

Transactions of the ASME

Journal-Bearing Performance for Combinations of Steady, Fundamental, and Low-Amplitude Harmonic Components of Load.	G. S. A. Shawki	449
Analytical Study of Journal-Bearing Performance Under Variable Loads	G. S. A. Shawki	457
Studies in Lubrication—XI	A. S. C. Ying, A. Charnes, and E. Saibel	465
Journal-Bearing Operation at Superlaminar Speeds	M. I. Smith and D. D. Fuller	469
The Dall Flow Tube	I. O. Mincer	475
Two- and Three-Dimensional Flow of Air Through Square-Edged Sonic Orifices	Alexander Weir, Jr., J. L. York, and R. B. Morrison	481
On the Theory of Discharge Coefficients for Rounded-Entrance Flowmeters and Venturis.	M. A. Rivas, Jr., and A. H. Shapiro	489
Biaxial Plastic Stress-Strain Relations of a Mild Steel for Variable Stress Ratios	Joseph Marin and L. W. Hu	499
A Method of Predicting the Effects of Notches in Uniaxial Fatigue	W. E. Dirkes	511
The Stress-Rupture Strength of Type 347 Stainless Steel Under Cyclic Temperature	E. E. Baldwin	517
Design Aspects of High-Temperature Fatigue With Particular Reference to Thermal Stresses	L. F. Coffin, Jr.	527
Quantitative Evaluation of Thermal-Shock Resistance.	S. S. Manson and R. W. Smith	533
Approximate Solution to Thermal-Shock Problems in Plates, Hollow Spheres, and Cylinders With Heat Transfer at Two Surfaces	A. Mendelson and S. S. Manson	545
A Survey of Aerodynamic Excitation Problems in Turbomachines	A. Sabatinski and F. Sisto	555
A Practical Approach to the Problem of Stall Flutter	Chi-Teh Wang, R. J. Vaccaro, and D. F. De Santo	565
The Flow in a Vee-Gutter Cascade	W. G. Cornsall	573
Determination of Mach Number From Pressure Measurements	F. W. Barry	581
Some Aerodynamic Investigations in Centrifugal Impellers	J. T. Hamrick	591
A Three-Dimensional Spherical Pitot Probe	J. C. Lee and J. E. Ash	603
The Combustion of Liquid-Fuel Spray	J. A. Bolt and T. A. Boyle	609
The Aerothermopressor—A Device for Improving the Performance of a Gas-Turbine Power Plant	A. H. Shapiro, K. R. Wadleigh, B. D. Gavril, and A. A. Fowle	617
A New Electrical Analog Method for the Solution of Transient Heat-Conduction Problems	G. Liebmann	655
Thermal Properties of Titanium Alloys and Selected Tool Materials	E. G. Loewen	667

TRANSACTIONS OF THE AMERICAN SOCIETY OF MECHANICAL ENGINEERS

VOLUME 78

APRIL 1956

NUMBER 3

Transactions

of The American Society of Mechanical Engineers

Published on the tenth of every month, except March, June, September, and December

OFFICERS OF THE SOCIETY:

J. W. BAKER, *President*

JOSEPH L. KOPP, *Treasurer*

C. E. DAVIS, *Secretary*

EDGAR J. KATH, *Asst. Treasurer*

COMMITTEE ON PUBLICATIONS:

OTTO DE LORENZI, *Chairman*

W. E. READER

JOHN DE S. COUTINHO

KERR ATKINSON

B. G. A. SEHOTSKY

R. A. CEDERBERG
H. N. WEINBERG *Junior Advisory Members*

GEORGE A. STETSON, *Editor*

K. W. CLAUDENHINO, *Managing Editor*
J. A. NORTH, *Asst. Managing Editor*

REGIONAL ADVISORY BOARD OF THE PUBLICATIONS COMMITTEE:

ROY L. FARMELL—I

A. D. BLACK—II

C. C. FRANK—III

FRANCIS C. SMITH—IV

H. M. CATHEN—V

C. R. EARLE—VI

M. B. HOGAN—VII

LEWIS HILANDER—VIII

Published monthly by The American Society of Mechanical Engineers. Publication office at 20th and Northampton Streets, Easton, Pa. The editorial department is located at the headquarters of the Society, 29 West Thirty-Ninth Street, New York 18, N. Y. Cable address, "Dynamic," New York. Price \$1.50 a copy, \$12.00 annually for Transactions and the *Journal of Applied Mechanics* to members, \$1.00 a copy, \$6.00 annually. Add \$1.50 for postage to all countries outside the United States, Canada, and Pan American Union. Changes of address must be received at Society headquarters seven weeks before they are to be effective on the mailing list. Please send old as well as new address. By-Law: The Society shall not be responsible for statements of opinions advanced in papers or printed in its publications (B13, Par. 4). Entered as second-class matter March 2, 1928, at the Post Office at Easton, Pa., under the Act of August 24, 1912. Copyrighted, 1955, by The American Society of Mechanical Engineers. Reprints from this publication may be made on condition that full credit be given the Transactions of the ASME and the author, and that date of publication be stated.

Journal-Bearing Performance for Combinations of Steady, Fundamental, and Low-Amplitude Harmonic Components of Load

By G. S. A. SHAWKI,¹ CAIRO, EGYPT

This paper presents the results of an experimental study of the effect, on journal-bearing performance, of superposing the low-amplitude harmonic to fundamental and steady components of a vertical cyclic bearing load of the form

$$P = P_0 + P_1 \sin(\omega_1 t) + P_n \sin(n\omega_1 t + \psi)$$

Amplitude ratio values (P_n/P_1) of between about 0.3 and 0.4 and frequency ratio values (n) of 2, 3, and 4 are considered. Test results exhibit a bearing performance somewhat similar to that obtained with sinusoidally alternating and fluctuating loads with critical changes in performance, at (ω_1/ω) (ratio of the rate of load application to that of journal rotation) slightly less than 0.5, of a character mainly dependent on the ratio (P_1/P_0) . The striking phenomenon encountered in the tests, however, is the appearance of secondary critical changes in the performance at submultiples of the one-half speed ratio, namely, at (ω_1/ω) slightly less than 0.25, 0.167, and 0.125 for second, third, and fourth superposed harmonic components of load. An explanation of this behavior is suggested. Further work on the subject is proceeding.

NOMENCLATURE

The following nomenclature is used in the paper:

- c = radial bearing clearance
- e = journal eccentricity
- F_f = total frictional force on journal
- n = frequency ratio of P_n to P_1
- N = rotational journal speed
- P = load applied per unit projected bearing area
- P_0 = steady component of P
- P_1 = fundamental component of P
- P_n = n th harmonic component of P
- r = radius of journal
- t = time
- W = total external load on bearing
- Δ = nondimensional quantity known as load criterion ($P\delta/\lambda N$). It is a measure of the load applied to a journal bearing for specified values of journal rotational speed, lubricant viscosity, and relative bearing clearance
- Δ_{av} = load criterion based on value of average load in cycle obtained with negative ordinates reversed

- Δ_{max} = load criterion based on value of maximum load in cycle
- δ = relative bearing clearance = c/r
- e = eccentricity ratio = e/c
- ϵ_{max} = maximum eccentricity ratio occurring in cycle
- λ = coefficient of viscosity of lubricant
- μ_{av} = coefficient of friction for journal, obtained by dividing average value of F_f in cycle, by value of average load (as per Δ_{av})
- σ_1 = ratio of rate of load application to that of journal rotation = ω_1/ω , referred to, in text, as speed ratio
- ψ = phase relationship between P_n and P_1 (see foregoing equation)
- ω = angular speed of journal rotation
- ω_1 = angular speed of application of P_1

INTRODUCTION

In a previous paper (1),² the fundamental problem of a journal bearing operating under variable loading conditions was discussed, and the bearing-performance characteristics were obtained for the relatively simple case of a vertical sinusoidal load with and without a deliberately imposed steady component of load.

The present study which forms a further contribution to the solution of the general problem, concerns itself with the effect, on the bearing behavior, of superposing a harmonic component with an amplitude only a fraction of that of the fundamental component. The ratios of the harmonic to fundamental amplitudes for the load waves presented are of the order of between 0.3 and 0.4. Three frequency ratios, viz., 2, 3, and 4, were used and for each ratio two values of the phase relationship, representing two extreme conditions, were tested.

In studying the effect of superposing the steady load component, only the cases in which the minimum or maximum load in the cycle assumed approximately a zero value were considered. This condition is based on test results with sinusoidally fluctuating loads and serves to show the relative behavior with "non-reversing" load waves.

Variations in the load criterion were obtained by changing only the journal rotational speed, and speed-ratio values between zero and unity were tested.

APPARATUS

The testing machine specially designed and built for the present investigations, Figs. 1 and 2, has been fully described (1). It simply comprises a full sleeve bearing, the journal being driven by a speed-controlled motor via a flexible coupling. The load is applied to the journal, through a lever system, by means of two helical compression springs actuated by variable throw eccentrics. The drive of the latter allows for the adjustment of the frequency ratio and the phase relationship between the two variable load components.

The journal displacement is measured by means of photo-

² Numbers in parentheses refer to the Bibliography at the end of the paper.

¹ Lecturer, Mechanical Engineering Department, Cairo University. Contributed by the Research Committee on Lubrication under the auspices of the Lubrication Activity of THE AMERICAN SOCIETY OF MECHANICAL ENGINEERS, and presented at the Second Annual ASME-ASLE Lubrication Conference, Indianapolis, Ind., October 10-12, 1955.

NOTE: Statements and opinions advanced in papers are to be understood as individual expressions of their authors and not those of the Society. Manuscript received at ASME Headquarters, October 14, 1954. Paper No. 55-LUB-15.

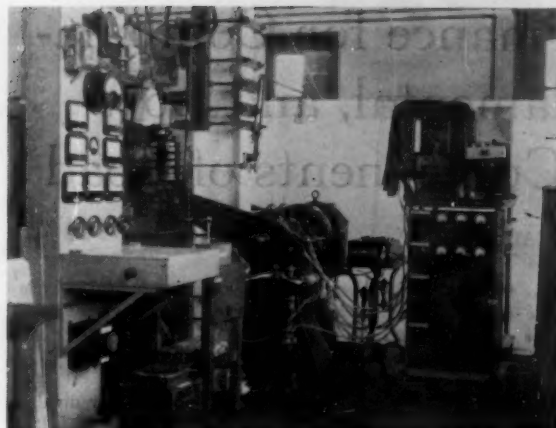


FIG. 1 GENERAL FRONT VIEW OF APPARATUS

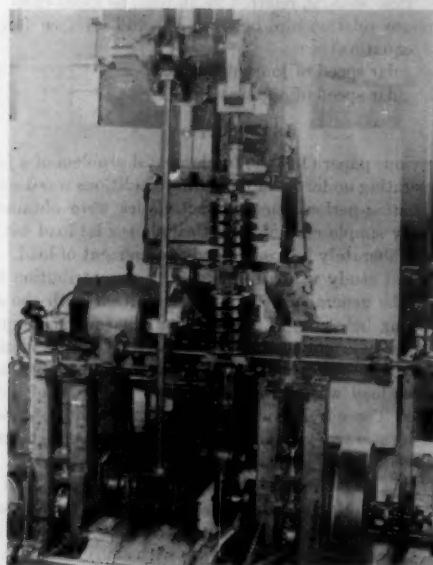


FIG. 2 GENERAL VIEW OF LOADING SYSTEM

electric pickup units coupled, through amplifiers, to a cathode ray tube.

The load wave is obtained under static conditions by measuring the lengths of the loading springs, and under dynamic conditions, by means of strain gages in the lever system connected to an oscilloscope.

Journal friction values are obtained from the power input to the journal. The oil temperature is measured by a thermocouple, and rotational speeds of journal and loading shafts by generator-type tachometers connected to voltmeters.

OUTLINE OF TEST PROCEDURE

The intercoupling of the eccentric drives was arranged to give the desired frequency ratio and phase relationship between the two sinusoidal load components. The adjustment of the eccentric throws provided for the required values of the component wave amplitudes. The steady load component was obtained

through the initial adjustment of the springs. The bearing was supplied, via four small holes at the ends of two horizontal diameters, with oil under an arbitrary pressure of 30 psi.

The apparatus was run under load for at least 90 min, during which period the electronic equipment was switched on and the various operating conditions adjusted to attain the steady state.

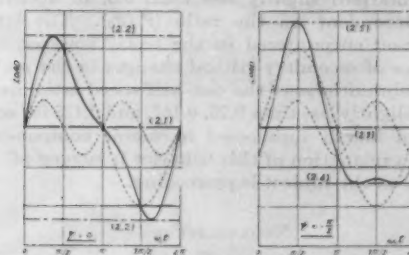
A complete set of observations was taken under the same conditions.

PRESENTATION OF RESULTS

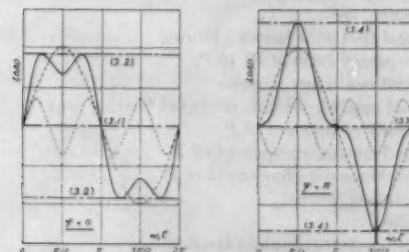
For fourteen load-wave forms tested, some system of notation would be desirable. Each wave form is hereby denoted by a number, the digit to the left giving the frequency ratio n and the decimal figure representing the serial number of the load wave for the particular frequency ratio. Fig. 3 shows the ideal forms of the load waves used in the experiments and Fig. 4 exhibits typical recordings thereof.

For each group of waves (same frequency ratio), the journal center loci, maximum eccentricity ratio (simply referred to as eccentricity ratio), load-carrying capacity, and friction results are discussed.

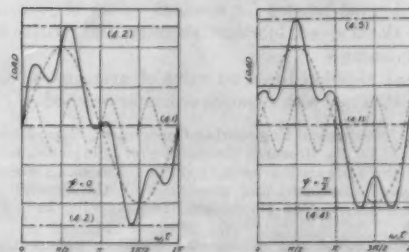
The journal center loci reproduced in the text are corrected for screen calibration only. No bending correction is applied owing to the uncertainty of this correction outside the region of maximum eccentricity and correlation points.



A. LOAD WAVES WITH SECOND HARMONIC COMPONENTS



B. LOAD WAVES WITH THIRD HARMONIC COMPONENTS



C. LOAD WAVES WITH FOURTH HARMONIC COMPONENTS

FIG. 3 IDEAL FORMS OF LOAD WAVES TESTED

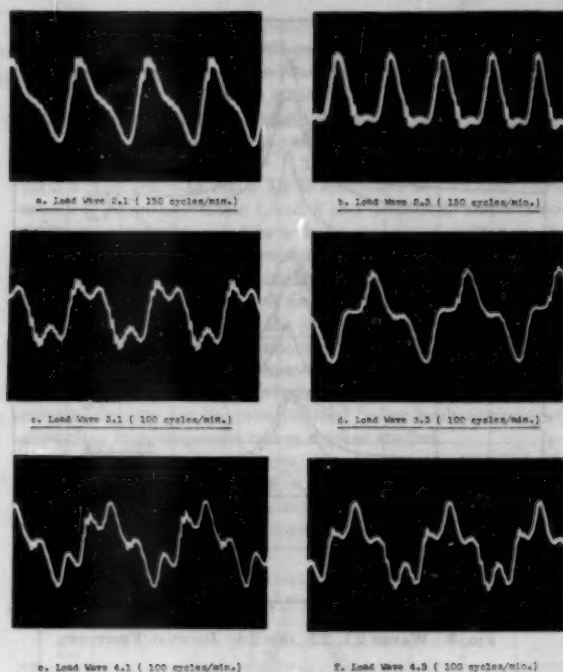


FIG. 4 SAMPLE RECORDINGS OF PRINCIPAL LOAD WAVES

It is considered convenient to reproduce some of the recordings to emphasize certain aspects of the bearing performance. The center of the graticule is to be regarded as the bearing center. It should also be understood that the sensitivities (or scales) in the X and Y directions are not quite the same, the smallest division representing between 0.4 and 0.6×10^{-3} in.

TESTS WITH SECOND-HARMONIC COMPONENTS

Journal Center Loci. Test results, Figs. 5 and 6, show, for waves 2.1 and 2.3, a general picture for the journal center locus not very different from that obtained for sinusoidally alternating loads (1). There is, however, in the neighborhood of $\sigma_1 = 0.25$, some tendency for the appearance of a secondary loop. It seems

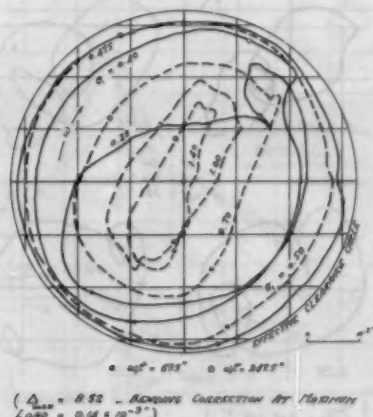


FIG. 5 WAVE 2.1: JOURNAL CENTER LOCI

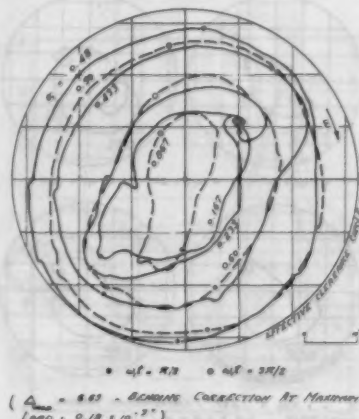


FIG. 6 WAVE 2.3: JOURNAL CENTER LOCI

that the effect of a second-harmonic component with such low amplitude ratio P_2/P_1 is insufficiently great as to bring considerable changes to the bearing behavior.

For the nonreversing load fluctuation 2.2, the journal locus was found to be shifted toward the steady load locus and the stages of journal path to simulate those obtained for sinusoidally fluctuating loads with $P_1/P_0 = 1$. For wave 2.4, however, the effect of the steady component did not seem to suppress to any considerable degree the whirl at the one-half speed ratio. It is suggested that with this wave form the journal is unloaded, in the cycle, with conditions simulating sudden release of load which were found to help in initiating the no-load whirl (3) and hence will support the journal oscillation at $\sigma_1 = 0.5$. Distinct from this wave is wave 2.5 in which the converse conditions are examined; the duration of the highest loads is far greater than the duration of the unloaded conditions in the bearing with the expected result of a seriously suppressed whirl and orbits mainly confined to only one quadrant of the clearance circle.

Maximum Eccentricity Ratio and Bearing-Load Capacity. The eccentricity curves for waves 2.1 and 2.3, Fig. 7, show that the peaks take place at a value of σ_1 between about 0.48 and 0.49. Only a slight relative increase in journal maximum eccentricity is noted in the neighborhood of $\sigma_1 = 0.25$.

The variation in eccentricity for wave 2.2 is gradual with a rather flat nature of the curves in the important region of the speed ratio. For wave 2.4, however, test results show that there is still a considerable increase in the maximum eccentricity ratio attaining maximum values at a speed ratio of about 0.48. An explanation for this behavior is given in the foregoing. Eccentricity results for wave 2.5 show only a slight increase in eccentricity and a rather flat nature of the curves in the region of the one-half speed ratio.

For this group of load waves, bearing design based on a steady load equal to the maximum load in the cycle seems to be of adequate safety for values of the speed ratio greater than about 0.8. In fact, the design on this basis would still be safe at lower values of the ratio with load waves for which journal whirl was obtained.

Friction. The curves obtained for wave 2.1, Fig. 8, exhibit some critical increase in friction values at σ_1 between about 0.48 and 0.49. A similar increase but somewhat less peaked is noted for waves 2.3 and 2.4 at $\sigma_1 \approx 0.48$. For waves 2.2 and 2.5, friction values were found constant over the entire range of speed ratios tested.

It can be seen that friction results fit in quite well with the general picture of behavior as drawn by eccentricity measure-

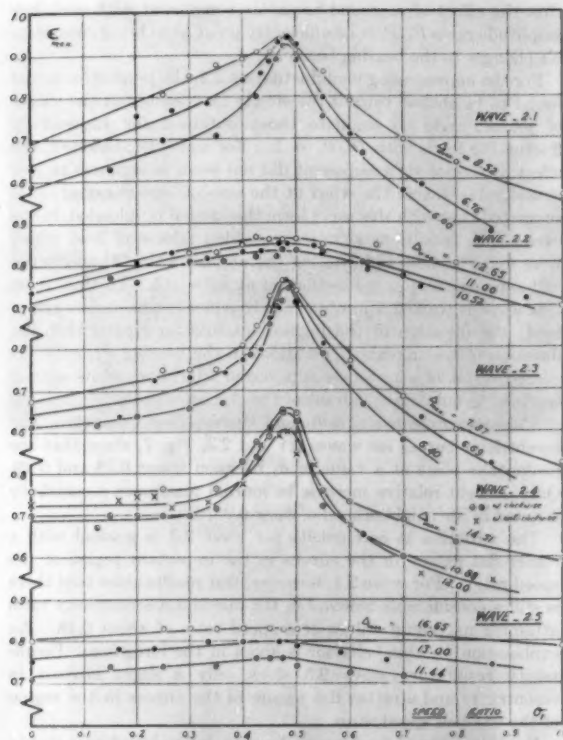


FIG. 7 WAVES WITH SECOND-HARMONIC COMPONENTS: CURVES OF MAXIMUM ECCENTRICITY RATIO

ments in the same manner as they do for sinusoidally alternating and fluctuating loads.

TESTS WITH THIRD-HARMONIC COMPONENTS

Journal Center Loci. An interesting phenomenon starts to appear quite clearly with these low-amplitude third harmonics. Loci for waves 3.1 and 3.3, Figs. 9 and 10, show that two secondary loops seem to come into existence in the neighborhood of

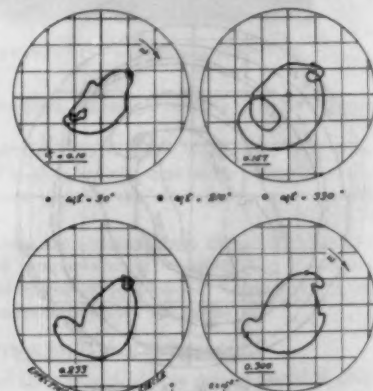


FIG. 9 WAVE 3.1: JOURNAL CENTER LOCI

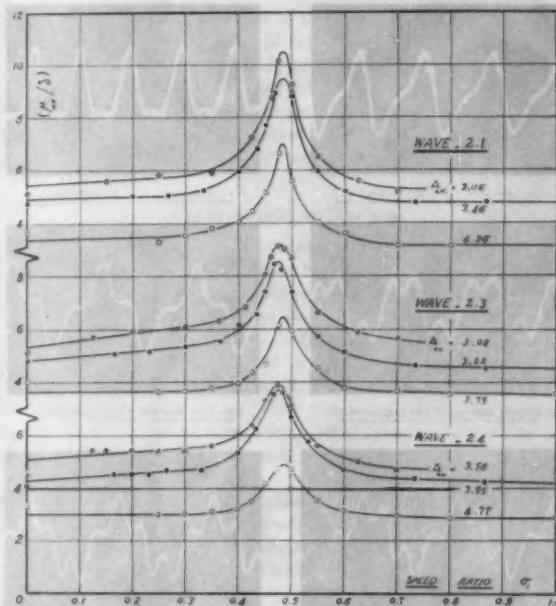


FIG. 8 WAVES 2.1, 2.3, AND 2.4: JOURNAL FRICTION

$\sigma_1 = 0.167$. It is not difficult to explain this feature of the journal path should the extreme case of a very high amplitude ratio P_3/P_1 be considered. Under such conditions, it would be reasonable to expect the appearance of three loops for the journal center path. The load wave would approach three sinusoidal load waves applied in one cycle and in the light of the results obtained with sinusoidally alternating loads, some critical increase in journal eccentricity and friction would be expected at the submultiple value of the one-half speed ratio corresponding to the third-harmonic component, viz., at a value of σ_1 slightly less than $0.5/3 = 0.167$. The presence of the loops appears more pronounced for wave 3.3, probably partly due to a higher value of the amplitude ratio P_3/P_1 (0.398 against 0.351). The orbits continue, after the foregoing value of σ_1 , to exhibit some circular

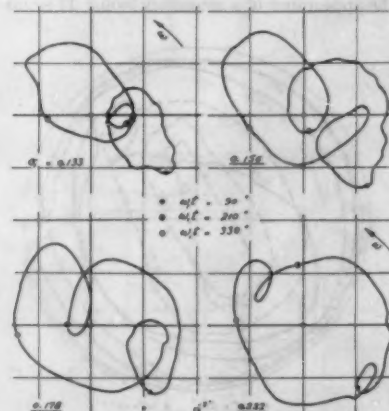


FIG. 10 WAVE 3.3: JOURNAL CENTER LOCI

whirl in the region of the one-half speed ratio and then, with increasing speed ratio, they collapse to some elliptic or dumbbell-shaped paths in stages somewhat similar to those experienced with sinusoidally alternating loads.

It is easy to show that a square wave form can be represented by a Fourier series in which the amplitudes of the first three component sine waves (with $n = 1, 3$, and 5 , respectively) are in the ratio $1:1/3:1/5$. As wave 3.1 is composed of two component waves of frequency ratios 1 and 3 and amplitude ratios 1 and 0.351 , it may be regarded as a first approximation to a square type of load wave, and the results of Burwell's theoretical study (2) may then be compared with the present experimental results. The journal center loci, Fig. 9, disagree with Burwell's loci which are composed of sections of the journal paths, first obtained by Swift (4), for the free oscillations of the journal center under a steady load. It is thought, however, that owing to the presence of terms other than the fundamental and third harmonic, the comparison may not be quite justified before loads composed of more than two component waves are first studied.

For convenience in reference, the speed ratio at which the maximum value of some relative increase in eccentricity or friction values takes place, or is expected to do so under favorable conditions, will be termed "critical speed ratio." It should be

understood, however, that the use of the term "critical" should not necessarily imply some actual critical change in the performance characteristics, but rather to refer to the speed ratio at which these changes may take place should the operating variables permit.

Test results show that the journal center path, for wave 3.2, is displaced in the direction of the steady load locus; there seems to exist, however, some tendency to whirl at the "fundamental" critical speed ratio. This is probably due to some stimulus to no-load whirl in a manner similar to that encountered with wave 2.4. The reason why the tendency appears at a somewhat lesser extent may be partly associated with the comparatively shorter duration of the unloaded conditions in the bearing for this wave.

The influence of the steady-load component in wave 3.4 was found to be quite effective in suppressing the journal center whirl.

Maximum Eccentricity Ratio and Bearing-Load Capacity. For waves 3.1 and 3.3, the eccentricity curves, Figs. 11 and 12, exhibit two relative increases in the range of speed ratio tested; rather slight at the "subharmonic" critical ratio and quite considerable at the fundamental critical ratio. As distinct from the above two waves, are waves 3.2 and 3.4 for which the steady component seems to suppress completely any increase in the eccentricity ratio in the neighborhood of the subharmonic critical

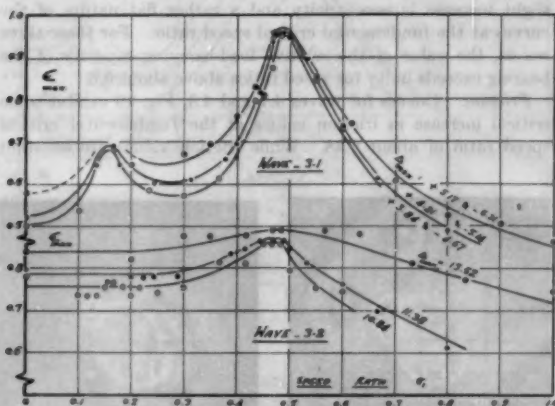


FIG. 11 WAVES 3.1 AND 3.2: CURVES OF MAXIMUM ECCENTRICITY RATIO

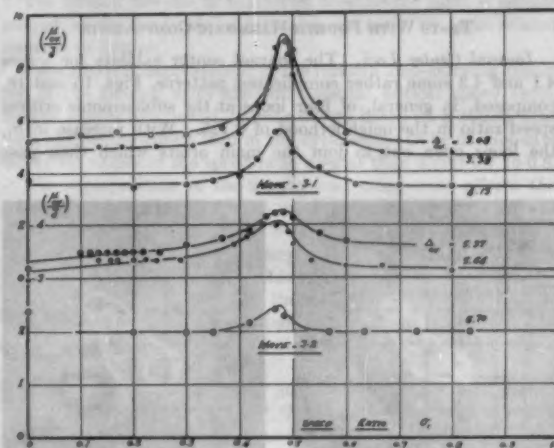


FIG. 13 WAVES 3.1 AND 3.2: JOURNAL FRICTION

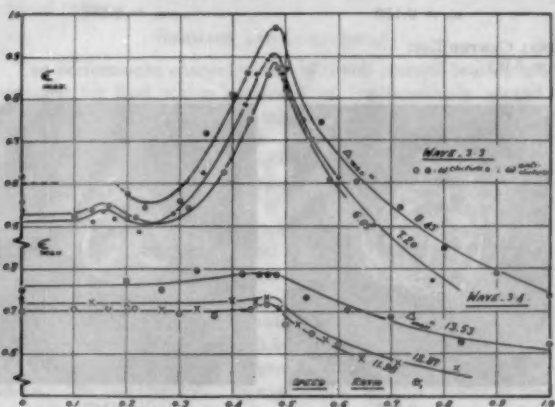


FIG. 12 WAVES 3.3 AND 3.4: CURVES OF MAXIMUM ECCENTRICITY RATIO

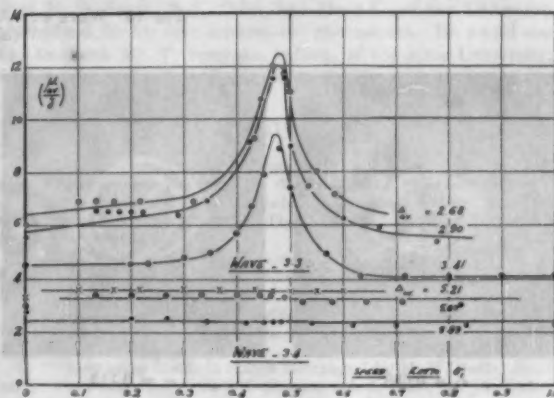


FIG. 14 WAVES 3.3 AND 3.4: JOURNAL FRICTION

ratio. While the curves for wave 3.4 show very little increase in the eccentricity ratio at the fundamental critical ratio, those for wave 3.2 show some appreciable increase for which an explanation is proposed in the foregoing.

For this group of load waves, bearing design based on a steady load equal to the maximum load in the cycle is of adequate safety for values of the speed ratio greater than about 0.7.

Friction. Test results show, for waves 3.1 and 3.3, Figs. 13 and 14, some critical increase in friction values at the fundamental critical speed ratio of about 0.48 with hardly any noticeable relative increase in the neighborhood of the subharmonic critical ratio. This is not difficult to visualize if reference be made to the results obtained for sinusoidally fluctuating loads with $P_1/P_0 = 1$, in which case the friction values were constant while some increase in eccentricity values was recorded. It seems that friction values do not appear to be affected until some considerable change in the operating conditions takes place, e.g., at the one-half speed ratio for sinusoidal loads. This attitude of friction variation in relation to eccentricity variation can be seen in the results of all load waves tested.

Constant friction values were obtained with wave 3.4, while some noticeable increase in friction was recorded for wave 3.2 at the fundamental critical speed ratio; this increase would be expected to accompany the tendency to journal whirl for this wave.

TESTS WITH FOURTH-HARMONIC COMPONENTS

Journal Center Loci. The journal center exhibits for waves 4.1 and 4.3 some rather complicated patterns, Figs. 15 and 16, composed, in general, of four loops at the subharmonic critical speed ratio in the neighborhood of 0.125. With increase in σ_1 , the loops open out to join the main orbits which then pass

through some familiar stages of locus as for sinusoidal loads. The appearance of four loops, at the subharmonic critical speed ratio, can be explained in the same way as given previously for waves with third-harmonic components.

Journal center loci for waves 4.2 and 4.5 were found to be considerably affected by the presence of the steady-load component. For wave 4.4, however, some tendency to journal whirl (in a manner similar to that experienced with wave 2.4 but to a lesser extent) was recorded at the fundamental critical speed ratio. This behavior can be explained on grounds of the unloaded conditions in the bearing as previously suggested for waves 2.4 and 3.2.

Maximum Eccentricity Ratio and Bearing-Load Capacity. Eccentricity curves, Figs. 17 and 18, show, for waves 4.1 and 4.3, some relative increase at the subharmonic critical speed ratio of about 0.12. They also show a considerable increase at the fundamental critical ratio of about 0.48, beyond which the eccentricity ratio decreases, the display of the curves being similar to those obtained for sinusoidal loads. For these two waves the relative load-carrying capacity exceeds unity for speed-ratio values higher than about 0.65.

Test results do not show, for waves 4.2, 4.4, and 4.5, any noticeable relative increase at the subharmonic critical speed ratio. While there is some tendency to journal whirl for wave 4.4, as discussed before, the curves for waves 4.2 and 4.5 show only a slight increase in eccentricity and a rather flat nature of the curves at the fundamental critical speed ratio. For these three waves, the value of the relative load-carrying capacity of the bearing exceeds unity for speed ratios above about 0.6.

Friction. Curves for waves 4.1 and 4.3, Fig. 19 exhibit some critical increase in friction values at the fundamental critical speed ratio of about 0.48. While friction values are constant

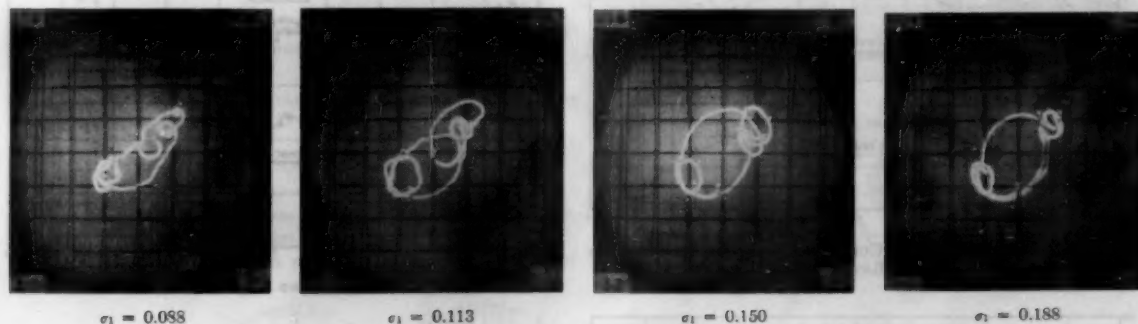


FIG. 15 WAVE 4.1: JOURNAL CENTER LOCI
($\Delta_{\max} = 6.0$.)

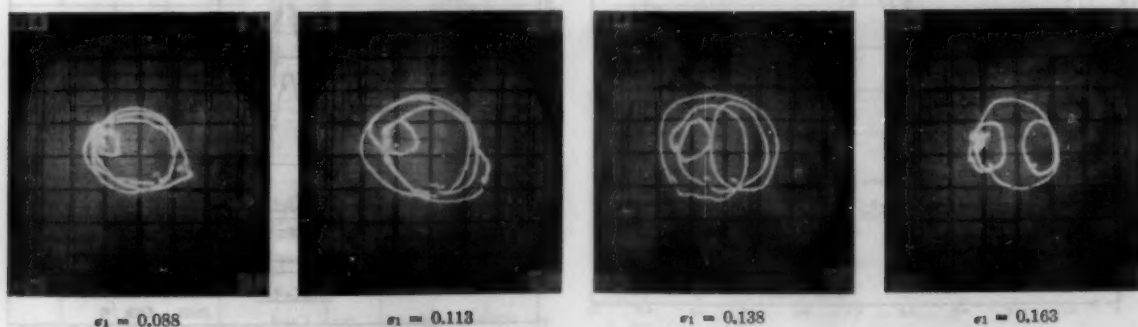


FIG. 16 WAVE 4.3: JOURNAL CENTER LOCI
($\Delta_{\max} = 5.89$.)

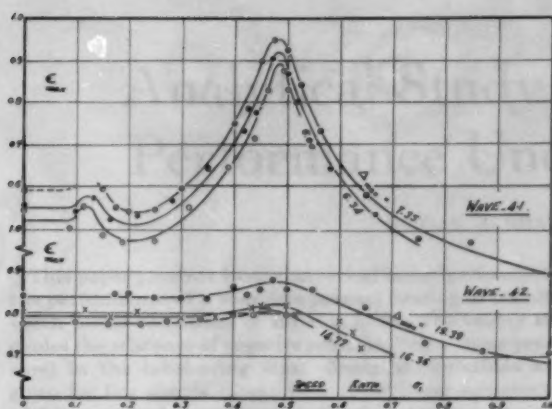


FIG. 17 WAVES 4.1 AND 4.2: CURVES OF MAXIMUM ECCENTRICITY RATIO

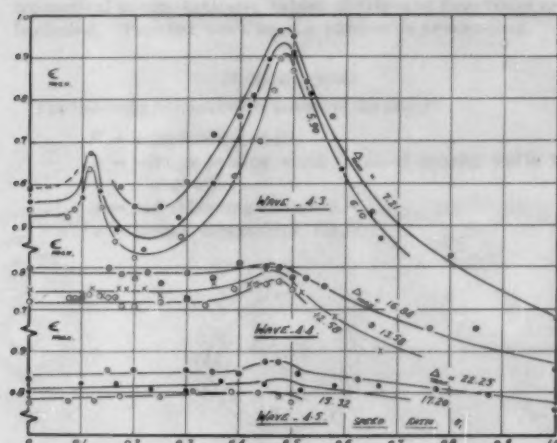


FIG. 18 WAVES 4.3, 4.4, AND 4.5: CURVES OF MAXIMUM ECCENTRICITY RATIO

over the entire range of speed ratio tested, for waves 4.2 and 4.5, there is some relative increase in friction for wave 4.4 accompanying the tendency to journal whirl at the fundamental critical ratio. For this group of load waves there does not seem to be any significant increase in friction values at the subharmonic critical ratio.

SUMMARY AND CONCLUSION

The performance characteristics of a full journal bearing are obtained for load waves composed of low-amplitude second, third, and fourth-harmonic components superposed on the fundamental component. The value of the amplitude ratio P_n/P_1 used in the tests is of the order of 0.3 to 0.4. The study includes the investigation of two extreme values of the phase relationship and also the effect of a deliberately imposed steady-load component adjusted to give maximum or minimum loads in the cycles approximately equal to zero.

The most striking phenomenon encountered in the tests is the appearance of the subharmonic critical speed ratio at a value which corresponds to the harmonic component involved, namely, in the neighborhood of 0.5/2, 0.5/3, and 0.5/4 for second, third and fourth harmonics, with journal center loci comprising 2, 3, and 4 loops, respectively. An explanation for this feature of behavior is put forward.

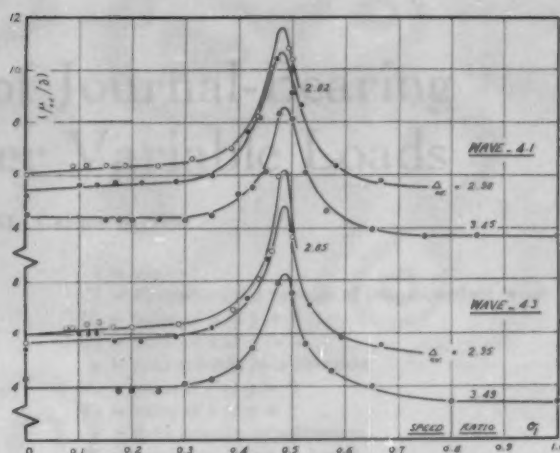


FIG. 19 WAVES 4.1 AND 4.3: JOURNAL FRICTION

The value of the phase relationship is found not to affect appreciably the presence of the subharmonic critical speed ratio though it is shown to have, in general, some influence on the bearing performance.

The critical increase in maximum eccentricity ratio is accompanied, at the fundamental critical speed ratio, by some related increase in friction.

Owing to the improvement in the relative load-carrying capacity of the bearing after the fundamental critical speed ratio, for the load waves tested, bearing design based on a steady load equal to the maximum load in the cycle seems to be of adequate safety for values of the speed ratio greater than about 0.7 to 0.8.

The superposition of the steady-load component affects the performance characteristics in a manner similar to that shown by sinusoidally fluctuating loads. For certain waves, with the intentionally imposed steady-load component, some tendency to journal center whirl was noted. This is attributed to some stimulus to no-load whirl brought in by the form of the wave. With the load fluctuations herein presented, no significant relative change in the bearing behavior was experienced at the subharmonic critical speed ratio.

Work has also been carried out for load waves with higher values of the amplitude ratio P_n/P_1 . The results of these investigations will be published in the future.

ACKNOWLEDGMENTS

The author wishes to express his indebtedness and gratitude to Prof. H. W. Swift, M.A., D.Sc., M.I.Mech.E., of the University of Sheffield, for his keen interest and able advice. He would also like to thank Mr. P. Freeman, B.Eng., of the same University, for his valuable assistance and encouragement.

BIBLIOGRAPHY

- 1 "Journal Bearing Performance Under Sinusoidally Alternating and Fluctuating Loads," by G. S. A. Shawki and P. Freeman, paper read before The Institution of Mechanical Engineers, April, 1955, to be published in Proceedings of The Institution of Mechanical Engineers, London, England.
- 2 "The Calculated Performance of Dynamically Loaded Sleeve Bearings (I)," by J. T. Burwell, *Journal of Applied Mechanics*, Trans. ASME, vol. 69, 1947, p. A-231.
- 3 "Whirling of a Journal Bearing: Experiments Under No-Load Conditions," by G. S. A. Shawki, *Engineering*, vol. 179, 1955, pp. 243-246.
- 4 "Fluctuating Loads in Sleeve Bearings," by H. W. Swift, *Journal of The Institution of Civil Engineers*, vol. 5, 1937, pp. 161-195.



The first of these is the fact that the population of the United States has increased from 22,000,000 in 1880 to 60,000,000 in 1900. This increase has been due to a number of causes, but the most important is the immigration of large numbers of foreign-born people. The second cause is the increase in the birth rate, which has been due to a number of causes, but the most important is the increase in the number of children born to each couple. The third cause is the decrease in the death rate, which has been due to a number of causes, but the most important is the improvement in medical science and the discovery of new drugs and remedies. The fourth cause is the increase in the life expectancy, which has been due to a number of causes, but the most important is the improvement in medical science and the discovery of new drugs and remedies. The fifth cause is the increase in the number of people living in cities, which has been due to a number of causes, but the most important is the improvement in medical science and the discovery of new drugs and remedies. The sixth cause is the increase in the number of people living in the West, which has been due to a number of causes, but the most important is the improvement in medical science and the discovery of new drugs and remedies. The seventh cause is the increase in the number of people living in the South, which has been due to a number of causes, but the most important is the improvement in medical science and the discovery of new drugs and remedies. The eighth cause is the increase in the number of people living in the North, which has been due to a number of causes, but the most important is the improvement in medical science and the discovery of new drugs and remedies. The ninth cause is the increase in the number of people living in the East, which has been due to a number of causes, but the most important is the improvement in medical science and the discovery of new drugs and remedies. The tenth cause is the increase in the number of people living in the West, which has been due to a number of causes, but the most important is the improvement in medical science and the discovery of new drugs and remedies.



The first of these is the fact that the population of the United States has increased from 22,000,000 in 1880 to 60,000,000 in 1900. This increase has been due to a number of causes, but the most important is the immigration of large numbers of foreign-born people. The second cause is the increase in the birth rate, which has been due to a number of causes, but the most important is the increase in the number of children born to each couple. The third cause is the decrease in the death rate, which has been due to a number of causes, but the most important is the improvement in medical science and the discovery of new drugs and remedies. The fourth cause is the increase in the life expectancy, which has been due to a number of causes, but the most important is the improvement in medical science and the discovery of new drugs and remedies. The fifth cause is the increase in the number of people living in cities, which has been due to a number of causes, but the most important is the improvement in medical science and the discovery of new drugs and remedies. The sixth cause is the increase in the number of people living in the West, which has been due to a number of causes, but the most important is the improvement in medical science and the discovery of new drugs and remedies. The seventh cause is the increase in the number of people living in the South, which has been due to a number of causes, but the most important is the improvement in medical science and the discovery of new drugs and remedies. The eighth cause is the increase in the number of people living in the North, which has been due to a number of causes, but the most important is the improvement in medical science and the discovery of new drugs and remedies. The ninth cause is the increase in the number of people living in the East, which has been due to a number of causes, but the most important is the improvement in medical science and the discovery of new drugs and remedies. The tenth cause is the increase in the number of people living in the West, which has been due to a number of causes, but the most important is the improvement in medical science and the discovery of new drugs and remedies.

Analytical Study of Journal-Bearing Performance Under Variable Loads

By G. S. A. SHAWKI,¹ CAIRO, EGYPT

This paper presents basic theoretical investigations into the performance of a complete journal bearing of infinite width under conditions of variable load. The theory excludes the existence of negative pressure (below vapor pressure) in the lubricating film. Analytical solutions are given for few simple cases; they show closer agreement with experiment than those attained by previous theory. Owing to the complexity of the equations involved in the analysis, solutions, in general, may be effected only by numerical computations; tables of relevant functions are included. Further work on the subject is proceeding.

NOMENCLATURE

The following nomenclature is used in the paper:

- B = axial bearing width
- b = relative bearing width (ratio of bearing width to diameter)
- c = radial bearing clearance
- e = journal eccentricity, Fig. 1

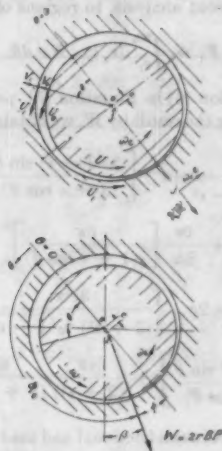


FIG. 1 NOTATION

- F_f = total frictional force on journal
- h = fluid-film thickness
- N = rotational journal speed
- P = load applied per unit projected bearing area
- p = fluid-film pressure
- r = radius of journal

¹ Lecturer, Mechanical Engineering Department, Cairo University. Contributed by the Research Committee on Lubrication under the auspices of the Lubrication Activity of THE AMERICAN SOCIETY OF MECHANICAL ENGINEERS, and presented at the Second Annual ASME-ASLE Lubrication Conference, Indianapolis, Ind., October 10-12, 1955.

NOTE: Statements and opinions advanced in papers are to be understood as individual expressions of their authors and not those of the Society. Manuscript received at ASME Headquarters, November 22, 1954. Paper No. 55-LUB-16.

- t = time
- U = circumferential velocity of journal surface = ωr
- U_0 = value of u at $y = 0$
- U_1 = value of u at $y = h$
- u = fluid velocity in x -direction
- V_0 = value of v at $y = 0$
- V_1 = value of v at $y = h$
- v = fluid velocity in y -direction
- W = total load acting on bearing
- x = distance measured along journal surface in direction of motion
- y = distance measured across fluid film
- z = distance measured along bearing axis
- α = angular rotation of journal = ωt
- β = angle between fixed line in space and load vector, measured in direction of journal rotation
- Δ = nondimensional quantity known as load criterion = $(P\delta^2/\lambda N)$
- Δ_0 = load criterion with load constant in both magnitude and direction
- Δ_1 = load criterion with load of fixed magnitude rotating at uniform speed
- δ = relative bearing clearance = c/r
- ϵ = eccentricity ratio = e/c
- ϵ_0 = eccentricity ratio for a load constant in both magnitude and direction
- η = relative load-carrying capacity of bearing, i.e., ratio of applied-load criterion to steady-load criterion that would produce the same maximum eccentricity ratio
- θ = angular position of any point in fluid measured from maximum film thickness end of line of centers, in direction of journal rotation
- θ_1 = value of θ at beginning of operative film
- θ_2 = value of θ at end of operative film
- λ = coefficient of viscosity of fluid
- μ_f = coefficient of friction for journal = F_f/W
- σ_1 = ratio of frequency of load application to that of journal rotation ω_1/ω (referred to, in text, as speed ratio)
- $\sigma_s = \omega_s/\omega$
- τ_x = shear stress in fluid in x -direction
- Φ = angle between load vector and minimum film thickness end of line of centers measured in direction of journal rotation
- Φ_0 = angle between maximum film thickness end of line of centers and load vector, measured in direction of journal rotation
- ω = angular speed of journal rotation
- ω_1 = angular speed of load application
- ω_s = angular speed of line of centers
- F_1 to F_4 = functions of ϵ and θ_2 , Equations [13] and [14]
- $f(\theta)$ = function of θ with ϵ as parameter, Equation [9]
- R_1, R_2, R_3 = functions of ϵ and θ_2 , Equation [18]

INTRODUCTION

Theoretical studies in dynamically loaded bearings were first

started by Harrison (5),² whose work was extended by Robertson (8), and the results used to explain the phenomenon of "oil-film whirl." An extensive treatment of the problem was later given by Swift (14). Subsequent contributors include Dick (4), Ott (6), and Burwell (1).

Apart from Ott, these authors assumed film continuity in the bearing; this entails the admission of negative film pressure. There are certain indications in experimental research (10) pointing to the nonexistence of negative film pressure as a major source of divergence between theory and experiment. For this reason a theory accounting for the incapability of fluids to stand tensile stress is put forward. Although Ott took the foregoing concept into consideration, his fundamental equations are open to objection (9, 10). He obtained approximate solutions to the equations giving the film extent in the bearing, but concluded that a formal mathematical solution was, in general, unattainable. It was therefore decided in the present work to obtain, by numerical methods, exact solutions to the problem in which the bearing performance is to be determined for specified external load.

ANALYTICAL TREATMENT

It is assumed that the operative lubricating film is confined to regions of positive pressure, that the flow is streamlined and that the fluid viscosity is uniform throughout the film.

(A) Fundamental Equations

Load Equations. It can be shown that a more general form of Reynolds differential equation (7) giving the pressure distribution in the lubricating film is

$$\frac{1}{6\lambda} \left[\frac{\partial}{\partial x} \left(h^3 \frac{\partial p}{\partial x} \right) + \frac{\partial}{\partial z} \left(h^3 \frac{\partial p}{\partial z} \right) \right] = \frac{\partial}{\partial x} (U_0 + U_1) h - 2 V_0 \dots [1]$$

which, for the usual case of a stationary bearing and assuming no side leakage, may be manipulated to yield the equation

$$\frac{\delta^2}{6\lambda} \left\{ \frac{\partial}{\partial \theta} \left[(1 + \epsilon \cos \theta)^3 \frac{\partial p}{\partial \theta} \right] \right\} = \omega \frac{\partial}{\partial \theta} (1 + \epsilon \cos \theta) + 2 \left(\frac{\partial \epsilon}{\partial t} \cos \theta + \epsilon \omega \sin \theta \right) \dots [2]$$

Integrating twice with respect to θ and evaluating the constants of integration for the boundary conditions

Film continuity: $[p]_{\theta=0}^{2\pi} = 0$

p = atmospheric or surrounding pressure at $\theta = 0$, the equation takes the nondimensional form

$$\left(\frac{p \delta^3}{\lambda N} \right) = 12\pi(1 - 2\sigma_s) \frac{\epsilon(2 + \epsilon \cos \theta) \sin \theta}{(2 + \epsilon^2)(1 + \epsilon \cos \theta)^2} + \frac{12\pi}{\epsilon} \left[\frac{1}{(1 + \epsilon \cos \theta)^3} - \frac{1}{(1 + \epsilon)^2} \right] \frac{\partial \epsilon}{\partial \alpha} \dots [3]$$

in which p represents, in fact, pressure rise above the surrounding pressure and N is assumed uniform but not zero.

The pressure, as shown by Equation [3], attains positive as well as negative values. As mentioned before, the film is considered inoperative in the regions where the equation necessitates negative pressure.

Neglecting frictional tractions with respect to fluid pressures, the load equations will be given by

² Numbers in parentheses refer to the Bibliography at the end of the paper.

$$\Delta \sin \Phi = (1 - 2\sigma_s) \left\{ \frac{6\pi\epsilon}{(2 + \epsilon^2) \sqrt{1 - \epsilon^2}} \sin^{-1} \left[\frac{\sqrt{1 - \epsilon^2} \sin \theta}{(1 + \epsilon \cos \theta)} \right] - \frac{6\pi\epsilon \sin \theta \cos \theta}{(2 + \epsilon^2)(1 + \epsilon \cos \theta)} \right\}_{\theta_1}^{\theta_2} + \frac{\partial \epsilon}{\partial \alpha} \left[\frac{6\pi}{\epsilon^2(1 + \epsilon \cos \theta)} + \frac{6\pi \cos \theta}{\epsilon(1 + \epsilon)^2} \right]_{\theta_1}^{\theta_2} \dots [4]$$

and

$$\Delta \cos \Phi = (1 - 2\sigma_s) \left[\frac{6\pi \cos \theta}{(2 + \epsilon^2)} + \frac{6\pi}{\epsilon(2 + \epsilon^2)(1 + \epsilon \cos \theta)} \right]_{\theta_1}^{\theta_2} + \frac{\partial \epsilon}{\partial \alpha} \left\{ \frac{6\pi}{(1 - \epsilon^2)^{3/2}} \sin^{-1} \left[\frac{\sqrt{1 - \epsilon^2} \sin \theta}{(1 + \epsilon \cos \theta)} \right] - \frac{6\pi \sin \theta}{\epsilon(1 - \epsilon^2)(1 + \epsilon \cos \theta)} + \frac{6\pi \sin \theta}{\epsilon(1 + \epsilon)^2} \right\}_{\theta_1}^{\theta_2} \dots [5]$$

Friction Equations. It can be shown that the shear stress in the fluid at the journal surface is given by

$$[\tau_x]_{y=0} = -\frac{\lambda \omega}{\delta} \left\{ \frac{1}{(1 + \epsilon \cos \theta)} + 6 \frac{\partial \epsilon}{\partial \alpha} \frac{\sin \theta}{(1 + \epsilon \cos \theta)^2} + 3(1 - 2\sigma_s) \left[\frac{\epsilon \cos \theta}{(1 + \epsilon \cos \theta)^2} + \frac{3\epsilon^2}{(2 + \epsilon^2)(1 + \epsilon \cos \theta)^2} \right] \right\} [6]$$

Owing to the uncertainty of treating the lubricant in the inoperative part of the film, the frictional resistance values will be confined, in the present analysis, to regions of positive pressure.

$$F_f = \int_{\theta_1}^{\theta_2} [\tau_x]_{y=0} B r d\theta \dots [7]$$

Substituting Equation [6] in Equation [7], performing the integration, and dividing the result by W , we obtain

$$\left(\frac{\mu_f}{\delta} \right) \Delta = \left\{ \frac{\pi}{\sqrt{1 - \epsilon^2}} \sin^{-1} \left[\frac{\sqrt{1 - \epsilon^2} \sin \theta}{(1 + \epsilon \cos \theta)} \right] \right\}_{\theta_1}^{\theta_2} + \frac{\partial \epsilon}{\partial \alpha} \left[\frac{6\pi}{\epsilon(1 + \epsilon \cos \theta)} \right]_{\theta_1}^{\theta_2} + (1 - 2\sigma_s) \left\{ \frac{3\epsilon^2 \pi}{(2 + \epsilon^2) \sqrt{1 - \epsilon^2}} \sin^{-1} \left[\frac{\sqrt{1 - \epsilon^2} \sin \theta}{(1 + \epsilon \cos \theta)} \right] + \frac{6\pi \sin \theta}{(2 + \epsilon^2)(1 + \epsilon \cos \theta)} \right\}_{\theta_1}^{\theta_2} \dots [8]$$

giving the relation between frictional and load criteria.

(B) Film Extent

As a first approximation to the determination of the film extent, the pressure function in Equation [3] is equated to zero. Therefore

$$\frac{(1 - 2\sigma_s) \epsilon(1 + \epsilon)^2}{\partial \epsilon / \partial \alpha (2 + \epsilon^2)} = \left[\cot \theta - \frac{(2 + \epsilon)}{(2 + \epsilon \cos \theta) \sin \theta} \right] = f(\theta) \dots [9]$$

The solution of Equation [9] is found to lead to two real and two complex roots. These latter roots are considered of no importance in the present study. It is, therefore, concluded that the pressure function attains, in general, zero values at precisely two points on the journal circumference.

The value of $\theta = \theta_1 = 0$ or 2π determines one end of the oper-

active film boundary. The other end θ_2 is the real root of the cubic equation in $(\tan \theta/2)$ obtained from Equation [9]. With θ_2 appearing as a limit of integration in load and friction equations, it seems that the numerical computation of θ_2 is a most suitable solution.

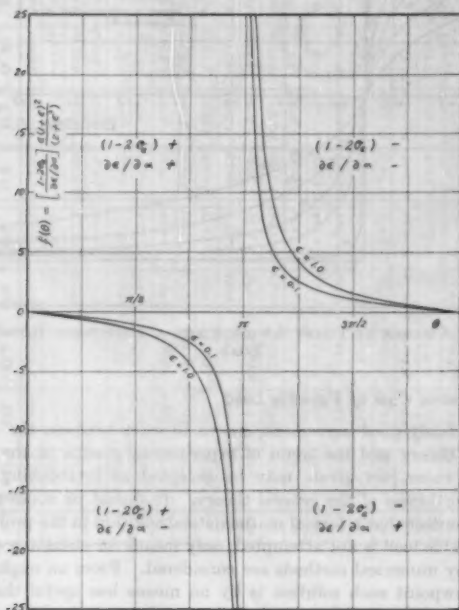


FIG. 2 $f(\theta)$ VERSUS θ

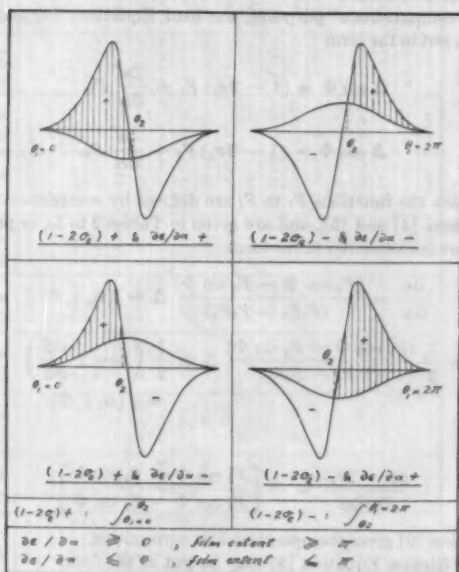


FIG. 3 COMBINATIONS OF PRESSURE WAVES

Should $f(\theta)$ in Equation [9] be plotted against θ , Fig. 2, a straight line parallel to the θ -axis would intersect the curve in points, the abscissas of which would give the film boundaries corresponding to the value of the left-hand side of the equation.

Table 1 is prepared for purposes of computation.

Fig. 3 shows the four possible combinations of the component pressure waves which lead to the different cases of the operative film position around the journal periphery under the conditions cited.

In the foregoing analysis the film is considered, for simplicity, to extend from θ_1 to θ_2 where the pressure function vanishes. It seems, therefore, that a more accurate solution would be obtained with the set of boundary conditions: $p = 0$ at $\theta_1 = 0$ and $p = 0 = \partial p / \partial \theta$ at θ_2 . This set, which is based on stability considerations, is found, however, to result in very complex expressions (10); it is doubtful whether the higher accuracy attained would justify the far too laborious task of obtaining solutions.

(C) Special Cases in Which $(\partial \epsilon / \partial \alpha) = 0$

This condition greatly simplifies the load and friction equations which reduce to

$$\Delta \sin \Phi = (1 - 2\sigma_s) \frac{6\pi^3 \epsilon}{(2 + \epsilon^2) \sqrt{1 - \epsilon^2}} \dots [10]$$

$$\Delta \cos \Phi = (1 - 2\sigma_s) \frac{12\pi \epsilon^3}{(2 + \epsilon^2) (1 - \epsilon^2)} \dots [11]$$

and

$$\left(\frac{\mu}{\delta} \right) \Delta = \frac{\pi^3}{\sqrt{1 - \epsilon^2}} + (1 - 2\sigma_s) \frac{3\pi^3 \epsilon^3}{(2 + \epsilon^2) \sqrt{1 - \epsilon^2}} \dots [12]$$

A Unidirectional Load of Constant Magnitude. For a fixed journal center position in the clearance circle, $\Delta = \Delta_0$, $\epsilon = \epsilon_0$, $\sigma_s = 0$. The results obtained, Figs. 4 and 5, are compared with earlier

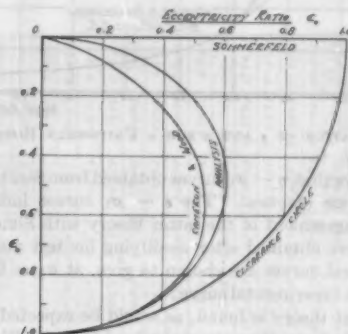


FIG. 4 JOURNAL CENTER LOCUS UNDER STEADY LOADS ($\delta = \infty$)

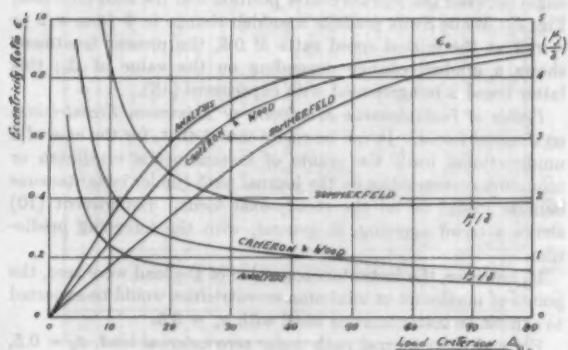


FIG. 5 LOAD CAPACITY AND FRICTION FOR A LOAD CONSTANT IN BOTH MAGNITUDE AND DIRECTION

theoretical investigations (2, 12). It should be pointed out that Cameron and Wood's results are based on the more accurate solution referred to previously, and that Sommerfeld's results are given only because they would be obtained from Swift's theory (14). It is evident that the results of the present work, for this special case of loading, show closer agreement with experiment than those obtained from Swift's theory.

A Uniformly Rotating Load of Constant Magnitude. A journal is subjected to a load constant in magnitude but rotating at a uniform angular speed ω_1 about the bearing center. In this case $\beta = \omega_1 t$ and $\Delta = \Delta_1$; therefore

$$\sigma_s = \frac{\partial}{\partial \alpha} (\beta + \Phi) = \frac{\omega_1}{\omega} = \sigma_1$$

The load equations are similar to those obtained in the previous case with $\Delta_1/(1 - 2\sigma_1)$ in place of Δ_s .

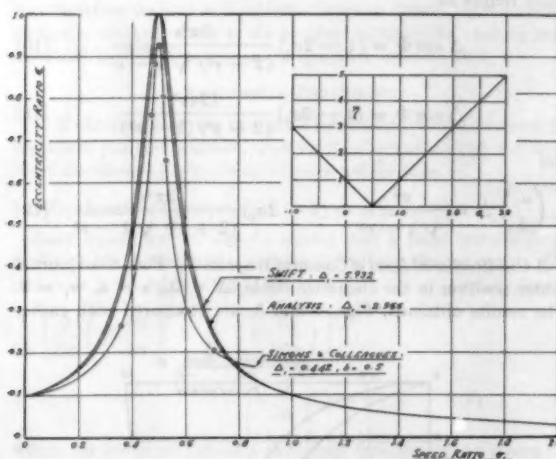


FIG. 6 VARIATION OF ϵ AND η FOR A UNIFORMLY ROTATING LOAD

Fig. 6 shows that $\eta - \sigma_1$ curves obtained from Swift's and present theories are identical. The $\epsilon - \sigma_1$ curves indicate, however, closer agreement of the latter theory with Simons' results (3) which were obtained after modifying his test machine (11). The theoretical curves are chosen to give, at $\sigma_1 = 0$, the same ϵ value as the experimental curve.

The present theory is found, as would be expected, to lead to friction values lower than those obtained from Swift's theory.

A most interesting result is the gradual change in Φ , the phase angle between the journal center position and the load direction, Fig. 7. While Swift predicts a sudden change in Φ from $\pi/2$ to $-\pi/2$ at the critical speed ratio of 0.5, the present treatment shows a gradual change depending on the value of Δ_1 ; this latter trend is in agreement with experiment (13).

Points of Instantaneous Maximum or Minimum Eccentricities on Journal Locus. It can be easily shown that, for the case of a unidirectional load, the points of instantaneous maximum or minimum eccentricities on the journal path (under instantaneous definite loads) lie on the steady-load locus. Experiment (10) shows a trend agreeing, in general, with the foregoing prediction.

If, however, the instantaneous value of the load were zero, the points of maximum or minimum eccentricities would be expected to exhibit an instantaneous whirl with $\sigma_s = 0.5$.

For a circular journal path under zero external load, $\sigma_s = 0.5$, and the eccentricity ratio assumes any value between zero and unity, the results being identical with Swift's findings.

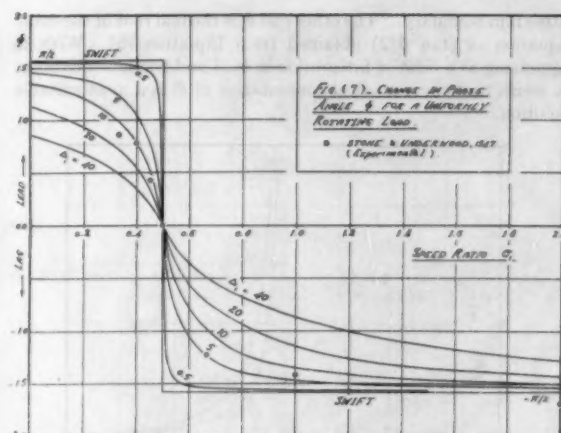


FIG. 7 CHANGE IN PHASE ANGLE Φ FOR A UNIFORMLY ROTATING LOAD

(D) General Case of Variable Load

The fairly good agreement, shown to exist between the suggested theory and the trend of experimental results in the few simple cases just given, may be accepted as establishing the trustworthiness of the general theory. It should be made clear at the outset that a formal mathematical solution to the problem of variable load is not attempted; only means for obtaining solutions by numerical methods are considered. From an engineering viewpoint such solution is by no means less useful than a strict mathematical handling of the problem which may prove far too laborious with no appreciable increase in the accuracy of the solutions effected.

For computational purposes, the load Equations [4] and [5] may be put in the form

$$\Delta \sin \Phi = (1 - 2\sigma_s) F_1 + \frac{\partial \epsilon}{\partial \alpha} F_2 \dots \dots \dots [13]$$

$$\Delta \cos \Phi = (1 - 2\sigma_s) F_3 + \frac{\partial \epsilon}{\partial \alpha} F_4 \dots \dots \dots [14]$$

(in which the functions F_1 to F_4 are defined by comparison with Equations [4] and [5], and are given in Tables 2 to 5), or probably more conveniently in the form

$$\frac{\partial \epsilon}{\partial \alpha} = \frac{(F_1 \cos \Phi - F_3 \sin \Phi)}{(F_1 F_4 - F_3 F_2)} \Delta = f(\alpha, \epsilon, \Phi) \dots \dots [15]$$

$$\frac{\partial \Phi}{\partial \alpha} = \frac{1}{2} \frac{(F_2 \cos \Phi - F_4 \sin \Phi)}{(F_1 F_4 - F_3 F_2)} \Delta + \frac{1}{2} \left(1 - 2 \frac{\partial \beta}{\partial \alpha} \right) = g(\alpha, \epsilon, \Phi) \dots \dots [16]$$

Also

$$\frac{(1 - 2\sigma_s)}{\partial \epsilon / \partial \alpha} = - \frac{[F_2 \cos \Phi - F_4 \sin \Phi]}{[F_1 \cos \Phi - F_3 \sin \Phi]} \dots \dots [17]$$

Equation [9] gives the operative film extremities.

The friction Equation [8] may be put in the form

$$\left(\frac{\mu_f}{\delta} \right) \Delta = R_1 + \frac{\partial \epsilon}{\partial \alpha} R_2 + (1 - 2\sigma_s) R_3 \dots \dots [18]$$

in which R_1 , R_2 , and R_3 are defined by comparison with Equation [8]; they are given in Tables 6 to 8.

The problem in which the resultant load is to be determined

TABLE 2 P_i

θ	$\epsilon=0.1$	$\epsilon=0.2$	$\epsilon=0.3$	$\epsilon=0.4$	$\epsilon=0.5$	$\epsilon=0.6$	$\epsilon=0.7$	$\epsilon=0.8$	$\epsilon=0.9$	$\epsilon=0.95$
0	0.0000	0.0000	0.0000	0.0000	0.0000	0.0000	0.0000	0.0000	0.0000	0.0000
10	0.0032	0.0069	0.0103	0.0135	0.0164	0.0190	0.0213	0.0232	0.0248	0.0260
20	0.0091	0.0182	0.0271	0.0356	0.0435	0.0508	0.0573	0.0629	0.0676	0.0713
30	0.0164	0.0324	0.0481	0.0633	0.0779	0.0918	0.1050	0.1173	0.1287	0.1391
40	0.0254	0.0507	0.0754	0.1000	0.1240	0.1474	0.1692	0.1894	0.2080	0.2251
50	0.0361	0.0721	0.1076	0.1424	0.1764	0.2094	0.2414	0.2723	0.3020	0.3304
60	0.0484	0.0967	0.1450	0.1921	0.2379	0.2823	0.3252	0.3665	0.4061	0.4440
70	0.0622	0.1243	0.1863	0.2471	0.3066	0.3646	0.4210	0.4758	0.5289	0.5802
80	0.0774	0.1547	0.2316	0.3071	0.3811	0.4534	0.5240	0.5927	0.6594	0.7241
90	0.0940	0.1913	0.2881	0.3833	0.4767	0.5682	0.6577	0.7451	0.8303	0.9134
100	0.1119	0.2291	0.3456	0.4603	0.5731	0.6839	0.7926	0.8991	1.0034	1.1055
110	0.1310	0.2680	0.4033	0.5367	0.6671	0.7944	0.9185	1.0393	1.1567	1.2706
120	0.1512	0.3080	0.4623	0.6143	0.7635	0.9088	1.0500	1.1870	1.3207	1.4509
130	0.1724	0.3500	0.5233	0.6943	0.8615	1.0266	1.1885	1.3461	1.5000	1.6454
140	0.1946	0.3939	0.5863	0.7743	0.9605	1.1344	1.3050	1.4721	1.6354	1.7871
150	0.2177	0.4396	0.6513	0.8643	1.0793	1.2612	1.4390	1.6134	1.7854	1.9449
160	0.2417	0.4871	0.7183	0.9643	1.1983	1.3882	1.5730	1.7474	1.9199	2.1094
170	0.2665	0.5363	0.7813	1.0643	1.3273	1.5253	1.7170	1.8904	2.0604	2.2709
180	0.2921	0.5873	0.8443	1.1643	1.4753	1.6823	1.8820	2.0504	2.2104	2.4284
190	0.3184	0.6403	0.9073	1.2643	1.6353	1.8553	2.0550	2.2004	2.3504	2.5809
200	0.3454	0.6953	0.9703	1.3643	1.8003	2.0303	2.2250	2.3254	2.4704	2.7284
210	0.3731	0.7523	1.0333	1.4643	1.9453	2.1053	2.3000	2.3504	2.5204	2.8709
220	0.4014	0.8113	1.0963	1.5643	2.0603	2.1803	2.2750	2.3254	2.4704	2.9984
230	0.4304	0.8723	1.1593	1.6643	2.1353	2.2553	2.2500	2.2504	2.3504	3.1209
240	0.4601	0.9353	1.2223	1.7643	2.2103	2.3303	2.1250	2.1254	2.2254	3.2384
250	0.4904	1.0003	1.2853	1.8643	2.2853	2.4053	2.0000	2.0004	2.1004	3.3509
260	0.5214	1.0673	1.3483	1.9643	2.3603	2.4803	1.8750	1.8754	1.9754	3.4584
270	0.5531	1.1363	1.4113	2.0643	2.4353	2.5553	1.7500	1.7504	1.8504	3.5609
280	0.5854	1.2073	1.4743	2.1643	2.5103	2.6303	1.6250	1.6254	1.7254	3.6584
290	0.6184	1.2803	1.5373	2.2643	2.5853	2.7053	1.5000	1.5004	1.6004	3.7509
300	0.6521	1.3553	1.6003	2.3643	2.6603	2.7803	1.3750	1.3754	1.4754	3.8384

TABLE 1 $f(\theta)$

θ	$\epsilon=0.1$	$\epsilon=0.2$	$\epsilon=0.3$	$\epsilon=0.4$	$\epsilon=0.5$	$\epsilon=0.6$	$\epsilon=0.7$	$\epsilon=0.8$	$\epsilon=0.9$	$\epsilon=0.95$	$\epsilon=1.00$
0	0.0000	0.0000	0.0000	0.0000	0.0000	0.0000	0.0000	0.0000	0.0000	0.0000	0.0000
10	0.0032	0.0069	0.0103	0.0135	0.0164	0.0190	0.0213	0.0232	0.0248	0.0260	0.0271
20	0.0091	0.0182	0.0271	0.0356	0.0435	0.0508	0.0573	0.0629	0.0676	0.0713	0.0740
30	0.0164	0.0324	0.0481	0.0633	0.0779	0.0918	0.1050	0.1173	0.1287	0.1391	0.1484
40	0.0254	0.0507	0.0754	0.1000	0.1240	0.1474	0.1692	0.1894	0.2080	0.2251	0.2404
50	0.0361	0.0721	0.1076	0.1424	0.1764	0.2094	0.2414	0.2723	0.3020	0.3304	0.3567
60	0.0484	0.0967	0.1450	0.1921	0.2379	0.2823	0.3252	0.3665	0.4061	0.4440	0.4794
70	0.0622	0.1243	0.1863	0.2471	0.3066	0.3646	0.4210	0.4758	0.5289	0.5802	0.6294
80	0.0774	0.1547	0.2316	0.3071	0.3811	0.4534	0.5240	0.5927	0.6594	0.7241	0.7864
90	0.0940	0.1913	0.2881	0.3833	0.4767	0.5682	0.6577	0.7451	0.8303	0.9134	0.9944
100	0.1119	0.2291	0.3456	0.4603	0.5731	0.6839	0.7944	0.9185	1.0393	1.1567	1.2706
110	0.1310	0.2680	0.4033	0.5367	0.6671	0.7944	0.9185	1.0393	1.1567	1.2706	1.3804
120	0.1512	0.3080	0.4623	0.6143	0.7635	0.9088	1.0500	1.1870	1.3207	1.4509	1.5764
130	0.1724	0.3500	0.5233	0.6943	0.8615	1.0266	1.1885	1.3461	1.5000	1.6454	1.7871
140	0.1946	0.3939	0.5863	0.7743	0.9605	1.1344	1.3050	1.4721	1.6354	1.7871	1.9449
150	0.2177	0.4396	0.6513	0.8643	1.0793	1.2612	1.4390	1.6134	1.7854	1.9449	2.1094
160	0.2417	0.4871	0.7183	0.9643	1.1983	1.3882	1.5730	1.7474	1.9199	2.0604	2.2709
170	0.2665	0.5363	0.7813	1.0643	1.3273	1.5253	1.7170	1.8904	2.0604	2.2104	2.4284
180	0.2921	0.5873	0.8443	1.1643	1.4753	1.6823	1.8820	2.0504	2.2104	2.3504	2.5809
190	0.3184	0.6403	0.9073	1.2643	1.6353	1.8553	2.0550	2.2004	2.3504	2.4704	2.7284
200	0.3454	0.6953	0.9703	1.3643	1.8003	2.0303	2.2250	2.3254	2.4704	2.5809	2.8709
210	0.3731	0.7523	1.0333	1.4643	1.9453	2.1053	2.2750	2.3504	2.4704	2.5809	2.9984
220	0.4014	0.8113	1.0963	1.5643	2.0603	2.1803	2.2500	2.3254	2.4704	2.5809	3.1209
230	0.4304	0.8723	1.1593	1.6643	2.1353	2.2553	2.2500	2.2504	2.3504	2.4704	3.2384
240	0.4601	0.9353	1.2223	1.7643	2.2103	2.3303	2.1250	2.1254	2.2254	2.3504	3.3509
250	0.4904	1.0003	1.2853	1.8643	2.2853	2.4053	2.0000	2.0004	2.1004	2.2104	3.4584
260	0.5214	1.0673	1.3483	1.9643	2.3603	2.4803	1.8750	1.8754	1.9754	2.0804	3.5609
270	0.5531	1.1363	1.4113	2.0643	2.4353	2.5553	1.7500	1.7504	1.8504	1.9504	3.6584
280	0.5854	1.2073	1.4743	2.1643	2.5103	2.6303	1.6250	1.6254	1.7254	1.8254	3.7509
290	0.6184	1.2803	1.5373	2.2643	2.5853	2.7053	1.5000	1.5004	1.6004	1.7004	3.8384
300	0.6521	1.3553	1.6003	2.3643	2.6603	2.7803	1.3750	1.3754	1.4754	1.5754	3.9209

ALL VALUES OF FUNCTION IN ABOVE TABLE ARE NEGATIVE
 $f(\theta) = -f(360^\circ - \theta)$

TABLE 3 P_i

θ	$\epsilon=0.1$	$\epsilon=0.2$	$\epsilon=0.3$	$\epsilon=0.4$	$\epsilon=0.5$	$\epsilon=0.6$	$\epsilon=0.7$	$\epsilon=0.8$	$\epsilon=0.9$	$\epsilon=0.95$	$\epsilon=1.00$
0	0.0000	0.0000	0.0000	0.0000	0.0000	0.0000	0.0000	0.0000	0.0000	0.0000	0.0000
10	0.0280	0.0702	0.1078	0.1502	0.1900	0.2266	0.2600	0.0101	0.0098	0.0094	0.0095
20	0.0643	0.1524	0.2329	0.3042	0.3690	0.4275	0.4791	0.0141	0.0105	0.0096	0.0090
30	0.1078	0.2604	0.3970	0.5165	0.6180	0.7019	0.7678	0.0170	0.0127	0.0096	0.0080
40	0.1581	0.3768	0.5497	0.7032	0.8317	0.9363	1.0177	0.0197	0.0143	0.0096	0.0062
50	0.2151	0.4656	0.6994	0.9779	1.1901	1.3753	1.5349	0.0223	0.0159	0.0096	0.0038
60	0.2707	0.5291	0.8256	1.2044	1.6760	1.9104	2.1094	0.0249	0.0185	0.0096	0.0018
70	0.3244	0.5967	0.9303	1.3084	2.0468	2.3795	2.7199	0.0271	0.0207	0.0096	0.0008
80	0.3800	0.6518	1.0290	1.4179	2.2001	2.5536	3.0739	0.0286	0.0219	0.0096	0.0004
90	0.4384	0.7043	1.1159	1.5269	2.3004	2.7355	3.2520	0.0298	0.0229	0.0096	0.0002
100	0.4993	0.7549	1.1940	1.6246	2.3932	2.9130	3.4292	0.0309	0.0239	0.0096	0.0001
110	0.5620	0.8032	1.2622	1.7146	2.4786	3.0877	3.6037	0.0318	0.0248	0.0096	0.0000
120	0.6264	0.8493	1.3217	1.7986	2.5571	3.2585	3.7760	0.0326	0.0256	0.0096	0.0000
130	0.6924	0.8934	1.3734	1.8766	2.6296	3.4219	3.9464	0.0333	0.0263	0.0096	0.0000
140	0.7599	0.9355	1.4182	1.9499	2.6961	3.5751	4.1127	0.0339	0.0269	0.0096	0.0000
150	0.8288	0.9756	1.4582	2.0186	2.7574	3.7194	4.2770	0.0344	0.0274	0.0096	0.0000
160	0.8990	1.0137	1.4954	2.0827	2.8135	3.8581	4.4399	0.0348	0.0278	0.0096	0.0000
170	0.9704	1.0498	1.5300	2.1422	2.8645	3.9924	4.5999	0.0351	0.0281	0.0096	0.0000
180	1.0431	1.0839	1.5629	2.1974	2.9113	4.1214	4.7569	0.0353	0.0283	0.0096	0.0000
190	1.1171	1.1160	1.5943	2.2491	2.9544	4.2394	4.9109	0.0355	0.0285	0.0096	0.0000
200	1.1924	1.1461	1.6243	2.2974	2.9936	4.3534	5.0719	0.0356	0.0286	0.0096	0.0000
210	1.2690	1.1741	1.6529	2.3424	3.0291	4.4624	5.2299	0.0357	0.0287	0.0096	0.0000
220	1.3468	1.2000	1.6800	2.3844	3.0610	4.5664	5.3849	0.0358	0.0288	0.0096	0.0000
230	1.4258	1.2240	1.7057	2.4234	3.0899	4.6564	5.5369	0.0359	0.0289	0.0096	0.0000
240	1.5059	1.2461	1.7299	2.4594	3.1159	4.7414	5.6849	0.0360	0.0290	0.0096	0.0000
250	1.5871	1.2664	1.7527	2.4924	3.1390	4.8214	5.8289	0.0361	0.0291	0.0096	0.0000
260	1.6694	1.2849	1.7741	2.5224	3.1594	4.8964	5.9699	0.0362	0.0292	0.0096	0.0000
270	1.7528	1.3016	1.7941	2.5494	3.1774	4.9664	6.1069	0.0363	0.0293	0.0096	0.0000
280	1.8373	1.3166	1.8127	2.5734	3.1930	5.0314	6.2399	0.0364	0.0294	0.0096	0.0000
290	1.9229	1.3299	1.8299	2.5944	3.2064	5.0914	6.3689	0.0365	0.0295	0.0096	0.0000
300	2.0096	1.3416	1.8456	2.6124	3.2179	5.1464	6.4929	0.0366	0.0296	0.0096	0.0000
310	2.0974	1.3519	1.8599	2.6274	3.2279	5.1964	6.6129	0.0367	0.0297	0.0096	0.0000
320	2.1863	1.3609	1.8729	2.6404	3.2359	5.2414	6.7289	0.0368	0.0298	0.0096	0.0000
330	2.2764	1.3686	1.8846	2.6514	3.2419	5.2814	6.8409	0.0369	0.0299	0.0096	0.0000
340	2.3677	1.3750	1.8949	2.6604	3.2459	5.3164	6.9489	0.0370	0.0300	0.0096	0.0000
350	2.4602	1.3799	1.9039	2.6674	3.2479	5.3464	7.0529	0.0371	0.0301	0.0096	0.0000
360	2.5539	1.3834	1.9116	2.6724	3.2489	5.3714	7.1539	0.0372	0.0302	0.0096	0.0000
370	2.6488	1.3856	1.9180	2.6764	3.2489	5.3914	7.2519	0.0373	0.0303	0.0096	0.0000
380	2.7449	1.3866	1.9231	2.6794	3.2479	5.4054	7.3469	0.0374	0.0304	0.0096	0.0000
390	2.8422	1.3864	1.9269	2.6814	3.2459	5.4134	7.4389	0.0375	0.0305	0.0096	0.0000
400	2.9407	1.3850	1.9294	2.6824	3.2429	5.4154	7.5269	0.0376	0.0306	0.0096	0.0000
410	3.0404	1.3824	1.9306	2.6824	3.2389	5.4114	7.6109	0.0377	0.0307	0.0096	0.0000
420	3.1414	1.3786	1.9306	2.6814	3.2329	5.4014	7.6909	0.0378	0.0308	0.0096	0.0000
430	3.2437	1.3736	1.9294	2.6794	3.2249	5.3844	7.7669	0.0379	0.0309	0.0096	0.0000
440	3.3473	1.3674	1.9269	2.6764	3.2149	5.3694	7.8389	0.0380	0.0310	0.0096	0.0000
450	3.4522	1.3599	1.9231	2.6724	3.2029	5.3464	7.9069	0.0381	0.0311	0.0096	0.0000
460	3.5584	1.3512	1.9180	2.6674	3.1879	5.3154	7.9709	0.0382	0.0312	0.0096	0.0000
470	3.6659	1.3413	1.9116	2.6604	3.1709	5.2764	8.0309	0.0383	0.0313	0.0096	0.0000
480	3.7747	1.3302	1.9039	2.6514	3.1519	5.2294	8.0869	0.0384	0.0314	0.0096	0.0000
490	3.8848	1.3179	1.8949	2.6404	3.1309	5.1744	8.1389	0.0385	0.0315	0.0096	0.0000
500	3.9962	1.3044	1.8846	2.6274	3.1079	5.1114	8.1869	0.0386	0.0316	0.0096	0.0000
510	4.1089	1.2897	1.8729	2.6124	3.0829	5.0364	8.2309	0.0387	0.0317	0.0096	0.0000
520	4.2229	1.2738	1.8599	2.5944	3.0559	4.9494	8.2709	0.0388	0.0318	0.0096	0.0000
530	4.3382	1.2567	1.8456	2.5734	3.0269	4.8504	8.3069	0.0389	0.0319	0.0096	0.0000
540	4.4548	1.2384	1.8299	2.5494	2.9959	4.7394	8.3389	0.0390	0.0320	0.0096	0.0000
550	4.5727	1.2189	1.8127	2.5224	2.9629	4.6164	8.3669	0.0391	0.0321	0.0096	0.0000
560	4.6919	1.1982	1.7941	2.4924	2.9279	4.4814	8.3909	0.0392	0.0322	0.0096	0.0000
570	4.8124	1.1764	1.7741	2.4594	2.8909	4.3344	8.4109	0.0393	0.0323	0.0096	0.0000
580	4.9342	1.1534	1.7527	2.4234	2.8519	4.1754	8.4269	0.0394	0.0324	0.0096	0.0000
590	5.0573	1.1292	1.7299	2.3844	2.8109	4.0044	8.4389	0.0395	0.0325	0.0096	0.0000
600	5.1817	1.1038	1.7057	2.3424	2.7679	3.8214	8.4469	0.0396	0.0326	0.0096	0.0000
610	5.3074	1.0772	1.6800	2.2974	2.7229	3.6264	8.4509	0.0397	0.0327	0.0096	0.0000
620	5.4344	1.0494	1.6529	2.2494	2.6759	3.4194	8.4509	0.0398	0.0328	0.0096	0.0000
630	5.5627	1.0204	1.6243	2.1974	2.6269	3.2004	8.4469	0.0399	0.0329	0.0096	0.0000
640	5.6923	0.9899	1.5943	2.1422	2.5759	2.9694	8.4389	0.0400	0.0330	0.0096	0.0000
650	5.8232	0.9580	1.5629	2.0827	2.5219	2.7264	8.4269	0.0401	0.0331	0.0096	0.0000
660	5.9554	0.9247	1.5300	2.0186	2.4659	2.4714	8.4109	0.0402	0.0332	0.0096	0.0000
670	6.0889	0.8900	1.4954	1.9499	2.4079	2.2044	8.3909	0.0403	0.0333	0.0096	0.0000
680	6.2237	0.8539	1.4582	1.8766	2.3479	1.9264	8.3669	0.0404	0.0334	0.0096	0.0000
690	6.3598	0.8164	1.4182	1.7986	2.2844	1.6364	8.3389	0.0405	0.0335	0.0096	0.0000
700	6.4972	0.7776	1.3734	1.7146	2.2179	1.3344	8.3069	0.0406	0.0336	0.0096	0.0000
710	6.6359	0.7376	1.3217	1.6246	2.1489	1.0194	8.2709	0.0407	0.0337	0.0096	0.0000
720	6.7759	0.6963	1.2622	1.5269	2.0779	0.6924	8.2309	0.0408	0.0338	0.0096	0.0000
730	6.9172	0.6537	1.1940	1.4179	2.0044	0.3544	8.1869	0.0409	0.0339	0.0096	0.0000
740	7.0598	0.6100	1.1159	1.2974	1.9279	0.0064	8.1389	0.0410	0.0340	0.0096	0.0000
750	7.2037	0.5652	1.0290	1.1624	1.8479	0.0000	8.0869	0.0411	0.0341	0.0096	0.0000
760	7.3488	0.5194	0.9303	1.0186	1.7644	0.0000	8.0309	0.0412	0.0342	0.0096	0.0000
770	7.4951	0.4726	0.8256	0.8643	1.6764	0.0000	7.9709	0.0413	0.0343	0.0096	0.0000
780	7.6426	0.4249	0.7032	0.6994	1.5760	0.0000	7.9069	0.0414	0.0344	0.0096	0.0000
790	7.7912	0.3764	0.5615	0.5165	1.4719	0.0000	7.8389	0.0415	0.0345	0.0096	0.0000
800	7.9409	0.3271	0.4032	0.3084	1.3646	0.0000	7.7669	0.0416	0.0346	0.0096	0.0000
810	8.0917	0.2770	0.2329	0.0633	1.2549	0.0000	7.6909	0.0417	0.0347	0.0096	0.0000
820	8.2436	0.2261	0.0508	0.0190	1.1434	0.0000	7.6129	0.0418	0.0348	0.0096	0.0000
830	8.3965	0.1744	0.0096	0.0000	1.0299	0.0000	7.5309	0.0419	0.0349	0.0096	0.0000
840	8.5504	0.1219	0.0000	0.0000	0.9144	0.0000	7.4449	0.0420	0.0350	0.0096	0.0000
850	8.7053	0.0696	0.0000	0.0000	0.7969	0.0000	7.3549	0.0421	0.0351	0.0096	0.0000
860	8.8612	0.0171	0.0000	0.0000	0.6774	0.0000	7.2609	0.0422	0.0352	0.0096	0.0000
870	9.0181	0.0000	0.0000	0.0000	0.5569	0.0000	7.1629	0.0423	0.0353	0.0096	0.0000
880	9.1760	0.0000	0.0000	0.0000	0.4354	0.0000	7.0609	0.0424	0.0354	0.0096	0.0000
890	9.3349	0.0000	0.0000	0.0000	0.3129	0.0000	6.9549	0.0425	0.0355	0.0096	0.0000
900	9.4948	0.0000	0.0000	0.0000	0.1904	0.0000	6.8449	0.0426	0.0356	0.0096	0.0000
910	9.6557	0.0000	0.0000	0.0000	0.0679	0.0000	6.7309	0.0427	0.0357	0.0096	

TABLE 8 R_h

θ	$\epsilon=0.1$	0.2	0.3	0.4	0.5	0.6	0.7	0.8	0.9	0.95
0	0.0000	0.0000	0.0000	0.0000	0.0000	0.0000	0.0000	0.0000	0.0000	0.0000
10	0.1557	0.2150	0.4172	0.5220	0.6095	0.6800	0.7360	0.7860	0.8320	0.8760
20	0.3082	0.5062	0.8716	1.4433	2.2006	3.1476	4.2980	5.6620	7.3480	9.3660
30	0.4543	0.8592	1.2396	1.5617	1.8334	2.0562	2.2330	2.3670	2.4730	2.5600
40	0.5920	1.1395	1.6370	2.0747	2.4492	2.7590	3.0060	3.1960	3.3340	3.4300
50	0.7129	1.3920	2.0189	2.5750	3.0577	3.4720	3.8190	4.0960	4.2940	4.4100
60	0.8192	1.6218	2.3793	3.0712	3.6820	4.2849	4.8790	5.4640	6.0390	6.6040
70	0.9057	1.8220	2.7011	3.5108	4.2928	5.0966	5.8920	6.6780	7.4540	8.2200
80	0.9695	1.9864	3.0034	3.8016	4.6087	5.4046	6.1910	6.9680	7.7350	8.4920
90	1.0076	2.1171	3.2436	4.0497	4.8578	5.6440	6.4210	7.1880	7.9450	8.6920
100	0.9990	2.1901	3.5230	4.3471	5.1570	5.9440	6.7170	7.4840	8.2450	8.9990
110	0.9506	2.1995	3.5230	4.3471	5.1570	5.9440	6.7170	7.4840	8.2450	8.9990
120	0.8714	2.0228	3.2422	4.0497	4.8578	5.6440	6.4210	7.1880	7.9450	8.6920
130	0.7653	1.8390	3.0034	3.8016	4.6087	5.4046	6.1910	6.9680	7.7350	8.4920
140	0.6347	1.5712	2.6678	3.4376	4.1742	4.9410	5.7070	6.4730	7.2390	7.9990
150	0.4844	1.2013	2.2013	2.9076	3.6735	4.4390	5.2040	5.9690	6.7340	7.4990
160	0.3199	0.9525	1.9034	2.5976	3.3635	4.1280	4.8930	5.6580	6.4230	7.1880
170	0.1483	0.5930	1.3376	2.3951	3.1627	3.9270	4.6910	5.4560	6.2210	6.9860
180	0.0871	0.3337	0.7710	1.5976	2.7331	4.2301	6.2705	8.5535	11.0167	13.6866
190	0.0361	0.1052	0.2492	0.6027	1.1817	2.1110	3.3865	5.0465	7.1330	9.6015
200	0.0166	0.0459	0.1052	0.2492	0.6027	1.1817	2.1110	3.3865	5.0465	7.1330
210	0.0086	0.0239	0.0525	0.1186	0.2631	0.5676	1.0000	1.6730	2.5840	3.7440
220	0.0046	0.0119	0.0262	0.0593	0.1316	0.2940	0.5200	0.8160	1.2740	1.9040
230	0.0024	0.0060	0.0134	0.0306	0.0676	0.1480	0.2630	0.4240	0.6340	0.9040
240	0.0012	0.0030	0.0067	0.0151	0.0331	0.0730	0.1310	0.2160	0.3340	0.4940
250	0.0006	0.0015	0.0034	0.0076	0.0166	0.0360	0.0640	0.1040	0.1540	0.2240
260	0.0003	0.0008	0.0017	0.0039	0.0086	0.0190	0.0340	0.0540	0.0840	0.1240
270	0.0001	0.0004	0.0009	0.0020	0.0046	0.0100	0.0180	0.0280	0.0440	0.0640
280	0.0000	0.0002	0.0005	0.0011	0.0024	0.0050	0.0090	0.0140	0.0220	0.0340
290	0.0000	0.0001	0.0003	0.0007	0.0015	0.0030	0.0050	0.0080	0.0120	0.0180
300	0.0000	0.0000	0.0001	0.0003	0.0007	0.0015	0.0030	0.0050	0.0080	0.0120

TABLE 9 R_h

θ	$\epsilon=0.1$	0.2	0.3	0.4	0.5	0.6	0.7	0.8	0.9	0.95
0	0.0000	0.0000	0.0000	0.0000	0.0000	0.0000	0.0000	0.0000	0.0000	0.0000
10	0.4991	0.4574	0.4221	0.3923	0.3655	0.3434	0.3255	0.3110	0.2990	0.2890
20	0.9992	0.9177	0.8408	0.7684	0.7003	0.6365	0.5765	0.5200	0.4660	0.4150
30	1.4993	1.3825	1.2800	1.1816	1.0872	0.9972	0.9110	0.8280	0.7480	0.6710
40	2.0000	1.8537	1.7265	1.6045	1.4865	1.3720	1.2610	1.1530	1.0480	0.9460
50	2.5017	2.3245	2.1730	2.0320	1.8910	1.7500	1.6090	1.4680	1.3270	1.1860
60	3.0034	2.8275	2.6444	2.4749	2.3064	2.1380	1.9690	1.7990	1.6290	1.4590
70	3.5051	3.3336	3.1270	2.9487	2.7697	2.5907	2.4110	2.2310	2.0510	1.8710
80	4.0068	3.8553	3.6179	3.4065	3.1951	2.9837	2.7723	2.5609	2.3495	2.1381
90	4.5085	4.3077	4.0492	3.7907	3.5322	3.2737	3.0152	2.7567	2.4982	2.2397
100	5.0102	4.7610	4.4625	4.1640	3.8655	3.5670	3.2685	2.9690	2.6695	2.3700
110	5.5119	5.2134	4.8649	4.5164	4.1679	3.8194	3.4709	3.1224	2.7739	2.4254
120	6.0136	5.6641	5.2656	4.8671	4.4686	4.0701	3.6716	3.2731	2.8746	2.4761
130	6.5153	6.1168	5.6683	5.2198	4.7713	4.3228	3.8743	3.4258	2.9773	2.5288
140	7.0170	6.5685	6.0700	5.5715	5.0730	4.5745	4.0760	3.5775	3.0790	2.5805
150	7.5187	7.0202	6.4717	5.9232	5.3747	4.8262	4.2777	3.7292	3.1807	2.6322
160	8.0204	7.4719	6.8734	6.2749	5.6764	5.0779	4.4794	3.8809	3.2824	2.6839
170	8.5221	7.9236	7.2751	6.6266	5.9781	5.3296	4.6811	4.0326	3.3841	2.7356
180	9.0238	8.3753	7.6768	6.9783	6.2798	5.5813	4.8828	4.1843	3.4858	2.7871
190	9.5255	8.8268	8.0783	7.3298	6.5813	5.8328	5.0843	4.3358	3.5873	2.8386
200	10.0272	9.2783	8.4798	7.6813	6.8828	6.0843	5.2858	4.4873	3.6888	2.8901
210	10.5289	9.7298	8.8813	8.0828	7.2843	6.4858	5.6873	4.8888	4.0903	3.2916
220	11.0306	10.2313	9.3328	8.4843	7.6858	6.8873	6.0888	5.2903	4.4918	3.7431
230	11.5323	10.7328	9.7843	8.9358	8.1373	7.3388	6.5403	5.7418	4.9433	4.1946
240	12.0340	11.2343	10.2858	9.4373	8.6388	7.8403	7.0418	6.2433	5.4448	4.6461
250	12.5357	11.7358	10.7873	9.9388	9.1403	8.3418	7.5433	6.7448	5.9463	5.1476
260	13.0374	12.2373	11.2888	10.4403	9.6418	8.8433	8.0448	7.2463	6.4478	5.6491
270	13.5391	12.7388	11.7903	10.9418	10.1433	9.3448	8.5463	7.7478	6.9493	6.1506
280	14.0408	13.2403	12.2918	11.4433	10.6448	9.8463	9.0478	8.2493	7.4508	6.6521
290	14.5425	13.7418	12.7933	11.9448	11.1463	10.3478	9.5493	8.7508	7.9523	7.1536
300	15.0442	14.2433	13.2948	12.4463	11.6478	10.8493	10.0508	9.2523	8.4538	7.6551

for given journal center displacement presents no obvious difficulties. On the other hand, the inverse problem which is encountered in bearing design is decidedly more difficult. Computing aids may be resorted to depending on the nature of the problem.

BIBLIOGRAPHY

- 1 "The Calculated Performance of Dynamically Loaded Sleeve Bearings," by J. T. Burwell, Part 1, *Journal of Applied Mechanics*, Trans. ASME, vol. 60, 1947, pp. A-231-A-245; Part 2, *Journal of Applied Mechanics*, Trans. ASME, vol. 71, 1949, pp. A-358-A-360; Part 3, *Journal of Applied Mechanics*, Trans. ASME, vol. 73, 1951, pp. 393-404.
- 2 "The Full Journal Bearing," by A. Cameron and W. L. Wood, *Proceedings of The Institution of Mechanical Engineers*, London, England, vol. 161, 1949, pp. 59-72.
- 3 "Discrepancies Between Theoretical and Observed Behaviour of Cyclically Loaded Bearings," by R. W. Dayton, E. M. Simons, and F. A. Fend, NACA TN 2545, 1951.
- 4 "Alternating Loads on Sleeve Bearings," by J. Dick, *Philosophical Magazine*, vol. 35, 1944, pp. 841-850.
- 5 "The Hydrodynamical Theory of the Lubrication of a Cylindrical Bearing Under Variable Load, and of a Pivot Bearing," by W. J. Harrison, *Trans. Cambridge Philosophical Society*, vol. 22, 1919, pp. 373-388.
- 6 "Zylindrische Gleitlager bei instationärer Belastung," by H. H. Ott, thesis, Eidgenössische Technische Hochschule, Zürich, Switzerland, 1948.
- 7 "On the Theory of Lubrication and Its Application to Mr. Beauchamp Tower's Experiments," by O. Reynolds, *Philosophical Trans. of the Royal Society of London, England*, vol. 177, series A, part 1, 1886, pp. 157-234.
- 8 "Whirling of a Journal in a Sleeve Bearing," by D. Robertson, *Philosophical Magazine*, vol. 15, 1933, pp. 113-130.
- 9 Review of Reference (6), by M. C. Shaw, *ASME Applied Mechanics Reviews*, vol. 2, 1949, p. 264.
- 10 "Journal Bearing Performance Under Variable Loads," by G. S. A. Shawki, thesis, University of Sheffield, England, 1952.
- 11 "The Hydrodynamic Lubrication of Cyclically Loaded Bearings," by E. M. Simons, *Trans. ASME*, vol. 72, 1950, pp. 805-816.
- 12 "Zur hydrodynamischen Theorie der Schmiermittelreibung," by A. Sommerfeld, *Zeitschrift für Mathematik und Physik*, vol. 50, 1904, pp. 97-153.
- 13 "Load-Carrying Capacity of Journal Bearings," by J. M. Stone and A. F. Underwood, *Quarterly Trans. of the Society of Automotive Engineers*, vol. 1, 1947, pp. 56-67.
- 14 "Fluctuating Loads in Sleeve Bearings," by H. W. Swift, *Journal of The Institution of Civil Engineers*, vol. 5, 1937, pp. 161-195.

Studies in Lubrication—XI

Slider Bearing With Transverse Curvature; Exact Solution¹

By A. S. C. YING,² A. CHARNES,³ AND E. SAIBEL,⁴ PITTSBURGH, PA.

An exact solution is developed for the Reynolds equation in the hydrodynamical theory of slider-bearing lubrication with side leakage for film thickness varying exponentially both in the direction of motion and symmetrically perpendicular to this direction. This solution is in the form of a rapidly convergent series from which calculations for the pressure distribution, total bearing load, frictional force, and so on, may be made conveniently for all length-to-width ratios, all entrance-to-exit clearance ratios, and all center-to-side clearance ratios. The results which were obtained previously by the perturbation method⁵ are shown to be quite accurate for small ratios of center-to-side clearance and, for the larger ratios, the error of the perturbation method is calculated. In fact, the present exact solution turns out to be as convenient to apply as the former approximate one and is recommended for practical consideration.

THEORY

THE usual notation is used, p and p' denote pressure, and h and h' the film thickness. The assumptions made are those which lead to the Reynolds equation⁶ and, although this paper will be concerned with the case of constant viscosity, the results can be applied when the viscosity is a function of pressure.⁷

The Reynolds equation for fluid lubrication is

$$\frac{\partial}{\partial x} \left(h^3 \frac{\partial p}{\partial x} \right) + \frac{\partial}{\partial y} \left(h^3 \frac{\partial p}{\partial y} \right) = 6\mu U \frac{\partial h}{\partial x} \dots \dots \dots [1]$$

$$\text{Assuming } \left. \begin{aligned} h &= ae^{bx}e^{cy} \quad \text{for } y \geq 0 \\ &= ae^{bx}e^{-cy} \quad \text{for } y \leq 0 \end{aligned} \right\} \dots \dots \dots [2]$$

where a , b , and c are known constants determined from the shape of the slider, the equation becomes

¹ This work was supported in part by funds from a contract of the Ordnance Corps, Department of the Army, with Carnegie Institute of Technology.

² Design Engineer, Pittsburgh-Des Moines Company; formerly, Assistant Professor, Department of Mathematics, Carnegie Institute of Technology.

³ Associate Professor, Department of Mathematics, Carnegie Institute of Technology.

⁴ Professor, Department of Mathematics, Carnegie Institute of Technology. Mem. ASME.

⁵ "On the Solution of the Reynolds Equation for Slider-Bearing Lubrication—III," by A. Charnes, E. Saibel, and A. S. C. Ying, Trans. ASME, vol. 75, 1953, pp. 507-513.

⁶ "Lubrication," by A. E. Norton, McGraw-Hill Book Company, Inc., New York, N. Y., 1942.

⁷ "On the Solution of the Reynolds Equation for Slider-Bearing Lubrication—II; The Viscosity a Function of the Pressure," by A. Charnes and E. Saibel, Trans. ASME, vol. 75, 1953, pp. 269-271.

Contributed by the Research Committee on Lubrication under the auspices of the Lubrication Activity of THE AMERICAN SOCIETY OF MECHANICAL ENGINEERS, and presented at the Second Annual ASME-ASLE Lubrication Conference, Indianapolis, Ind., October 10-12, 1955.

NOTE: Statements and opinions advanced in papers are to be understood as individual expressions of their authors and not those of the Society. Manuscript received at ASME Headquarters, March 3, 1955. Paper No. 55-LUB-13.

$$\frac{\partial^2 p}{\partial x^2} + \frac{\partial^2 p}{\partial y^2} + 3b \frac{\partial p}{\partial x} + 3c \frac{\partial p}{\partial y} = \frac{6b\mu U}{a^2} e^{-2bx} e^{-2cy} \text{ for } y \geq 0 \dots [3]$$

$$\frac{\partial^2 p'}{\partial x^2} + \frac{\partial^2 p'}{\partial y^2} + 3b \frac{\partial p'}{\partial x} - 3c \frac{\partial p'}{\partial y} = \frac{6b\mu U}{a^2} e^{-2bx} e^{2cy} \text{ for } y \leq 0 \dots [4]$$

and the boundary conditions are that the pressure is zero on the exterior edge of the slider and that the pressure and the rate of flow in the y -direction are continuous on the common boundary.

SOLUTION

The solution of Equation [3] may be obtained readily as

$$p(x, y) = p_p(x, y) + p_c(x, y) \dots \dots \dots [5]$$

where $p_p(x, y)$ is the particular integral and $p_c(x, y)$ is the complementary function, and they satisfy, respectively, the equations

$$\frac{\partial^2 p_p}{\partial x^2} + \frac{\partial^2 p_p}{\partial y^2} + 3b \frac{\partial p_p}{\partial x} + 3c \frac{\partial p_p}{\partial y} = \frac{6b\mu U}{a^2} e^{-2bx} e^{-2cy} \dots [6]$$

$$\frac{\partial^2 p_c}{\partial x^2} + \frac{\partial^2 p_c}{\partial y^2} + 3b \frac{\partial p_c}{\partial x} + 3c \frac{\partial p_c}{\partial y} = 0 \dots \dots \dots [7]$$

For the particular integral, p_p will be in the form

$$p_p = e^{-2cy} F(x)$$

Substituting this into Equation [6], we have the differential equation for $F(x)$

$$F''(x) + 3bF'(x) - 2c^2F(x) = \frac{6b\mu U}{a^2} e^{-2bx} \dots \dots \dots [8]$$

and its solution is

$$F(x) = -\frac{3b\mu U}{a^2(b^2 + c^2)} (e^{-2bx} - \beta_1 e^{\alpha_1 x} - \beta_2 e^{\alpha_2 x})$$

where

$$\alpha_1 = \frac{1}{2} (-3b + \sqrt{9b^2 + 8c^2})$$

$$\alpha_2 = \frac{1}{2} (-3b - \sqrt{9b^2 + 8c^2})$$

The integration constants β_1 and β_2 are so chosen that p_p will be as simple as possible. This is effected by making $p_p = 0$ at $x = 0$ and $x = B$. Using these boundary conditions we find

$$\left. \begin{aligned} \beta_1 &= \frac{\frac{-bB}{2} - e^{-\frac{\sqrt{9b^2+8c^2}}{2} B}}{\frac{\sqrt{9b^2+8c^2}}{2} B - e^{-\frac{\sqrt{9b^2+8c^2}}{2} B}} \\ \beta_2 &= \frac{\frac{\sqrt{9b^2+8c^2}}{2} B - e^{-\frac{bB}{2}}}{\frac{\sqrt{9b^2+8c^2}}{2} B - e^{-\frac{\sqrt{9b^2+8c^2}}{2} B}} \end{aligned} \right\} \dots \dots \dots [9]$$

and the particular integral is

$$p_p = -\frac{3b\mu U}{a^2(b^2 + c^2)} (e^{-2bx} - \beta_1 e^{\alpha_1 x} - \beta_2 e^{\alpha_2 x}) e^{-2cy} \quad [10]$$

For complementary function p_c , the solution can be put in the following form by separation of variables

$$p_c = e^{-\frac{3bx}{2}} (C \sin ix + D \cos ix) e^{-\frac{3cy}{2}} (E \sinh jy + F \cosh jy)$$

where

$$i = \sqrt{k^2 - \frac{9b^2}{4}} \quad \text{and} \quad j = \sqrt{k^2 - \frac{9c^2}{4}}$$

Since $p = p_p = 0$ and $p_c = 0$ at $x = 0$ and $x = B$, then $D = 0$ and $i = n\pi/B$ which leads to

$$k = \sqrt{\frac{n^2\pi^2}{B^2} + \frac{9b^2}{4}} \quad \left. \begin{array}{l} \text{and} \\ j = \sqrt{\frac{n^2\pi^2}{B^2} + \frac{9(b^2 + c^2)}{4}} = j_n \end{array} \right\} \dots\dots\dots [11]$$

Therefore the general solution is

$$p = -\frac{3b\mu U}{a^2(b^2 + c^2)} (e^{-2bx} - \beta_1 e^{\alpha_1 x} - \beta_2 e^{\alpha_2 x}) e^{-2cy} + e^{-\frac{3bx}{2}} e^{-\frac{3cy}{2}} \sum_{n=1,2,3} \sin \frac{n\pi x}{B} (E_n \sinh j_n y + F_n \cosh j_n y) \quad [12]$$

where E_n and F_n will be determined by the conditions at $y = L/2$ and the common boundary.

From the condition, $p = 0$ at $y = L/2$

$$\sum_{n=1,2,3} \left(E_n \sinh \frac{j_n L}{2} + F_n \cosh \frac{j_n L}{2} \right) \sin \frac{n\pi x}{B} = -\frac{3b\mu U}{a^2(b^2 + c^2)} e^{-\frac{cL}{4}} \left(e^{-\frac{bx}{2}} - \beta_1 e^{\frac{\sqrt{9b^2 + 8c^2}}{2} x} - \beta_2 e^{-\frac{\sqrt{9b^2 + 8c^2}}{2} x} \right) \quad [13]$$

The expression on the right-hand side of Equation [13] vanishes at the edge $x = 0$ and $x = B$. Such a function can be represented by the series

$$\sum_{n=1,2,3} A_n \sin \frac{n\pi x}{B} \quad [14]$$

in which the coefficients A_n are calculated by using the formula

$$A_n = \frac{2}{\beta} \int_0^B \frac{3b\mu U}{a^2(b^2 + c^2)} e^{-\frac{cL}{4}} \left(e^{-\frac{bx}{2}} - \beta_1 e^{\frac{\sqrt{9b^2 + 8c^2}}{2} x} - \beta_2 e^{-\frac{\sqrt{9b^2 + 8c^2}}{2} x} \right) \sin \frac{n\pi x}{B} dx$$

from which it follows that

$$A_n = \frac{6b\mu U}{a^2(b^2 + c^2)B} e^{-\frac{cL}{4}} \left[1 - (-1)^n e^{-\frac{bB}{2}} \right] \frac{2(b^2 + c^2) \frac{n\pi}{B}}{\left(\frac{b^2}{4} + \frac{n^2\pi^2}{B^2} \right) \left(\frac{9b^2 + 8c^2}{4} + \frac{n^2\pi^2}{B^2} \right)} \quad [15]$$

Substituting Equation [14] into Equation [13] and equating the corresponding coefficients for $\sin n\pi x/B$, we have

$$E_n \sinh \frac{j_n L}{2} + F_n \cosh \frac{j_n L}{2} = A_n \dots\dots\dots [16]$$

For the continuity equation at the common boundary, we have to know the pressure distribution p' for $y \leq 0$. This can easily be found by replacing y with $-y$ in Equation [12]

$$p' = -\frac{3b\mu U}{a^2(b^2 + c^2)} (e^{-2bx} - \beta_1 e^{\alpha_1 x} - \beta_2 e^{\alpha_2 x}) e^{2cy} + e^{-\frac{3bx}{2}} e^{\frac{3cy}{2}} \sum_{n=1,2,3} \sin \frac{n\pi x}{B} (-E_n \sinh j_n y + F_n \cosh j_n y) \quad [17]$$

It is obvious that p and p' are symmetrical with respect to y , also $p = p'$ automatically at $y = 0$. The boundary condition remaining to be satisfied is that the rate of flow in y -direction is continuous, i.e.

$$-\frac{h^2}{12\mu} \frac{\partial p}{\partial y} = -\frac{h'^2}{12\mu} \frac{\partial p'}{\partial y}$$

Since $h = h'$ at $y = 0$ (see Equation [2])

$$\frac{\partial p}{\partial y} = \frac{\partial p'}{\partial y} \quad [18]$$

By differentiating Equations [12] and [17] and substituting together with Equation [15] into Equation [18], we find

$$E_n j_n - \frac{3c}{2} F_n = -2ce^{\frac{cL}{4}} A_n \dots\dots\dots [19]^*$$

From Equations [16] and [19], we find

$$\left. \begin{array}{l} E_n = \frac{\frac{3c}{2} - 2ce^{\frac{cL}{4}} \cosh \frac{j_n L}{2}}{j_n \cosh \frac{j_n L}{2} + \frac{3c}{2} \sinh \frac{j_n L}{2}} A_n \\ F_n = \frac{j_n + 2ce^{\frac{cL}{4}} \sinh \frac{j_n L}{2}}{j_n \cosh \frac{j_n L}{2} + \frac{3c}{2} \sinh \frac{j_n L}{2}} A_n \end{array} \right\} \dots\dots\dots [20]$$

The final solution is Equation [12] for $y \geq 0$ and Equation [17] for $y \leq 0$ with α_1, α_2 given by Equation [8], β_1, β_2 by Equation [9], E_n, F_n by Equation [20], j_n by Equation [11], and A_n by Equation [15].

PERFORMANCE CHARACTERISTICS

The characteristics treated in the present paper are (a) total load and (b) the total frictional force. Other characteristics such as center of pressure, oil flow, etc., can be obtained from the known pressure distribution.

(a) *Total Load.* Making the customary assumption, namely, that the slope of the slider is small and that consequently the vertical component of the pressure against the slider is equal to the pressure itself, we have

* The same equation can be obtained by setting $\frac{\partial p}{\partial y} = 0$. This follows from the symmetry $\left(\frac{\partial p}{\partial y} = -\frac{\partial p'}{\partial y} \right)$ and continuity $\left(\frac{\partial p}{\partial y} = \frac{\partial p'}{\partial y} \right)$ properties.

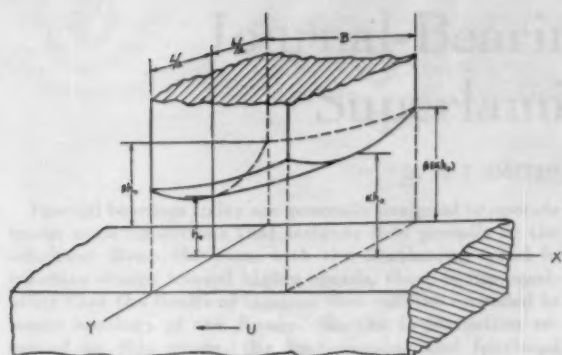


FIG. 1

$$W = 2 \int_{y=0}^{y=L/2} \int_{x=0}^{x=B} p \, dx \, dy$$

where p is given by Equation [12]. The result is

$$W = -\frac{6b\mu U}{\alpha(b^2 + c^2)} \left(\frac{1 - e^{-2bB}}{2b} + \beta_1 \frac{1 - e^{\alpha_1 B}}{\alpha_1} + \beta_2 \frac{1 - e^{\alpha_2 B}}{\alpha_2} \right) \frac{1 - e^{-cL}}{2c} + 2 \sum_{n=1,2,3}^{\infty} \frac{\frac{n\pi}{B}}{\frac{9b^2}{4} + \left(\frac{n\pi}{B}\right)^2} \frac{1 - (-1)^n e^{-\frac{3bB}{2}}}{\frac{9c^2}{4} - j_n^2} \left\{ e^{-\frac{3cL}{4}} \left[-\frac{3c}{2} A_n - j_n \left(E_n \cosh \frac{j_n L}{2} + F_n \sinh \frac{j_n L}{2} \right) \right] + E_n j_n + \frac{3c}{2} F_n \right\} \dots [21]$$

(b) Total Frictional Force. If S_x is the shearing stress component in the x -direction

$$S_x = \frac{\mu U}{h} + \frac{h}{2} \frac{\partial p}{\partial x}$$

and

$$F = 2 \int_{y=0}^{y=L/2} \int_{x=0}^{x=B} S_x \, dx \, dy$$

The evaluation of F can be simplified using integration by parts as follows

$$F = 2 \int_{y=0}^{y=L/2} \int_{x=0}^{x=B} \frac{\mu U}{h} \, dx \, dy + \int_{y=0}^{y=L/2} \int_{x=0}^{x=B} h \frac{\partial p}{\partial x} \, dx \, dy$$

$$= 2 \int_{y=0}^{y=L/2} \int_{x=0}^{x=B} \frac{\mu U}{h} \, dx \, dy + \int_{y=0}^{y=L/2} \left(h p \Big|_0^B - \int_{x=0}^{x=B} p \frac{\partial h}{\partial x} \, dx \right) \\ = 2 \int_{y=0}^{y=L/2} \int_{x=0}^{x=B} \frac{\mu U}{h} \, dx \, dy + \int_{y=0}^{y=L/2} \int_{x=0}^{x=B} p \frac{\partial h}{\partial x} \, dx \, dy$$

knowing $p = 0$ at $x = 0$ and $x = B$.

With $h = \alpha e^{b_1 x} e^{c y}$ for $y = 0$ the result is

$$F = \frac{\mu U (2c^3 + 5b^3)}{\alpha(b^2 + c^2)} \frac{1 - e^{-bB}}{b} \frac{1 - e^{-\frac{cL}{2}}}{c} \\ + \frac{3b^2 \mu U}{\alpha(b^2 + c^2)} \left[\beta_1 \frac{1 - e^{(\alpha_1 + b)B}}{\alpha_1 + b} + \beta_2 \frac{1 - e^{(\alpha_2 + b)B}}{\alpha_2 + b} \right] \frac{1 - e^{-\frac{cL}{2}}}{c} \\ - \sum_{n=1,2,3}^{\infty} \frac{ab \frac{n\pi}{B}}{\frac{b^2}{4} + \left(\frac{n\pi}{B}\right)^2} \frac{1 - (-1)^n e^{-\frac{bB}{2}}}{\frac{c^2}{4} - j_n^2} \\ \left\{ e^{-\frac{cL}{4}} \left[-\frac{c}{2} A_n - j_n \left(E_n \cosh \frac{j_n L}{2} + F_n \sinh \frac{j_n L}{2} \right) \right] + E_n j_n + F_n \frac{c}{2} \right\} \dots [22]$$

NUMERICAL EXAMPLE

As a comparison of results with those from the approximate method, we calculate the total load and total frictional force for a square ($L = B$) slider having a ratio (α) of film thickness at entrance to exit of 2 (see Fig. 1) and various ratios (β) of side-to-center clearances. The results are listed in Tables 1 and 2 together with those from the perturbation method. The percentage of error for the latter method is seen to increase as β increases. This is to be expected.

TABLE 1

$\beta =$	Exact \bar{W} (present paper)	Approximate \bar{W} (perturbation method)	Per cent error
1.00	0.01130 $\frac{6\mu UB^2}{h_0^3}$	0.01130 $\frac{6\mu UB^2}{h_0^3}$	0
1.02	0.01110	0.01109	-0.09
1.20	0.00963	0.00914	-5.10
1.50	0.00719	0.00652	-9.35

TABLE 2

$\beta =$	Exact F (present paper)	Approximate F (perturbation method)	Per cent error
1.00	0.1259 $\frac{6\mu UB^2}{h_0^3}$	0.1259 $\frac{6\mu UB^2}{h_0^3}$	0
1.02	0.1250	0.1250	0
1.20	0.1130	0.1180	2.61
1.50	0.1028	0.1074	4.48

Journal-Bearing Operation at Superlaminar Speeds

By M. I. SMITH¹ AND D. D. FULLER²

Journal bearings today are generally designed to operate under such conditions that laminar flow prevails in the lubricant film. However, with the continuing trend in machine design toward higher speeds, there is the possibility that the limits of laminar flow may be exceeded in many bearings of the future. In the investigation reported in this paper, the load-carrying and frictional characteristics of a journal bearing were studied at speeds ranging up to five times the critical speed. The "critical speed" is defined as that rotational velocity which just causes breakdown of laminar flow.

NOMENCLATURE

The following nomenclature is used in the paper:

- c = radial clearance, in.
- D = bearing diam, in.
- f = coefficient of friction, dimensionless
- h = film thickness, in.
- K, K' = constants, dimensionless
- L = bearing length, in.
- m = clearance ratio, mils/in.
- N = speed, rpm
- p = pressure, psi
- P = load per unit projected area, psi
- q = flow rate per unit width, in³/sec
- r = bearing radius, in.
- Re = Reynolds number, dimensionless
- U = journal velocity, in/sec
- x = linear co-ordinate in direction of motion, in.
- ϵ = eccentricity ratio, dimensionless
- ρ = lubricant mass density, lb sec²/in.⁴
- μ = lubricant viscosity, reyns, lb sec/in.²
- μ' = lubricant viscosity, centipoises, dyne sec/cm²
- ν = kinematic viscosity, centistokes
- θ = angular co-ordinate measured from point of maximum film thickness
- τ = shear stress, psi
- ϕ = attitude angle

INTRODUCTION

In one of the very few instances in which hydrodynamic theory has been applied successfully to predict breakdown or instability of laminar flow, Taylor analyzed the fluid motion in the annular film between rotating concentric cylinders (1).³ For the case of an

unloaded journal bearing, Taylor's instability criterion may be given in the form of a critical Reynolds number

$$Re_{cr} = \frac{\rho U_{cr} c}{\mu} = 41.1 \sqrt{\frac{r}{c}} \quad [1]$$

In terms of the usual dimensions employed in the lubrication literature, the critical speed in rpm is given by

$$N_{cr} = 77,400 \frac{\nu}{m^{3/2} D} \quad [2]$$

These relations were confirmed quite well by Wilcock (2), who noted anomalous increases in the frictional torque developed in relatively lightly loaded journal bearings above this critical speed. Taylor observed visually that at speeds in excess of the critical value, the flow in the cylindrical annulus assumed a regular vortex pattern which persisted over some range before degenerating into a truly turbulent motion. The frictional characteristics were such as to suggest that the vortical flow corresponded to the "transition" region found in other systems between the laminar and turbulent-flow regimes, such as, for example, in pipe flow (3).

THEORETICAL ANALYSIS OF TURBULENCE

The performance characteristics of bearings are usually deduced from Reynolds differential equation

$$\frac{\partial}{\partial x} \left[h^3 \frac{\partial p}{\partial x} \right] + \frac{\partial}{\partial z} \left[h^3 \frac{\partial p}{\partial z} \right] = 6\mu U \frac{dh}{dx} \quad [3]$$

This is derived from the equations of continuity and Navier-Stokes, and assumes the existence of laminar flow in the lubricant film.

Sommerfeld's simplified analysis (4) neglected the influence of axial flow and permitted the pressure gradient to be expressed as

$$\frac{dp}{dx} = 6\mu U \frac{h - h^*}{h^3} \quad [4]$$

where h^* is the film thickness at the position of maximum pressure.

This latter relation results from the formal manipulation of the basic laminar equations. However, in such a development, it may be shown that the flow of lubricant may be considered to be due to the additive effects of a pure shear flow, upon which is superimposed a flow due to a pressure gradient in a fixed-walled passage.

In attempting to evolve an expression similar to Equation [4] applying to the turbulent regime, it was not found possible to proceed along the formal lines employed previously, since the equations of turbulent motion contain so-called Reynolds stresses, which are unknown quantities requiring empirical data for evaluation. Therefore the foregoing principle of superposition was assumed; i.e., it was assumed that the flow of lubricant could be attributed to the separate effects of a turbulent shear and a pressure flow. That the shear component of flow is no longer laminar above a critical speed could be accepted from the previously cited work of Taylor and Wilcock. The critical question then arose: What is the nature of the pressure flow compo-

¹ Technical Service Laboratory, Socony Mobil Oil Company, Brooklyn, N. Y.; former graduate student, Department of Mechanical Engineering, Columbia University, New York, N. Y.

² Professor of Mechanical Engineering, Columbia University, New York, N. Y.; The Franklin Institute Laboratories for Research and Development, Philadelphia, Pa.

³ Numbers in parentheses refer to the Bibliography at the end of the paper.

Contributed by the Lubrication Activity Committee and presented at the ASME-ASLE Second Lubrication Conference, Indianapolis, Ind., October 10-12, 1955.

NOTE: Statements and opinions advanced in papers are to be understood as individual expressions of their authors and not those of the Society. Manuscript received at ASME Headquarters, September 15, 1955. Paper No. 55-LUB-26.

nent at supercritical Reynolds numbers? There appeared to be no way of drawing upon earlier theory to predict definitely whether it would remain laminar, or whether it, too, would become unstable and break into turbulence. If it did, in fact, retain its laminar characteristics, then Equation [4] would be valid, and the load-carrying capacity of the supercritical bearing would be essentially that of a laminar one, although friction would be expected to be higher due to the turbulent shear flow. On the other hand, what sort of performance might result from the pressure flow becoming turbulent? This possibility had not been analyzed up to the present time and, in order to study a bearing critically in the laboratory, a theory based upon turbulence of the pressure component was developed. The performance of the bearing was then expected to indicate definitely the actual nature of the pressure flow.

Concerning the shear component of flow, it might be noted that a turbulent shear-velocity profile has not yet been defined without the introduction of empirical constants, thus far undetermined (5). However, for the purpose at hand, it is necessary to know merely the flow rate attributable to shear alone. Since this flow must be symmetrical about the channel mid-point, the rate is the same as that under laminar-flow conditions

$$q_s = \frac{U h}{2} \quad [5]$$

In a pressure flow in a passage, the pressure gradient under turbulent conditions is proportional to the average cross-sectional velocity raised to a power approaching 2, as compared to the value of this exponent of unity for laminar flow. Taking, then, the gradient as proportional to the average velocity squared

$$\frac{dp}{dx} = -\frac{K}{h} \frac{\rho u_{avg}^2}{2} \quad [6]$$

where the negative sign indicates that the pressure decreases in the direction of mean motion. The quantity of flow attributable to the pure pressure effect is

$$q_p = u_{avg} h \quad [7]$$

Neglecting side leakage, continuity of flow demands that

$$q_s + q_p = \text{const} = \frac{U}{2} h^* \quad [8]$$

These equations lead to the relations for the turbulent pressure gradients in a bearing

$$\left. \begin{aligned} \frac{dp}{dx} &= K' \rho U^2 \frac{(h - h^*)^2}{h^3}, & h > h^* \\ \frac{dp}{dx} &= -K' \rho U^2 \frac{(h - h^*)^2}{h^3}, & h < h^* \end{aligned} \right\} \quad [9]$$

K' represents $K/4$ and is an empirical constant. Equation [9] was solved for a journal bearing, where

$$h = c[1 + \epsilon \cos \theta] \quad [10]$$

The boundary conditions imposed were those of the "half Sommerfeld" solution derived by Gumbel for laminar operation (6). That is, the arc of positive pressure was taken to extend over the region $0 \leq \theta \leq \pi$, while the remainder of the film was assumed to be at atmospheric pressure. Comparisons of the turbulent bearing were drawn with Gumbel's laminar solution.

As a result of this analysis, there emerged three outstanding differences between turbulent and laminar pressure films.

1 Although the empirical constant K remained in the pressure equation, it was found that the turbulent pressure profile at a

given eccentricity ratio was much flatter than the sharply peaked profile characteristic of laminar flow.

Turbulent pressure variation

$$\begin{aligned} p &= K \rho U^2 \frac{r}{c} \frac{\epsilon^2}{2 \sqrt{1 - \epsilon^2}} \left[\text{arc cos} \frac{\cos \theta + \epsilon}{1 + \epsilon \cos \theta} \right. \\ &\quad \left. + \frac{\sin \theta (\cos \theta + \epsilon) \sqrt{1 - \epsilon^2}}{(1 + \epsilon \cos \theta)^2} \right], \quad 0 \leq \theta \leq \theta^* \\ p &= K \rho U^2 \frac{r}{c} \frac{\epsilon^2}{2 \sqrt{1 - \epsilon^2}} \left[\pi - \text{arc cos} \frac{\cos \theta + \epsilon}{1 + \epsilon \cos \theta} \right. \\ &\quad \left. - \frac{\sin \theta (\cos \theta + \epsilon) \sqrt{1 - \epsilon^2}}{(1 + \epsilon \cos \theta)^2} \right], \quad \theta^* \leq \theta \leq \pi \dots [11] \end{aligned}$$

Here θ^* is the angle corresponding to the position of maximum pressure, and is given by

$$\cos \theta^* = -\epsilon \dots [12]$$

Laminar pressure variation

$$p = \frac{6 \mu U r}{c^2} \frac{\epsilon (2 + \epsilon \cos \theta) \sin \theta}{(2 + \epsilon^2)(1 + \epsilon \cos \theta)^2} \dots [13]$$

2 An exact expression could be obtained to describe the eccentricity locus of a turbulent bearing. At a given eccentricity, the attitude angle measured between the line of centers and load line in the direction of rotation was smaller than that of laminar operation.

Turbulent locus

$$\tan \phi = \frac{2(\text{arc sin } \epsilon - \epsilon \sqrt{1 - \epsilon^2})}{\log_e (1 - \epsilon^2) + \epsilon^2} \dots [14]$$

Laminar locus

$$\tan \phi = -\frac{\pi \sqrt{1 - \epsilon^2}}{2\epsilon} \dots [15]$$

3 The foregoing two factors placed a turbulent pressure film in a much better position to support an applied load, so that the load-carrying capacity was indicated as being considerably superior to that of a similar bearing which maintained laminar flow in the film under the same conditions of operation.

Turbulent load-carrying capacity

$$\frac{P}{K \rho N^2 r^3} \left(\frac{c}{r} \right) = \frac{\pi^2 (\text{arc sin } \epsilon - \epsilon \sqrt{1 - \epsilon^2})}{900 \sin \phi} \dots [16]$$

Laminar load-carrying capacity

$$\frac{P}{\mu N} \left(\frac{c}{r} \right)^3 = \frac{\pi^2 \epsilon}{10(2 + \epsilon^2) \sqrt{1 - \epsilon^2} \sin \phi} \dots [17]$$

$\sin \phi$ is most easily evaluated for a given value of ϵ from Equations [14] and [15], respectively.

With these points serving as a guide for comparison, the behavior of a journal bearing was then observed in the laboratory.

DESCRIPTION OF APPARATUS

The apparatus was designed with the object of attaining a fairly low critical speed, while holding power losses to reasonable values. Several methods might have been employed to measure the thickness of the lubricant film. The simplest, and one which lends itself to a high degree of precision, is the measurement of displacement of a "floating" bearing, corrected for the deflection of the journal produced by the load.

A lubricant of low kinematic viscosity was required to depress

the critical speed. Since load was never applied until the shaft was in motion, "lubricity" in the lubricant was of secondary importance. Consequently, water was used as the test lubricant. In addition to its low viscosity, water possessed an additional advantage in that its fairly good viscosity index and high specific heat minimized the error in the estimate of average film viscosity, which is a function of temperature. This is a factor which is generally troublesome to define in any lubrication study.

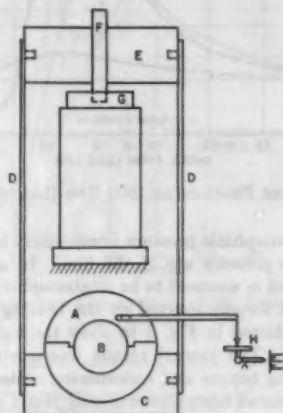


FIG. 1 SCHEMATIC DIAGRAM OF APPARATUS

A 3-in. \times 3-in. bronze bearing (A in Fig. 1) of split construction was employed. The shaft (B) was stainless steel. Lubricant was introduced through a single $\frac{1}{8}$ -in. hole in the bearing crown. The clearance ratio was 2.93 mils per in., a value which was calculated to remain constant under the conditions prevailing during operation. The shaft was supported at either end by rolling-contact bearings, and was driven through belted pulleys by a $\frac{1}{2}$ -hp variable-speed d-c motor.

Load was applied hydraulically to the test bearing through a hydrostatic shoe (C), which was suspended by thin straps (D) from a yoke (E). A ball bearing (F), positioned at the center of the yoke, was seated in the piston (G). Delivery of high-pressure water at the shoe-bearing interface effectively "floated" the bearing, so that the frictional torque developed could be counterbalanced on a laboratory-platform balance (H) without interference from the loading mechanism.

Displacement of the bearing was measured by two air gages which were positioned against the outer periphery of the bearing, each at a 45-deg angle with the load line. The combination of "Plunjet" air-gage heads and rotameter provided an amplification factor of 2000:1. The gage readings at each increment of load were referred to the concentric no-load positions, and corrected for journal deflection to enable calculation of eccentricity and attitude angle. The maximum estimated error in eccentricity ratios measured in duplicate runs amounted to ± 0.02 . Where whirling of the unloaded bearing occurred at high speeds, extrapolation of the gage readings was necessary to establish the concentric position, and then the maximum estimated error increased to ± 0.035 .

Film pressures along the median plane were obtained by means of five taps which were connected by flexible plastic tubing to a manifold and thence to a pair of pressure gages. Provision was made to rotate the bearing enabling the pressure to be recorded in increments of $7\frac{1}{2}$ deg over an arc of 255 deg.

Accurate measurements of film temperatures to permit estimation of average viscosity are extremely difficult to make. It was

arbitrarily assumed in this work that the average temperature in the film was the arithmetic mean of the inlet and outlet temperatures. The latter was calculated from the power loss in the bearing, lubricant flow rate, and thermal gradients in the bronze. At the highest speed investigated, an error not exceeding 6 per cent may have been made in the viscosity calculated in this manner. This limit of uncertainty is much smaller than that encountered in subjecting viscous lubricants of lower specific heat to high rates of shear.

FRICTIONAL CHARACTERISTICS AT NO LOAD

The frictional characteristics of the unloaded bearing were used as the criterion to determine the mode of flow in the lubricant film. Under laminar-flow conditions, the shear stress is given by

$$\tau = \mu \frac{U}{c} \quad [18]$$

The shear stress may be defined in a manner similar to that commonly employed in other fields of fluid dynamics

$$\tau = f \frac{\rho U^2}{2} \quad [19]$$

Here f is a coefficient of friction and is a function of the Reynolds number. In the laminar bearing

$$f = \frac{2\mu}{\rho UC} = \frac{2}{Re} \quad [20]$$

In turbulent flow, the coefficient of friction is related to the Reynolds number by the function

$$f = \frac{\text{const}}{Re^b}, \quad 0 < b < 1 \quad [21]$$

Fig. 2 presents a log-log plot of experimental data for f (calculated from $f = \text{torque}/\pi \rho U^2 r^2 L$) versus the Reynolds number. The form of the graph is similar to those commonly observed in other fluid systems, in that regions of laminar, "transition," and turbulent flow were quite sharply delineated. Taylor's calculated critical Reynolds number is indicated on the graph, and it is seen that it is actually very close to the point of departure from laminar behavior, as observed by test. The constants of Equation [21] were evaluated in the turbulent region at no load, so that the coefficient of friction could be expressed as

$$f = \frac{0.078}{Re^{0.43}} \quad [22]$$

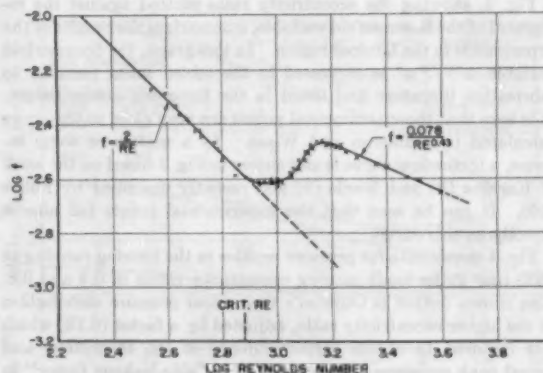


FIG. 2 FRICTION AS A FUNCTION OF REYNOLDS NUMBER (UNLOADED BEARING)

Actually, for the four highest values of Reynolds number, it was found necessary to load the bearing slightly in order to suppress whirling, and the points shown on the graph were obtained by extrapolation to zero load.

With the assurance that the coefficient of friction of the concentric (unloaded) bearing afforded a clear indication of the mode of flow in the lubricant film, the performance of the loaded bearing was studied.

PERFORMANCE AT SUBCRITICAL REYNOLDS NUMBERS (LAMINAR CONDITIONS)

The bearing was run at 900, 1300, and 1800 rpm, corresponding to 0.47, 0.68, and 0.94 of Taylor's critical speed. In this region, bearing theory has been well developed, and operation has been observed by many investigators. This study included the laminar region in order to determine the degree of conformance of the bearing with laminar theory and to develop a degree of confidence in the data obtained from the test machine. The work of Cameron and Wood probably represents the most complete mathematical analysis of the 360-deg finite journal bearing (7), and their results were used as the basis for comparison. The simplified analysis of Gümbel, in which side leakage is neglected, also was used for comparative purposes.

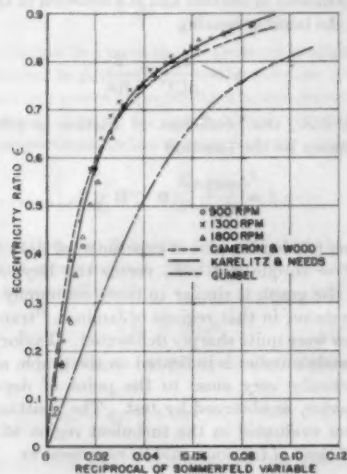


FIG. 3 Load-Carrying Capacity in the Laminar Region

Fig. 3, showing the eccentricity ratio plotted against the reciprocal of the Sommerfeld variable, summarizes the results of the experiments in the laminar region. In this graph, the Sommerfeld variable $\mu'N/Pm^2$ is expressed in the mixed units peculiar to lubrication literature and listed in the foregoing nomenclature. It is seen that the experimental points are very close to the curve calculated by Cameron and Wood. As a matter of some interest, a theoretical curve is also shown in Fig. 3 based on the work of Karelitz (8) and Needs (9) and recently described by Fuller (10). It can be seen that the experimental points fall almost directly on this curve.

Fig. 4 shows data for pressure profiles in the bearing running at 1800 rpm under loads causing eccentricity ratios of 0.4 and 0.8. Also shown dotted is Gümbel's theoretical pressure distribution at the higher eccentricity ratio, adjusted by a factor (0.78) which was required to obtain correspondence of the theoretical and actual peak pressures. Reduced by the "side-leakage factor" in this manner, the theoretical curve closely approximated the actual pressure profile. The greatest variation was found in the

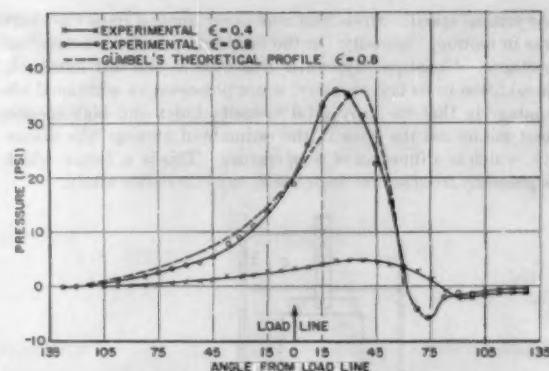


FIG. 4 Pressure Profiles at 1800 RPM (Laminar Operation)

region of subatmospheric pressure immediately behind the trailing edge of the pressure arc of the film. In analytical treatments, this region is assumed to be at atmospheric pressure.

The frictional torques exerted on the bearing and journal at 1800 rpm are plotted in Fig. 5 to show the variation with eccentricity ratio. The journal torque was calculated from the measured bearing torque and eccentricity. Also shown dotted are curves calculated from Cameron and Wood's analysis. The frictional behavior of the test bearing conformed quite closely to that predicted.

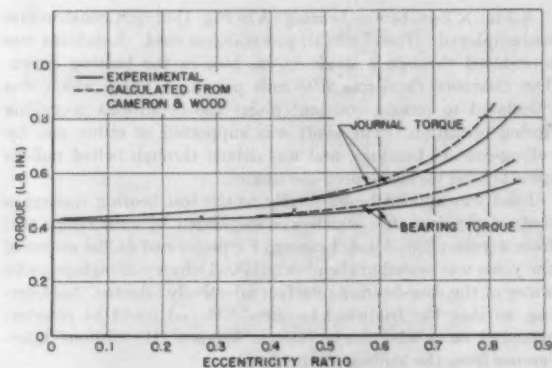


FIG. 5 Frictional Torque at 1800 RPM (Laminar Operation)

PERFORMANCE AT SUPERCRITICAL REYNOLDS NUMBERS

The bearing was run at a somewhat higher temperature and at eight speeds, ranging from 2400 to 7450 rpm, with the latter representing 5.17 times the critical speed calculated from Equation [2].

Eccentricity ratio-load curves at 3000 and 7450 rpm are drawn in Figs. 6 and 7, together with the theoretical laminar curves calculated for the finite (Cameron and Wood) and infinite (Gümbel) journal bearing. At speeds somewhat beyond the critical value, the former theoretical laminar treatment described load-carrying capacity very well. With increasing speed, there was a drift toward the behavior of the infinite laminar bearing. There was, however, no approach to the vast increase in load-carrying capacity which would have resulted from a turbulent-pressure flow in the lubricant film.

Pressure readings along the median plane at eccentricity ratios of 0.8 at these two speeds are given in Fig. 8. Also shown dotted

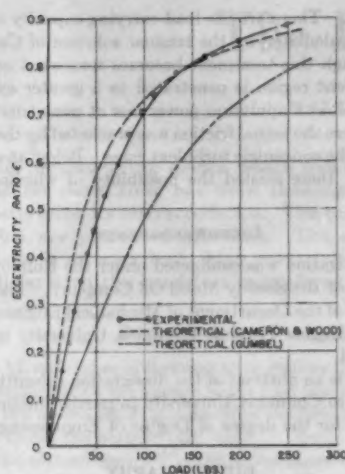


FIG. 6 Load-Carrying Capacity at 3000 RPM (SUPERLAMINAR OPERATION)

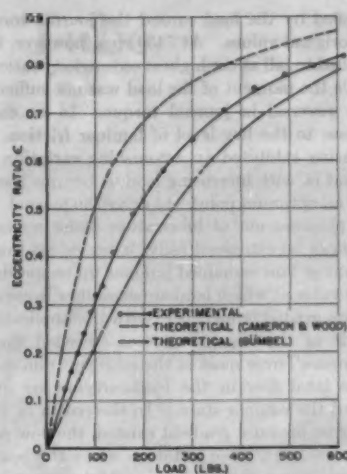


FIG. 7 Load-Carrying Capacity at 7450 RPM (SUPERLAMINAR OPERATION)

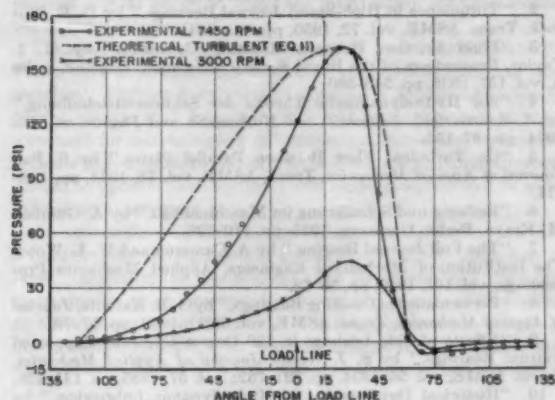
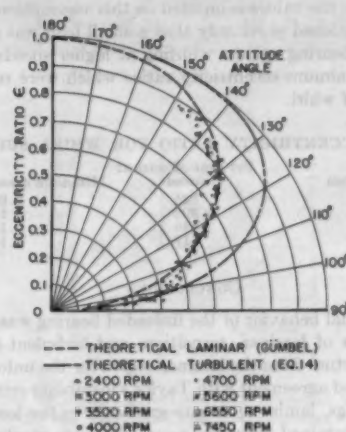
FIG. 8 Pressure Profiles for Operating Conditions Above the Critical Speed ($\epsilon = 0.8$)

FIG. 9 Eccentricity Loci for Operating Conditions Above the Critical Speed

is the theoretical turbulent profile calculated from Equation [11] and adjusted to have the same peak value as that recorded at the higher speed. It is readily apparent that the sharply peaked profile characteristic of laminar-pressure flow was maintained despite the turbulence of the shear component of flow. Indicative of the somewhat greater load-carrying capacity at higher speeds, the maximum pressure measured at 3000 rpm was 75 per cent of Gumbel's theoretical maximum value, whereas 109 per cent was recorded at 7450 rpm.

Points taken at all eight supercritical speeds are plotted in the polar diagram of Fig. 9, where the theoretical turbulent and laminar eccentricity loci calculated from Equations [14] and [15], respectively, are also shown. In this respect, too, the bearing performed in laminar fashion.

The frictional torques exerted on the bearing and journal at 3000, 4700, and 7450 rpm are shown in Fig. 10. Also tabulated for comparison are the no-load torques which would have been developed, had laminar flow prevailed in the film. It is seen that the initially high friction at light load was greatly reduced by the imposition of load. At the lowest speeds, the bearing torques leveled off at high eccentricity ratios, while the compensating

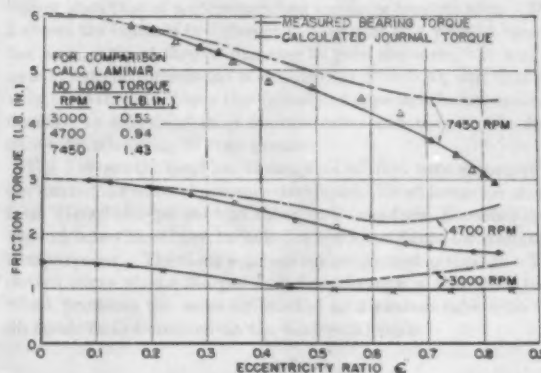


FIG. 10 Friction Torque for Operating Conditions Above the Critical Speed

moments applied by the load caused the journal torques to return to their original values. At 7450 rpm, however, the bearing torque continued to fall at the highest eccentricity ratio which was attained, while the moment of the load was not sufficiently great to cause any reversal in journal torque. In no case did the torque decrease to the low level of laminar friction. Thus the turbulent bearing exhibited an astonishing variation of friction with load; that is, with increasing load, it became less difficult—at least up to an optimum point—to drive the journal.

While the phenomenon of lubrication under nonlaminar-flow conditions cannot be explained fully, it is evident that the pressure component of flow remained laminar up to speeds exceeding five times the value at which laminar shear flow became unstable. As the pressure gradients increased with the application of load, the magnitude of the viscous stresses exceeded the turbulent "Reynolds stresses" over most of the lubricant film cross section. Therefore the total flow in the load-carrying arc of the bearing approached the laminar state. In the crown of the bearing, where little or no pressure gradient existed, the flow probably remained turbulent. In those instances where the bearing torque attained virtually constant values at high eccentricity ratios, calculations of friction were carried out, assuming a pure laminar flow in the converging arc of the film and a turbulent flow in the diverging half. It was found that the actual friction was somewhat less than the values computed on this assumption.

It was mentioned previously that a small load was required to stabilize the bearing against whirling at higher speeds. Table 1 shows the minimum eccentricity ratios which were required for suppression of whirl.

TABLE 1 ECCENTRICITY RATIO FOR WHIRL SUPPRESSION

Speed, rpm	Per cent of critical speed	Minimum eccentricity ratio
4700	325	0.07
5500	392	0.10
6550	446	0.12
7450	517	0.13

CONCLUSIONS

The frictional behavior of the unloaded bearing was such as to define regions of laminar, transition, and turbulent flow. The point of departure from the laminar region for the unloaded bearing was in good agreement with Taylor's instability criterion. For loaded bearings, laminar pressure gradients in the load-carrying film were maintained to speeds some five times greater than the

critical speed. Therefore the load-carrying capacity of the bearing could be calculated by the laminar solution of Cameron and Wood, although this treatment becomes somewhat conservative as the turbulent region is penetrated to a greater extent. The bearing exhibited a minimum power loss at eccentricity ratios of 0.6 to 0.8, where the actual friction was bracketed by the calculated laminar and the concentric turbulent cases. Below an eccentricity ratio of 0.15, there existed the possibility of whirling at higher speeds.

ACKNOWLEDGMENTS

This investigation was conducted under the Employee Educational Grant of the Socony Mobil Oil Company. The assistance of the faculty of the Department of Mechanical Engineering and of the Eugene Higgins Trust at Columbia University is gratefully acknowledged.

This paper is an abstract of the dissertation submitted by Melvin I. Smith to Columbia University in partial fulfillment of the requirements for the degree of Doctor of Engineering Science.

BIBLIOGRAPHY

- 1 "Stability of a Viscous Liquid Contained Between Two Rotating Cylinders," by G. I. Taylor, *Trans. of the Royal Society of London, England, series A*, vol. 223, 1923, pp. 289-343.
- 2 "Turbulence in High-Speed Journal Bearings," by D. F. Wilcock, *Trans. ASME*, vol. 72, 1950, pp. 825-834.
- 3 "Fluid Friction Between Rotating Cylinders," by G. I. Taylor, *Proceedings of the Royal Society of London, England, series A*, vol. 157, 1936, pp. 546-560.
- 4 "Zur Hydrodynamische Theorie der Schmiermittelreibung," by A. Sommerfeld, *Zeitschrift für Mathematik und Physik*, vol. 50, 1904, pp. 97-155.
- 5 "On Turbulent Flow Between Parallel Plates," by S. Pai, *Journal of Applied Mechanics*, *Trans. ASME*, vol. 75, 1953, pp. 109-114.
- 6 "Reibung und Schmierung im Maschinenbau," by A. Gümbel, M. Krayn, Berlin, Germany, 1925, pp. 110-126.
- 7 "The Full Journal Bearing," by A. Cameron and W. L. Wood, *The Institution of Mechanical Engineers, Applied Mechanics Proceedings*, vol. 161, 1949, pp. 59-72.
- 8 "Performance of Oil-Ring Bearings," by G. B. Karelitz, *Journal of Applied Mechanics*, *Trans. ASME*, vol. 52(1), 1930, pp. 57-70.
- 9 "Effects of Side Leakage in 120-Degree Centrally Supported Journal Bearings," by S. J. Needs, *Journal of Applied Mechanics*, *Trans. ASME*, vol. 56, 1934, pp. 721-732; vol. 57, 1935, pp. 135-138.
- 10 "Historical Development of Hydrodynamic Lubrication," by D. D. Fuller, published as part of "Fundamentals of Friction and Lubrication in Engineering," by the American Society of Lubrication Engineers, 1954, 196 pp.

The Dall Flow Tube

By I. O. MINER,¹ PROVIDENCE, R. I.

A primary flowmetering device which has been in use in England for some time has been thoroughly investigated to determine its characteristics. The results of this investigation are presented herewith. The outstanding characteristic is an amazingly high metering differential in comparison with the head loss engendered.

INTRODUCTION

SEVERAL new types of flow-metering devices have appeared in literature or on the market in the past few years. One of these is a device which is a modified venturi tube produced in England under the name, "Dall Tube."² Some claims made for this device seemed contrary to the performance that would be expected from theoretical considerations. The company by which the author is employed has made a comprehensive study of this new type of flowmetering primary element, and it is the purpose of this paper to make the information obtained available to those interested.

Tests were conducted in an industrial hydraulic laboratory.³ Flows were determined by calibrated volumetric tanks and stop watches. Further description of the tests is deemed unnecessary except to say that large-bore inverted hook-gage manometers were used for measuring low differential pressures, and test results indicate that technique and care were adequate in nearly all cases. Actual test points have been included on most curves to give some indication of accuracy.

An examination of the Dall flow tube gives the impression that a fluid flowing through it will be subject to a very high loss of head. Actually, the loss is lower than for any other known primary device which operates by developing pressures dependent on the acceleration of the fluid. Those experienced in the art of flow measurement are even more amazed at the remarkably low pressure drop caused by a Dall flow tube than are the uninitiated.

OPERATION OF DALL FLOW TUBE

Fig. 1 shows a cross section through a typical Dall flow tube. Note that the flow first strikes a dam at *a*, which would be expected to increase the head loss. There is a narrow cylindrical section on either side of the throat slot. Therefore, after the flow passes through the inlet cone it encounters a sharp edge at *b* and then another sharp edge at *c*. The flow next has to traverse the open throat slot, after which it strikes two more sharp edges, *d* and *e*. At point *f* the flow undergoes sudden enlargement to the pipe diameter. The cones are steep in addition to being truncated, and the whole device is only about 2 diameters long. The recovery cone has an included angle of about 15 deg. There are no graceful curves as in venturi tubes, nozzles, and other devices

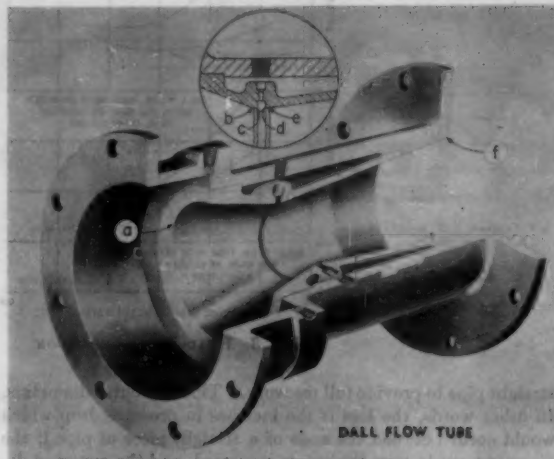


FIG. 1 DALL FLOW TUBE

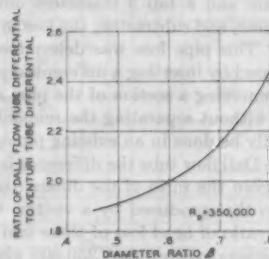


FIG. 2 RATIO OF DALL-FLOW-TUBE DIFFERENTIAL TO HERSCHEL-TYPE VENTURI-TUBE DIFFERENTIAL

which are intended to accelerate or decelerate a fluid with minimum loss.

The differential pressure produced by a Dall flow tube is much higher than that of a corresponding nozzle or venturi tube. Fig. 2 shows the increase in differential over that of a venturi tube of the same ratio of throat diameter to pipe diameter. It will be noted that the differential is doubled for $\beta = 0.60$, and that for very large throats, where the velocity of approach factor causes a decrease in effectiveness of venturi tubes and nozzles, the Dall flow-tube advantage is even greater.

Fig. 3 shows the head loss through a Dall flow tube expressed in per cent of differential pressure developed. Head losses for short-form Herschel-type venturi tubes and long-form Herschel-type venturi tubes have been included in the same figure for comparative purposes. The three solid curves are plotted against β . The dotted curve shows the per cent loss through a Dall flow tube which produces the same differential as a venturi tube with the diameter ratio indicated on the horizontal scale.

HEAD LOSS

The head-loss figures throughout this paper indicate the loss caused by a differential producer when it is followed by sufficient

¹ Vice-President in Charge of Engineering, Builders-Providence, Inc., Division of B-I-F Industries (Formerly, Builders Iron Foundry). Mem. ASME.

² Made by George Kent Ltd., Luton, Bedfordshire, England.

³ B-I-F Industries, Inc., Providence, R. I.

Contributed by the Research Committee on Fluid Meters and presented at the Annual Meeting, New York, N. Y., November 28-December 3, 1954, of THE AMERICAN SOCIETY OF MECHANICAL ENGINEERS.

NOTE: Statements and opinions advanced in papers are to be understood as individual expressions of their authors and not those of the Society. Manuscript received at ASME Headquarters, August 27, 1954. Paper No. 54-A-130.

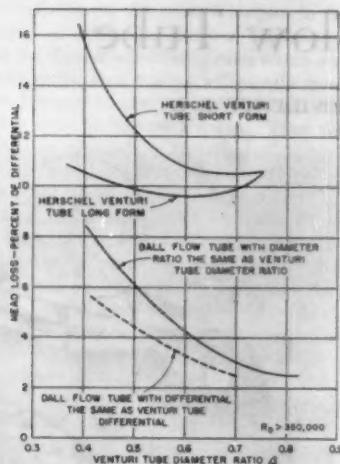


FIG. 3 HEAD-LOSS COMPARISON

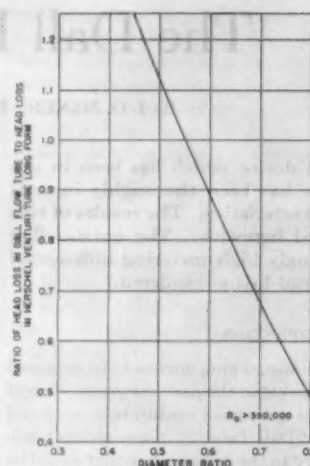


FIG. 4 HEAD-LOSS RATIO

straight pipe to provide full recovery. This is about 5 diameters. In other words, the loss is the increase in pressure drop which would occur between the ends of a straight piece of pipe if the pipe were cut in two, the pieces separated, and the metering device inserted between them. For the Dall flow tube this loss was determined by measuring the pressure drop between a tap 1 diameter upstream and a tap 5 diameters downstream of the differential producer, and subtracting the loss in a piece of pipe 6 diameters long. This pipe loss was determined by test. The increased loss caused by inserting a differential producer in a section of pipe by removing a section of the pipe and inserting the metering device without separating the remaining pipe sections (as would normally be done in an existing piping system) is less. In the case of the Dall flow tube the difference is substantial.

In Fig. 2 is shown the ratio of the differential produced by a Dall flow tube to that produced by a venturi tube or a nozzle. Fig. 4 shows the ratio of head loss of these two types of devices (at Reynolds numbers greater than 350,000 where the ratio becomes constant).

It will be noted that the head loss of the Dall flow tube varies from about 0.5 to 1.3 times the head loss in a venturi tube of corresponding β . In other words, part of the phenomenal performance of the Dall flow tube is dependent on the increase in differential. However, the head loss, even with a given β , is less for the Dall flow tube when the diameter ratio is greater than 0.552.

CALIBRATION

The typical calibration of a Dall flow tube is more like that of an orifice than that of a venturi tube. Fig. 5 shows the calibration of an 8-in. \times 5.85-in. Dall flow tube ($\beta = 0.732$). The coefficient is higher at low Reynolds numbers as in the case of an orifice. The increase in coefficient starts about pipe Reynolds number 350,000. Fig. 6 shows coefficients for Dall flow tubes of various ratios plotted against β .

It has been suggested that the Society consider the tolerance of a primary metering device to be twice the standard deviation. This gives a 20:1 probability that the error of any specimen will not exceed the tolerance.⁴ At the time of going to press the author estimates that there is a 20:1 chance that the coefficient

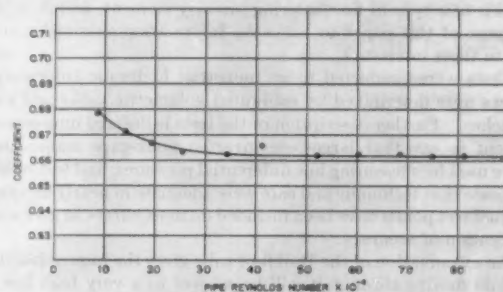
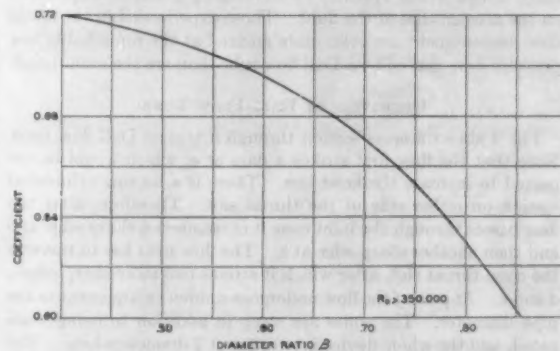
FIG. 5 CALIBRATION OF 8.00-IN. \times 5.85-IN. DALL FLOW TUBE

FIG. 6 DALL FLOW-TUBE COEFFICIENT VERSUS DIAMETER RATIO

as shown on this curve is within 1 per cent of the actual value for any Dall flow tube of 6-in. or greater pipe diameter and β between 0.4 and 0.75. Although a tremendous amount of Dall flow-tube testing has been done, not enough calibrations are available to determine the standard deviation, as has been done with some differential producers. Fig. 6 applies to all Dall flow tubes of 6-in. line size or over.

EFFECT OF ROUNDING SHARP EDGES OF TUBE

Tests were made to determine the effects of rounding the sharp edges in a Dall flow tube. An 8-in. \times 5.85-in. tube was used for

⁴"On the Evaluation of Accuracy of the Coefficient of Discharge in the Basic Flow-Measurement Equation," by A. L. Jorissen, Trans. ASME, vol. 75, 1953, pp. 1323-1326.

the tests. First, the tube was calibrated as manufactured. Following this test, sharp edge *a* (Fig. 1) was slightly rounded with emery cloth. The coefficient dropped 0.4 per cent. Sharp edge *c* at the leading edge of the throat slot was next slightly rounded. There was no further change in the calibration. The edge at the downstream side of the slot was then slightly rounded, and again there was no further change in the calibration. In view of the small change effected by imparting a slight radius to three sharp edges, we machined a $1/16$ -in. radius on edge *a*. The coefficient dropped 1 per cent below its original value (0.6 per cent more drop than for slight rounding). A $1/16$ -in. radius was then machined on edge *c*, and the coefficient increased 0.4 per cent, making it 0.6 per cent lower than originally. Finally, a $1/16$ -in. radius was machined on edge *d*, and the coefficient remained 0.6 per cent below its original value when all edges were sharp.

UPSTREAM DISTURBANCES

In keeping with other primary devices, the Dall flow tube is sensitive to upstream disturbances. In many cases it is more sensitive than the most commonly used primary devices, but it is by no means more sensitive than all other differential producers under all installation conditions. The error caused by various upstream disturbances when no allowance is made for a change in coefficient is shown in Figs. 7, 8, 8(a), 8(b), 9, and 10.

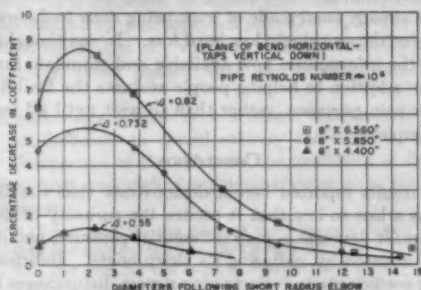


FIG. 7 EFFECT OF SHORT-RADIUS ELBOW UPSTREAM FROM DALL FLOW TUBE

Fig. 7 shows the effect of a single elbow upstream for three different β ratios. Fig. 8 shows the effect of a gate valve, opened one third, with its stem parallel to the inlet tap, and the portion of the gate in the stream on the same side as the inlet tap in the Dall flow tube. Fig. 8(a) shows the effect of rotating the valve so that its stem took the positions shown by the abscissa. The valve remained $1/3$ open, it was located 5 ft ($7\frac{1}{2}$ pipe diameters) upstream, and the inlet pressure tap was at the 90-deg position. Fig. 8(b) shows the effect of a gate valve with various openings when located 5 ft upstream, with the stem parallel with the inlet tap.

Fig. 9 shows the effect of a 6-in. \times 8-in. increaser ahead of Dall flow tubes of three different β ratios. Note that in all cases the error reverses. The coefficient starts off too high with no straight pipe between the increaser and the Dall flow tube, then the coefficient becomes too low as the straight pipe ahead of the Dall flow tube is increased, and finally the coefficient rises to its standard value.

Fig. 10 shows the effect of a 10-in. \times 8-in. reducer upstream from the Dall flow tube. The test points for $\beta = 0.73$ were quite erratic for some reason which we were not able to determine. It is probable that there is an actual instability in the flow pattern with this particular disturbance.

A question arose as to how close a particular type of disturbance could be located to the throat when placed in the downstream

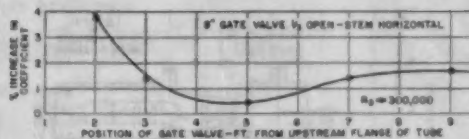


FIG. 8 EFFECT OF GATE VALVE UPSTREAM

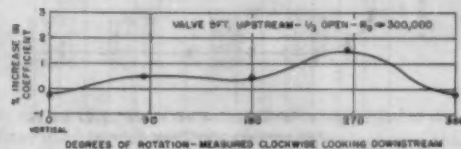


FIG. 8(a) GATE VALVE 5 FT UPSTREAM, $1/3$ OPEN, $R_D \approx 300,000$

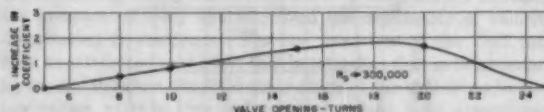


FIG. 8(b) GATE VALVE 5 FT UPSTREAM, STEM HORIZONTAL, $R_D \approx 300,000$

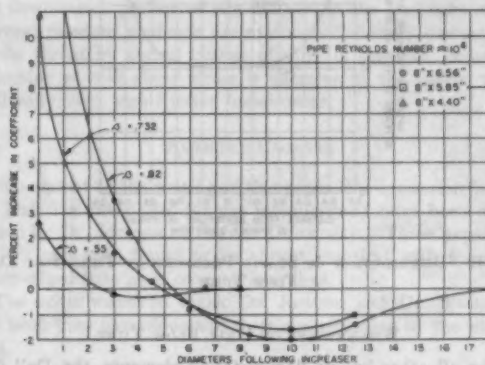


FIG. 9 EFFECT OF 6-IN. \times 8-IN. INCREASER 11 IN. LONG PRECEDING DALL FLOW TUBE

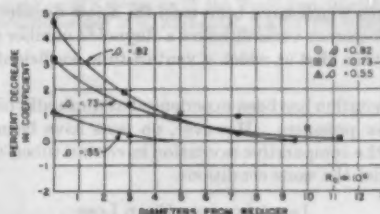


FIG. 10 EFFECT OF 10-IN. \times 8-IN. REDUCER 12 IN. LONG UPSTREAM FROM FLOW TUBE

cone. Fig. 11 indicates the type of disturbance and its effect. It will be noted that there is no observable change when the position of the disturbing object is increased beyond one throat diameter downstream from the throat slot. The coefficient was about 0.3 per cent higher than standard, but this is believed to be due to test inaccuracies rather than to the object in the diffuser.

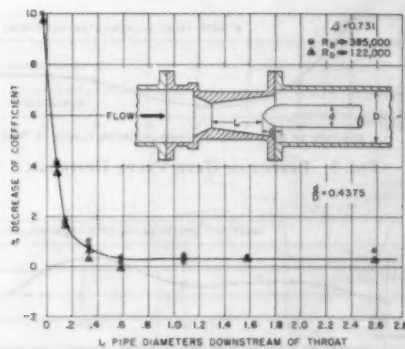


FIG. 11 INTERFERENCE TEST

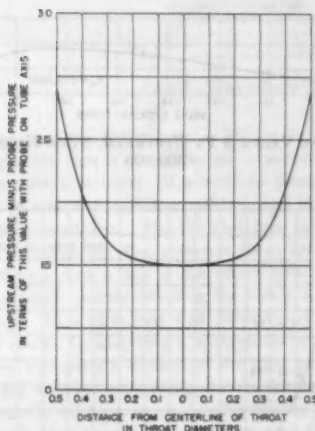


FIG. 12 DISTRIBUTION OF STATIC PRESSURE AT THROAT OF DALL FLOW TUBE

WEAKNESSES OF DALL FLOW TUBE

Like all other known flow-metering elements, the Dall flow tube fails to be outstanding in all respects. Its weaknesses are: (1) A standard Dall flow tube is not suitable for measuring the flow of fluids containing solids which are apt to settle out in the throat slot; (2) more straight pipe is required than for some primary devices which have been used for a few decades; (3) the coefficient becomes variable below a Reynolds number considerably higher than that at which a venturi-tube coefficient starts to vary.

Some cavitation has been experienced at unusually high velocities and low pressures. However, no tests have been made to determine the comparative cavitation in venturi tubes, orifices, or nozzles under the same conditions.

INVESTIGATING HEAD LOSS

It was stated previously that the more one knows about flow-metering, the more mystified he is apt to be by the low head loss of a Dall flow tube. Some investigation has been made, and it sheds considerable light on the reason for the high differential, but it does not indicate why the head loss is lower than that for a venturi tube of the same diameter ratio, provided this ratio is above 0.552. A test probe was used to explore the variation in static pressure in the plane of the throat slot of a 6-in. Dall flow tube with a 0.354 β ratio. A U-tube manometer was connected

to the test probe and to the inlet tap of the Dall flow tube. The probe was moved across a diameter in the plane of the throat slot. The probe was fitted with a slot in the side and was kept parallel with the axis of the Dall flow tube since it was desired to pick up the approximate static pressure rather than an impact pressure.

Fig. 12 shows the ratio between the manometer indication with the probe in various positions and the differential pressure when the probe was on the axis of the tube. It will be noted that the static pressure decreases to provide 2.4 times as much differential at the wall as at the center of the Dall flow tube. Further investigation is necessary to find out more about this gradual increase in differential as the probe is moved from the axis of the tube, but it is easy to see that a change in the direction of the flow lines can be largely responsible.

An attempt is being made by Dr. John R. Weske at the University of Maryland to photograph stream-flow lines through a Dall flow tube made of methyl methacrylate. It is hoped that eventually there will be a complete explanation for the extremely low loss of head through a Dall flow tube.

FURTHER EXPERIMENTATION

Experiments are under way or planned, to determine the effect of elbows in more than one plane, permissible manufacturing tolerances for all dimensions, and the straight pipe required to completely eliminate the effect of partially closed valves. Mention has already been made of work being done to determine the reasons for the amazingly low head loss. It was thought best to present the information now available and stimulate further research in addition to helping people evaluate the Dall flow tube for their own purposes, rather than to wait until all tests have been completed.

CONCLUSION

Test results reported herein demonstrate that the Dall flow tube has a loss so low that it excites the curiosity of flowmeter engineers; it develops a high differential pressure; and it is only slightly affected by radiusing its sharp edges. Information regarding coefficients and effects of upstream disturbances has been given to enable researchers and users to install it properly.

Discussion

A. L. JORISSEN.⁵ The writer's first experience with the Dall flow tube was the calibration of a 24.02-in. \times 17.544-in. tube ($\beta = 0.7302$) in the Hydraulic Laboratory at Cornell University in 1953. The calibration curve exhibits the same trend as that shown by the author's Fig. 5. However, the coefficient of discharge does not become constant until a relatively high value of the pipe Reynolds number (approximately 700,000) is reached. The constant value of the coefficient of discharge is equal to 0.661, which agrees remarkably well with the value read from the author's Fig. 6.

The head loss, taken as the difference in pressure between a section situated one pipe diameter upstream and a section situated five pipe diameters downstream of the Dall tube is extremely low and amounts to less than 2 per cent of the Dall-tube differential at Reynolds numbers above 500,000. Even taking into account the fact that for $\beta = 0.7302$ the ratio of Dall-tube differential to venturi-tube differential would be approximately equal to 2.2, Fig. 2, this still indicates that the Dall tube tested has a much smaller head loss than a comparable venturi tube.

More recently, an extensive series of tests was undertaken by the writer to determine the effect on various flowmetering de-

⁵ Professor of Civil Engineering; Head, Department of Hydraulics and Hydraulic Engineering, Cornell University, Ithaca, N. Y. Mem. ASME.

TABLE 1 DALL-TUBE TEST RESULTS

L_a , ft.-in.	L_a/D	8" X 4-in.		8" X 4.4-in.		8" X 5-in.		8" X 5.2-in.	
		Venturi tube C	z	Dall tube C	z	Venturi tube C	z	Dall tube C	z
Tests without straightening vanes									
0.....	0	0.9834	-0.02	0.7117	+0.24	0.9843	-0.34	0.6862	-0.48
4-4.....	6.5	0.9833	-0.03	0.7096	-0.05	0.9836	-0.41	0.6859	-0.52
10-0 1/4.....	13.5	0.9832	-0.04	0.7103	+0.05	0.9851	-0.26	0.6877	-0.26
19-4 1/4.....	28	0.9841	+0.05	0.7106	+0.09	0.9860	-0.17	0.6909	+0.20
27-7 1/4.....	41	0.9836	...	0.7100	...	0.9877	...	0.6905	...
Tests with straightening vanes									
0.....	0
4-4.....	6.5	0.9840	-0.12	0.7090	-0.43	0.9885	-0.23	0.6881	-1.10
10-0 1/4.....	13.5	0.9845	-0.06	0.7127	-0.09	0.9910	+0.02	0.6950	-0.10
19-4 1/4.....	28	0.9851	-0.01	0.7136	+0.05	0.9907	-0.01	0.6969	+0.17
27-7 1/4.....	41	0.9852	...	0.7133	...	0.9908	...	0.6957	...

vices of two short-radius elbows in orthogonal planes. These tests are part of a research project conducted in the Hydraulic Laboratory at Cornell University under the sponsorship of Builders-Providence, Inc. The test run is an experimental pipe 8 in. in diam, under a static head of 80 ft. Tests were run without and with straightening vanes at the upstream end of the approach pipe, immediately after the two elbows. The results of the tests are summarized in Table 1 of this discussion.

L_a is the length of approach pipe between the two elbows and the tube tested, D the pipe diameter, C the coefficient of discharge, and z the difference (in per cent) between the coefficient of discharge for a particular condition and that obtained for the same tube with a length of approach pipe 27 ft 7/4 in. (41 D) long. It should be noted that any value of z smaller than 0.2 per cent is insignificant, being smaller than the possible experimental error.

A first conclusion is that even a length of approach pipe of 41 D is not sufficient to cancel entirely the effect of the two elbows. Comparison of the values of the coefficient of discharge obtained without and with straightening vanes gives the following differences:

- 0.15 per cent for the 8-in. X 4-in. venturi tube
- 0.47 per cent for the 8-in. X 4.4-in. Dall tube
- 0.31 per cent for the 8-in. X 5-in. venturi tube
- 0.90 per cent for the 8-in. X 5.2-in. Dall tube

This indicates that the Dall tube is somewhat more sensitive than the venturi tube to the effect of two short-radius elbows in orthogonal planes and that this effect is more marked at larger values of β .

This conclusion also is substantiated by a study of the values of z in Table 1.

J. R. WESKE.^{*} The author's statement to the effect that a

^{*} Visiting Research Professor, Institute for Fluid Dynamics, University of Maryland, College Park, Md. Mem. ASME.

captive vortex ring was observed at the discontinuity of diameter at diffuser discharge of the Dall tube and his suggestion that this annular vortex contributes to the measured low head loss appear confirmed by investigations of Perkins and Hazen,⁷ who found that a corresponding captive vortex in a wind tunnel increased the pressure recovery and improved the uniformity of velocity distribution downstream. The low head loss of the Dall tube may be attributed to the fact that in retarding flow as in boundary layers and diffusers, the fluid shear stress at the wall drops to very low values, even to zero and negative values, from a maximum which occurs away from the wall.⁸ This is as may be expected since the central stream will entrain the fluid near the wall previously retarded by adverse pressure gradients. It occurs in the downstream portion of any diffuser; in the Dall tube strong adverse pressure gradients are established directly downstream of the throat by abrupt change of slope of the wall; hence the reduction of wall shear stress is effective in the region where ordinarily very high friction losses occur.

AUTHOR'S CLOSURE

Subsequent to the writing of this paper, the expansion factors for Dall flow tubes used for gas measurement have been determined by Dr. Jorissen at Cornell University. These expansion factors have been found to be almost identical with those for sharp-edged flat plate concentric orifices.

The writer wishes to thank Dr. Jorissen and Dr. Weske for the work they have done and their contributions to the discussion.

⁷ "Some Recent Advances in Boundary Layer and Circulation Control," by C. D. Perkins and D. Z. Hazen, Proceedings of the Fourth Anglo-American Aeronautical Conference, Royal Aeronautical Society, 1953, pp. 189-224.

⁸ "Investigation of Separation of the Turbulent Boundary Layer," by G. B. Schubauer and P. S. Klebanoff, NACA TR 1030, 1951.

Two- and Three-Dimensional Flow of Air Through Square-Edged Sonic Orifices

By ALEXANDER WEIR, JR.,¹ J. L. YORK,² AND R. B. MORRISON,³ ANN ARBOR, MICH.

In this investigation, the two-dimensional flow of air through rectangular, and the three-dimensional axisymmetrical flow of air through circular, square-edged, sonic orifices were examined under pressure ratios ranging from 1.894 to 42.0 (upstream stagnation pressure/downstream static pressure). Mass-flow measurements were made using a primary metering system, rather than another orifice or nozzle, and optical techniques were used to obtain pictures of the flow upstream, within the thickness of the orifice plate, and downstream of the orifice. Evidence is presented in this paper which indicates that square-edged sonic orifices can be treated as sonic nozzles by utilizing the concept that the air "turning the corner" of the orifice plate, in effect, makes its own nozzle. It is believed that this interpretation of experimental observations is in full agreement with established principles of aero- and thermodynamics.

NOMENCLATURE

The following nomenclature is used in the paper:

- A = area, sq ft
- A_t/A_E = area of "effective throat"/total orifice area
- c_p = specific heat at constant pressure, Btu/lb/deg F
- c_v = specific heat at constant volume, Btu/lb/deg F
- D = diameter of circular orifice, or distance between rectangular orifice plates, in.
- G = mass velocity, lb/sec/sq ft
- g_c = conversion factor for mass and force units = 32.2
- h = enthalpy, Btu/lb
- K = const
- M = molecular weight of air = 29
- Ma = Mach number = velocity of gas/velocity of sound at same conditions
- n = pound-moles = pounds/ M
- P_0 = stagnation pressure, psia
- P = static pressure, psia
- p = static pressure, lb force per sq ft
- R = universal gas constant = 1544 ft-lb force/lb-mass/deg F
- r = distance of fluid particle from upstream corner of orifice plate, in.
- T_0 = stagnation temperature, deg R
- T = static temperature, deg R

- v = velocity, fps
- v_s = sonic velocity, fps
- w = mass flow rate, lb mass/sec
- Z = compressibility factor = PV/nRT
- z = width of rectangular orifice, in.
- Δ = radius of "effective void space," in.
- δ = deflection angle of streamline passing through oblique shock wave, deg
- γ = ratio of heat capacities = c_p/c_v = 1.4 for air
- ρ = density, lb mass/cu ft
- ρ' = ρ/g_c
- ϕ_w = angle of inclination of oblique shock wave, deg
- μ = angle of inclination of Mach wave, deg

INTRODUCTION

The phenomenon of critical flow of air through orifices was first observed experimentally in 1839 by Saint Venant and Wantzel (1).⁴ Stokes (2) reviewed this work in 1846, and proved invalid the previous assumption that the pressure in the orifice was equal to the pressure in the space where discharge occurred. Several decades later, in 1885, Wilde (3) observed critical flow of air both for discharge into a vacuum and into a vessel whose pressure was greater than atmospheric, but it remained for Osbourne Reynolds (4) in the same year to deduce that the velocity of the gas at the minimum area was equal to the velocity of sound in the gas.

Sonic nozzles have been used extensively as metering devices since, for constant upstream conditions, the mass-flow rate is not a function of downstream conditions. In recent years, however, the use of square-edged sonic orifices as critical-flow provers has been questioned. In this investigation the two-dimensional flow of air through rectangular, and the three-dimensional axisymmetrical flow of air through circular, square-edged, sonic orifices was examined under pressure ratios ranging from 1.894 to 42.0 (upstream stagnation pressure/downstream static pressure). Mass-flow measurements were made using a primary metering system, rather than another orifice or nozzle, and optical techniques were used to obtain pictures of the flow upstream, within the thickness of the orifice plate, and downstream of the orifice.

The existence of supersonic flow within the orifice itself, as evidenced by the presence of oblique shock waves in the typical schlieren picture shown in Fig. 1, indicates that attempts to extrapolate concepts which were satisfactory for subsonic flow into the trans- and supersonic-flow regimes which exist in square-edged sonic orifices will not be successful. In other words, such useful dimensionless parameters as the Reynolds number, the pressure ratio across the orifice, and the orifice-to-pipe diameter ratio are not applicable to sonic orifices; the actual upstream pressure and orifice diameter must be used instead.

Evidence is presented in this paper which indicates that square-edged sonic orifices can be treated as sonic nozzles by utilizing the concept that the air turning the corner of the orifice plate, in effect, makes its own nozzle. It is believed that this interpretation of experimental observations is in full agreement with established principles of aero- and thermodynamics.

⁴ Numbers in parentheses refer to the Bibliography at the end of the paper.

¹ Lecturer, Department of Chemical and Metallurgical Engineering and Associate Research Engineer, Engineering Research Institute, Aircraft Propulsion Laboratory, University of Michigan.

² Associate Professor, Department of Chemical and Metallurgical Engineering, University of Michigan. Mem. ASME.

³ Associate Professor, Department of Aeronautical Engineering, University of Michigan.

Contributed by the Research Committee on Fluid Meters and presented at the Annual Meeting, New York, N. Y., November 28-December 3, 1954, of THE AMERICAN SOCIETY OF MECHANICAL ENGINEERS.

NOTE: Statements and opinions advanced in papers are to be understood as individual expressions of their authors and not those of the Society. Manuscript received at ASME Headquarters, August 16, 1954. Paper No. 54-A-112.

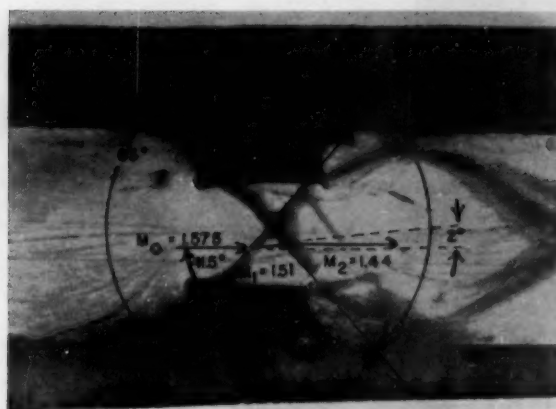


FIG. 1 SCHLIEREN PHOTOGRAPH OF TWO-DIMENSIONAL SONIC ORIFICE

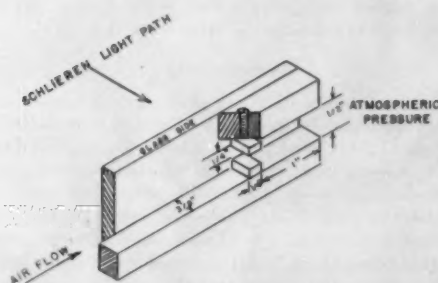


FIG. 2 SCHLIEREN TEST SECTION

DESCRIPTION OF EQUIPMENT AND EXPERIMENTAL TECHNIQUE

The photograph shown in Fig. 1 was obtained with a conventional "balanced" schlieren system (5). The schlieren light beam was passed through a glass-sided test section. The method of inserting blocks in this test section to make rectangular two-dimensional orifices is indicated in Fig. 2. In addition to the 0.250×0.375 -in. orifice, photographs also were taken of a 0.133×0.375 -in. orifice as well as of $1/2$ of a 0.750×0.875 -in. orifice (obtained by removing one of the blocks in Fig. 2). This technique thus allows observation of the flow through the orifice itself.

Mass-flow measurements were made with 0.128×0.375 -in. and 0.250×0.375 -in. rectangular orifices, constructed from $1/8$ -in.-thick brass plate, and with 0.122-in., 0.188-in., 0.253-in., and 0.390-in.-diam circular orifices, which were made from $1/16$ -in.-thick stainless steel. Both rectangular and circular orifices were constructed with a 90-deg edge upstream. Pressure and temperature measurements were made in an approach section, 5 ft long, upstream of the orifice, 1-in., schedule-40 pipe being used for circular-orifice tests and a rectangular duct ($1/2 \times 3/8$ in. ID) for the rectangular-orifice tests. As in the two-dimensional orifices used for schlieren photographs, Fig. 2, the width of the rectangular approach section was equal to the width ($1/2$ in.) of the rectangular orifices used for mass-flow experiments.

The primary standard for air mass-flow measurements was the change in the mass of air stored in the high-pressure system upstream of the orifice, analogous to the weighing tanks used for liquid metering. The mass of air in the system at any time was determined from pressure and temperature measurements together with the Beattie-Bridgeman equation of state (6). The technique of determining the orifice flow rate by the rate of mass de-

crease in the air-supply system was compared to the flow rate measured by a subsonic orifice designed to ASME standards. No detectable difference in the flow rates obtained by the two methods was observed.

The volume of the air-storage tanks and piping was measured to be 169.57 cu ft by weighing the water to fill them. The temperature of the air in the storage system was measured by thermocouples inserted into the air-storage tank, using a potentiometer with a precision of 0.1 deg F. A calibrated 2000-pai laboratory test gage with 10-lb increments indicated the pressure in the air-supply system. The pressure upstream of the orifice was maintained constant by two dome control valves in parallel operated by adjusting nitrogen pressure above the diaphragm. No variation in orifice upstream pressure during a run was ever observed with this system.

Leakage of the entire system was evaluated a number of times during the experimental work reported here. Pressures and temperatures in the air-storage tanks were measured as for mass-flow tests. The average leakage measured corresponded to critical flow at the storage-tank pressure through an orifice with an area of 0.0000092 sq in. A maximum error of 0.025 per cent results from neglecting the leakage rate for the largest orifice tested and 0.33 per cent for the smallest orifice tested. This leakage is greater than actually exists for it includes leaks through the orifice control valves in shutoff position, which would not be encountered during a test run.

The orifices for mass-flow tests always discharged directly into the atmosphere with no piping, valves, or other restrictions downstream. As shown in Fig. 2, the photographs were made on systems with a 1-in. length of rectangular duct downstream. Thus no questionable downstream pressures were obtained.

THEORY

One-Dimensional Flow Through Ideal Nozzle. Utilizing the concept of mass velocity, or mass flow per unit area, we can express the mass velocity at any location in an isentropic nozzle, in terms of upstream stagnation conditions, by combining the conservation of mass, conservation of energy, the perfect-gas law, and the definition of Mach number to obtain (12)

$$G = w/A = \frac{g_c P_0}{\sqrt{\gamma_0}} \text{Ma} \left(\frac{1}{1 + \frac{\gamma-1}{2} \text{Ma}^2} \right)^{\frac{\gamma+1}{2(\gamma-1)}} \quad [1]$$

It can be shown from Equation [1] that the maximum mass velocity of a perfect gas occurs in a reversible nozzle when the Mach number is 1. Since the mass-flow rate is constant, sonic velocity will occur at the minimum cross-sectional area or throat of the nozzle. Then

$$G_{\text{max}} = w_{\text{max}}/A_{\text{throat}} = \frac{\gamma_0}{\sqrt{\gamma_0 R/M}} \left(\frac{2}{\gamma+1} \right)^{\frac{\gamma+1}{2(\gamma-1)}} \frac{P_0}{\sqrt{T_0}} \quad [2]$$

Thus, for a sonic nozzle, the mass velocity at the throat is determined only by the stagnation temperature and pressure; i.e., the total upstream pressure and temperature, and is not a function of downstream conditions.

Two-Dimensional Flow Around a Corner. In the foregoing idealized one-dimensional-flow theory, it was assumed that the flow in the throat possessed velocity only in the x -direction, while upstream of the nozzle the velocity was equal to zero, an isentropic process being used to connect the two regions. However, with a square-edged orifice, some particles must travel in the y -direction before passing through the orifice. By equating the centrifugal force on these particles to the net pressure force, it is possible to

show that the pressure gradient encountered by the particle turning the corner is

$$\frac{dp}{dr} = \frac{\rho'v^2}{r} \quad [3]$$

For air at 60 F and 1 atm traveling at sonic velocity, Equation [3] indicates that a particle 0.1 in. from the corner would encounter a pressure gradient of about 2000 psia per in., or at a distance 0.002 in. from the corner, a pressure gradient of 10,000 psia per in., although these obviously cannot coexist. Because of these high pressure gradients, the air is diverted away from the corner, leaving a low-pressure zone in the region near the corner.

It would be very desirable to know the velocity and pressure distribution near the corner as the transition from subsonic to supersonic flow occurs. Equation [3] cannot be integrated, without assuming some variation of ρ and v with either P or r since ρv^2 would not be a constant in the region near the corner. Binder (7) and others treat a somewhat similar case of an incompressible fluid flowing in a pipe bend and indicate that near the inner radius the velocity is directly proportional to the radius, while the velocity near the outer radius is inversely proportional to the radius of curvature. We will make a similar simplifying assumption to obtain a relation between the velocity of the fluid and the distance from the upstream corner of the orifice plate; i.e., that the velocity is directly proportional to the distance from the corner, r , in the region nearest the corner where the viscous forces predominate, and further from the corner is inversely proportional to the distance from the corner until free-stream conditions are reached. For such an assumption, the velocity distribution at the

$$w = \rho A v = K(r)(Pv) \quad [4]$$

Such a curve is shown in the lower portion of Fig. 3 for the velocities and pressures in the upper part of Fig. 3.

We also can draw a rectangular distribution of Pv so that the area contained in this rectangle is equal to the area under the smooth curve. In the lower portion of Fig. 3 this is shown in dotted lines. The shaded area above the smooth curve, but contained in the rectangle, is equal to the shaded area under the smooth curve in the region near the corner or at $r = 0$. We can therefore represent the mass flow through the orifice by assuming a rectilinear distribution of pressure and velocity over an area smaller than the actual orifice area, rather than determining the actual pressure and velocity distribution across the entire orifice. For example, for a rectangular orifice with a distance between the orifice plates of D (and a constant width of the orifice and upstream channel of s) the effective area of the orifice would be

$$A_{eff} = s(D - 2\Delta) \quad [5]$$

and the mass flow through the orifice would be

$$w = \rho A v = \rho_{throat} v_{sc} s(D - 2\Delta) \quad [6]$$

where the density at the throat could be obtained from the one-dimensional nozzle equations and the velocity is sonic across the distance $D - 2\Delta$. Equation [6] thus indicates that the one-dimensional nozzle equations can be applied to a square-edged sonic orifice by using an effective void distance, Δ .

Interaction of Oblique Shock Waves in Two-Dimensional Orifices. Using the hypothesis that the air turning the corner "makes its own nozzle," we can explain the appearance of the oblique shock waves in the photograph of the two-dimensional orifice shown in Fig. 1. Consider the path of a fluid particle near the corner of the orifice. Upstream of the orifice, its velocity and Mach number are small, but as it passes through the throat, it reaches sonic velocity and the Mach number is 1. Downstream of the throat, the flow is supersonic, with a Mach number greater than 1, because of the curvature of the "effective void space" of radius Δ . The supersonic velocity results from the increase in effective nozzle area, in accordance with Equation [1]. However, as the fluid particle rounds the corner, it encounters the solid wall of the orifice plate. This change in direction results in a compression and an oblique shock wave originates from the wall.

By measurement of the intersection angles of the oblique shock waves in the center of the stream, it is possible to compute the mass-flow rate of air through the orifice. Consider a streamline near the center of the orifice, one whose path is marked by $D-E-F-G-H$ in Fig. 4, which is a schematic drawing of Fig. 1. If the Mach number Ma_0 is known at point E and the area represented by the line $B-B'$, it would be possible to compute the area represented by the line $A-A'$, since the Mach number at point D is 1 and line $A-A'$ represents the throat. Considering the edge of the effective void spaces $A-B$ and $A'-B'$ as representing the contour of a nozzle, the mass flow at section $A-A'$ will be equal to the mass flow at $B-B'$, and from (12)

$$\frac{\gamma_t Ma_t A_t P_t}{v_{st}/g_0} = \frac{\gamma_E Ma_E A_E P_E}{v_{sE}/g_0} \quad [7]$$

The subscript E represents conditions at point E (or anywhere in the triangle $B-C-B'$) and the subscript t represents conditions at the effective throat along the line $A-A'$ in Fig. 4. Assuming that γ is constant (perfect-gas law) and the flow from point D to point E is isentropic (since this is upstream of any shock waves and is not near the corner), plus the knowledge that the Mach number at the effective throat is equal to 1, gives (12)

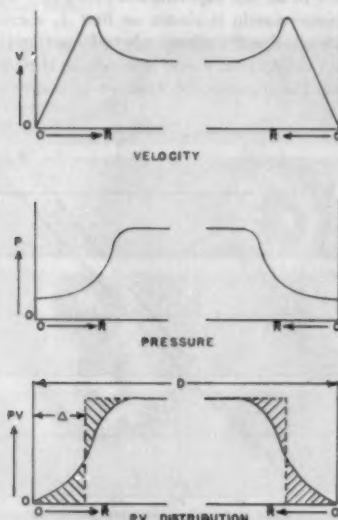


FIG. 3 CONDITIONS AT ORIFICE INLET

orifice inlet would look as shown in the top graph in Fig. 3. The pressure distribution for this velocity distribution, Equation [3], would look as shown in the center of Fig. 3.

The distance r is directly proportional to the area of a two-dimensional orifice and the pressure is proportional to the density. Therefore the area under a plot of Pv versus r will be proportional to the mass rate of flow through the orifice, or

$$\frac{A_t}{A_g} = Ma_g \left[\frac{\frac{\gamma+1}{2}}{1 + \frac{\gamma-1}{2} Ma_g^2} \right]^{\frac{\gamma+1}{2(\gamma-1)}} \dots \dots \dots [8]$$

Knowing that A_g is the total cross-sectional area of the orifice, Equation [8] permits calculation of A_t , the area of the "effective throat," if Ma_g can be determined. This value of A_t can be substituted in Equation [1] or [2] to determine the mass flow of air through the orifice.

Ma_g (or Ma_0) can be determined by a solution of the shock-wave pattern in the schlieren photographs, as sketched in Fig. 4.

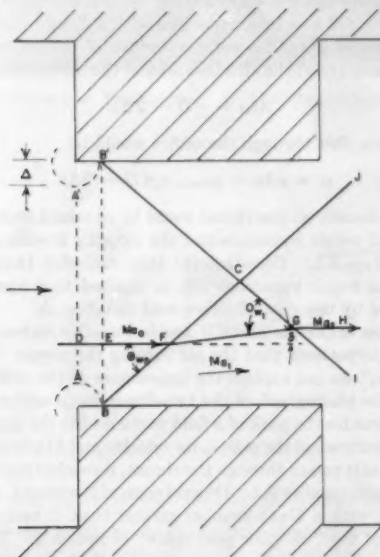


FIG. 4 SHOCK-WAVE PATTERN OF FIG. 1

The angles $B'C-B$ and $J-C-I$ can be measured. The shock wave BC is inclined at an angle ϕw_0 to the entering flow, and this angle is equal to one half the measured angle $B'C-B$. It can be shown that the deflection angle δ is the same for both shock waves, and the angle of inclination (ϕw_1) of the second shock wave, CI , to its entering flow, Ma_1 , is equal to δ plus one half the measured angle $J-C-I$. Although it is not required that the angle $B'C-B$ be equal to the angle $J-C-I$ for the solution of the problem, when the measured angles are equal (as was found to be the case experimentally)

$$\phi w_1 = \phi w_0 + \delta$$

It has been shown (5, 8, 9, 10, 11) that Ma_0 , Ma_1 , ϕw_0 , and δ are related by the following equations

$$\frac{\tan(\phi w_0 - \delta)}{\tan \phi w_0} = \frac{Ma_1 \sin(\phi w_0 - \delta)}{Ma_0 \sin \phi w_0} \dots \dots \dots [9]$$

$$Ma_1^2 \sin^2(\phi w_0 - \delta) = \frac{2 + (\gamma - 1) Ma_0^2 \sin^2 \phi w_0}{2\gamma Ma_0^2 \sin^2 \phi w_0 - (\gamma - 1)} \dots \dots \dots [10]$$

There are two equations and three unknowns, Ma_0 , Ma_1 , and δ , since ϕw_0 was obtained experimentally. However, these equations apply to both shock waves (BC and CI) and since δ is the same for both shock waves, and the Mach number of the flow

leaving the first shock wave (Ma_1) must be equal to the Mach number of the flow entering the second shock wave, it is possible to obtain a unique solution for Ma_0 , Ma_1 , and δ . Since Ma_0 or Ma_g can thus be determined from angle measurements of the shock-wave intersection in schlieren photographs, the value obtained can be substituted in Equation [8] to obtain the ratio of the effective throat area to the total area of the orifice. Equation [2] can be rewritten, for air flow, as

$$G_{orifice} = \frac{w}{A_{orifice}} = (A_t/A_g)(76.35)(P_0/\sqrt{T_0}) \dots \dots [11]$$

so that we have an expression for the mass velocity through a critical orifice, based on the orifice cross-sectional area, in terms of the upstream stagnation temperature and pressure.

EXPERIMENT

Two-Dimensional Orifices. It was found that the same shock-wave pattern existed between the orifice plates for the 0.250-in. \times 0.375-in. orifice for upstream pressures from 27.5 to 173 psia. From Fig. 1 the solution of the shock-wave interaction indicates that the Mach number upstream of the shock-wave intersection is 1.575. Using Equation [8] the ratio of the effective throat area to the total orifice area is

$$A_t/A_g = 1.575 \left(\frac{1.2}{1 + 0.2(1.575)^2} \right)^3 = 0.8125 \dots \dots [12]$$

This value of the area ratio may be substituted in Equation [11] to obtain the mass velocity through a 0.250-in. rectangular orifice as a function of upstream stagnation conditions. In Fig. 5 a plot of mass velocity as a function of pressure ratio (the downstream pressure in all the experiments performed was 14.5 psia) for an ideal sonic nozzle is shown as line A, corresponding to Equation [2], while line B corresponds to Equation [11] and indicates the mass velocity that would be expected through a 0.250-in. orifice based on the schlieren-photograph measurements.

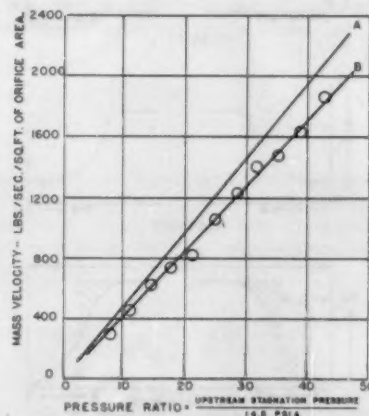


FIG. 5 MASS VELOCITY AS FUNCTION OF PRESSURE RATIO

Experimental values obtained by storage-tank measurements also are plotted in Fig. 5. At least eight simultaneous readings of the air storage-system pressure and temperature, and elapsed time were made during each run. Thus a plot of P/TZ versus time was a straight line containing at least eight points. Actual experimental points were used to calculate the mass-flow rate for each run, rather than the slope of the line, for ease in calculations; therefore each value of the mass-flow rate obtained at different

pressures was supported by eight experimental points. The original experimental readings, plots of P/TZ versus time, and tabulated values of the mass-flow rate for each run are given in reference (12). About 1000 points were obtained with the various orifices tested and space limitations prevent their presentation here.

By removing one of the blocks in this orifice, it is possible to obtain one half of a 0.750-in. orifice. A small hole drilled through the side of the channel opposite to the remaining block allows the supersonic flow through the orifice to encounter a lower pressure at this point, and results in an expansion or Mach wave. From schlieren photographs the expansion wave was found to be inclined to the flow at an angle μ , of 50 deg. It can be shown (5, 8, 9, 10) for a Mach wave that for $\mu = 50$ deg

$$Ma_0 = 1/\sin 50 = 1/0.76604 = 1.305 \dots [13]$$

and from Equation [8]

$$A_t/A_g = 0.9364 \text{ (for } D = 0.750 \text{ in.)} \dots [14]$$

Schlieren photographs were also obtained inside a rectangular orifice with the distance between the orifice plates equal to 0.133 in. In Fig. 6 a few of these photographs are shown, with upstream stagnation pressures ranging from 22.0 psia (subsonic flow) through 28 psia (sonic) to 214.5 psia. (The downstream static pressure was in all cases 14.5 psia.) These photographs indicate that when sonic flow is established, the shock-wave pattern does not change with upstream pressure or pressure ratio. An analysis of the shock-wave pattern is given in Fig. 7 which indicates that the Mach number upstream of the first shock wave corresponds to 1.82. The ratio of the area of the effective throat to the total orifice area is, from Equation [8], 0.6845 for a 0.133-in. rectangular orifice.

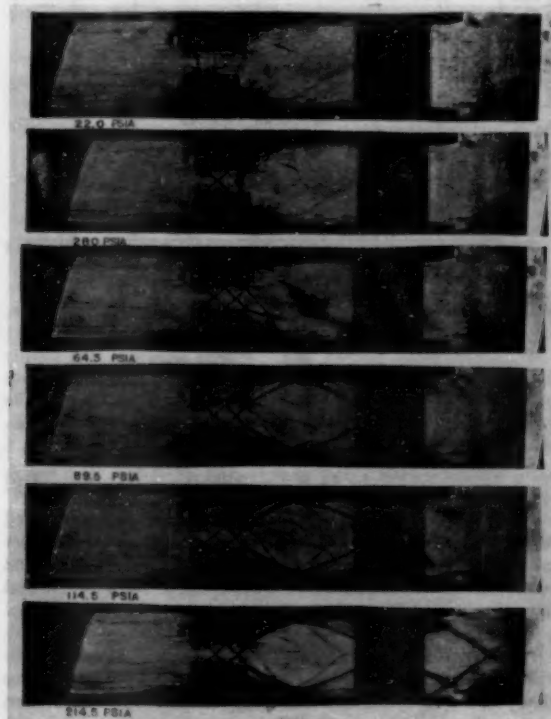


FIG. 6 SCHLIEREN PHOTOGRAPHS OF 0.133-IN. ORIFICE

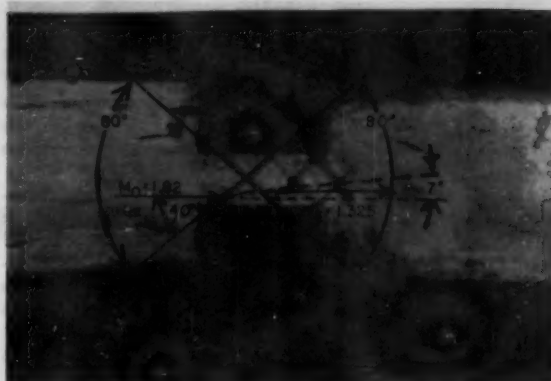


FIG. 7 SCHLIEREN PHOTOGRAPH OF 0.133 X 0.375-IN. ORIFICE

Similar values of the area ratio were obtained with mass-flow measurements in a 0.128 x 0.375-in. rectangular orifice, with upstream stagnation pressures as high as 515 psia. No change in the area ratio due to different upstream pressures was observed.

The values of the effective area ratio permit calculation of the value of Δ , the radius of the effective void space in Equation [5]. Fig. 3 indicates that as long as the orifice plates were far enough apart to prevent mutual interference effects from the opposite corners of the orifice plate, the magnitude of Δ would be independent of the distance between the orifice plates. Since

$$A_t/A_g = z(D - 2\Delta)/zD \dots [15]$$

for a rectangular orifice of width z and a distance between the orifice plates of D , we can use the values of A_t/A_g given in Equations [12] and [14] to calculate numerical values of Δ for two-dimensional flow. A value of Δ equal to 0.02341 in. was obtained for the 0.250-in. and 0.750-in. orifices, while a value of Δ of 0.02098 in. was obtained for the 0.133-in. rectangular orifice. Thus, in two-dimensional flow, Δ in addition to being independent of upstream pressure, or pressure ratio across a sonic orifice, is also independent of D for values of D equal to or greater than 0.250 in.

Three-Dimensional Orifices. The foregoing discussion is concerned only with two-dimensional flow; that is, flow in only the



FIG. 8 CYLINDER IN SUPERSONIC STREAM (REFERENCE 13)

x and y -directions. With a circular orifice, flow also occurs in the z -direction; hence we can only qualitatively apply our concept of flow through two-dimensional orifice to the three-dimensional case. However, three-dimensional flow exists around a body of revolution as well as through a circular orifice. If a cylinder is placed head on into a stream, the resulting flow pattern near the corner can be considered as that obtained if our circular orifice were turned "inside out."

Fig. 8 (reference 13) is a horizontal knife-edge schlieren photograph of a cylinder inserted longitudinally in a stream whose Mach number is about 1.4. The flow in front of the detached wave is supersonic, but the flow in the region behind the detached shock wave and in front of the cylinder is subsonic since the detached wave may be treated as a normal shock wave. The low-pressure zone created by the air turning the corner is plainly visible, as is the oblique shock wave originating from the wall at the end of the low-pressure zone.

There is little doubt, then, that a similar flow pattern occurs in a circular orifice plate as occurs between rectangular orifice plates. The effective void space or low-pressure zone extends around the periphery of the orifice, and a conical shock wave probably originates at the downstream edge of the low-pressure zone.

For a circular orifice the ratio of the effective throat to the total area of the orifice would be

$$A_t/A_E = (D - 2\Delta)^2/D^2 \dots \dots \dots [16]$$

and the mass velocity through the orifice under critical conditions would be that predicted from Equation [11].

Since optical data could not be obtained with circular orifices, a correspondingly larger number of mass-flow measurements were made to establish the radius of the effective void space, Δ . For example, with the 0.390-in-diam orifice, 31 runs containing at least 8 points each were made at pressures ranging from 27.5 to 615 psia. The distribution of the experimental data for this orifice indicated a probable error of 1.2 per cent, with $A_t/A_E = 0.90$ being the median value. A value of $\Delta = 0.010$ in. was obtained with the 0.390-in-diam orifice and the same value was obtained with the 0.253-in-diam orifice. Lower values of Δ were obtained for the smaller orifices.

COMPARISON OF TWO AND THREE-DIMENSIONAL ORIFICES

In Fig. 9 all of the experimental mass flows obtained in this investigation, for four two-dimensional orifices, and four three-dimensional orifices are plotted versus pressure ratio. The linear relationship between mass flow and pressure ratio for sonic square-edged orifices is evident. Mass-flow rates from 0.024 lb per sec to 1.4 lb of air per sec were obtained with pressure ratios as high as 40/1.

The values of Δ , the radius of the effective void space, are plotted versus D in Fig. 10. The radius of the effective void space Δ , appears to be constant for values of D greater than about $1/4$ in.

The effective area ratio A_t/A_E is plotted versus D in Fig. 11. Since Δ is constant for values of D greater than $1/4$ in., for two-dimensional flow

$$A_t/A_E = (D - 0.04682)/D \dots \dots \dots [17]$$

and for three-dimensional flow

$$A_t/A_E = (D - 0.020)^2/D^2 \dots \dots \dots [18]$$

For smaller values of D in three-dimensional flow, smaller values of Δ were obtained, probably as a result of mutual interference effects. A median value of A_t/A_E of 0.878 was obtained with the 0.188-in-diam orifice, while a median value of A_t/A_E of

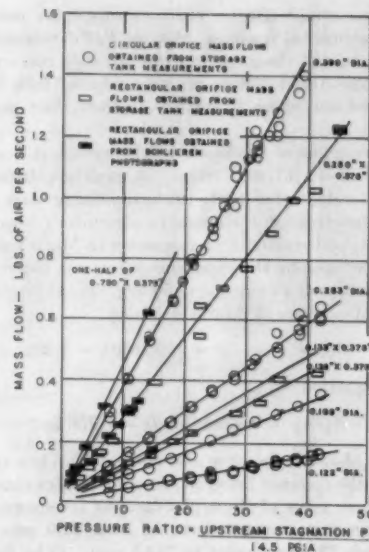


FIG. 9 EXPERIMENTAL MASS FLOWS VERSUS PRESSURE RATIO

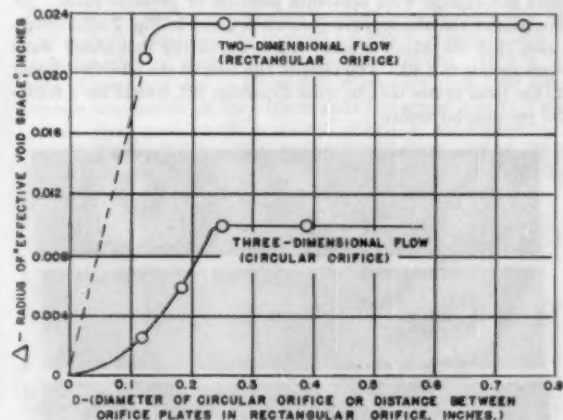


FIG. 10 VALUES OF Δ , RADIUS OF EFFECTIVE VOID SPACE, VERSUS D

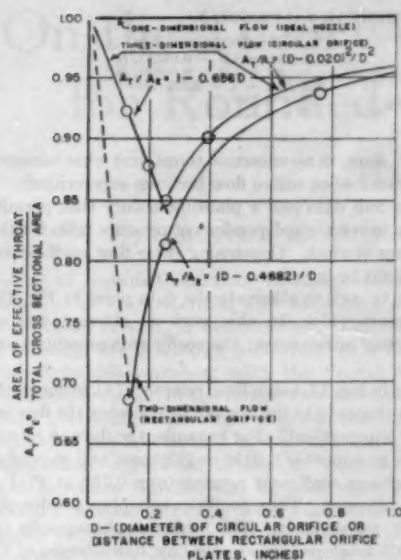
0.920 was obtained with a 0.122-in-diam orifice. These values are plotted in Fig. 11 and happen to fall on a straight line with the origin. Thus, for values of D less than 0.25 in., the effective area ratio in three-dimensional flow can be represented by

$$A_t/A_E = 1 - 0.656D \dots \dots \dots [19]$$

Fig. 11 represents, then, the "correction factor" to be applied to sonic-nozzle equations (reversible, adiabatic flow of a perfect gas through an ideal nozzle) to allow their use with square-edged sonic orifices. It adequately represents all of the experimental data obtained in this investigation.

DISCUSSION

The concept of flow through sonic orifices presented indicates that parameters useful in correlating subsonic-orifice data are not necessarily applicable to sonic orifices. For example, it is the actual magnitude of the upstream pressure, not the pressure ratio

FIG. 11 EFFECTIVE-AREA RATIO A_1/A_2 VERSUS D

across the orifice, which determines the mass-flow rate through a sonic orifice. The effect of approach velocity is automatically included in the flow equations presented here, since total or stagnation pressure, rather than static pressure, is used. However, for air at 60 F, an approach velocity of 600 fps would be required before the stagnation pressure would be 2 per cent greater than the static-pressure reading upstream of the orifice.

It is also very important that the actual orifice diameter, not a diameter ratio, be used in sonic-orifice calculations. In Fig. 12 a plot of D versus Δ is presented which includes not only the data for circular, square-edged sonic orifices obtained in this investigation, but also values of Δ calculated (12) from other data recently published in the ASME Transactions. All of the published data in which there is no doubt that sonic velocity actually occurred in the test orifice are plotted on this graph. This graph resolves some of the apparent discrepancies in the literature if one realizes that different flow coefficients will be obtained with different-diameter orifices, even if the orifice-to-pipe diameter ratio is constant.

Since the maximum value of Δ for circular orifices was found to be 0.010 in., all orifice-plate thicknesses greater than this value should give the same results. The circular orifices tested were constructed with an orifice plate thickness of $1/16$ in. Some additional experiments, however, were performed with a 0.122-in.-diam sonic orifice with an orifice-plate thickness of $1/4$ in. (12). No difference in the flow rate between the two thicknesses of orifice plate was observed. It is necessary that the orifice-plate thickness be sufficient to prevent mechanical deformation of the orifice plate. With rectangular orifices, deformation of $1/16$ -in. stainless-steel orifice plates along the $3/8$ -in. width occurred with upstream pressures near 600 psia. Hence $1/4$ -in.-thick plates were used for the experiments with rectangular orifices reported here. Differences in downstream geometry, such as beveling the downstream edge of a square-edged orifice plate, should make no difference in the mass-flow rate through a sonic orifice, if the normal part of the orifice plate is at least 0.010 in. thick. Obviously, downstream geometry should be such that sonic velocity actually occurs in the throat of the test orifice since a second throat downstream results in a subsonic test orifice.

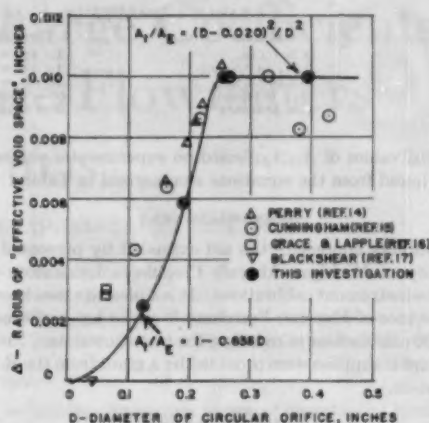


FIG. 12 COMPARISON OF CIRCULAR, SQUARE-EDGED, SONIC ORIFICE DATA

SUMMARY AND CONCLUSIONS

Two- and three-dimensional flow of air through square-edged sonic orifices results in the formation of a low-pressure zone at the upstream corner of the orifice plate. If the diameter of a circular orifice or the distance between the orifice plates of a two-dimensional rectangular orifice is designated as D , and if the distance that the low-pressure zone or effective void region extends into the stream is designated by Δ , then sonic velocity occurs in the effective throat of dimension $D - 2\Delta$ and the mass rate of flow through the orifice will be that predicted for one-dimensional, reversible, adiabatic flow of a perfect gas through an ideal nozzle whose throat diameter is $D - 2\Delta$.

Values of Δ were determined experimentally by shock-wave analysis of schlieren photographs, and by mass-flow measurements based on the decrease in mass of air stored in a system of known volume. The same values of Δ were obtained by the two methods for two-dimensional orifices. The value for Δ in two-dimensional flow is greater than in three-dimensional flow, however. The results of these experiments indicated:

1 The magnitude of Δ is independent of the pressure ratio between 1.894 and 40 (ratio of upstream total pressure to downstream static pressure), as well as of the absolute value of the upstream pressure.

2 The magnitude of Δ is independent of orifice diameter for large values of D . In the case of air, this corresponds to a D greater than $1/4$ in. Smaller values of Δ are obtained as D is decreased below this minimum, Δ approaching 0 as D approaches 0.

The maximum mass velocity through a square-edged orifice is

$$G = \left[\frac{\gamma g_c}{R/M} \right]^{1/2} \left[\frac{2}{\gamma + 1} \right]^{(\gamma+1)/2(\gamma-1)} \left[\frac{P_0}{\sqrt{T_0}} \right] \left[\frac{A_t}{A_B} \right]$$

For air flow, in engineering units, this equation reduces to

$$G = 76.35(P_0/\sqrt{T_0})(A_t/A_B)$$

where

- G = mass velocity, lb/sec/sq ft of total orifice area
- P_0 = upstream total or stagnation pressure, psia
- T_0 = upstream total or stagnation temperature, deg R
- A_t/A_B = area of effective throat/total orifice area
 - = $(D - 2\Delta)^2/D^2$ in three-dimensional flow through circular orifices
 - = $(D - 2\Delta)/D$ in two-dimensional flow through rectangular orifices

TABLE 1 VALUES OF A_t/A_E BASED ON EXPERIMENTAL VALUES OF Δ

D (in.)	Three-dimensional flow	Two-dimensional flow
$D > 1/4$ in.	$A_t/A_E = (D - 0.020)^{1/2}/D^2$	$A_t/A_E = (D - 0.0468)/D$
$D(1/8 \text{ to } 1/4 \text{ in.})$	$A_t/A_E = 1 - 0.656(D)$	$A_t/A_E = (D - 0.0468)/D$
$D(0 \text{ to } 1/8 \text{ in.})$	$A_t/A_E = 1 - 0.656(D)$	$A_t/A_E = 1 - 2.373(D)$
Max D tested	$D = 0.390$	$D = 0.750$
Min D tested	$D = 0.122$	$D = 0.128$

Numerical values of A_t/A_E , based on experimental values of Δ , may be found from the equations summarized in Table 1.

ACKNOWLEDGMENT

The authors appreciate the aid extended by personnel of the University of Michigan Aircraft Propulsion Laboratory during numerous instrument calibrations. It is a pleasure to acknowledge the assistance of Florence Forschner Weir for her performance of over 2500 calculations in reducing the mass-flow data. Necessary photographic supplies were provided by a grant from the Research Corporation.

BIBLIOGRAPHY

- 1 "Mémoire et expériences sur l'écoulement de l'air, déterminé par les différences de pressions considérables," by L. Wantael and A. J. C. Saint Venant, *Journal de l'École Royale Polytechnique*, series 1, vol. 16, 1839, pp. 85-122.
- 2 "Report of Recent Researches in Hydrodynamics," by G. G. Stokes, Reports of Meetings of the British Association for the Advancement of Science, vol. 1 (relating to the 16th Meeting), 1846.
- 3 "On the Velocity With Which Air Rushes Into a Vacuum, and on Some Other Phenomena Attending the Discharge of Atmospheres at Higher Into Atmospheres of Lower Density," by H. Wilde, Proceedings of the Manchester Literary and Philosophical Society, vol. 25, 1885, p. 17.
- 4 "On the Flow of Gases," by O. Reynolds, Proceedings of the Manchester Literary and Philosophical Society, vol. 25, 1885, p. 55.
- 5 "Elements of Aerodynamics of Supersonic Flows," by A. Ferri, The Macmillan Company, New York, N. Y., 1949.
- 6 "A New Equation of State for Fluids," by J. A. Beattie and O. C. Bridgeman, Proceedings of the American Academy of Arts and Sciences, vol. 63, 1928, p. 298.
- 7 "Fluid Mechanics," by R. C. Binder, Prentice Hall, Inc., New York, N. Y., second edition, 1949.
- 8 "Introduction to Theoretical Gas Dynamics," by R. Sauer, Springer-Verlag OHG, 1943, Berlin, Germany, translation by F. K. Hill and R. A. Alpher, J. W. Edwards, Ann Arbor, Mich., 1947.
- 9 "Foundations of Aerodynamics," by A. M. Kuethe and J. D. Schetzler, John Wiley & Sons, Inc., New York, N. Y., 1950.
- 10 "Introduction to Aerodynamics of a Compressible Fluid," by H. W. Liepmann and A. E. Puckett, John Wiley & Sons, Inc., New York, N. Y., 1947.
- 11 "Notes and Tables for Use in the Analysis of Supersonic Flow," Staff of the Ames 1 by 3 foot Supersonic Wind Tunnel Section, National Advisory Committee for Aeronautics, NACA TN 1428, 1947.
- 12 "Two- and Three-Dimensional Flow of Air Through Square-Edged Sonic Orifices," by A. Weir, Jr., PhD Dissertation, University of Michigan, February, 1954 (copies may be obtained from University Microfilms, Ann Arbor, Mich.).
- 13 This photograph was obtained in 1948 in the University of Michigan Supersonic Wind Tunnel by Joseph Rutkowski, now Associate Professor of Aeronautical Engineering, Wayne University, Detroit, Mich.
- 14 "Critical Flow Through Sharp-Edged Orifices," by J. A. Perry, Jr., Trans. ASME, vol. 71, 1949, p. 757.
- 15 "Orifice Meters With Supercritical Compressible Flow," by R. G. Cunningham, Trans. ASME, vol. 73, 1951, p. 625.
- 16 "Discharge Coefficients of Small-Diameter Orifices and Flow Nozzles," by H. P. Grace and C. E. Lapple, Trans. ASME, vol. 73, 1951, p. 639.
- 17 "NACA Sonic-Flow-Orifice Temperature Probe in High-Gas-Temperature Measurement," by P. L. Blackshear, Jr., Trans. ASME, vol. 75, 1953, p. 51.

Discussion

P. L. BLACKSHEAR, JR.¹ It is certainly a pleasure to have

¹ Aeronautical Research Scientist, National Advisory Committee for Aeronautics, Cleveland, Ohio.

the authors show, in no uncertain terms, just what becomes of the vena contracta when orifice flow becomes supercritical. It is reassuring to find data and a plausible theory that permit orifice coefficients to remain independent of pressure ratio for the range of conditions studied. Concerning these flow coefficients, a few remarks might be in order.

It might be well to eliminate the data point in Fig. 12, taken from reference (17). In this work no attempt was made to measure actual orifice areas; the coefficients presented were relative.

The data in Fig. 12, taken from reference (4), bring up the question: What happens to the flow coefficient when the flow is critical or slightly supercritical? For example, the data in reference (4) were taken in orifices of 0.0156 in. thickness and showed a variation in discharge coefficient ranging from 0.756 at $P_1/P_2 = 2$ to 0.843 at $P_1/P_2 \rightarrow \infty$. These coefficients imply a Δ value of 0.026 D to 0.046 D , respectively. The schlieren photographs of Fig. 6 show a well-developed supersonic flow downstream of the vena contracta at a $P_1/P_2 = 2$ (the photograph labeled 28.0 psia). One would expect that the mechanism which applied to the higher pressure-ratio flows would apply here, and hence would apply in the region of varying coefficients reported in reference (4). Could the authors define geometry and pressure-ratio limitations that would reconcile this seeming inconsistency?

AUTHORS' CLOSURE

The authors are pleased that Mr. Blackshear agrees with our interpretation of experimental observations. With respect to Mr. Blackshear's (17) data point used in Fig. 12, the fact that the flow coefficients reported were relative, not absolute, values for the 0.040 in.-diam orifice should give a high value of Δ , which presently is slightly below our curve. The actual magnitude of Mr. Blackshear's flow coefficient is, however, not so significant as his observation (17) that "in no case was there any recordable deviations in flow coefficients as pressure ratios exceeded 3.2." Mr. Blackshear performed "exhaustive tests" with pressure ratios up to 9 (total upstream pressure/downstream static pressure) since a previous investigator (14) had indicated that the flow coefficient increased with pressure ratio after the critical-pressure ratio had been reached. Mr. Blackshear apparently is referring to this work (14 not 4) in the last paragraph of his comments.

In (14), the discharge coefficient was reported to have increased from 0.756 at a pressure ratio of 1.895 to 0.843 at a pressure ratio of 6.8 with $1/16$ in. (not 0.0156 in.) thick orifice plates. Five orifices with diameters ranging from 0.1564 to 0.2500 in. were tested, but no distinction was made between the results obtained with the different orifice diameters. Only values of Δ computed from the experiments (14) performed when the valve downstream of the test orifice was wide open were plotted in Fig. 12. In other words, the same value of the flow coefficient of 0.84 was used to compute Δ for all five orifice diameters. Unfortunately, insufficient details of Mr. Perry's (14) experiments are reported to be positive of the reason for the apparent increase in flow coefficient but, to answer Mr. Blackshear's question specifically, there is no doubt in the authors' minds that the same mechanism which applies to our data over the entire pressure ratio range of 1.895 to 40 also applies to the range from 1.895 to 6.8. There was no indication of any change in the flow coefficient in our data in the pressure ratio range from 1.895 to 40.

On the Theory of Discharge Coefficients for Rounded-Entrance Flowmeters and Venturis

By MIGUEL A. RIVAS, JR.,¹ AND ASCHER H. SHAPIRO,² CAMBRIDGE, MASS.

A theory of rounded-entrance flowmeters, based on a consideration of the potential and boundary-layer flows in a converging nozzle, is constructed. Curves are presented showing the discharge coefficient as a function of diameter Reynolds number, with the "total equivalent length-diameter ratio" of the nozzle as a parameter. The equivalent frictional length-diameter ratio of the contraction section of the ASME long-radius nozzle is presented. The theoretical curves of discharge coefficient versus diameter Reynolds number are in good agreement with experiment over a range of Reynolds number from 1 to 10^4 . The theory provides a rational framework for correlating and extrapolating experimental results; it shows the effects of contraction shape and location of pressure taps; it furnishes values of discharge coefficient for untested designs; and it suggests precautions to be taken in design, installation, and operation.

NOMENCLATURE

The following nomenclature is used in the paper:

- A = cross-sectional area of cylindrical portion of nozzle (Fig. 1)
- C_D = discharge coefficient of meter, defined by Equation [4]
- D = diameter of cylindrical portion of nozzle (Fig. 1)
- f_{APP} = integrated apparent friction coefficient, defined by Equation [2]
- L = length of cylindrical portion of nozzle (Fig. 1)
- L_{eq} = equivalent frictional length of contraction section
- $L' = L + L_{eq}$
- p = pressure
- r = radius in cylindrical co-ordinates (Fig. 6)
- Re_D = diameter Reynolds number, $\rho V D / \mu$
- Re_x = length Reynolds number, $\rho V x / \mu$
- s = arc length along wall (Fig. 6)
- u = velocity component in x -direction
- U = potential-flow velocity at wall, outside of boundary layer
- v = velocity component in r -direction
- V = volume-mean velocity in cylindrical portion of nozzle
- w = mass rate of flow
- x = axial distance from beginning of cylindrical section
- y = distance normal to wall
- δ = boundary-layer thickness
- δ^* = boundary-layer displacement thickness

¹ Graduate Student, Massachusetts Institute of Technology. Assoc. Mem. ASME.

² Professor of Mechanical Engineering, Massachusetts Institute of Technology. Mem. ASME.

Contributed by the Research Committee on Fluid Meters and presented at the Annual Meeting, New York, N. Y., November 28-December 3, 1954, of THE AMERICAN SOCIETY OF MECHANICAL ENGINEERS.

NOTE: Statements and opinions advanced in papers are to be understood as individual expressions of their authors and not those of the Society. Manuscript received at ASME Headquarters, April 19, 1954. Paper No. 54-A-98.

- ρ = mass density
- μ = coefficient of viscosity
- θ = boundary-layer momentum thickness
- ψ = stream function, defined by Equation [8]

Subscripts

- (₀) = signifies stagnation reservoir upstream of nozzle
- (₁) = signifies beginning of cylindrical section
- (₂) = signifies location of downstream static-pressure tap

INTRODUCTION

Statement of Problem. The flowmeter nozzle and the venturi meter have an ancient and important engineering history whose past and present significance are attested by the vast literature (1)² describing flow-calibration tests under manifold conditions.

² Numbers in parentheses refer to the Bibliography at the end of the paper.

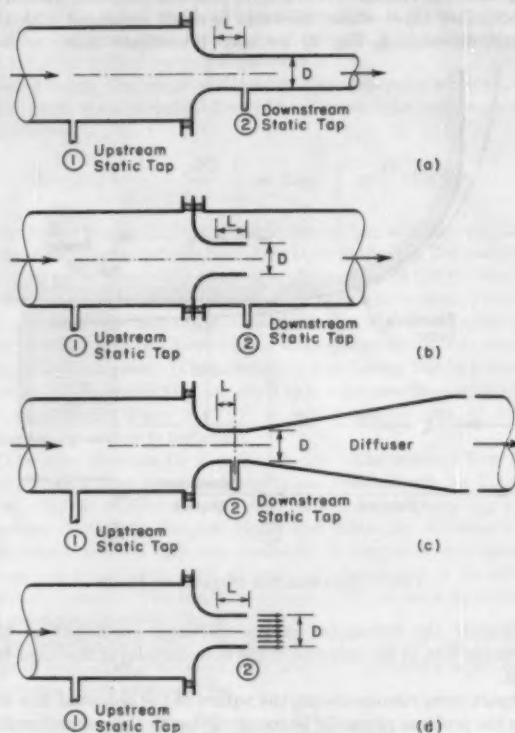


FIG. 1 FLOWMETER CONFIGURATIONS TO WHICH PRESENT THEORY IS APPLICABLE

(D is diameter of cylindrical section of accelerated jet; L is length of cylindrical section from end of contraction section to downstream static-pressure tap.)

Consequently, it comes as a surprise to find that, at least to the authors' knowledge, there is no basic theory of such flowmeters. Kretschmer (2) attempted to formulate such a theory, but did not perceive the central role of the boundary-layer development, and was therefore unable to arrive at quantitative results. It is the purpose of this paper to present a fundamental theory and to show how the predicted discharge coefficients compare with experimental data.

Assumptions

So different are the flow phenomena in a sharp-edged orifice meter and in a rounded-entrance flowmeter that separate analytical treatments are necessary. In this paper we shall consider only the rounded-entrance flowmeter in which there is no vena contracta. Fig. 1 shows some of the configurations to which the present theory is applicable. In each case there is a smooth contraction from a large-diameter to a small-diameter pipe, and following the contraction there is a short length of constant-diameter pipe preceding the downstream static-pressure tap. The solid surfaces are assumed to be smooth; more specifically, the surface-roughness dimensions are assumed to be negligible as compared with the boundary-layer thickness. Only incompressible, steady flow is considered.

Description of Flow in Rounded-Entrance Meter

We now discuss qualitatively the details of the flow in a rounded-entrance meter and how these details influence the discharge coefficient.

High Reynolds Numbers. When the Reynolds numbers are so large that the viscous effects are, for practical purposes, limited to a boundary layer whose thickness is small compared with the nozzle dimensions, Fig. 2, we may investigate more or less

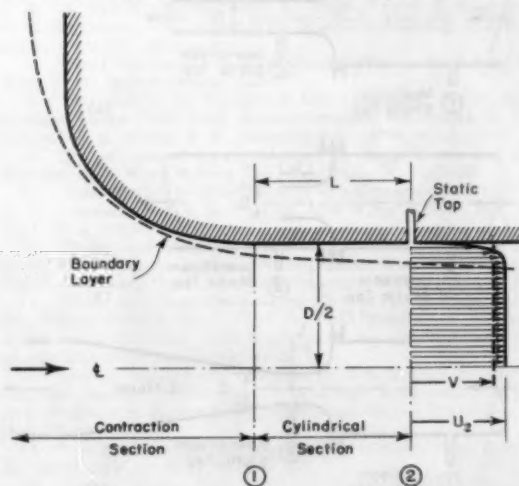


FIG. 2 ILLUSTRATES DETAILS OF FLOW

separately the influences on the discharge coefficient of the potential flow in the core and of the boundary-layer flow near the wall.

Apart from viscous effects, the nature of the potential flow enters the problem primarily in connection with the nonuniformity of the pressure and velocity distributions in the plane of the downstream static-pressure tap. In general the streamlines in this plane have a slight curvature and, accordingly, there is a pressure gradient normal to the streamlines of such direction that

the pressure at the wall is less than that on the center line. Therefore the downstream static-pressure tap measures a pressure less than the average over the cross section, and, by Bernoulli's equation, leads to an inferred velocity greater than the average. From this reasoning it is seen that the assumption of the flow being uniform in the exit plane of the nozzle would lead to a discharge coefficient of less than unity even if viscosity were completely absent. However, the streamline curvature which generates this effect diminishes as the length-diameter ratio L/D of the straight section increases. Indeed, when on both sides of the pressure tap there are straight sections having lengths of the order of $1/4$ diameter or more, it is shown in the example described later that the nonuniformity of the potential flow in plane 2 is negligibly small. In what follows we shall assume that L/D is sufficiently large to permit the assumption of uniform flow in the potential core at section 2.

The nature of the potential flow associated with a given contraction shape also influences the discharge coefficient indirectly because the boundary-layer development to be described is controlled in part by the longitudinal pressure gradients established by the potential flow.

Turning now to the boundary layer, its growth depends on (a) viscous effects, (b) changes in radius of the contraction section which require changes in boundary-layer thickness to accommodate a given boundary-layer flow, and (c) pressure gradients. For a typical contraction section, the example worked out later shows that up to nearly the end of the contraction section the effect of the falling pressure gradient is predominant, and the boundary layer becomes thinner; shortly before the beginning of the cylindrical section, viscosity becomes predominant, and the boundary layer becomes thicker, Fig. 2.

Very Low Reynolds Numbers. When the Reynolds number is very small, the foregoing picture is modified in that the boundary layer occupies all, or nearly all, of the cross-sectional area. The conceptual picture of a potential flow and a boundary-layer flow which may be treated separately is then invalid, and the analytical treatment is very difficult. However, when the Reynolds numbers are so low as to be in the "creeping" range, i.e., inertia forces are negligible compared to viscous forces, dimensional reasoning suggests a powerful scheme for generalizing a small amount of experimental data.

The Discharge Coefficient

To illustrate how the discharge coefficient depends on frictional effects, let us begin with a model in which there is no friction whatsoever in the contraction, so that the boundary layer begins to form only at the beginning of the cylindrical section, Fig. 2. Then Bernoulli's equation gives

$$p_0 - p_1 = \frac{\rho}{2} V^2 \quad [1]$$

Between sections 1 and 2 we may account for friction by analogy with pipe friction in fully developed flow by writing

$$p_1 - p_2 = 4\bar{f}_{APP} \frac{L}{D} \frac{\rho}{2} V^2 \quad [2]$$

where \bar{f}_{APP} is a "mean apparent friction factor" over the length L and is defined by this equation. It is called "apparent" (3) because it includes the effects of changes in momentum flux as well as of the usual wall friction on the pressure drop; it is called "mean" because the local apparent friction factor varies with axial distance (3, 4, 5).

Now, adding Equations [1] and [2], we get

$$p_0 - p_2 = \frac{\rho}{2} V^2 \left(1 + 4\bar{f}_{APP} \frac{L}{D} \right) \quad [3]$$

The discharge coefficient is defined as the ratio of the actual flow passing through the nozzle to the flow which would pass for the same pressure drop if the flow were frictionless. Using Bernoulli's equation, and the continuity equation $w = \rho AV$, together with Equation [3], we get

$$C_D = \frac{\rho AV}{A \rho \sqrt{2(p_0 - p_2)/\rho}} = \frac{1}{\sqrt{1 + 4f_{AFF} \left(\frac{L}{D}\right)}} \quad [4]$$

An alternate expression may be obtained for the case in which a potential core exists at section 2. Letting U_2 denote the velocity in the potential core at section 2, Bernoulli's equation written for any streamline not entering the boundary layer is $p_0 - p_2 = \rho U_2^2/2$, and thus Equation [4] shows that

$$C_D = V/U_2 \quad [5]$$

In other words, the discharge coefficient is equal to the ratio of the mean velocity to the potential core velocity at section 2.

Thus far we have not considered friction in the contraction section. At high Reynolds numbers, i.e., when a potential core exists, Equation [5] for C_D is valid regardless of where the boundary layer begins to develop, whether in the contraction or in the cylindrical section. The expression for C_D given by Equation [4], however, may be regarded as approximately valid when there is friction in the contraction section provided that L is replaced by L' , where the latter is interpreted as a pseudo length equal to the sum of L and an equivalent frictional length L_{eq} for the contraction section. Thus

$$C_D = \frac{1}{\sqrt{1 + 4f_{AFF} \frac{L + L_{eq}}{D}}} = \frac{1}{\sqrt{1 + 4f_{AFF} \frac{L'}{D}}} \quad [6]$$

Plan of Procedure

In what follows we shall first consider the simple case where the contraction section is replaced by an equivalent length of tube, in which case the discharge coefficient may be found from Equation [6] in conjunction with existing theoretical solutions (5, 6, 7, 8, 9) for the value of f_{AFF} in the entry of a tube. Subsequently we shall apply boundary-layer theory to determine the equivalent length of the contraction section, thus completing the picture of how friction influences the discharge coefficient of a rounded-entrance flowmeter.

ANALYSIS OF MODEL IN WHICH CONTRACTION SECTION IS REPLACED BY EQUIVALENT FRICTIONAL LENGTH

In the model of Fig. 3 the contraction section is replaced by the equivalent length L_{eq} , and the flow is assumed to enter the tube at section 1 with uniform velocity and no boundary layer. If L/D is of the order of $1/2$ or greater this model will adequately portray orders of magnitudes, even with very rough estimates of L_{eq} , inasmuch as the fluid velocities (and correspondingly the frictional stresses) are on the average very much less in the contraction section than in the cylindrical section.

Comparison With Boundary Layer on Flat Plate. Near $x = 0$, where the boundary layer is thin compared with the tube radius, the flow in the boundary layer is substantially like that on a flat plate, except that in the tube there is a falling pressure gradient as compared with zero pressure gradient for the flat plate in an infinite stream. However, the theoretical investigations of (5) concerning the boundary-layer development in a tube demonstrate that in the region of thin boundary layers the pressure gradient has a virtually negligible effect on the velocity profile and rate of growth of the boundary layer.

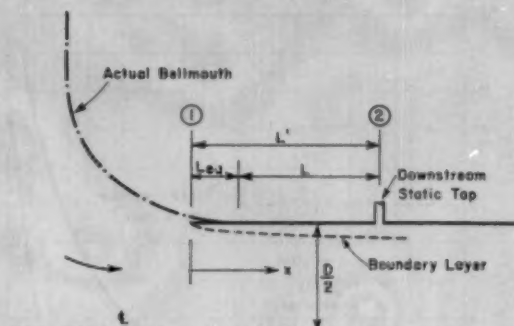


FIG. 3 SIMPLIFIED MODEL IN WHICH CONTRACTION SECTION IS REPLACED BY EQUIVALENT FRICTIONAL LENGTH INTO WHICH FLOW ENTERS WITH UNIFORM VELOCITY AND NO BOUNDARY LAYER

Conditions for Boundary Layer to be Laminar. Because of the generally strong falling pressure gradient in the contraction section, the boundary layer beginning at $x = 0$ may be expected to be laminar, provided that the contraction section is designed to avoid appreciable suction peaks on the wall. Furthermore, since the falling pressure gradient in the cylindrical section (due to friction) is favorable to the maintenance of laminar boundary layers, the longitudinal length required for the flat-plate-like boundary layer to become turbulent may be expected to be at least as great as in the case of a flat plate with no pressure gradient. For the latter it is known that, in a stream of moderate initial turbulence, the length Reynolds number of transition $Re_{x,t}$ is of the order of $5(10)^5$. Experiments in the entries of tubes (3, 4, 5) demonstrate the validity of the foregoing arguments.

Accordingly, the range of diameter Reynolds number $Re_{D,t}$ in which the flow up to section 2 may be expected to be laminar, is of the order of

$$Re_{D,t} = \frac{\rho V D}{\mu} = \frac{\rho V L}{\mu} \frac{D}{L} = Re_{x,t} \frac{D}{L} \cong \frac{D}{L} (5)(10)^5$$

In most flowmeters L/D is of the order of $1/2$; accordingly, the range of $Re_{D,t}$ for which the boundary layer in the length L may be expected to be completely laminar is of the order of $(10)^5$. Many flowmeters of interest have values of $Re_{D,t}$ less than this. Therefore we reach the important conclusion that the assumption of laminar flow up to the downstream static-pressure tap will cover many practical cases. This assumption underlies the following discussion. Subsequently we shall say a few words concerning the range where $Re_{D,t} > (10)^5$, in which range part of the boundary-layer flow is turbulent.

Theoretical Solution for Laminar Entry. The laminar flow in the entry of a tube has been investigated theoretically by Bousinesq (6), by Schiller (7), by Atkinson and Goldstein (8), by Langhaar (9), and by Shapiro, Siegel, and Kline (5). All these investigations led, by different methods, to results which agree within a few per cent, and all may be considered to be substantially correct. The results of reference (5) are used hereafter and are summarized by Fig. 4.

The experimental results of reference (4), carried out in the range of $Re_{x,t}/Re_{D,t}^2$ between 10^{-6} and 10^{-8} , yielded a mean experimental curve expressed by

$$4f_{AFF}(x/D) = 13.74 \sqrt{Re_{x,t}/Re_{D,t}}$$

which shows excellent agreement with Fig. 4.

Determination of Discharge Coefficient. From Equation [6] and Fig. 4 it is evident that C_D depends only on the single parameter

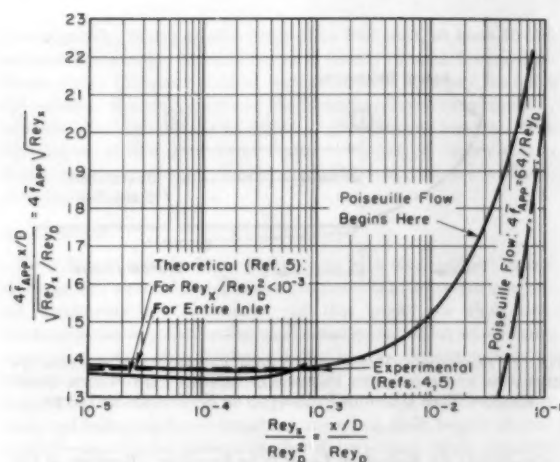


FIG. 4 THEORETICAL CURVES OF APPARENT FRICTION FACTOR FOR LAMINAR ENTRY OF TUBE, ACCORDING TO SHAPIRO, SIEGEL, AND KLINE (4)

$(L'/D)/Rey_D$, irrespective of the individual values of L'/D and Rey_D . Thus it is possible to construct the universal curve of Fig. 5(a).

Given the value of L'/D for a particular flowmeter, and using Equation [6] in conjunction with Fig. 4, the curves of Figs. 5(b) and 5(c) may be established, showing C_D as a function of L'/D and of Rey_D .

Boundary Layer Partially Turbulent. The curves of Fig. 5 are valid only up to values of Rey_D of about $(10)^6$, after which the point of transition lies upstream of section 2, and the boundary layer is turbulent over a portion of its length.

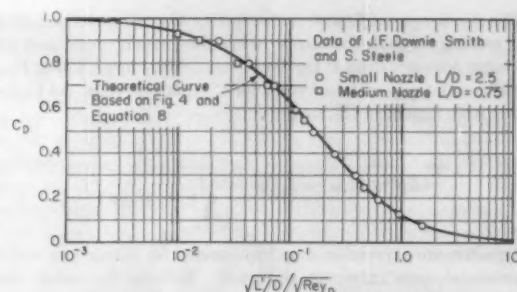
Experiments in the entries of tubes (3) indicate that, after some peculiarities associated with the onset of turbulence, the local apparent friction zone factor in the turbulent zone is generally slightly less than the average apparent friction factor in the laminar zone preceding transition, and that, as x increases, the value of f_{app} in the turbulent zone decreases slightly and gradually approaches the asymptotic value for fully developed turbulent pipe flow.

With these experimental facts in mind, and taking note of Equation [6], we may expect that as Rey_D increases beyond the limit of laminar flow, the curves of Fig. 5 will continue to increase slightly and will then remain virtually constant no matter how large Rey_D becomes.

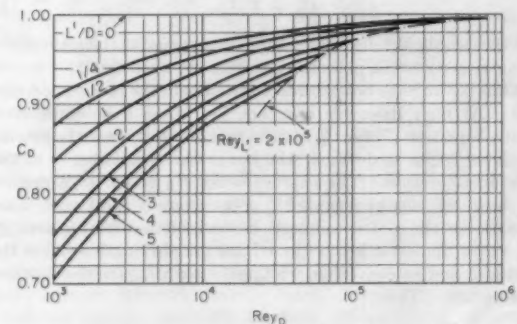
EQUIVALENT FRICTIONAL LENGTH OF CONTRACTION SECTION

Outline of Procedure. By the "equivalent frictional length" L_{eq} of the contraction section, we mean that fictitious length of straight tube of diameter D which, if placed before the actual length of cylindrical tube of length L , would lead to a discharge coefficient identical with the discharge coefficient produced by the actual combination of bellmouth and cylindrical section. In order to find L_{eq} the following procedure is employed: (a) Boundary-layer theory is employed to determine the boundary-layer properties at section 2, and, from Equation [5], the discharge coefficient C_D ; (b) inserting the latter into Equation [6], the value of $4f_{app}L'/D$ is computed; (c) from Fig. 4 the value of L'/D may then be found; (d) by subtraction of L/D , the value of L_{eq}/D is computed.

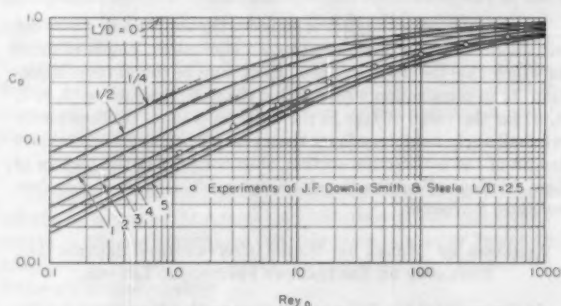
An iterative procedure is required to determine the boundary-layer growth, involving an initial calculation of the pressure dis-



(a) Universal curve showing C_D as function of single parameter $\sqrt{L'/D} / \sqrt{Rey_D}$



(b) C_D versus Rey_D for various values of L'/D , in high range of Rey_D . Line marked $Rey_L' = 2(10)^6$ represents approximately the limit to which the approximation of laminar flow is valid, although under favorable conditions the limit might reach 10^6 .



(c) Similar to (b), but for low range of Rey_D .

FIG. 5 THEORETICAL CURVES OF C_D FOR LAMINAR FLOW

tribution of the potential flow, computation of the boundary-layer growth, recalculation of the potential flow, and so on, until convergence is obtained.

Specific Contraction Contour Chosen for Study. The equivalent length of the contraction depends both on the shape of the contraction and on the diameter Reynolds number, Rey_D . The results presented in this paper are for the standard ASME elliptical contour (11) shown in Fig. 6.

Since the contour of Fig. 6 is not very different from that used on other flow nozzles and venturis, and inasmuch as the discharge coefficient does not usually depend decisively on the equivalent length of the contraction, the equivalent length found for the contour of Fig. 6 may often with little error be used for other contrac-

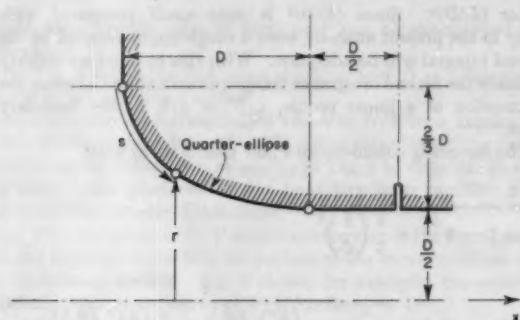


FIG. 6 ASME ELLIPTICAL CONTRACTION SECTION SELECTED FOR SPECIFIC CALCULATIONS

tion contours, subject, however, to the precautions discussed in Section 7.

Potential Flow Solution (First Approximation). We now present the potential-flow solution for the contraction section of Fig. 6. Steady, incompressible, nonviscous flow is assumed, and the x, r -system of cylindrical co-ordinates shown in Fig. 6 is employed. The velocity components in the x and r -directions are denoted by u and v , respectively.

The equation of continuity is

$$\frac{\partial}{\partial x}(ur) + \frac{\partial}{\partial r}(vr) = 0 \dots \dots \dots [7]$$

This equation is the necessary and sufficient condition for the existence of Stokes' stream function, defined by

$$ur = \partial\psi/\partial r; \quad vr = -\partial\psi/\partial x \dots \dots \dots [8]$$

Since all the streamlines originate in a reservoir where conditions are uniform, and viscous stresses are ignored, the flow is irrotational. Therefore we may write

$$\partial u/\partial r = \partial v/\partial x \dots \dots \dots [9]$$

Substituting the expressions for u and v given by Equation [8] into Equation [9] and expanding, we get

$$\frac{\partial^2 \psi}{\partial x^2} + \frac{\partial^2 \psi}{\partial r^2} - \frac{1}{r} \frac{\partial \psi}{\partial r} = 0 \dots \dots \dots [10]$$

which is Laplace's equation in cylindrical co-ordinates.

We now have a boundary-value problem in which we must find the solution to Equation [10] subject to the following boundary conditions: (a) The flow follows the contour. This may be expressed by assigning constant values of ψ to the axis ($r = 0$) and to the wall streamlines.

(b) In the cylindrical section "far downstream" of the contraction the flow is uniform and parallel. This may be expressed by setting

$$\psi = (2r/D)^2 \psi_{\text{wall}}$$

on a downstream plane normal to the axis, based on an arbitrary value of zero for ψ on the axis. Tentatively it was assumed that the flow was uniform and parallel at the downstream static tap, and the subsequent calculations demonstrated that this plane was indeed sufficiently far from the contraction to justify the assumption.

(c) Far upstream of the contraction the flow approaches asymptotically a spherically symmetrical sink flow.

Manageable methods for solving Equation [10] analytically, subject to the foregoing boundary conditions, are not known. Consequently, solutions may be obtained only by numerical

methods. That best-suited to the purpose, and the one used here, is the well-known relaxation method of Southwell (12). The details of the calculations are too lengthy to be given here, but the outcome is that the value of ψ is found at the net points of an orthogonal grid. Then, by numerical differentiation of Equations [8], the velocity components u and v may be computed as functions of x and r . From the values of u and v may be calculated the speed $U = \sqrt{u^2 + v^2}$. Then, by Bernoulli's equation, the pressure p may be found at any x and r through the relation

$$p = p_0 - \rho U^2/2$$

where p_0 is the total pressure, or the pressure far upstream of the contraction.

For our present purpose the significant result of the potential-flow solution is the velocity distribution at the wall, shown in Fig. 7 in dimensionless terms. Two features stand out:

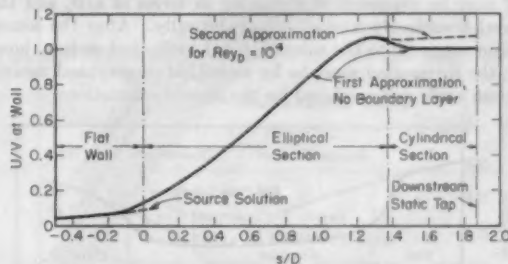


FIG. 7 POTENTIAL-FLOW VELOCITY DISTRIBUTION ON NOZZLE WALL FOR NOZZLE OF FIG. 6.

(Solid line shows first approximation, based on no boundary layer, $Re_D \rightarrow \infty$. Dashed line shows second approximation for $Re_D = 10^4$.)

(a) There is a velocity peak slightly upstream of the cylindrical section, followed by a deceleration. This is probably inevitable in nozzles having cylindrical measuring sections (13), and throws some doubt on the earlier assumption that the flow is laminar in the cylindrical section. For the moderately adverse pressure gradient of Fig. 7, the close comparison between the measured discharge coefficient and that computed in this paper with the assumption of laminar flow indicates, however, that the assumption of laminar flow is valid. The same would not necessarily be true, however, for other nozzle forms in which more severe adverse pressure gradients prevailed.

(b) The velocity distribution becomes flat at a distance of about $0.2D$ downstream of the contraction section, thus demonstrating that the streamlines at that point have become parallel, and justifying the choice of downstream boundary condition for solution of the potential flow problem.

Boundary-Layer Solution (First Approximation). For practical calculations of laminar boundary layers the integral method of von Karman and Pohlhausen is suitable as regards both simplicity and accuracy, at least when severe adverse pressure gradients are absent. The method has been cast in a particularly convenient form by Thwaites (10) for two-dimensional boundary layers. Rott and Crabtree (14) have extended Thwaites' method to the axially symmetric case, with the restriction that the local boundary-layer thickness is small compared with r . This last implies that Re_D is not too small.

The procedure of Rott and Crabtree, which we use here, states that the momentum thickness θ at a given location s is given by

$$\theta^2 = a \frac{\mu}{\rho} r^{-2} U^{-3} \int_{-\infty}^s r^2 U^{1/2} ds \dots \dots \dots [11]$$

where U is the potential-flow velocity immediately outside the

boundary layer, and where a and b are semiempirical constants having the values $a = 0.45$ and $b = 6$. It is assumed for Equation [11] that the quantity $\theta^2 r^2 U^3$ goes to zero far upstream of the elliptical contraction section.

Rearranging Equation [11] in dimensionless form, with V as the reference velocity and D as the reference length, we obtain

$$\left(\frac{\theta}{D}\right)^2 \text{Rey}_D = 0.45 \left(\frac{r}{D}\right)^2 \left(\frac{U}{V}\right)^4 \int_{-\infty}^{s/D} \left(\frac{U}{V}\right)^6 \left(\frac{r}{D}\right)^2 d\left(\frac{s}{D}\right) \quad \dots [12]$$

The value of r/D as a function of s/D is known from the nozzle contour, Fig. 6. Moreover, the value of U/V is known as a function of s/D from the potential flow solution, Fig. 7. Consequently Equation [12] may be integrated to give $(\theta/D)\sqrt{\text{Rey}_D}$ as a function of s/D . For the region of the potential-flow source solution (i.e., upstream of the elliptical section), both r/D and U/V may be expressed algebraically in terms of s/D , and the integral accordingly worked out analytically. After the source solution merges into the solution for the elliptical section, however, the integration must be by numerical or graphical means; Simpson's rule was employed for the present calculations.

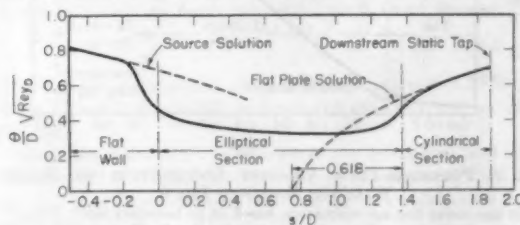


FIG. 8 FIRST APPROXIMATION TO BOUNDARY-LAYER MOMENTUM THICKNESS AS A FUNCTION OF ARC LENGTH, CORRESPONDING TO FIRST APPROXIMATION TO VELOCITY DISTRIBUTION SHOWN IN FIG. 7

The results of the integration are shown in Fig. 8, with $(\theta/D)\sqrt{\text{Rey}_D}$ plotted against s/D .

Equivalent Length (First Approximation). The foregoing results are restricted to the case where $\theta/D \ll 1$. Since $(\theta/D)\sqrt{\text{Rey}_D}$ is seen from Fig. 8 to be of the order of 0.5 in the region of interest, we are limited to values of Rey_D in excess of about 1000.

In order to evaluate U_2/V , consider a tube flow with uniform velocity U in a potential core and in which at any value of x there is a boundary layer of thickness δ . Letting u represent the velocity in the boundary layer at a distance y from the wall, we may write from continuity considerations that

$$\frac{\pi}{4} D^2 V = \frac{\pi}{4} (D - 2\delta)^2 U + \int_0^\delta \pi (D - 2y) u \, dy$$

This may be rearranged algebraically to give

$$\frac{U}{V} = \frac{1}{1 - 4 \frac{\delta}{D} \int_0^1 \left(1 - \frac{u}{U}\right) d\left(\frac{y}{\delta}\right) + 4 \left(\frac{\delta}{D}\right)^2 \int_0^1 \left(1 - 2 \frac{y}{\delta} \frac{u}{U}\right) d\left(\frac{y}{\delta}\right)} \quad \dots [13]$$

We recognize the first integral in the denominator of this expression as giving the usual definition of the displacement thickness, δ^*

$$\frac{\delta^*}{\delta} = \int_0^1 \left(1 - \frac{u}{U}\right) d\left(\frac{y}{\delta}\right)$$

Regarding the second integral, we see that it is associated with the

factor $(\delta/D)^2$. Since $(\delta/D)^2$ is very small compared with unity in the present analysis, even a rough approximation to the second integral will be adequate. With this in mind we quickly evaluate the second integral as being approximately $1/3$, using the assumption of a linear profile, $u/U = y/\delta$, in the boundary layer.

The foregoing considerations now enable us to write

$$\frac{U}{V} = \frac{1}{1 - 4 \frac{\delta^*}{D} + \frac{4}{3} \left(\frac{\delta}{D}\right)^2} = \frac{1}{1 - 4 \left(\frac{\delta^*}{\theta}\right) \left(\frac{\theta}{D}\right) + \frac{4}{3} \left(\frac{\delta}{\theta}\right)^2 \left(\frac{\theta}{D}\right)^2} \quad \dots [14]$$

For a given value of Rey_D , Fig. 8 gives a first approximation to the value of θ/D at section 2. Moreover, the integral method of boundary-layer calculation permits us to compute the values of δ^*/θ and δ/θ at section 2. Consequently, we may, from Equation [14], compute V/U_2 , which, according to Equation [5], is the discharge coefficient C_D .

Having found (in this first approximation) C_D as a function of Rey_D , it is then possible, as explained earlier, to determine (again in first approximation) L_{eq}/D as a function of Rey_D , using Equation [6] and Fig. 4.

Iterative Improvement of Solution. As explained previously, the first approximation presented in the foregoing is incorrect because the effect of the boundary layer on the potential flow has been neglected. Since the displacement thickness of the boundary layer depends on Rey_D , it follows that Rey_D also influences the effective boundary of the potential flow, the distribution of U/V for the potential flow, and the effective length of the contraction section.

In order to follow undeviatingly the iterative procedure previously outlined, therefore, it would appear to be necessary to work out the relaxation solution of the potential flow for many Reynolds numbers, and, furthermore, to repeat this at each iteration. All this would involve a prohibitive amount of labor. An approximate but simple procedure, the assumptions of which appear to be quite plausible, was used instead.

The type of approximation which is appropriate stems from an appreciation that, in computing θ/D at the downstream static tap from Equation [12], the greatest contribution by far to the integral is that of the cylindrical section. This comes about because U/V appears to the fifth power in the integrand and because, according to Fig. 7, $(U/V)^5$ is generally much smaller than unity except in the cylindrical section. In the cylindrical section the flow is almost one dimensional except for the boundary-layer flow. Therefore the one-dimensional value of U/V in the cylindrical section may be found for a given boundary-layer thickness from simple continuity considerations.

The modified iterative procedure is therefore based on a model in which viscosity does not affect the potential-flow solution up-

stream of the cylindrical section, and in which the presence of the boundary layer in the cylindrical section increases in a one-dimensional manner the U/V values which would otherwise prevail. Equation [14] allows us to compute how U/V varies with x/D , inasmuch as the calculation method gives us θ/D as a function of x/D .

The iteration procedure used for calculating the equivalent

length for a specific value of Rey_D may now be summarized as follows:

(a) Fig. 8 shows the first approximation to θ/D as a function of s/D in the cylindrical section.

(b) Calculate the corresponding values of U/V from Equation [14]. Multiply the values of U/V from Equation [14] by the first approximation values of U/V shown in Fig. 7 to determine how the constriction produced by the boundary layer modifies the potential-flow velocity distribution.

(c) Plot the values of U/V determined in step (b) in Fig. 7, and fair the resulting curve into the portion of the curve upstream of the cylindrical section. Fig. 7 shows, for example, the second approximation to the curve of U/V for $Rey_D = 10^4$.

(d) With the U/V curve of step (c), calculate the θ/D distribution by integrating Equation [12]. This represents the second approximation to θ/D as a function of s/D .

(e) Starting with the second approximation to θ/D determined in (d), repeat steps (a) through (d) and thus find the third approximation. Continue the iteration procedure until satisfactory convergence is attained. The latter was achieved in the fifth approximation.

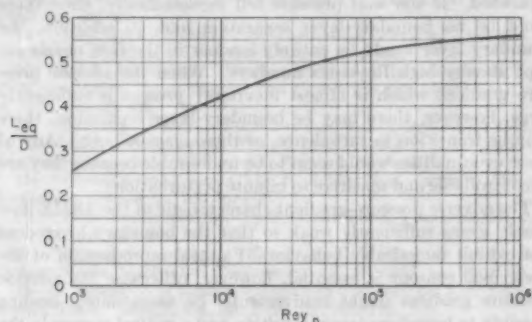


FIG. 9 EQUIVALENT LENGTH OF CONTRACTION SECTION VERSUS Rey_D FOR CONTOUR OF FIG. 6

Having in this way adequately determined θ_s/D as a function of Rey_D , L_{eq}/D was established as a function of Rey_D in the manner already outlined. The results of these calculations are presented in Fig. 9 where L_{eq}/D is plotted against Rey_D for the fifth approximation. The equivalent length decreases from a value of about 0.56 at $Rey_D = 10^3$ to a value of about 0.25 at $Rey_D = 1000$. For reasons given previously, it would be unsafe to employ the present analysis below a Reynolds number of about 1000.

COMPARISON WITH EXPERIMENTAL RESULTS

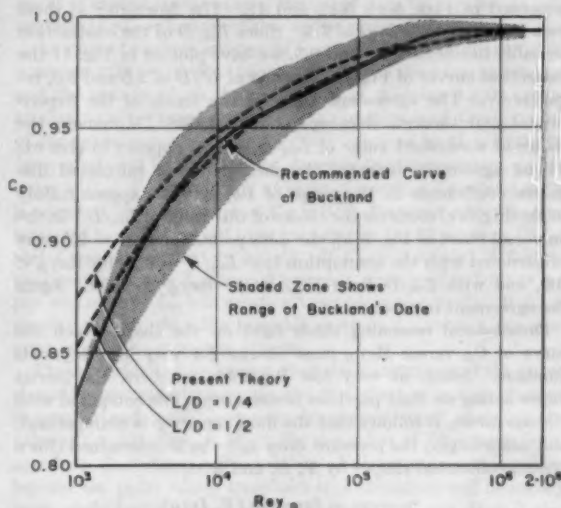
Data of Buckland for ASME Long-Radius Nozzle (11, 16). Using Fig. 9 to determine L_{eq}/D , and using Fig. 4 for determining $4f_{APP} L'/D$, Equation [6] may be employed for determining C_D versus Rey_D for the ASME flowmeter nozzle. Curves so computed are shown in Fig. 10(a) for values of L/D of 0.25 and 0.50.

Also shown in Fig. 10(a) are the experimental results of Buckland (16), found from tests of ten nozzles of different sizes but with the ASME contour, using water and oil as the flowing fluids. In Buckland's experiments the values of L/D for the cylindrical portions of the nozzles ranged from 0.35 to 0.58, with the bulk of the data (except for low Rey_D) referring to a value of 0.50.

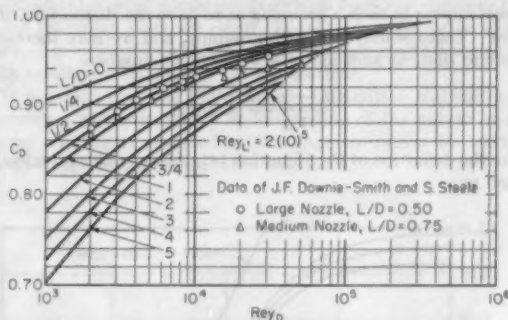
The computed curve for $L/D = 0.50$ is seen to fit the experimental data as well as Buckland's recommended curve, except in the range of Rey_D below 4000, where the experimental data are admittedly inaccurate. The theory also reflects faithfully the manner in which Reynolds number influences the discharge co-

efficient. The break in the curve at $Rey_D \approx 5(10^3)$ is the result of the point of transition from a laminar to a turbulent boundary layer moving upstream of the downstream static tap; because the turbulent skin-friction coefficient exceeds the laminar skin friction and varies only slightly with Reynolds number, the curve of C_D versus Rey_D does not continue upward toward unity, but instead becomes nearly level. This is in accord with the discussion given previously concerning this phenomenon.

Data of Downie Smith and Steele (17). Although the experiments of Downie Smith and Steele were made with contraction sections different from that to which Fig. 9 applies, it is, nevertheless, of interest to compare the theory based on Fig. 9 with the experimental results.



(a) ASME nozzle of Fig. 6



(b) Data of Downie Smith and Steele

FIG. 10 COMPARISON OF THEORETICAL AND EXPERIMENTAL RESULTS

In Fig. 10(b) are plotted curves of C_D versus Rey_D for various values of L/D , based on Equation [6], Fig. 4 and Fig. 9. Also shown are the experimental data of reference (17) for two nozzles, one with $L/D = 0.50$ and the other with $L/D = 0.75$. The agreement between theory and experiment is seen to be of the order of 1 per cent except for the high Reynolds-number data of the medium nozzle, data which behave unexplainably.

A further comparison with the data of Downie Smith and Steele is shown on the universal curve of Fig. 5(a). The agreement again is gratifying.

FLOW COEFFICIENT AT LOW REYNOLDS NUMBERS

For Reynolds numbers less than about 1000, the foregoing results cannot be expected to retain their accuracy. Unfortunately, there is no simple way of determining the equivalent length at low Reynolds numbers, nor is it known for that matter whether the concept of an equivalent length is valid.

Having found, however, that the equivalent length of the contraction section is important but not decisive, we may adopt an heuristic attitude and attempt to infer the equivalent length at low Reynolds numbers by simply superposing experimental curves on Fig. 5(c).

For this purpose we turn to the experimental results at very low Reynolds numbers of Downie Smith and Steel (17), which are presented in Figs. 5(a), 5(c), and 11. The flowmeter of these tests had a value of L/D of 2.5. Since L_{eq}/D of the contraction probably lies between 0 and 0.5, we have plotted in Fig. 11 the theoretical curves of Fig. 5 for values of L'/D of 2.5 and 3.0, respectively. The agreement between the forms of the experimental and theoretical curves is remarkable. Moreover, the choice of a constant value of $L_{eq}/D = 0.19$ appears to give excellent agreement between the measured and calculated discharge coefficients in the range of Re_D below approximately 1000. Fig. 5(c) confirms the choice of this value of L_{eq}/D . In the universal chart of Fig. 5(a), the data points for $L/D = 2.5$ were constructed with the assumption that $L_{eq}/D = 0.19$ for $Re_D < 800$, and with L_{eq}/D from Fig. 9 for $Re_D > 1000$. Again the agreement is good.

Dimensional reasoning sheds light on the shape which the curve of C_D versus Re_D must assume for very low Reynolds numbers. Since, at very low Reynolds numbers, the inertia forces acting on fluid particles become negligible compared with viscous forces, it follows that the fluid density ρ is unimportant, and accordingly, the pressure drop $p_0 - p_2$ is determined (for a given geometrical shape) by V , D , and μ

$$p_0 - p_2 = \text{function}(V, D, \mu)$$

For dimensional homogeneity to prevail, the quantities V , D , and μ must appear in such a grouping as to have the dimensions of a stress. There is only one such grouping, and we may therefore conclude that, at sufficiently low Reynolds numbers

$$\frac{(p_0 - p_2)D}{V\mu} = \text{const}$$

From the definition of C_D , Equation [4], this may be equivalently stated as

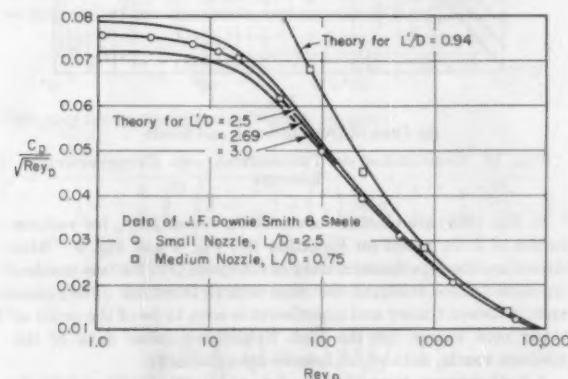


FIG. 11 COMPARISON OF THEORETICAL WITH EXPERIMENTAL RESULTS AT LOW REYNOLDS NUMBERS

$$C_D = \text{const} \sqrt{Re_D}$$

which shows that for very small values of Re_D , the discharge coefficient varies as the square root of the Reynolds number.

To illustrate this point, Fig. 11 represents $C_D/\sqrt{Re_D}$ as a function of Re_D . The fact that both the experimental and theoretical results approach horizontal asymptotes at low values of Re_D confirms the validity of the dimensional reasoning presented in the foregoing.

DISCUSSION OF VARIABLES IN FLOWMETER DESIGN

The analyses presented in this paper of flowmeter performance give some insight into what are the important factors to be considered in flowmeter design, construction, and installation, and indicate certain precautions which should be taken to insure reproducible and reliable results.

Shape of Contraction Contour. The contour of the contraction section influences the equivalent length of the latter. Most important, however, is the way in which the pressure distribution on the contour determines whether the flow in the nozzle is laminar or turbulent, and whether the flow is fully attached or partially separated. If the wall pressure fell monotonically, then there could be no boundary-layer separation and, in addition, the boundary layer would be entirely laminar in the flow nozzle except at very high Reynolds numbers. When the adverse pressure gradient which is almost inevitably present is sufficiently large, however, there may be boundary-layer separation, there may be transition to turbulence, or there may be both. Any of these eventualities would seem to be undesirable because they are uncontrollable and sensitive to minute perturbations.

The adverse pressure-gradient characteristic of the ASME flow nozzle seems sufficiently weak so that the boundary layer does not exhibit undesirable behavior. Faithful reproduction of the prescribed contour is essential, however, otherwise the adverse pressure gradient might inadvertently be accentuated, leading possibly to boundary-layer transition and a radical change in the discharge coefficient.

Position of Downstream Pressure Tap. It would seem desirable to place the downstream static tap in a region where the streamlines no longer have curvature. According to Fig. 7, this sets the minimum desirable value of L/D at about $1/4$. In addition, there should be about $1/4$ diameter of straight section downstream of the static pressure tap.

Accurate location of the pressure tap is very important; Fig. 5 shows how a small change in L/D may produce significant alterations in C_D .

Apart from the foregoing, it is important to keep in mind that the static tap is in a region where the boundary-layer thickness may be smaller than the diameter of the pressure hole. In order to avoid large errors in static pressure reading, therefore, the pressure hole must be meticulously constructed.

Roughness or Initial Turbulence. Either wall roughness or initial turbulence will decrease the value of Re_D at which the point of laminar transition moves into the flow nozzle. Either of these occurrences, by changing the friction factor, would alter the discharge coefficient.

BIBLIOGRAPHY

- 1 "A Bibliographical Survey of Flow Through Orifices and Parallel-Throated Nozzles," by T. H. Redding, Chapman and Hall, Ltd., London, England, 1952.
- 2 "Strömungsform und Durchflusssahl der Messdrosseln," by F. Kretschmer, *Forschungsheft* 381, 1936, 28 pages.
- 3 "Friction Coefficients in the Inlet Length of Smooth Round Tubes," by A. H. Shapiro and R. Douglas Smith, NACA TN No. 1785, November, 1948.
- 4 "Experimental Investigation of the Effects of Cooling on Friction and on Boundary-Layer Transition for Low-Speed Gas Flow at

the Entry of a Tube," by S. J. Kline and A. H. Shapiro, NACA TN 3048, November, 1953.

5 "Friction Factor in the Laminar Entry Region of a Smooth Tube," by A. H. Shapiro, Robert Siegel, and S. J. Kline, Proceedings of the Second U. S. National Congress of Applied Mechanics, pp. 733-741, June, 1954.

6 "Hydrodynamique," by J. Boussinesq, Comptes Rendus, vol. 110, 1890, pp. 1160, 1238; vol. 113, 1891, pp. 9-49.

7 "Die Entwicklung der Laminaren Geschwindigkeitsverteilung und ihre Bedeutung für Zähigkeitsmessungen," by L. Schiller, Zeitschrift für angewandte Mathematik und Mechanik, Bd. 2, Heft 2, 1922, pp. 96-106.

8 "Modern Developments in Fluid Dynamics," by the Fluid Motion Panel of the Aeronautical Research Committee and others, edited by S. Goldstein, Clarendon Press, Oxford, England, vol. 1, 1938, pp. 304-308.

9 "Steady Flow in the Transition Length of a Straight Tube," by H. L. Langhaar, Journal of Applied Mechanics, Trans. ASME, vol. 64, 1942, pp. A-55-A-58.

10 "Approximate Calculation of the Laminar Boundary Layer," by B. Thwaites, Aeronautical Quarterly of the Royal Aeronautical Society, vol. 1, 1949, pp. 245-280.

11 ASME Power Test Codes:

"Information on Instruments and Apparatus,"

"Part 5, Measurement of Quantity of Materials,"

"Chapter 4, Flow Measurement by Means of Standardized Nozzles and Orifices," The American Society of Mechanical Engineers, 1940, pp. 28, 40.

12 "Relaxation Methods in Theoretical Physics," by R. V. Southwell, The Clarendon Press, Oxford, England, 1946.

13 "Über Änderungen der Stromungsform in Messdüsen," by F. Kretschmer, Forschung auf dem Gebiete des Ingenieurwesens, vol. 9, 1938, pp. 35-40.

14 "Simplified Laminar Boundary-Layer Calculations for Bodies of Revolution and for Yawed Wings," by N. Rott and L. F. Crabtree, Institute of Aeronautical Sciences, Preprint No. 359.

15 "Grenzschicht Theorie," by H. Schlichting, Verlag G. Braun, Karlsruhe, Germany, 1951, p. 105.

16 "Fluid-Meter Nozzles," by B. O. Buckland, Trans. ASME, vol. 56, 1934, pp. 827-832.

17 "Rounded-Approach Orifices," by J. F. Downie Smith and Sydney Steele, Mechanical Engineering, vol. 57, 1935, pp. 760, 780.

18 "Calibration of Rounded Approach Orifices," by J. F. Downie Smith, Trans. ASME, vol. 56, 1934, pp. 791-793.

Discussion

S. J. KLINE.⁴ This paper is a valuable contribution to the understanding of flow in rounded-entrance nozzles. It provides a long step toward meeting the objectives of the authors, and it should also be of assistance in correctly interpreting friction data in the entrance zone of tubes.

⁴ Assistant Professor of Mechanical Engineering, Stanford University, Stanford, Calif. Mem. ASME.

The curves presented by the authors amply illustrate the very important effect of L/D , on discharge coefficient at fixed Reynolds numbers. And the authors quite properly stress the importance of this fact in regard to downstream tap location in flowmetering. The authors also discuss the effect of wall boundary-layer transition. Some further discussion of the importance of transition might also be appropriate. While it is true that the transition zone usually begins at a length Reynolds number of around 5×10^5 as stated by the authors, available experiments show it may start as low as 8×10^4 and as high as 4×10^6 . It follows from these facts that the bump at the beginning of the flat zone, shown on Buckland's curve in Fig. 10(a) of the paper, might vary over a similar range. And since the actual location is determined as the result of several subtle causes, the use of data from previous calibrations is somewhat unreliable in the zone near transition.

An item of obvious interest in connection with this paper is the accuracy with which the theory predicts the discharge coefficient and the zone in which the results of Fig. 9 giving L_{eq}/D can be applied to other nozzle contours. Examination of Equation [4] of the paper shows that the accuracy required in $4\sqrt{f_{APP}}L/D$, the term computed by flow theory, depends to a large extent on the value of C_D . For example, if an error of less than 1 per cent in C_D is required, and the value of C_D is 0.90, the error which can be tolerated in $4\sqrt{f_{APP}}L/D$ is 11 per cent and in L_{eq} 22 per cent (if L_{eq} and L are approximately equal). If C_D is 0.30 and if L_{eq} approximately equals L , then a 3 per cent error in $4\sqrt{f_{APP}}L/D$ or a 6 per cent error in L_{eq} will create a 1 per cent error in C_D . If L_{eq} is smaller than L , then the tolerable error in L_{eq} for a 1 per cent error in C_D becomes even larger.

These considerations suggest that the calculations of the paper should be particularly accurate and the effect of minor changes in contour and initial boundary layer very small when (a) the value of $(L'/D)/Re_{yD}$ is small, (b) the value of L' is large compared to L_{eq} . Obviously, neither of these comments applies beyond the point where transition to a turbulent wall boundary layer might begin. If conditions (a) and (b) are met, then it also follows that the curve of Fig. 9 can be used to predict discharge coefficients for other nozzle contours with excellent accuracy provided transition does not occur. In fact, even the much cruder method of reference (3) of the paper has been used by the writer with excellent results under these conditions.

It is hoped that the Fluid Meters Committee will soon avail themselves of the increased understanding of the nature of discharge coefficients provided by this paper to review the current code for possible improvement of standards.

Biaxial Plastic Stress-Strain Relations of a Mild Steel for Variable Stress Ratios

By JOSEPH MARIN¹ AND L. W. HU,² STATE COLLEGE, PA.

The main objective in the study reported in this paper was to provide further experimental checks on the validity of the simple flow theory of plasticity. In this investigation, biaxial stresses were produced by subjecting tubular specimens to internal pressure and axial tension. The tests were made on specimens machined from cold-drawn seamless-steel tubing. Most of the tests were performed under variable biaxial-stress ratios but in order to provide the necessary control data and basic biaxial strength properties, a series of constant stress-ratio tests also was conducted. Eight different types of variable stress-ratio tests were devised to determine the validity of the simple flow theory. The results of these tests do not support the theory. A test also was made to check the validity of the distortion-energy criterion as used in the simple flow theory. The differences between the theoretical and experimental results for this test were too great to be explained as due to experimental error or material anisotropy. A special variable stress-ratio test also was conducted to compare certain requirements of both the slip and simple flow theory. The results from this test were in poor agreement with the simple flow theory and in approximate agreement with the slip theory. An investigation was made to determine the validity of the so-called "loading function" as required by the various plasticity theories. These test results do not agree with the concept of the isotropic expansion of loading functions.

INTRODUCTION

MANY theories have been proposed for expressing the plastic stress-strain relations in metals subjected to combined states of stress. To select the most adequate theory it is necessary to obtain by experiment actual plastic stress-strain relations and to compare these results with those predicted theoretically. In searching for the best available theory it is also advisable to verify the validity of various assumptions and requirements of the plasticity theories. This paper presents plastic stress-strain relations for both constant and variable stress ratios and special tests for verifying certain requirements of the plasticity theories. Results from both the foregoing types of tests will then be compared to values predicted by a theory to determine the accuracy of the theory.

TEST PROCEDURE

Material Tested and Specimens. The material tested in this investigation was a mild steel designated as SAE 1020. The nominal composition, in addition to iron and normal impurities,

¹ Professor and Head of Engineering Mechanics, Pennsylvania State University. Mem. ASME.

² Assistant Professor of Engineering Mechanics, Pennsylvania State University.

Contributed by the Metals Engineering Division and presented at the Annual Meeting, New York, N. Y., November 28-December 3, 1954, of THE AMERICAN SOCIETY OF MECHANICAL ENGINEERS.

NOTE: Statements and opinions advanced in papers are to be understood as individual expressions of their authors and not those of the Society. Manuscript received at ASME Headquarters, October 26, 1954. Paper No. 54-A-243.

consists of 0.19 per cent carbon, 0.48 per cent manganese, 0.24 per cent silicon, 0.013 per cent phosphorus, and 0.043 per cent sulphur. The material was supplied in the form of commercial cold-drawn seamless-steel tubing with an outside diameter of 1 1/2 in. and inside diameter of 5/8 in. The mechanical properties of steel tested in the longitudinal direction were as follows: Yield strength at 0.002 in./in. offset, 74,900 psi; ultimate strength, 79,500 psi; elongation in 2-in. gage length, 9.5 per cent; modulus of elasticity, 28.0×10^6 psi; Poisson's ratio, 0.27.

The specimens for the various combined stress tests were made from the steel tubing by machining on both the inside and outside to a wall thickness of 0.050 in. and inside diameter of 1.000 in. The ends of the specimen were threaded to permit the application of axial tension in addition to internal pressure. Details of the specimen design are given in Fig. 1 of reference (1).³

Testing Machine and Strain Gages. The testing machine used to apply the axial tension and internal pressure to the specimen is described in reference (2). The elastic and plastic strains during loading were determined by the use of SR-4 strain gages and a specially designed clip-type electric strain gage as described in reference (2).

CONSTANT STRESS-RATIO TESTS

Constant biaxial stress-ratio tests were made in order to provide control test data and to supply basic information on biaxial properties of the material tested. In these tests the ratio of the principal stresses was maintained essentially constant by keeping a constant ratio between the internal pressure and the axial load during the loading of the specimen.

The stress-strain relations up to the maximum load, for various values of the principal stress ratios, are given for the axial and tangential stresses in Fig. 1. For all tests the deformations up to the maximum load were small and less than 0.5 per cent for most tests. It was then sufficiently accurate to use nominal stress and strain values based on the original specimen dimensions and gage length in place of the true stress and strain values. The values of the nominal axial and tangential stresses are for a thin-walled cylinder, respectively

$$\sigma_a = \frac{P}{\pi(d_i + t)t} \dots \dots \dots [1]$$

$$\sigma_t = \frac{pd_i}{2t} \dots \dots \dots [2]$$

where d_i = initial internal diameter, t = initial wall thickness, P = total axial load, and p = internal pressure.

Based on the relations plotted in Fig. 1, values of yield strength were obtained using an equivalent offset strain as explained in reference (2) and using a value of 0.002 in. per in. offset strain for evaluating the yield stress in simple tension. A comparison of these biaxial yield strengths and values predicted by the maximum-shear and distortion-energy theories is shown in Fig. 2(a). An examination of the graph in Fig. 2(a) shows that the distortion-energy theory is in approximate agreement with the test data.

³ Numbers in parentheses refer to the Bibliography at the end of the paper.

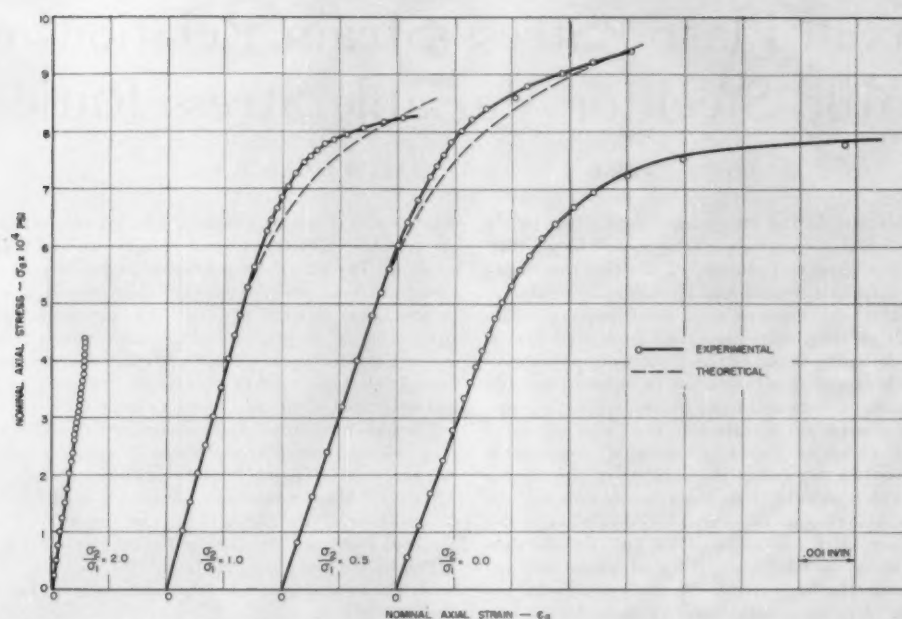


FIG. 1(a) COMPARISON OF AXIAL STRESS-STRAIN RELATIONS WITH THEORETICAL VALUES FOR CONSTANT STRESS RATIOS

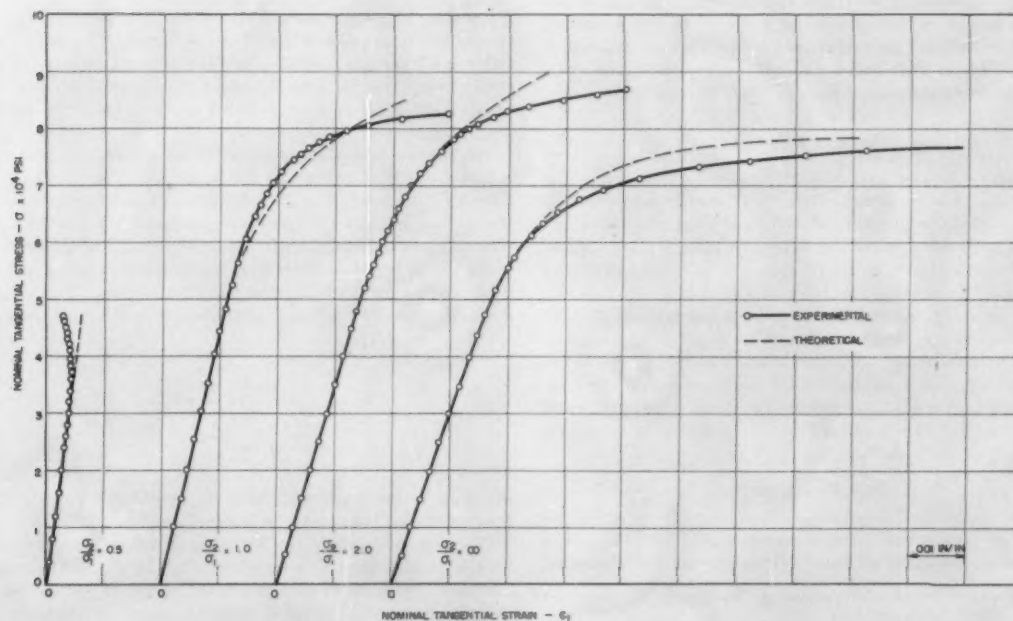


FIG. 1(b) COMPARISON OF TANGENTIAL STRESS-STRAIN RELATIONS WITH THEORETICAL VALUES FOR CONSTANT STRESS RATIOS

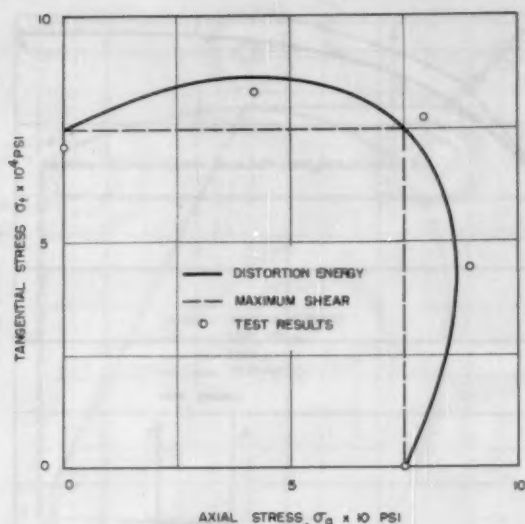


FIG. 2(a) COMPARISON OF YIELD STRENGTHS WITH THEORIES OF FAILURE FOR CONSTANT STRESS RATIO TESTS

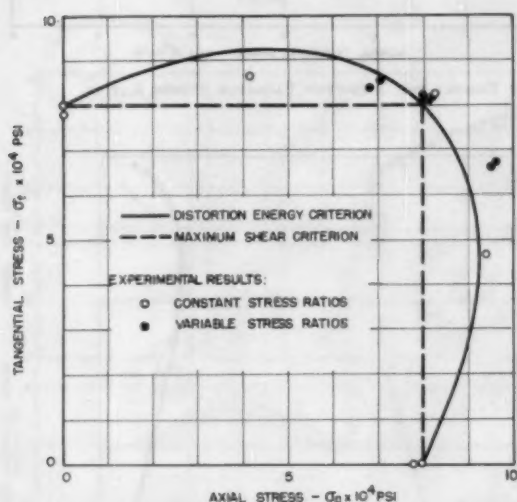


FIG. 2(b) COMPARISON OF FRACTURE STRESSES WITH THEORETICAL VALUES FOR CONSTANT AND VARIABLE STRESS RATIOS

The plastic stress-strain relations as predicted by the simple flow theory (3) are shown in Fig. 1. In determining the theoretical values of the plastic strain-stress relation in this paper, a simple tension plastic stress-strain equation of the form

$$\epsilon = k\sigma^n \dots \dots \dots [3]$$

was used. For the steel test, values of $k = 8.53 \times 10^{-10}$ and $n = 7.45$ were found.

By the simple flow theory it can be shown that the increments of the axial and tangential plastic strains in terms of the axial and tangential stresses are

$$\delta \epsilon_a = \frac{1}{\sigma} \left(\frac{\partial \bar{\epsilon}}{\partial \sigma} \right) \left[\sigma_a - \frac{\sigma_t}{2} \right] \delta \sigma \dots \dots \dots [4]$$

$$\delta \epsilon_t = \frac{1}{\sigma} \left(\frac{\partial \bar{\epsilon}}{\partial \sigma} \right) \left[\sigma_t - \frac{\sigma_a}{2} \right] \delta \sigma \dots \dots \dots [5]$$

where $\bar{\sigma}$ and $\bar{\epsilon}$ are the effective stress and strain, respectively, with values of

$$\bar{\sigma} = \sqrt{\sigma_a^2 - \sigma_a \sigma_t + \sigma_t^2} \dots \dots \dots [6]$$

$$\bar{\epsilon} = \int \sqrt{\frac{4}{3} [(\delta \epsilon_a)^2 + (\delta \epsilon_t)^2 + (\delta \epsilon_s)^2]} \dots \dots [7]$$

A comparison between these theoretical relations and the actual values, as given in Fig. 1, shows that the simple flow theory is in approximate agreement with the test results. A comparison is given in Fig. 2 (b) between the actual values of the ultimate bi-axial strengths and the values predicted by the theories of failure. An examination of this figure shows that the distortion-energy criterion is in approximate agreement with the test results.

VARIABLE STRESS-RATIO TESTS

In practice, loads may be applied so that the combined stress ratio does not remain constant as in the tests just described. For this reason, various kinds of variable stress-ratio tests were conducted in this investigation to determine the influence of varying stress ratios on the plastic stress-strain relations. In addition, these variable stress-ratio tests also provided a further check on the adequacy of the flow theory.

Two types of variable stress-ratio tests were conducted. In one type designated as the "two-step" test a stress is applied in the axial direction only to a selected value. Then in addition, the specimen is subjected to the stress in the tangential direction only, to fracture, Fig. 3. This latter stage of loading results in a varying stress ratio (σ_t/σ_a) as σ_t increases while σ_a remains constant. The stress-strain relations for the foregoing two-step loading are shown in Fig. 3. The theoretical stress-strain relations based on the simple flow theory are shown in Fig. 3. Test results are given in Fig. 4 for initial loading in the tangential direction with subsequent loading in the axial direction.

A new type of variable stress-ratio test designated as "three-step" test also was made. The paths of loading used for these tests are described in Fig. 5. With initial stressing in the tangential direction the loading paths used were O-A-B-D, O-A-B-E, and O-F-G-E. Three tests similar to the foregoing were made with initial stressing in the axial in place of the tangential direction. Figs. 6 to 12 show the stress-strain relations for each of these tests as designated by the legend on these figures.

The plastic stress-strain relations based on the simple flow theory are represented in Figs. 3 to 12. A comparison of the actual curves with these theoretical relations indicates that there is fair agreement between the simple flow theory and the test results for variable stress ratios.

TEST ON THE VALIDITY OF THE DISTORTION-ENERGY CRITERION

In the usual simplified form of the flow theory (4) it is assumed that the yielding surface is defined by the distortion-energy criterion as represented in Fig. 2(a). To determine the validity of this yield surface, a variable stress-ratio test was conducted by using a loading path as shown in Fig. 12. The loading path described in Fig. 12 was produced by alternate application of axial tensile loads and internal pressures, in such a way that the effective stress

$$\bar{\sigma} = \sqrt{\frac{1}{2} [(\sigma_a - \sigma_t)^2 + (\sigma_t - \sigma_r)^2 + (\sigma_r - \sigma_a)^2]}$$

remained constant on the inner surface of the specimen. The strains produced during the foregoing loading process are shown

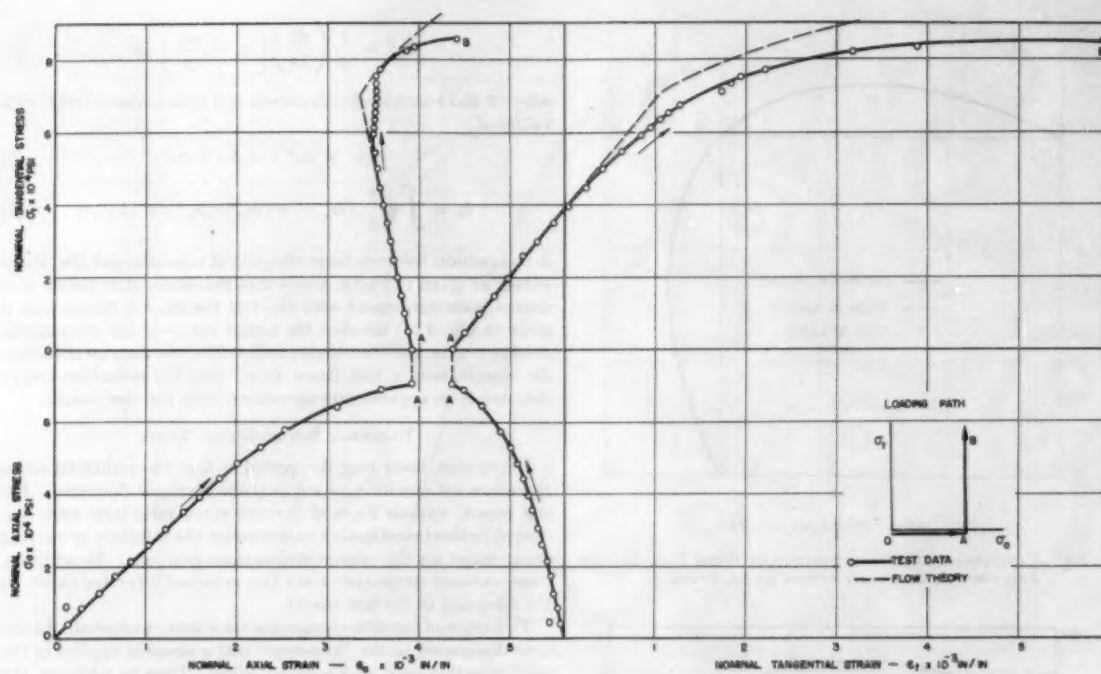


FIG. 3 COMPARISON OF STRESS-STRAIN RELATIONS WITH FLOW THEORY FOR TWO-STEP VARIABLE STRESS RATIOS

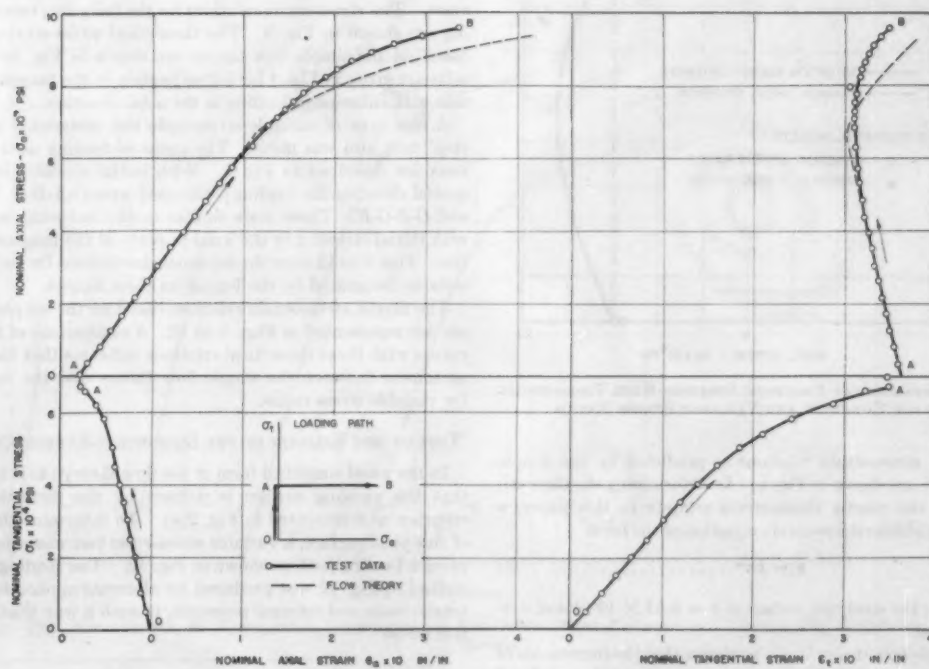


FIG. 4 COMPARISON OF STRESS-STRAIN RELATIONS WITH FLOW THEORY FOR TWO-STEP VARIABLE STRESS RATIOS

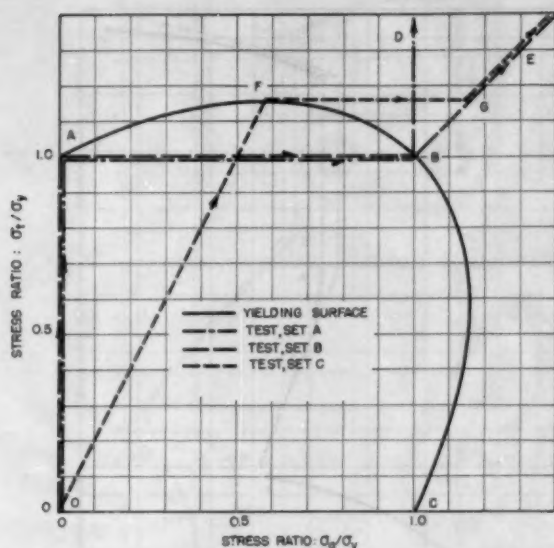


FIG. 5 LOADING PATHS FOR THREE-STEP VARIABLE STRESS-RATIO TESTS

in Fig. 13 for both the axial and the tangential directions. According to the distortion-energy criterion there should be no additional plastic strains produced when the path of loading follows the distortion-energy ellipse. Fig. 14 shows that this requirement is not fulfilled, since for both the axial and tangential directions there is considerable variation in the plastic strains. These changes are of such magnitude that they cannot be considered as due to experimental errors; that is, the large variations in the plastic strains show that the distortion-energy criterion is not valid.

TEST TO DISTINGUISH BETWEEN SLIP AND FLOW THEORIES

A test, similar to that reported in reference (5), was made to determine which theory—the slip (6) or simple flow theory—agrees best with the actual behavior. To describe this test consider that $O-A-J-B$ in Fig. 15 represents the distortion-energy strength criterion corresponding to the proportional limit. A tubular specimen was first subjected to internal pressure at a constant stress ratio so that the path of loading was along $O-F$. The specimen was then stressed in the axial direction only to point G . Then for subsequent loading and according to the simple flow theory the loading surface now becomes the ellipse $C-G-D$; that is, by the simple flow theory plastic deformation would not occur if the specimen is loaded along or within the loading surface represented by the ellipse shown. The specimen was subjected to load increments represented by points $G-I$

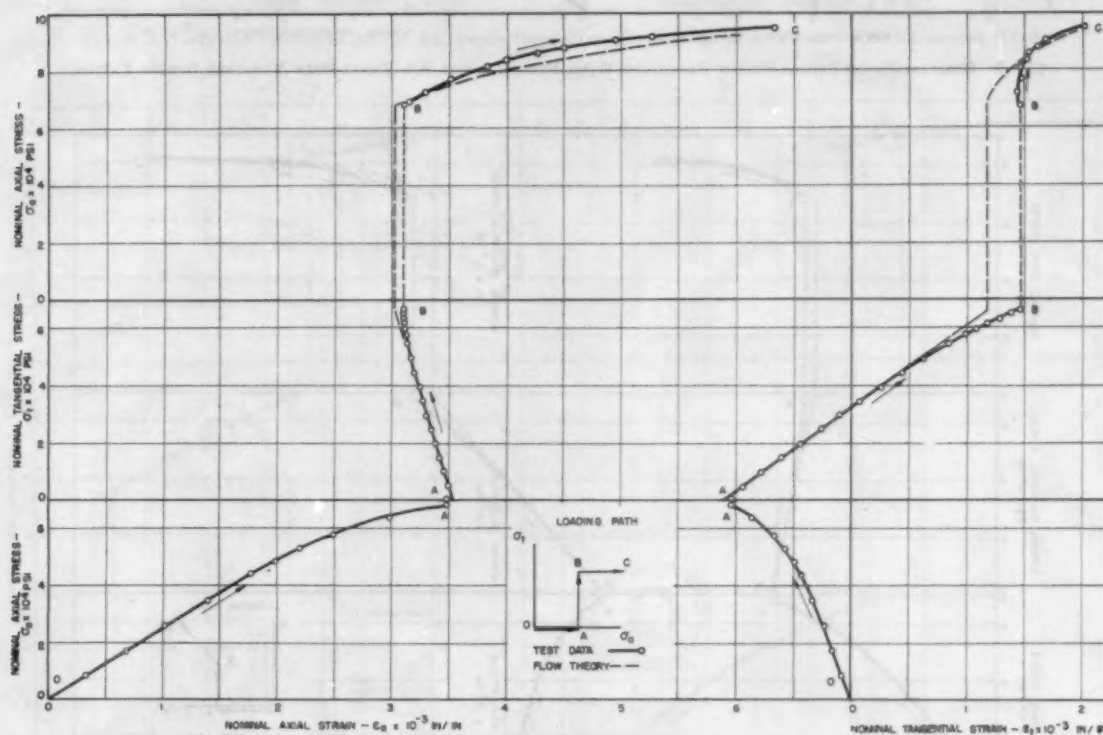


FIG. 6 COMPARISON OF STRESS-STRAIN RELATIONS WITH FLOW THEORY FOR THREE-STEP VARIABLE STRESS RATIOS

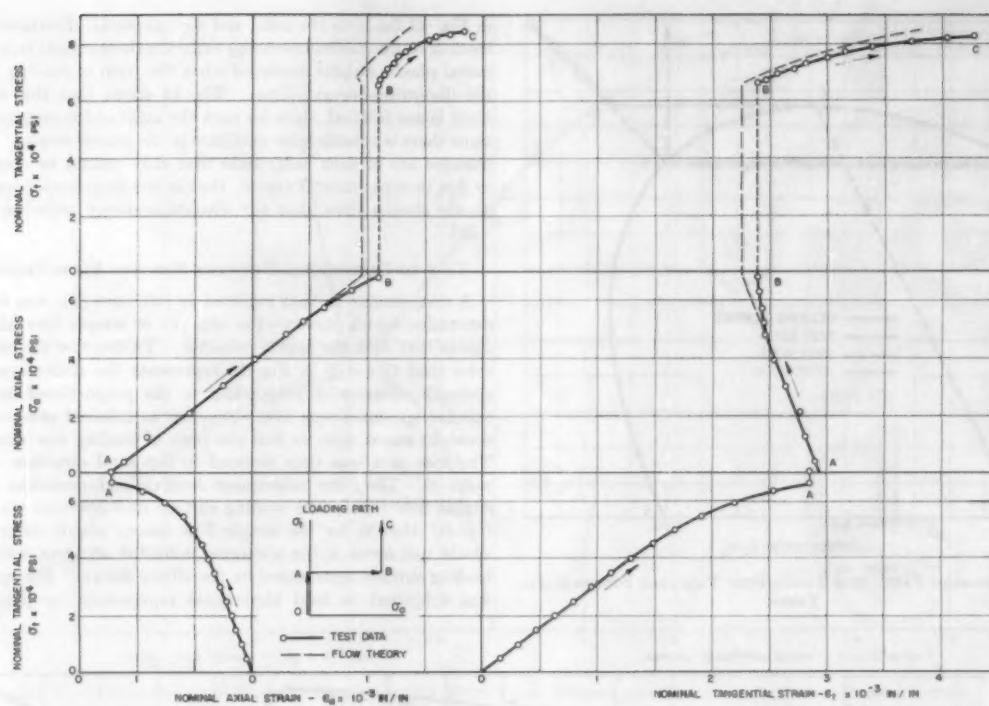


FIG. 7 COMPARISON OF STRESS-STRAIN RELATIONS WITH FLOW THEORY FOR THREE-STEP VARIABLE STRESS RATIOS

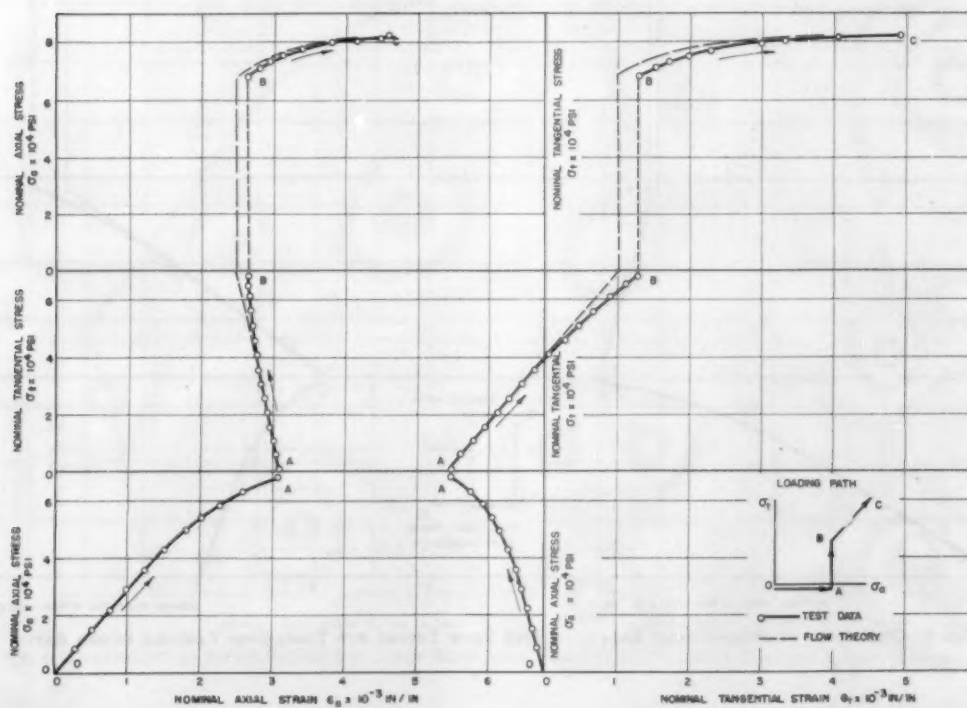


FIG. 8 COMPARISON OF STRESS-STRAIN RELATIONS WITH FLOW THEORY FOR THREE-STEP VARIABLE STRESS RATIOS

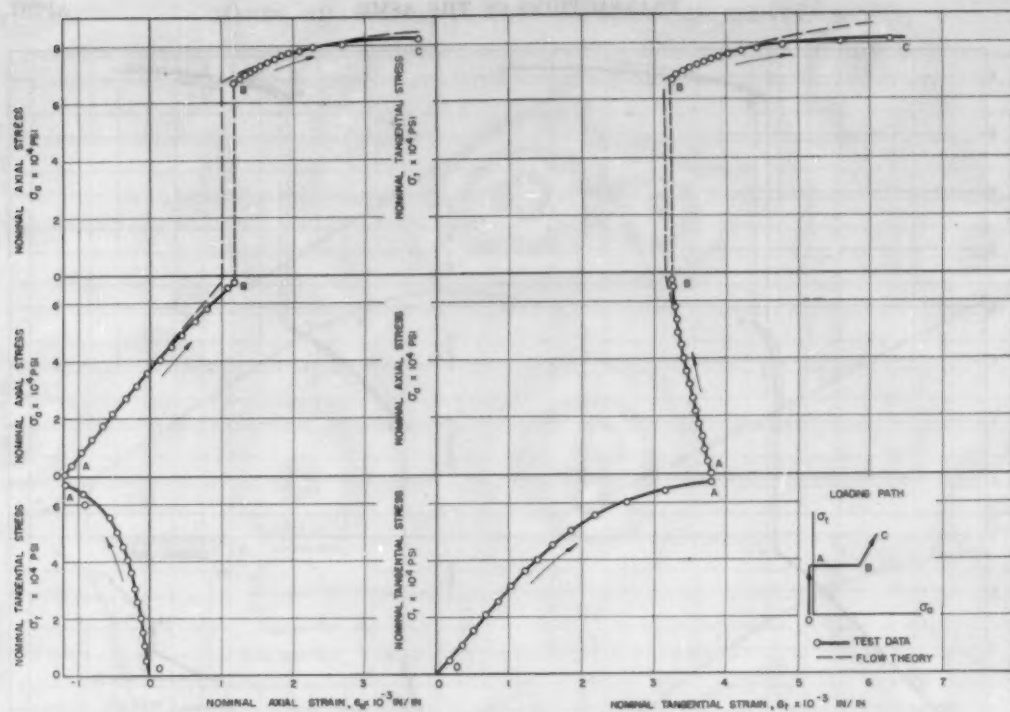


FIG. 9 COMPARISON OF STRESS-STRAIN RELATIONS WITH FLOW THEORY FOR THREE-STEP VARIABLE STRESS RATIOS

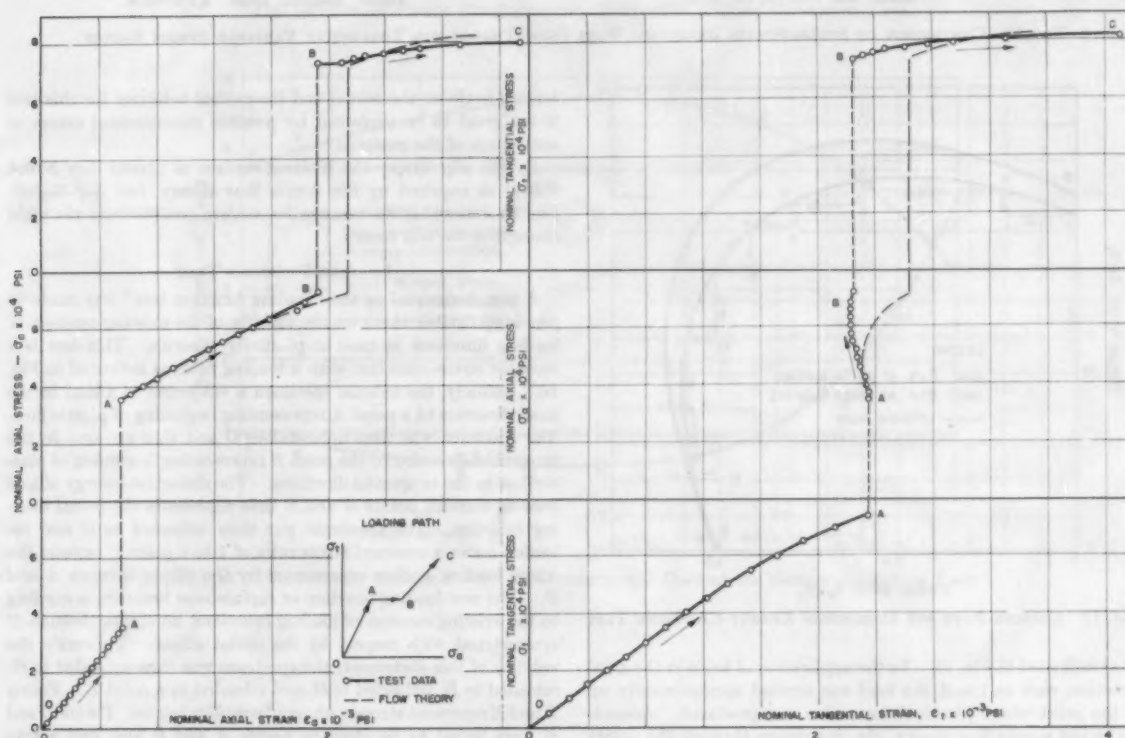


FIG. 10 COMPARISON OF STRESS-STRAIN RELATIONS WITH FLOW THEORY FOR THREE-STEP VARIABLE STRESS RATIOS

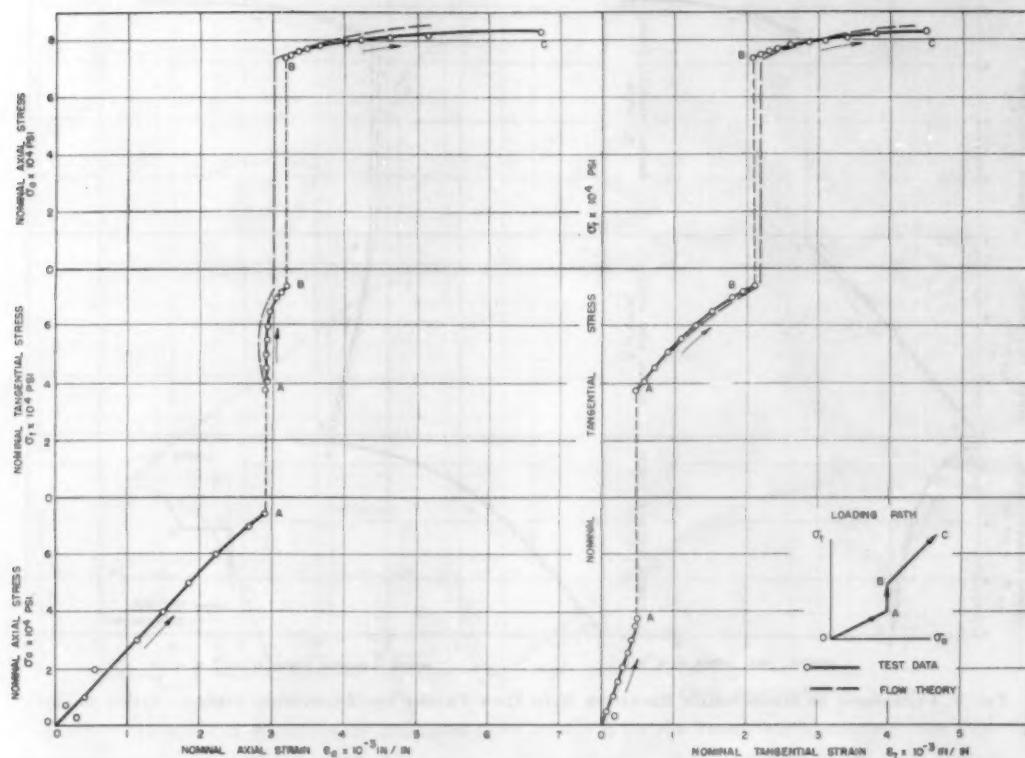


FIG. 11 COMPARISON OF STRESS-STRAIN RELATIONS WITH FLOW THEORY FOR THREE-STEP VARIABLE STRESS RATIOS

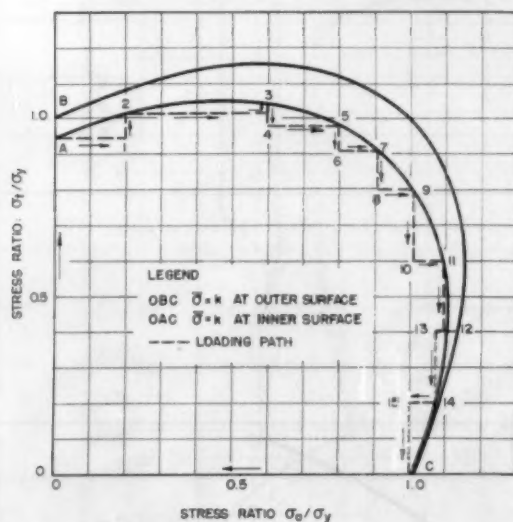


FIG. 12 LOADING PATH FOR DISTORTION ENERGY CRITERION TEST

23 as indicated in Fig. 15. In the application of loads in the axial direction, such as 1 to 2, the load was applied approximately up to the point where plastic deformation was produced. According to the simple flow theory, the line drawn through the points G2, 4, 6-22 should coincide with the yield ellipse G-D. The dif-

ference between the actual and theoretical behavior for this test is too great to be explained by possible experimental errors or anisotropy of the material.

By the slip theory the limiting surface of plastic flow is not C-G-D as required by the simple flow theory, but A-F-G-J-B. Fig. 15 shows that the test results confirm qualitatively the yield concept of the slip theory.

LOADING FUNCTION TEST

A test designated as the "loading function test" was made to provide a further check on the validity of the existing concept of loading functions as used in plasticity theories. This test is a variable stress-ratio test with a loading path as indicated in Fig. 16. Initially, the tubular specimen is subjected to a load in the axial direction to a point A representing beginning of plastic flow. The specimen was then unloaded to O and thus stressed in the tangential direction to the point B representing beginning of plastic flow in the tangential direction. The distortion-energy ellipse passing through points A and B then represents the initial loading function. The specimen was then unloaded to O and reloaded under a constant stress ratio of 1 to a point C beyond the initial loading surface represented by the ellipse through A and B. The new loading function or surface now becomes, according to the existing concept of loading functions, an ellipse through C symmetrical with respect to the initial ellipse. To verify the validity of this statement, the specimen was thus unloaded to O, reloaded to D, unloaded to O, and reloaded to a point E. Points D and E represent stresses where plastic flow begins. Points D and E were found to be close to points A and B and well within the loading surface through C as required by the existing con-

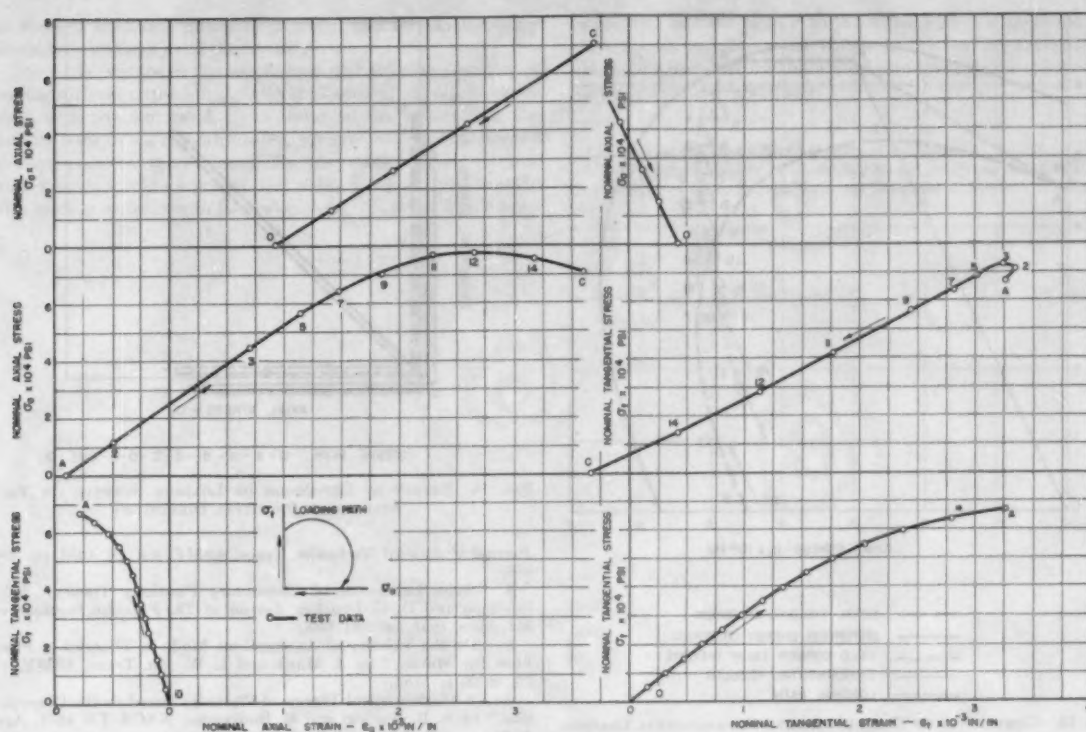


FIG. 13 STRESS-STRAIN RELATIONS FOR DISTORTION ENERGY CRITERION TEST

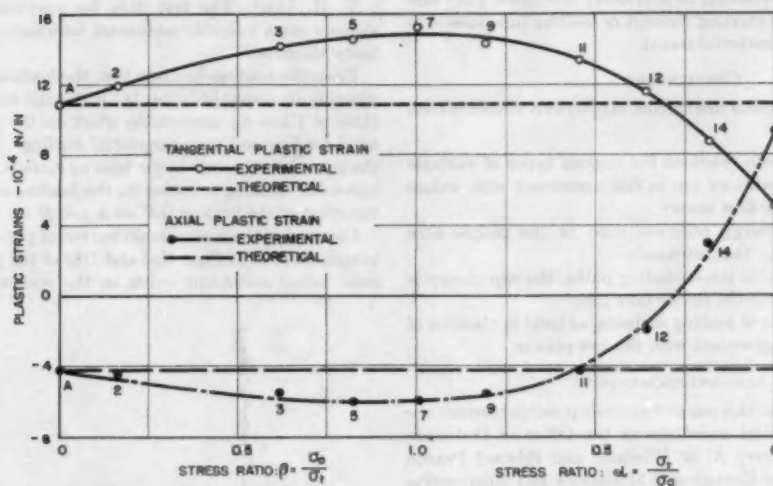


FIG. 14 VARIATION OF PLASTIC STRAIN COMPONENTS FOR DISTORTION ENERGY CRITERION TEST

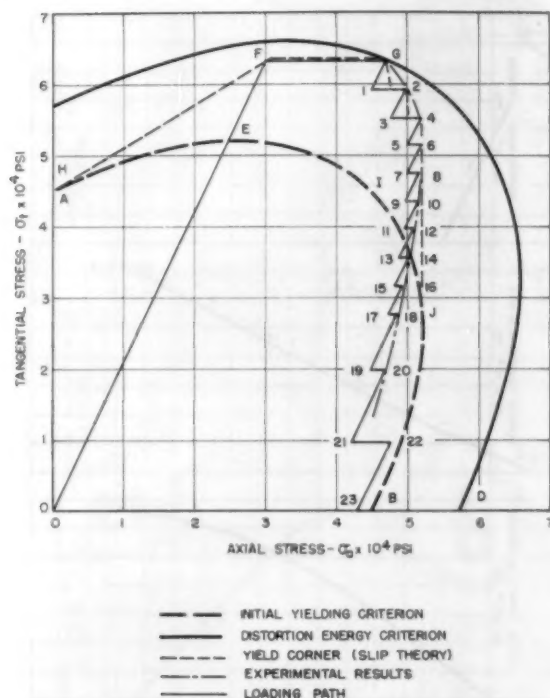


FIG. 15 COMPARISON OF THEORETICAL AND EXPERIMENTAL LOADING FUNCTIONS

cepts of loading functions. Further stresses to points beyond C and unloading with reloading, as previously described, gave further evidence that the existing concept of loading functions cannot be applied for the material tested.

CONCLUSIONS

Tests on steel specimens made from cold-drawn seamless-steel tubing showed that:

- 1 Plastic stress-strain relations for various types of variable biaxial stress-ratio conditions are in fair agreement with values predicted by the simple flow theory.
- 2 The distortion-energy criterion used in the simple flow theory is not verified by the test results.
- 3 For certain variable stress-loading paths, the slip theory is in better agreement than the simple flow theory.
- 4 Existing concepts of loading surfaces, as used in theories of plasticity, are not in agreement with the test results.

ACKNOWLEDGMENTS

The study reported in this paper was made possible through the sponsorship and financial assistance of the Office of Ordnance Research. Messrs. Harry A. B. Wiseman and Edward Paxson of the Departments of Engineering Mechanics and Engineering Research, assisted in obtaining the test results.

BIBLIOGRAPHY

- 1 "Plastic Stress-Strain Relations of Alcoa 14S-T6 for Variable Stress Ratios," by J. Marin, L. W. Hu, and J. F. Hamburg, *Proceedings of American Society for Metals*, vol. 45, 1953, pp. 686-709.
- 2 "Plastic Stress-Strain Relations for 75S-T6 Aluminum Alloy Subjected to Biaxial Tensile Stresses," by J. Marin, B. H. Ulrich, and W. P. Hughes, *NACA TN 2425*, August, 1951.
- 3 "Determination of Theoretical Plastic Stress-Strain Relations for Variable Combined Stress Ratios," by L. W. Hu and J. Marin,

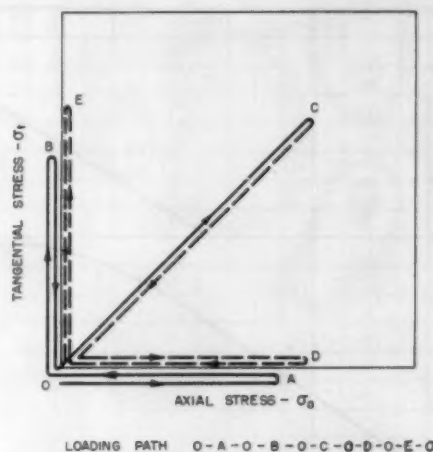


FIG. 16 EFFECT OF EXPANSION OF LOADING SURFACE ON YIELD STRESSES IN PRINCIPAL DIRECTIONS

Journal of Applied Mechanics, Trans. ASME, vol. 74, 1952, pp. 485-488.

4 "Some Extensions of Elementary Plasticity Theory," by F. Edelman and D. C. Drucker, *Journal of The Franklin Institute*, vol. 251, June, 1951, pp. 581-605.

5 "On the Validity of Assumptions Made in Theories of Plastic Flow for Metals," by J. Marin and L. W. Hu, *Trans. ASME*, vol. 75, 1953, p. 1181.

6 "A Mathematical Theory of Plasticity Based on the Concept of Slip," by S. B. Batdorf and B. Budiansky, *NACA TN 1871*, April, 1949.

Discussion

T. H. LIN.⁴ The test data for varying ratios of principal stresses are a valuable additional information for checking plasticity theories.

From the loading-function test, the loading beyond the proportional limit along O-C (Fig. 16) with axial stress-tangential stress ratio of 1 has no appreciable effect on the yield stress for pure axial loading and pure tangential loading. This seems to show the existence of corner in the loading surface. As seen in Fig. 17, herewith, creating a corner on the loading surface may decrease the effect of the loading O-C on A and B on the loading surface.

Comparing the stress-strain curves of pure axial load and pure tangential load in Figs. 1(a) and 1(b) of the paper, it is seen that some initial anisotropy exists in the specimen. As theories to

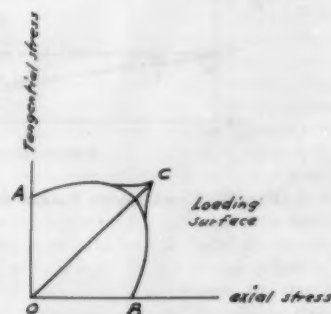


FIG. 17

⁴ University of Detroit, Detroit, Mich.

be checked are based on initial isotropy, this initial anisotropy probably introduces some discrepancy.

The authors state in the conclusions that existing concepts of loading surfaces as used in theories of plasticity, are not in agreement with the test results. It seems to the writer that the authors refer to the smooth loading surfaces with unique normal at every point on the surface. The test results shown disagree with smooth loading surfaces, but seem to agree qualitatively with loading surfaces with corner on these surfaces. Slip theory

by Batdorf and Budiansky⁶ to the writer's knowledge is the first plasticity theory giving this corner in the loading surface, and slip theory proposed by the writer⁴ also predicts the existence of corner in the loading surfaces.

⁶ Reference (6) of the Bibliography of the paper.

⁴ "A Proposed Theory of Plasticity Based on Slips," by T. H. Lin, Proceedings of U. S. Second National Congress of Applied Mechanics, 1954.

A Method of Predicting the Effects of Notches in Uniaxial Fatigue¹

By W. E. DIRKES,² DAYTON, OHIO

This paper approaches the problem of correlating notched and unnotched test data from observations of how the material may be considered to be affected under repeated stresses. A semigraphical method of extrapolating notched test data is developed. Although data available do not conclusively prove the observations reported herein, neither does presently available information refute the views presented. Individual observations are gathered together to form a picture which is intended as an aid to designers in visualizing possible trends even though complete test data are not available.

INTRODUCTION

THE phenomenon of progressive fracture of metals under repeated loads, generally referred to as fatigue failures, has been investigated extensively, and the physical laws governing such failures are gradually being uncovered. A definition of the mechanism of failure is particularly difficult owing to the large number of variables which have been found to affect test results. Significant contributions have been made by a great number of investigators, for example, H. F. Moore (1)³ has studied the effects of various specimen sizes, Peterson and Lessells (2), and Almen (3) have investigated surface strengthening, while Gough (4) and Dolan and Yen (5) have reported some effects of crystal structure. Findley (6) has shown that attempts to correlate dynamic failures with theories of static failure have been only partially successful for a single material. Much of the work to date has consisted of either empirical correlation of test data or the development of mathematical solutions which satisfy only special cases. The attempt is made herein to analyze fatigue data in a manner which permits prediction of the effects of notches.

DEFINITIONS

The symbols and nomenclature used in this paper are those recommended by the ASTM Committee E-9 and are defined in the ASTM "Manual on Fatigue Testing," except for the use and definition of the term "stress ratio:"

- A = stress ratio = S_a/S_m
- S_{max} = maximum stress
- S_a = alternating stress amplitude
- S_m = mean stress
- K_f = theoretical stress-concentration factor
- K_f = fatigue strength-reduction factor

ANALYSIS OF NOTCH EFFECTS UNDER REPEATED LOADS

When alternating-mean stress diagrams are drawn for some

¹ The opinions expressed are those of the author and do not necessarily represent the official views of the United States Air Force.

² Captain, USAF; Materials Laboratory, Wright Air Development Center, Wright-Patterson Air Force Base.

³ Numbers in parentheses refer to the Bibliography at the end of the paper.

Contributed by the Metals Engineering Division and presented at the Annual Meeting, New York, N. Y., November 28-December 3, 1954, of THE AMERICAN SOCIETY OF MECHANICAL ENGINEERS.

NOTE: Statements and opinions advanced in papers are to be understood as individual expressions of their authors and not those of the Society. Manuscript received at ASME Headquarters, September 16, 1954. Paper No. 54-A-180.

specified number of cycles, a family of curves can be formed from the test data for unnotched and notched specimens, as shown in Figs. 1-3. These and the following figures were prepared from the data taken from references (7 and 8).

The material in an unnotched and notched specimen is identical except for normal variations which occur between any two samples of metal. Therefore it can be assumed that the mechanism of failure of unnotched and notched specimens is identical, if the same state of stress is maintained in each. The problem then becomes one of determining the proper means of expressing a relationship between fatigue curves of unnotched and notched specimens such that the existing stress conditions are satisfied. The assumption just made is not entirely correct, for greater plasticity and cold-working are likely to occur near the surface of notched specimens than in unnotched specimens, but these may be such localized effects that the resulting analysis will not be affected appreciably. Assume further that the relationship between notched and unnotched test data can be expressed along lines of constant stress ratio; that is, the transformation between any notched curve and the "parent" unnotched curve is a point-to-point relationship designated by any line drawn from the origin of the co-ordinate axes. This second assumption is based on the concept that at the instant the maximum nominal stress is applied to a notched specimen, the specimen will react to the total stress, since there is no apparent method for a test specimen to separate the stress into dynamic and static components.

Let K_f define the relationship between a notched and the unnotched curve along any stress-ratio line. This is equivalent to the statement

$$K_f = \frac{S_{max}}{S_{max}'}$$

where S_{max}' designates the maximum nominal stress computed for a notched specimen. Similarly

$$K_f = \frac{S_m + S_a}{S_m' + S_a'}$$

and since K_f was assumed to affect each stress component equally

$$K_f = \frac{S_m}{S_m'} = \frac{S_a}{S_a'}$$

K_f was determined in this manner for Figs. 1-3, and the K_f -values are given along the notched curves in the figures.

The usefulness of a strength-reduction factor is complicated by the fact that K_f varies for each stress level. As tensile stress is applied to a notched, ductile material, the notch may deform due to elongation of the material. As the tensile stress is increased, the notch is stretched and becomes less severe. Thus the stress concentration is partially relieved and K_f will change. Local plasticity may occur at the root of a notch even though the maximum stress calculated is below the elastic limit for the material and K_f may consequently vary within the nominally elastic range. Therefore K_f is defined for a specified ratio of the nominal stress components for any given specimen and notch.

If a notch is deformed, thus reducing the strength-reduction factor as increased tensile stresses are applied to a specimen, the

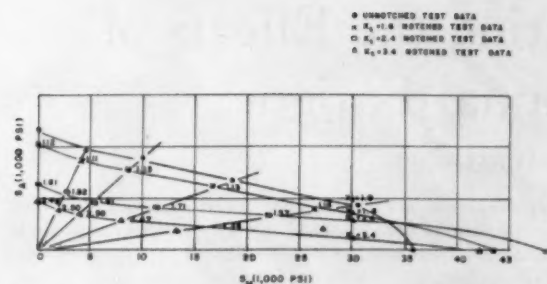


FIG. 1 ALTERNATING-MEAN STRESS DIAGRAM FOR 2014-T6 ALUMINUM ALLOY ROUND SPECIMENS, FOR 10^7 CYCLES (SEE REFERENCE 7)

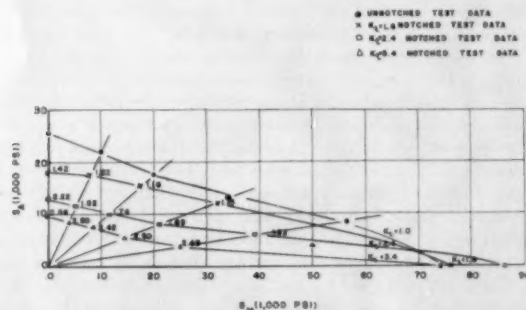


FIG. 2 ALTERNATING-MEAN STRESS DIAGRAM FOR 2024-T4 ALUMINUM ALLOY ROUND SPECIMENS, FOR 10^7 CYCLES (SEE REFERENCE 7)

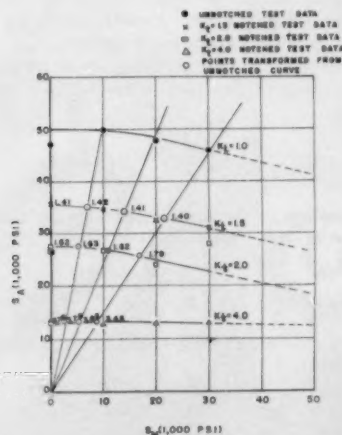


FIG. 3 ALTERNATING-MEAN STRESS DIAGRAM FOR SAE 4130 SHEET STEEL SPECIMENS, FOR 10^7 CYCLES (SEE REFERENCE 8)

maximum value of K_f can be predicted as the value of K_f for a minimum tensile stress. However, when $S_m = 0$, a fully reversed stress cycle is applied and the effect of the compression of the material must be considered. The minimum value of K_f can be seen as the point where $S_m = 0$, or at the point where the specimen is tested statically. There is some deviation in this since the static stress necessary to cause failure in a notched specimen may vary appreciably from the ultimate stress in unnotched specimens, but this point is beyond the area for design consideration except for designs requiring a very short lifetime. The K_f -variation will be affected by residual stresses and cold-working but the general trend has been discussed to show that K_f varies

from a high value near the point where $S_m = 0$ to a minimum near the point where $S_m = 0$.

Since the unnotched curve is assumed to define the fatigue characteristics of a material, if the K_f -variation is known for a given stress-concentration factor, the notched curve for the material can be calculated. This K_f -relationship is described for a specified number of cycles. K_f would be constant at all stress levels only if the material were extremely brittle. In such a case, the alternating-mean stress diagram would consist of a family of parallel lines. Fatigue tests with glass have shown this characteristic (9).

It should be noted that the data for Figs. 1-3 were obtained from S - N curves each of which was plotted from data obtained from tests of as little as four specimens. Even with this limitation, it is possible to see several important trends in the data. Considerable scatter exists, so the K_f -variations were checked by plotting several other curves for the same data, but no significant variation in trends was noticed. The plotted points lie generally along straight lines, except in the region where compressive stresses occurred; that is, completely reversed stress cycles on the crystals resisting the stresses caused a different action than stress cycles which were applied to stress the bonds in only one direction, and the trends of the curves varied slightly in this region. The deviation of test data from straight lines is probably a function of the test material as well as the stresses applied.

The concept just expressed ignores the effects of triaxial stresses present. Even though the load is applied along the major axis, triaxial and biaxial stresses actually occur within round and flat specimens, respectively, yet the results can be expressed in terms of the nominal applied stresses. Since sufficient test data are not available for analysis of brittle materials, this discussion is limited to ductile materials. If test data were available for brittle materials, according to the concept presented, the value of K_f should remain nearly constant for all levels of mean stress, and K_f would be nearly equal to K_t .

Also, if the unnotched curve is definitive for the material, the direction of curvature in notched curves should follow the same directional trends. The significant factors determined by inspection of the alternating-mean stress diagrams are as follows:

- The linear portion of each curve extends into the plastic stress range.
- The greatest K_f -variation occurs when the load cycle includes compressive stresses.
- The K_f -values are nearly constant over a wide segment of the curves, particularly for the lower values of K_f .
- The linear portions of the curves decrease in slope as the K_f -parameter is increased.
- The calculated K_f -values are smaller than the corresponding K_t -values.

The points listed are significant from a design standpoint. If unnotched test data are available for a material and information is desired about notched test data, reasonably accurate alternating-mean stress curves can be approximated for notched specimens by use of the notched fatigue strength determined from a single S - N curve with the $K_f = S_m/S_m'$ relationship, the ultimate tensile stress, and the trends listed in the foregoing.

PREDICTING EFFECTS OF NOTCHES

An illustrative example will show how the concepts expressed in the foregoing can be utilized in estimating the fatigue characteristics for a given material and notch. Considering the alternating-mean stress curve for 2014-T6 aluminum alloy, shown in Fig. 1, the notched curve can be constructed for the type specimen used for $K_t = 2.4$ using a single reference fatigue strength and the ultimate tensile strength. In order to stay within the linear por-

tion of the curve, the test data should be obtained in the region where S_a' is greater than S_a . One such point is that where $S_a' = 23.4$ kips and $S_a = 8.6$ kips. Referring to Fig. 4, this point is plotted on the graph as point *a*. The slope of the linear portion of any notched curve varies from that of the unnotched curve to a limiting value defined by the S_a -axis. These two limiting conditions for the slope of the linear portion of the notched curve are shown in Fig. 4(b).

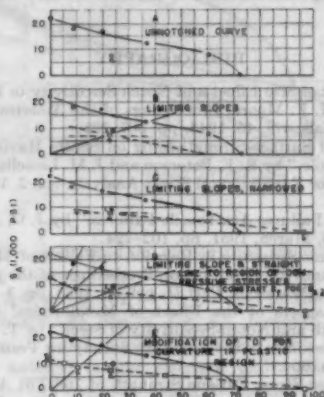


FIG. 4 CONSTRUCTION OF AN ALTERNATING-MEAN STRESS CURVE

Since the unnotched curve defines the fatigue strength under various combinations of stress for a given material, and each notched curve is assumed to follow the trends established by the parent curve, an additional limitation on the slope of the linear portion of the notched curve is imposed. Within the plastic region of the material, the unnotched curve is concave downward. In order to satisfy this trend, the slope of the linear portion of the notched curve must be limited by the horizontal line through *a* and the line drawn between *a* and the point determined by a static tensile test, labeled point *b* in Fig. 4(c). As the stress-concentration factor is increased, these two limiting lines tend to converge, thereby simplifying the choice of an assumed notched curve.

K_f can be determined at a single point on the notched alternating-mean stress curve from each notched S - N curve. If K_f is assumed to be constant for the region where compressive stresses are encountered and the remainder of the curve is assumed to be a straight line to point *b*, Fig. 4(d) can be constructed. Fig. 4(d) gives reliable limiting values for the notched alternating-mean stress curve. The right and left-hand parts of the curve show lower and upper limiting values, respectively, for the fatigue strengths. There are insufficient data available to derive a more exact analysis, but some additional approximations can be made.

The slopes of the notched curves vary only slightly in the region where $K_f \leq 2.0$, and the right-hand portion of the notched curve can be assumed a straight line with $K_f \geq 3.0$. The region $2.0 < K_f < 3.0$ is a transition region. Since the notch used in this example lies within the transition region, assume there is some noticeable curvature in the plastic region, which also specifies that the slope varies slightly from that of the straight line, *a-b*. Thus it is possible to approximate the line *c-a-b* in Fig. 4(e), where *c* is the point where $S_a = S_m$. At *c*, K_f is 1.8. Assume K_f remains constant for the region *d-c*, and the remaining part of Fig. 4(e) can be constructed.

Fig. 4(e) cannot be derived accurately, but depends on the amount of data available and the experience and judgment of the engineer. Therefore the discussion of accuracy will be limited

to Fig. 4(d) in which the right and left-hand parts of the curve are lower and upper limits, respectively. Fig. 5 shows the comparison of the alternating-mean stress curve plotted from actual data, a reproduction of Fig. 4(d), and a straight line drawn between the terminal points of the curve.

In Fig. 5 the largest error found in the type of construction used in Fig. 4(d) is at the point $S_a = S_m$, or $A = 1$. The error is about 12 per cent. The straight-line assumption, which is widely used at present, has an error in the maximum stress of 25 per cent when compared along the $A = 1$ stress ratio line. A minimum error of at least 4 per cent occurs in experimental data due to residual stresses, test-machine accuracy and temperature variations, which indicates that the bounding fatigue-curve values can be used advantageously for extrapolation of test data. It is even more important to note that for the data presented on 2014-T6 aluminum alloy, the straight-line assumption errs on the

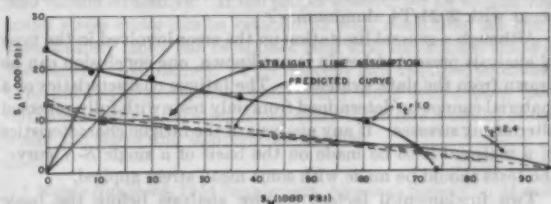


FIG. 5 COMPARISON OF ACTUAL AND CONSTRUCTED ALTERNATING-MEAN STRESS CURVES FOR 2014-T6 ALUMINUM ALLOY

unsafe side of the desired stress while the error in the method presented herein does not have this inherent failing.

If greater accuracy and reliability are desired, the fatigue strength should also be determined for completely reversed stress cycles. With the data from two S - N curves and the static ultimate strength, a reliable alternating-mean stress curve for notched specimens can be constructed from an unnotched alternating-mean stress curve for the material.

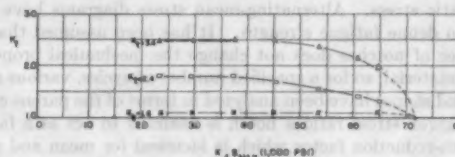


FIG. 6 EFFECTIVE STRESS-CONCENTRATION FACTOR VERSUS EFFECTIVE PEAK STRESS FOR 2014-T6 ALUMINUM ALLOY

Fig. 6 presents the K_f versus S_{max}/K_f variations for 2014-T6 aluminum alloy. The curves follow a pattern which may be useful in checking extrapolated curves, but are presented here primarily to indicate the range over which K_f remains constant.

LIMITATIONS OF METHOD

The sample construction in Fig. 4 shows that the relationships derived in this paper do not give a precise mathematical solution. The accuracy of curves constructed as proposed depends upon the amount and the accuracy of the data available as well as the judgment of the designer. Another factor which is probably more important is that the relationships as presented are only satisfactory for a large number of cycles. If additional data were available for 10^6 and 10^7 cycles, since the S - N curves are nearly flat in this region, very little variation should occur. It should be noted that the greatest deviation in the curves presented occurs with 2024-T4 aluminum alloy, and the flat portion of the

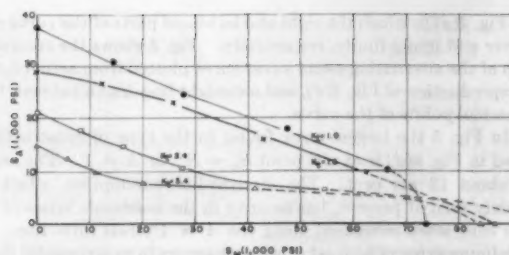


FIG. 7 ALTERNATING-MEAN STRESS DIAGRAM FOR 2014-T6 ALUMINUM ALLOY ROUND SPECIMENS, FOR 10^7 CYCLES (SEE REFERENCE 7)

S - N curves for this material was found to be beyond 10^7 cycles for some of the test conditions. Fig. 7 shows the trends for fewer cycles. Only data for 2014-T6 are shown, but the same trends occur with 2024-T4 aluminum.

Although a general limitation on the error involved in the type of analysis presented herein is not known, one conclusion can be drawn from the data available. The fatigue characteristics of a material cannot be determined from only tests with fully reversed alternating stresses. If any analysis of the fatigue characteristics of a material is to be made on the basis of a single S - N curve, the tests should be made with some mean stress applied.

Two fundamental factors require analysis before the basic physical laws governing fatigue can be defined: (a) Although the relationship between K_t and K_f is considered to be a function of both notch shape and material, the relationship has not yet been determined. (b) There is little known as yet about the actual biaxial and triaxial stresses encountered in notched specimens, and the relationship these stresses have to fatigue failures for a wide range of ductilities and mean stresses is not known.

SUMMARY

The fatigue-strength variation of materials with mean stresses for a specified number of cycles to failure has been discussed in terms of the amplitude of the alternating stress superimposed on the static stress. Alternating-mean stress diagrams have been used to define fatigue strength. It has been assumed that the presence of notches does not change the mechanical properties of the material, so for a specified number of cycles, various notch sizes and shapes have been analyzed in terms of the parent curve. For a given stress ratio a notch is assumed to act as a fatigue strength-reduction factor which is identical for mean and alternating stresses. The many variables which affect fatigue strength of a material have not been ignored, but a pattern has been established which is intended as an outline from which many other variables may be investigated.

The concept of fatigue as developed from the original assumption is satisfactory for the axial-load data available on ductile materials providing the relationships developed are used for large numbers of cycles. This type of analysis provides a means of predicting the notched fatigue strengths of materials if the unnotched fatigue strength is known for various stress ratios. The following minimum notched test data are required:

- 1 The fatigue strength with a static load greater than the peak alternating load.
- 2 The static tensile strength.

The trends presented in this paper were checked with all of the data available in the two referenced reports. No other data were found for such extensive test series of notched and unnotched specimens as were found in these two reports. Although the analysis has not been proved conclusively, it is in agreement with the test data available for both aluminum and steel.

ACKNOWLEDGMENT

The analysis of fatigue as presented in this paper has been developed from discussions on specific points with Prof. J. O. Smith of the University of Illinois, Dr. A. Herzog, and W. J. Trapp, of the Materials Laboratory at Wright Air Development Center. Acknowledgment is also made of the time spent by Prof. T. J. Dolan and H. T. Corten of the University of Illinois, in reviewing the paper. The author wishes to thank them for the time they have contributed and the interest they have shown in this analysis.

BIBLIOGRAPHY

- 1 "A Study of Size Effect and Notch Sensitivity in Fatigue Tests of Steel," by H. F. Moore, Proceedings of the American Society for Testing Materials, vol. 45, 1945, pp. 507-521.
- 2 "Effect of Surface-Strengthening on Shafts Having a Fillet or a Transverse Hole," by R. E. Peterson and J. M. Leesells, Proceedings of the Society for Experimental Stress Analysis, vol. 2, 1944, pp. 191-199.
- 3 "Fatigue Failures Are Tensile Failures," by J. O. Almen, *Product Engineering*, March, 1951, pp. 102-124.
- 4 "Crystalline Structure in Relation to Failure of Metals—Especially by Fatigue," by H. J. Gough, Proceedings of the American Society for Testing Materials, Part II, vol. 33, 1933, pp. 3-114.
- 5 "Some Aspects of the Effect of Metallurgical Structure on Fatigue Strength and Notch-Sensitivity of Steel," by T. J. Dolan and C. S. Yen, Proceedings of the American Society for Testing Materials, vol. 48, 1948, p. 664.
- 6 "Combined-Stress Fatigue Strength of 768-T61 Aluminum Alloy With Superimposed Mean Stresses and Corrections for Yielding," by W. N. Findley, NACA TN 2924, Washington, D. C., May, 1953.
- 7 "Fatigue Properties of Aluminum Alloys at Various Direct Stress Ratios," by B. J. Lavan and A. A. Blatherwick, WADC TR 52-306, Part I, Wright-Patterson Air Force Base, Ohio, 1952.
- 8 "Axial-Load Fatigue Tests on Notched Sheet Specimens of 24S-T3 and 76S-T6 Aluminum Alloys and of SAE 4130 Steel With Stress Concentration Factor of 1.5," by H. J. Grover, W. S. Hyler, and L. R. Jackson, NACA TN 2639, Washington, D. C.
- 9 W. J. Trapp, Verbal Communication.

Discussion

R. E. PETERSON.⁴ The procedure proposed by Captain Dirkes is in remarkably good agreement with test data for the cases covered. However, it does depend on running fatigue tests for any variation in geometry. In many design problems, one must make an estimate without the benefit of special tests, and it is of interest to see what one would obtain in this instance. The yield, tensile, and unnotched fatigue strengths of ordinary engineering materials are available to designers, as are also a variety of theoretical stress-concentration factors. A design rule is usually a simplification in which the error is on the safe side. Referring to Fig. 8, based on Captain Dirkes' Fig. 5, the simplest design rule for a notched member under alternating stress is

$$S_{kt} = S_e / K_t$$

where

- S_{kt} = design stress for notched member
 S_e = unnotched fatigue strength
 K_t = stress-concentration factor (theoretical)

To account for mean stress, the simplest rule is to connect S_{kt} of Fig. 8 with the yield strength, S_y , or tensile strength, S_t , by means of a straight line.⁵ As seen from Fig. 8, this procedure results in values well on the safe side of the test points. Incidentally,

⁴ Manager, Mechanics Department, Westinghouse Research Laboratories, East Pittsburgh, Pa.

⁵ "Factor of Safety and Working Stress," by C. R. Soderberg, Trans. ASME, vol. 52, Part 1 (1930), p. APM 52-2. See also "Stress Concentration Design Factors," by R. E. Peterson, John Wiley & Sons, Inc., New York, N. Y. (1953), p. 15.

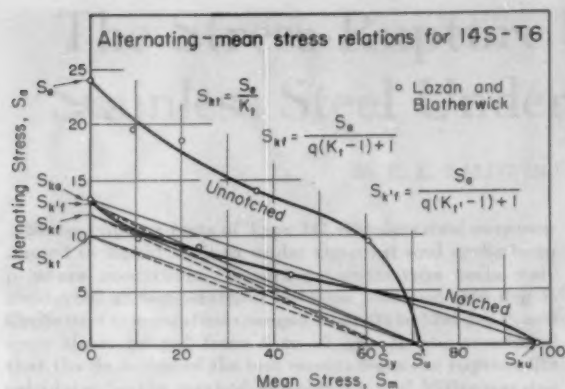


FIG. 8

Captain Dirkes mentioned the widely used straight-line assumption as being in error on the unsafe side, referring to the straight dashed line of Fig. 5 drawn to the notched tensile strength value (see also top straight line of Fig. 8); however, this does not correspond with usual design procedure. With regard to estimating the notched fatigue strength under alternating stress conditions one can use more elaborate methods⁶ as indicated on

Fig. 8, wherein average notch-sensitivity factors⁶ and the Mises criterion⁶ are used and these come closer to the test results. However, in a large percentage of cases, these design refinements are probably not justifiable. At best, design rules are not as satisfactory as actual tests and the writer is in agreement with Captain Dirkes in that wherever possible supporting test data be obtained and utilized.

AUTHOR'S CLOSURE

Mr. Peterson's comments are appreciated, particularly the information regarding common design practices. Inspection of Fig. 5, considering Mr. Peterson's comments, shows that the area of greatest error with conventional-design procedures is that where high mean stresses are applied.

The original interest in developing a more accurate design procedure was caused by the need for weight saving in aircraft and missile structures. If the proper contour for an alternating-mean stress curve can be established with reasonable accuracy, then a safety factor can be applied such that the original shape of the curve is maintained. This concept still requires additional experimental investigation, particularly since recent tests have indicated that modification is necessary if the test material creeps under the stress and temperature applied.

⁶ *Metals Handbook*, 1954 Supplement, American Society for Metals, Cleveland, Ohio, p. 101.

The Stress-Rupture Strength of Type 347 Stainless Steel Under Cyclic Temperature¹

By E. E. BALDWIN,² SCHENECTADY, N. Y.

Stress-rupture tests of Type 347 stainless steel were conducted in liquid sodium under constant and cyclic temperature conditions. Constant-temperature tests were conducted at temperatures between 1000 and 1200 deg F. Cyclic-test temperatures ranged from 416 to 1294 deg F, and cycle times ranged from 6 to 12 hr. It was concluded that the deviation of the test results from the rupture life calculated by the method of Robinson and Miller was due to transient creep of the steel under cyclic-temperature changes.

OBJECT

THE trend in design of power plants, both mobile and stationary, is the continual increase in maximum operating temperature for increased efficiency. Included in this trend are steam plants operating at higher temperatures and pressures, gas turbines with their high-temperature gaseous combustion products, and more recently, the application of nuclear reactors to power production.

Concurrent with this design trend are the increased requirements of the materials of construction used for the fabrication of these plants. These materials must withstand the higher operating temperature without serious loss of strength and have adequate resistance to the corrosive atmospheres which are present.

Among the materials that have been shown suitable for the foregoing applications are the austenitic stainless steels and of these Type 347 stainless steel has had wide usage. Its chemical composition (18 per cent chromium, 8 per cent nickel, plus tantalum and columbium) results in a material with relatively good mechanical strength at temperatures up to 1300 F (704 C), and resistance to corrosive attack by many heat-transfer mediums.

During the operation of power-producing equipment, the calculated constant design temperatures are never, in effect, constant. Varying power-load demands, scheduled and unscheduled shutdowns, and other scheduled and unscheduled events, depending upon the type of plant and its operation, result in an operating temperature that fluctuates in a cyclic manner.

Investigations have shown that the rupture and creep strengths of metals are reproducible and predictable at constant temperature, but are seriously affected by cyclic-temperature changes (1, 2).³ As a result, cyclic-temperature changes in a power plant may seriously shorten its total operating life.

¹ This paper was submitted to the Metallurgy Department of Rensselaer Polytechnic Institute in partial fulfillment of the requirements for the degree of Master of Science in Metallurgical Engineering.

² Materials Engineering Section, Knolls Atomic Power Laboratory, operated for the U. S. Atomic Energy Commission by the General Electric Company.

³ Numbers in parentheses refer to Bibliography at end of the paper. Contributed by the Metals Engineering Division and presented at the Annual Meeting, New York, N. Y., November 28—December 3, 1954, of THE AMERICAN SOCIETY OF MECHANICAL ENGINEERS.

NOTE: Statements and opinions advanced in papers are to be understood as individual expressions of their authors and not those of the Society. Manuscript received at ASME Headquarters, October 20, 1954. Paper No. 54-A-231.

This investigation was undertaken to determine the effect of several types of cyclic-temperature changes on the stress-rupture strengths of Type 347 stainless steel, to compare the test results with values of cyclic-temperature rupture life calculated by the method of Robinson and Miller (2, 3), and to attempt to offer a plausible explanation for any deviation of the experimental from the calculated results.

PROCEDURE

Material. The material tested in this investigation was 1-in.-diam, centerless ground, annealed bar stock. The chemical composition of the steel, as determined by mill analysis, is listed in Table 1.

TABLE 1 TYPE 347 STAINLESS STEEL TESTED⁴

Element	Per cent	Element	Per cent
C	0.047	Si	0.44
Cr	17.83	S	0.012
Ni	10.40	P	0.025
Cr + Ta	0.91	Mn	1.73
		Fe	Balance

⁴ Supplier, G. O. Carlson. Heat No. 49175.

Equipment. The stress-rupture testing was conducted at the Knolls Atomic Power Laboratory, using the three-bar rupture furnaces illustrated in Figs. 1 and 2. These furnaces consist of an austenitic stainless-steel container made of 5-in. Schedule 40 pipe welded shut at the bottom with 1/4-in.-thick plate, and fitted at the top with a flange, and a 1/2-in.-thick bolted cover.

Provision is made to insert three complete load-bar and specimen assemblies through the cover. These assemblies provide the means for applying a tensile load to the specimen while it is immersed in liquid metal.

The specimens tested in this apparatus, Figs. 3 and 4, were in the form of cylindrical tensile specimens, having a 1-in. gage length, and a gage diameter of 0.160 ± 0.005 in. Elongation at rupture was determined by measuring the over-all length of the specimen before and after completion of the test, assuming that all plastic deformation occurred in the 1-in. gage section.

A tensile load was applied to the specimen by means of split rings bearing against the 0.330-in.-diam heads, Fig. 5. The split rings were held in place by the lower support ring at the bottom and the load-bar coupling at the top.

The lower support ring was fastened to the containing tube, which has a flange welded to its top end, Fig. 6, and the load bar was fastened to the knife-edge assembly. The knife-edge assembly was welded to one end of a flexible Type 347 stainless-steel bellows, and a flange was welded to the other end. The complete assembly was inserted into the liquid-metal container through ports in the cover, and bolted to the container cover. Aluminum O-ring seals between the flanges prevented leakage of the protective inert-gas atmosphere.

The sodium container with its three specimen and load-bar assemblies was inserted into a nichrome-wound resistance furnace. Temperature was determined by chromel-alumel thermocouples which were inserted into a protection tube. This tube was welded to the liquid-metal container cover at the top and immersed in the liquid metal at the bottom at the same height as the specimen.

FIG. 1 (right) AND FIG. 2 (below)
LIQUID-METAL STRESS-RUPTURE
FURNACE

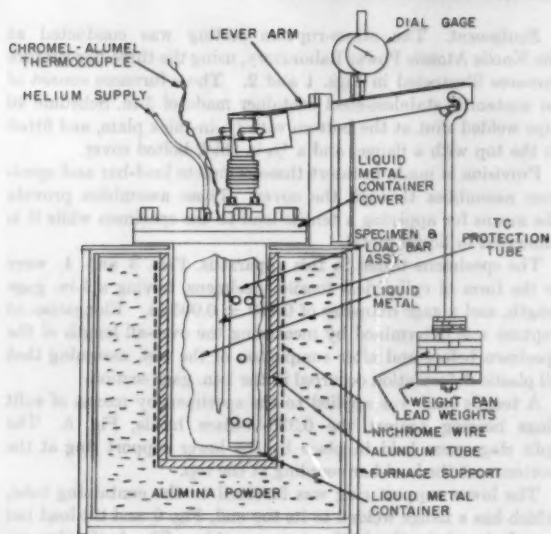
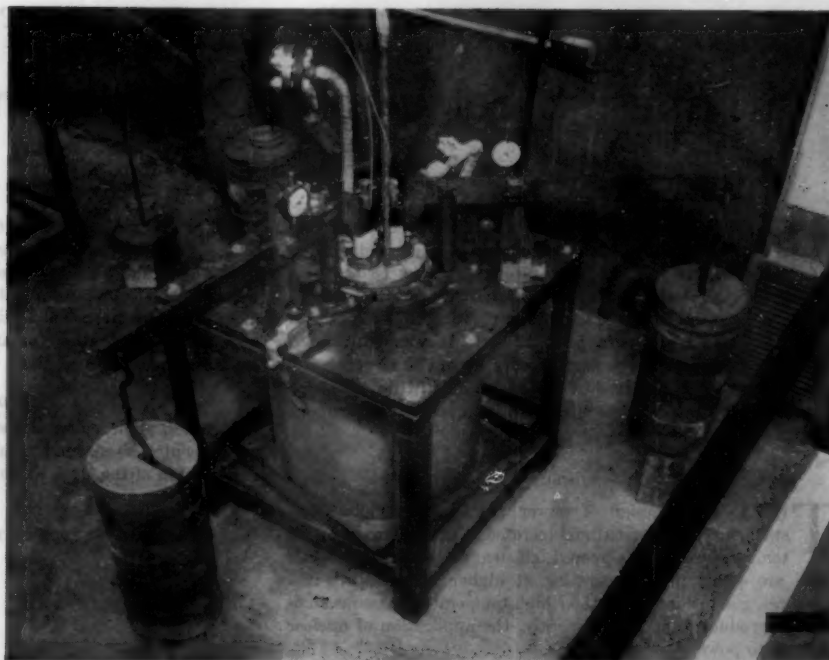


Fig. 2

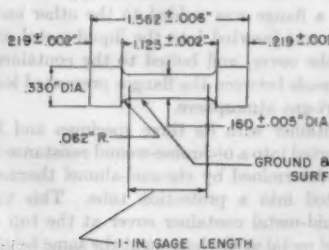


FIG. 4 LIQUID-METAL STRESS-RUPTURE SPECIMEN

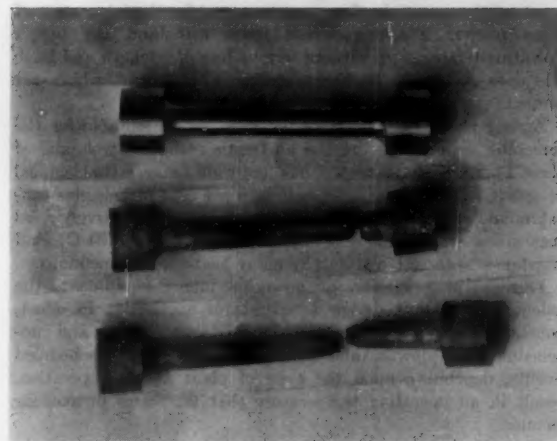


FIG. 3 STRESS-RUPTURE SPECIMENS

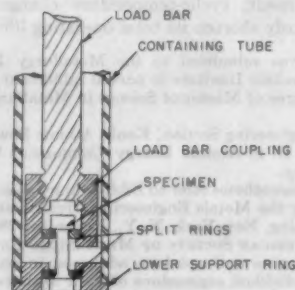


FIG. 5 SPECIMEN AND LOAD-BAR ASSEMBLY—LOWER PORTION

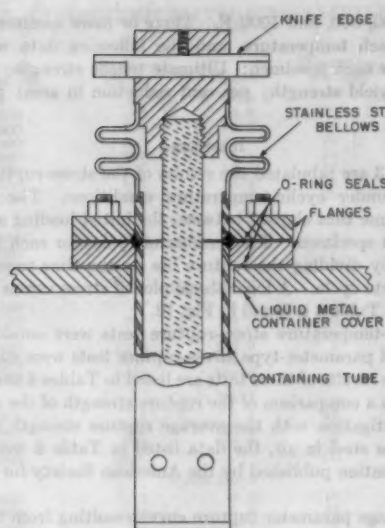


FIG. 6 SPECIMEN AND LOAD-BAR ASSEMBLY—UPPER PORTION

Tensile stresses were applied to the specimen by means of lead weights and a lever-arm arrangement. The lever arm had a 5 to 1 ratio, so that a 1-lb weight would exert a force of 5 lb on the specimen and produce a tensile stress of 250 psi in its gage length.

A 0.001-in. dial gage was mounted on the lever arm at a point from the lever-arm fulcrum equidistant to the length between the fulcrum and the load-bar knife edge. This dial gage was used to determine specimen elongation during loading and test, but was not accurate enough for determination of time-elongation curves.

The liquid metal used in these tests was sodium, currently of interest as a heat-transfer medium for nuclear-power plants. Investigations have been conducted which have shown that liquid sodium is noncorrosive to austenitic stainless steels when the oxygen content is kept low (4, 5). Before filling the liquid-metal container, the sodium was purified by filtering it through a porous stainless-steel filter at a temperature slightly above its melting point (208 F), to remove insoluble oxides. Sodium purity was maintained throughout the test by evacuating the liquid-metal container before filling and maintaining a protective atmosphere of helium over the liquid metal during testing.

Temperature of the rupture furnaces was controlled by two methods. For cyclic-temperature tests, the temperature was regulated by a Wheelco program controller, Model 72251B. In the event of a temperature overshoot, either as the result of a thermocouple failure or malfunctioning of the program controller, a Brown Pyr-O-Vane controller, Model 105C4PS-22, was used as a limit control. If the temperature of the furnace exceeded the limit-control temperature, a warning horn sounded, indicating malfunction of the equipment. For rupture tests conducted at constant temperature a Brown Pyr-O-Vane controller was substituted for the Wheelco controller. Temperature of the furnaces during test was recorded on a six-point Leeds and Northrup Micromax recorder. A recording of temperature was made approximately every 3 min.

Short-time tensile tests of the material under investigation were made on a Baldwin universal testing machine of a 60,000-lb capacity. Specimens were in the form of standard 0.505-in.-diam ASTM tensile specimens (6) tested at a crosshead speed of approximately 0.05 ipm. For the elevated-temperature tests, the

specimen temperature was maintained by a Hevi-Duty multiple-unit electric furnace, Type M-3018, controlled by a Foxboro potentiometer controller, Model 4041-40F. The 0.2 per cent offset yield strength was determined from the load-elongation curves recorded by a microformer-type extensometer and a Baldwin microformer stress-strain recorder, Model 91.

Tests. The tests conducted in this investigation were of three types: Cyclic-temperature stress-rupture tests in sodium; constant-temperature stress-rupture tests in sodium; short-time tensile tests in air.

Concurrent with this investigation, constant-temperature parameter-type stress-rupture tests in air were conducted on samples of the same material by the Materials and Processes Laboratory, Large Steam Turbine and Generator Department, General Electric Company.

The cyclic-temperature stress-rupture tests were conducted under two general types of cyclic-temperature conditions:

Temperature variation in a sawtooth cycle (continual fluctuation between an upper and lower-temperature limit)

Temperature variation in a square-wave cycle (upper and lower-temperature limits, and a residence time at each limit)

The temperature and cycle-time conditions that existed in each of the cyclic-temperature tests are listed in Table 2 and are plotted in Figs. 7 to 11.

TABLE 2 CYCLIC-TEMPERATURE CONDITIONS

Cycle no.	Cycle type	Cycle time, hr	Max temp, deg F	Min temp, deg F	Mean temp, deg F
1	Square wave	12	1000	416	608
2	Square wave	12	1200	468	834
3	Sawtooth	8	1104	850	1007
4	Sawtooth	7.4	1294	698	996
5	Square wave	6	1218	970	1094

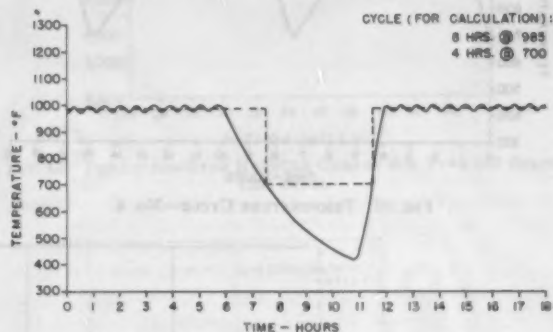


FIG. 7 TEMPERATURE CYCLE—No. 1

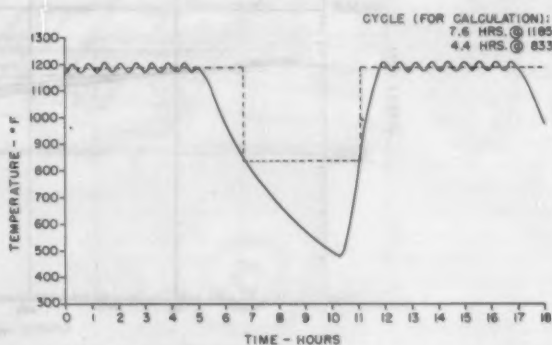


FIG. 8 TEMPERATURE CYCLE—No. 2

The constant-temperature stress-rupture tests were conducted at 1000, 1100, and 1200 F; (a) to determine the constant-temperature stress-rupture properties of the material under investigation in a temperature range similar to that of the cyclic-temperature stress-rupture tests, and (b) combined with the data from the Materials and Processes Laboratory, Large Steam Turbine and Generator Department, to establish a parameter-type stress-rupture curve for this material.

Short-time tensile tests were conducted at room temperature,

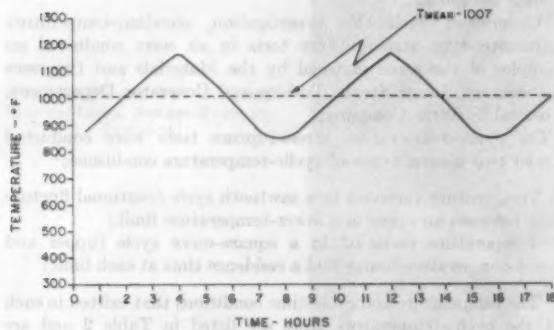


FIG. 9 TEMPERATURE CYCLE—No. 3

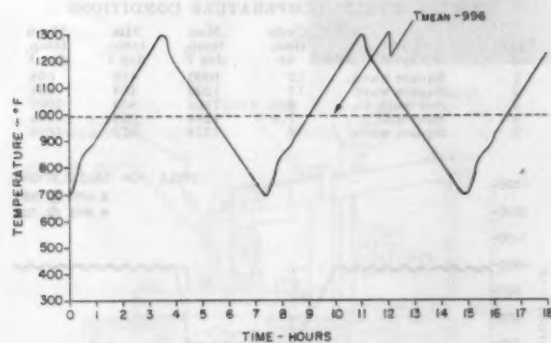


FIG. 10 TEMPERATURE CYCLE—No. 4

200, 400, 600, 800, and 1000 F. Three or more specimens were tested at each temperature, and the following data were determined for each specimen: Ultimate tensile strength; 0.2 per cent offset yield strength; per cent reduction in area; per cent elongation.

RESULTS

In Table 3 are tabulated the results of the stress-rupture tests conducted under cyclic-temperature conditions. The rupture life is the time that elapsed between the initial loading and rupture of each specimen. The number of cycles for each test was calculated by dividing the rupture life by the time required for each complete cycle. A logarithmic plot of stress versus rupture life listed in Table 3 is found in Fig. 12.

Constant-temperature stress-rupture tests were conducted in sodium, and parameter-type stress-rupture tests were conducted in air. The results of these tests are listed in Tables 4 and 5.

To obtain a comparison of the rupture strength of the material under investigation with the average rupture strength of Type 347 stainless steel in air, the data listed in Table 6 were taken from information published by the American Society for Testing Materials.

The average parameter rupture curve resulting from the data listed in Tables 4, 5, and 6 is plotted in Fig. 13. The log-stress log-time rupture curves resulting from the data listed in Tables 4 and 6 are illustrated in Fig. 14.

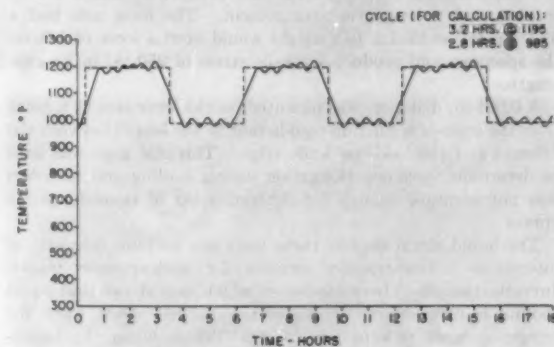


FIG. 11 TEMPERATURE CYCLE—No. 5

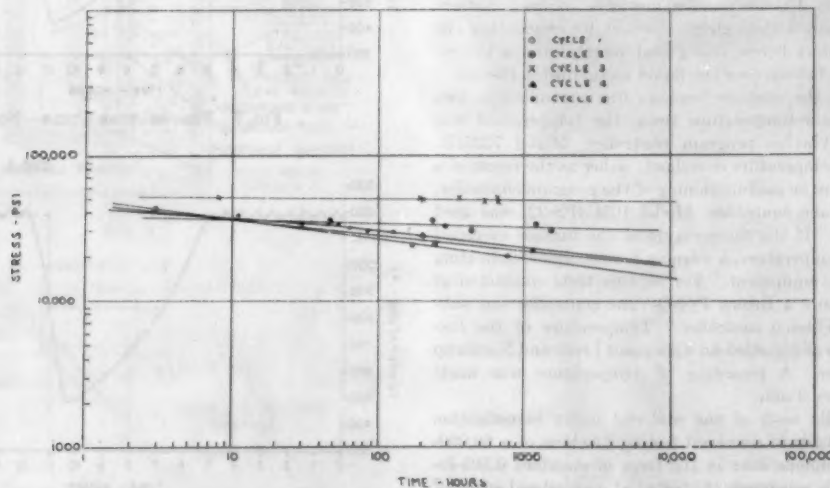


FIG. 12 CYCLIC-TEMPERATURE STRESS-RUPTURE TYPE 347 STAINLESS STEEL

TABLE 3 CYCLIC-TEMPERATURE STRESS-RUPTURE TESTS IN SODIUM

Stress, psi	Rupture life, hr	Cycles	Elongation, per cent	Reduction of area, per cent
Cycle No. 1				
52000	7	0.6	20	68
51000	196	16.3	33	64
51000	360	30.0	32	68
50500	197	16.5	26	52
50000	671	56.0	33	65
49500	541	45.1	35	64
49000	671	56.0	26	43
Cycle No. 2				
28000	202	16.9	5	4
24000	246	20.5	7	2
22000	1145	95.5	4	7
Cycle No. 3				
36250	47	5.9	33	69
36250	230	29.5	30	36
32500	269	36.2	14	19
32500	1218	182.0	9	12
30000	457	64.7	9	19
30000	1583	198.0	5	15
Cycle No. 4				
45375	3	0.4	47	50
24000	173	23.4	17	20
20000	785	106.2	9	15
16000	Disc.	...	(2) ^a	(5) ^a
Cycle No. 5				
42000	3	0.5	42	70
38000	11	1.9	46	64
34000	47	8.1	23	40
34000	53	9.1	25	32
32000	65	11.2	20	34
30000	130	22.4	18	30

^a Specimen: unloaded, unbroken.

TABLE 4 CONSTANT-TEMPERATURE STRESS-RUPTURE TESTS IN SODIUM

Temp, deg F	Stress, psi	Rupture life, hr	$P^a \times 10^{-3}$	Elongation, per cent	Reduction of area, per cent
1000	51000	506	23.1	27	45
1000	50000	819	33.3	26	36
1000	49000	863	33.4	19	32
1000	48000	896	33.5	21	25
1000	46000	2041	34.1	15	25
1100	42000	111	34.4	23	32
1100	38000	226	35.0	16	34
1100	36000	337	35.2	12	16
1100	24000	329	35.4	10	9
1100	32000	295	35.2	18	22
1100	32000	498	35.4	8	2
1200	28000	84	36.8	12	19
1200	24000	142	26.9	11	13
1200	22000	782	37.0	6	7

^a $P = T(20 + \log t)$, where T = absolute temperature, deg R, and t = rupture life, hr.^b Temperature overshoot during test.

TABLE 5 PARAMETER STRESS-RUPTURE TESTS IN AIR

Temp, deg F	Stress, psi	Rupture life, hr	$P \times 10^{-3}$	Elongation, per cent	Reduction of area, per cent
1000	40000	2008	34.0	16	19
1050	50000	41	32.6	27	68
1100	32000	249	34.9	30	34
1200	20000	393	37.8	6	6
1200	25000	78	36.4	21	21
1250	15000	439	38.7	5	7
1350	20000	7	37.8	33	36
1350	10000	158	40.3	15	13

TABLE 6 AVERAGE STRESS-RUPTURE STRENGTH OF TYPE 347 STAINLESS STEEL (5)

Rupture time, hr	Stress ^a	Stress ^a	Stress ^a	Stress ^a	Stress ^a	Stress ^a
	800	900	1000	1100	1200	1300
10 ¹	64000	60000	54000	40000	28000	20000
10 ¹	$P \times 10^{-3}$	27.7	29.9	32.1	34.3	36.5
10 ¹	60000	56000	49000	35000	23000	14000
10 ¹	$P \times 10^{-3}$	29.0	31.2	33.5	35.6	38.1
10 ¹	60000	52000	36000	27000	17500	10500
10 ¹	$P \times 10^{-3}$	30.2	32.6	35.0	37.4	39.8
10 ¹	58000	50000	33000	22000	18000	7500
10 ¹	$P \times 10^{-3}$	31.6	34.0	36.3	39.0	41.5

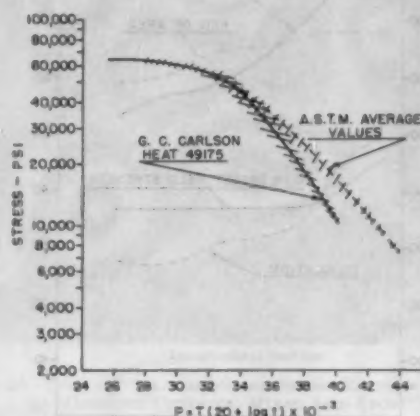
^a Stress in pounds per square inch.

FIG. 13 PARAMETER-TYPE RUPTURE CURVES FOR TYPE 347 STAINLESS STEEL

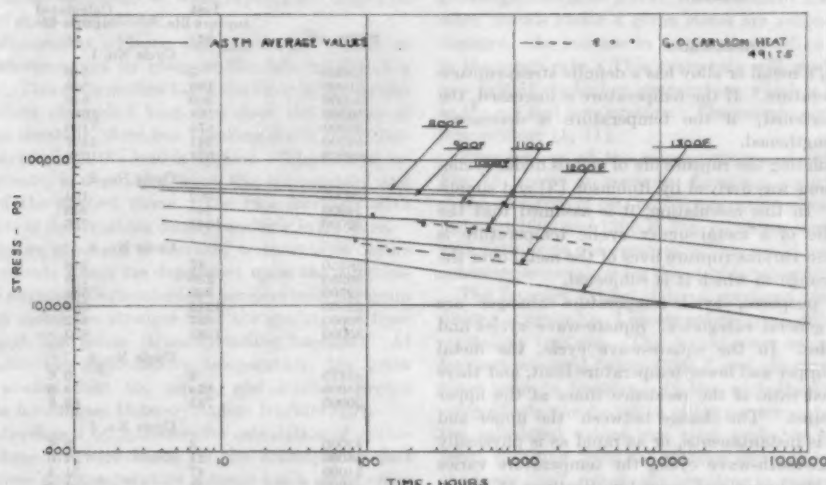


FIG. 14 STRESS RUPTURE OF TYPE 347 STAINLESS STEEL

The results of short-time tensile tests conducted in air at temperatures ranging from 70 to 1000 F are listed in Table 7. These tensile properties are plotted as a function of temperature in Fig. 15.

TABLE 7 SHORT-TIME TENSILE PROPERTIES OF TYPE 347 STAINLESS STEEL

Temp, deg F	Ultimate tensile strength, psi	0.2 per cent offset yield strength, psi	Elongation, per cent	Reduction of area, per cent
70	87700	45700	50	68
200	78700	40800	45	68
400	67300	37000	33	66
600	60200	36700	31	65
800	57200	36900	27	61
1000	52800	36000	28	59

NOTE: The values in this table are the average of three or more specimens tested at each temperature.

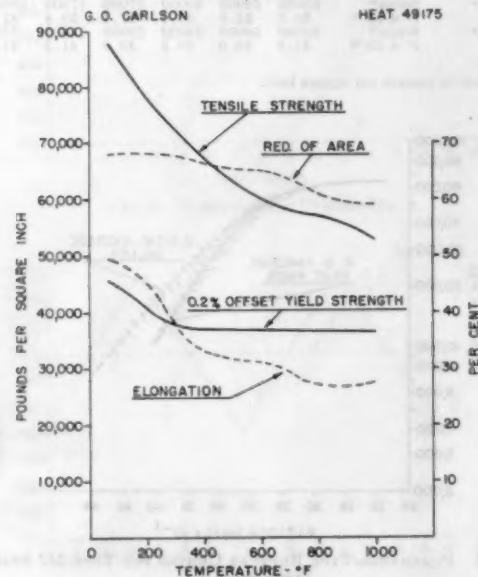


FIG. 15 SHORT-TIME TENSILE PROPERTIES—TYPE 347 STAINLESS STEEL

DISCUSSION

For a given stress, a metal or alloy has a definite stress-rupture life at a given temperature. If the temperature is increased, the rupture life is shortened; if the temperature is decreased, the rupture life is lengthened.

A method of calculating the rupture life of metals under cyclic-temperature conditions was derived by Robinson (3) and simplified by Miller (2). In this calculation, it is assumed that the resultant rupture life of a metal under cyclic temperature is the summation of the various rupture lives of the metal over the cyclic-temperature range to which it is subjected.

For calculation purposes, cyclic-temperature changes are classified into two general categories: Square-wave cycles and sawtooth-wave cycles. In the square-wave cycle, the metal is alternately at an upper and lower-temperature limit, and there is a definite and fixed ratio of the residence times at the upper and lower temperatures. The change between the upper and lower temperatures is instantaneous, or as rapid as is physically possible. In the sawtooth-wave cycle, the temperature varies constantly between the upper and lower temperatures at a constant rate.

The mathematical relationships used to calculate the rupture life of a metal or alloy under cyclic-temperature conditions are as follows (2):

Square Wave

$$L = \frac{L_1(R + 1)}{R + L_1/L_2} \quad [1]$$

where

L = rupture life for square-wave cycle

L_1 = rupture life at high temperature

L_2 = rupture life at low temperature

R = ratio of residence time at high temperature to residence time at low temperature

Sawtooth Wave

$$L = L_T \frac{2.3 P \Delta T / T^3}{\sinh(2.3 P \Delta T / T^3)} \quad [2]$$

where

L = rupture life for sawtooth cycle

L_T = rupture life at mean temperature

T = mean temperature in degrees Rankine

ΔT = difference between maximum and mean temps

P = parameter for the stress considered $T(20 + \log t)$

Using these formulas, calculations were made of the expected rupture life for the stresses and temperature cycles studied in this investigation. The results of these calculations and the deviation of the test from the calculated life in one direction.

Examination of the data in Table 8 indicates that for two of the temperature cycles investigated, cycles Nos. 1 and 4, there was deviation of the test from the calculated life in one direction. In cycle No. 1, the experimentally determined rupture life was less than that predicted by calculation, and in cycle No. 4 the experimentally determined rupture life was greater than that predicted by calculation. In all other cycles (Nos. 2, 3, and 5), the experimentally determined rupture lives showed both positive and negative deviations from the calculated life.

TABLE 8 COMPARISON OF CALCULATED AND TEST RUPTURE LIFE UNDER CYCLIC-TEMPERATURE CHANGES

Stress, psi	Test rupture life, hr	Calculated rupture life, hr	Deviation of test from calculated rupture life, per cent
Cycle No. 1			
52000	8	540	-98.7
51000	196	946	-79.2
51000	360	946	-62.0
50500	198	1086	-81.8
50000	671	1190	-43.6
49500	541	1427	-62.1
49000	671	1680	-60.0
Cycle No. 2			
28000	202	194	+4.1
24000	246	443	-44.5
22000	1145	755	+51.8
Cycle No. 3			
36250	47	218	-78.4
36250	236	218	+8.5
32500	289	584	-56.5
32500	1218	584	+108.4
30000	437	862	-49.4
30000	1583	862	+84.3
Cycle No. 4			
45375	3	0.6	+362.0
24000	173	53.8	+221.0
20000	785	83.9	+835.0
Cycle No. 5			
42000	3	9.4	-68.1
38000	11	21.0	-47.7
34000	47	51.4	-8.6
34000	53	51.4	+3.1
32000	65	83.5	-27.1
30000	130	93.7	+38.7

There are three possible reasons for the deviations shown between the calculated and the test results:

Assumptions made as to wave form for calculating cyclic-temperature rupture life.

Deformation mechanisms taking place in the specimens during test.

Errors introduced by experimental conditions.

Assumptions Made for Calculations. Examination of the time-temperature plots for the various temperature cycles investigated, Figs. 7 to 11, shows that none of the temperature cycles investigated satisfied the requirements of true square-wave or sawtooth-wave cycles as defined. In cycles Nos. 1 and 2, there was no residence time at the lower-temperature limit, but a continuous change in temperature between the residence times at the upper temperature. In cycle No. 5, although there were residence times at the upper and lower temperatures, the temperature change between the upper and lower limits was not instantaneous but changed at a definite and relatively slow rate. In addition, at the higher-temperature limit in cycles Nos. 1 and 2 and at both the upper and lower-temperature limits in cycle No. 5, the temperature was not constant but underwent small cyclic changes.

For calculation purposes, temperature cycles Nos. 1, 2, and 5 were considered square-wave cycles having limits defined by the broken-line curves in Figs. 7, 8, and 11.

A similar deviation from the rigid definition of sawtooth wave occurs in cycles Nos. 3 and 4. Cycle No. 4 (Fig. 10) most closely approximates a sawtooth cycle, but deviates from the ideal by having heating and cooling rates which vary during each cycle. Cycle No. 3 (Fig. 9) deviated from the ideal cycle in that there is not an instantaneous but a gradual change from cooling to heating at the lower-temperature limit plus the fact that there is a change in heating and cooling rates during the cycle. In both cases, however, the cycles are assumed to be sawtooth cycles, and rupture lives are calculated with the applicable formula.

Since, as shown in the foregoing, the temperature cycles investigated did not meet the requirements of cycle shape upon which Equations [1] and [2] are based, close agreement between experimental and calculated results cannot be expected. However, since the results of rupture tests under cycles Nos. 2, 3, and 5 show both positive and negative deviations from the calculated results, the formulas for calculating cyclic-temperature rupture life give some indication of what rupture life might be expected, but not exact predictions.

Deformation Mechanisms. Plastic deformation of metals at elevated temperatures occurs by creep or the deformation of a metal with time. This deformation takes the form of an elongation in the direction of applied load, but since the volume of the metal remains constant, there is a "necking down" or reduction of the area over which the load is applied. The rate of extension, or creep rate, is dependent upon the temperature and the magnitude of the applied stress. The rate increases with increasing amounts of deformation, finally resulting in fracture.

Fracture or rupture of metals at elevated temperatures occurs by one of two methods which are dependent upon the temperature. Below the so-called "equicohesive" temperature, the grain boundaries of the metal are stronger than the grains, and fracture occurs through the grains (transcrystalline fracture). At temperatures above the equicohesive temperature, the grain boundaries are weaker than the grains, and fracture occurs through the grain boundaries (intercrystalline fracture) (9).

The formulas developed by Robinson for calculation of cyclic-temperature rupture life were based on the assumptions that (a) for a given stress and temperature a metal has a given creep rate and rupture life, and (b) under cyclic-temperature changes

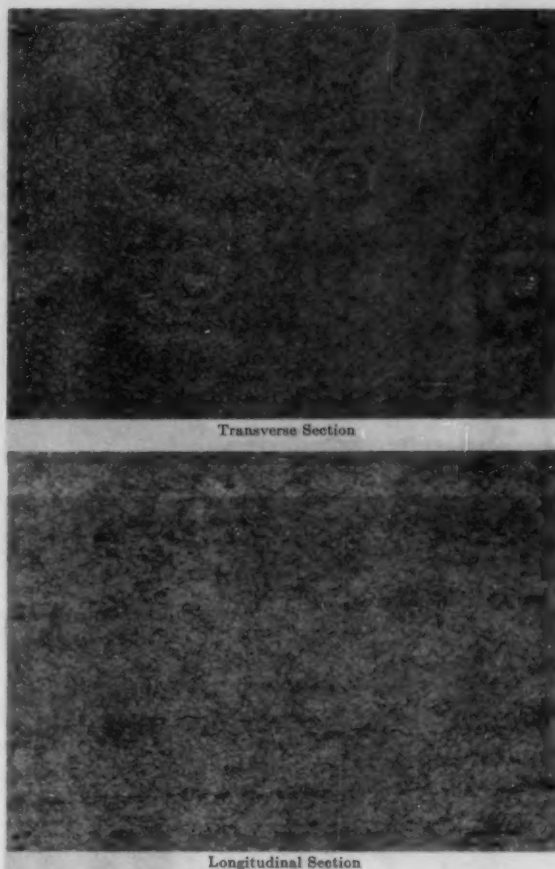
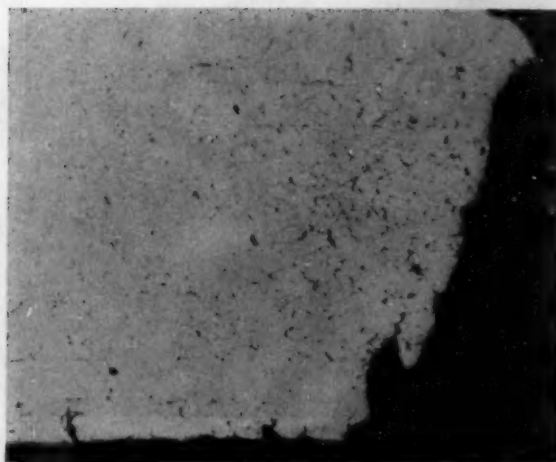


FIG. 16 TYPE 347 STAINLESS-STEEL STRESS-RUPTURE SPECIMEN—AS MACHINED, UNTESTED, MIXED ACID ETCH; $\times 100$

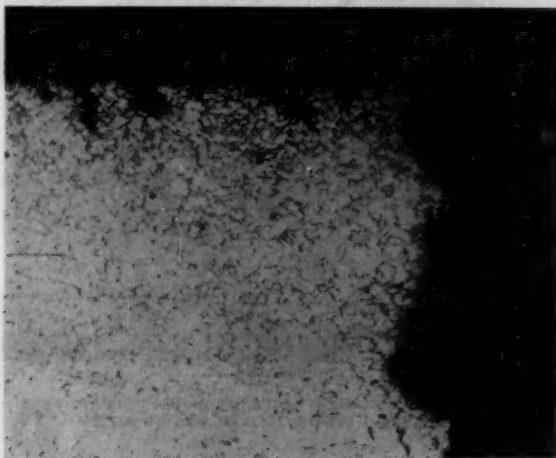
the resultant creep and rupture life was the summation of these properties for each increment of temperature in the cycle (3, 10). Investigations have shown that transient creep conditions occur when metals under a given stress are subjected to temperature changes. An increase in temperature will cause a sharp increase in the creep rate. This creep rate will gradually decrease to a new rate at the higher temperature, which is higher than the rate at the original temperature. The reverse occurs on a decrease in temperature (1, 11).

Examination of the microstructure of the original material, Fig. 16, shows an equiaxed fine-grain structure. Examination of the structure of constant-temperature stress-rupture specimens tested at 1000 and 1200 F, Fig. 17, shows intercrystalline fracture with little or no deformation. This would indicate that the equicohesive temperature for this steel is below 1000 F.

The fracture exhibited by a specimen tested under the conditions of cycle No. 1 shows severe grain deformation and transcrystalline fracture. This would seem to indicate that (a) the fracture occurred below 1000 F and (b) severe creep had taken place prior to fracture. In line with the findings on transient creep effects, the deviation of the experimental rupture lives from the calculated values was most probably caused by increased creep resulting from the sudden increase in temperature from the lower limit, eventually resulting in rupture at a temperature below 1000 F and at a time shorter than the calculated value.



1000 F (538 C)



1200 F (649 C)

FIG. 17 CONSTANT-TEMPERATURE STRESS-RUPTURE SPECIMENS—LONGITUDINAL SECTION THROUGH FRACTURE, MIXED ACID ETCH; $\times 100$

Fracture of specimens tested under the other cyclic-temperature conditions was of an intercrystalline type.

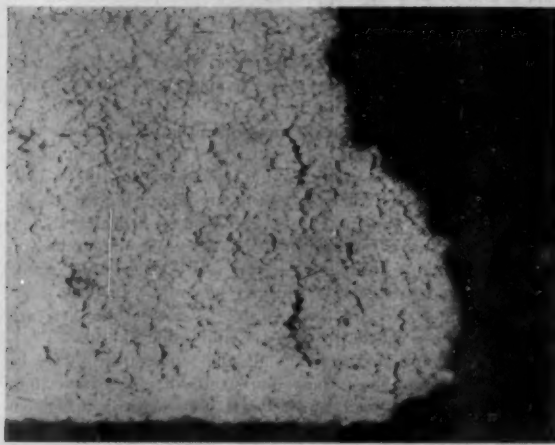
The deviation of the experimental rupture lives from the calculated values in temperature cycle No. 4 might also be explained by transient creep effects. In this case, the decrease in creep rate by the sudden decrease in temperature from the upper limit could have more than offset the increased creep rate resulting from the temperature increase, resulting in a rupture life longer than that calculated.

Experimental Conditions. The equipment used in this investigation could have influenced the results obtained.

During cyclic-temperature changes, the load bar and specimen expanded and contracted, the magnitude of the dimensional change being determined by the coefficient of thermal expansion of the austenitic stainless steel used for their construction and the magnitude of the temperature change. Since the bellows was, in effect, a spring, its expansion caused a reduction, and contraction an increase in the load applied to the specimen. This resulted in a minor cyclic stress being imposed on the specimen in addition to the cyclic-temperature changes.



Temperature Cycle No. 1



Temperature Cycle No. 2

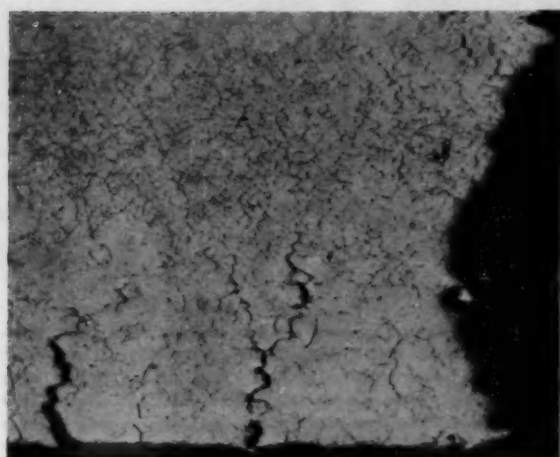
FIG. 18 CYCLIC-TEMPERATURE STRESS-RUPTURE SPECIMENS—LONGITUDINAL SECTION THROUGH FRACTURE, MIXED ACID ETCH; $\times 100$

Specimen and load-bar assemblies were removed from the liquid-metal container without draining the sodium. Although a flow of helium was kept over the sodium during these operations, there was most probably some contamination of the sodium by oxygen, which might have resulted in corrosion of the specimens. In Table 9 are listed the maximum and minimum weight changes of the specimens for each test condition.

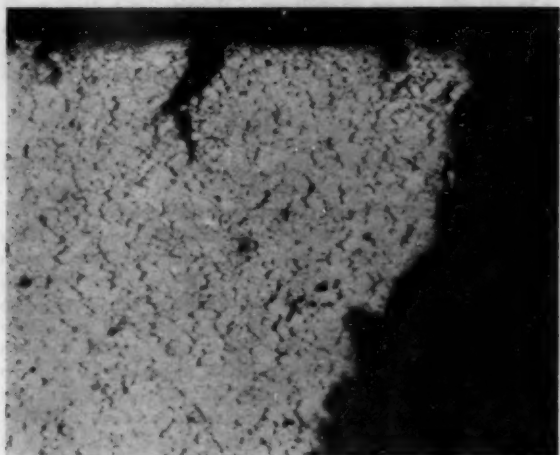
TABLE 9 RANGE OF SPECIMEN WEIGHT CHANGES

Test condition	Weight change, mg/cm ²	
	Maximum	Minimum
1000 F	-3.02	-1.99
1100 F	+0.17	+0.12
1200 F	-4.46	-0.15
Cycle No. 1	-3.42	+0.02
Cycle No. 2	-0.47	-0.06
Cycle No. 3	-2.84	-0.75
Cycle No. 4	-3.50	-0.73
Cycle No. 5	-4.01	-0.01

There was a wide range in weight changes as shown in Table 9, but there was no correlation between the weight change exhibited and the time and temperature of the test. Examination of Figs. 16 to 20 indicates that a major fraction of the weight loss of the



Temperature Cycle No. 3



Temperature Cycle No. 4

FIG. 19 CYCLIC-TEMPERATURE STRESS-RUPTURE SPECIMENS—LONGITUDINAL SECTION THROUGH FRACTURE, MIXED ACID ETCH; $\times 100$

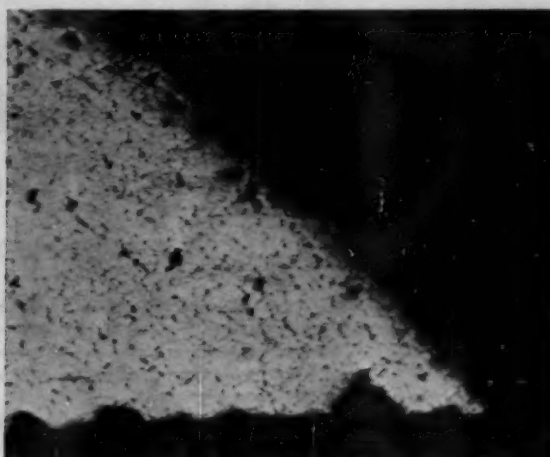
specimens was probably due to loss of particles of metal adjacent to the fracture during steam cleaning of the specimens after their removal from the sodium.

The cyclic-test temperatures were controlled by a Wheelco controller, which involved cutting a circular cam to the shape necessary for the particular cycle of interest. As shown in Figs. 7 to 11, there was some cyclic variation at the constant control temperatures. This was due either to roughness on the edge of the cam or the high heat capacity of the furnace and liquid-metal container.

CONCLUSIONS

From the results obtained in this investigation, the following conclusions can be drawn:

- 1 The mathematical expressions developed by Robinson for



Temperature Cycle No. 5

FIG. 20 CYCLIC-TEMPERATURE STRESS-RUPTURE SPECIMENS—LONGITUDINAL SECTION THROUGH FRACTURE, MIXED ACID ETCH; $\times 100$

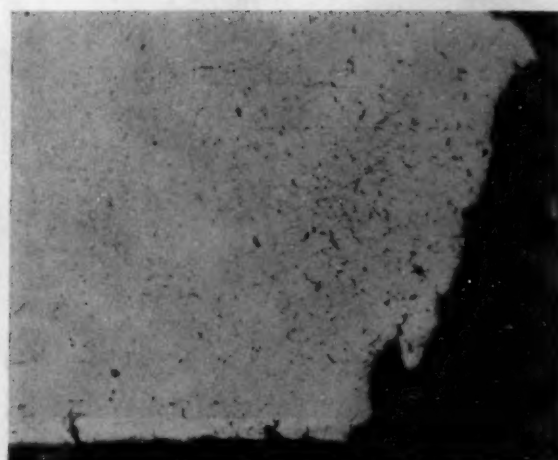
calculating the stress-rupture life of steels under cyclic-temperature conditions give results which are only an approximation of the expected life.

- 2 The deviation of the test from the calculated life is due to the transient creep conditions that exist under cyclic-temperature changes, which are not considered in the Robinson and Miller formulas.

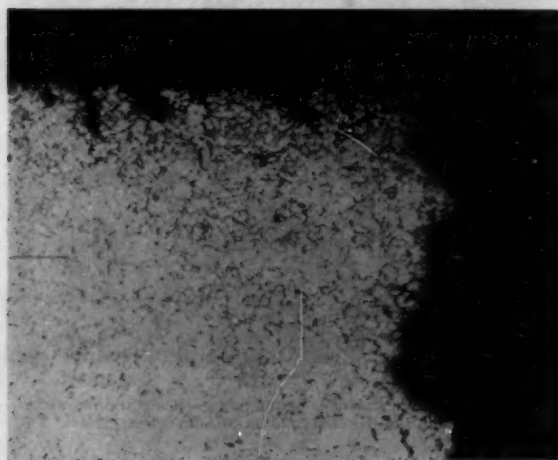
- 3 The rupture life determined for Type 347 stainless steel under a given cyclic-temperature condition is true only for that condition and cannot be extrapolated to similar conditions with any degree of accuracy.

BIBLIOGRAPHY

- 1 "The Cyclic Temperature Acceleration of Strain in Heat-Resisting Alloys," by G. R. Brophy and D. E. Furman, *Trans. ASM*, vol. 30, 1942, p. 1115.
- 2 "Effect of Temperature Cycling on the Rupture Strength of Some High-Temperature Alloys," by J. Miller, ASTM, Special Technical Publication No. 165, 1954, p. 53.
- 3 "Effect of Temperature Variation on Long-Time Rupture Strength of Steels," by Ernest L. Robinson, *Trans. ASME*, vol. 74, 1952, pp. 777-781.
- 4 "Liquid Metals Handbook," Rev., NAVEXOS-P-733, June, 1952.
- 5 "Liquid Sodium, a Noncorrosive Coolant," by R. F. Koenig and S. R. Vandenberg, *Metal Progress*, vol. 61, March, 1952, p. 71.
- 6 "Tension Testing of Metallic Materials," ASTM Specification E8-52T, Fig. 8, 1952, p. 1393.
- 7 "A Time-Temperature Relationship for Rupture and Creep Stresses," by F. R. Larson and J. Miller, *Trans. ASME*, vol. 74, 1952, pp. 765-775.
- 8 "The Elevated-Temperature Properties of Stainless Steels," ASTM, Special Technical Publication No. 124, 1952.
- 9 "Properties of Metals at Elevated Temperatures," by G. V. Smith, McGraw-Hill Book Company, Inc., New York, N. Y., 1950.
- 10 "Effect of Temperature Variation on the Creep Strength of Steels," by Ernest L. Robinson, *Trans. ASME*, vol. 60, 1938, pp. 253-259.
- 11 "Transient Plastics Deformation," by R. P. Carreker, J. G. Leschen, and J. D. Lubahn, *Trans. AIME*, vol. 180, 1949, pp. 139-146.



1000 F (538 C)



1200 F (649 C)

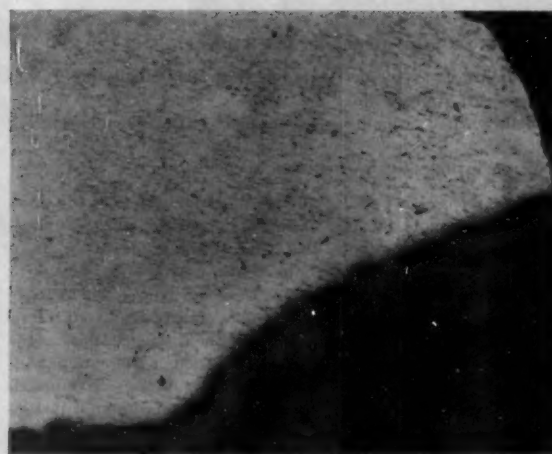
FIG. 17 CONSTANT-TEMPERATURE STRESS-RUPTURE SPECIMENS—LONGITUDINAL SECTION THROUGH FRACTURE, MIXED ACID ETCH; $\times 100$

Fracture of specimens tested under the other cyclic-temperature conditions was of an intercrystalline type.

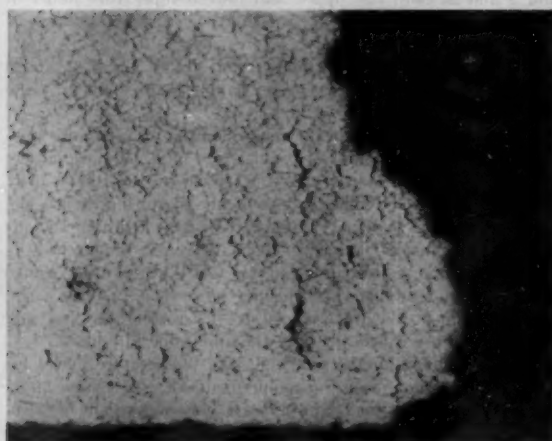
The deviation of the experimental rupture lives from the calculated values in temperature cycle No. 4 might also be explained by transient creep effects. In this case, the decrease in creep rate by the sudden decrease in temperature from the upper limit could have more than offset the increased creep rate resulting from the temperature increase, resulting in a rupture life longer than that calculated.

Experimental Conditions. The equipment used in this investigation could have influenced the results obtained.

During cyclic-temperature changes, the load bar and specimen expanded and contracted, the magnitude of the dimensional change being determined by the coefficient of thermal expansion of the austenitic stainless steel used for their construction and the magnitude of the temperature change. Since the bellows was, in effect, a spring, its expansion caused a reduction, and contraction an increase in the load applied to the specimen. This resulted in a minor cyclic stress being imposed on the specimen in addition to the cyclic-temperature changes.



Temperature Cycle No. 1



Temperature Cycle No. 2

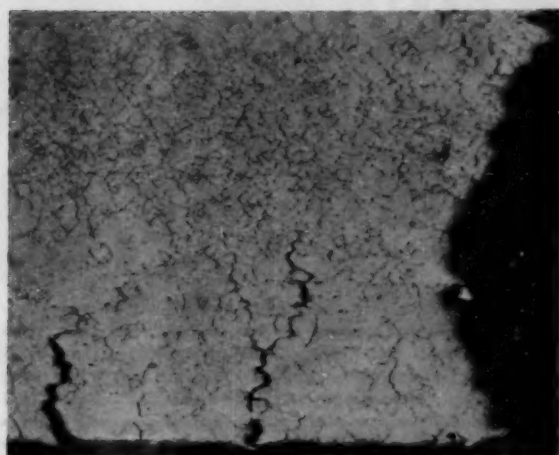
FIG. 18 CYCLIC-TEMPERATURE STRESS-RUPTURE SPECIMENS—LONGITUDINAL SECTION THROUGH FRACTURE, MIXED ACID ETCH; $\times 100$

Specimen and load-bar assemblies were removed from the liquid-metal container without draining the sodium. Although a flow of helium was kept over the sodium during these operations, there was most probably some contamination of the sodium by oxygen, which might have resulted in corrosion of the specimens. In Table 9 are listed the maximum and minimum weight changes of the specimens for each test condition.

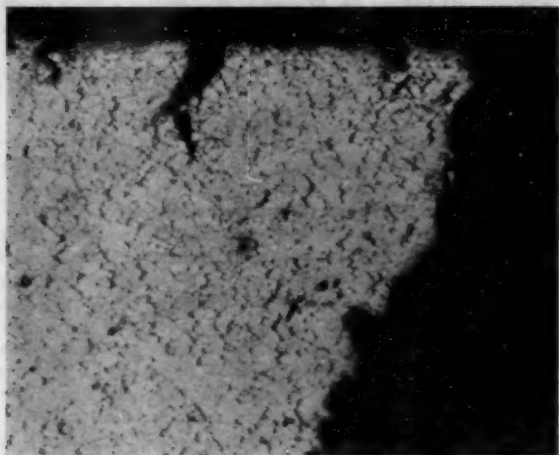
TABLE 9 RANGE OF SPECIMEN WEIGHT CHANGES

Test condition	Weight change, mg/cm ²	
	Maximum	Minimum
1000 F	-3.02	-1.99
1100 F	+0.17	+0.12
1200 F	-4.46	-0.15
Cycle No. 1	-3.42	+0.02
Cycle No. 2	-0.47	-0.06
Cycle No. 3	-2.84	-0.75
Cycle No. 4	-3.50	-0.73
Cycle No. 5	-4.01	-0.01

There was a wide range in weight changes as shown in Table 9, but there was no correlation between the weight change exhibited and the time and temperature of the test. Examination of Figs. 16 to 20 indicates that a major fraction of the weight loss of the



Temperature Cycle No. 3



Temperature Cycle No. 4

FIG. 19 CYCLIC-TEMPERATURE STRESS-RUPTURE SPECIMENS—LONGITUDINAL SECTION THROUGH FRACTURE, MIXED ACID ETCH; $\times 100$

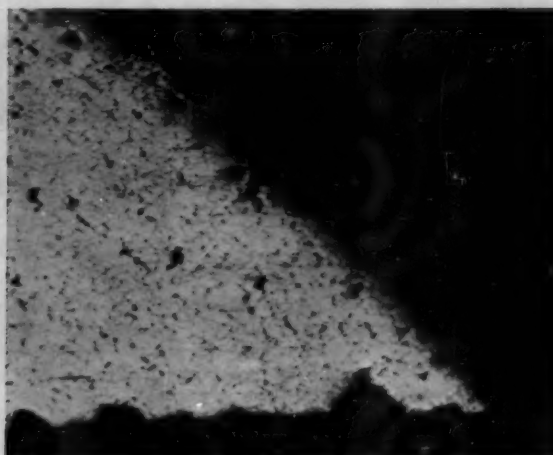
specimens was probably due to loss of particles of metal adjacent to the fracture during steam cleaning of the specimens after their removal from the sodium.

The cyclic-test temperatures were controlled by a Wheelco controller, which involved cutting a circular cam to the shape necessary for the particular cycle of interest. As shown in Figs. 7 to 11, there was some cyclic variation at the constant control temperatures. This was due either to roughness on the edge of the cam or the high heat capacity of the furnace and liquid-metal container.

CONCLUSIONS

From the results obtained in this investigation, the following conclusions can be drawn:

- 1 The mathematical expressions developed by Robinson for



Temperature Cycle No. 5

FIG. 20 CYCLIC-TEMPERATURE STRESS-RUPTURE SPECIMENS—LONGITUDINAL SECTION THROUGH FRACTURE, MIXED ACID ETCH; $\times 100$

calculating the stress-rupture life of steels under cyclic-temperature conditions give results which are only an approximation of the expected life.

2 The deviation of the test from the calculated life is due to the transient creep conditions that exist under cyclic-temperature changes, which are not considered in the Robinson and Miller formulas.

3 The rupture life determined for Type 347 stainless steel under a given cyclic-temperature condition is true only for that condition and cannot be extrapolated to similar conditions with any degree of accuracy.

BIBLIOGRAPHY

- 1 "The Cyclic Temperature Acceleration of Strain in Heat-Resisting Alloys," by G. R. Brophy and D. E. Furman, *Trans. ASM*, vol. 30, 1942, p. 1115.
- 2 "Effect of Temperature Cycling on the Rupture Strength of Some High-Temperature Alloys," by J. Miller, *ASTM, Special Technical Publication No. 165*, 1954, p. 53.
- 3 "Effect of Temperature Variation on Long-Time Rupture Strength of Steels," by Ernest L. Robinson, *Trans. ASME*, vol. 74, 1952, pp. 777-781.
- 4 "Liquid Metals Handbook," Rev., NAVEXOS-P-733, June, 1952.
- 5 "Liquid Sodium, a Noncorrosive Coolant," by R. F. Koenig and S. R. Vandenberg, *Metal Progress*, vol. 61, March, 1952, p. 71.
- 6 "Tension Testing of Metallic Materials," *ASTM Specification E8-52T*, Fig. 8, 1952, p. 1393.
- 7 "A Time-Temperature Relationship for Rupture and Creep Stresses," by F. R. Larson and J. Miller, *Trans. ASME*, vol. 74, 1952, pp. 765-775.
- 8 "The Elevated-Temperature Properties of Stainless Steels," *ASTM, Special Technical Publication No. 124*, 1952.
- 9 "Properties of Metals at Elevated Temperatures," by G. V. Smith, McGraw-Hill Book Company, Inc., New York, N. Y., 1950.
- 10 "Effect of Temperature Variation on the Creep Strength of Steels," by Ernest L. Robinson, *Trans. ASME*, vol. 60, 1938, pp. 253-259.
- 11 "Transient Plastic Deformation," by R. P. Carreker, J. G. Leschen, and J. D. Lubahn, *Trans. AIME*, vol. 180, 1949, pp. 139-146.

Design Aspects of High-Temperature Fatigue With Particular Reference to Thermal Stresses

By L. F. COFFIN, JR.,¹ SCHENECTADY, N. Y.

A criterion for fatigue failure has been proposed, based on experiments carried out on test specimens subjected both to constrained thermal cycling and constant-temperature strain cycling. This criterion relates the number of cycles to failure with the plastic strain change per cycle. The application of such a criterion to design, where thermal-stress fatigue is the principal factor, is discussed from fundamental and practical viewpoints. From such a criterion it is possible to predict the life of a certain machine part for a calculated thermal stress, or conversely, the thermal stress permitted for a certain limiting number of cycles of stress.

INTRODUCTION

Thermal transients in large high-temperature machines represent a serious problem for the designer. Examples include temperature gradients in large steam turbines with rapid start-ups, welds between ferritic and austenitic materials, complex pipe assemblies, and many others. Here temperature gradients or mismatch in expansion of structural materials or expansion under conditions of constraint leads to thermal stresses which may be quite severe. Plastic deformation may occur in such situations, which, if cyclic conditions prevail, can lead to cracking by fatigue in an otherwise ductile metal. The situation can be particularly severe in nuclear-power equipment.

The particular problem facing the designer is the evaluation of calculated stresses in excess of the yield stress of the material, these stresses arising from transient thermal conditions. Generally the part in question may receive only a limited number of thermal cycles during its life. The reduction in stress to values where conventional fatigue-design procedures are applicable may be difficult from a design point of view, or impractical because of the particular operating conditions imposed on the component. Thus a design procedure, which is based on a limited number of thermal cycles and which permits some plastic deformation, would have many applications in equipment operating at high temperatures.

Studies on thermal stress fatigue have appeared in the literature in the past few years (1 to 8).² More recently, an experimental investigation of one high-temperature structural material, Type 347 stainless steel, was carried out on a laboratory scale at the Knolls Atomic Power Laboratory (9, 10). From the results of that study it was possible to formulate a mathematical

relationship for predicting failure of the test specimens under constrained cyclic thermal conditions. A later investigation (11) showed that a similar relationship could be expressed for strain-cycling to failure at constant temperature.

In the present paper the application of this experimental relationship to high-temperature design is discussed. The method represents a departure from conventional fatigue-design procedures; however, it appears to offer a rational approach to the problem. Although much work needs to be done to substantiate the method for various specific applications, it is presented here for the consideration and discussion of those working on high-temperature design problems.

A CRITERION FOR FAILURE BY FATIGUE

In the experimental program referred to (9, 10), test specimens in the form of thin-walled tubes were subjected to alternate high and low temperatures while constrained so as to prevent axial deformation. The reversed stress and strain so produced resulted in transverse cracking of the tubes by a fatigue process. It was then possible to obtain a fatigue curve of temperature change versus cycles to failure. At the same time the apparatus permitted the measurement of the stress change which accompanied each temperature cycle.

In an attempt to interpret the test results so obtained from a fundamental viewpoint, a quantity called the total plastic-strain change was calculated for each specimen. This quantity was defined as the plastic strain absorbed by the specimen regardless of sign. Thus, if the plastic strain developed in a test specimen when being heated is $\Delta\epsilon_p$, for each complete cycle the plastic strain absorbed is $2\Delta\epsilon_p$. For the entire test to failure this quantity would be $2N\Delta\epsilon_p$, if $\Delta\epsilon_p$ remains constant or $\Sigma 2N_i\Delta\epsilon_{p_i}$, if $\Delta\epsilon_p$ is found to change as a result of continuous cycling. We shall say more later about the change in $\Delta\epsilon_p$ with cycling.

It was at first felt that a reasonable criterion for fatigue failure might be that the quantity $2N\Delta\epsilon_p$ was constant under all cyclic conditions. As seen in Fig. 1, this is not the case. Here the total plastic-strain change is plotted against the logarithm of the cycles to failure for Type 347 stainless steel in the annealed state and cold-worked by torsion and tension. It is immediately observed that, as the cycles to failure increase, the total plastic strain absorbed by the specimen also increases, the increase being exponential rather than linear. When the data were plotted on a logarithmic basis for both co-ordinates, Fig. 2, a straight-line relationship was found. It is seen that by extrapolating the data the linear relationship can be extended to pass through the point representing the simple static tension test, where N , the number of cycles, is considered to be 0.25 and $\Delta\epsilon_p$ is the fracture ductility as measured by the reduction in area.

It is possible to write by a simple expression the relationship between the plastic-strain change $\Delta\epsilon_p$ and the cycles to failure N . This relationship for the data of the annealed material as given in Fig. 2 is

$$N^{1/2} \Delta\epsilon_p = 0.36 \dots \dots \dots [1]$$

¹ Research Associate, Knolls Atomic Power Laboratory, General Electric Company. Mem. ASME.

² Numbers in parentheses refer to the Bibliography at the end of the paper.

Contributed by the Metals Engineering Division and presented at the Annual Meeting, New York, N. Y., November 28-December 3, 1954, of THE AMERICAN SOCIETY OF MECHANICAL ENGINEERS.

NOTE: Statements and opinions advanced in papers are to be understood as individual expressions of their authors and not those of the Society. Manuscript received at ASME Headquarters, December 1, 1954. Paper No. 54-A-252.

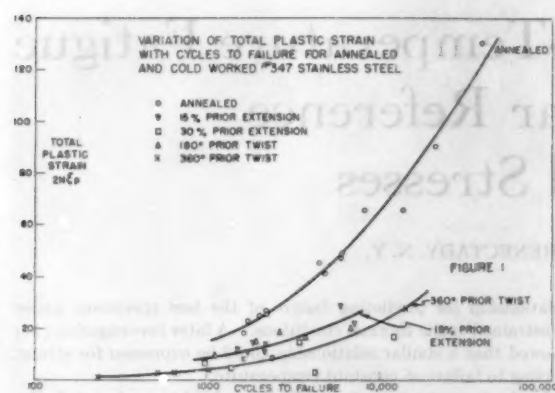


FIG. 1 VARIATION OF TOTAL PLASTIC STRAIN WITH CYCLES TO FAILURE FOR ANNEALED AND COLD-WORKED NO. 347 STAINLESS STEEL

The exponent $1/2$, appears at the present time to be fortuitous.

As has been indicated, the failure criterion as given by Equation [1] is obtained for specimens constrained so that there is no net strain. This means that the sum of the strain components—elastic, plastic and thermal—is at all times zero or, expressed somewhat differently, the elastic and plastic strains are continually balanced by the thermal strain. Hence the fatigue-failure criterion expressed in Equation [1] is obtained under conditions of cyclic temperature. Actually, the tests were conducted by varying the high and low temperature while maintaining the mean temperature at a constant value of 350 C.

Recently another series of experiments was reported (11), in which specimens were strain-cycled while maintaining the temperature constant and equal to the mean temperature of the foregoing tests. A good fit for the failure data obtained was found to be

$$N^{0.43} \Delta \epsilon_p = 0.23 \dots \dots \dots [2]$$

The similarity of this equation with Equation [1] is noted, despite the fact that in one case the temperature is cycled, while in the other the temperature is held constant.

Test data sufficiently complete to permit the formulation of the foregoing type of equations are very difficult to find in the literature, since most fatigue data are obtained by stress-cycling without measurement of the strain or by strain-cycling without measuring the stress. Both stress and strain quantities are required to formulate Equations [1] and [2]. However, an experimental investigation carried out by Lui, Lynch, Ripling, and Sachs (12) for high strain-low cycle fatigue of 24 ST aluminum gives some data for which the relationship

$$N^{1/2} \Delta \epsilon_p = 0.56 \dots \dots \dots [3]$$

gives a good fit. Table 1 compares the results of the plastic-strain change as obtained experimentally in reference (12) with that as calculated by Equation [3]. Although the agreement with Equation [3] is good, it must be admitted, however, that

TABLE 1 COMPARISON OF DATA OF REFERENCE (12) WITH CALCULATED RESULTS FROM EQUATION [3]

Strain amplitude	Stress amplitude, psi	Elastic strain amplitude	Cycles to failure	Plastic-strain change (experimental)	Plastic-strain change (calculated from Equation [3])
0.12	86500	0.0087	7	0.223	0.212
0.15	91000	0.0091	4	0.282	0.280
0.20	90500	0.0091	2	0.382	0.396
0.30	94000	0.0094	1	0.582	0.560

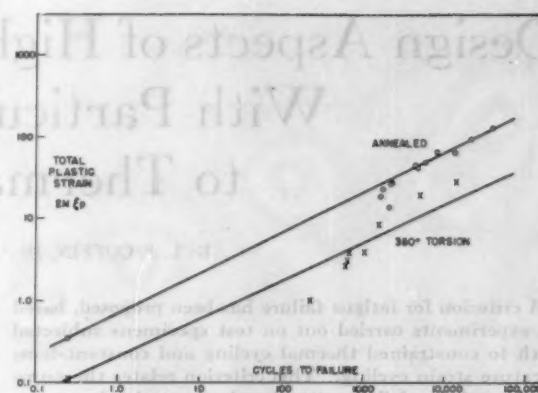


FIG. 2 VARIATION OF TOTAL PLASTIC STRAIN WITH CYCLES TO FAILURE NO. 347 STAINLESS STEEL

these test data do not serve as a critical test of the significance of the equation. It is evident that more experimental results are required before complete justification of the use of this form of equation can be established.

Comparison of Equations [1], [2], and [3] indicates that the general form of the equation used for the mathematical representation of fatigue failure in terms of the plastic-strain change is

$$N^k \Delta \epsilon_p = C \dots \dots \dots [4]$$

where k and C are constants. The significance of these constants in terms of mechanical properties of the materials considered is the subject of the following section.

FUNDAMENTAL ASPECTS OF THE EQUATION

There are several sound reasons for establishing a criterion for fatigue failure based on the plastic-strain change. First, a study of the literature on the basic mechanism for fatigue in ductile metals reveals that fatigue cracks originate in regions of a crystal where slip has occurred, and never in regions where there is no evidence of slip. For example, the work of Gough and Hansen (13) on the changes in microstructure in iron, steel, and copper under cyclic stresses showed that plastic deformation (slip) took place both for cyclic stresses which did not lead to fatigue failure, as well as for those which produced fracture by fatigue. They observed, however, that the fatigue crack was initiated in the region of slip. The work of Ewing and Humphrey (14), Stanton and Barstow (15), Rosenhain (16), subsequent studies by Gough (17), Wood and his co-workers (18), and many others have confirmed this viewpoint. Recently Forsyth (19) has carried out a detailed study of the mechanism of slip in aluminum as a result of stress-cycling. Hence the use of the plastic strain as a measure of slip would appear from fundamental considerations to be a rational variable in establishing a fatigue-failure criterion.

A second reason for the soundness of the failure criterion given by Equation [4] is the close relationship it appears to have with the basic mechanical properties of metallic materials, as depicted by the flow-stress curve and the fracture ductility. To show this, it is first necessary to consider the cyclic stress-strain behavior in metals. It is well known that under an imposed cyclic stress or strain a hysteresis loop of stress against strain is established. Subsequent changes in this loop occur very slowly with time (10), as will be discussed later. If the cyclic stress is increased, the hysteresis loop is broadened and is re-established at a higher strain value. Thus it is possible to construct, for a particular material at a particular temperature, a curve of cyclic stress versus cyclic strain which resembles the flow stress curve

obtained for monotonic loading. Some typical stress-strain curves taken from reference (10) are shown in Fig. 3. These data were obtained for constrained thermal cycling of annealed and cold-worked stainless steel. Similar sets of curves can be obtained for constant-temperature cycling.

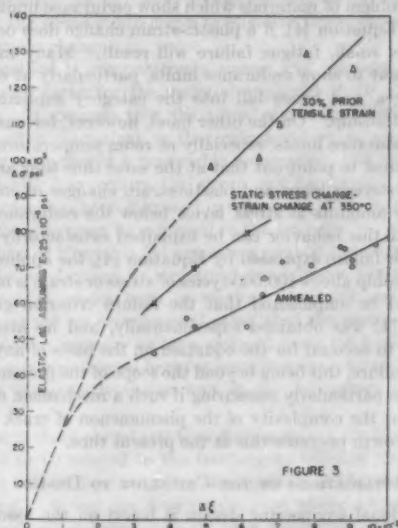


FIG. 3 RELATIONSHIP BETWEEN STRESS AND STRAIN CHANGE FOR NO. 347 STAINLESS-STEEL SPECIMENS DURING THERMAL CYCLING

The cyclic stress-strain curve and the flow-stress curve are not identical, but appear to be related.³ The difference in the two curves can be attributed to the Bauschinger effect (the nonlinearity of stress and strain upon reversing the loading direction), which broadens the hysteresis loop. The difference between the two curves is shown in Fig. 3. Here the static stress-strain curve (with doubled co-ordinates) of annealed stainless steel at 350 C is compared with cyclic data. It will be observed that the doubled flow-stress curve is somewhat higher than the cyclic stress-strain curve. The behavior observed for this material appears to be generally true for metals.

Having established that the flow-stress curve bears a direct relationship to the cyclic stress-strain curve, use can be made of this curve in assessing the behavior of various metals subject to cyclic loading. Consider, for example, two different metals with distinctly different flow-stress curves. When both are subjected to the same cyclic stress, that metal with the greater flow stress will undergo considerably less strain change and consequently considerably less plastic-strain change. When both metals are given the same cyclic strain, the plastic-strain change of the metal having the higher flow-stress curve will be only slightly less. This is because its elastic-strain change is greater and the resulting plastic-strain change is found by subtracting the elastic strain from the total strain change. Thus, on the basis of the plastic-strain change, a wide difference in cycles to failure would occur for stress-cycling, while little difference exists under strain-cycling.

A knowledge of the plastic-strain change in a particular metal is not in itself sufficient to determine the number of cycles for failure. In addition, the fracture ductility of the metal can be

³ To construct a cyclic stress-strain curve, the stress change is plotted against the strain change, and hence, gives peak-to-peak values. For purposes of comparison, the stress and strain co-ordinates of the flow stress curve must be doubled.

shown to be important. This can be seen from the data given in Fig. 2 for both annealed and cold-worked Type 347 stainless steel subjected to constrained thermal-cycling. The equation for failure of the annealed metal is given by Equation [1], while for the cold-worked material one finds that

$$N^{0.536} \Delta \epsilon_p = 0.103 \quad [5]$$

It will be noted that the exponent has changed but slightly while the constant on the right-hand side has decreased considerably and reflects the lower ductility of the cold-worked metal. In fact, in Equations [1], [2], [3], and [5] the exponent, for all practical purposes, can be considered to be 0.5, while the quantity C (given in Equation [4]) varies as the ductility of the metal varies.

It is not clear, at the present time, just how the fracture ductility as measured in the tension test relates to failure by fatigue. A comparison of the total plastic strain absorbed by the material is particularly pertinent. In Fig. 2 it is seen that as the cycles for failure are increased, the total plastic strain increases. For failure occurring after 10,000 strain cycles, the total plastic strain is 66. This is compared to a fracture ductility of 0.64 for simple tension. This hundredfold factor in the two ductility values would certainly point to a different mechanism between deformation and fracture. Nevertheless, the test results to date indicate that fracture ductility from monotonic loading is related to fracture in cyclic loading.

FACTORS AFFECTING THE HYSTERESIS LOOP AND PLASTIC-STRAIN CHANGE

An important aspect of the criterion appears when one considers such factors as temperature, strain rate, and creep effects in the cyclic loading of materials. It is well known, for example, that the stress which a given material can resist without failure for a predetermined number of cycles decreases with increasing temperature. Effects of oxidation or of metallurgical changes can account in part for some of this effect at high temperatures. In the temperature range where these factors are not important, however, the decrease in fatigue resistance can be accounted for by the increased hysteresis loop and correspondingly the increased plastic-strain change brought on by the reduced flow stress. Thus in Equation [4] if the plastic-strain change is increased, while the fracture ductility (and hence k) remains constant, the cycles required for failure decrease.

Strain-rate effects do not appear to have an important influence on fatigue-resistance for most metals at room temperature. At higher temperatures the flow-stress curve and the cyclic stress-strain curve are strongly influenced by the strain rate. Cheve-nard (20) has shown that hysteresis loops for nickel at 400 C are markedly strain-rate sensitive, becoming narrower as the periodic time of the cycle is decreased. Thus the concept of the plastic strain offers a rational method for accounting for strain-rate effects on failure, and Equation [4] appears to be a reasonable criterion for predicting failure under such conditions. Unfortunately, there is little experimental evidence useful for purposes of comparison.

Creep and relaxation effects are also important in metals under elevated temperature and cyclic loading, particularly in cases where the material is held under stress for long periods of time between cycles. Relaxation of the thermally induced stresses has the effect of increasing the width of the hysteresis loop when cyclic conditions prevail, thus increasing the plastic-strain change. Results of tests of this sort are reported in reference (10), where it is shown that the cycles-to-failure decrease with increasing hold times at the high temperatures.

One important factor in establishing the validity and scope of Equation [4] is the stability of the hysteresis loop with cycling.

If changes in the hysteresis loop occur, it would be difficult to establish a particular value for $\Delta\epsilon_p$. However, as pointed out earlier, the hysteresis loop generally appears to be quite stable for a particular cyclic stress or strain. Previous results (10) have shown, however, that at least for Type 347 stainless steel certain cyclic-dependent changes do occur. It was shown that for annealed stainless steel some strain hardening takes place, although the amount is slight. Table 2 shows some data taken from reference (11) on the strain hardening of annealed Type 347 stainless steel at 350 C for various cyclic strains. It is apparent that the stress change and consequently the plastic-strain change do not undergo any significant changes with cycling.

TABLE 2 CYCLIC STRAIN-HARDENING EFFECTS—ANNEALED NO. 347 STAINLESS STEEL 350 C

Total strain change	Cycles	Stress change, psi	Elastic-strain change	Plastic-strain change
0.01	10	82000	0.0033	0.0067
	100	86000	0.0034	0.0066
	1000	80000	0.0027	0.0073
0.02	10	100000	0.0040	0.0160
	100	112000	0.0045	0.0155
	1000	108000	0.0043	0.0157
0.03	10	145000	0.0058	0.0242
	100	125000	0.0050	0.0250
	1000

TABLE 3 CYCLIC STRAIN-SOFTENING EFFECTS—COLD-WORKED NO. 347 STAINLESS STEEL

(0.82 in./in. prior torsional strain)					
Temp. deg C	Total strain change	Cycles	Stress change, psi	Elastic- strain change	Plastic- strain change
350	0.01	10	190000	0.0076	0.0024
		100	175000	0.0070	0.0030
		1000	159000	0.0064	0.0036
25	0.01	10	204000	0.0068	0.0032
		100	193000	0.0064	0.0026
		1000	184000	0.0061	0.0039

An interesting effect, reported in references (10) and (11), is the apparent softening of cold-worked stainless steel with strain cycling. The effect is not associated with annealing, since the softening occurs as readily at room temperature as at higher temperatures. Table 3 shows some results for Type 347 stainless steel obtained at 350 C and at room temperature. It is apparent from Table 3 that the softening of the material has a pronounced effect on the plastic-strain change, and some care must be used in applying it under such conditions.

Because of the large amount of plastic strain capable of being absorbed by the material during cyclic straining, certain metallurgical processes which are strain-sensitive might be expected to occur as a result of the cycling process. As a result, changes in the hysteresis loop can take place, which would not occur in single-phase metals. The most important example of this is the well-known strain-aging phenomenon in ferritic metals. Much work still needs to be done in studying the relationship between hysteresis loops and strain-sensitive metallurgical processes, since any process which changes the hysteresis loop will have a pronounced effect on the fatigue resistance of the metal.

LIMITS OF APPLICATION OF THE RELATIONSHIP

The criterion for fatigue failure as expressed by Equation [4] has been derived from data in which failure occurs in less than 100,000 cycles. This is well below the number of cycles usually employed to establish endurance limits or fatigue stresses where no endurance limit exists. It may well be that this relationship is equally valid for failures in cycles of loading above 100,000. However, from practical considerations its use may be limited for larger cycles by the difficulty of determining the plastic strain. For example, if Equation [1] is solved for $\Delta\epsilon_p$ when $N = 100,000$, the plastic-strain change involved is 0.0011 in. per in. For failure after 10^6 cycles, the plastic-strain change becomes 0.00036.

Such low strains are very difficult to measure experimentally since they are determined by the difference in two larger strains, the total strain and the elastic strain.

Aside from the difficulty in determining the plastic-strain change for low stress-high cycle fatigue failure, one is also faced with the problem of materials which show endurance limits. According to Equation [4], if a plastic-strain change does occur, no matter how small, fatigue failure will result. Many materials do not appear to show endurance limits, particularly at elevated temperatures, and hence fall into the category explainable by such a relationship. On the other hand, however, ferrous metals do have endurance limits, especially at room temperature. It is also of interest to point out that at the same time they are found to have hysteresis loops and plastic-strain changes of small but measurable amounts at stress levels below the endurance limits (13). Until this behavior can be explained satisfactorily by the criterion for failure expressed by Equation [4], the application of the relationship above 100,000 cycles of stress or strain is in doubt.

It should be emphasized that the failure criterion given by Equation [4] was obtained experimentally, and no attempt is made here to account for the equation on the basis of any mechanism for failure, this being beyond the scope of the present paper. It would be particularly reassuring if such a mechanism could be devised, but the complexity of the phenomenon of crack nucleation and growth prevents this at the present time.

APPLICATIONS OF THE CRITERION TO DESIGN

Conventional engineering design is based on the assumption that the material behaves elastically throughout. The use of the plastic strain in a design criterion represents a distinct departure from the present design philosophy. The advantages of this criterion have been discussed from the point of view of material behavior. The disadvantages of the method appear when one considers calculating plastic strains.

There appear to be at least two ways available for the designer to determine the plastic strain change in the fatigue criterion. One way is to actually perform a plastic-stress analysis on the part in question. This is often very difficult, since very few solutions are available, and these may not be sufficiently complete to apply to the problem under consideration. Only in cases where the geometry is comparatively simple, such as in simple bending, rotational symmetry, etc., can solutions be found. Very often the solution desired is for partially plastic deformation, that is, where a portion of the structure is plastic and the balance elastic. These solutions are much more complex than when the structure is treated as completely elastic or completely plastic. Hence, until the field of plastic-stress analysis is developed to the extent of elastic-stress analysis, the designer must resort to other techniques.

A second method available to the designer for determining the plastic-strain change is to calculate the elastic strains in a particular part (including local stresses at holes, fillets, etc.), assuming the material is elastic throughout. This is readily done by evaluating the elastic stresses and converting these to strains. Then, with the aid of a cyclic stress-strain curve of a form similar to Fig. 3 and from the calculated elastic-strain change, a stress change can be determined. From this information the plastic-strain change then is

$$\Delta\epsilon_p \approx \Delta\epsilon_e' - \frac{\Delta\sigma}{E} \quad [6]$$

Here $\Delta\epsilon_p$ is the plastic-strain change calculated for application into Equation [4], $\Delta\epsilon_e'$ is the fictitious elastic strain calculated by assuming the material is elastic throughout, the $\Delta\sigma$ is the stress change which would actually be developed by the component,

and E is the elastic modulus of elasticity. Note that $\Delta\epsilon_p'$ is the range of strain experienced by the part during the thermal cycle. Note also that the relation [6] is expressed for the case of unidirectional stress. For combined stresses the equation can be easily modified by using effective stresses and strains, by replacing E by the quantity $3E/2(1 + \nu)$ and by converting the co-ordinates of the cyclic stress-strain curve to effective stress change and effective strain change.

The method is comparatively simple and requires the cyclic stress-strain curve for the material applicable to the particular problem. It assumes that the actual strain distribution in the component is equivalent to that calculated on an elastic basis. In many cases this is a reasonable assumption, but occasionally when plastic flow occurs the strain can be greatly enhanced. This problem has been discussed in reference (11). In such situations great care must be exercised in the analysis.

The form of Equation [4] suggests a method for accounting for accumulative damage in structural components for a complex loading which varies both in number of cycles and severity. There is as yet no experimental proof that the method is valid, but because it appears to be a rational basis for handling such situations, it is presented here for completeness. An experimental program is currently under way in our laboratory to test the method.

Earlier it was pointed out that the constant C in Equation [4] appeared to be related to the fracture ductility of the material and that failure resulted when the quantity $N^{1/2}\Delta\epsilon_p$ equaled the quantity C . Hence, for a particular case where a specific number of cycles has been absorbed at a particular plastic strain, failure is determined by whether the quantity $N^{1/2}\Delta\epsilon_p$ is more or less than C . As a result the quantity $N^{1/2}\Delta\epsilon_p$ can be thought of as a measure of damage. If such is the case, it then becomes a useful method for calculating a factor of safety in design or of damage by cumulative cycling. For example, a factor of safety for particular design conditions can be expressed as

$$f = \frac{C}{N^{1/2}\Delta\epsilon_p} \quad [7]$$

where C is the value of $N^{1/2}\Delta\epsilon_p$ at failure, N the number of cycles expected in the application, and $\Delta\epsilon_p$ the plastic strain.

When the thermal loading on the part is such as to produce a variety of different thermal cycles, the problem can be resolved by determining the number of cycles expected at each strain level. For each strain level, one can evaluate a particular $N_i^{1/2}\Delta\epsilon_{pi}$ and the summation of all the increments then applied to find the factor of safety or

$$f = \frac{C}{\sum_{i=1}^n N_i^{1/2} \Delta\epsilon_{pi}} \quad [8]$$

It remains to be proved whether the damage, defined in the foregoing, is linear with the actual damage accumulated by the material.

AREAS OF UNCERTAINTY

The design criterion, as outlined, is based on laboratory test results. Before the criterion can be applied with assurance to specific components found in practice, considerably more experimentation is required. In particular, the following areas need to be explored in more detail:

- 1 Cyclic straining with a steady stress superimposed.
- 2 Effect of rate of cycling.
- 3 Influence of grain size and other metallurgical factors.

- 4 Effect of corrosive atmospheres.
- 5 Metallurgical changes resulting from welding.
- 6 Size effect.
- 7 Relationship of temperature change with cyclic stress.
- 8 Phase relationship of cyclic temperature and stress.

The last two items are under study at the present time in our laboratory under the sponsorship of the Piping Code Committee of the American Standards Association. In addition, investigation of a variety of structural materials should be undertaken to substantiate the work already done on stainless steel.

CONCLUSIONS

A design criterion for fatigue of structural components under conditions of constant or cyclic elevated temperatures is discussed. The fundamental and practical aspects of the criterion are considered.

BIBLIOGRAPHY

- 1 "Experience With Austenitic Steels in High-Temperature Service in the Petroleum Industry," by M. E. Hoimberg, Trans. ASME, vol. 73, 1951, pp. 733-742.
- 2 "Cyclic Heating Tests of Main Steam Piping Joints Between Ferritic and Austenitic Steels—Sewaren Generating Station," by H. Weisberg, Trans. ASME, vol. 71, 1949, pp. 643-649.
- 3 "Thermal Shock and Other Comparison Tests of Austenitic and Ferritic Steels for Main Steam Piping," by W. D. Stewart and W. G. Schreits, Trans. ASME, vol. 73, 1951, pp. 1043-1060.
- 4 Ibid., vol. 75, 1953, pp. 1051-1072.
- 5 "Some Considerations in the Joining of Dissimilar Metals for High-Temperature, High-Pressure Service," by O. R. Carpenter, N. C. Jensen, J. L. Oberg, and R. D. Wylie, Proceedings of the ASTM, vol. 50, 1950, pp. 809-857.
- 6 "Thermal Fatigue and Thermal Shock," by H. Thiesch, Welding Research Council Bulletin Series, No. 10, April, 1952.
- 7 "Cyclic Heating Tests of Main Steam Piping Materials and Welds—Sewaren Generating Station," by H. Weisberg and H. M. Soldan, Trans. ASME, vol. 76, 1954, p. 1085.
- 8 "Thermal-Shocking Austenitic Stainless Steels With Molten Metals," by R. A. Tidball and M. M. Shrut, Trans. ASME, vol. 76, 1954, p. 639.
- 9 "Apparatus for the Study of Effects of Cyclic Thermal Stresses on Ductile Metals," by L. F. Coffin, Jr., and R. P. Wesley, Trans. ASME, vol. 76, 1954, pp. 923-930.
- 10 "A Study of the Effects of Cyclic Thermal Stresses on a Ductile Metal," by L. F. Coffin, Jr., Trans. ASME, vol. 76, 1954, pp. 931-950.
- 11 "The Problem of Thermal Stress Fatigue in Austenitic Steels at Elevated Temperatures," by L. F. Coffin, Jr., American Society for Testing Materials, 1954, Special Technical Publication No. 165.
- 12 "Low Cycle Fatigue of Aluminum Alloy 24 ST in Direct Stress," by S. I. Lui, J. S. Lynch, E. J. Ripling, and G. Sachs, Trans. AIME, vol. 175, 1948, p. 469.
- 13 "Behavior of Metals Subjected to Repeated Stresses," by H. J. Gough and D. Hansen, Proceedings of the Royal Society of London, England, vol. 104, series A, 1923, p. 539.
- 14 "The Fracture of Metals Under Repeated Alternations of Stress," by J. A. Ewing and J. W. C. Humphrey, Philosophical Transactions of the Royal Society of London, England, vol. 200, series A, 1903, p. 241.
- 15 "The Resistance of Materials to Impacts," by T. E. Stanton and L. Barstow, Proceedings of the Institution of Civil Engineers, part 4, vol. 166, 1905-1906.
- 16 "Deformation and Fracture in Iron and Steel," by W. Rosenhain, Journal of the Iron and Steel Institute, vol. 70, 1906, p. 189.
- 17 "Crystalline Structure in Relation to Failure of Metals—Especially by Fatigue," by H. J. Gough, Proceedings of the ASTM, vol. 33, 1933, p. 3.
- 18 "Effects of Alternating Strain on the Structure of a Metal," by W. A. Wood and R. B. Davies, Proceedings of the Royal Society of London, England, vol. 220, series A, 1953, pp. 255-266.
- 19 "Some Further Observations on the Fatigue Process in Pure Aluminum," by P. J. E. Forsyth, Journal of the Institute of Metals, vol. 82, 1954, pp. 449-455.
- 20 "Les propriétés mécaniques dites secondaires: frottement interne, relaxation visqueuse, réactivité, coefficient de Poisson," by P. Chevenard, Rev. Metall., vol. 15, 1943, p. 289.

Discussion

J. J. MURPHY.⁴ The author is to be commended for following up his previously presented experimental results with this effort to develop them in terms of a simple design criterion. Both the fundamental and practical aspects are of interest but whether the fundamental aspects prove correct or not, the designer will find such an approach a very practical one which can be adjusted as necessary as more experience and test data are developed.

Markl⁵ found a relation of the type given by Equation [4] fitted his room-temperature fatigue tests on carbon-steel piping assemblies quite well but utilized the total strain rather than the plastic portion only. He also found that a value of $k = 0.2$ fitted his results best. A limited number of fatigue tests on thin stainless-steel expansion joints available to the writer indicate a value of k of about 0.3. It would seem that if the author were to include a portion of the nominally elastic portion of the strain an equally good correlation with the test data would be found. The author's value of k of about 0.5 hinges on the assumption that the approximating straight line must pass through the point describing performance in the simple static tensile test. The value of k would increase if this point were ignored. It may be desirable, therefore, to limit the range of applicability of the approximation and establish the best value of k for the range of N selected.

The author, in Equations [7] and [8], suggests a method of evaluating combinations of different thermal-strain cyclic loadings. The assumption is made that, for a given strain, the damage varies as N^k . A more satisfactory and customary approach would be to assume the fractional damage varies directly as N leading to the following relations

$$f_i = \frac{C^{1/k}}{N_i (\Delta \epsilon_{pi})^{1/k}}$$

$$f = \frac{C^{1/k}}{\sum_{i=1}^n N_i (\Delta \epsilon_{pi})^{1/k}}$$

⁴Section Engineer, Mechanical Development Division, The M. W. Kellogg Company, New York, N. Y. Mem. ASME.

⁵"Fatigue Tests of Piping Components," by A. R. C. Markl, Trans. ASME, vol. 74, 1952, pp. 287-303.

AUTHOR'S CLOSURE

The author appreciates the comments of Mr. Murphy since they represent the point of view of the design engineer who must convert to practical application the basic or fundamental knowledge of material behavior. Mr. Murphy's first question relates to the most useful form of expression for a finite-cycle fatigue criterion. The advantages of using the total-strain (elastic plus plastic) range rather than just the plastic component are quite obvious from engineering considerations. It would indeed be possible to break down the experimental results into fairly limited ranges of cycles to failure and to represent this information by a number of relationships between the total strain (or elastically calculated stress) and cycles to failure. However, from the point of view of simplicity in the application of basic material behavior, it would be more desirable to have a single relationship available for predicting failure in finite cycle fatigue of a particular material, the constants for which have physical meaning in terms of other, more well-known, properties. With the substantiation of this form of relation, it would not be necessary to obtain experimental determination of the constants, but rather to use those constants already known or obtainable in much simpler tests. This is the aim of the author in proposing a single relationship covering the range of cycles from simple tension to high-cycle fatigue.

Mr. Murphy's second comment relates to the modification of Equations [7] and [8] such that the fractional damage is linear with respect to the number of cycles to which the specimen is subjected, rather than the level of plastic strain. The modification suggested is indeed a more correct form for design purposes where cycles, rather than plastic strain, is the independent variable. The unsuitability of Equation [8] is apparent if one considers the same test from two points of view. For example, a test run for 1000 cycles at a particular plastic-strain range produces a degree of damage which is exactly that if one considers breaking the test into two 500-cycle periods at the same strain level. The denominator of Equation [8] for the first situation is $1000^{1/k} \Delta \epsilon_p$, while in the second case it is $(500^{1/k} + 500^{1/k}) \Delta \epsilon_p$, which is obviously different. For Mr. Murphy's modification, however, each denominator is $1000 \Delta \epsilon_p^2$.

Quantitative Evaluation of Thermal-Shock Resistance

By S. S. MANSON¹ AND R. W. SMITH,² CLEVELAND, OHIO

The dependence of thermal-shock resistance on two parameters k and $\sigma_f/E\alpha$ (when k is conductivity, σ_f the fracture stress, E the elastic modulus, and α the coefficient of thermal expansion) is experimentally demonstrated by the fact that the relative ratings of two materials may change with a change of quench severity. The theory of thermal-shock resistance of a disk quenched at the periphery is developed, making use of the results of Jaeger. Two criteria for failure are considered; namely, the maximum normal-stress criterion, and the criterion of maximum "risk of rupture" based on the Weibull statistical theory. Equipment for subjecting these specimens to a wide range of quench severities of known surface heat-transfer coefficients is described, and results are presented for thermal-shock tests of steatite and glass disks. The results for steatite are then utilized for determination of thermal-shock parameters by four independent methods, the results showing good agreement.

INTRODUCTION

THE thermal-shock resistance of brittle materials is usually described in qualitative terms. Only recently has interest been directed at the establishment of a quantitative basis for evaluating thermal-shock resistance.

The need for this quantitative basis has been indicated by analysis and by experiments which demonstrated that materials which may be superior to others in one type of test may prove inferior in another type of test. A recent study (1)³ of beryllium oxide and aluminum oxide in air and in water quenches serves to illustrate this phenomenon. Disks of beryllium oxide were considerably superior in thermal-shock resistance to similar disks of aluminum oxide when air-quenched, but the order of superiority was reversed when the disks were water-quenched. The reason for this behavior is that thermal-shock resistance is governed by two, and in some cases by more than two, parameters involving properties of the material. For the class of materials which obey the critical-stress theory of failure, the significant parameters are $\sigma_f/E\alpha$ and k , where k is the thermal conductivity, σ_f is the fracture strength, E the elastic modulus, and α the coefficient of thermal expansion. In mild quenches, such as still air, thermal-shock resistance is governed by a combination of k and $\sigma_f/E\alpha$; hence beryllium oxide proves superior to aluminum oxide owing to its very high thermal conductivity. In severe quenches, however, the governing parameter is $\sigma_f/E\alpha$ only, and the high thermal conductivity of the beryllia is ineffective in raising the

thermal-shock resistance above the alumina which has a superior combination of strength, elastic modulus, and temperature coefficient of expansion.

For materials in which failure is governed not only by the maximum stress but also by the distribution of stress within the body, additional material properties are required for evaluation of the relative strengths of materials in thermal shock. These properties are extensively discussed in reference (2), and a brief outline of the significant variables will be presented in this paper.

Thermal-shock resistance cannot therefore be described as "good" or "bad," nor can it be described as a single parameter, such as $k\sigma_f/E\alpha$, as is often done. Rather, two or more parameters must be ascertained, and suitable formulas or graphical representations must be derived for properly combining the parameters under arbitrary conditions of test geometry and quench severity.

In reference (3) a method is described whereby the thermal-shock parameters $\sigma_f/E\alpha$ and k may be determined from static tests on ring specimens of the required material. No experimental verification was presented, however, of the validity of the parameters as so determined for predicting the behavior of the material under arbitrary thermal-shock conditions. One of the purposes of the present investigation was, therefore, to study the actual behavior of several brittle materials over a wide range of thermal-shock conditions, and to compare the parameters as obtained by several independent methods with each other. The method of reference (3) was not specifically evaluated in this investigation, although it has considerable merit. Some of the methods developed for convenient application of available equipment may have advantage over the method of reference (3). For example, in examining materials with high conductivity it may be difficult to produce fracture in a static test, whereas a thermal-shock test under severe condition of surface heat transfer provides a simpler means for producing fracture. The method of determining conductivity may also have some merit over that of reference (3) in terms of simplicity. The work described is part of a general program being conducted at the Lewis Laboratory of the NACA to determine the behavior of materials under conditions of thermal stress and was performed between 1952 and 1954.

THEORY

The critical-stress theory and the statistical theory of thermal-shock resistance are to be applied to the specific case of a thin disk thermally insulated at both faces and subjected to heat removal at the rim only. This specimen configuration was found to be very practical for experimental testing. Because no heat flow occurs across the faces, the disks can be regarded as infinite cylinders for purposes of thermodynamic analysis. The theory for the temperature problem of an infinite cylinder initially at constant temperature and subjected to sudden surface heat removal has been worked out by Carslaw and utilized by Jaeger (4) to solve the stress problem. Jaeger's solution is not directly applicable to the disk since the infinite cylinder represents a case of plane strain, whereas the disk represents a case of plane stress. Comparison of the theory for the two cases (5) indicates, however, that the final results differ from each other only by the

¹ Chief, Strength of Materials Branch, NACA Lewis Flight Propulsion Laboratory.

² Aeronautical Research Scientist, NACA Lewis Flight Propulsion Laboratory.

³ Numbers in parentheses refer to the Bibliography at the end of the paper.

Contributed by the Metals Engineering Division and presented at the Annual Meeting, New York, N. Y., November 28-December 3, 1954, of THE AMERICAN SOCIETY OF MECHANICAL ENGINEERS.

NOTE: Statements and opinions advanced in papers are to be understood as individual expressions of their authors and not those of the Society. Manuscript received at ASME Headquarters, December 1, 1954. Paper No. 54-A-263.

factor $(1-\mu)$; hence the results of Jaeger can be directly applied by the removal of the Poisson's ratio term μ .

Critical-Stress Theory. According to this theory, failure is postulated to occur when the stress anywhere within the disk reaches a certain critical value σ_f . For the type of quench under consideration, peak stress occurs at the rim of the disk. Fig. 1 shows the solution for the rim-stress problem of the thin disk, as

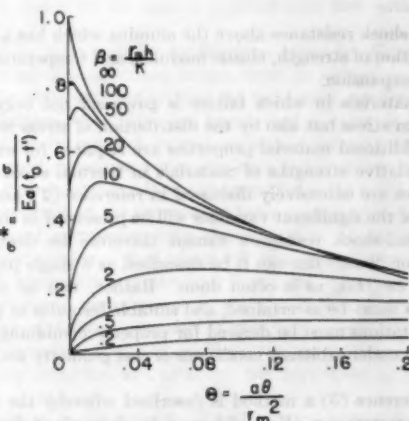


Fig. 1 DIMENSIONLESS STRESS VERSUS DIMENSIONLESS TIME FOR VARIOUS VALUES OF DIMENSIONLESS HEAT TRANSFER

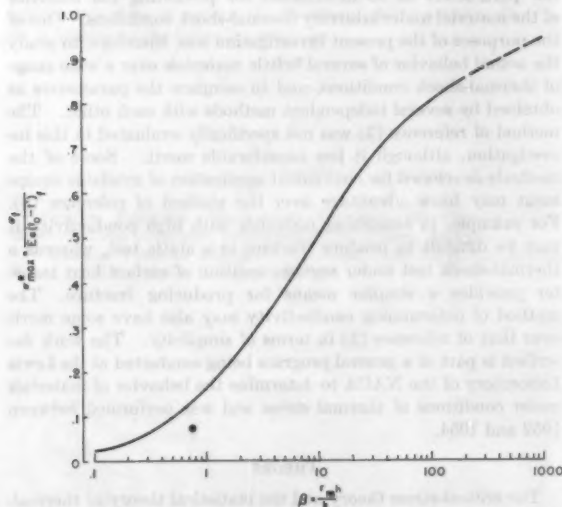


Fig. 2 MAXIMUM DIMENSIONLESS STRESS VERSUS DIMENSIONLESS HEAT TRANSFER

adapted from Jaeger's solution (4) of the infinite cylinder. On the horizontal axis is plotted dimensionless time θ , on the vertical axis dimensionless stress σ^* for a number of selected values of Biot's modulus β . For each value of β there occurs a maximum value of σ^* . If the minimum temperature difference causing failure is determined, then fracture will occur at the maximum point on the curve. Hence a plot of σ^*_{max} versus β , as shown in Fig. 2, represents the relationship among the variables required for the thermal-shock problem. Thermal-shock resistance is herein defined as the lowest temperature difference $(t_0 - t_f)_f$ at which failure occurs for a given condition of surface heat-transfer

coefficient, h . Fig. 2 shows that the thermal-shock resistance for a specimen of given size is a function of the parameter $\sigma_f/E\alpha$ and the thermal conductivity k . Although it is possible to fit an empirical equation to this curve (as was done for the case of the flat plate in reference 1), it has been found most convenient to work with the relation in its graphical form.

Statistical Theory. The stress at which fracture occurs merits detailed examination. First, it is necessary to postulate a criterion of fracture; then it is necessary to ascertain a suitable measure of fracture stress for practical use.

It is common to assume that fracture occurs in a brittle material when a critical normal stress is reached at any point in the body. In some cases a critical shear stress is postulated. Obviously, these assumptions cannot always be valid since in many cases the measured stress at fracture depends on the stress distribution in the test specimen. Thus it is common for measured tensile-strength values to be considerably lower than modulus of rupture (bend-test) values. Although part of the discrepancy can often be explained on the basis of bending stresses induced by eccentricity in the tensile test and on differences in elastic modulus in tension and compression (6), the most widely accepted explanations are based on the statistical theories of strength proposed by Tucker (7) and by Weibull (8).

The Weibull formulation is based on the concept of flaw distribution in brittle materials and on a simple mathematical hypothesis relating the stress in each element to its contribution to risk of rupture. Thus, if a body is under uniform stress σ , the risk of rupture is greater than if only a small region near the surface is subjected to the stress σ , while the remainder of the body is subjected to stresses lower than σ . It is for this reason that when the modulus-of-rupture specimen is subjected to a surface stress equal to the failure stress in a tensile test, the risk of rupture is low compared to the risk of rupture at rupture in the tensile test. If it is hypothesized that fracture occurs at equal risks of rupture, then it can be demonstrated that the surface stress in the modulus-of-rupture test can be several times the tensile strength. Weibull (8) has derived the necessary relations, and the concepts have been applied with considerable success by Frankel (9) in explaining the fracturing conditions of mortar beams under various loading conditions.

Application of Weibull Theory to Thermal-Shock Problem. The Weibull concept of risk of rupture has been applied by the present authors to the thermal-shock problem of a thin circular disk (2). A brief outline of the approach is given in the Appendix. The significant conclusions will now be discussed.

Fig. 3 shows (2) that the stress distribution at the time of maximum surface stress is steeper the higher the value of β . Hence it might be expected that higher surface stresses would be permissible before rupture occurs for the higher values of β , in the same manner that higher surface stresses are permissible in the modulus-of-rupture test to compensate for the steeper stress gradient compared to the tensile test. Although this is true, the magnitude of permissible increase is modified by the fact that the risk of rupture does not necessarily reach a maximum when the surface stress is a maximum. Figs. 4 and 5 demonstrate the effect. In Fig. 4 dimensionless stress is plotted as a function of radius at each of several values of dimensionless time for a value of $\beta = 10$. When $\theta = 0.02$ the stress at the surface is a maximum. But the stress gradient is steep, and only a small portion of the disk at the surface is under high stress. At a later time $\theta = 0.05$ the surface stress has decreased slightly, but stresses in other locations have risen. A greater volume of material is now under relatively high stress, although no point is at a stress quite as high as the surface stress when it was a maximum. Fig. 5 shows a plot of relative risk of rupture for $\beta = 10$, $n = 3$ as a function of time, indicating that rupture probably occurs at

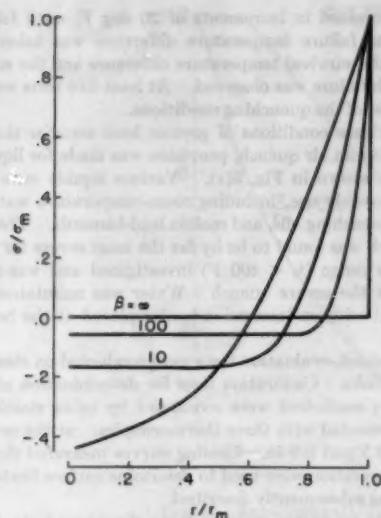
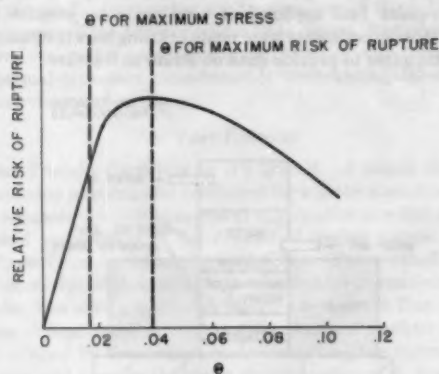


FIG. 3 RELATIVE STRESS DISTRIBUTION AT TIME OF MAXIMUM STRESS

FIG. 5 RISK OF RUPTURE AS A FUNCTION OF DIMENSIONLESS TIME, $\beta = 10, n = 3$

some time after maximum surface stress has been reached. In Fig. 6 the stress distributions are shown for the instants when the risks of rupture are a maximum for several values of β . It is seen that the stress distributions are more nearly similar than at the times when surface stresses are a maximum. The consequence is that, although the different quench severities do result in considerable difference in stress distributions at the time of maximum stress, the stress distributions are nearly independent of quench severity at the time of maximum risk of rupture, that is, at the time when rupture most probably occurs. Thus the correction for stress distribution affected by quench is likely to be small.

Fig. 6 also serves to clarify the type of strength value that governs fracture. The tensile stress distributions for these quench severities are approximately linear, varying from zero in the region at $r/r_m = 0.65$ to a maximum at $r/r_m = 1.0$. The compressive stresses are neglected since they are small, and according to the Weibull theory do not contribute to risk of rupture in any case. These stress distributions could be simulated by a modified modulus-of-rupture test as indicated in Fig. 7.

Four-point loading is used to provide uniform bending moment between the two inner loads. The distance between the inner loads is selected to place approximately the same volume under stress in the modulus-of-rupture test as in the disk. The depth of the specimen is taken as twice the region of the disk subjected

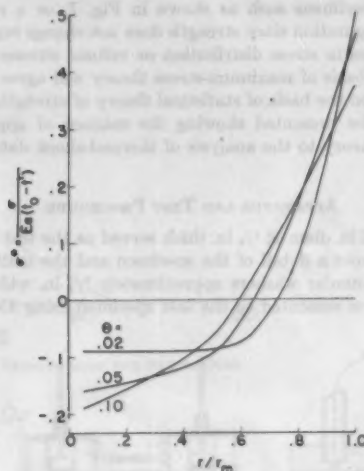
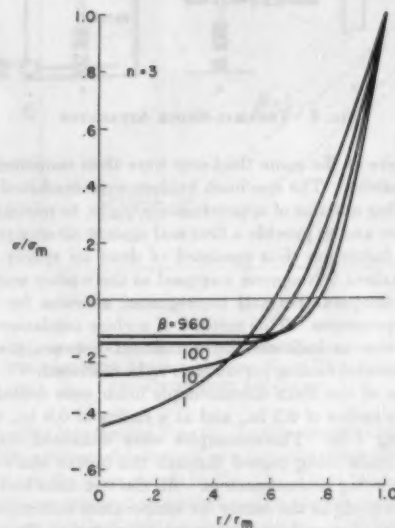
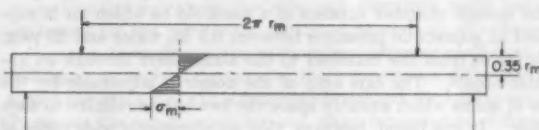
FIG. 4 STRESS DISTRIBUTION AT VARIOUS VALUES OF DIMENSIONLESS TIME FOR $\beta = 10$ FIG. 6 STRESS DISTRIBUTION AT TIME OF MAXIMUM RISK OF RUPTURE FOR $n = 3$ 

FIG. 7 SUGGESTED BEND-TEST-SPECIMEN CONFIGURATION TO APPROXIMATE THERMAL-SHOCK STRESS DISTRIBUTION WITHIN A DISK

to tensile stress ($2 \times 0.35 r_m$). The dimensions are not critical, since modulus of rupture results are not sensitive to small-volume effects. In any case, it is indicated by the theory that the fracture stress to be used in the thermal-shock parameters is not the conventional tensile strength as is frequently used.

It can thus be seen that if fracture strength is determined by means of specimens such as shown in Fig. 7, or a reasonably similar configuration since strength does not change rapidly with small changes in stress distribution or volume stressed, correlation on the basis of maximum-stress theory will agree well with correlation on the basis of statistical theory of strength. An example will be presented showing the manner of applying the statistical theory to the analysis of thermal-shock data on steatite.

APPARATUS AND TEST PROCEDURE

A disk of 2 in. diam \times $1/4$ in. thick served as the test specimen. Fig. 8(a) shows a detail of the specimen and the method of insulation. Annular washers approximately $1/4$ in. wide and $1/16$ in. thick were cemented to the test specimen using 3M cement.

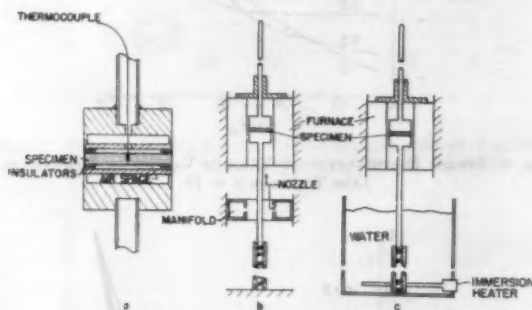


FIG. 8 THERMAL-SHOCK APPARATUS

Solid washers of the same thickness were then cemented to the annular washers. The specimen holders were machined to provide a bearing annulus of approximately $1/16$ in. to minimize path for heat flow and to provide a firm seal against air or water leakage. The insulation thus consisted of dead air spaces and insulating washers. Neoprene was used as the washer material at the lower temperatures and impregnated asbestos for slightly higher temperatures. This method of surface insulation proved quite effective as indicated by agreement between theoretical and experimental cooling curves later to be described.

For some of the disks thermocouple holes were drilled at the center, at a radius of 0.5 in., and at a radius of 0.9 in., the disk radius being 1 in. Thermocouples were cemented into these holes, the leads being passed through the hollow shaft to continuous-recording potentiometers. All the test disks had at least one thermocouple at the center for temperature indication.

Two types of quenching equipment were used as illustrated in Figs. 8(b) and (c). Fig. 8(b) schematically shows the apparatus for air quenching. The specimen is heated to a uniform temperature in a furnace and then lowered into the quenching region. The quench chamber consists of a manifold to which air is supplied at adjustable pressures between 0.3 in. water and 20 psig. Air issues from the manifold to the atmosphere through an annular nozzle. The exit area of the nozzle is adjustable by the use of shims which suitably space the two halves relative to each other. It was found, however, that an adequately wide range of surface heat-transfer coefficient could be obtained by using a single spacing of 0.020 in.; hence all the results presented were obtained in this manner. The temperature of the disk was suc-

cessively increased in increments of 20 deg F, until failure occurred. The failure temperature difference was taken as the average of the survival temperature difference and the successive one at which failure was observed. At least five tests were averaged for most of the quenching conditions.

To investigate conditions of greater heat transfer than those available with an air quench, provision was made for liquid-bath quenches as shown in Fig. 8(c). Various liquids were investigated for possible use, including room-temperature water, boiling water, quenching oils, and molten lead-bismuth. The boiling-water quench was found to be by far the most severe for the low-temperature range ($t_0 < 400$ F) investigated and was used exclusively for the severe quench. Water was maintained at the boiling point with an immersion heater placed at the bottom of the tank.

Thermal shock-evaluation tests were conducted on steatite and plate-glass disks. Calibration tests for determination of surface heat-transfer coefficient were conducted by using stainless-steel disks instrumented with three thermocouples: at the center and at radii of 0.5 and 0.9 in. Cooling curves measured during the quenching operation were used to determine surface heat-transfer coefficient, as subsequently described.

Other tests conducted were modulus-of-rupture tests, thermal-conductivity measurements, and thermal-expansion measurements. The bend tests were made to determine some of the material properties entering into thermal-shock theory. Centerpoint and four-point load applications were made on steatite bars. Some of these experiments were made utilizing bars instrumented with strain gages to provide data on strain to fracture.

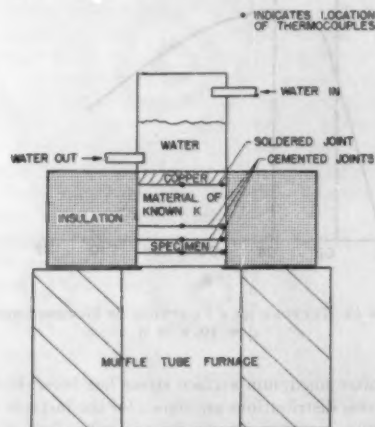


FIG. 9 THERMAL-CONDUCTIVITY APPARATUS

An apparatus schematically shown in Fig. 9 was devised to measure thermal conductivity of thermal-shock specimens. Heat is caused to flow vertically through a disk of known conductivity and through a stack of three thermal-shock disks cemented together. Since the thermocouples are essentially imbedded in the cement interface between the test specimens, it is desirable to use a cement of high conductivity in order to minimize the temperature drop at the interface. A mixture of Sauerisen No. 1 cement and powdered silver was found satisfactory. Radial heat flow is restricted to a negligible amount by insulation placed around the periphery of the disks. When steady-state axial heat flow is established, temperature readings at the upper and lower surfaces of the reference disk and the sandwiched thermal-shock disk are obtained. Thermal conductivity of the test specimen is then equal to the ratio of temperature drop per inch of

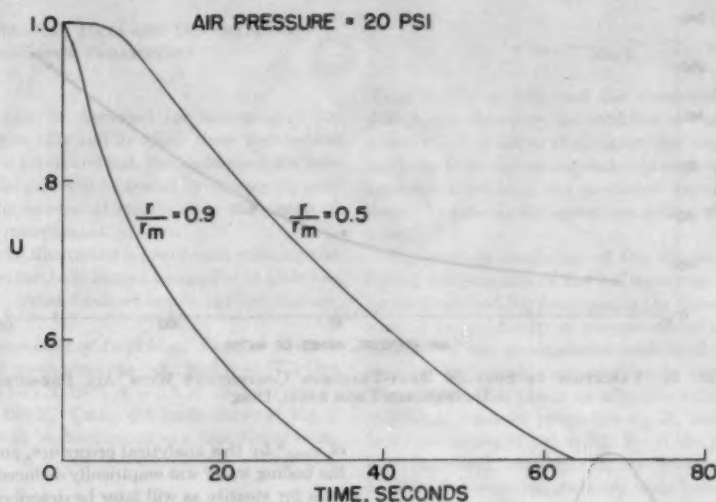


FIG. 10 EXPERIMENTAL TRANSIENT-TEMPERATURE DISTRIBUTION FOR STEEL DISK

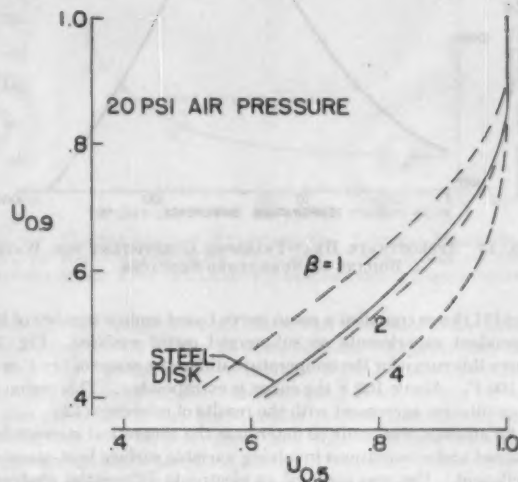
thickness of the reference disk to that of the thermal-shock specimen multiplied by the known thermal conductivity of the reference material. By varying the temperature of the furnace, the temperature of the test material may be varied, thus permitting a determination of the variation of conductivity with temperature.

Thermal-expansion measurements were accomplished with a commercial interferometer.

TEST RESULTS

Heat-Transfer Coefficient for Air Quench. A simple method of determining heat-transfer coefficient for a given quench condition is to compare the cooling curves at any location in a disk of known physical properties with the theoretical cooling curves for arbitrarily assigned heat-transfer coefficients. This method requires the knowledge of thermal diffusivity (in order to nondimensionalize the time scale), and conductivity (to convert Biot modulus values to heat-transfer values). An alternate method that has been devised by the authors makes use of cooling curves at two stations, and permits the direct determination of β , from which the heat-transfer coefficient can be computed. Thus information is required only on thermal conductivity. Since this method establishes β without information on other physical properties, it is of considerable value in the testing of new materials, as will later be shown. However, its use will now be demonstrated in connection with the determination of surface heat-transfer coefficients.

Published tables (for example, reference 10) present data on U versus Θ at a given radius as a function of β . The data are difficult to apply directly in a material of unknown physical properties since Θ and β both contain unknowns. The difficulty can be overcome if cooling curves are experimentally obtained at two stations, as for example in Fig. 10, which shows the measured temperature variation at the 50 per cent and 90 per cent radius as a function of time for a steel disk, similar in size to the test specimens, subjected to cooling air at a manifold pressure of 20 psi. Using time as a parameter, $U_{0.9}$ can be cross-plotted against $U_{0.5}$, as shown by the solid curve in Fig. 11. The dashed curves in Fig. 11 are cross plots of the theoretical data from reference (10) for the two stations at arbitrarily assigned values of β , using nondimensional time as the parameter for cross-plotting. From the figure it is apparent that β is approximately 1.8, and using the known thermal conductivity of the steel $k = 113$ Btu-in/hr-deg F-sq ft the surface heat-transfer coefficient is readily computed

FIG. 11 METHOD OF DETERMINING β BY COMPARISON OF EXPERIMENTAL TEMPERATURE MEASUREMENTS WITH THEORETICAL CURVES FOR DIFFERENT β -VALUES

to be $h = 204$ Btu/hr-deg F-sq ft. In this manner the heat-transfer coefficients were determined as a function of manifold air pressure, the results being shown in Fig. 12. These heat-transfer coefficients were assumed to apply for all materials tested.

Heat-Transfer Coefficient for Boiling Water. Cooling curves obtained for water quenching of the steel disk indicated that this quench was considerably more severe than the highest air-pressure quench. However, the surface heat-transfer coefficient proved to be extremely variable and therefore could not be evaluated by the previously described procedure. Various investigators have shown the surface heat-transfer coefficient for boiling water to be a function of the temperature difference between the surface of the submerged body and the boiling water. However, the relationship for any given temperature difference depends, among other things, upon the nature and condition of the heating surface. For this reason the results of different investigators sometimes differ appreciably. Fishenden and Saun-

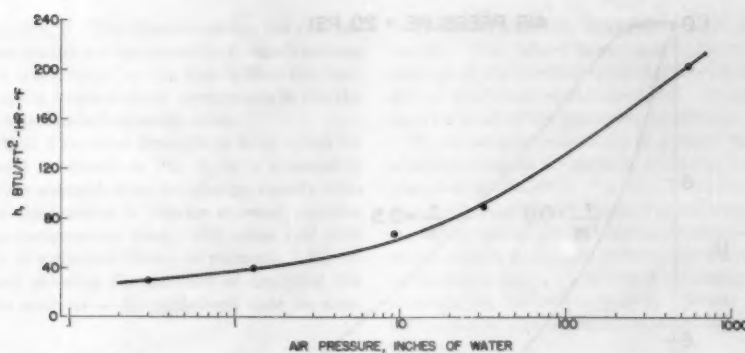


FIG. 12 VARIATION OF SURFACE HEAT-TRANSFER COEFFICIENT WITH AIR PRESSURE DETERMINED FROM STEEL DISK

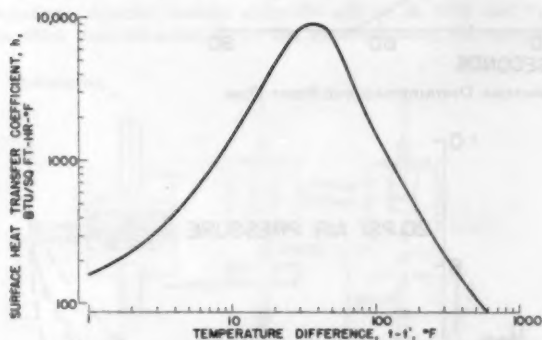


FIG. 13 APPROXIMATE HEAT-TRANSFER COEFFICIENT FOR WATER BOILING ON SUBMERGED SURFACES

ders (11) have compiled a mean curve based upon a number of independent experiments on submerged metal surfaces. Fig. 13 shows this curve for the temperature-difference range of $t - t' = 1$ to 100 F. Above 100 F the curve is extrapolated. This region is in qualitative agreement with the results of reference (12).

An attempt was made to determine the theoretical stresses developed under conditions involving variable surface heat-transfer coefficient. Use was made of an electronic differential analyzer to calculate temperature distribution and rim stress within the disk using techniques described in (13). The heat-transfer curve of Fig. 13 was simulated with the computer by fitting three fourth-degree polynomials to successive regions of the curve. The results are shown in Fig. 14 where maximum nondimensional stress at the rim is shown as a function of initial temperature difference.

It will be seen later by deduction from the air-quench data, that the values of σ_{\max}^* associated with the boiling-water quench appear to be higher than those indicated in Fig. 14. A more suitable value for σ_{\max}^* , at least for steatite, is approximately 0.95. In part the discrepancy may be due to the fact that surface heat-transfer coefficient is severely dependent on material and surface condition. Reference (12) shows, for example, that at a given temperature difference the heat-transfer coefficient may vary by a factor of 10 or greater, depending upon the metal. No data are available for the ceramic materials used in the present experiments. Further, all available data refer to steady-state conditions of heat transfer, whereas the heat transfer in the present tests occurs under rapidly changing temperature conditions. Because of uncertainties associated with the determination

of σ_{\max}^* by this analytical procedure, an effective value for h for the boiling water was empirically deduced from the thermal-shock data for steatite as will later be described. This value of 18,000 Btu/hr-sq ft-deg F produces the same σ_{\max}^* stress as the variable h associated with the boiling-water quench.

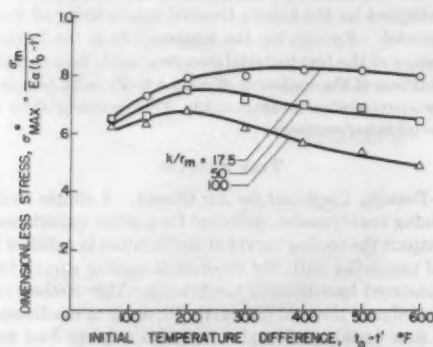


FIG. 14 EFFECT OF INITIAL TEMPERATURE DIFFERENCE ON MAXIMUM DIMENSIONLESS STRESS FOR WATER BOILING AT PERIPHERY OF A SUBMERGED DISK

(Symbols represent points at which computations were made.)

Strain at Fracture. From an average of six steatite specimens of the approximate dimensions shown in Fig. 7, the strain at fracture, which is numerically equal to σ_f/E , was 650×10^{-4} .

Coefficient of Thermal Expansion. The coefficient of thermal expansion α for steatite as measured with a commercial dilatometer was 6.3×10^{-6} per deg F over the temperature range of 100 to 400 F.

Thermal Conductivity. Thermal conductivity for steatite and glass, as measured with the apparatus in Fig. 8, was found to be nearly constant over the temperature range from 200 to 600 F. For steatite $k = 17.5 \pm 1.0$ and for glass $k = 8.5 \pm 0.4$ Btu-in/hr-deg F-sq ft.

Resistance to Thermal Shock. The experimental data on fracture temperatures for steatite and glass are presented in later figures (Figs. 15 and 21) in connection with various methods of data correlation. A number of duplicate tests were conducted under each of several conditions of air-quench severity and under boiling water. The individual data points are shown as circles; the arithmetical average of the points at each condition is shown by a diamond. Points A to D represent air quenches and point E represents the boiling-water quench.

METHODS OF CORRELATING DATA AND DETERMINING THERMAL-SHOCK PARAMETERS

Critical Stress Theory

Several methods will now be discussed for determining the thermal-shock parameters $\sigma_f/E\alpha$ and k . Once these parameters have been determined by a given method, their adequacy for predicting thermal-shock resistance will be tested by comparing predicted results with the experimental results over the range of heat-transfer coefficients investigated.

A detailed analysis will be illustrated for each case utilizing the steatite data. Some of the methods cannot be applied to glass because of inadequate data. Other methods can be applied, but details will be omitted.

Method I: Direct Measurement of Individual Physical Properties. Based on the direct measurements described $k = 17.5$ Btu-in/hr-deg F-sq ft, $\sigma_f/E = 650 \times 10^{-3}$, $\alpha = 6.3 \times 10^{-6}$ per deg F, and therefore $\sigma_f/E\alpha = 103$ F. Using the basic curve of Fig. 2 the fracture temperature can be determined as a function of heat-transfer coefficient. Fig. 15 shows the comparison of the pre-

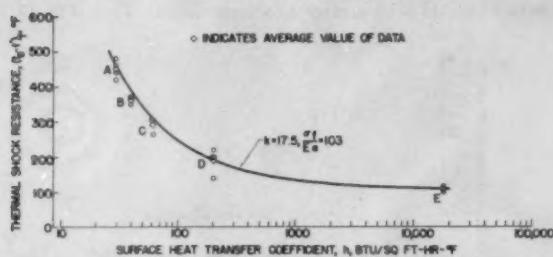


FIG. 15 COMPARISON OF EXPERIMENTAL THERMAL-SHOCK RESISTANCE FOR STEATITE WITH PREDICTED CURVE BASED UPON DIRECT MEASUREMENTS OF PHYSICAL PROPERTIES

dicted and experimental results. Good correlation is obtained for the data points representing the average thermal-shock resistance for each of the four severities of air quench. Since some doubt exists as to the precise heat-transfer coefficient associated with the boiling-water quench, the data have been plotted at $\bar{h} = 18,000$ Btu/sq ft-hr-deg F corresponding to $\sigma^*_{max} = 0.95$ where the mean of the thermal-shock tests best coincides with the predicted curve. The correlation thus serves to determine the approximate heat-transfer coefficient for this type of quench. This value of \bar{h} will later be used for correlation of the data for glass. The precise value of \bar{h} is not critical in this range.

Method II: Direct Measurement of Conductivity Combined With Single Thermal-Shock Test. Since the apparatus of Fig. 9 provides a simple and convenient method of determining thermal conductivity without need for any specimens other than the usual thermal-shock disk, it is apparent that a method involving the use of directly measured conductivity would not be especially objectionable. On the other hand, it would be desirable to avoid the need for direct measurement of σ_f/E and α . Thus a single thermal-shock test can be combined readily with the directly measured value of k to provide a convenient method. If the shock test is conducted at a known value of h , then β can be determined since k is known. From Fig. 2, σ^*_{max} can be determined, and using the measured value of $(t_b - t_f)_f$, the value of $\sigma_f/E\alpha$ can be computed.

As an example, consider the use of $k = 17.5$ Btu-in/hr-deg F-sq ft combined with the mild air-quench data $(t_b - t_f)_f = 450$ F at $h = 30$ Btu/hr-sq ft-deg F. The computed value for $\beta = 1.72$, and from Fig. 2

$$\sigma^*_{max} = \frac{\sigma_f}{E\alpha(t_b - t_f)_f} = 0.222$$

Thus $\sigma_f/E\alpha = 100$, and the computed variation of $(t_b - t_f)_f$ with h is as shown by the solid line in Fig. 16 passing through the point A. It is noted that, again, the use of $\bar{h} = 18,000$ Btu/hr-sq ft-deg F for the boiling-water quench results in reasonably good agreement between the predicted curve and the experimental data. In general the agreement with the other air-quench data is good.

The method consisting of the direct measurement of k and failure temperature in the boiling-water quench would constitute an ideal method for determining the thermal-shock parameters in view of the simplicity of the procedure and required equipment. Because of the uncertainties associated with the effective heat-transfer coefficient some sacrifice in accuracy can be expected. The method also yields an effective value of $\sigma_f/(E\alpha)$ where the individual material properties σ_f , E , and α refer to their values at temperatures of 200 to 300 F. If the properties change widely with increased temperature, the effective values of $\sigma_f/E\alpha$ can be obtained by supplementary tests involving milder quenches.

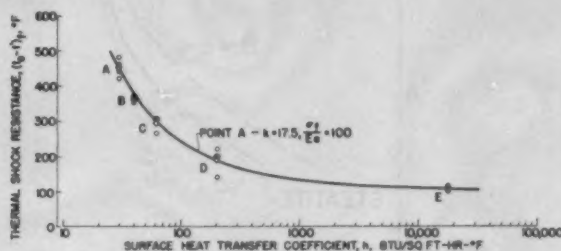


FIG. 16 COMPARISON OF EXPERIMENTAL THERMAL-SHOCK RESISTANCE FOR STEATITE WITH PREDICTED CURVE BASED ON ONE THERMAL-SHOCK TEST AND DIRECT MEASUREMENT OF CONDUCTIVITY

Method III: Single Thermal-Shock Test Combined With Measured Cooling Curves at Two or More Stations. As previously described (Fig. 11) the effective value of β for a given quenching condition can be obtained by cross-plotting of the cooling curves at two stations. If the heat-transfer coefficient is known, the conductivity can be determined and then combined with the single thermal-shock test, as in Method II, to determine $\sigma_f/E\alpha$.

Fig. 17 shows, for example, the experimental cross plot of $U_{0.5}$ versus $U_{0.5}$ for steatite under an air quench at 20 psi manifold pressure. The apparent value of β is approximately 10, from which the computed value of k is 20 Btu-in/hr-deg sq ft. From the value of β and the fracture-temperature difference the value of $\sigma_f/E\alpha$ is 96. The predicted curve based on $k = 20$ and $\sigma_f/E\alpha$ is shown in Fig. 18. The agreement with the other data is reasonably good. It will be noted that some disagreement occurs between the value of k as determined from the apparatus of Fig. 9 and the value determined from the cooling curves. In the determination of k from the cooling curves some margin is left to judgment as to the proper value of β ; therefore the value of k as so determined must be regarded as approximate. The approximation is compensated, however, by application of the thermal-shock test to determine an effective value of $\sigma_f/E\alpha$. Thus the values $k = 20$, $\sigma_f/E\alpha = 96$ fit the experimental data very well. Furthermore, high quantitative agreement among results from different methods should not be expected because of the approximations involved and because of experimental scatter.

Method IV: Two or More Thermal-Shock Tests. Investigation of two thermal-shock characteristics of a material has the satisfying advantage that the behavior under extreme conditions is

directly determined, and other cases are usually interpolations between the two which can be predicted with confidence. For this case continuous-recording potentiometers can be avoided, as well as equipment for measuring thermal conductivity. The disadvantage is, however, that two or more thermal-shock tests must be conducted, preferably under widely differing conditions of quench severity, thus necessitating either two different thermal-

represents a range of combinations of k and $\sigma_f/E\alpha$ determined in this manner to be compatible with the data point A , while curve D shows combinations compatible with the data point D . The point of intersection of the two curves establishes a value of k and $\sigma_f/E\alpha$ compatible with both data points. If only two data points are available, a single point of intersection will be established, and no independent check will be available on its validity. If more than two data points are used, the convergence of the curves to a single point of intersection acts as a check on the validity of theory and experimental data. If the curves do not pass through a single point, all the points of intersection must be considered.

The method produces best results when temperature differences at fracture differ greatly from one data point to another. Under this condition the curves of Fig. 19 intersect at a large angle, and the point of intersection is relatively insensitive to small experimental error. When the fracture-temperature differences among the data points are nearly equal, the curves become nearly parallel, and the point of intersection is very sensitive to experimental error. Obviously, greater weight should be placed on the points associated with widely different thermal-shock resistances when interpreting curves which do not converge to a single point. From Fig. 19,

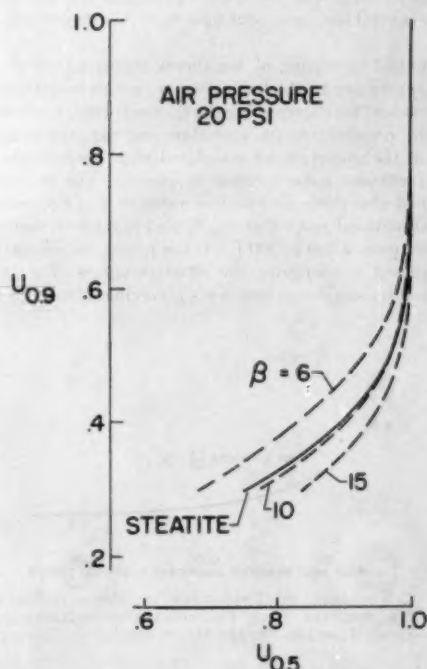


FIG. 17 METHOD OF DETERMINING β BY THE COMPARISON OF EXPERIMENTAL TEMPERATURE MEASUREMENTS WITH THEORETICAL CURVES FOR DIFFERENT β -VALUES

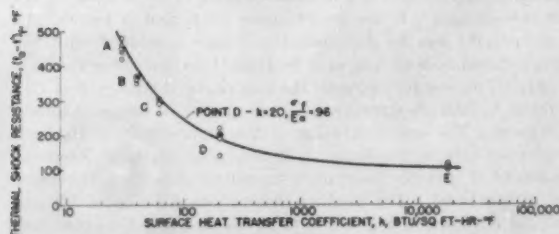


FIG. 18 COMPARISON OF EXPERIMENTAL THERMAL-SHOCK RESISTANCE FOR STEATITE WITH PREDICTED CURVE BASED UPON ONE THERMAL-SHOCK TEST AND THE INDIRECT DETERMINATION OF THERMAL CONDUCTIVITY FROM COOLING CURVES

shock rigs or a single thermal-shock rig having considerable flexibility in quench severity.

The method of analysis is illustrated in Fig. 19. Assume that any two or more of the points A , B , C , D , and E in Fig. 15 are available as basic data. Each datum point is individually analyzed to determine combinations of k and $\sigma_f/E\alpha$ with which it is compatible. This can be achieved by assigning arbitrary values of k , computing β from the known value of h , determining σ_f^* for this value of β from Fig. 2, and computing $\sigma_f/E\alpha$ from σ_f^* and the experimental value of $(t_b - t_f)_c$. Thus curve A in Fig. 19

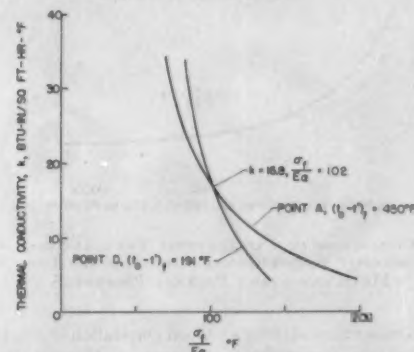


FIG. 19 DETERMINATION OF THERMAL-SHOCK PARAMETERS FOR STEATITE MUTUALLY SATISFYING FAILURE DATA AT TWO QUENCH SEVERITIES, A AND D

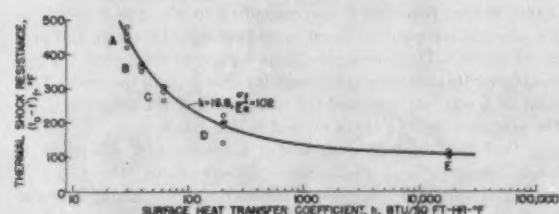


FIG. 20 COMPARISON OF EXPERIMENTAL THERMAL-SHOCK RESISTANCE OF STEATITE WITH RESULTS PREDICTED FROM FAILURE DATA AT TWO QUENCH SEVERITIES, A AND D

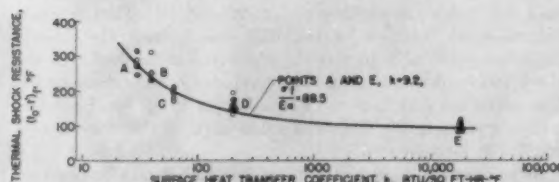


FIG. 21 COMPARISON OF EXPERIMENTAL THERMAL-SHOCK DATA FOR GLASS WITH PREDICTED CURVE DERIVED FROM TWO THERMAL-SHOCK TESTS

using points A and D, the thermal-shock parameters are $k = 16.8$ Btu-in/hr-sq ft-deg F, $\sigma_f/E\alpha = 102$, which agree well with the determinations by the previous methods. Fig. 20 shows the good correlation between the predicted curve based on these parameters and the experimental data.

Fig. 21 shows a similar correlation for glass using points A and E. The heat-transfer coefficient for point E was taken as 18,000 Btu/hr-sq ft-deg F based on examination of the steatite data. The actual values, of course, may differ appreciably from this value since h is a function of material; but in the absence of more suitable data the present assumption is made. The fit with the experimental data in the intermediate range of quench severity is seen to be reasonably good considering the limited amount of data and data scatter.

The values of k and $\sigma_f/E\alpha$ as determined by this procedure may not agree exactly with the properties of the material as determined from conventional physical tests. For example, if these parameters are variable with temperature, then this method will provide effective values which will be useful in the prediction of thermal-shock resistance at intermediate quench severities. The parameters as calculated by Methods II, III, and IV are caused to fit at least one experimental datum point. If one parameter is somewhat in error, the other then compensates for it with the result that the combined parameters will accurately predict thermal-shock resistance for quench severities in the vicinity of the test.

Statistical Theory of Strength

In reference (2) two methods are outlined for analyzing thermal-shock data on the basis of the statistical theory of strength. In one method the value of n is independently determined by a series of strength tests, and this value is used in conjunction with two thermal-shock tests to predict the thermal-shock behavior over the complete range of conditions of quench severity. Actually, any of the four methods used in the present paper could be combined with a known value of n to predict the thermal-shock behavior. The second method described involves the indirect determination of n making use of a measured conductivity and two thermal-shock tests. Analysis of the data on steatite in (2) by both methods led to a value of n in the vicinity of 20. For such a large value of n it would be expected that the statistical theory would lead to the same predicted behavior as the critical-stress theory.

SUMMARY OF RESULTS

Based on theoretical investigations and on thermal-shock experiments with steatite and glass, covering a wide range of quench severity, the following results are believed valid:

1 Thermal-shock resistance of most brittle materials is a function of two or more parameters, the relative importance of each parameter depending on the quench severity.

2 Adequate theory is presented to permit prediction of thermal-shock resistance of thin circular disks subjected to peripheral quench of arbitrary heat-transfer coefficient by both the maximum-stress criterion of fracture and by the statistical theory of fracture.

3 Use of the Weibull statistical theory of failure leads to very nearly the same results as the application of the maximum-stress theory for steatite. For a material which is equally sensitive to flaws throughout its volume, fracture does not necessarily occur at the time the surface stress is a maximum, but rather at a later time when the stress gradient and surface stress have been reduced. For a material which is sensitive primarily to surface flaws, no correction to the critical-stress theory is required for correlation of data of a series of similar disks subjected to differences only in quench severity. Some correction may be required if thermal-shock data on small disks are to be extended to

disks of larger size or to other types of specimens involving an increase of surface area. Consideration of conditions at fracture also suggest that the effective fracture stress corresponds to the results of a modified modulus-of-rupture test, rather than the tensile strength frequently used.

4 Suitable equipment has been devised to permit testing of materials over a wide range of quench severity. The heat-transfer coefficients for the air-quench equipment were determined primarily by use of steel disks of known thermal conductivity. Simple equipment has also been devised for measuring thermal conductivity by making direct use of the thermal-shock-disk specimen.

5 Four methods are described for experimentally determining the thermal-shock parameters k and $\sigma_f/E\alpha$. These involve: I—the direct measurement of the individual pertinent physical properties; II—the measurement of thermal conductivity and thermal-shock testing under a single condition of quench severity; III—measurement of cooling curves at two or more stations in conjunction with thermal-shock testing at a single condition of quench severity; and IV—thermal-shock testing under two or more conditions of quench severity. All methods produced similar predictions of thermal-shock resistance over the complete experimental range.

Method II represents the most simple and convenient method if the boiling-water quench is used as the thermal-shock test. Some sacrifice in accuracy might be necessary because of uncertainties associated with the effective heat-transfer coefficient of boiling water. Also, small experimental errors may lead to relatively larger errors in the prediction of failure temperature under mild conditions of thermal shock because the experimentally available point is at one of the extremes of the curve. Method IV has the advantage of permitting the use of two thermal-shock tests under widely differing conditions of quench severity—such as boiling water and air. The normal conditions involving intermediate quench severity are thus more accurately predicted by the curve passing through the extreme conditions. When material properties are variable with temperature, this method provides effective values of k and $\sigma_f/E\alpha$ which are useful in the prediction of intermediate thermal-shock resistance.

6 Although the thermal-shock parameters for steatite as determined by the various methods have general validity in a wide variety of applications, caution must be exercised in their application in cases involving sufficiently high temperature to cause changes in physical properties and to cases involving stress states substantially different from that involved in the surface cooling of a thin circular disk.

ACKNOWLEDGMENT

The authors wish to express their gratitude to Mr. Clive M. Yeomans for his assistance in the design of experimental equipment and in the performance of much of the experimental tests.

BIBLIOGRAPHY

- 1 "Behavior of Materials Under Conditions of Thermal Stress," by S. S. Manson, NACA TN 2933, 1953.
- 2 "Theory of Thermal Shock Resistance of Brittle Materials Based on Weibull's Statistical Theory of Strength," by S. S. Manson and R. W. Smith, *Journal of the American Ceramic Society*, January, 1955, pp. 18-27.
- 3 "The Ring Test and Its Application to Thermal Shock Problems," by Wilhelm Buessom, Office of Air Research, Wright-Patterson Air Force Base, June, 1950.
- 4 "On Thermal Stresses in Circular Cylinders," by J. C. Jaeger, *Philosophical Magazine*, vol. 36, 1945, pp. 418-428.
- 5 "Theory of Elasticity," by S. Timoshenko, McGraw-Hill Publishing Company, New York, N. Y., 1934, pp. 209-210.
- 6 "Precise Tensile Properties of Ceramic Bodies," by W. H. Duckworth, *Journal of the American Ceramic Society*, vol. 34, 1951, pp. 1-9.

7 "Statistical Theory of the Effect of Divisions and Method of Loading Upon the Modulus of Rupture of Beams," by John Tucker, Jr., Proceedings of the ASTM, vol. 41, 1941, pp. 1072-1094.

8 "A Statistical Theory of the Strength of Materials," by W. Weibull, Proceedings of the Royal Swedish Institute of Engineering Research, no. 151, 1939, 45 pages.

9 "Relative Strengths of Portland Cement Mortar in Bending Under Various Conditions of Loading," by J. P. Frankel, *Journal of the American Concrete Institute*, vol. 20, September, 1948, pp. 21-32; Proceedings, vol. 45.

10 "Some Mathematical Considerations on the Heating and Cooling of Steel," by T. F. Russell, First Report of Alloy Steel Re-

search Committee, Iron and Steel Institute, Reprint, May, 1941. Tables reproduced in "The Flow of Heat in Metals," by J. B. Austin, ASM publication, 1942.

11 "An Introduction to Heat Transfer," by M. Fishenden and O. A. Saunders, The Clarendon Press, Oxford, England, 1950, p. 177.

12 "Heat Transfer to Water Boiling Under Pressure," by E. A. Farber and R. L. Scoria, Trans. ASME, vol. 70, 1948, pp. 369-384.

13 "Application of Finite Difference Techniques to Heat Flow Problems Using the Electronic Differential Analyzer," by R. M. Howe, Engineering Research Institute, University of Michigan, Ann Arbor, Mich., May, 1954.

Nomenclature

a = thermal diffusivity, $= \frac{k}{\rho c}$
 α = linear coefficient of expansion
 β = heat-transfer ratio (Biot modulus) $= \frac{r_m h}{k}$
 c = specific heat capacity
 E = modulus of elasticity (Young's modulus)
 h = coefficient of heat transfer between surroundings at t' and surface at t_s
 n = material constant arising in statistical theory of strength
 ρ = density
 σ = normal stress
 σ_f = fracture stress
 σ^* = dimensionless stress $= \frac{\sigma}{E\alpha(t_0 - t')}$
 σ^*_{max} = maximum dimensionless stress occurring for given conditions
 t = temperature of point at time θ
 t' = temperature of surroundings (in some cases it may be convenient to arbitrarily take $t' = 0$)
 t_0 = original uniform base temperature (in some cases it may be convenient to arbitrarily take $t_0 = 0$)
 U = temperature at given time — temperature of cooling medium
 U = initial uniform temperature — temperature of cooling medium
 θ = time
 Θ = relative time ratio $\left(\text{Fourier modulus} = \frac{k\theta}{\rho c r_m^2} = \frac{a\theta}{r_m^2} \right)$
 k = thermal conductivity
 r = radius
 r_m = normal distance from axis or mid-plane to surface
 S = probability of fracture

Units	
English	Cgs
in. ² hr ⁻¹	cm ² sec ⁻¹
deg F ⁻¹	deg C ⁻¹
dimensionless	dimensionless
Btu lb ⁻¹ deg F ⁻¹	cal gm ⁻¹ deg C ⁻¹
lb in. ⁻²	dyne cm ⁻²
Btu hr ⁻¹ deg F ⁻¹ ft ⁻²	cal sec ⁻¹ deg C ⁻¹ cm ⁻²
dimensionless	dimensionless
lb ft ⁻²	gm cm ⁻²
lb in. ⁻²	dyne cm ⁻²
lb in. ⁻²	dyne cm ⁻²
dimensionless	dimensionless
dimensionless	dimensionless
deg F	deg C
deg F	deg C
deg F	deg C
hr	sec
dimensionless	dimensionless
Btu-in. hr ⁻¹ deg F ⁻¹ ft ⁻²	cal sec ⁻¹ deg C ⁻¹ cm ⁻¹
in.	cm
in.	cm
dimensionless	dimensionless

STATISTICAL THEORY OF FAILURE APPLIED TO THERMAL SHOCK

Volumetric Sensitivity to Flaws. Consider the probability of failure S_i of a unit volume of material to be a function of stress alone according to a distribution curve such as Fig. 22. The probability of failure S_f for a specimen of volume V under uniform stress is related to the probability of failure S_i for a unit volume of the material by the following fundamental equation of statistical theory

$$S_f = 1 - e^{-V \ln(1 - S_i)} \quad [1]$$

Weibull defines risk of rupture R as the negative of the exponent in Equation [1]

$$R \equiv -V \ln(1 - S_i) \quad [2]$$

As stress level increases so does probability of rupture S_i . Since S_i is by definition a probability, and is therefore restricted to numerical values between 0 and 1, Equation [2] states that risk of rupture R increases both with increasing stress and increasing volume of material under stress. R is therefore taken as a measure of likelihood of failure. If the material is assumed to be isotropic in the sense that the probability of rupture starting at any point within the body is equal for a given stress, then Equation [2] can be written in infinitesimal form

$$dR = f(\sigma_i) dV \quad [3]$$

For the entire volume

$$R = \int_V f(\sigma_i) dV \quad [4]$$

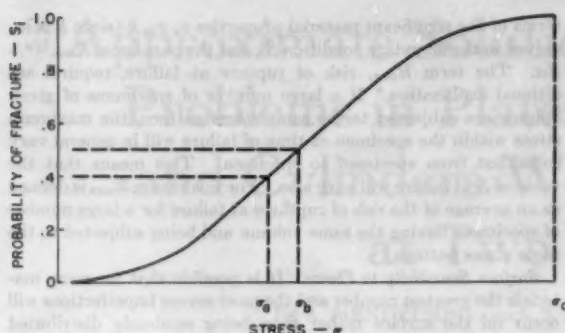


FIG. 22 PROBABILITY OF FRACTURE AS A FUNCTION OF STRESS

Probability of rupture is then defined as

$$S_f = 1 - e^{-\int V f(\sigma) dV} \quad [5]$$

Weibull found that distribution curves for various materials could be fitted well by the convenient analytical form

$$f(\sigma) = \left(\frac{\sigma}{\sigma_0}\right)^n \quad [6]$$

where σ_0 is a material stress constant and n is a material constant characterizing the shape of the failure-distribution curve. For the limiting case of $n = \infty$, the probability of rupture S_f is zero for all values of $\sigma < \sigma_0$, and S_f is unity for $\sigma > \sigma_0$; therefore this case corresponds exactly to the critical-stress theory of failure, σ_0 being the failure stress of the material.

Substituting Equation [6] into Equation [4]

$$R = \frac{1}{\sigma_0^n} \int V \sigma^n dV \quad [7a]$$

or for the disk

$$R = \frac{2\pi}{\sigma_0^n} \int_0^{r_m} \sigma^n r dr \quad [7b]$$

Equation [1] expressing probability of failure S_f as a function of risk of rupture can be written now for the more general case of variable stress distribution

$$S_f = 1 - e^{-\frac{1}{\sigma_0^n} \int V \sigma^n dV} \quad [8]$$

This equation permits the determination of the material properties σ_0 and n from a series of tension or bend tests as described by Weibull.

Considering the problem of a thin disk subjected to a known rate of heat transfer at the rim, it is first necessary to calculate R at various time intervals measured from the start of the quench in order to determine the time of maximum R . Since it is convenient to work with dimensionless stress

$$\sigma^* = \frac{\sigma}{E\alpha(t_0 - t')}$$

this substitution is made into Equation [7b]

$$R = \frac{2\pi}{\sigma_0^n} [E\alpha(t_0 - t')]^n \int_0^{r_m} \sigma^{*n} r dr \quad [9]$$

Dimensionless stress distribution can be calculated from series expressions of Jaeger or, as was done here, calculated from published

temperature data such as Russell's. Since, in general, the stress distribution cannot be expressed in a form which can be readily integrated, this curve was approximated by dividing the curve into three sections and fitting these with parabolas as shown in Fig. 23. Weibull considers the contribution of compressive stress toward failure to be negligible for brittle materials, which are relatively strong in compression. For this reason the integration is performed over the region of tensile stress only. The subdivisions are selected to be bounded by radii r_m , r_B , r_C , and r_D at which the stresses are σ_m^* , $2\sigma_m^*/3$, $\sigma_m^*/3$, and 0, respectively. Each region is approximated by a parabola of the form

$$\sigma^* = p + qr^2 \quad [10]$$

where for region mB

$$p = \frac{(2r_m^2 - 3r_B^2)\sigma_m^*}{3(r_m^2 - r_B^2)} \quad \text{and} \quad q = \frac{\sigma_m^*}{3(r_m^2 - r_B^2)} \quad [11]$$

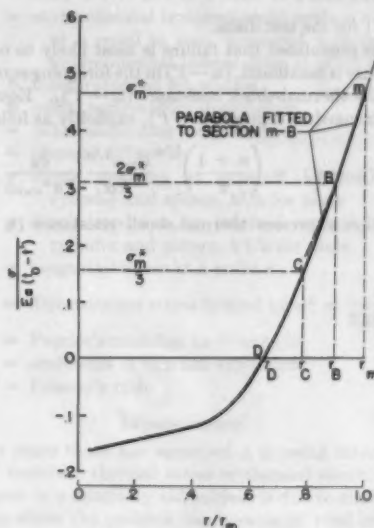
FIG. 23 REPLACEMENT OF STRESS-DISTRIBUTION CURVE BY THREE PARABOLAS $\beta = 10$, $\Theta = 0.05$

Fig. 23 illustrates how well region mB was fitted in such a manner for $\beta = 10$, $\Theta = 0.05$. Parabolas fitted to regions BC and CD were equally good approximations. The contribution to risk of rupture for each of the regions can be integrated separately according to Equation [7b] with the substitution $\sigma = \sigma^* E\alpha(t_0 - t')$ and then summed to give the following expression for R

$$R = \frac{[E\alpha(t_0 - t')]^n \pi}{\sigma_0^n (n+1)} \left(\frac{\sigma_m^*}{3}\right)^n r_m^n \left[(3^{n+1} - 2^{n+1}) + (2^{n+2} - 3^{n+1} - 1) \left(\frac{r_B}{r_m}\right)^2 + (2 - 2^{n+1}) \left(\frac{r_C}{r_m}\right)^2 - \left(\frac{r_D}{r_m}\right)^2 \right] \quad [12]$$

A plot of R versus time measured from start of quench permits the determination of maximum risk of rupture R_{max} , surface stress $\sigma_{m,B}$ at this time, and the corresponding radii ratios $(r_B/r_m)_B$, $(r_C/r_m)_B$, and $(r_D/r_m)_B$. These latter quantities are functions of the boundary condition $\beta = (r_m h)/k$.

Define

$$\phi(\beta, n) \equiv \frac{1}{3} \left[(3^{n+1} - 2^{n+1}) + (2^{n+2} - 3^{n+1} - 1) \left(\frac{r_B}{r_m} \right)_R^2 + (2 - 2^{n+1}) \left(\frac{r_c}{r_m} \right)_R^2 - \left(\frac{r_D}{r_m} \right)_R^2 \right]^{1/n} \quad [13]$$

$$P(\beta, n) \equiv \frac{\sigma_{\max}^* R}{\sigma_{\max}^*} \quad [14]$$

where σ_{\max}^* is the maximum dimensionless surface stress occurring during the quench.

The parameters ϕ and P once calculated for the desired range of β and n can be permanently filed in the form of graphs or tables (2). Maximum risk of rupture can now be written in simplified form making use of Equations [13] and [14]

$$R_{\max} = \frac{\pi [E\alpha(t_0 - t')]^n}{\sigma_0^n (n+1)} P^n \sigma_{\max}^* \phi^n \quad [15]$$

since $r_m = 1$ for the test disks.

Since it is postulated that failure is most likely to occur when risk of rupture is maximum, $(t_0 - t')$ in the foregoing equation is by definition the thermal-shock resistance $(t_0 - t')_f$. Equation [15] can be rearranged to express $(t_0 - t')_f$ explicitly as follows

$$(t_0 - t')_f = \left(\frac{n+1}{\pi} \right)^{1/n} \frac{R_{\max}^{1/n}}{E\alpha} \frac{\sigma_0}{P \sigma_{\max}^* \phi} \quad [16]$$

This equation expresses thermal-shock resistance $(t_0 - t')_f$ in

terms of the significant material properties n , σ_0 , k (since k is involved in the boundary condition β), and the parameter $R_{\max}^{1/n}/E\alpha$. The term R_{\max} , risk of rupture at failure, requires additional explanation. If a large number of specimens of given volume are subjected to the same stress pattern, the maximum stress within the specimen at time of failure will in general vary somewhat from specimen to specimen. This means that the value of R at failure will vary also. For this reason R_{\max} is defined as an average of the risk of ruptures at failure for a large number of specimens having the same volume and being subjected to the same stress pattern.

Surface Sensitivity to Flaws. It is possible that for some materials the greatest number and the most severe imperfections will occur on the surface rather than being randomly distributed throughout the volume of the material. For thermal-shock specimens of the type used in the present investigation in which the maximum stress always occurs at the surface, and in which the surface area is constant, the stress at fracture would then be independent of quench severity. Thus the data would reveal an apparent correlation with the maximum-stress theory of fracture even though the relevant statistical theory would show that the fracture stress is dependent upon amount of surface area under maximum stress, and in general upon distribution of stress on the surface. Valuable information for resolving the applicable fracture theory would be obtained by testing specimens in which the ratio of surface to volume is varied over wide limits; or in which a nonuniform distribution of surface stress is induced; however, such tests were not included within the scope of the present study.

Approximate Solution to Thermal-Shock Problems in Plates, Hollow Spheres, and Cylinders With Heat Transfer at Two Surfaces

BY A. MENDELSON¹ AND S. S. MANSON,² CLEVELAND, OHIO

An approximate method for computing transient thermal stresses in hollow cylinders, plates, and hollow spheres is presented. The method makes use of polynomial approximations to the temperature distribution by means of which the partial differential equation of the problem is reduced to a set of first-order ordinary differential equations. Nonuniform initial temperature distribution and heat transfer from both surfaces can be treated without difficulty making possible the practical solution of problems with relatively little labor for which an exact solution requires a great expenditure of labor and time. Several examples are presented and compare favorably with more accurate solutions.

NOMENCLATURE

The following nomenclature is used in the paper:

- a = inner radius of hollow cylinder or sphere, as ratio of outer radius, b
- a_i = coefficient in approximating polynomial
- b = outer radius of cylinder or sphere
- b_i, c_i = coefficients defined in text
- e = base of natural logarithms
- E = Young's modulus
- h, h' = heat-transfer coefficients at outer and inner surfaces, respectively
- k = thermal conductivity
- l = thickness of plate
- n = number of stations used
- $P_i(r)$ = polynomials defined in text
- r = radius to arbitrary position in cylinder or sphere as ratio of outer radius, b
- x = distance to arbitrary position in plate as ratio of thickness, l
- t = time
- T = ratio of temperature, at time τ and radius r or position x , to maximum temperature in body, measured with reference to environmental temperature at surface r equal to 1 or x equal to 1. This environmental temperature is always taken as zero. This dimensionless temperature

ratio is henceforth referred to simply as temperature

- $T(a), T(1)$ = temperature at r or x equal to a and 1 respectively
- T_s' = environmental temperature at surface r equal to a , or x equal to zero, measured with reference to environmental temperature at other surface
- T_j = temperature at j th station
- $T(r, 0)$ = initial temperature distribution
- ΔT = initial maximum temperature
- α = thermal diffusivity
- β = Biot's modulus at external surface, hb/k for cylinder and sphere, hl/k for plate
- β' = Biot's modulus at internal surface, $h'a/k$ for cylinder and sphere, $h'l/k$ for plate
- σ = tangential stress at a point r
- σ^* = dimensionless stress defined by $\sigma^* = \frac{\sigma}{E\mu(1-\nu)\Delta T}$
- τ = Fourier's modulus, $t\alpha/b^2$ or $t\alpha/l^2$
- μ = coefficient of thermal expansion
- ν = Poisson's ratio

INTRODUCTION

In recent years there has appeared a growing interest in the problem of transient thermal stress or thermal shock. This renewed interest in a relatively old subject is due to the many new applications where the problem has become of vital importance, such as jet engines, nuclear power plants, and high-speed missiles subjected to aerodynamic heating.

Many of the problems of thermal shock described in the literature are generally confined to bodies with geometric symmetry, such as uniform plates, circular cylinders, and spheres. For such bodies the stresses at any time due to temperature gradients can easily be obtained if the temperature distribution is known, particularly if the temperature distribution exhibits similar symmetrical properties (see, for example, reference 1).³ The chief difficulty is therefore not in evaluating the stress but in evaluating the temperature distribution at a given time after conditions are suddenly changed.

The exact solution of the transient temperature problems in plates, cylinders, and spheres has been extensively treated in the literature (2). These solutions in general are in the form of infinite series of trigonometric functions for the plate and sphere and Bessel functions for the cylinder (2). The arguments of these functions are obtained by first solving a transcendental equation (in trigonometric or Bessel functions) for its roots, each root being associated with one term of the infinite series. The coefficients of the functions in the infinite series are obtained from the initial temperature distribution making use of the orthogonality relation between the functions. The process is

³ Numbers in parentheses refer to the Bibliography at the end of the paper.

¹ Aeronautical Research Scientist, NACA Lewis Flight Propulsion Laboratory.

² Chief, Strength of Materials Branch, NACA Lewis Flight Propulsion Laboratory.

Contributed by the Metals Engineering Division and presented at the Annual Meeting, New York, N. Y., November 28-December 3, 1954, of THE AMERICAN SOCIETY OF MECHANICAL ENGINEERS.

NOTE: Statements and opinions advanced in papers are to be understood as individual expressions of their authors and not those of the Society. Manuscript received at ASME Headquarters, December 1, 1954. Paper No. 54-A-264.

very laborious and furthermore is very slowly convergent for high values of surface heat-transfer coefficient and for low values of time. For the case of a hollow cylinder, for example, numerical values have been obtained in only special cases (heat-transfer coefficient either 0 or ∞ , reference 3).

The object of this paper is to present a simple approximate method for obtaining transient stresses in plates, cylinders, and spheres. The method used is essentially an extension of the collocation procedure (4) applied to partial differential equations. Use is made of polynomial approximations to reduce the partial differential equation of the problem to a finite set of ordinary differential equations. The method is general in nature and can be applied to two and three-dimensional problems, such as the solution of Laplace's equation or the biharmonic equation for the stress function. For the one-dimensional transient thermal stress problem, the method is particularly suitable, for the final set of ordinary differential equations to be solved are all of the first order.

The method is presented in detail for determining the stresses in an infinitely long hollow circular cylinder with arbitrary initial temperature distribution and arbitrary surface heat-transfer coefficients and environmental temperatures. The stresses for the plate and the sphere are obtained similarly and the basic equations for these cases are presented in an Appendix. The extension to other two and three-dimensional problems is self-evident.

TRANSIENT TEMPERATURE DISTRIBUTION IN HOLLOW CYLINDER

The differential equation for the transient temperature distribution in an infinitely long hollow circular cylinder with angular symmetry is

$$\left. \begin{aligned} \frac{\partial T}{\partial \tau} &= \frac{\partial^2 T}{\partial r^2} + \frac{1}{r} \frac{\partial T}{\partial r} \quad a \leq r \leq 1 \\ \tau &> 0 \\ \frac{\partial T}{\partial r} \Big|_{r=a} &= \frac{\beta'}{a} [T(a) - T_s'] \\ \frac{\partial T}{\partial r} \Big|_{r=1} &= -\beta T(1) \\ T &= T(r, 0) \text{ at } \tau = 0 \end{aligned} \right\} \dots [1]$$

The exact solution of Equations [1] can be obtained in terms of a complicated infinite series of Bessel functions, the arguments of the different terms in the series being obtained as the infinite number of solutions of a transcendental equation in Bessel functions (2). Numerical solutions have been obtained only in special cases.

In the present paper Equations [1] are solved approximately by making use of polynomial approximations as explained in detail in Appendix 1. The temperature at any time is assumed to be given by a polynomial passing through n radial stations in the cylinder. Making use of this polynomial, Equations [1] are reduced to a set of ordinary linear first-order differential equations of the form

$$\left. \begin{aligned} \frac{dT_1}{d\tau} &= b_{11}T_1 + b_{12}T_2 + \dots + b_{1n}T_n + c_1 \\ \frac{dT_2}{d\tau} &= b_{21}T_1 + b_{22}T_2 + \dots + b_{2n}T_n + c_2 \\ &\vdots \\ \frac{dT_n}{d\tau} &= b_{n1}T_1 + b_{n2}T_2 + \dots + b_{nn}T_n + c_n \end{aligned} \right\} \dots [2]$$

where the T_i are the temperatures at n -stations in the cylinder and the b_{ij} and c_i are constants depending on a, β, β', T_s' . It will subsequently be shown that 3 or 4 stations will suffice for most practical applications. The problem is then reduced to solving Equations [2] for the n -temperatures T_i as functions of τ . This can, of course, be done by any of several standard methods. The method generally adopted in this paper makes use of simple matrix algebra and is explained in detail in Appendix 2. Once the temperatures have been determined, the stresses at any time can be calculated.

TRANSIENT STRESSES IN CYLINDER

The tangential thermal stresses in a circular cylinder are given by

$$\sigma^*(r) = \frac{1}{1-a^2} \int_a^1 T r dr + \frac{1}{r^2} \int_a^r T r dr - T(r) \quad [3]$$

Attention will be directed only to tangential stresses. The radial and axial stresses, of course, can be calculated in a similar manner. At the surfaces where the maximum stresses generally occur, the tangential stresses are given by

$$\left. \begin{aligned} \sigma^*(a) &= \frac{2}{1-a^2} \int_a^1 T r dr - T(a) \\ \sigma^*(1) &= \frac{2}{1-a^2} \int_a^1 T r dr - T(1) \end{aligned} \right\} \dots [4]$$

It is shown in Appendix 3 that the stresses can also be obtained from a knowledge of the time history of the surface stresses only. Thus

$$\left. \begin{aligned} \sigma^*(a) &= -\frac{2}{1-a^2} \left\{ \int_0^\tau [\beta T(1) + \beta' T(a)] d\tau \right. \\ &\quad \left. - \beta' T_s' \tau - \int_a^1 T(r, 0) r dr \right\} - T(a) \\ \sigma^*(1) &= \sigma^*(a) + T(a) - T(1) \end{aligned} \right\} \dots [5]$$

For a solid cylinder, the rim stress becomes

$$\left. \begin{aligned} \sigma^*(1) &= -2\beta \int_0^\tau T(1) d\tau - T(1) + 2 \int_0^1 T(r, 0) r dr \\ \text{or} \\ \sigma^*(1) &= \sigma_0^*(1) + T(1, 0) - T(1) - 2\beta \int_0^\tau T(1) d\tau \end{aligned} \right\} \dots [6]$$

where $\sigma_0^*(1)$ is the initial rim stress (zero for uniform initial temperature distribution) and $T(1, 0)$ is the initial rim temperature (equal to 1 for uniform initial distribution).

Having determined the temperature at n -points from the solution of Equations [2], the stresses can be calculated by means of either Equations [4] or [5]. If Equations [4] are used the integral can be evaluated directly by means of the Newton-Cotes quadrature formulas (5), so that the final formula for the stress is of the simple form

$$\sigma^* = \sum_{j=1}^n k_j T_j \quad [7]$$

If Equations [5] are used, only the surface temperatures are required. Equations [5] are particularly useful, if the solution of

the temperature problem is obtained by using an electronic differential analog computer. Several numerical examples of the method will now be given in detail.

EXAMPLES

1 Consider a solid cylinder with a constant initial temperature distribution, $T(r, 0) = 1$. Let $n = 3$ with the three stations taken at $r = 0, 1/3, 1$. Upon substituting the polynomials given in Appendix 1, the set of differential equations to be solved become

$$\left. \begin{aligned} \frac{dT_1}{d\tau} &= -44T_1 + 64T_2 - (20 + 4\beta)T_3 \\ \frac{dT_2}{d\tau} &= 5T_1 - 16T_2 + (11 + 1.5\beta)T_3 \\ \frac{dT_3}{d\tau} &= -10T_1 + 32T_2 - (22 + 9\beta)T_3 \end{aligned} \right\} \dots [8]$$

Equations [8] have been solved by two methods: First, by using the standard exponential solution, and then by using the infinite matrix series as explained in Appendix 2. The exponential solution for $\beta = 30$ is

$$T_1 = 1.563 e^{-5.307\tau} - 1.079 e^{-43.307\tau} + 0.516 e^{-304.47\tau}$$

$$T_2 = 1.090 e^{-5.307\tau} + 0.0892 e^{-43.307\tau} - 0.179 e^{-304.47\tau}$$

$$T_3 = 0.0672 e^{-5.307\tau} + 0.0546 e^{-43.307\tau} + 0.878 e^{-304.47\tau}$$

By a Newton-Cotes quadrature formula (5)

$$\int_0^1 T_r dr = \frac{1}{6} \left(T_1 \cdot 0 + 4T_r \frac{1}{2} + T_3 \cdot 1 \right) = \frac{1}{3} T_2 + \frac{1}{6} T_3$$

and by Equation [4]

$$\begin{aligned} \sigma^*(1) &= \frac{2}{3} T_2 + \frac{1}{3} T_1 - T_3 = \frac{2}{3} (T_2 - T_1) \\ &= 0.682 e^{-5.307\tau} + 0.0231 e^{-43.307\tau} - 0.705 e^{-304.47\tau} \end{aligned}$$

from which the stress can be plotted as a function of τ , and the maximum value of $\sigma^*(1)$ determined.

Alternately, using the infinite matrix solution given in Appendix 2 results for T_1

$$\begin{aligned} T_1 &= 1 - 270\tau + 8.148 \times 10^4 \frac{\tau^2}{2!} - 24.78 \times 10^8 \frac{\tau^3}{3!} \\ &+ 75.42 \times 10^8 \frac{\tau^4}{4!} - 229.6 \times 10^{10} \frac{\tau^5}{5!} + 698.9 \times 10^{12} \frac{\tau^6}{6!} \\ &- 2128 \times 10^{14} \frac{\tau^7}{7!} + 6476 \times 10^{16} \frac{\tau^8}{8!} \\ &- 10,720 \times 10^{18} \frac{\tau^9}{9!} + \dots \end{aligned}$$

Using similar equations for T_2 and T_3 , the stress can then be calculated from either Equations [4] or [6]. The same results are obtained using either method. However, the matrix-series method appears in general to produce results more rapidly. For the value of $\beta = 30$, a maximum stress of 0.64 is obtained compared to the theoretically exact solution of 0.67. Thus with only 3 stations the error in maximum stress is about 5 per cent at this relatively high value of β . For more reasonable values of β , the error is much less as can be seen from Fig. 1 where $\sigma^*(1)$ has been plotted against τ for various values of β . Since, in most cases of practical interest, the parameter sought is the maximum stress, rather than the complete variation of stress with time, the discrepancies between the solid and dotted curves in the

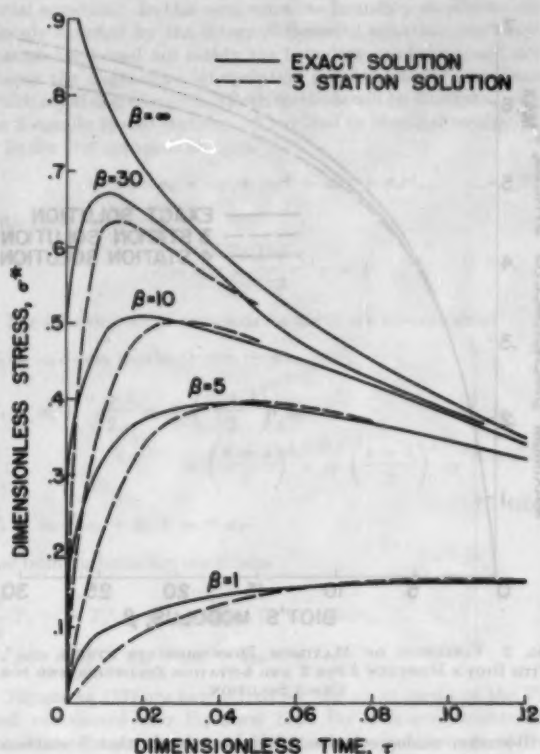


FIG. 1 VARIATION OF DIMENSIONLESS STRESS σ^* WITH DIMENSIONLESS TIME τ FOR VARIOUS VALUES OF β FOR 3-STATION SOLUTION AND FOR EXACT SOLUTION

lower time range are of little significance. The approximations predict the maximum stress with a good degree of accuracy. By using one or two more stations the complete stress-time curve can be accurately obtained.

In Fig. 2, σ_{max}^* has been plotted against β for a 3-station solution, a 4-station solution, and a 10-station solution obtained on an electronic differential analyzer. The differential-analyzer solution is identical with the exact solution as given in reference (6) and was run in order to check the accuracy of the analyzer for subsequent hollow cylinder computations. Further information on the use of an electronic differential analyzer in solving temperature-distribution problems is given in reference (7). It is seen from Fig. 2 that 3 stations are, in general, adequate for determining the maximum stress, with 4 stations giving some improvements in accuracy at high values of β .

2 As a second example, the case where the initial temperature distribution is not uniform is considered. No difficulty is added to the problem. Equations [2] are solved in the same manner as before, taking into account the initial values of the T_i . The stresses are then calculated as before. The case treated is that of a solid cylinder using 3 stations with two different initial temperature distributions given by

$$T(r, 0) = r^3$$

and

$$T(r, 0) = \frac{2-r^4}{2}$$

The results are plotted for $\beta = 10$ in Fig. 3 and compared with

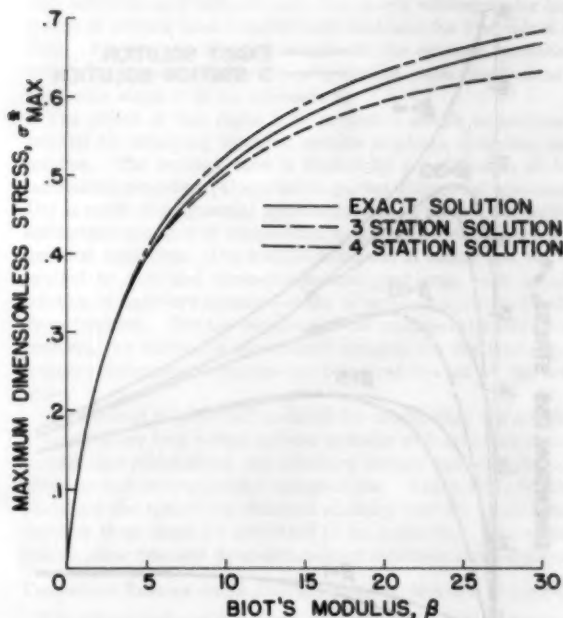


FIG. 2 VARIATION OF MAXIMUM DIMENSIONLESS STRESS σ_{\max}^* WITH BIOT'S MODULUS β FOR 3 AND 4-STATION SOLUTIONS, AND FOR EXACT SOLUTION

a 10-station analog solution. It is seen again that 3 stations give adequate accuracy.

3 As another example, we take the case of a hollow circular cylinder with uniform initial temperature distribution and the following boundary conditions:

On external surface: $\beta = 10$

On internal surface: Case (a) $\beta' = 5$, $T_e' = 0$
Case (b) $\beta' = 5$, $T_e' = 2$

Internal radius of cylinder: $a = 1/2$

The method for handling these cases is the same as previously used. Three stations were taken, at $r = 1/2, 3/4, 1$. A polynomial was passed through these stations and the coefficients in Equations [2] obtained. Equations [2] were then solved as previously, and the stresses obtained from either Equations [4] or [5]. The results are plotted in Fig. 4 and compared with a 10-station analog-computer solution. Again it is seen that 3 stations are adequate for determining the maximum stresses.

DISCUSSION

Although only a few examples have been presented, it is apparent that the method used is very general in nature and can be applied to widely different conditions with little increase in labor. From the curves presented it appears that, for reasonable initial and boundary conditions, 3 stations will give sufficient accuracy for many engineering purposes. For cases where steeper gradients can be expected, it may be necessary to use a greater number of stations; or the stations may be judiciously chosen unequally spaced to favor the sections which have steeper gradients, without appreciably increasing the labor involved.

An examination of the general equation for transient stress in a hollow cylinder as given in reference (6) demonstrates the almost hopeless task of obtaining numerical answers for general boundary

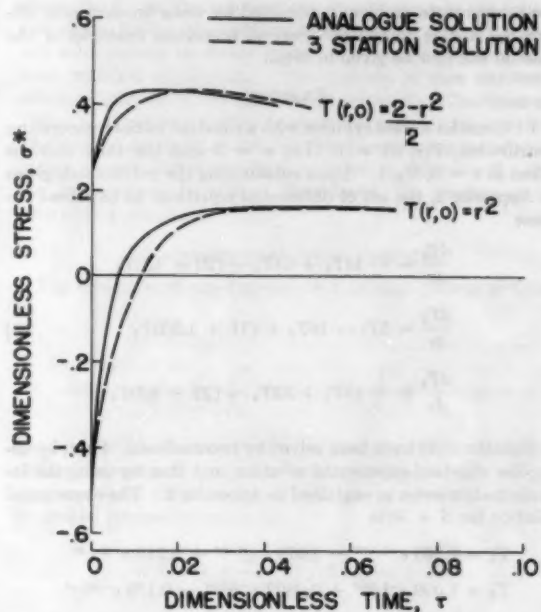


FIG. 3 VARIATION OF DIMENSIONLESS STRESS σ^* WITH DIMENSIONLESS TIME τ FOR A SOLID CYLINDER WITH NONUNIFORM INITIAL TEMPERATURE DISTRIBUTION USING 3 STATIONS AND USING A 10-STATION DIFFERENTIAL-ANALYZER SOLUTION. $\beta = 10$

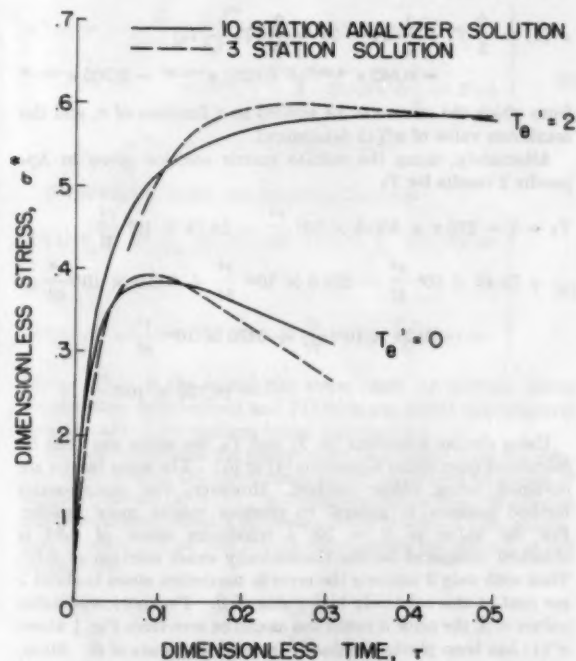


FIG. 4 VARIATION OF DIMENSIONLESS STRESS σ^* WITH DIMENSIONLESS TIME τ FOR HOLLOW CYLINDER, FOR 3-STATION SOLUTION, AND FOR 10-STATION ANALOG SOLUTION. $a = 1/2$, $\beta = 10$, $\beta' = 5$

conditions without the use of special computing machinery. The present method, therefore, even if a larger number of stations than indicated in this paper were used, would still result in a great saving of computing time.

The solution of plate and sphere problems by this method requires no basic extension. Polynomials are chosen as for the cylinder and substituted into the appropriate differential equations for plate or sphere. The equations are given in Appendix 4. The solution assumes exactly the same form as previously discussed. It is also to be noted that the existence of heat sources within the body adds no additional difficulty. The correct differential equation must be used, although it may be necessary in this case to use a greater number of stations.

BIBLIOGRAPHY

- 1 "Theory of Elasticity," by S. Timoshenko and J. N. Goodier, McGraw-Hill Book Company, Inc., New York, N. Y., 1951.
- 2 "Conduction of Heat in Solids," by H. S. Carslaw and J. C. Jaeger, Clarendon Press, Oxford, England, 1947.
- 3 "Thermal Stresses in Non-Ductile High-Temperature Materials," by F. J. Bradshaw, Royal Aircraft Establishment Technical Note No.: met. 100, February, 1949.
- 4 "Approximations to Functions and to the Solutions of Differential Equations," by R. A. Frazer, W. P. Jones, and S. W. Skan, ARC Technical Rep., 1937, R. and M. No. 1799, March, 1937.
- 5 "Numerical Calculus," by W. E. Milne, Princeton University Press, Princeton, N. J., 1949.
- 6 "On Thermal Stresses in Circular Cylinders," by J. C. Jaeger, *Philosophical Magazine*, 7th series, vol. 36, 1945, p. 418.
- 7 "Application of Difference Techniques to Heat Flow Problems Using the Electronic Differential Analyzer," by R. M. Howe, Engineering Research Institute, University of Michigan, Ann Arbor, Mich., May, 1954.

Appendix 1

POLYNOMIAL APPROXIMATION TO TEMPERATURE DISTRIBUTION

Consider a circular hollow cylinder as shown in Fig. 5, with inner radius a , outer radius 1. The differential equation for the

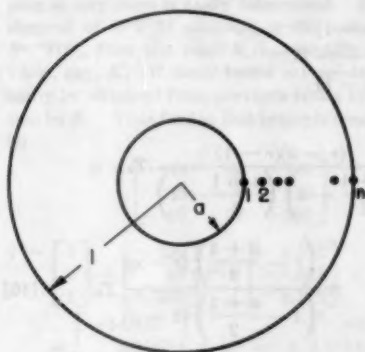


FIG. 5 HOLLOW CYLINDER WITH n -STATIONS

transient temperature distribution, the boundary conditions and initial conditions are as given in Equations [1]; n -stations are established in the cylinder as shown. These stations need not necessarily be equally spaced. It is now desired to approximate the temperature distribution in this cylinder at any time by a polynomial in r , taking on prescribed initial values at n -stations. This polynomial when substituted into the partial differential equation reduces it to an ordinary differential equation which when satisfied at each of the n -stations results in n ordinary first-order differential equations. In this approach the polynomials should also satisfy the boundary conditions of Equations [1]. These polynomials will therefore in general be of degree $n + 1$.

In an alternate approach, the differential equation is first transformed to an integro-differential equation by integrating with

respect to r and making use of the boundary conditions. The assumed polynomial is then substituted into this integro-differential equation. In this case, since the boundary conditions are already satisfied by the integro-differential equation, the polynomials used need not satisfy the boundary conditions, and are simply the Lagrangian interpolation polynomials for n -stations which are of degree $n - 1$. Both methods will be illustrated here for 3 equally spaced stations. They lead to identical results.

In the first approach let

$$T = a_0 + a_1 r + a_2 r^2 + a_3 r^3 + a_4 r^4 \dots \dots \dots [9]$$

with the 3 stations at

$$r = a, r = \frac{a+1}{2}, r = 1$$

The following set of equations for the a_i are now obtained

$$\left. \begin{aligned} T_1 &= a_0 + a a_1 + a^2 a_2 + a^3 a_3 + a^4 a_4 \\ T_2 &= a_0 + \frac{a+1}{2} a_1 + \left(\frac{a+1}{2}\right)^2 a_2 \\ &\quad + \left(\frac{a+1}{2}\right)^3 a_3 + \left(\frac{a+1}{2}\right)^4 a_4 \\ T_3 &= a_0 + a_1 + a_2 + a_3 + a_4 \end{aligned} \right\} \dots [10]$$

$$\left. \begin{aligned} \frac{\beta'}{a} T_1 - \frac{\beta'}{a} T_4 &= a_1 + 2a a_2 + 3a^2 a_3 + 4a^3 a_4 \\ -\beta T_3 &= a_1 + 2a_2 + 3a_3 + 4a_4 \end{aligned} \right\}$$

Equations [10] are now solved for the a_i 's in terms of the T_i and substituted into Equation [9]. For a larger number of stations a larger number of simultaneous equations must be solved, and the labor becomes cumbersome. However, the required polynomial can be obtained very simply in another fashion without solving Equations [10]. The temperature distribution can be written as follows

$$T = P_1(r)T_1 + P_2(r)T_2 + P_3(r)T_3 \dots \dots \dots [11]$$

where the P_i are station functions which have the following characteristics

$$\left. \begin{aligned} P_i(r) &= 1 & \text{when } r = r_i \\ P_i(r) &= 0 & \text{when } r = r_j \quad i \neq j \end{aligned} \right\} \dots \dots [12]$$

Furthermore, in order to satisfy the boundary conditions, all the polynomials except P_1 have zero slope at r equal to a , and all but P_2 have zero slope at r equal to 1 whereas P_1 has the proper slope at r equal to a to satisfy the boundary condition there, and P_3 has the proper slope at r equal to 1. Such polynomials can be written by inspection, thus

$$\left. \begin{aligned} P_1(r) &= \frac{\left(r - \frac{a+1}{2}\right)(r-1)(r-b_1)}{\left(\frac{a-1}{2}\right)(a-1)(a-b_1)} \\ P_2(r) &= \frac{(r-a)(r-1)^2}{\frac{1}{16}(a-1)^4} \\ P_3(r) &= \frac{(r-a)^2 \left(r - \frac{a+1}{2}\right)(r-b_2)}{(1-a)^2 \left(\frac{1-a}{2}\right)(1-b_2)} \end{aligned} \right\} \dots [13]$$

where b_1 and b_2 are chosen to satisfy the boundary conditions. Equations [11] and [13] will automatically satisfy Equations [10], once the constants b_1 and b_2 are determined. These can easily be found as follows

$$\left. \frac{dT}{dr} \right|_{r=a} = T_1 \left. \frac{dP_1}{dr} \right|_{r=a} = \frac{\beta'}{a} (T_1 - T_s')$$

or

$$P_1(a) \left[\frac{1}{r - \frac{a+1}{2}} + \frac{2}{r-1} + \frac{1}{r-b_1} \right] \bigg|_{r=a} T_1 = \frac{\beta'}{a} (T_1 - T_s')$$

but $P_1(a) = 1$, therefore

$$\left(\frac{2}{a-1} + \frac{2}{a-1} + \frac{1}{a-b_1} \right) T_1 = \frac{\beta'}{a} (T_1 - T_s')$$

$$b_1 = a - \frac{T_1}{\left(\frac{\beta'}{a} + \frac{4}{1-a} \right) T_1 - \frac{\beta'}{a} T_s'}$$

Similarly, for b_2

$$\left. \frac{dT}{dr} \right|_{r=1} = T_2 \left. \frac{dP_2}{dr} \right|_{r=1} = -\beta T_2$$

$$\text{or} \quad \left(\frac{2}{r-a} + \frac{1}{r - \frac{a+1}{2}} + \frac{1}{r-b_2} \right) \bigg|_{r=1} = -\beta$$

therefore

$$b_2 = 1 + \frac{1}{\frac{4}{1-a} + \beta}$$

It is seen from the foregoing that the extension to more stations is relatively simple. Substituting now into the differential Equations [1] and evaluating it at $r = a$, $(a+1)/2$ and 1 results in the following 3 equations

$$\left. \begin{aligned} \frac{dT_1}{dr} &= \left[\frac{-22}{(1-a)^2} + \frac{9a-1}{a^2(a-1)} \beta' \right] T_1 + \frac{32}{(1-a)^2} T_2 \\ &\quad - \left[\frac{10}{(1-a)^2} + \frac{2\beta}{1-a} \right] T_1 - \left[\frac{9a-1}{a^2(a-1)} \beta' \right] T_s' \\ \frac{dT_2}{dr} &= \left[\frac{8}{(1-a)^2} - \frac{3}{1-a^2} + \frac{3a+1}{2(1-a^2)} \frac{\beta'}{a} \right] T_1 \\ &\quad - \frac{16}{(1-a)^2} T_2 + \left[\frac{\left(3 + \frac{1-a}{2} \beta \right) (5+3a)}{(1-a)(1-a^2)} \right. \\ &\quad \left. - \frac{4+(1-a)\beta}{(1-a)^2} \right] T_3 - \frac{3a+1}{2(1-a^2)} \frac{\beta'}{a} T_s' \\ \frac{dT_3}{dr} &= \left[\frac{-10}{(1-a)^2} - \frac{2}{(1-a)} \frac{\beta'}{a} \right] T_1 + \frac{32}{(1-a)^2} T_2 \\ &\quad + \left[\frac{4a-26}{(1-a)^2} + \frac{4+(a-9)\beta}{1-a} \right] T_3 + \frac{2}{(1-a)} \frac{\beta'}{a} T_s' \end{aligned} \right\} \dots [14]$$

for the solid cylinder, where a becomes zero, the

$$\lim_{r \rightarrow 0} \frac{1}{r} \frac{dP}{dr} = \frac{d^2P}{dr^2} \bigg|_{r=0}$$

and results in the first of Equations [8] in the text.

It is to be noted that in obtaining the coefficients in Equations [14] it is not necessary to actually expand the polynomials of Equations [13] when evaluating the derivatives at a particular station. For example

$$\frac{dP_1}{dr} = P_1 \left[\frac{1}{r - \frac{a+1}{2}} + \frac{2}{r-1} + \frac{1}{r-b_1} \right]$$

$$\frac{d^2P_1}{dr^2} = -P_1 \left[\frac{1}{\left(r - \frac{a+1}{2} \right)^2} + \frac{2}{(r-1)^2} + \frac{1}{(r-b_1)^2} \right] + P_1 \left[\frac{1}{r - \frac{a+1}{2}} + \frac{2}{r-1} + \frac{1}{r-b_1} \right]^2$$

These can readily be evaluated, with the help of Equations [12].

For a given cylinder under known environmental conditions, a, β, β', T_s' are known and Equations [14] can be solved for T_1, T_2 , and T_3 as functions of r .

In the second method the differential equation is first integrated using the appropriate boundary conditions. The following integro-differential equation results

$$\frac{\partial}{\partial r} \left[\int_r^1 \frac{dr_1}{r_1} \int_a^{r_1} T r dr + \frac{1}{\beta} \int_a^1 T r dr \right] = -T + \beta' [T(a) - T_s'] \left[\ln r - \frac{1}{\beta} \right] \dots [15]$$

The boundary conditions are already included in this equation and a simple Lagrangian interpolation polynomial is therefore chosen for T . For three equally spaced stations this polynomial is simply

$$T = \frac{\left(r - \frac{a+1}{2} \right) (r-1)}{\left(a - \frac{a+1}{2} \right) (a-1)} T_1 + \frac{(r-a)(r-1)}{\left(\frac{a+1}{2} - a \right) \left(\frac{a+1}{2} - 1 \right)} T_2 + \frac{\left(r - \frac{a+1}{2} \right) (r-a)}{\left(1 - \frac{a+1}{2} \right) (1-a)} T_3 \dots [16]$$

Equation [16] is substituted into [15] and the resultant equation is evaluated at the three stations. This leads to three ordinary differential equations which after some algebraic manipulation reduce identically to Equations [14].

Appendix 2

MATRIX SERIES FOR TEMPERATURE DISTRIBUTION

Equation [2] can be solved by any of a number of standard methods. The solution in general will be given by a set of exponentials. It was found that the standard matrix solution is advantageous for this problem, and it will therefore be outlined here, although it can be found in standard texts on matrices.

Equation [2] can be written in matrix notation as

$$\frac{dT}{dr} = BT \dots \dots \dots [17]$$

where the c 's have been taken as zero, and

$$T = \begin{bmatrix} T_1 \\ T_2 \\ \vdots \\ T_n \end{bmatrix} \quad B = \begin{bmatrix} b_{11} & b_{12} & \dots & b_{1n} \\ b_{21} & b_{22} & \dots & b_{2n} \\ \vdots & \vdots & \ddots & \vdots \\ b_{n1} & b_{n2} & \dots & b_{nn} \end{bmatrix}$$

The solution of Equation [17] is

$$T = e^{Br} T(0) \dots \dots \dots [18]$$

where $T(0)$ is the initial distribution and e^{Br} is the exponential matrix defined by the usual exponential series

$$e^{Br} = I + Br + B^2 \frac{r^2}{2!} + B^3 \frac{r^3}{3!} + \dots \dots \dots [19]$$

and I is the identity matrix.

The matrix e^{Br} can be obtained in closed form by use of Sylvester's theorem. The labor involved is essentially the same as solving Equations [2] by the standard exponential substitution, and little would be gained by this approach. However, it is simpler to use the exponential series [19] directly, since it was found that in general it converges rapidly for the problems considered.

Substituting series [19] into [18] gives

$$T = T(0) + BT(0)r + B[BT(0)] \frac{r^2}{2!} + \dots \dots \dots [20]$$

The foregoing series can easily be evaluated since each term involves the product of an $n \times n$ matrix and a column. Also, the series alternates in sign and the maximum possible error in stopping at any term is easily determined. Furthermore, if b_n is an element of $B^n T(0)$ and b_{n-1} is the corresponding element of $B^{n-1} T(0)$, then the ratio b_n/b_{n-1} rapidly approaches a constant value, say, K . If more terms are needed, therefore, they can easily be obtained from previous terms by successive multiplication by K . Thus for the first example treated in the text, for $\beta = 30$

$$B = \begin{bmatrix} -44 & 64 & -140 \\ 5 & -16 & 56 \\ -10 & 32 & -292 \end{bmatrix} \quad T(0) = \begin{bmatrix} 1 \\ 1 \\ 1 \end{bmatrix}$$

$$\begin{aligned} T = & \begin{bmatrix} 1 \\ 1 \\ 1 \end{bmatrix} + \begin{bmatrix} -120 \\ 45 \\ -270 \end{bmatrix} r + \begin{bmatrix} 4.596 \\ -1.644 \\ 8.148 \end{bmatrix} \times 10^4 \frac{r^2}{2} \\ & + \begin{bmatrix} -14.482 \\ 5.0557 \\ -24.778 \end{bmatrix} \times 10^8 \frac{r^3}{6} + \begin{bmatrix} 44.297 \\ -15.408 \\ 75.417 \end{bmatrix} \times 10^8 \frac{r^4}{24} \\ & + \begin{bmatrix} -134.94 \\ 46.914 \\ -229.579 \end{bmatrix} \times 10^{10} \frac{r^5}{120} + \begin{bmatrix} 410.81 \\ -142.82 \\ 698.88 \end{bmatrix} \times 10^{13} \frac{r^6}{720} \\ & + \begin{bmatrix} -1250.6 \\ 434.76 \\ -2127.5 \end{bmatrix} \times 10^{14} \frac{r^7}{5040} \\ & + \begin{bmatrix} 3807.0 \\ -1323.5 \\ 6476.5 \end{bmatrix} \times 10^{16} \frac{r^8}{40,320} + \dots \end{aligned}$$

By taking ratios of successive columns the constant K is seen to be -304.42 . Therefore additional columns can be obtained by simply multiplying by this constant. If the c 's are not zero, the additional particular solution can easily be found.

Appendix 3

ALTERNATE STRESS EQUATION

The differential equation can be written as follows

$$\frac{\partial}{\partial r} (rT) = \frac{\partial}{\partial r} \left(r \frac{\partial T}{\partial r} \right) \dots \dots \dots [21]$$

Integrating with respect to r and making use of the boundary conditions gives at $r = 1$

$$\frac{\partial}{\partial r} \int_a^1 T r dr = -\beta T(1) - \beta' [T(a) - T_e'] \dots \dots [22]$$

or

$$\int_a^1 T r dr = - \int_0^r [\beta T(1) + \beta' T(a)] dr + \beta' T_e' r + f(r) \dots [23]$$

From the initial condition

$$f(r) = \int_a^1 T(r, 0) r dr$$

therefore

$$\begin{aligned} \int_a^1 T r dr = & \int_a^1 T(r, 0) r dr \\ & - \int_0^r [\beta T(1) + \beta' T(a)] dr + \beta' T_e' r \dots \dots [24] \end{aligned}$$

Substituting into Equations [4] of the text results in

$$\begin{aligned} \sigma^*(1) = & - \frac{2}{1-a^2} \left\{ \int_0^r [\beta T(1) + \beta' T(a)] dr \right. \\ & \left. - \beta' T_e' r - \int_a^1 T(r, 0) r dr \right\} - T(1) \dots [25] \\ \sigma^*(a) = & \sigma^*(1) + T(1) - T(a) \end{aligned}$$

Appendix 4

PLATES AND SPHERES

A similar method as discussed for the cylinder can be used for the plate and sphere. The differential equations and the boundary conditions under consideration are:

For the plate

$$\begin{aligned} \frac{\partial T}{\partial r} = \frac{\partial^2 T}{\partial x^2} \quad 0 \leq x \leq 1 \quad r > 0 \\ \frac{\partial T}{\partial x} \Big|_{x=0} = -\beta' [T_e' - T(0)] \\ \frac{\partial T}{\partial x} \Big|_{x=1} = -\beta T(1) \end{aligned} \dots \dots [26]$$

For the sphere

$$\begin{aligned} \frac{\partial T}{\partial r} = \frac{\partial^2 T}{\partial r^2} + \frac{2}{r} \frac{\partial T}{\partial r} \quad a \leq r \leq 1 \quad r > 0 \\ \frac{\partial T}{\partial r} \Big|_{r=a} = \frac{\beta'}{a} [T(a) - T_e'] \\ \frac{\partial T}{\partial r} \Big|_{r=1} = -\beta T(1) \end{aligned} \dots [27]$$

As for the case of the cylinder, the temperature is assumed to be

given by a polynomial passing through a given number of stations and satisfying the boundary conditions. These polynomials are substituted into Equations [26] or [27] and the equations satisfied at the n chosen stations. This gives n first-order differential equations.

The Plate. Consider three stations taken at $x = 0, 1/2, 1$. The temperature is assumed to be given by the polynomial

$$T = \frac{(x - b_1)(x - 1/2)(x - 1)^2}{1/2 b_1} T_1 + \frac{x^2(x - 1)^2}{1/16} T_2 + \frac{x^2(x - 1/2)(x - b_2)}{1/2(1 - b_2)} T_3 \dots \dots [28]$$

where b_1 and b_2 are determined by the boundary conditions and are given by

$$\left. \begin{aligned} b_1 &= \frac{T_1}{\beta' T_1' - (4 + \beta') T_1} \\ b_2 &= \frac{5 + \beta}{4 + \beta} \end{aligned} \right\} \dots \dots [29]$$

Substituting into Equation [26] and evaluating at $x = 0, 1/2$, and 1 results in the following three equations for the temperatures at the three stations

$$\left. \begin{aligned} \frac{dT_1}{d\tau} &= - \left(\frac{11}{2} + 4\beta' \right) T_1 + 8T_2 \\ &\quad - \left(\beta + \frac{5}{2} \right) T_3 + 4\beta' T_3' \\ \frac{dT_2}{d\tau} &= \left(2 + \frac{\beta'}{2} \right) T_1 - 4T_2 \\ &\quad + \left(2 + \frac{\beta}{2} \right) T_3 - \frac{\beta'}{2} T_3' \\ \frac{dT_3}{d\tau} &= - \left(\frac{5}{2} + \beta' \right) T_1 + 8T_2 \\ &\quad - \left(\frac{11}{2} + 4\beta \right) T_3 + \beta' T_3' \end{aligned} \right\} \dots [30]$$

It is to be noted that if the temperature is known to be symmetric about the mid-plane of the plate ($\beta' = \beta$, $T_1' = 0$, and $T(x, 0)$ is symmetric about the mid-plane), then greater accuracy can be obtained by taking the origin $x = 0$ at the mid-plane, letting x range from -1 to 1 , and considering only the half plate $0 \leq x \leq 1$. Equations [30] can still be used with $\beta' = T_1' = 0$ and noting that β and τ are now defined in terms of the half thickness.

After solving Equations [30] for the temperatures T_1 , T_2 , and T_3 the stresses can be computed from the relation

$$\sigma^* = \int_0^1 T dx + 3(2x - 1) \int_0^1 T(2x - 1) dx - T \quad [31]$$

For the symmetric case with x ranging from -1 to 1 the stress is given by

$$\sigma^* = \int_0^1 T dx - T \dots \dots [32]$$

The integrals can again be evaluated by Newton-Cotes quadrature formulas (4). An alternate formula for the stress can be derived in a similar manner to the one obtained for the cylinder in Appendix 3

$$\left. \begin{aligned} \sigma^*(0) &= -T(0) + \int_0^1 \left[\left(\beta + \frac{3}{2} \right) T(1) \right. \\ &\quad \left. - \left(2\beta' + \frac{3}{2} \right) T(0) \right] d\tau + 2\beta' T_1' \tau \\ &\quad + 4 \int_0^1 T(x, 0) dx - 6 \int_0^1 T(x, 0) x dx \\ \sigma^*(1) &= -T(1) - \int_0^1 \left[\left(2\beta + \frac{3}{2} \right) T(1) \right. \\ &\quad \left. - \left(\beta' + \frac{3}{2} \right) T(0) \right] d\tau - \beta' T_1' \tau \\ &\quad - 2 \int_0^1 T(x, 0) dx + 6 \int_0^1 T(x, 0) x dx \end{aligned} \right\} \dots [33]$$

The Sphere. A hollow sphere with inner radius a , and outer radius 1 is considered. The polynomials chosen are the same as those for the cylinder, the final set of ordinary differential equations being different because of the difference in the basic partial differential equations. For the three stations at $r = a, (a + 1)/2, 1$, the equations to be solved are

$$\left. \begin{aligned} \frac{dT_1}{d\tau} &= \left[\frac{-22}{(1-a)^2} + \frac{10a-2}{a(a-1)} \beta' \right] T_1 + \frac{32}{(1-a)^2} T_2 \\ &\quad - \left[\frac{10}{(1-a)^2} + \frac{2\beta}{1-a} \right] T_3 - \frac{10a-2}{a(a-1)} \beta' T_3' \\ \frac{dT_2}{d\tau} &= \left[\frac{8}{(1-a)^2} - \frac{6}{1-a^2} + \frac{2a}{1-a^2} \beta' \right] T_1 \\ &\quad - \frac{16}{(1-a)^2} T_2 + \left[\frac{a+3}{1-a^2} \frac{(1-a)\beta+6}{1-a} \right. \\ &\quad \left. - \frac{(1-a)\beta+4}{(1-a)^2} \right] T_3 - \frac{2a}{1-a^2} \beta' T_3' \\ \frac{dT_3}{d\tau} &= - \left[\frac{10}{(1-a)^2} + \frac{2}{1-a} \beta' \right] T_1 + \frac{32}{(1-a)^2} T_2 \\ &\quad - \left[\frac{22}{(1-a)^2} + \frac{10-2a}{1-a} \beta \right] T_3 + \frac{2}{1-a} \beta' T_3' \end{aligned} \right\} \dots [34]$$

For the solid sphere, where a becomes zero, the

$$\lim_{r \rightarrow 0} \frac{2}{r} \frac{dP}{dr} = 2 \frac{d^2P}{dr^2} \bigg|_{r=0}$$

After solving Equation [34] for the temperatures, the stresses are computed from the equation

$$\sigma^*(r) = \frac{2 + \frac{a^2}{r^3}}{1 - a^2} \int_a^1 T r^2 dr + \frac{1}{r^2} \int_a^r T r^2 dr - T \dots [35]$$

At the two surfaces this becomes

$$\left. \begin{aligned} \sigma^*(1) &= \frac{3}{1-a^2} \int_a^1 T r^2 dr - T_3 \\ \sigma^*(a) &= \frac{3}{1-a^2} \int_a^1 T r^2 dr - T_1 \end{aligned} \right\} \dots \dots [36]$$

Alternate equations for the stresses can be obtained as for the cylinder and plate

$$\sigma^*(1) = -\frac{3}{1-a^3} \left\{ \int_0^1 [\beta T(1) + a\beta' T(a)] dr - a\beta' T_a' r - \int_a^1 T(r,0)r^2 dr \right\} - T(1) \quad \dots [37]$$

$$\sigma^*(a) = \sigma^*(1) + T(1) - T(a)$$

Discussion

FRANK KREITH.⁴ The authors have presented a useful method for computing transient thermal stresses and their technique yields values for maximum thermal stresses in a hollow cylinder which agree closely with the results of more accurate solutions. The boundary conditions selected for the sample problem provide, however, for a relatively large thermal resistance at the surface so that no severe temperature gradients occur at small values of time in the vicinity of the surface. Such problems are encountered when combustion is initiated in various jet devices or in firing guns. To determine the thermal stresses a short time after the wall temperature undergoes a sudden and rapid change

⁴ Associate Professor of Mechanical Engineering, Lehigh University, Bethlehem, Pa. Assoc. Mem. ASME.

requires a large number of points near the surface if the collocation method is applied directly to the differential equations. An alternate procedure for such cases has been suggested by F. Erdogan⁵ and has been used with considerable success.⁶

Using Laplace transforms, the thermal problem can be solved in the transform plane (either exactly or by approximate methods) and the Laplace transforms of the stresses can be calculated directly. For small values of time the inverse transforms can be obtained without difficulty by using asymptotic expansions of the stresses in the transform plane to find the inverse transforms.

AUTHORS' CLOSURE

The authors wish to thank Professor Kreith for his comments. It is pointed out in the paper that, for the case of very steep temperature gradients, more closely spaced stations may be needed in the vicinity of these temperature gradients. Under such conditions, the method suggested by Professor Kreith may indeed be helpful.

⁵ PhD thesis by F. Erdogan, Lehigh University, Bethlehem, Pa., in preparation.

⁶ "An Investigation of Thermal Stresses With Applications to Hollow Cylinders," Frankford Arsenal Interim Report, DA-316-034-ORD-1658, June, 1955.



Fig. 1 Variation of normalized stress with normalized time for a hollow cylinder with a surface thermal resistance

Figure 1 shows the variation of normalized stress with normalized time for a hollow cylinder with a surface thermal resistance. The curve starts at 1.0 for $\tau/a^2 = 0$ and decreases monotonically, approaching 0 as τ/a^2 increases. The y-axis is labeled σ/σ_0 and ranges from 0 to 1.0. The x-axis is labeled τ/a^2 and ranges from 0 to 1.0. The curve is labeled σ/σ_0 and τ/a^2 .

The authors wish to thank Professor Kreith for his comments. It is pointed out in the paper that, for the case of very steep temperature gradients, more closely spaced stations may be needed in the vicinity of these temperature gradients. Under such conditions, the method suggested by Professor Kreith may indeed be helpful.

... the ... of the ...

... the ... of the ...

... the ... of the ...

$$\begin{aligned} & \dots \\ & \dots \\ & \dots \end{aligned}$$

... the ... of the ...

$$\dots$$

... the ... of the ...

$$\dots$$

Discussion

... the ... of the ...

A Survey of Aerodynamic Excitation Problems in Turbomachines

By A. SABATIUK¹ AND F. SISTO,¹ WOOD RIDGE, N. J.

The important blade-excitation phenomena in turbomachines are reviewed with respect to the theory extant in the literature and with respect to typical experimental results. The mechanisms of flutter, forced excitation, and rotating stall are discussed broadly and the importance of subharmonic resonance in turbine blades is introduced. Finally, general topics worthy of further consideration are enumerated and avenues for future research are delineated.

INTRODUCTION

THE study of aeroelastic problems dates from the late 1920's when Birnbaum, Wagner, and Glauert made the fundamental, pioneering contributions. Since that time the field, as applied to aircraft structures, has grown in scope and complexity, attesting to the stimulus received from the ever-increasing problems encountered in the industry. An excellent bibliography is given in reference (1).²

During the past decade a considerable body of literature has come into existence concerning the aeroelastic problems of turbomachine blading. As with the airplane-wing problem, this growing attention has been demanded by industrial problems of the first magnitude. Before launching into this brief review of the subject at its present stage of development, it would be well to define briefly the various categories into which the excitation phenomena are usually divided.

Under certain combinations of flow conditions and blade structural properties it is possible for turboblades to execute self-excited and self-sustained vibrations. Since these vibrations may arise with completely uniform and time-invariant flow, they satisfy the criterion of self-excitation; a periodic process is generated from a nonperiodic source of energy. The generic name of this class of phenomena is "flutter."

Under specific conditions of flow and cascade geometry it is also possible for self-oscillations of the fluid to take place. Since blade flexibility is not required to initiate or sustain this phenomenon the mechanism is essentially distinct from flutter. The flow nonuniformities once being set up in a turbomachine or in a cascade, it is possible for these periodic pulsations to buffet the blades to resonance, provided the frequency of the excitation and some blade natural frequency are consonant or harmonic. The fluid oscillations are termed propagating, or "rotating," stall.

The third classification is the usual or conventional forced excitation due to the periodic passage of the turboblades through a disturbance in the air stream. The situation can only be achieved

artificially in a single cascade, but in an actual turbomachine the disturbances may arise out of a variety of causes. A particularly interesting case, for example, is afforded by the passage of an uninstalled blade through the rotating-stall disturbances generated by another stage.

A brief consideration will reveal that there are, of necessity, interactions among the phenomena. A schematic block diagram of possible first-order interactions is displayed in Fig. 1. For emphasis two specific mechanisms are traced out with separate legends.

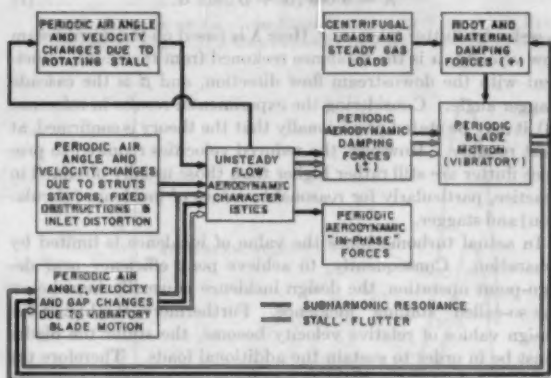


FIG. 1 SCHEMATIC DIAGRAM OF AERODYNAMICALLY EXCITED BLADE-VIBRATION PHENOMENA

FLUTTER

Potential Flows. As is well known from classical unsteady aerodynamics, the type of aeroelastic instability known as flutter can occur with completely potential flow. Considering a single wing, or blade, it is known (2) that in order for this unstable situation to arise there must be coupling between two degrees of freedom, at least for subsonic flow. It has been fairly well demonstrated, by a variety of methods (3, 4), that conventional turboblade vibrations are not excited by this mechanism. The required air-stream velocity is too high.

Owing to the different geometry encountered upon considering a blade in cascade, it was thought for a time that interference effects among the fluttering blades in the cascade could contribute to a realistic lowering of the critical value of the so-called reduced velocity $\lambda = V/(\omega b)$. Here V is air-stream velocity, ω is the flutter (circular) frequency, which is always close to the blade natural frequency, and b is the blade semichord. However, recent theoretical (5, 6) and experimental (7) studies have shown that the pure interference effects, due to vibration of neighboring blades, do not alter the nonstationary aerodynamic reactions sufficiently to account for the lowered critical speeds actually encountered in practice. Furthermore, when only the "interference effect" is considered, the flutter phenomenon still depends on coupling between the torsional and bending degrees of freedom. In practice, vibratory motion is observed to be predominantly in a single mode, bending, or torsion. The theoretical investigations, how-

¹ Project Engineer, Wright Aeronautical Division, Curtiss-Wright Corporation.

² Numbers in parentheses refer to the Bibliography at the end of the paper.

Contributed by the Aviation Committee and presented at a joint session of the Aviation Division and American Rocket Society at the Diamond Jubilee Semi-Annual Meeting, Boston, Mass., June 19-23, 1955, of THE AMERICAN SOCIETY OF MECHANICAL ENGINEERS.

NOTE: Statements and opinions advanced in papers are to be understood as individual expressions of their authors and not those of the Society. Manuscript received at ASME Headquarters, March 29, 1955. Paper No. 55-SA-40.

ever, have been confined to compressor-type stagger (which is called positive.) Actually, turbine stagger should also be investigated before interference flutter is completely written off.

Another effect, obtained only in cascade flow, and which has received some consideration, may be termed the nonuniform-flow-field effect. The alteration of the ordinary nonstationary aerodynamic reactions arises out of the motion of the blades in a flow field which has a gradient of the oncoming flow velocity in the direction normal to the blade chords. This gradient is, in turn, due to the steady portion of the circulation associated with each blade in the cascade. Consequently, this might equally well be termed an incidence effect. Theoretical investigations of this effect are several in number (8, 9, 10), with experimental confirmation being rather meager (8). All of these investigations have indicated that a single-degree-of-freedom flutter is indeed possible. (Bending is usually considered.) A rather simple criterion has been developed by Söhngen (10), valid for small gap/chord ratios. For a pure bending motion he finds that λ must exceed

$$\lambda = 8 \cos(\alpha + \beta) / \sin \alpha \dots \dots \dots [1]$$

in order for flutter to occur. Here λ is based on the downstream flow velocity, α is the incidence reckoned from the chord, coincident with the downstream flow direction, and β is the cascade stagger angle. Considering the experimental results in reference (8), it may be stated provisionally that the theory is confirmed, at least roughly. However, the reduced velocities required to produce flutter are still rather higher than those usually obtained in practice, particularly for reasonable values of incidence (circulation) and stagger.

In actual turbomachines the value of incidence is limited by separation. Consequently, to achieve peak efficiency near design-point operation, the design incidence is usually kept below the so-called "stalling" incidence. Furthermore, the higher the design values of relative velocity become, the stiffer the blades must be in order to sustain the additional loads. Therefore the value of λ does not increase as rapidly as one might suppose with increasing design values of the air-stream velocity. In fact, for a particular comparison of two stages, the one with the higher relative velocity might very well have the lower λ due to a larger semichord b .

Equation [1] is plotted in Figs. 2 and 3 to indicate the combinations that produce critical reduced velocities. It is significant that turbine stagger appears to be far less susceptible to flutter than compressor stagger. In contradiction of this apparent tendency, Shioiri (9) has investigated, by simplified model, the susceptibility to flutter of three staggers ($0, \pm\pi/4$) at values of λ satisfying Equation [1] and found only the turbine stagger ($\beta = -45^\circ$) to have a critical flutter velocity. If V_m is the vector mean velocity through the cascade, it can be shown that Shioiri's requirements that λ (based on V_m) = 10, and steady circulation/pitch = $0.8 V_m$ are completely equivalent to Equation [1]. It appears that there is more to be learned about this particular effect before its importance can be completely assessed.

At part-speed operation the situation is somewhat changed. The forward stages in a compressor, for example, tend toward higher incidence as the machine speed is decreased since the axial component of the through-flow velocity decreases faster than the peripheral blade speed. Consequently, larger incidences are attained, but only at the expense of reduced relative velocities, and consequently reduced λ 's. The operating line of such a stage tends to parallel a line of constant β in Fig. 2. Once the incidence for separation is trespassed the flutter mechanism is altered radically. This point is taken up again in the next section. However, in the transition region near actual separation the nonuniform-flow-field effect may be of some importance.

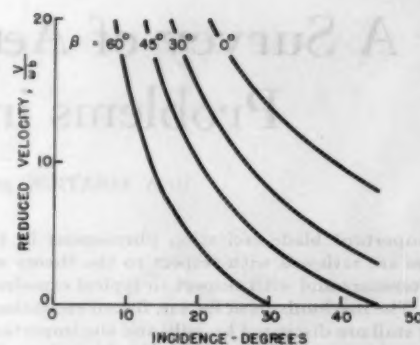


FIG. 2 PURE BENDING COMPRESSOR-BLADE FLUTTER CRITERION ACCORDING TO REFERENCE (10). VALID FOR SMALL GAP/CHORD

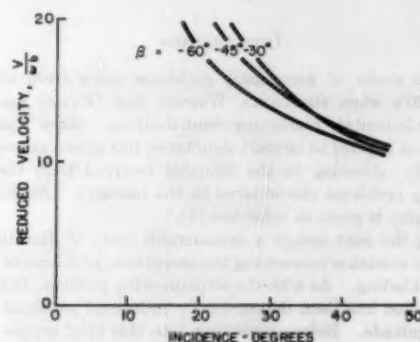


FIG. 3 PURE BENDING TURBINE-BLADE FLUTTER CRITERION ACCORDING TO REFERENCE (10). VALID FOR SMALL GAP/CHORD

Stalled Flows. The alterations in the flutter mechanism (chiefly the radical lowering of the reduced velocity) which occur when an airfoil approaches stalling incidence have been studied for some time. As far back as 1936 Studer (11) reported an exhaustive series of tests demonstrating the major features of single-wing stall flutter. He rightly surmised that the change in behavior was due to the periodic breakaway and reattachment of the flow during the cycle of oscillation. Considering the bending degree of freedom for concreteness, it was thought for some time that a certain phase lag between the instantaneous incidences at reattachment and at separation was necessary to sustain the single-degree-of-freedom vibratory motion (11, 12). It appears, however, that in so far as bending flutter is concerned, a negative slope of the normal force versus incidence curve has a more direct bearing upon the susceptibility to flutter (13, 14). Pearson (15) reports excellent correlation with actual regions of instability in the normal force versus incidence plane by using the negative-slope criterion.

In order to examine some of the implications of the modern stall-flutter approach as set forth in references (13) and (14), some selected experimental results may be exhibited here. Initially, it is important to test the very concept of the normal force coefficient under dynamic conditions. Fig. 4 displays the results of one such investigation where the steady component of the normal force coefficient of cascaded cantilever compressor blades has been measured during flutter in a wind tunnel. The data for 500 and 600 fps air velocities correlate fairly well on the coefficient basis. It is not meant to imply that this coefficient does not change with large Mach-number variations. However, away from the choking

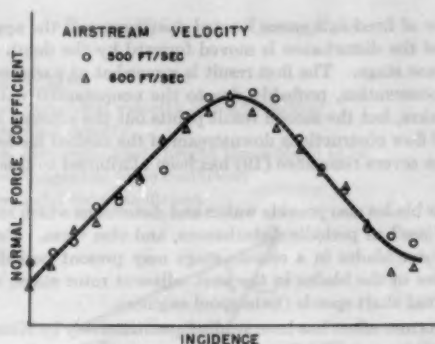


FIG. 4 MEASURED STEADY COMPONENT OF NORMAL FORCE COEFFICIENT OF A FLUTTERING BLADE
(Conventional compressor-blade sections arranged in cascade tunnel and supported as cantilevers.)

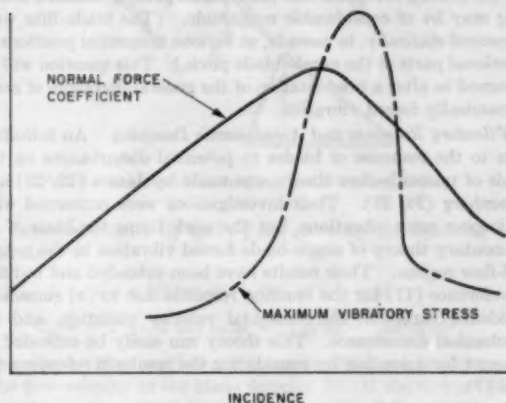


FIG. 5 VIBRATORY STRESS SUPERIMPOSED ON FIG. 4

condition, it is expected that the coefficient changes will be small for moderate changes in velocity or Mach number.

In Fig. 5 the simultaneously observed vibratory stresses are superposed on the normal force-coefficient curve. The critical dependence of this bending flutter on the slope of the normal force curve is at once apparent.

Figs. 6, 7, and 8 illustrate the effect on the flutter of typical cascaded compressor blades of (a) leading-edge radius, (b) stagger, (c) blade spacing. In each case the only quantity which was varied, aside from incidence, was the parameter whose effect was being studied. The vibratory stresses are the maximum for a complete range of incidence with other parameters held fixed. Since the maximum vibratory amplitude (or stress) is probably directly related to the maximum negative slope of the normal force curve (13, 15), these figures give a good indication of how the magnitude of this slope varies with the quantities being studied.

Full-scale engine and compressor-rig confirmation of the salient features of stall flutter are contained in reference (14) and other unpublished results. Rather than use the normal force versus incidence plane, it is more convenient to correlate high vibratory stress in the pressure-coefficient versus flow-coefficient plane. The latter quantities are usually calculated in conventional turbomachine tests, and a correspondence between the two sets of quantities can be established if desired.

Future Research. The force-coefficient approach which has been discussed in the foregoing might be termed the quasi-steady

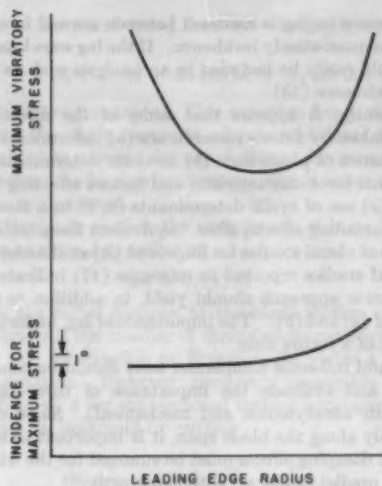


FIG. 6 EFFECT OF LEADING-EDGE RADIUS ON VIBRATORY FLUTTER STRESS OF CASCADDED COMPRESSOR BLADES IN A WIND TUNNEL

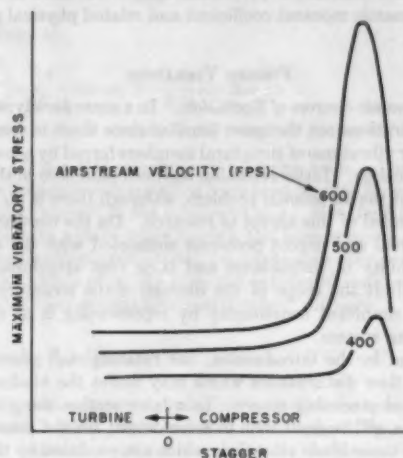


FIG. 7 EFFECT OF CASCADE STAGGER ON FLUTTER STRESS INDUCED IN CANTILEVER COMPRESSOR BLADES MOUNTED IN WIND TUNNEL

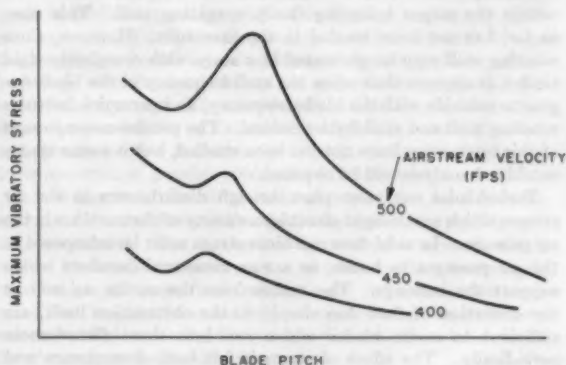


FIG. 8 EFFECT OF GAP/CHORD RATIO ON VIBRATORY STRESS DEVELOPED DURING FLUTTER OF CANTILEVER COMPRESSOR BLADES IN WIND TUNNEL

approach, since no lag is assumed between normal force and instantaneous quasi-steady incidence. If the lag were known, however, it could easily be included in an analysis such as that presented in reference (13).

Consequently, it appears that some of the directions that should be taken by future research are (a) determination of size and importance of phase lags, (b) accurate determination of dynamic normal force characteristic and factors affecting this characteristic, (c) use of cyclic determinants (6, 9) in a theory to account for cascading effects, after "equivalent linearization" (16), and (d) use of visual studies for improved physical understanding. Some visual studies reported in reference (17) indicate that the interferometric approach should yield, in addition to (d), good estimates of (a) and (b). The importance of lag, under (a), will be the subject of a future note.

Engine and full-scale component tests should be conducted to determine and evaluate the importance of three-dimensional effects (both aerodynamic and mechanical). Since conditions vary radially along the blade span, it is important to know how forcing and damping effects must be summed for the whole blade in order to predict flutter amplitude correctly.

In concluding this section it seems safe to remark that should torsional flutter prove to be troublesome in turbomachines, a similar theoretical and experimental attack will have to be made on the dynamic moment coefficient and related physical parameters.

FORCED VIBRATION

Aerodynamic Sources of Excitation. In a sense aerodynamically forced vibrations are the most familiar since there is some background for vibrations of structural members forced by other physical mechanisms. Little attention has been paid here to the "elastic" side of the aeroelastic problem, although there is no belittlement intended of this aspect of research. On the contrary, there are very real and urgent problems connected with the strength and durability of turboblades and their root attachments. In order to limit the scope of the discussion the structural model has been simplified consistently by representing it as a simple mass-spring system.

As noted in the introduction, the rotating-stall phenomenon generates flow disturbances which may buffet the blades in succeeding and preceding stages. In a later section the generation mechanism will be dealt with in more detail; for the present consideration those blade vibrations which are produced by these disturbances may be treated like any other forced vibrations once the magnitudes of the disturbances are known. A special case which requires a separate treatment is the vibration of the blades within the stages initiating the propagating stall. This case, so far, has not been treated in the literature. However, since rotating stall may be generated in a stage with completely rigid blades, it appears that when the stall frequency of the blade begins to coincide with the blade frequency, an interaction between rotating stall and stall flutter occurs. The precise consequences of this interaction have not yet been studied, but it seems that a combined analysis will be required.

Turboblades may also pass through disturbances in the air stream which are brought about by a variety of obstructions in the air passage. In axial-flow machines struts must be interposed in the air passages to house, or act as, structural members which support the bearings. The wakes from the struts, as well as the distortion of flow due simply to the obstruction itself, are sufficient to excite blades which run into these disturbances periodically. The effect of struts is felt both downstream and upstream. Schöngen (18) has shown that an upstream potential disturbance cannot pass through a row of fixed inlet vanes. On the other hand downstream potential disturbances are amplified

by a row of fixed exit vanes located upstream, and the apparent source of the disturbance is moved forward by the depth of the guide-vane stage. The first result is somewhat at variance with actual observation, probably due to the nonpotential nature of strut wakes, but the second result points out the extreme importance of flow obstructions downstream of the excited blades. At least one severe resonance (19) has been attributed to this latter cause.

Stator blades also provide wakes and distortions which rotating blades "see" as periodic disturbances, and vice versa. Furthermore, rotor blades in a certain stage may present periodic disturbances to the blades in the next adjacent rotor stage, due to differential shaft speeds (twin-spool engines).

The former effect has been studied quantitatively by Kemp and Sears (20) for potential flows. In compressor-blade configurations they found the fluctuating component of the lift to be rather small, up to 18 per cent of the steady lift in extreme cases. On the other hand, some static tests in reference (21) indicate that the fluctuating lift on turbine-rotor blades passing behind a nozzle ring may be of considerable magnitude. (The blade lifts were measured statically, in cascade, at various tangential positions of fractional parts of the nozzle-blade pitch.) This question will be returned to after a brief citation of the general literature of aerodynamically forced vibration.

Vibratory Response and Aerodynamic Damping. An introduction to the response of blades to potential disturbances on the basis of unsteady-flow theory was made by Isaacs (22, 23) and Greenberg (24, 25). Their investigations were concerned with helicopter rotor vibrations, but the work forms the basis of an elementary theory of single-blade forced vibration in the potential-flow regime. Their results have been extended and codified in reference (17) for the bending response due to (a) sinusoidal incidence variation, (b) sinusoidal velocity variation, and (c) mechanical disturbance. This theory can easily be extended to account for cascading by considering the results in references (6) and (7).

In this respect it may be noted that the major quantity limiting the amplitude of blade vibration, assuming resonance, is the aerodynamic damping. This quantity has long been known for the single blade. Recent theoretical developments (26) indicate that an exact solution of the aerodynamic damping in staggered cascades is at hand. The results of numerical calculations utilizing this theory are anticipated with interest. From the known results for special values of stagger, spacing, and interblade phase angles (5, 6, 27), however, it appears that the aerodynamic damping in the linear or potential-flow range will always be positive. In general, decreased spacing, decreased interblade phase, and decreased λ all tend to lower the aerodynamic damping.

The importance of aerodynamic damping has been pointed out by many investigations (3, 4). Without such damping the majority of blade vibrations would result in nearly instantaneous rupture of the turboblades or their attachments. The reason for this critical behavior is that other forms of damping are exceedingly small. Material damping in conventional materials, with the exception of some promising plastic constructions, is insufficient to limit vibratory amplitudes to safe values. Mechanical damping in the root attachment is difficult to maintain in the presence of a strong centrifugal-force field, particularly over a range of rotational speeds.

Subharmonic Resonance. In order to reveal some features of aerodynamically forced vibrations it is of interest to investigate the fluctuating force on a turbine blade on the basis of the simplest cascade theory. Assuming inviscid, incompressible, two-dimensional flow (see Fig. 9) it is possible, by a simple momentum balance, to show that the force on any blade is given by

$$F_T = q_0 C_T \delta A \quad F_A = q_0 C_A \delta A$$

where

$$q_0 = \frac{1}{2} \rho U^2$$

U = peripheral velocity of blade section

ρ = fluid density

δA = elemental blade height times blade pitch

C_T = tangential force coefficient

C_A = axial force coefficient

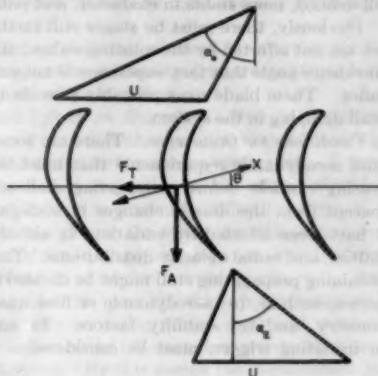


FIG. 9 TURBINE-BLADE CASCADE NOMENCLATURE

The force coefficients C_T and C_A are given by the following expressions

$$C_T = 2[(\tan \alpha_0 + \tan \alpha_1)\phi^2 - \phi]$$

$$C_A = -1 + (2 \tan \alpha_0)\phi + (\tan^2 \alpha_1 - \tan^2 \alpha_0)\phi^2$$

where ϕ is the "flow coefficient," the ratio of the axial component of the flow velocity to the blade velocity U . If the turbine disk turns at a constant speed, the blade force in the θ -direction is proportional to

$$C_\theta = C_T \cos \theta + C_A \sin \theta$$

θ is the direction of blade vibration at the radial station under consideration.

Assume now that disturbances in the velocity pass periodically through the blades, α_1 remains substantially unchanged due to the preceding stator blades, and α_2 (a relative gas angle) also remains substantially unchanged. Consequently, adopting the quasi-steady approach (disregarding unsteady-flow time lags between force and flow angles), the derived value of C_θ can be used as the forcing function in terms of ϕ . For specific blade geometry, in fact, one can write

$$F_\theta = q_0 \delta A (a_0 + a_1 \phi + a_2 \phi^2)$$

where the a 's are constants. For a simple cosinusoidal variation in ϕ , i.e.

$$\phi = \phi_0 (1 + \sigma \cos \omega t)$$

where ω is the frequency of the ϕ variation and t is time, a strong second harmonic component in the forcing function may be expected. In fact, applying this driving term to a simple mass-spring system, one obtains

$$m \ddot{x} + m \omega_0^2 x = q_0 \delta A \{ [a_0 + a_1 \phi_0 + a_2 (1 + \sigma^2/2^2) \phi_0^2] + \sigma [a_1 \phi_0 + 2a_2 \phi_0^2] \cos \omega t + \sigma^2 [1/2 a_2 \phi_0^2] \cos 2\omega t \}$$

where m is the blade mass, x is the vibratory displacement, and ω_0 is the blade natural frequency. Assuming the rotor inertia is

so great that the wheel speed does not change, it is possible to write simply

$$x + \omega_0^2 x = A_0 + A_1 \cos \omega t + A_2 \cos 2\omega t \dots \dots [2]$$

where the A 's are constants. This equation has a simple solution. When the blade begins to vibrate additional terms in x must be added to account for aerodynamic damping. For the present purpose the blade-vibratory velocity is ignored and only its position is considered.

Due to the blade motion the variation in ϕ is no longer dependent on ωt alone, but rather on

$$\omega t + x/(R/z)$$

where R is the radial distance to the blade section under consideration and z is the number of disturbances per revolution.

Making this substitution in Equation [2] yields a distinctly nonlinear equation. However, since it is reasonable to expect that $|x/(R/z)| \ll 1$ for conventional turbine arrangements, the problem may be linearized by putting

$$\sin \frac{x}{R/z} = \frac{1}{2} \sin \frac{2x}{R/z} = \frac{x}{R/z}$$

$$\cos \frac{x}{R/z} = \cos \frac{2x}{R/z} = 1$$

and so arrive at

$$x + \left(\omega_0^2 + \frac{A_1}{R/z} \sin \omega t + \frac{2A_2}{R/z} \sin 2\omega t \right) x = A_0 + A_1 \cos \omega t + A_2 \cos 2\omega t \dots \dots [3]$$

Equation [3] is a Hill equation with forcing term. The properties of the homogeneous equation have been studied for particular forms of the "ripple" in the coefficient of x . For the Hill-Meissner equation (a square-wave ripple), the homogeneous equation exhibits subharmonic resonance; i.e., resonance may occur when ω_0 is a submultiple of ω . In fact, the permissible values of ω for the so-called "heteroparametric excitation" (16) are

$$\frac{\omega_0}{\omega} = \frac{1}{2}, \frac{2}{3}, \frac{3}{4}, \dots; \frac{1}{4}, \frac{2}{5}, \frac{3}{6}, \dots; \frac{1}{6}, \frac{2}{7}, \frac{3}{8}, \dots$$

It would seem extremely profitable to study solutions of Equation [3] with forcing terms included since apparently some turbine-blade vibrations can be correlated on the basis of subharmonic resonance.

Such vibrations have been difficult to correlate, in the past, since the decreasing pressure gradient through the blade passages tends to inhibit separation of the flow (except perhaps in small local regions). Furthermore, the large number of nozzle blades has usually precluded the coincidence of the rotor-blade natural frequency with the fundamental, or a harmonic, of the nozzle-excitation frequency. The consideration of subharmonics greatly alters the possibilities of excitation. However, remedial action in a specific turbine is extremely difficult to foresee due to the dense spectrum of possible subharmonic frequencies.

Future Research. In citing items of importance for future research in forced vibrations the elastic aspects of the problem are to be considered. The mechanical behavior of a tapered, offset, twisted blade with various types of root fixation in a centrifugal-force field is still imperfectly understood. A better understanding of the "transfer function" of such blades would be extremely welcome. This remark, of course, is of equal importance in all the phenomena discussed in this paper.

In so far as aerodynamic forcing is concerned, the remarks at the conclusion of the Flutter section apply here as well. In addition, the aerodynamic structure of strut and blade wakes

should be explored, and the response of blades to such nonpotential disturbances should be investigated.

Full-scale component-rig resonance studies (14) have confirmed the general features of aerodynamically forced vibrations. It is equally important that such tests now be directed to a study of the decay of wakes and potential disturbances with axial distance. Theory indicates that the potential disturbance decays exponentially (18), but quantitative confirmation is lacking. Due to the mechanical requirements involved, resonance testing is most effectively accomplished on rotating machines.

ROTATING STALL

Definition. Rotating or propagating stall is a phenomenon which manifests itself in the components of turbomachinery as regions of stalled or separated flow rotating at some fraction of component speed and in the same direction. Although compressor-surge studies (28) have indicated that the phenomenon accompanies surge, its behavior during such operation is not pertinent to the discussion since continuous surge operation cannot be tolerated. On the other hand, rotating stall accompanying surge-free performance has been tolerated probably since the operation of the first centrifugal compressor. To be more specific, propagating stall is the successive stalling and unstalling of the blades in a cascade when the mean flow approaching the cascade is at an incidence angle which is near or beyond the stall point. A triggering action, perhaps the wake of some upstream blade or strut, chokes one or more passages of a blade row. This results in a flow spill from the passage entry which is choked to the passages on either side as shown in Fig. 10. The blades immediately

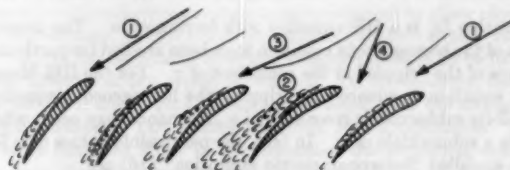


FIG. 10 STALL PROPAGATION

- 1 Mean approach velocity relative to cascade (near stall incidence angle).
- 2 Passage inlet—right blade has stalled and choked the passage causing flow spill at (2) in both directions.
- 3 Local approach velocity relative to blades on left (increased incidence angle).
- 4 Local approach velocity relative to the blades on the right (reduced incidence angle). Stall propagates from right to left.

to the left become subjected to higher incidence angles, separation, consequent stall, and a perpetuation of the process. At the blade to the right, the spill flow tends to reduce the incidence angle, stabilize the flow, and minimize the tendency for continuation of the process. Thus the stall propagates along the cascade from right to left. In the rotating machine this phenomenon is called rotating stall and the flow spill is tangential rather than radial. The process is thoroughly described in references (28) and (29).

The flow process involved can be termed unsteady only within the individual blade passages of the affected blade rows. Across any flow annulus throughout the length of the machine the flow rate is constant with time. In an axial-flow multistage machine the resulting rotating wakes affect the downstream blade rows, while the spill process propagates a measurable effect upstream. However, it is usually difficult to detect the existence of the phenomenon some distance upstream of the inlet-blade row or downstream of the exit-blade row.

In considering the axial-flow multistage machine, there exist at least two important types of blade rows (and their respective flow processes) which must be studied. One type is the initiating (or generating) blade row which has been described briefly in this

section. The other type of blade row is one which is operating at an incidence angle below the stall, as is usually the case with some downstream stage, and which is subjected to the rotating wakes of the generating blade row. The operating incidence angles are intermittently increased to the stall value as the wakes rotate past the individual blades. The process then becomes very similar to that of the generating blade row, and the result may be a further generation of rotating stall perfectly synchronized with the original stall. This means that the stall pattern becomes well defined, more stable in character, and reinforced in amplitude. Obviously, there must be stages still further downstream which are not affected by the rotating wakes; that is, the increase of incidence angle that they experience is not sufficient to stall the blades. These blade rows probably provide the major portion of stall damping in the system.

Necessary Conditions for Occurrence. There are some definite geometric and aerodynamic requirements that must be fulfilled by an operating cascade before propagating stall will occur. This is apparent from the drastic changes in stall-pattern behavior that have been affected by variations in airfoil sections, cascade solidities, and radial velocity distributions. The requirements for obtaining propagating stall might be divided into three basic categories, such as, (a) aerodynamic or flow qualities, (b) cascade geometry, and (c) stability factors. In addition, a stimulus, or initiating trigger, must be considered a necessary factor.

The major flow qualities break down primarily into the magnitude of the blade relative flow velocity and the cascade-incidence angle. Reference (28) indicates that a lower limit of velocity exists below which a propagating stall is not generated. It is reasonable to assume that an upper limit of velocity exists at a value which chokes all the passages of the cascade making it impossible for the spill, or transport mechanism, to function. This implies that for a given cascade there is a limited range of relative velocity within which propagating stall can be generated. This range may or may not vary with changes in incidence angle. The incidence-angle requirements involved in the definition of propagating stall are rather difficult to analyze in detail. Generally speaking, the only requirement is that the incidence angle be at a value which lies near, or within, the aerodynamically stalled operating region of the cascade. There is no indication that an upper limit to incidence angle exists (that is, a value of the incidence beyond which propagating stall can no longer be generated). The stall point of a cascade is a function of the detailed geometry of the blades and the blade-row assembly as well as boundary-layer and free-stream flow conditions. Operating Reynolds number, compressibility effects, and flow turbulence level are, therefore, highly influential factors. Sears (30) and Stenning (31) have discussed some of these factors in proposing explanations for the behavior of rotating stall.

The cascade geometry is extremely important in determining whether propagating stall is possible. Blades or vanes capable of providing a lift force must be arranged in a somewhat uniform and continuous, though not necessarily endless, cascade. The blades must be packed so closely that the aerodynamic performance of the cascade does not reflect directly the isolated airfoil performance of the individual blades. In other words, if the spill or flow-transport mechanism is to function, the blade-passage flows must be sensitive to the stall, or flow separation, of the blades that form the passage. Iura and Rannie (29) demonstrated that reducing the solidity, which was accomplished by removal of alternate blades in each blade row, virtually eliminated the multiple rotating stall pattern. This would imply that there is a minimum value of solidity below which propagating stall cannot occur in a cascade of a particular blade section and stagger. Airfoil geometry appears to be another highly significant factor.

Huppert and Benser (32) reported a stage in which rotating stall did not exist. The unusual feature of the stage was the extremely high camber of the tip section. Iura and Rannie reported changes in the radial location of the propagating stall pattern that were affected primarily by blade-section alterations.

Stability factors for rotating stall are provided by uniformity of the pressures, the mass-flow distribution, and the symmetry in the geometry of the passage parts. Almost every imaginable turbomachine component is designed with tangential uniformity in its blade rows, flow ducts, inlet and exit spinners, and various support struts.

An initiating stimulus, required for starting the spill mechanism, is supplied by the wakes of upstream struts or blades, or by the turbulence of the inlet flow.

Resultant Effects on Operation. Rotating stall provides desirable as well as undesirable qualities that influence the operating characteristics of a turbomachine component. Experimental results indicate that evaluation of the effects of stall on aerodynamic performance is extremely difficult. First, it is apparent that under the proper throttling conditions certain multistage units have exhibited surge-free and over-all stall-free performance despite operation of one or more stages in stall. Rotating stall probably made this possible through its tangential transport mechanism. By obviating radial flows and minimizing consequent disruption of the full-span flow process there was no serious loss in efficiency. By this means the phenomenon has provided a very advantageous extension of the operating region beyond the stall-limit line that apparently should have been associated with the machine.

On the other hand, rotating stall has exhibited the ability to promote over-all compressor stall and surge by causing downstream stages to reinforce a stall pattern which was instigated by only one or two upstream blade rows. This effect limits the peak pressure-ratio capabilities of the compressor at a particular equivalent speed. The disturbing factor is that the beneficial condition might occur at one speed while the harmful situation might occur at another operating speed of the same machine. This indicates that rotating stall may be extremely influential in establishing the surge or stall-limit line of the component.

In addition to its effects on aerodynamic performance, rotating stall has a very detrimental effect on the life of physical parts. Stall patterns provide the nearby stages with an environment of fairly well-defined periodic pulses of appreciable amplitude, so that excitation forces are available to vibrate the blades. The frequency spectrum of rotating stall is so vast and complete that it is virtually impossible to avoid resonance with blade natural frequencies. This resonant excitation, as discussed earlier, can cause excessive vibratory stresses in the vanes of stationary blade rows as well as in rotor blades.

Samples of Behavior. The behavior pattern of rotating stall is quite complex, but when the phenomenon is coupled with multistage operating characteristics and engine-geometry effects, it becomes virtually impossible to segregate the detailed influences and traits for study. The cascade and single-stage tests of Emmons, Pearson, and Grant (28), and the three-stage tests of Iura and Rannie (29) were quite successful in providing insight into the nature of the phenomenon by minimizing the number of unrelated variables. The following paragraphs summarize the more prominent features of stall behavior reported in the literature.

The two-dimensional plane cascade tests (28) indicate that an endless blade row is not a requirement for occurrence of propagating stall. As long as the blade-row geometry is not interrupted, stall propagates across the cascade from one end to the other and then repeats the same process by starting each time at the original end of the cascade. The direction of propagation is always the

same and the over-all flow rate is constant with time. Fig. 11 indicates that propagation rates (measured by hot-wire anemometers at the inlet and exit of the cascade) are the same and that the measured patterns are synchronized. The stall region encompasses one, two, three or more blades simultaneously, providing a greater amplitude downstream than upstream. There is an indication that a limit of through velocity exists below which the intermittent stall does not occur. There is obviously an upper limit to this velocity, since eventually all blade passages are choked and the flow-spill mechanism cannot function. Probably the most significant observation to be made is that one blade row of rigidly supported blades is sufficient to generate a well-defined propagating stall pattern.

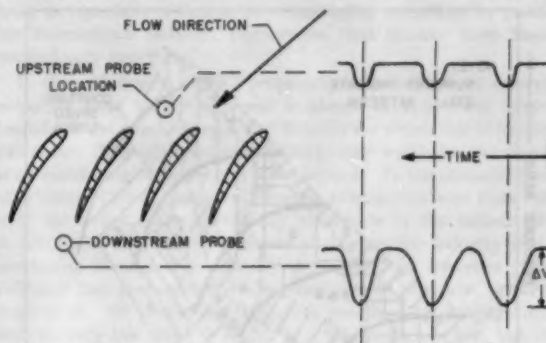


FIG. 11 SCHEMATIC INDICATION OF UPSTREAM AND DOWNSTREAM EFFECTS OF PROPAGATING STALL IN A CASCADE

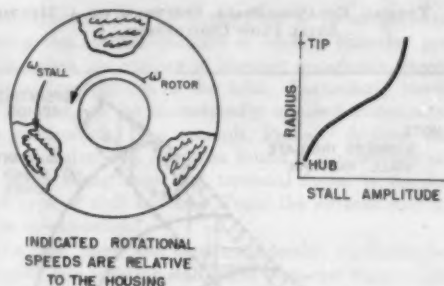


FIG. 12 TYPICAL THREE-CELL ROTATING STALL PATTERN AND RESULTANT RADIAL AMPLITUDE DISTRIBUTION

Single-stage machines add some features to the behavior pattern by virtue of their three-dimensional nature. Radial differences in blade-section geometry, in solidity, and in operating incidence angles force a selective process which makes a particular propagating pattern dominate each specific operating point (i.e., a given speed, weight flow, and pressure ratio). Radial flows caused by centrifugal effects and annulus variation, in addition to tip clearance and shrouding effects, complicate the isolation of a pure rotating-stall manifestation still further.

Generally speaking, the existence of an endless cascade with a finite circumference forces the stall pattern into an arrangement of evenly spaced stall regions, or cells, around the annulus. Fig. 12 indicates such a typical pattern. There is a measurable radial depth and tangential breadth of the stall regions which, along with the number of cells, change with the operating point.

Rotating stall in multistage units possesses all the attributes of the single-stage stall in addition to some further complicating features. The selection of the one dominating stall pattern must rest on a greater majority of blade sections, solidities, incidence

angles, etc. Conceivably there are many instigating combinations just as there are many damping factors. Damping is accomplished not only by aerodynamically unstalled stages but also by combinations of blade rows desiring to instigate a different rotating stall pattern, i.e., a pattern of more or fewer stall regions with some other frequency. This creates an instability of pattern which causes an intermittent jumping or hunting between two stall patterns. For instance, reference (29) indicates that the rotating stall can alternate between a three-stall pattern and a four-stall pattern at a fairly rapid rate while the unit is operating at one steady-state condition. A spectrum of the stall patterns that are possible in a multistage axial-flow compressor is shown in Fig. 13.

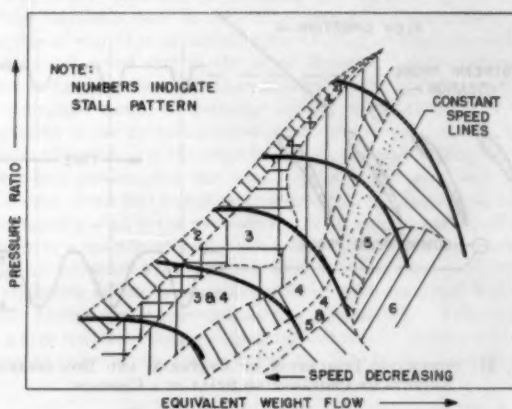


FIG. 13 TYPICAL ROTATING-STALL SPECTRUM OF A MULTISTAGE AXIAL FLOW COMPRESSOR

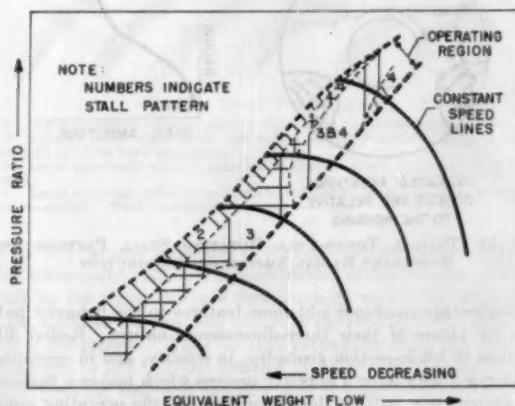


FIG. 14 LIMITED STALL SPECTRUM RESULTING FROM APPLICATION OF COMPRESSOR OF FIG. 13 IN A GAS-TURBINE ENGINE

Gas turbine-engine stall patterns exhibit the same characteristics that were described for the stall pattern of the multistage unit with two major differences. First, the range of occurrence and the type of stall pattern are limited to the operating line or operating region of the engine; that is, a good deal of the spectrum that might be found in component tests is eliminated completely because the engine will not operate at the necessary conditions. Fig. 14 indicates the limited spectrum of stall associated with a gas-turbine engine.

An engine can exhibit slightly new and different characteristics because it has additional possible sources of stimuli or excitation.

Factors such as shaft critical speeds, engine-order vibrations, combustion roughness, etc., may contribute vibration excitation, and passage geometry might provide some changes in flow conditions, all of which could have consequent effect on the rotating-stall behavior.

Proposed Further Studies of the Phenomenon. In order to control or eliminate completely the rotating-stall phenomenon in turbomachinery it is essential to determine the finite limits of the various factors which comprise the necessary and sufficient conditions for occurrence. Airfoil-geometry factors, cascade-geometry limits, Reynolds number, and flow qualities must be recognized and catalogued so thoroughly that the phenomenon can be eliminated completely by removing any one of the requirements. Another noteworthy consideration is that complete removal of stall is not always necessary. A substitution of one pattern for another may be an excellent method for eliminating a bad resonance condition or a poor performance characteristic.

Such a knowledge of the stall behavior may provide a simple means for improving the designs of gas turbines without resorting to the complexity of variable geometry, bleed, etc. It appears that the problems of surge and accelerating characteristics of turbomachines will not be resolved without a thorough understanding of this elusive flow process. What can be accomplished in this direction is not known, but mastery of the phenomenon is not inconceivable.

CONCLUSIONS

A survey of the important aerodynamic excitation phenomena that are known to exist in turbomachines has been presented in rather general form. No attempt has been made to establish the relative importance of each phenomenon since this is determined by the design and operating condition of the particular machine. Although each phenomenon can occur only within specific limits of geometry and flow conditions, several excitations may exist simultaneously.

Aerodynamic excitation phenomena can decrease aerodynamic performance and penalize seriously the useful life of turboblades. Exceptionally high vibratory stresses may be obtained which, in turn, cause blade failures through fatigue. A thorough understanding of the excitation mechanism is required before these dangerous conditions can be eliminated.

The assessment of detrimental character of a phenomenon must be determined by the vibratory-stress amplitude to which it is capable of buffeting a blade. A study aimed at evaluating the excitation capabilities of the various mechanisms necessarily involves an understanding of the inherent damping factors. Heretofore, the aerodynamic damping has been studied in the linear range. It appears, however, that more attention should now be devoted to the important nonlinear range as well as to the amplitude-limiting features of nonlinear excitation. Mechanical damping, enhanced by unconventional blade and attachment design, may supply additional potent means for minimizing vibration amplitudes.

There is much progress to be made in all phases of the blade-excitation problem. Apparently, there are no signs of saturation in the development of new experimental detection techniques or in the application of advanced analytical procedures. The great advances in gas-turbine design during the past decade are, in a large measure, directly attributable to the development of the aircraft gas turbine where high performance with low weight and small size have been the constant goals. Thus, as performance is improved to meet these requirements and blade loadings increase as a result, it is reasonable to assume that excitation problems will keep pace. The solutions to these problems will come only from increased knowledge and understanding of the details which are schematically portrayed in Fig. 1.

BIBLIOGRAPHY

- 1 "Introduction to the Study of Aircraft Vibration and Flutter," by R. N. Scanlan and R. Rosenbaum, The Macmillan Company, New York, N. Y., 1951.
- 2 "Experimental Aerodynamic Derivatives of a Sinusoidally Oscillating Airfoil in Two-Dimensional Flow," by R. L. Halfman, NACA TN 2465, November, 1951.
- 3 "Vibration Problems in Gas Turbines, Centrifugal and Axial-Flow Compressors," by J. F. Shannon, British ARC R and M No. 2226, March, 1945.
- 4 "The Stress Problem of Vibrating Compressor Blades," by J. R. Schnittger, *Journal of Applied Mechanics*, Trans. ASME, vol. 77, March, 1955, pp. 57-64.
- 5 "Unsteady Aerodynamic Reactions on Airfoils in Cascade," by F. Sisto, *Journal of the Aeronautical Sciences*, vol. 22, 1955, pp. 297-302.
- 6 "A Theoretical Investigation of the Flutter Characteristics of Compressor and Turbine Blade Systems," by Frank Lane and Chih Wang, WADC Technical Report under Contract No. AF 33 (616)-25, 1954.
- 7 "An Investigation of the Flexure-Torsion Flutter Characteristics of Aerofoils in Cascade," by G. M. Lilley, The College of Aeronautics, Cranfield, Report No. 60, May, 1952.
- 8 "Self-Induced Vibrations of Turbo-Machine Blades," by Ch. Belletot and J. L. d'Epina, *Brown-Boveri Review*, vol. 37, October, 1950, pp. 368-376.
- 9 "Flutter in Cascading Blades. I. General Theory and Stability of Pure Bending Flutter," by Junpei Shioiri, Bulletin of the Government Mechanical Laboratory, Tokyo, Japan, No. 3, 1954.
- 10 "Luftkräfte an einem schwingenden Schaufelkranz kleiner Teilung," by H. Söhngen, *Zeitschrift für angewandte Mathematik und Physik*, vol. 4, 1953, p. 267.
- 11 "Experimentelle Untersuchungen über Flügelschwingungen," by H. L. Studer, Mitteilungen aus dem Institut für Aerodynamik, Eidgenössische Hochschule, Zurich, Switzerland, No. 4/5, 1936.
- 12 "Aerodynamic Hysteresis as a Factor in Critical Flutter Speed of Compressor Blades at Stalling Conditions," by A. Mendelson, *Journal of the Aeronautical Sciences*, vol. 16, 1949, pp. 645-652.
- 13 "Stall-Flutter in Cascades," by F. Sisto, *Journal of the Aeronautical Sciences*, vol. 20, 1953, pp. 598-604.
- 14 "The Aerodynamics of Compressor Blade Vibration," by H. Pearson, Proceedings of the Fourth Anglo-American Aeronautical Conference, 1953, pp. 127-162.
- 15 "Cascade Blade Flutter and Wake Excitation," by J. F. W. Parry and H. Pearson, *Journal of the Royal Aeronautical Society*, vol. 58, 1954, pp. 505-508.
- 16 "Non-Linear Mechanics," by N. Minorsky, Edwards Bros., Inc., Ann Arbor, Mich., 1947.
- 17 "Single Degree of Freedom Flutter of Compressor Blades in Separated Flow," by J. R. Schnittger, *Journal of the Aeronautical Sciences*, vol. 21, 1954, pp. 27-36.
- 18 "Durchgang einer Potentialstörung durch einen Leitschaufelkranz," by H. Söhngen, *Ingenieur-Archiv*, Bd. 20, 1952, pp. 13-18.
- 19 "Test Experience With Naval Gas Turbines," by Commander (E) G. F. A. Trewhay, *The Oil Engine and Gas Turbine*, vol. 22, May, 1954, p. 36.
- 20 "Aerodynamic Interference Between Moving Blade Rows," by N. H. Kemp and W. R. Sears, *Journal of the Aeronautical Sciences*, vol. 20, 1953, pp. 585-597.
- 21 "Pressure Distribution Measurements on a Turbine Rotor Blade Passing Behind a Turbine Nozzle Lattice," by Hausenblas, NACA TM 1173, September, 1947.
- 22 "Airfoil Theory for Flows of Variable Velocity," by Rufus Isaacs, *Journal of the Aeronautical Sciences*, vol. 12, 1945, pp. 113-118.
- 23 "Airfoil Theory for Rotating Wing Aircraft," by Rufus Isaacs, *Journal of the Aeronautical Sciences*, vol. 13, 1946, pp. 218-220.
- 24 "Airfoil in Sinusoidal Motion in a Pulsating Stream," by J. M. Greenberg, NACA TN 1326, June, 1947.
- 25 "Some Considerations on an Airfoil in an Oscillating Stream," by J. M. Greenberg, NACA TN 1372, August, 1947.
- 26 "Premiers Elements d'un Calcul de L'Amortissement Aerodynamique des Vibrations d'Aubes de Compresseurs," by Robert Legendre, *La Recherche Aeronautique*, no. 37, January-February, 1954, pp. 3-10.
- 27 "Lift and Moment Equations for Oscillating Airfoils in an Infinite Unstaggered Cascade," by A. Mendelson and R. W. Carroll, NACA TN 3263, October, 1954.
- 28 "Compressor Surge and Stall Propagation," by H. W. Emons, C. E. Pearson, and H. P. Grant, Trans. ASME, vol. 77, 1955, pp. 455-469.
- 29 "Observations of Propagating Stall in Axial-Flow Compressors," by T. Iura and W. D. Rannie, Mechanical Engineering Laboratory, California Institute of Technology, Pasadena, Calif., Report No. 4, April, 1953.
- 30 "On Asymmetric Flow in an Axial-Flow Compressor Stage," by W. R. Sears, *Journal of Applied Mechanics*, Trans. ASME, vol. 75, 1953, pp. 57-62.
- 31 "Stall Propagation in Cascades of Airfoils," by A. H. Stenning, *Journal of the Aeronautical Sciences*, vol. 21, 1954, pp. 711-713.
- 32 "Some Stall and Surge Phenomena in Axial-Flow Compressors," by M. C. Huppert and W. A. Benser, *Journal of the Aeronautical Sciences*, vol. 20, 1953, pp. 835-845.

Discussion

H. P. GRANT.³ The authors' broad survey of flutter problems is especially valuable in encouraging attention to possible interactions between phenomena that usually have been studied only provincially.

In their discussion of stall propagation the authors on several occasions refer to the apparent existence of upper and lower bounds on the mean through-flow velocity for which this behavior can occur. The upper bound (choking) may well exist, but there is no convincing evidence of a lower bound. In the cascade tests of reference (28) of the paper, distinct propagation was reported over the entire range of velocity attainable in the tunnel (90 to 600 fps). The rate of decrease of propagation velocity with decreasing through-flow velocity in Table 1 of reference (28) indicates that propagation would cease only at zero flow, or very close to it. Of course any buffeting produced by propagating stall at very low flows is slight, and the frequency low, but it apparently does not vanish and must still be reckoned as a possible source of mechanical and aerodynamic excitation.

A. H. STENNING.⁴ The authors are to be congratulated for presenting this concise summary of blading vibration problems at a time when the number of theories apparently exceeds the number of investigators in the field. Particularly bewildering to the layman are the diametrically opposed statements made by the protagonists. For example, Pearson⁵ declares that torsional stall flutter has not been found in compressors and cascades, while Wang⁶ says that torsional flutter is the only important type of stall flutter! Would the authors care to comment on this situation?

In the past there has been considerable confusion between stall flutter and rotating stall, since whenever the first phenomenon might occur, the second is almost certain to be present. Is there any firm evidence of stall flutter occurring in compressors, and has any blade failure occurred which can be attributed to stall flutter rather than rotating stall?

With reference to the section in the paper on rotating stall, we have not found any meaningful lower limit on relative velocity below which rotating stall ceases to occur. At relative velocities of the order of 100 fps rotating stall still appeared in a single-stage axial compressor tested at M.I.T. Contrary to the authors' statement, an upper limit to incidence angle above which rotating stall does not occur has been found on both a circular cascade and a single-stage compressor. Reynolds-number effects can be very strong and a reduction in Re from 240,000 to 150,000 in one case eliminated one of the stall patterns completely.

³ Flow Corporation, Cambridge, Mass.

⁴ Assistant Professor of Mechanical Engineering, Massachusetts Institute of Technology, Cambridge, Mass.

⁵ Reference (14) of the Bibliography of the paper.

⁶ "A Practical Approach to the Problem of Stall Flutter," by C. Wang, R. J. Vaccaro, and D. F. De Santo, published in this issue, pp. 565-572.

AUTHORS' CLOSURE

The authors wish to thank Dr. Grant and Professor Stenning for their enlightening discussions.

In reply to Professor Stenning's questions we may remark that vibratory data on compressor rotor blades are reasonably meager and quite difficult to obtain. Consequently one cannot conduct all the experiments which one would like to design. Nevertheless, some general observations may be made.

A typical graph of blade stress versus rpm generally exhibits a plateau of fairly uniform vibratory stress amplitude over a certain range. At one, two, or several particular values of rpm a stress peak may be found superimposed on this plateau level. The usual supposition is that the plateau is due to stall flutter and each peak is caused by a rotating-stall resonance.

Since the plateau value for a particular configuration can exceed the vibratory stress margin as determined by a modified Goodman diagram, it would be possible to fatigue a blade intentionally by prolonged operation at that level. Conversely, operation over the narrow rpm band near a resonance could fatigue the blade more rapidly in point of number of cycles, but this precise condition could be expected to occur much more infrequently due to the "sharpness" of the resonance peaks. It is probable that failures attributable to stall phenomena simply reflect the cumulative fatigue damage due to vibratory behavior of both types. (One may realize that a typical blade frequency of 278 cps represents one million repetitive stress cycles per hour.) Only if a compressor were purposely operated over a very precise schedule of rpm's could the damage be attributed solely to stall flutter or solely to rotating stall.

To the authors' knowledge, no case of torsional stall flutter has been diagnosed in rotating machinery. Its occurrence in cascades, however, has been detected.

Since both discussers have commented on the bounds of through velocity beyond which rotating stall is not detected, some clarification of the presented thoughts is in order. The conclusion drawn, regarding the lower limit of through velocity, was an interpretation of the results of cascade tests described in reference (28). A plot of incidence angle versus velocity yielded a negatively sloped lower bound of incidence angle (for the start of stall propagation). These results would provide a lower velocity limit if plotted with interchanged axes; of course it would be desirable to conduct the experiment over a wider range of incidence angles.

Professor Stenning has pointed out the significance of Reynolds number effects in relation to the propagation phenomenon. It is reasonable to assume that the lower velocity limit, when it is a finite value other than zero, is probably established mostly by Reynolds number considerations.

Relative to the upper-incidence angle limit, there was no definite information in the literature that such a limit was ever determined for the complete range of operating velocities. Professor Stenning indicates that an upper limit was recognized and measured in several specific instances. It is reasonable to assume that at certain flow velocities a given cascade would experience local sonic regions when operated at high incidence angles. This would choke the passage flow and inhibit stall propagation and thus provide an upper limit of incidence angle. However, it is difficult to see how this limit-producing effect could exist for the lower range of through velocities. In other words, no one has as yet reported tests which defined accurately and completely the area in a velocity-incidence angle plot within which propagating stall existed in a specific cascade. It is felt that this degree of definition is necessary.

A Practical Approach to the Problem of Stall Flutter¹

By CHI-TEH WANG,² R. J. VACCARO,³ AND D. F. DE SANTO,⁴ NEW YORK, N. Y.

A method is presented in this paper whereby the real part of the dynamic moment derivative may be obtained from a flutter test on a single blade oscillating in torsion alone in the stall region. These data may be used to predict the critical flutter velocity and frequency of a blade with the same geometrical properties oscillating with two degrees of freedom and having arbitrary elastic and inertial properties. It is possible that the present method can be used to predict the flutter speed and frequency of a cantilever blade by either a representative section or a Rayleigh-type analysis.

NOMENCLATURE

The following nomenclature is used in the paper:

- $a_{M\alpha}$ = real part of dynamic moment derivative
- $b_{M\alpha}$ = imaginary part of dynamic moment derivative
- b = semichord of airfoil, ft
- $C_{M\alpha}$ = total dynamic moment derivative
- EA = elastic axis (axis of rotation) position, per cent of airfoil chord aft of leading edge
- k = reduced frequency, $\omega b/V$
- I = mass moment of inertia about EA, lb-sq ft/ft span
- I' = dimensionless mass moment of inertia about EA, $I' = I/2pb^4$
- M = mass, lb/ft span
- M' = dimensionless mass, $M' = M/2pb^3$
- S = mass unbalance about EA, negative for center of gravity aft of EA, lb-ft
- S' = dimensionless mass unbalance about EA, $S' = S/2pb^3$
- \bar{q}_α = dimensionless displacement in torsion, radians
- V = air speed, fps
- α = angular deflection about EA (angle of attack), deg
- ω = flutter frequency, cycles per sec (cps)
- ω_α = natural frequency in torsion, cps
- ω_δ = natural frequency in bending, cps
- ρ = air density, pcf

INTRODUCTION

Since the inception of axial-flow aircraft gas turbines the fatigue and eventual failure of compressor blades has been of considerable concern to blade designers. It is generally conceded that nearly all blade vibration is of aerodynamic origin and is usually associated with stall flows. (The vibration may be caused by stall flutter of the blades or by the phenomenon of rotating stall.)

¹ The work reported in this paper was carried out under the sponsorship of Office of Scientific Research, U. S. Air Force, Contract AF 18 (600)-1372.

² Professor of Aeronautical Engineering, New York University. (Deceased April 22, 1955).

³ Research Associate, New York University.

⁴ National Science Foundation Fellow, New York University.

Contributed by the Aviation Division and presented at a joint session of the Aviation Division and American Rocket Society, at the Diamond Jubilee Semi-Annual Meeting, Boston, Mass., June 19-23, 1955, of THE AMERICAN SOCIETY OF MECHANICAL ENGINEERS.

NOTE: Statements and opinions advanced in papers are to be understood as individual expressions of their authors and not those of the Society. Manuscript received at ASME Headquarters, May 17, 1955. Paper No. 55-SA-69.

A program has been initiated at the Guggenheim School of Aeronautics of New York University to study the stall flutter of blade systems. As a first step, the problem of stall flutter of a single blade or airfoil has been studied briefly. A practical method is proposed whereby from the flutter-test results of a single airfoil oscillating with a single degree of freedom, the critical flutter frequency and velocity for a blade with two degrees of freedom can be calculated. Possibly the method could be applied to cantilever blades by using either a representative section or a Rayleigh-type analysis.

REVIEW OF PREVIOUS WORK

Before we outline our method, let us review the previous work done by other investigators; notably the work of Victory and Mendelson.

Victory (1)⁵ sought to explain the predominantly torsional modes generally conceded as characteristic of stall flutter by modifying only the aerodynamic torsional damping in the classical theory. It was her contention that a reduction of the torsional damping in the stall region was responsible for the lower flutter speeds and predominantly torsional modes. In order to demonstrate this theory, Victory employed values of the torsional damping from forced-oscillation tests made at the National Physical Laboratories in England. The airfoil used by NPL was similar to one used by Studer (2) for actual stall-flutter tests under almost identical conditions and it was possible to compare the empirical theory with actual flutter results; the agreement between calculated and experimental flutter speeds appeared satisfactory.

A different type of modification to the classical theory was employed by Mendelson (3). He proceeded on the assumption that the absolute magnitudes of the aerodynamic forces and moments remain the same in the stall region as they are at zero incidence, but that the vector magnitudes of these quantities are altered. This change is caused by the lag of the aerodynamic damping and restoring forces behind the velocities and displacements in the stall region, thus giving rise to a type of aerodynamic hysteresis effect. Hence Mendelson modified the classical expressions for lift and moment by including a lag angle in only those terms which stem from displacement or velocity of the airfoil. He then proceeded to obtain an empirical relation between the aerodynamic lag angle and the steady-state lift curve. In order to evaluate his theory, Mendelson calculated flutter speeds for a wing tested by Bollay and Brown (4), and found that if the lag angle took on positive values, the flutter speeds dropped accordingly. Thus the theory apparently compared favorably with the experimental results.

In a review of the available methods for predicting flutter speeds in the stall region, Halfman et al. (5) applied the two methods just discussed, to predict the flutter speed of a wing tested by Bollay and Brown (4). For this case the Victory method did not give good results. A closer examination of the Mendelson method indicated that the drop in flutter speeds was also accompanied by a drop in the flutter frequency, which is contrary to the usual experimental results. In addition, they ob-

⁵ Numbers in parentheses refer to the Bibliography at the end of the paper.

served that the assumed values of aerodynamic lag were opposite in sign to the behavior in forced motion. They proceeded to demonstrate that indeed Mendelson had obtained his solution for the aerodynamic lag angle in the wrong range and that a second solution existed which exhibited the correct trends for both the flutter speed and frequency. However, the second solution did not result in an accurate prediction of the flutter speed. The problem of predicting the flutter speed of a blade in the stall region is still without adequate solution, and the exact status remains somewhat nebulous.

THE PROPOSED METHOD

In the high-incidence range where stalling conditions govern the aerodynamics, a theoretical approach to the problem is at present untenable. It is possible, nevertheless, to obtain aerodynamic data experimentally by forced oscillation tests; however, a large amount of data must be collected to insure the inclusion of the flutter point which is not previously known. Another method of obtaining aerodynamic data is proposed which eliminates not only the large amount of data required but the complexity of the forcing mechanism as well. This method utilizes single-degree-of-freedom flutter tests to obtain the aerodynamic data. If the blade is allowed only the torsional degree of freedom, the equation of motion in the absence of structural damping and under the assumption of harmonic time dependence is

$$\left[I' \left(\frac{\omega_a^2}{\omega^2} - 1 \right) - \frac{1}{k^2} C_{M\alpha} \right] \ddot{q}_\alpha = 0 \dots \dots \dots [1]$$

where I' is the nondimensional polar moment of inertia about the elastic axis, ω_a is the torsional natural frequency and ω the flutter frequency, k is the reduced frequency, $C_{M\alpha}$ is the oscillatory moment derivative $\partial C_M / \partial \alpha$, and q_α is the magnitude of torsional amplitude. Assume that $C_{M\alpha}$ can be written as the sum of a real and imaginary part. Thus we have

$$I' \left(\frac{\omega_a^2}{\omega^2} - 1 \right) - \frac{1}{k^2} (a_{M\alpha} + ib_{M\alpha}) = 0 \dots \dots \dots [2]$$

The real and imaginary parts of Equation [2] must be satisfied separately. From the imaginary part

$$\frac{b_{M\alpha}}{k^2} = 0 \dots \dots \dots [3]$$

The condition states that the imaginary part of the oscillatory moment derivative must be zero for flutter to occur or that the torsional damping must be zero.

The real part of the equation yields dynamic moment derivative

$$a_{M\alpha} = k^2 I' \left(\frac{\omega_a^2}{\omega^2} - 1 \right) \dots \dots \dots [4]$$

Hence for a given value of elastic axis location, a series of single-degree-of-freedom flutter tests may be performed, utilizing arbitrary values for the dimensionless moment of inertia I' and the torsional frequency ω_a with the angle of attack α as variable. For each angle of attack tested, a critical frequency and velocity will result from which k and, therefore, $a_{M\alpha}$ may be calculated. It must be emphasized again that the values of k and $a_{M\alpha}$ thus obtained are independent of the choice of I' and ω_a . The significance of this result lies in the fact that for this particular case it is possible to obtain an aerodynamic derivative from a flutter rather than a forced-oscillation investigation.

Stall flutter for a system with two degrees of freedom has been observed experimentally to occur with a predominantly tor-

sional mode. If the seemingly random flexural motion truly has no effect other than to provide excitation for the torsional mode, then the results for the single-degree-of-freedom case may be employed to predict stall-flutter speeds for a two-degree-of-freedom system. Equation [4] may be resolved in the following form

$$\frac{\omega}{\omega_a} = \left[\frac{1}{1 + \frac{a_{M\alpha}}{k^2 I'}} \right]^{1/2} \dots \dots \dots [5]$$

Thus, for a fixed elastic axis position and angle of attack, values of $a_{M\alpha}$ and k may be obtained from the single-degree-of-freedom results. These may be employed in Equation [5] with the values of I' and ω_a dictated by the two-degree-of-freedom system to compute the value of the flutter frequency. This is combined with the known value of the reduced frequency and blade semi-chord to yield the critical velocity. The air force $a_{M\alpha}$ will of course be affected by changes in airfoil shape and Reynolds number. Therefore the single-degree-of-freedom data must be available for the same airfoil shape, and the dependency of $a_{M\alpha}$ on Reynolds number must be known if the results are to be applicable to systems with vastly different elastic properties. The effects of Reynolds number have not been considered here.

THE EXPERIMENTAL PROGRAM

Flutter experiments have been carried out in the 7 × 10-ft wind tunnel at the Guggenheim School of Aeronautics of New York University. A single airfoil is positioned between two large wings or "end plates" which are spaced 1 ft apart and span the wind-tunnel test section from floor to ceiling, thus furnishing a two-dimensional air stream. To permit observation of the blade during testing, one end plate is equipped with plastic windows on both the exterior and the interior sides. Fig. 1 is a view of this

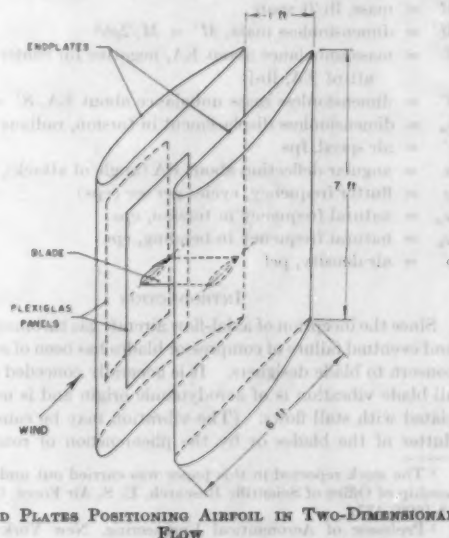


FIG. 1 END PLATES POSITIONING AIRFOIL IN TWO-DIMENSIONAL FLOW

apparatus, looking downstream. Each end plate houses one half of the "flutter mechanism," Fig. 2, which supports the blade at both ends and permits it to translate vertically and to rotate about a prescribed elastic axis, but which prevents the blade from having any tendency to roll. Both the translatory or flexural motion and the rotary or torsional motion are restrained by calibrated springs; thus the elasticity of the blade is well defined.

For the single-degree-of-freedom tests, rectangular blocks of

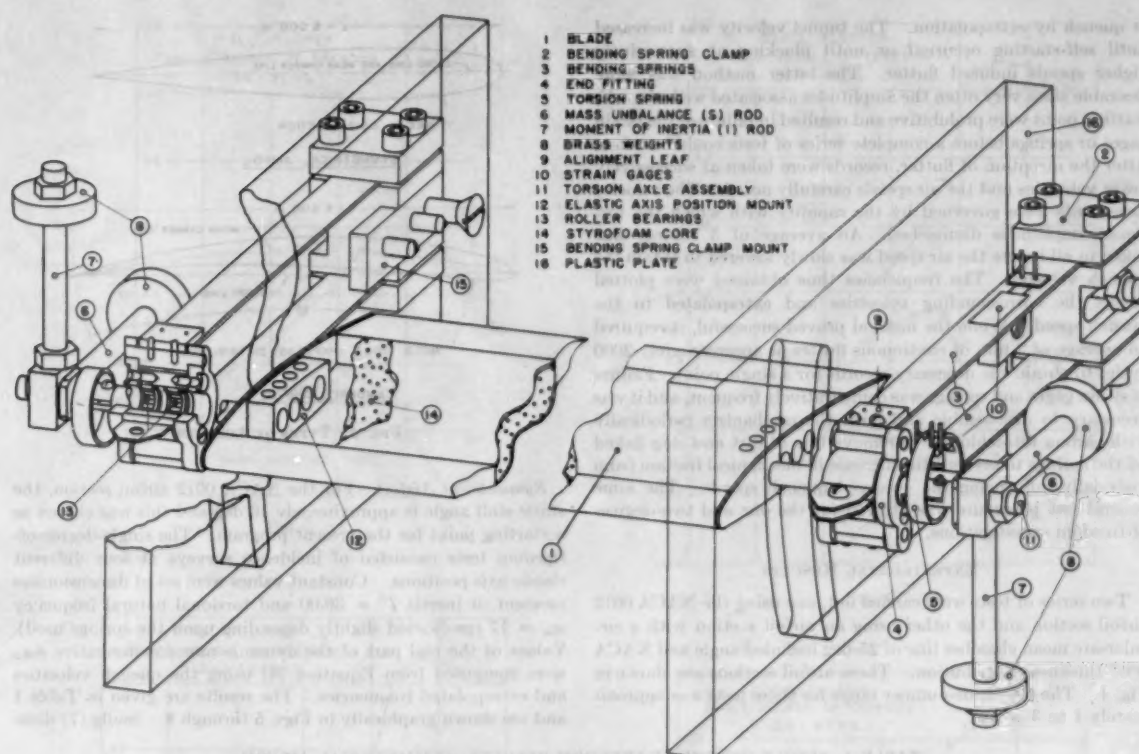


FIG. 2. COMPOSITE OF FLUTTER MECHANISM

wood cut to fit exactly were placed between the bending springs, and the springs were clamped to them with parallel clamps. Virtually no bending motion was possible once the clamps were tightened. The recording mechanism was a two-channel direct-inking oscillograph with two high-gain d-c amplifiers. The air speed was obtained roughly from an inclined manometer and a more accurate value was taken on a precision alcohol manometer capable of reading 0.001 in. of alcohol.

The procedure employed in stall-flutter testing is quite different from that used in the classical regime. For the classical case, as the tunnel speed is increased, damped oscillations begin to appear and finally, at some well-defined point, a constant-amplitude flutter occurs. If the tunnel velocity is lowered below this point, the flutter quenches. Hence the flutter oscillation occurs at the lowest critical velocity where instability can exist. This is not true in the case of stall flutter. In this case the point of initial instability must be passed (on the velocity scale) and flutter does not occur spontaneously until a point called the self-starting point is reached. After the flutter oscillation has been established, however, it is possible to obtain the point of initial instability by lowering the tunnel velocity until the flutter quenches. As the tunnel velocity is lowered, the flutter amplitude gradually diminishes but then drops to zero abruptly at the quench point. Thus, in stall flutter, a type of amplitude hysteresis loop is traversed. A typical plot of amplitude versus velocity is shown in Fig. 3. Similar results were obtained by Sisto (6) using the theory of nonlinear vibrations.

For the airfoil shape and Reynolds-number range under investigation, it appears that an upper quench point exists beyond which flutter is no longer possible. As the mean incidence was increased, the range of instability decreased until for an elastic

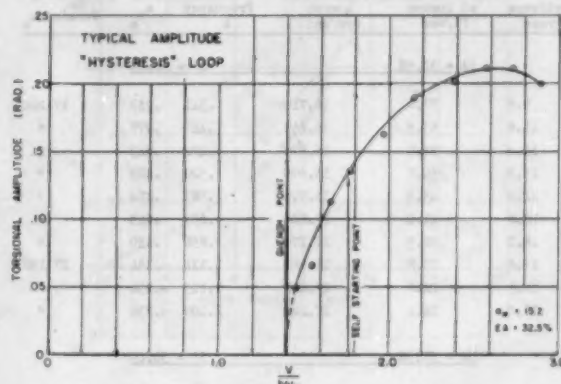


FIG. 3

axis position of 32.5 per cent chord flutter could not be observed at all for incidence angles above 20 deg. The maximum incidence angle increased as the elastic axis was moved rearward. For incidence angles close to the maximum, it was possible to accelerate the wind tunnel through the range of instability and not encounter flutter. At any velocity above the quench, but below the self-starting point, the blade could be artificially triggered by plucking it, and the flutter thus excited would acquire the proper amplitude corresponding to the existing velocity.

Since the quench velocity was not previously known, it would have been impractical to attempt to obtain a record at this point. Therefore a test procedure was adopted which provided the data

at quench by extrapolation. The tunnel velocity was increased until self-starting occurred or until plucking at successively higher speeds induced flutter. The latter method was more desirable since very often the amplitudes associated with the self-starting point were prohibitive and resulted in failure of the strain gages or springs before a complete series of tests could be taken. After the inception of flutter, records were taken at successively lower velocities and the air speeds carefully noted. The velocity increments were governed by the rapidity with which the torsional amplitudes diminished. An average of 5 records was taken in all before the air speed was slowly lowered to obtain the quench velocity. The frequencies thus obtained were plotted versus the corresponding velocities and extrapolated to the quench speed. While the method proved successful, it required an average of 2 min of continuous flutter or approximately 2000 cycles to obtain the necessary records for a single point. Failure of strain gages and springs was comparatively frequent, and it was necessary to disassemble and flush the mechanism periodically with carbon tetrachloride to remove bits of dirt and slag flaked off the springs to prevent the increase in mechanical friction from materially influencing the observed quench speeds. The same general test procedure was utilized for the one and two-degree-of-freedom investigations.

EXPERIMENTAL RESULTS

Two series of tests were carried out, one using the NACA 0012 airfoil section and the other using an airfoil section with a circular-arc mean chamber line of 25-deg included angle and NACA 0007 thickness distribution. These airfoil sections are shown in Fig. 4. The Reynolds-number range for these tests was approximately 1 to 3×10^6 .

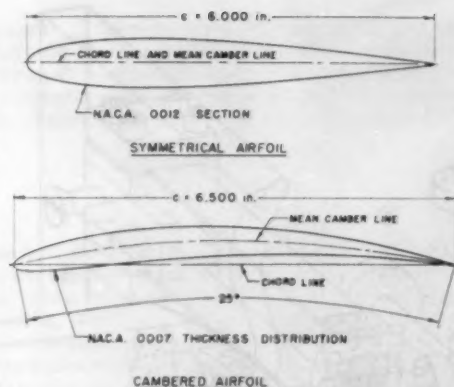


FIG. 4 TYPES OF AIRFOILS

Symmetrical Airfoil. For the NACA 0012 airfoil section, the static stall angle is approximately 10 deg and this was chosen as a starting point for the present program. The single-degree-of-freedom tests consisted of incidence surveys at four different elastic axis positions. Constant values were set of dimensionless moment of inertia $I' = 36.00$ and torsional natural frequency $\omega_n = 17$ cps (varied slightly depending upon the springs used). Values of the real part of the dynamic moment derivative $a_{M\alpha}$ were computed from Equation [4] using the quench velocities and extrapolated frequencies. The results are given in Table 1 and are shown graphically in Figs. 5 through 8. Smilg (7) dem-

TABLE 1 SINGLE-DEGREE-OF-FREEDOM RESULTS—SYMMETRICAL AIRFOIL

Mean Incidence Degrees	Velocity at Quench ft/sec	Extrapolated Frequency at Quench cyc/sec	Reduced Frequency k	$a_{M\alpha}$	Natural Frequency in Torsion ω_n	Mean Incidence Degrees	Velocity at Quench ft/sec	Extrapolated Frequency at Quench cyc/sec	Reduced Frequency k	$a_{M\alpha}$	Natural Frequency in Torsion ω_n
EA = 32.5% $I' = 36.00$						EA = 42.5% $I' = 36.00$					
9.9	77.0	16.725	.341	.253	17.224	10.4	76.4	16.02	.330	.544	17.098
11.6	63.5	16.255	.417	.277	"	11.7	56.4	16.08	.448	.945	"
12.4	55.9	16.870	.474	.343	"	13.3	56.7	16.22	.475	.901	"
13.3	50.1	16.890	.529	.402	"	14.2	46.9	16.36	.547	.995	"
14.2	45.5	16.900	.583	.474	"	14.7	43.5	16.47	.604	1.020	"
15.2	41.0	17.100	.655	.525	"	15.3	39.8	16.75	.660	.699	"
16.1	31.5	17.175	.856	.150	"	16.4	29.7	16.97	.897	.438	"
17.0	23.8	17.180	1.134	-.154	17.152	16.9	27.9	17.00	.958	.383	"
17.9	24.1	17.200	1.123	-.254	"	17.3	28.0	17.03	.955	.263	"
19.0	24.4	17.220	1.109	-.336	"	18.1	25.5	17.05	1.051	.200	"
EA = 71.5% $I' = 36.00$						19.0	24.6	17.05	1.087	.238	"
10.7	61.4	16.690	.422	.514	17.138	21.0	26.5	17.16	1.030	-.275	"
11.6	56.1	16.510	.462	.594	"	22.0	27.0	17.20	1.000	-.425	"
12.4	50.9	16.550	.511	.679	"	EA = 47.5% $I' = 36.00$					
13.3	49.3	16.600	.529	.663	"	9.8	77.6	15.330	.310	.760	16.927
14.2	45.3	16.665	.577	.690	"	10.7	65.5	15.480	.371	.970	"
15.2	35.9	16.850	.738	.676	"	11.4	62.2	15.720	.397	.999	"
15.9	27.7	17.030	.965	.422	"	12.9	51.3	15.890	.486	1.127	"
16.8	25.2	17.110	1.065	.131	"	13.0	47.9	15.930	.522	1.244	16.911
18.1	24.8	17.170	1.086	-.161	"	15.0	30.8	16.475	.838	1.397	"
19.0	25.1	17.120	1.071	.083	"	16.0	26.8	16.650	.975	1.082	"
20.0	24.9	17.200	1.086	-.305	"	17.4	25.4	16.732	1.033	.826	"
21.0	26.4	17.230	1.023	-.399	"	18.6	24.3	16.750	1.084	.816	"
22.2	27.0	17.250	1.000	-.468	"	20.1	23.7	16.795	1.110	.715	"
						21.0	23.6	16.820	1.119	.489	"
						22.0	22.7	16.842	1.167	.402	"

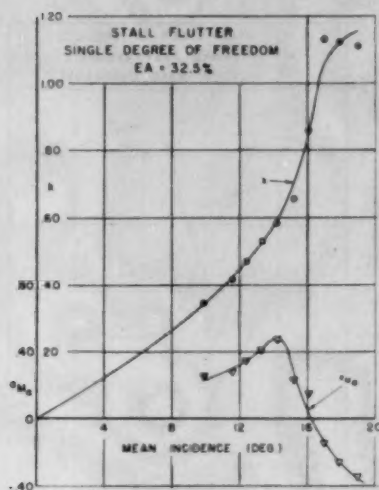


FIG. 5

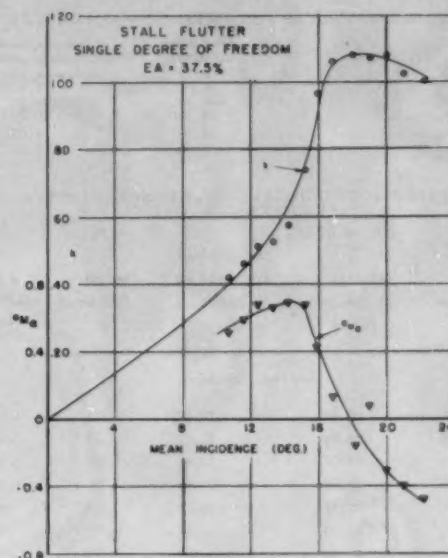


FIG. 6

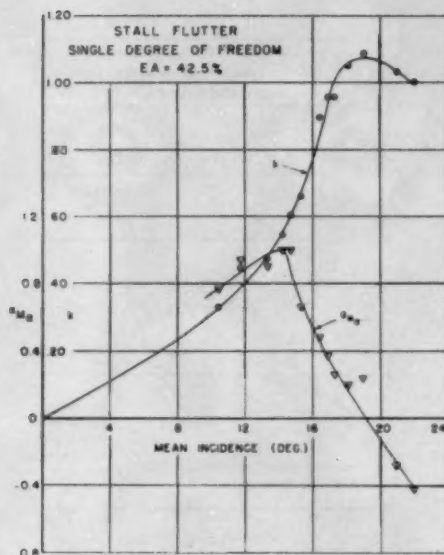


FIG. 7

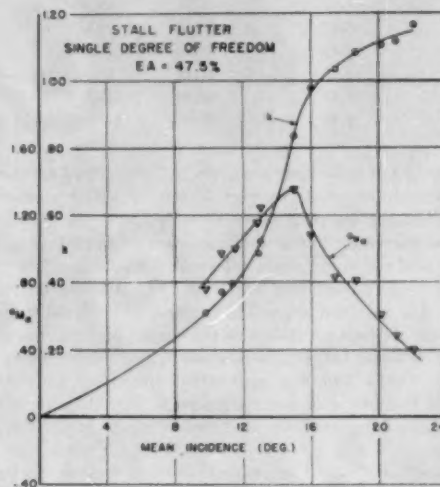


FIG. 8

onstrated that at zero incidence single-degree-of-freedom torsional flutter cannot exist for elastic axis positions aft of the 25 per cent chord. Therefore the flutter velocity is infinite at $\alpha = 0$ for the present series of tests; and hence the reduced frequency curves have been faired to the origin. According to Equation [4]

$$a_{Ma} = 0 \text{ if } k = 0$$

but the behavior of a_{Ma} in the incidence range 0 to 10 deg is not known. Halfman, et al. (5) have shown by forced-oscillation tests that for a constant value of k , the variation of the total moment derivative in pitch is similar in shape to the steady-state curve. This may also be true in the present case for variable k

since the shape of the dynamic moment-derivative curve is similar to that of the static curve. As might be expected, the magnitude of a_{Ma} increases as the elastic axis position is moved rearward; however, the shape remains relatively unchanged.

In order to determine whether or not the single-degree-of-freedom results could be employed to predict critical velocity and frequency for two-degree-of-freedom flutter, the bending mode was released and tests were made using moment of inertia and torsional natural frequency different from those used in the single-degree-of-freedom tests. For the symmetrical airfoil both low and high values of mass unbalance were tested to determine the effect of this parameter. The elastic-axis position for the two series of tests was held fixed at 37.5 per cent. Values for the remaining physical parameters are given in Table 2.

TABLE 2 VALUES FOR PHYSICAL PARAMETERS

	Low mass unbalance	High mass unbalance
S'	-6.73	-14.12
I'	18.00	24.39
M'	104.56	104.56
ω_n	24.140	20.751
ω_h	8.04	8.01
ω_n/ω_h	2.98	2.59

TABLE 3 TWO-DEGREE-OF-FREEDOM RESULTS—SYMMETRICAL AIRFOIL

EA = 37.5% $M' = 104.56$

Mean Incidence Degree	Velocity At Quench ft/sec	Extrapolated Frequency at Quench cyc/sec	Reduced Frequency k	Flutter Coefficient $\frac{Y}{b\omega_n}$
Low Mass Unbalance				
9.20	98.99	21.50	.341	2.610
10.90	76.89	22.42	.452	2.030
12.50	67.05	22.91	.536	1.768
15.20	47.16	23.69	.789	1.240
17.9	37.31	23.98	1.009	.984
20.0	34.35	24.02	1.098	.906
22.0	35.12	24.15	1.080	.926
High Mass Unbalance				
9.8	75.51	19.03	.396	2.320
11.9	62.62	19.94	.500	1.921
13.4	56.74	20.36	.564	1.740
15.2	44.63	21.17	.743	1.369
18.0	33.49	21.27	.998	1.027
20.0	32.18	21.39	1.040	.987
21.6	31.50	21.37	1.066	.966

The results of these tests are given in Table 3 and are shown as the experimental points in Figs. 9 and 10. The predicted reduced-frequency curve is taken directly from Fig. 6, while the predicted curves for flutter coefficient are computed using Equation [5] and the appropriate values of I' and ω_{na} . The results from Equation [5] are combined with k to obtain the flutter coefficient. For both the low and high values of mass unbalance, the agreement between predicted values employing single-degree-of-freedom data and two-degree-of-freedom test values is very satisfactory. At the high angles of attack the discrepancy between predicted and test values is attributed to the difficulties encountered in obtaining accurate air-speed readings in the low velocity range.

Cambered Airfoil. The cambered-airfoil section used in the second series of flutter tests was chosen so as to approximate the shape of a typical modern axial-flow compressor-blade cross section located about 75 per cent of the way from root to tip of one of the blades in the early stages of the compressor, Fig. 4. This was done with a view to the potential application of the proposed method to a "representative-section" type of stall-flutter analysis of compressor blades.

The test program for the cambered airfoil constituted an abbreviated version of the program carried out for the symmetrical section. The single-degree-of-freedom incidence survey was carried out with the elastic axis located at 37 per cent chord on the mean camber line; the mean angle-of-attack range was from about 18 to 27 deg above the angle of zero lift. In this test values of the dimensionless moment of inertia $I' = 26.40$ and $\omega_n \cong 18.20$ cps were used. Values of ω_{na} were computed as before and are presented in Table 4 and Fig. 11.

The two-degree-of-freedom flutter investigation for the cam-

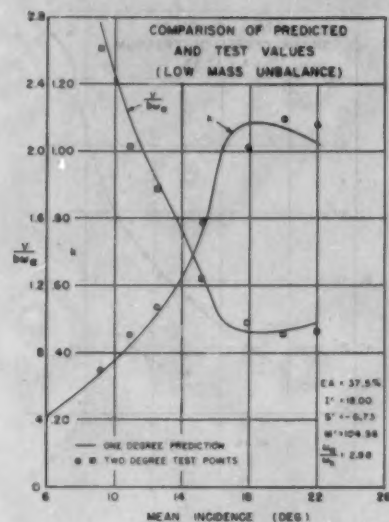


FIG. 9

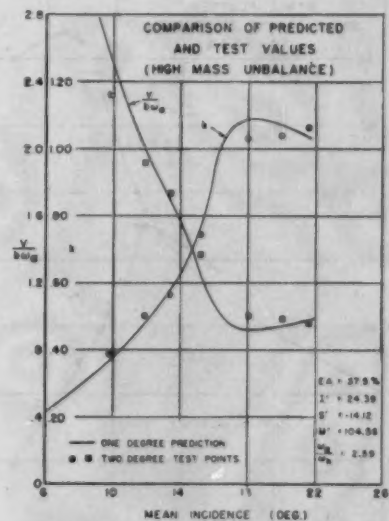


FIG. 10

bered airfoil was conducted by unlocking the bending mode and decreasing I' from 26.40 to 19.905, thereby increasing ω_n from about 18.20 to 20.95 cps. The values of the parameters are given in Table 5.

The two-degree-of-freedom results, given in Table 5 and indicated by points in Fig. 12, were obtained as in the case of the symmetrical airfoil, and agree well with the single-degree-of-freedom predicted results. While not enough data have been accumulated in this rather short experimental investigation to evaluate the effect of airfoil shape, the results seem to indicate that the flutter behavior is not materially altered by the change from symmetrical to relatively highly cambered sections. Thus the proposed method appears quite promising in the practical analysis of compressor-blade stall flutter.

TABLE 4 SINGLE-DEGREE-OF-FREEDOM RESULTS—CAMBERED AIRFOIL

Mean Incidence Degrees	Velocity at Quench ft/sec	Extrapolated Frequency at Quench cy/sec	Reduced Frequency k	α_{M_0}	Natural Frequency 18 Torsion ω_n
17.7	117.61	16.40	.350	.762	18.23
19.4	61.02	16.90	.470	.954	"
20.9	52.07	17.20	.575	1.077	"
22.4	41.32	17.46	.693	1.143	"
23.9	37.39	17.60	.813	1.148	18.17
26.4	29.40	17.80	1.030	1.176	"

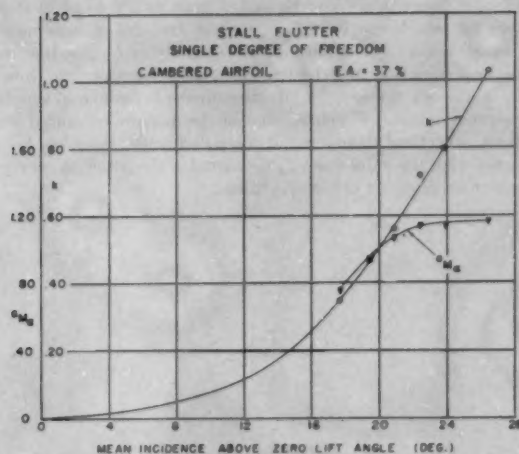


FIG. 11

TABLE 5 VALUES OF PARAMETERS

S'	-11.67
I'	19.905
M'	95.52
ω_n	20.95
α_n	6.82
ω_n/α_n	3.07

BIBLIOGRAPHY

- 1 "Flutter at High Incidence," by M. Victory, British Aeronautical Research Council, R and M No. 2048, 1943.
- 2 "Experimentelle Untersuchungen über Flugschwingungen," by H. L. Studer, Mitt. aus dem Institut für Aerod., Eidgenössische Tech. H. S., Zurich, Switzerland, No. 415, 1936.
- 3 "Effect of Aerodynamic Hysteresis on Critical Flutter Speed at Stall," by A. Mendelson, NACA RM E 8 BO4, 1943.
- 4 "Some Experimental Results on Wing Flutter," by W. Bollay and C. D. Brown, *Journal of the Aeronautical Sciences*, vol. 8, 1941, pp. 313-318.
- 5 "Evaluation of High-Angle-of-Attack Aerodynamic-Derivative Data and Stall-Flutter Prediction Technique," by R. L. Halfman, H. C. Johnson, and S. M. Haley, NACA Technical Note No. 2533, 1951.
- 6 "Stall-Flutter in Cascades," by F. Sisto, *Journal of the Aeronautical Sciences*, vol. 20, 1953, pp. 598-604.
- 7 "The Instability of Pitching Oscillations of an Airfoil in Subsonic Incompressible Potential Flow," by B. Smilg, *Journal of the Aeronautical Sciences*, vol. 16, 1949, pp. 691-696.

TABLE 6 TWO-DEGREE-OF-FREEDOM RESULTS—CAMBERED AIRFOIL

EA = 37%		$M' = 95.52$		
Mean Incidence Degrees	Velocity at Quench ft/sec	Extrapolated Frequency at Quench cy/sec	Reduced Frequency k	Flutter Coefficient $\frac{V}{\omega_n}$
17.9	87.25	18.87	.368	2.45
20.4	59.13	20.35	.586	1.655
22.4	53.50	20.60	.655	1.500
24.9	39.25	20.85	.904	1.100

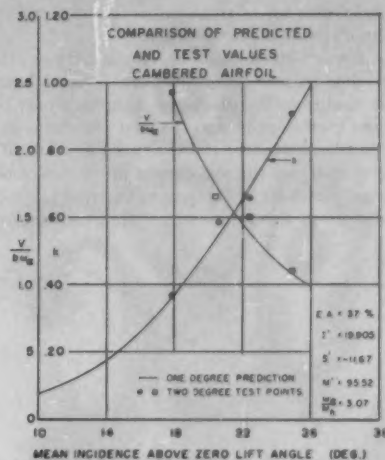


FIG. 12

Discussion

R. L. HALFMAN.⁶ The authors are to be congratulated for clearing away some of the haze usually surrounding the stall-flutter problem, at least for the case where the flutter is essentially a torsional oscillation about a definite axis. For compressor blades this case may well be of considerable importance along with the companion problem of rotating stall.

Although the authors state that they have conducted a series of tests to obtain the real part of the dynamic moment coefficient in a single-degree-of-freedom flutter in order to predict a two-degree-of-freedom flutter, the writer prefers to adopt a somewhat different viewpoint. It is entirely possible to view the single-degree-of-freedom-flutter data as the results of the testing of a somewhat simplified scaled flutter model. That is to say, the model can be restricted to simple rotation because the "full-scale" wing (the two-degree-of-freedom case) is not expected to exhibit translational motion during flutter. The time-scale factor, which is the ratio of the torsional natural frequencies, and the mass-scale factor can be calculated simply in each case. The length-scale factor is unity. Because of the importance of Reynolds-number effects, the corresponding model and full-scale tests are quite rightly carried out at essentially the same Reynolds numbers. The normal use of scale factors to transform the scale model (single-degree-of-freedom) data to predictions of full-scale (two-degree-of-

⁶ Associate Professor of Aeronautical Engineering, Massachusetts Institute of Technology, Cambridge, Mass.

freedom) flutter points is exactly equivalent to the prediction process used by the authors. The excellent agreement of results presented in the paper can be thought of as validating the assumptions underlying the scale-model experiments.

The suggestion of the authors that their procedure may be used to predict flutter of a cantilever blade appears quite logical from the writer's point of view. The two-dimensional single-degree-of-freedom flutter tests can be interpreted as simplified "typical section" flutter tests of a properly scaled model of the cantilever wing and predictions can be made by applying the appropriate scale factors. The possible extension of the authors' method to stall flutter actually involving more than one degree of freedom is then seen to coincide with the testing of an appropriately scaled flutter model to a greater extent than to the usual measurement of aerodynamic derivatives.

Although it was not emphasized by the authors, the single-degree-of-freedom measurements are perhaps more significant as a set of test conditions for which the imaginary part of the dynamic-moment coefficient is zero than for the values of the real part which can be deduced. For example, if the bald assumptions are made that, for the purposes of prediction of the flutter curves in Figs. 9 and 10 of the paper, the real part of the dynamic-moment coefficient is also zero so that the wing will flutter

at its natural torsional frequency, then the agreement between predicted and measured flutter points is practically unchanged.

The authors are to be commended for conducting a careful set of experiments well designed to obtain a maximum amount of information without becoming bogged down in a welter of non-linear effects.

AUTHORS' CLOSURE

The authors would like to express their thanks to Prof. R. L. Halfman of Massachusetts Institute of Technology, for his careful review of the paper and for his interesting comments. His scaled flutter-model viewpoint is considered valuable in that it constitutes an independent justification of the method.

Professor Halfman states that the authors' single-degree-of-freedom measurements may be looked upon as a set of test conditions for which the imaginary part of the dynamic moment derivative is zero. The authors' statement that $b_{Ma} = 0$ arose from the assumption that the structural damping was zero; however, this is not the case for the measurements made and is only an approximation. Recently, one of the authors measured the systems' structural damping and computed actual values of b_{Ma} ; together with the values of a_{Ma} presented in the paper, these represent an accurate set of test conditions.



Fig. 9



Fig. 10

The Flow in a Vee-Gutter Cascade

By W. G. CORNELL,¹ EVENDALE, OHIO

A theory is presented, yielding the wake shape, the total pressure loss, and the drag force of two-dimensional vee-gutter profiles in unstaggered cascade array, for incompressible, steady, potential flow directed normal to the cascade axis. The results, for all gutter-included angle and blockage ratio, are compared to two and three-dimensional experimental results, showing good agreement. Approximate theories are presented, valid at high blockage ratio and either at small or large gutter angle.

NOMENCLATURE

The following nomenclature is used in the paper:

- A_s = function in expression for μ
- B_s = function in expression for μ
- b = breadth of gutter along cascade axis
- C_c = contraction coefficient
- C_D = drag coefficient
- D = drag force on a gutter
- d_1, d_2 = inlet, outlet diameter of conical nozzle
- $F(b/t, \alpha)$ = function in expression for μ
- $G(\alpha)$ = function in asymptotic expression for μ
- $H(\alpha)$ = function in asymptotic expression for μ
- p = static pressure
- p_T = total pressure
- Δp_T = total pressure loss of cascade
- q = integer
- R, Z = cylindrical co-ordinates
- r, s = integers ($r > s$)
- l = pitch of cascade along cascade axis
- $W = \phi + i\psi$ = complex potential
- w = fluid velocity
- w_1 = velocity upstream of cascade
- w_2 = velocity downstream of cascade
- w_3 = velocity after mixing of wakes and jets
- Y, X = rectangular co-ordinates
- $z = x + iy$ = complex position variable
- α = gutter included half angle
- β_s = function in expression for μ
- ϵ = function in expression for μ
- ξ = complex position variable
- λ = total pressure loss coefficient of cascade
- μ = wake width as fraction of pitch l
- ξ = dummy variable of integration
- ρ = fluid-mass density

INTRODUCTION

In afterburners of modern aircraft gas-turbine power plants and in other combustion systems, various bluff bodies are used for flameholders, creating low-velocity regions downstream in order to stabilize combustion. One of the most frequently used

¹ Aerodynamicist, Aircraft Gas Turbine Division, General Electric Company. Mem. ASME.

Contributed by the Aviation Division and presented at a joint session of the Aviation Division and the American Rocket Society at the Diamond Jubilee Semi-Annual Meeting, Boston, Mass., June 19-23, 1955, of THE AMERICAN SOCIETY OF MECHANICAL ENGINEERS.

NOTE: Statements and opinions advanced in papers are to be understood as individual expressions of their authors and not those of the Society. Manuscript received at ASME Headquarters, April 25, 1955. Paper No. 55-SA-53.

configurations is the vee-gutter flameholder, composed of concentric annular rings of vee cross section with apex upstream. In the design of vee-gutter flameholders, a method is needed to predict the effect of vee-gutter geometry on aerodynamic forces on the gutters, total pressure loss, and wake shape.

The present theory idealizes the configuration as a two-dimensional cascade of vee-gutter profiles; that is, an infinite number of equally spaced profiles of infinite span, a section normal to the span being shown in Fig. 1. The profiles are idealized as infinitesimally thin vee-shaped plates of included angle 2α and breadth b along the cascade axis which is normal to the upstream flow.

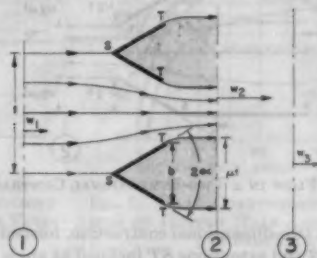


FIG. 1 FLOW IN A VEE-GUTTER CASCADE

The upstream flow, infinitely far ahead of the cascade, at station 1, is taken as a uniform flow of velocity w_1 normal to the cascade axis. Stagnation streamlines will proceed undeflected from station 1 to stagnation points at S on the apex of each profile. These streamlines then split and become the outside surfaces of the profiles, flowing smoothly off the trailing edges T . Since in an actual, viscous fluid, the flow cannot negotiate the sharp turn at the trailing edges in order to proceed upstream along the inside surfaces of the profiles, it will be assumed that the flow separates from the profile at the trailing edges. The streamlines extending downstream from the trailing edges will be taken as "free streamlines," enclosing "dead-water" regions or wakes, extending infinitely far downstream to station 2. At station 2 the flow consists of wakes of extent μl parallel to the cascade axis, and intervening jets of extent $(1 - \mu)l$. In the wakes, the velocity is taken as zero, in the jets at a constant value w_3 , normal to the cascade axis. The static pressure will be considered uniform across both wakes and jets at station 2. Thus the static pressure in the entire wakes will be taken constant at the downstream value p_2 . As a boundary condition, then, the static pressure will be constant at p_2 along the free streamlines.

It will be assumed that the flow is two-dimensional, steady, incompressible, irrotational, nonviscous, and free of body forces. As a consequence, the velocity w_2 in the jets will exceed the inlet velocity w_1 . Further, the total pressure

$$p_T = p + \frac{1}{2}(\rho w^2)$$

will be constant in the flow from 1 to 2, so that no losses will be accounted for in the process of formation of the jets.

The wakes and jets are then assumed to mix at constant momentum, since no mechanism is present to afford a force external to the fluid, between station 2 and station 3, located farther

downstream. The flow at station 3 is characterized by uniform velocity w_3 normal to the cascade axis and equal, from continuity considerations, to the inlet velocity w_1 . The static pressure will be taken as uniform at p_3 , a lower value than the inlet static pressure p_1 , since a total pressure loss will be computed in the mixing.

The problem may be stated as follows: Given a vee-gutter cascade defined geometrically by α , b/t , and an upstream flow velocity w_1 , it is required to find the wake thickness/pitch ratio μ , the drag force D (normal to the cascade axis) on each profile, and the total pressure loss

$$\Delta p_T = p_{T1} - p_{T3}$$

FLOW IN THE WAKES AND JETS

The flow between stations 1 and 2 is considered first. The vee-gutter flow configuration shown in Fig. 1 is seen to be identical, under the assumptions made, to the configuration shown in Fig. 2,

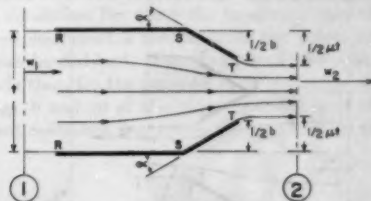


FIG. 2 FLOW IN A TWO-DIMENSIONAL CONTRACTION

that of flow in a two-dimensional contraction, formed of two semi-infinite walls RS and extensions ST inclined at angle α to RS and having breadth $b/2$ measured normal to RS . At station 1, infinitely far ahead of the contraction, the velocity is w_1 . The flow discharges into stagnant fluid having static pressure p_2 and forms a vena contracta of breadth $(1 - \mu)t$ at station 2, infinitely far downstream. Von Mises (1)³ has given the desired potential-flow solution for the two-dimensional contraction, in order to predict flow coefficients for discharge from such openings, utilizing the free-streamline theory of Helmholtz and Kirchhoff (2). The results, in the present nomenclature, are as follows: The wake thickness/pitch ratio μ is given by

$$\mu = 1 - \frac{1 - b/t}{1 + F(\alpha, b/t)} \quad [1]$$

where

$$F(\alpha, b/t) = \frac{\sin \alpha}{\pi} \sum_{q=1}^{1/2r} [A_q \cos(s\beta_q) + B_q \sin(s\beta_q)]$$

$r, s =$ arbitrary integers, $r > s$, $r/s = \pi/\alpha$

$$\beta_q = (2q - 1)\alpha/s$$

$$A_q = 2 \ln(1 - \cos \beta_q)$$

$$B_q = 2(1/\epsilon - \epsilon) \ln(\epsilon^{2/s} + 1 - 2\epsilon^{1/s} \cos \beta_q)$$

$$B_q = 2(1/\epsilon - \epsilon) \ln \left(\frac{\epsilon^{1/s} \sin \beta_q}{1 - \epsilon^{1/s} \cos \beta_q} \right)$$

$$\epsilon = (1 - \mu)^2/(1 - b/t)$$

In order to evaluate $F(\alpha, b/t)$ for chosen α , b/t , the integers r, s are chosen to yield the minimum number of series terms. It is to be noted that computation is restricted to values of α which are integral fractions of π . This restriction is not troublesome, however, since graphical interpolation can be used on the results. Numerical results are shown in Figs. 3 and 4 where μ is shown as a function of α and b/t for the complete range $0 < \alpha < 180^\circ$,

³ Numbers in parentheses refer to Bibliography at end of paper.

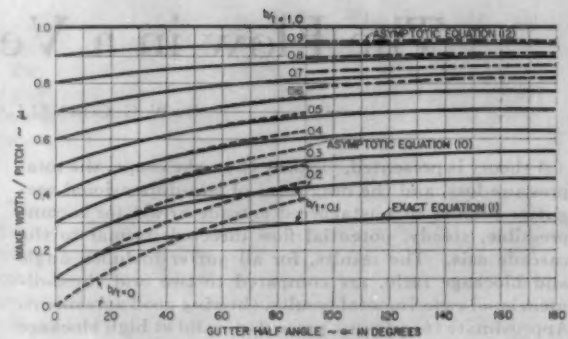


FIG. 3 WAKE-WIDTH PARAMETER μ AS A FUNCTION OF GUTTER HALF ANGLE α FOR VARIOUS BLOCKAGE b/t

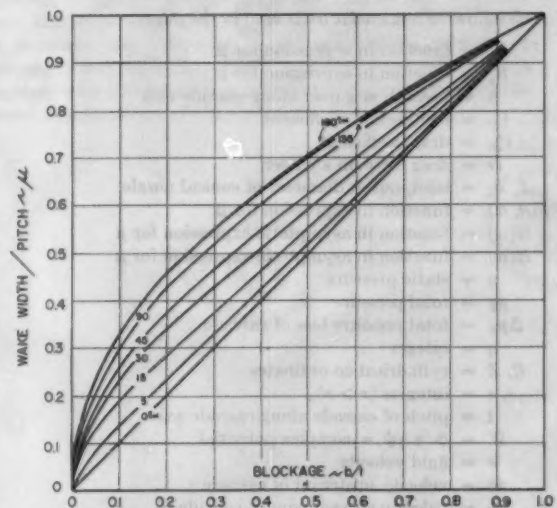


FIG. 4 WAKE-WIDTH PARAMETER μ AS A FUNCTION OF BLOCKAGE b/t FOR VARIOUS GUTTER HALF ANGLE α

$0 < b/t < 1$. Also shown in Fig. 3 are results of two asymptotic theories discussed later in the paper.

TOTAL PRESSURE LOSS

The total pressure loss

$$\Delta p_T = p_{T1} - p_{T3}$$

may be written as

$$\Delta p_T = p_1 - p_3 + \frac{1}{2} \rho (w_3^2 - w_1^2) \quad [2]$$

by definition of

$$p_T = p + (1/2)\rho w^2$$

and since $p_{T1} = p_{T3}$.

The principle of conservation of momentum may be applied for forces normal to the cascade axis and acting on a strip of fluid of breadth t , containing a wake and two halves of a jet, extending between stations 2 and 3. The result is

$$p_2 - p_3 = \rho[w_3^2 - w_1^2(1 - \mu)] \quad [3]$$

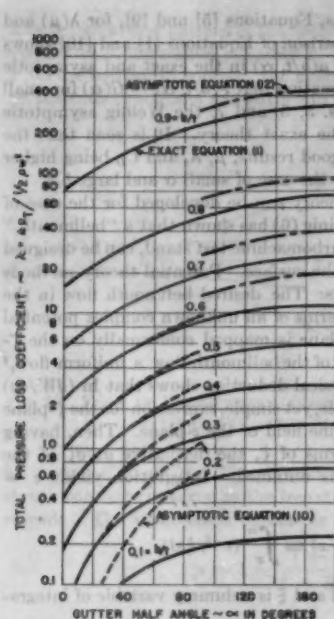


FIG. 5 TOTAL PRESSURE-LOSS COEFFICIENT λ AS A FUNCTION OF GUTTER HALF ANGLE α FOR VARIOUS BLOCKAGE b/t

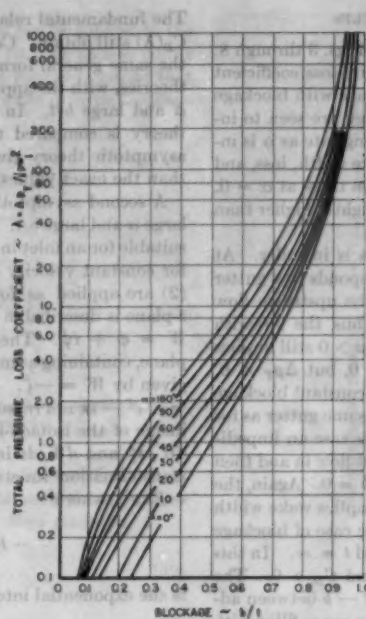


FIG. 6 TOTAL PRESSURE-LOSS COEFFICIENT λ AS A FUNCTION OF BLOCKAGE b/t FOR VARIOUS GUTTER HALF ANGLE α

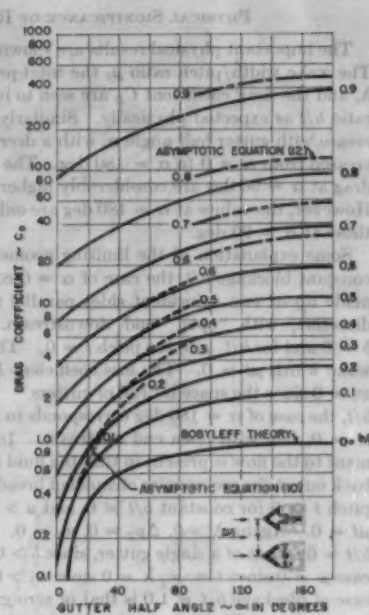


FIG. 7 DRAG COEFFICIENT C_D AS A FUNCTION OF GUTTER HALF ANGLE α FOR VARIOUS BLOCKAGE b/t

The principle of conservation of mass may be applied to the same strip, extended to station 1, to yield

$$w_1/w_2 = w_2/w_2 = 1 - \mu \quad [4]$$

Combination of Equations [2], [3], and [4] yields the nondimensional total pressure-loss coefficient as

$$\lambda = 2\Delta p_T / \rho w_1^2 = \mu^2 / (1 - \mu)^2 \quad [5]$$

The loss coefficient λ is seen to be a function only of μ , which is given by Equation [1] in terms of α , b/t . Numerical results are shown in Figs. 5 and 6 where λ is shown as a function of α and b/t . Also shown in Fig. 5 are the results of the asymptotic theories.

THE PROFILE DRAG FORCE

The principle of conservation of momentum may be applied to the previous strip of fluid, extended to station 1, to yield the drag force on a profile as

$$D = (p_1 - p_2)t + \rho w_1^2 - \rho w_2^2(1 - \mu) \quad [6]$$

Since the total pressure is unchanged between stations 1 and 2, the Bernoulli relation yields

$$p_1 - p_2 = \frac{1}{2} \rho (w_2^2 - w_1^2) \quad [7]$$

Combining Equations [4], [6], and [7] yields the nondimensional drag coefficient as

$$C_D \equiv D / (1/2) \rho w_1^2 b = (t/b) \mu^2 / (1 - \mu)^2 \quad [8]$$

which, with Equation [5], may be written as

$$C_D = (t/b) \lambda \quad [9]$$

which might have been deduced physically. The product of drag

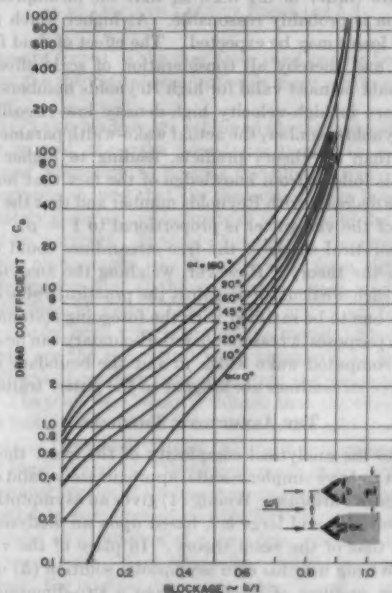


FIG. 8 DRAG COEFFICIENT C_D AS A FUNCTION OF BLOCKAGE b/t FOR VARIOUS GUTTER HALF ANGLE α

coefficient and blockage, $C_D b/t$, is seen to be a function only of μ , or alternately of λ , and therefore of α and b/t from Equation [1]. Numerical results are shown in Figs. 7 and 8, where C_D is shown as a function of α and b/t . The drag coefficient for the case of a single vee-gutter, $b/t = 0$, has been given previously by Bobyleff (3). Also shown in Fig. 7 are the results of the asymptotic theories.

PHYSICAL SIGNIFICANCE OF RESULTS

The important physical results are shown in Figs. 3 through 8. The wake width/pitch ratio μ , the total pressure-loss coefficient λ , and the drag coefficient C_D are seen to increase with blockage ratio b/t as expected physically. Similarly, they are seen to increase with gutter half angle α , with a decreasing rate as α is increased from $\alpha = 0$ to $\alpha = 180$ deg. The wake width, loss, and drag at $\alpha = 90$ deg are considerably higher than those at $\alpha = 0$. However, the values at $\alpha = 180$ deg are only slightly higher than those at $\alpha = 90$ deg.

Some explanation of the limiting geometries is in order. At constant blockage b/t , the case of $\alpha = 0$ corresponds to a gutter made up of two coincident sides parallel to the upstream flow direction, with "open" end downstream. Thus the breadth $b = 0$ and for $b/t \neq 0$, the pitch $t = 0$. Thus $\mu > 0$ still implies wake width $\mu t = 0$. The loss coefficient $\lambda > 0$, but $\Delta p_T = 0$, $w_1 = 0$ since the space is "full of gutters." At constant blockage b/t , the case of $\alpha = 180$ deg corresponds to the same gutter as for $\alpha = 0$, but with open end upstream. In this case an impediment to the flow is present in that the fluid must flow in and then back out of the rectangular channel of breadth $b = 0$. Again, the pitch $t = 0$ for constant $b/t \neq 0$, and $\mu > 0$ implies wake width $\mu t = 0$. Again, $\lambda > 0$, $\Delta p_T = 0$, $w_1 = 0$. The case of blockage $b/t = 0$ is that of a single gutter, since $b > 0$ and $t = \infty$. In this case $\mu = 0$ since $t = \infty$, $\lambda = 0$ since $w_1 > 0$, and $C_D > 0$. The case of blockage $b/t = 1.0$ is that of zero gap $t = b$ between adjacent plates. In this case $\mu = 1.0$ (downstream space filled with wakes), $\lambda = \infty$, and $C_D = \infty$ since $w_1 = 0$.

The effect of compressibility has been ignored for simplicity of analysis. Luckily, in modern afterburner practice Mach numbers are low (order of 0.1–0.2), so that the incompressible approximation is probably reasonable. At higher Mach numbers, additional losses may be expected. The effect of fluid friction is neglected, and thereby all consideration of scale effects. The theory should be most valid for high Reynolds numbers; i.e., for large gutters in high-velocity high-density low-viscosity fluids. At low Reynolds number, the actual wake-width parameter μ will be larger than the theory predicts, leading to higher loss and drag. This follows from knowledge of the fact that nozzle flow coefficients decrease with Reynolds number and that the "flow coefficient" of the vee-gutter is proportional to $1 - \mu$.

The theoretical shape of the free streamlines could be calculated from the theory. However, weighing the analytical complexity of such a calculation against the practical value of the results leads one to be satisfied with the foregoing statement. For estimation purposes, a reasonable wake boundary can be sketched, using the computed wake width μt and the boundary condition that the free streamlines are tangent to the gutter trailing edges.

THE ASYMPTOTIC THEORIES

Owing to the analytical complexity of the exact theory, it is convenient to have simpler results, approximately valid over part of the range of variables. Weinig (4) gives an asymptotic theory, valid for small α and large b/t , based upon an analysis entirely similar to that of the exact theory. In place of the von Mises solution, Weinig uses his own asymptotic solution (5) of the potential flow problem of discharge from a two-dimensional contraction, for the case $\alpha \rightarrow 0$, $b/t \rightarrow 1$. Weinig's results are as follows

$$\mu \sim 1 - \frac{1 - b/t}{1 + G(\alpha)} \quad [10]$$

where

$$G(\alpha) \equiv \frac{4}{\pi^2} \alpha \left[1 + 0.085 \left(1 - \frac{2\alpha}{\pi} \right)^2 \right]$$

The fundamental relations, Equations [5] and [9], for $\lambda(\mu)$ and $C_D(\lambda)$ still obtain. Comparison of Equations [1] and [10] shows the same general form of $\mu(b/t, \alpha)$ in the exact and asymptotic theories, with the approximation that $F(b/t, \alpha) \sim G(\alpha)$ for small α and large b/t . In Figs. 3, 5, and 7, the Weinig asymptotic theory is compared to the exact theory. It is seen that the asymptotic theory gives good results, μ , λ , and C_D being higher than the exact values, for the case of small α and large b/t .

A second asymptotic theory can be developed for the case of large α and large b/t . Weinig (6) has shown that a "bellmouth," suitable for an inlet in a turbomachine test stand, can be designed for constant velocity on the surface. Potential theory methods (2) are applied as follows: The desired bellmouth flow in the z -plane is describable in terms of an unknown complex potential $W = \phi + i\psi$. The z -plane is mapped conformally on the ξ -plane, containing as image of the bellmouth flow a uniform flow,² given by $W = -\xi$. Physical deduction shows that $\ln(dW/dz) = -e^{\xi} - i\pi$ is a reasonable, yet simple, expression for the ξ -plane image of the isotach-isocline field of the z -plane. Then, having $dW/d\xi$ and dW/dz in terms of ξ , the derivative $dz/d\xi$ of the transformation function is obtained. Integration yields $z = -Ei(e^{\xi})$, where

$$-Ei(-x) \equiv \int_x^{\infty} (e^{-t}/t) dt$$

is the exponential integral and ξ is a dummy variable of integra-

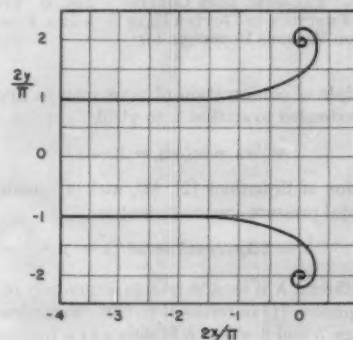


FIG. 9 SICI SPIRAL

tion. Further investigation shows that the bellmouth contour is the Sici spiral shown in Fig. 9, where $z = x + iy$ and

$$\left. \begin{aligned} \frac{2x}{\pi} &= \frac{2}{\pi} Ci(\alpha) \\ \frac{2y}{\pi} &= 1 + \frac{2}{\pi} Si(\alpha) \end{aligned} \right\} \dots\dots\dots [11]$$

and

$$Ci(\alpha) \equiv - \int_{\alpha}^{\infty} (\cos \alpha/\alpha) d\alpha$$

and

$$Si(\alpha) \equiv (\pi/2) - \int_{\alpha}^{\infty} (\sin \alpha/\alpha) d\alpha$$

are, respectively, the cosine and sine integrals.

The angle α is the local inclination of the bellmouth contour.

² Taking velocity proportional to the positive potential derivative.

The potential flow pattern of the bellmouth can be applied to the vee-gutter configuration as shown in Fig. 10. At chosen points P on the bellmouth contour, the upstream flow is taken as that off the trailing edges of vee-gutters in a cascade of large blockage

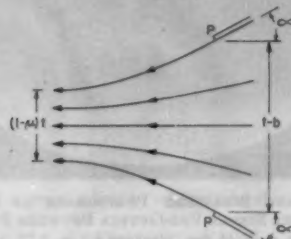


FIG. 10 FLOW IN VEE-GUTTER CASCADE OF LARGE GUTTER HALF ANGLE α AND LARGE BLOCKAGE b/t

b/t and half angle α . The downstream portions of the bellmouth contour are taken as the free streamlines of the vee-gutter cascade. The wake-width parameter μ is then given by

$$\mu \sim 1 - \frac{1 - b/t}{1 + H(\alpha)} \quad [12]$$

where

$$H(\alpha) \equiv \frac{2}{\pi} Si(\alpha)$$

Again, Equations [5] and [9] give $\lambda(\mu)$ and $C_D(\lambda)$. The same general form of $\mu(b/t, \alpha)$ is obtained as in Equations [1] and [10], with the approximation that $F(b/t, \alpha) \sim H(\alpha)$ for large α and large b/t . In Figs. 3, 5, and 7 the present asymptotic theory is compared to the exact theory. The asymptotic theory gives fairly good results, the range of validity being restricted to very large α and b/t , and μ , λ , and C_D being higher than the exact values.

COMPARISON WITH EXPERIMENTAL RESULTS

Noreen (7) tested single vee-gutters of 90 deg included angle ($\alpha = 45$ deg) and various widths b in a rectangular channel (span = 2 in., wall spacing $t = 4$ in.). The blockage ratios b/t were 0.5, 0.625, 0.75. Tests were made with air at velocities from 25 to 90 fps and with and without combustion. Pressure drop across the vee-gutter section was determined by measurement of wall static pressure before and behind the vee-gutter. In Fig. 11 are shown test values of loss coefficient λ plotted as a function of b/t , compared with the theoretical curve for $\alpha = 45$ deg. Measured losses with combustion exceed those predicted theoretically. Measured losses without combustion are less than theory predicts. The undoubtedly imperfectly square edges of the vee-gutter trailing edges probably are partially responsible for the relatively low loss of the cold tests. Thus the theory assumes that the wake leaves tangent to the vee-gutter surface at the trailing edge. If the edge is slightly rounded, the flow will follow the contour, leading to a thinner wake, and hence lower loss.

In the case of the hot tests, additional losses occur due to heat addition. The disparity between theory and experiment is least at high blockage b/t , becoming higher as b/t is decreased. This is to be expected, since the theory's assumption of wake-pressure constant at the downstream value becomes less valid as blockage is decreased. In the case of low-blockage cascades, the actual wake pressure is somewhat below the downstream value, giving rise to relatively high drag, thick wake, and large loss compared to the theoretical value. As blockage is increased, strong ac-

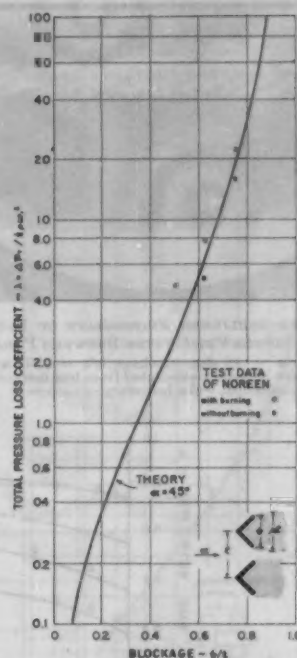


FIG. 11 COMPARISON OF THEORY AND EXPERIMENT FOR SINGLE VEE-GUTTER BETWEEN PARALLEL WALLS. GUTTER HALF ANGLE $\alpha = 45$ DEG AND VARIOUS BLOCKAGE b/t

celerations are forced in the flow from inlet to jets between the wakes, and the theoretical assumption is more nearly representative of fact.

Noreen (7) also made spark schlieren photographs of the wake flow. In general, the wake boundaries tended to roll up into vortices and ultimately to become turbulent. Examination of the photographs showed that the theoretical wake boundary lay approximately along an eye estimate of the locus of the centers of the rolled-up vortices. Typical photographs are shown in Fig. 12. In the photographs, the flow proceeds from right to left. The upper trailing edge of the vee-gutter is seen, and the light field is the field of flow. The vertical marks at the top of the photographs were 1 in. apart on the model. Shown in the photographs are the theoretical wake boundary, as well as the "effective" wake boundary computed from the measured loss coefficient. The theoretical wake is thinner than the effective wake in the hot tests, the converse being true in the cold tests.

Test data of Grey and Wilsted (8) are shown, compared with theory, in Figs. 13 and 14. Tests were made in air with axisymmetrical conical nozzles of various cone-angle and diameter ratio. The original data were presented in the form of curves of contraction coefficient as a function of cone angle, diameter ratio, and nozzle pressure ratio. For comparison with the present vee-gutter theory, the original data were extrapolated to unity pressure ratio and reworked into the form of wake-width parameter μ as a function of gutter half angle α and blockage b/t , for the equivalent two-dimensional case, defined as that one having the same fraction of blocked area as the three-dimensional case of the experiment. Thus, with d_1 and d_2 , respectively, the inlet and outlet diameters of the conical nozzle, the blockage ratio of the equivalent vee-gutter is given by

$$\left(\frac{b}{t}\right)_{eq} \equiv 1 - \left(\frac{d_2}{d_1}\right)^2 \quad [13]$$

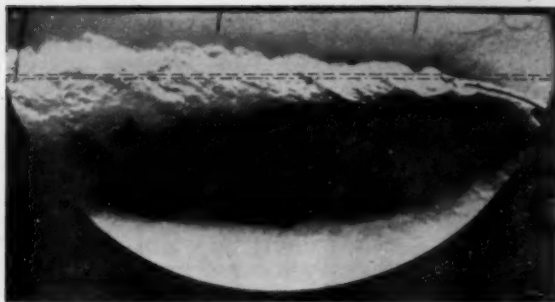


FIG. 12(a) SPARK SCHLIEREN PHOTOGRAPH OF FLOW WITH COMBUSTION OVER SINGLE VEE-GUTTER BETWEEN PARALLEL WALLS (Gutter half angle $\alpha = 45$ deg, blockage $b/t = 0.75$, and inlet velocity $w_1 = 48.7$ fps. Wake boundary calculated from loss measurements — — —; theoretical wake boundary — — — —.)



FIG. 12(b) SPARK SCHLIEREN PHOTOGRAPH OF FLOW WITHOUT COMBUSTION OVER SINGLE VEE-GUTTER BETWEEN PARALLEL WALLS (Gutter half angle $\alpha = 45$ deg, blockage $b/t = 0.75$, and inlet velocity $w_1 = 46.5$ fps. Wake boundary calculated from loss measurements — — —; theoretical wake boundary — — — —.)

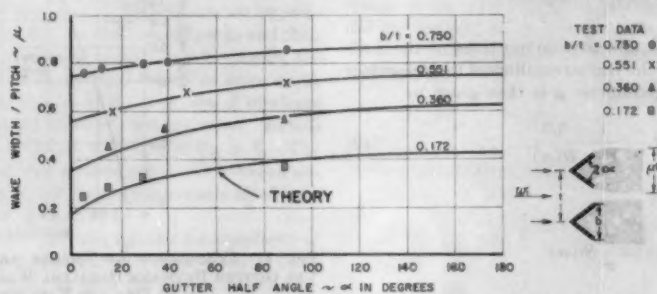


FIG. 13 COMPARISON OF THEORY AND EXPERIMENT FOR AXISYMMETRIC CONICAL NOZZLES WITH VARIOUS HALF ANGLE α AND BLOCKAGE b/t

The contraction coefficient is related to μ and b/t by

$$C_c = \frac{1 - \mu}{1 - \frac{b}{t}} \quad [14]$$

from the geometry of the configuration shown in Fig. 1.

The validity of this comparison of two and three-dimensional flows is well known. The classical example is the fact that the theoretical contraction coefficient for a two-dimensional sharp-edged orifice (long slit) is very nearly equal to the experimental value for circular sharp-edged orifices (2). Other examples are cited by Weinig (9), the author (10), and as given later in this paper.

The limitations of the validity of such comparisons of two and three-dimensional flows are principally governed by the following consideration: If a three-dimensional flow with radial co-ordinate denoted by R and axial co-ordinate by Z be compared with a two-dimensional flow with "comparable" co-ordinates denoted by Y and X , then a comparison such as that discussed is based upon the following imputed co-ordinate transformation

$$\left. \begin{aligned} X &= Z \\ Y &= R^2 \end{aligned} \right\} \quad [15]$$

Consideration of the nonlinear nature of the Y, R -relation quickly indicates that the comparison is valid only for flows in which the radial (R) components of velocity are relatively small. In cases where large radial velocities exist, a vee-gutter in the three-dimensional R, Z -space transforms into a gutter of curved elements in the two-dimensional Y, X -space. Only for the cases of small radial velocity does a vee-gutter in R, Z become

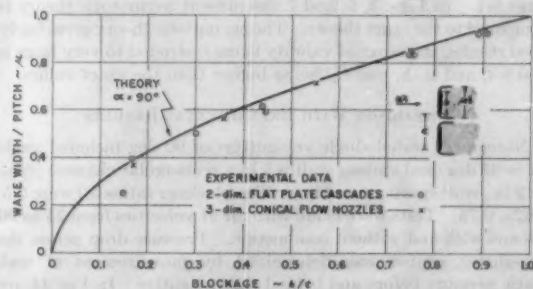


FIG. 14 COMPARISON OF THEORY AND EXPERIMENT FOR AXISYMMETRIC CONICAL NOZZLES AND FLAT PLATE CASCADES WITH HALF ANGLE $\alpha = 90$ DEG AND VARIOUS BLOCKAGE b/t

(approximately) a vee-gutter in Y, X . Thus in the vee-gutter case, for gutters of small half angle α , the comparison is most valid. Further, for large blockage (and hence small velocity along the cascade axis) most validity is found. Examination of Fig. 13 shows good agreement between theory and experiment. Best agreement is noted at high blockage b/t , as expected, and at high gutter half angle α . This latter is unexpected from the foregoing considerations. However, a further factor probably is responsible for overriding this: At high gutter angle, the "effective blockage" is greater and more acceleration is forced upon the jets between the wakes, leading to more accurate theoretical prediction (similarly to the effect discussed previously under the effect of blockage b/t). Fig. 14 shows theory and experiment for the case of $\alpha = 90$ deg, wake-width parameter μ being shown as a function of blockage b/t . Good agreement is obtained.

The data of Betz and Petersohn (11) on two-dimensional cascades of sharp-edged flat plates—equivalent to the case of $\alpha = 90$ deg—are also shown in Fig. 14. Tests were made with air and also with water discharging into atmospheric air. The velocity in the jets between the wakes was reported, calculated from static pressure measurements downstream of the cascade. In the present comparison, wake-width parameter μ was calculated from $tw_1 = (1 - \mu)w_2$, the continuity relation, using experimental values of w_1/w_2 . It is noted that the experimental values of μ are less than those predicted theoretically, an effect no doubt partially due to imperfect sharpness of plate edges.

Figs. 15, 16, and 17 show test results of Langer (12), who measured forces with a two-component balance on cascades of the profiles shown, corresponding to vee-gutters of half angle $\alpha = 90$,

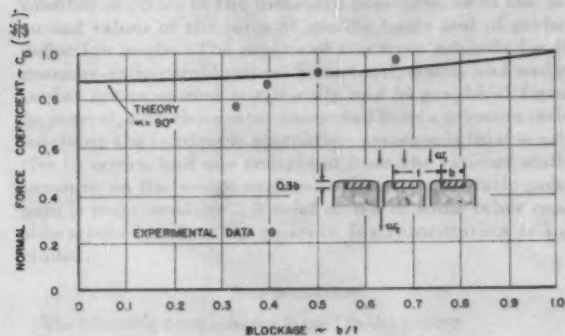


FIG. 15 COMPARISON OF THEORY AND EXPERIMENT FOR CASCADES OF GUTTER HALF ANGLE $\alpha = 90$ DEG AND VARIOUS BLOCKAGE b/t

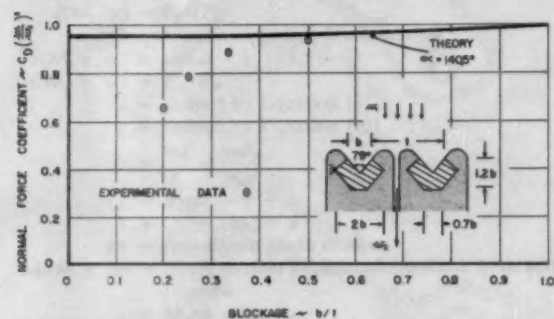


FIG. 16 COMPARISON OF THEORY AND EXPERIMENT FOR CASCADES OF GUTTER HALF ANGLE $\alpha = 140.5$ DEG AND VARIOUS BLOCKAGE b/t

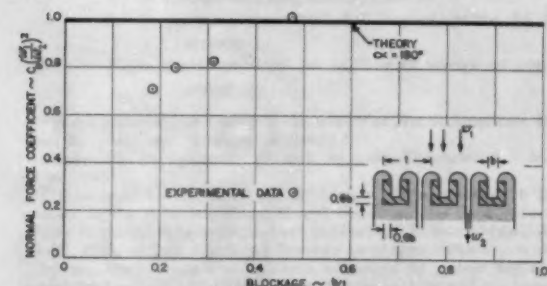


FIG. 17 COMPARISON OF THEORY AND EXPERIMENT FOR CASCADES OF GUTTER HALF ANGLE $\alpha = 180$ DEG AND VARIOUS BLOCKAGE b/t

140.5, 180 deg, and to various blockages b/t . The data are shown as normal force coefficient $C_N(w_1/w_2)^2$, or drag coefficient based on jet velocity w_2 , as a function of blockage b/t . It is noted that at low blockage b/t experimental drag coefficient is generally less than that predicted theoretically, an unexpected result. However, agreement improves with increasing blockage, as expected. At high blockage, experimental drag coefficients exceed theoretical values, as expected.

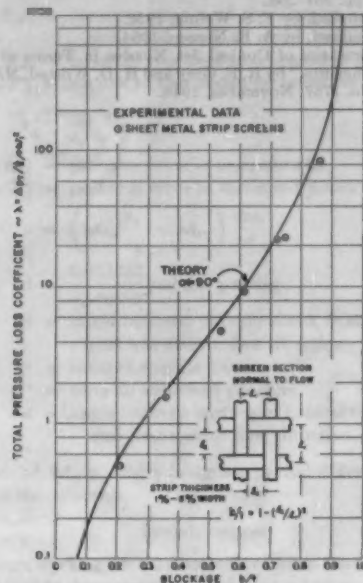


FIG. 18 COMPARISON OF THEORY AND EXPERIMENT FOR FLOW NORMAL TO SHEET-METAL STRIP SCREENS. HALF ANGLE $\alpha = 90$ DEG AND VARIOUS BLOCKAGE b/t

Experimental data of Flachsbart (13) are shown in Fig. 18, compared with the theory. The data are shown as total pressure-loss coefficient λ as a function of blockage b/t , for tests with air in three-dimensional screens formed of rectangularly woven thin sheet-metal strips, with flow normal to the plane of the screen. The original three-dimensional data have been converted to equivalent two-dimensional data on the basis of equal blocked-area ratio, as previously discussed. Good agreement is noted between theory and experiment, measured losses being lower, probably due to slight rounding of the plate edges. This comparison of theory and experiment was first noted by Weinig (9) in his study of ribbon parachutes.

CONCLUSION

The present theory gives a reasonable means of predicting the performance of high blockage cascades of vee-gutter profiles, yielding the wake shape, the total pressure loss, and the drag force of the profiles. Consequently, the effect of design choice of blockage and gutter angle can be predicted prior to proof-testing of afterburner flame holders of vee-gutter type.

ACKNOWLEDGMENTS

The author is indebted to Dr. F. S. Weinig for many suggestions, to Mr. A. E. Noreen for obtaining the experimental data of reference (7), and to Messrs. H. A. Fremont, J. E. Worsham, and J. W. Vdovick for many helpful discussions and references to combustion literature.

BIBLIOGRAPHY

- 1 "Berechnung von Ausfluss- und Überfallzahlen," by R. von Mises, *Zeitschrift des Vereines deutscher Ingenieure*, bd. 61, 1917, no. 21, pp. 447-452; no. 22, pp. 469-474; no. 23, pp. 493-498.
- 2 "Hydrodynamics," by H. Lamb, Dover Publications, New York, N. Y., sixth edition, 1945.
- 3 By D. Bobyleff, *Journal of the Russian Physico-Chemical Society*, vol. 13, 1881.
- 4 Unpublished, by F. S. Weinig, 1951.
- 5 "Ausfluss aus einer Düse," by F. S. Weinig, *Ingenieur-Archiv*, bd. 11, 1940, pp. 264-268.
- 6 Unpublished, by F. S. Weinig, 1952.
- 7 Unpublished, by A. E. Noreen, 1954.
- 8 "Performance of Conical Jet Nozzles in Terms of Flow and Velocity Coefficients," by R. E. Grey and H. D. Wilsted, NACA Technical Note, No. 1757, November, 1948.
- 9 "Parachutes With Canopies Composed of Self-Supporting Ribbons," by F. S. Weinig, HQAMC, Wright Field, Technical Report No. F-TR-2148-ND, GS-AAF-Wright Field No. 22, 1947, pp. 13-14.
- 10 "The Stall Performance of Cascades," by W. G. Cornell, Proceedings of the Second U. S. National Congress of Applied Mechanics, Ann Arbor, Mich., 1954.
- 11 "Anwendung der Theorie der freien Strahlen," by A. Betz and E. Petersohn, *Ingenieur-Archiv*, bd. 2, 1931, pp. 190-211.
- 12 "Bremswirkung von Windschutzgittern," by R. Langer, Ergebnisse der Aerodynamischen Versuchsanstalt zu Göttingen, IV Lieferung, 1932, pp. 138-141.
- 13 "Widerstand von Seidengasfilter, Runddraht- und Blechstreifensieben mit quadratischen Maschen," by O. Flachsart, Ergebnisse der Aerodynamischen Versuchsanstalt zu Göttingen, IV Lieferung, 1932, pp. 112-118.

Determination of Mach Number From Pressure Measurements¹

By F. W. BARRY,² EAST HARTFORD, CONN.

This paper contains a discussion of the errors introduced by using various combinations of measured pressures to compute Mach number, especially in supersonic flow. Pressures measured with total, static, conical, and two-dimensional wedge probes are considered. A procedure is developed for estimating the effect on computed Mach number of errors in the measured pressures, or in the assumed values of the ratio of specific heats and of probe-deflection angle. The results of the error analysis for 10 pressure-ratio combinations from total, static, and wedge probes are presented analytically and in graphical form. In general, a Mach number computed from a pressure ratio involving the isentropic stagnation pressure is least sensitive to errors, and one computed from the ratio of static pressure on the wedge surface to free-stream static pressure is most sensitive. A brief review of some other considerations in choosing pressure instrumentation is included.

NOMENCLATURE

The following nomenclature is used in the paper:

- $a(M, \gamma) = P_t/P$
 $b(M, \gamma) = P_t'/P$
 $c(M, \gamma, \alpha) = P/P_1$
 $d(M_1, \gamma) = P_t'/P_1$
 $E(M) =$ error in computed Mach number
 $e(M, \gamma, \alpha) = \tan \omega$
 $f(M, \gamma, \alpha) = P_L/P_a$
 $G =$ defined by Equation [8]
 $g =$ defined by Equation [10]
 $h = \frac{cM}{c} - \frac{eM\alpha}{e\alpha c}$
 $j = 2\gamma m^2 - \gamma + 1$
 $k = (\gamma - 1)m^2 + 2$
 $M =$ free-stream Mach number
 $M_1(M, \gamma, \alpha) =$ Mach number behind oblique shock from wedge probe
 $m = M \sin \alpha$
 $n = \left(M_1 M - M_{1a} \frac{eM}{e\alpha} \right) \frac{dM_1}{d}$
 $P =$ free-stream static pressure
 $P_t =$ free-stream stagnation pressure
 $P_t' =$ pressure measured by impact probe in free stream
 $P_1 =$ static pressure on surface of wedge or conical probe

- $P_a' =$ pressure measured by impact probe behind oblique shock from wedge probe
 $P_L =$ larger of two measured pressures
 $P_S =$ smaller of two measured pressures
 $r = \frac{e_\gamma c_\alpha}{e_\alpha c} - \frac{c_\gamma}{c}$
 $r(M) =$ probable error in computed M
 $r(P) =$ probable error in measured pressure
 $s = \left(M_{1a} \frac{e_\gamma}{e_\alpha} - M_{1\gamma} \right) \frac{dM_1}{d}$
 $t = 0.017453$
 $t = e_\alpha \cos^2 \omega$ radians per deg
 $\alpha =$ angle between oblique shock from wedge probe and free-stream flow direction
 $\gamma =$ ratio of specific heats
 $\epsilon P =$ error in measured pressure
 $\omega =$ angle between surface of conical or wedge probe and free-stream flow direction.

Subscripts M , M_1 , α , and γ designate partial differentiation with respect to the subscript.

INTRODUCTION

Engineers working with subsonic flows have the results of years of experience to draw upon in arriving at solutions to instrumentation problems. Engineers working with supersonic flows, on the other hand, do not have such a large background of experience. The relative newness of the study of supersonic flows, coupled with the large increases in the number of supersonic wind tunnels and the operation of missiles at supersonic speeds, emphasizes the need for a periodic evaluation of the instruments and techniques used for measuring these flows.

Of the various compressible-flow parameters which one may wish to determine experimentally, Mach number is nearly always the most important. The fact that a calibration of a supersonic wind tunnel is largely a matter of determining the Mach-number distribution in the test section attests to the significance of this parameter.

With the exception of Mach wave-angle measurements in supersonic flow, no means for measuring Mach number directly exists.³ Usually pressures are measured and the Mach number computed from some pressure ratio. This paper presents the results of a theoretical analysis of methods for determining Mach number by combinations of pressures measured with total (pitot), static, conical, and wedge probes. The available theories for supersonic flow about axially symmetric cones or two-dimensional wedges are used. The results for conical or wedge probes are applied only when the flow is entirely supersonic since the validity of these theories is questionable in mixed flow. The analysis includes a study of the effect on the computed Mach number of errors in measured pressures, in assumed ratio of specific heats, or in wedge deflection angle in order to provide engineers with a

¹ Some material developed by the author at North American Aviation, Inc., has been included (reference 3).

² Research Department, United Aircraft Corporation. Assoc. Mem. ASME.

Contributed by the Aviation Division and presented at a joint session of the Aviation Division and the American Rocket Society at the Diamond Jubilee Semi-Annual Meeting, Boston, Mass., June 19-23, 1955, of THE AMERICAN SOCIETY OF MECHANICAL ENGINEERS.

NOTE: Statements and opinions advanced in papers are to be understood as individual expressions of their authors and not those of the Society. Manuscript received at ASME Headquarters, January 11, 1955. Paper No. 55-SA-23.

³ Mach number is the reciprocal of the sine of the Mach angle. Other methods for determining Mach number require that at least two quantities be measured and a value for the ratio of specific heats be assumed.

BIBLIOGRAPHY

- 1 "Berechnung von Ausfluss- und Überfallszahlen," by R. von Mises, *Zeitschrift des Vereines deutscher Ingenieure*, bd. 61, 1917, no. 21, pp. 447-452; no. 22, pp. 469-474; no. 23, pp. 493-498.
- 2 "Hydrodynamics," by H. Lamb, Dover Publications, New York, N. Y., sixth edition, 1945.
- 3 By D. Bobyleff, *Journal of the Russian Physico-Chemical Society*, vol. 13, 1881.
- 4 Unpublished, by F. S. Weinig, 1951.
- 5 "Ausfluss aus einer Düse," by F. S. Weinig, *Ingenieur-Archiv*, bd. 11, 1940, pp. 264-268.
- 6 Unpublished, by F. S. Weinig, 1952.
- 7 Unpublished, by A. E. Noreen, 1954.
- 8 "Performance of Conical Jet Nozzles in Terms of Flow and Velocity Coefficients," by R. E. Grey and H. D. Wilsted, NACA Technical Note, No. 1757, November, 1948.
- 9 "Parachutes With Canopies Composed of Self-Supporting Ribbons," by F. S. Weinig, HQAMC, Wright Field, Technical Report No. F-TR-2148-ND, GS-AAF-Wright Field No. 32, 1947, pp. 13-14.
- 10 "The Stall Performance of Cascades," by W. G. Cornell, Proceedings of the Second U. S. National Congress of Applied Mechanics, Ann Arbor, Mich., 1954.
- 11 "Anwendung der Theorie der freien Strahlen," by A. Betz and E. Petersohn, *Ingenieur-Archiv*, bd. 2, 1931, pp. 190-211.
- 12 "Bremswirkung von Windschutzgittern," by R. Langer, Ergebnisse der Aerodynamischen Versuchsanstalt zu Göttingen, IV Lieferung, 1932, pp. 138-141.
- 13 "Widerstand von Seidengasfilter, Runddraht- und Blechstreifensieben mit quadratischen Maschen," by O. Flachsbart, Ergebnisse der Aerodynamischen Versuchsanstalt zu Göttingen, IV Lieferung, 1932, pp. 112-118.

Determination of Mach Number From Pressure Measurements¹

By F. W. BARRY,² EAST HARTFORD, CONN.

This paper contains a discussion of the errors introduced by using various combinations of measured pressures to compute Mach number, especially in supersonic flow. Pressures measured with total, static, conical, and two-dimensional wedge probes are considered. A procedure is developed for estimating the effect on computed Mach number of errors in the measured pressures, or in the assumed values of the ratio of specific heats and of probe-deflection angle. The results of the error analysis for 10 pressure-ratio combinations from total, static, and wedge probes are presented analytically and in graphical form. In general, a Mach number computed from a pressure ratio involving the isentropic stagnation pressure is least sensitive to errors, and one computed from the ratio of static pressure on the wedge surface to free-stream static pressure is most sensitive. A brief review of some other considerations in choosing pressure instrumentation is included.

NOMENCLATURE

The following nomenclature is used in the paper:

- $a(M, \gamma) = P_t/P$
- $b(M, \gamma) = P_t'/P$
- $c(M, \gamma, \alpha) = P/P_t$
- $d(M, \gamma) = P_n'/P_t$
- $E(M) = \text{error in computed Mach number}$
- $e(M, \gamma, \alpha) = \tan \omega$
- $f(M, \gamma, \alpha) = P_L/P_g$
- $G = \text{defined by Equation [8]}$
- $g = \text{defined by Equation [10]}$
- $h = \frac{cM}{e} - \frac{cMc_\alpha}{e_\alpha c}$
- $j = 2\gamma m^2 - \gamma + 1$
- $k = (\gamma - 1)m^2 + 2$
- $M = \text{free-stream Mach number}$
- $M_1(M, \gamma, \alpha) = \text{Mach number behind oblique shock from wedge probe}$
- $m = M \sin \alpha$
- $n = \left(M_1 M - M_{1a} \frac{eM}{e_\alpha} \right) \frac{dM_1}{d}$
- $P = \text{free-stream static pressure}$
- $P_t = \text{free-stream stagnation pressure}$
- $P_t' = \text{pressure measured by impact probe in free stream}$
- $P_1 = \text{static pressure on surface of wedge or conical probe}$

$P_n' = \text{pressure measured by impact probe behind oblique shock from wedge probe}$

$P_L = \text{larger of two measured pressures}$

$P_g = \text{smaller of two measured pressures}$

$$r = \frac{e_\gamma}{e_\alpha} \frac{c_\alpha}{c} - \frac{c_\gamma}{c}$$

$r(M) = \text{probable error in computed } M$

$r(P) = \text{probable error in measured pressure}$

$$s = \left(M_{1a} \frac{e_\gamma}{e_\alpha} - M_{1\gamma} \right) \frac{dM_1}{d}$$

$$t = \frac{0.017453}{e_\alpha \cos^2 \omega} \text{ radians per deg}$$

$\alpha = \text{angle between oblique shock from wedge probe and free-stream flow direction}$

$\gamma = \text{ratio of specific heats}$

$eP = \text{error in measured pressure}$

$\omega = \text{angle between surface of conical or wedge probe and free-stream flow direction.}$

Subscripts M , M_1 , α , and γ designate partial differentiation with respect to the subscript.

INTRODUCTION

Engineers working with subsonic flows have the results of years of experience to draw upon in arriving at solutions to instrumentation problems. Engineers working with supersonic flows, on the other hand, do not have such a large background of experience. The relative newness of the study of supersonic flows, coupled with the large increases in the number of supersonic wind tunnels and the operation of missiles at supersonic speeds, emphasizes the need for a periodic evaluation of the instruments and techniques used for measuring these flows.

Of the various compressible-flow parameters which one may wish to determine experimentally, Mach number is nearly always the most important. The fact that a calibration of a supersonic wind tunnel is largely a matter of determining the Mach-number distribution in the test section attests to the significance of this parameter.

With the exception of Mach wave-angle measurements in supersonic flow, no means for measuring Mach number directly exists.³ Usually pressures are measured and the Mach number computed from some pressure ratio. This paper presents the results of a theoretical analysis of methods for determining Mach number by combinations of pressures measured with total (pitot), static, conical, and wedge probes. The available theories for supersonic flow about axially symmetric cones or two-dimensional wedges are used. The results for conical or wedge probes are applied only when the flow is entirely supersonic since the validity of these theories is questionable in mixed flow. The analysis includes a study of the effect on the computed Mach number of errors in measured pressures, in assumed ratio of specific heats, or in wedge deflection angle in order to provide engineers with a

¹ Some material developed by the author at North American Aviation, Inc., has been included (reference 3).

² Research Department, United Aircraft Corporation, Assoc. Mem. ASME.

Contributed by the Aviation Division and presented at a joint session of the Aviation Division and the American Rocket Society at the Diamond Jubilee Semi-Annual Meeting, Boston, Mass., June 19-23, 1955, of THE AMERICAN SOCIETY OF MECHANICAL ENGINEERS.

NOTE: Statements and opinions advanced in papers are to be understood as individual expressions of their authors and not those of the Society. Manuscript received at ASME Headquarters, January 11, 1955. Paper No. 55-SA-28.

³ Mach number is the reciprocal of the sine of the Mach angle. Other methods for determining Mach number require that at least two quantities be measured and a value for the ratio of specific heats be assumed.

rational means for choosing instrumentation and for estimating the accuracy of the computed Mach number.

DETERMINING MACH NUMBER FROM PRESSURE MEASUREMENTS

The isentropic stagnation pressure P_1 may be measured in a subsonic stream by a total pressure probe. An impact probe placed in a supersonic stream, on the other hand, measures a pressure lower than the stagnation pressure. The ratio between the measured impact pressure and the ideal stagnation pressure, P_i'/P_1 , is the well-known ratio of stagnation pressure across the normal shock and is a function of only Mach number and the ratio of specific heats, γ . Consequently, if one can measure both the impact pressure and the stagnation pressure, and if one assumes a value for γ , one can calculate the corresponding Mach number. This method for determining Mach number can be used when the flow accelerates through the speed of sound isentropically, as in a supersonic wind tunnel. In this instance the stagnation pressure in the section ahead of the tunnel throat is usually assumed to equal the stagnation pressure in the test section, except in a boundary layer or behind a shock from a model. This method is often used because of its simplicity and the small size of the probe.

Sometimes the stagnation pressure cannot be measured and some other pressure ratio is used to determine Mach number. For example, the Mach number may be calculated from measured impact and static pressures. The ratio of impact to static pressure is likewise a function of Mach number and γ . This is shown in Fig. 1 by the line labeled $\omega = 0$ deg. This method is used to

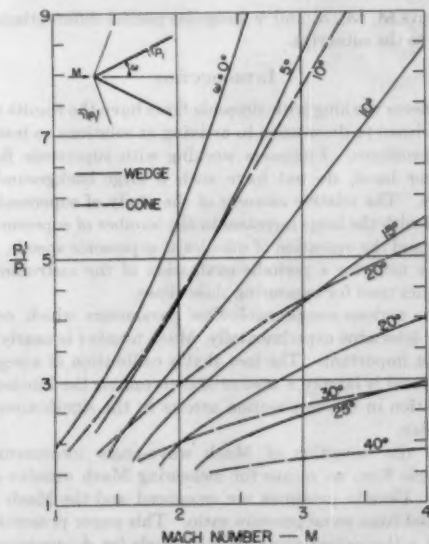


FIG. 1 P_i'/P_1 AS A FUNCTION OF M AND ω FOR TWO-DIMENSIONAL AND CONICAL PROBES

determine the Mach-number profile in a boundary layer on a plane wall because the static pressure usually can be measured conveniently by a tap in the wall or by a probe near the wall as proposed in reference (1).⁴

A pressure measured on the surface of a wedge or conical probe also may be used in conjunction with the impact pressure to determine Mach number. The static pressure on the surface of a wedge may be expressed by the oblique-shock relations as a

⁴ Numbers in parentheses refer to the Bibliography at the end of the paper.

function of the free-stream static pressure and Mach number, and the angle ω between the wedge surface and the undisturbed streamlines. Therefore the ratio of impact pressure to surface pressure P_i'/P_1 , depends upon the Mach number γ and the flow deflection angle. Similarly, the ratio of impact pressure to the surface pressure on a cone depends upon the Mach number γ and cone angle (2). This ratio is shown in Fig. 1 for wedge and conical probes.

The static pressure ratio (P_1/P) for wedge probes has an undesirable characteristic as shown in Fig. 2. Two Mach numbers, rather than one, may correspond to a given pressure ratio. If this is the situation, only an approximate value of the Mach number or another measured pressure can resolve the indeterminacy in Mach number.

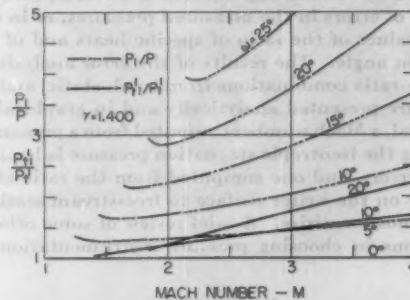


FIG. 2 P_1/P AND P_i'/P_1 AS FUNCTIONS OF M AND ω FOR TWO-DIMENSIONAL PROBES

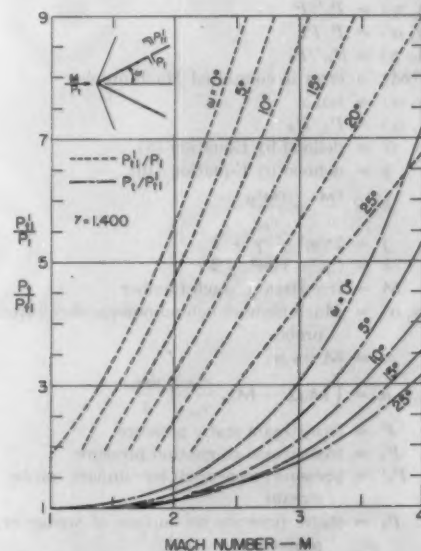


FIG. 3 P_i'/P_1 AND P_i'/P_1 AS FUNCTIONS OF M AND ω FOR TWO-DIMENSIONAL PROBES

The impact pressure behind the bow wave, rather than the free-stream impact pressure, may be read by a total pressure tube which can be attached to a wedge or cone probe. Theoretically, this impact pressure $P_{i'}$ does not depend on the position of the impact tube with respect to the two-dimensional wedge-probe surface providing the tube is behind the bow wave. The ratio of the measured impact pressure to the surface static pressure is

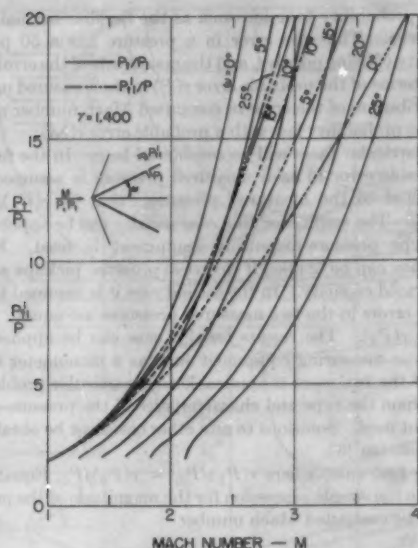


FIG. 4 P_1/P_1 and P_1'/P_1 AS FUNCTIONS OF M AND ω FOR TWO-DIMENSIONAL PROBES

plotted in Fig. 3 for a number of wedge probes. Any analysis of a conical probe with an impact tube behind the conical shock must include an additional variable of the impact-tube location to describe the probe geometry because of the nonuniform flow between the conical shock and the conical-probe surface (2). A higher value of $P_{n'}$ would be measured by an impact probe near the cone surface than would be measured by a probe just behind the conical shock.

A number of pressure ratios can be formed from pairs of these five pressures (P_0 , P_1 , P_1' , $P_{n'}$, P , and P_1), see Figs. 1 through 5. Three ratios are limiting cases corresponding to $\omega = 0$. Additional pressure-ratio combinations are available if an asymmetric probe is used, or if both conical and wedge probes are used. As discussed in the next section, a Mach number computed from some combinations is inherently more accurate than one computed from some other combinations.

ANALYSIS OF ERRORS

In the usual wind tunnel or flight-test techniques, it is inevitable that some errors will occur in pressure measurements because of undesirable characteristics in the installation. Some of the prevalent sources of error are probe misalignment, poor construction of probes, and the inaccuracies of the manometers or electric pressure-sensing devices. Although errors may be reduced by careful procedures, they cannot be eliminated completely. Therefore the effects of anticipated errors must be evaluated in order to determine the probable accuracy of the computed Mach number. As a corollary, the error analysis provides a guide for choosing measuring techniques so that the probable error in Mach number will be minimized.

To determine the Mach number, two pressures are measured and a value of the ratio of specific heats is assumed. If a wedge or conical probe is used, the effective probe deflection angle ω also must be estimated from information on the probe geometry, boundary-layer growth on the probe surface, and alignment with the free-stream flow. The effects of errors in the two pressures, the ratio of specific heats γ and in the angle ω will be considered separately.

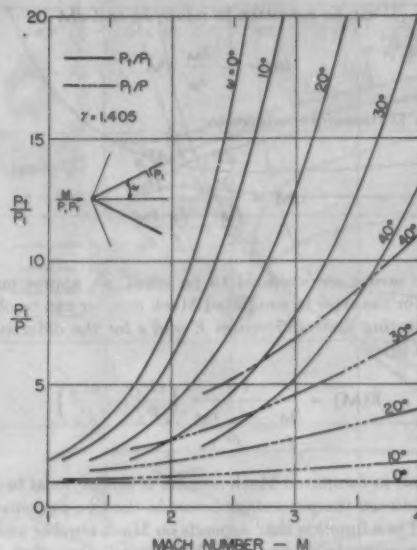


FIG. 5 P_1/P_1 and P_1/P_1 AS FUNCTIONS OF M AND ω FOR CONICAL PROBES

The effect of errors in measured pressures on the computed values of various flow parameters has been analyzed in reference (3). Only the three pressure-ratio combinations formed from P_0 , P_1 , and P were considered, and it was assumed that the error in one measured pressure is equal in magnitude to the error in the other measured pressure. Lord and Beasall (4) present an analysis of the error in computed Mach number for the same three pressure ratios when the relative magnitudes of the errors in the two pressures are not equal. Both references consider the extreme case in which the pressure errors are opposite in sign, while this paper assumes that the errors in both measured pressures follow a symmetrical probability distribution. Thus the errors in the two measured pressures are assumed to have a 50 per cent probability of being the same sign. Therefore the probable error in Mach number, computed from Equation [9] of this paper, is less than the error given in the two references. This paper also considers seven additional pressure-ratio combinations, and it includes an analysis of the effect of an error in the ratio of specific heats.

Errors in Measured Pressures. For an arbitrary pair of measured pressures the pressure ratio is a function of M , γ , and α

$$\frac{P_L}{P_S} = f(M, \gamma, \alpha) \quad [1]^*$$

Differentiating

$$\frac{dP_L}{P_L} - \frac{dP_S}{P_S} = \frac{f_M}{f} dM + \frac{f_\gamma}{f} d\gamma + \frac{f_\alpha}{f} d\alpha \quad [2]$$

To determine the effect of errors in pressure measurements alone, we set $d\gamma = 0$ and require that the total differential of the deflection angle ω be zero. Therefore, since $e = \tan \omega$, we may write

$$de = e_M dM + e_\gamma d\gamma + e_\alpha d\alpha = 0 \quad [3]$$

* Actually ω rather than α is an independent variable, but since no analytical expressions for oblique shock functions involving M , γ , and ω are available one must introduce another variable. The angle α is the most convenient one and it is related to the deflection angle ω by the expression $e(M, \gamma, \alpha) = \tan \omega$.

Equation [3] can be rewritten to relate $d\alpha$ and dM

$$d\alpha = -\frac{e_M}{e_a} dM \quad [4]$$

Equation [2] therefore reduces to

$$dM = \frac{\frac{dP_L}{P_L} - \frac{dP_S}{P_S}}{\frac{f_M}{f} - \frac{f_a}{f} \frac{e_M}{e_a}} \quad [5]$$

Since the errors are assumed to be small, an approximate expression for the error in computed Mach number can be obtained by substituting finite differences E and ϵ for the differentials in Equation [5]

$$E(M) = \frac{1}{\frac{f_M}{f} - \frac{f_a}{f} \frac{e_M}{e_a}} \left(\frac{eP_L}{P_L} - \frac{eP_S}{P_S} \right) \quad [6]$$

The error in computed Mach number is proportional to the difference between the percentage errors in the two measured pressures, and to a function that depends on Mach number and which pair of pressures is measured. This general expression may be used for any combination of errors in the measured pressures. A somewhat more useful form of Equation [6] is obtained if it is assumed that the errors in the measured pressures follow a sym-

metrical probability function such as the familiar normal probability curve. Thus the error in a pressure has a 50 per cent probability of being positive, and the magnitude of the error will be given in terms of the probable error $r(P)$ in the measured pressure. The distribution of the error in computed Mach number also will follow the probability law with a probable error $r(M)$.

Two particular cases will be considered here. In the first case the probable error in each measured pressure is assumed to be proportional to the measured pressure; that is, $r(P_L)/P_L = r(P_S)/P_S$. The results for this case usually can be applied when analog-type pressure-measuring equipment is used. For example, they can be applied if electrical pressure pickups are used at their rated capacity. In the second case it is assumed that the probable errors in the two measured pressures are equal; that is, $r(P_L) = r(P_S)$. The results for this case can be applied when digital-type measuring equipment such as a manometer is used. Which of the two cases is applicable to a particular problem will depend upon the type and characteristics of the pressure-sensing equipment used. Solutions to any other case may be obtained by using Equation [6].

In the first case, where $r(P_L)/P_L = r(P_S)/P_S$, Equation [6] reduces to the simple expression for the magnitude of the probable error in the computed Mach number

$$r(M) = G \frac{r(P_L)}{P_L} = G \frac{r(P_S)}{P_S} \quad [7]$$

where

TABLE 1 EQUATIONS DEFINING FUNCTIONS USED IN ERROR ANALYSIS OF PITOT, STATIC, AND TWO-DIMENSIONAL WEDGE PROBES

(Refer to Appendix for formulas for quantities appearing in these equations.)

MEASURED PRESSURE RATIO		G	g	$\frac{dM}{d\gamma}$	$\frac{dM}{d\omega}$
P_t/P	a	$\frac{\sqrt{2}}{a_M/a}$	$\frac{\sqrt{1+1/a^2}}{a_M/a}$	$-\frac{a\gamma/a}{a_M/a}$	
P_t^1/P	b	$\frac{\sqrt{2}}{b_M/b}$	$\frac{\sqrt{1+1/b^2}}{b_M/b}$	$-\frac{b\gamma/b}{b_M/b}$	
P_t/P_t^1	a/b	$\frac{\sqrt{2}}{a_M/a - b_M/b}$	$\frac{\sqrt{1/a^2 + 1/b^2}}{a_M/a - b_M/b}$	$-\frac{a\gamma/a - b\gamma/b}{a_M/a - b_M/b}$	
P_t/P	1/c	$-\frac{\sqrt{2}}{h}$	$-\frac{\sqrt{c^2+1}}{h}$	$\frac{r}{h}$	$\frac{1}{h} \frac{c_a}{c}$
P_t/P_t^1	ac	$\frac{\sqrt{2}}{a_M/a + h}$	$\frac{\sqrt{c^2+1/a^2}}{a_M/a + h}$	$\frac{r - a\gamma/a}{a_M/a + h}$	$-\frac{1}{h} \frac{c_a/c}{a_M/a + h}$
P_{t1}/P_t	d	$\frac{\sqrt{2}}{n}$	$\frac{c\sqrt{1+1/a^2}}{n}$	$\frac{s - d\gamma/d}{n}$	$-\frac{1}{n} \frac{d_M M_{1a}/d}{n}$
P_t^1/P_t	bc	$\frac{\sqrt{2}}{b_M/b + h}$	$\frac{\sqrt{c^2+1/b^2}}{b_M/b + h}$	$\frac{r - b\gamma/b}{b_M/b + h}$	$-\frac{1}{h} \frac{c_a/c}{b_M/b + h}$
P_t/P_{t1}	ac/d	$\frac{\sqrt{2}}{h + a_M/a - n}$	$\frac{\sqrt{1/a^2 + (c/d)^2}}{h + a_M/a - n}$	$\frac{r - a\gamma/a + d\gamma/d - s}{h + a_M/a - n}$	$\frac{1}{h + a_M/a - n} \frac{d_M M_{1a}/d - c_a/c}{n}$
P_{t1}/P_t^1	d/bc	$\frac{-\sqrt{2}}{h + b_M/b - n}$	$\frac{-\sqrt{(c/d)^2 + 1/b^2}}{h + b_M/b - n}$	$\frac{r - b\gamma/b + d\gamma/d - s}{h + b_M/b - n}$	$\frac{1}{h + b_M/b - n} \frac{d_M M_{1a}/d - c_a/c}{n}$
P_{t1}^1/P	d/c	$\frac{-\sqrt{2}}{h - n}$	$\frac{-\sqrt{(c/d)^2 + 1}}{h - n}$	$\frac{r + d\gamma/d - s}{h - n}$	$\frac{1}{h - n} \frac{d_M M_{1a}/d - c_a/c}{n}$

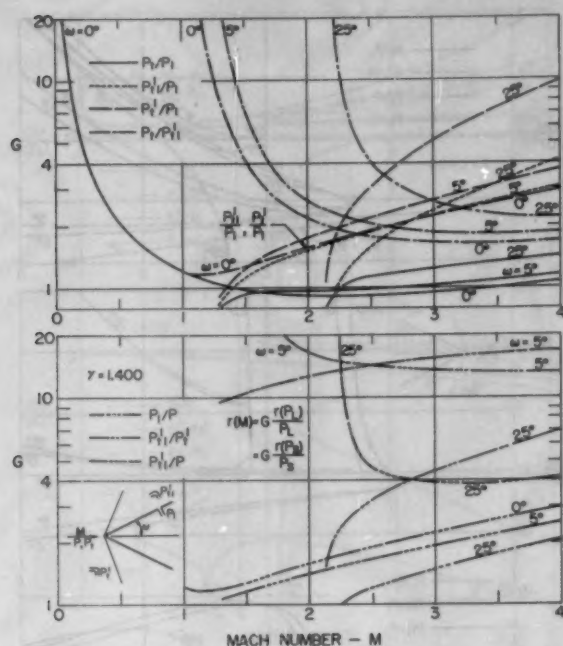


FIG. 6 FUNCTION G FOR TWO-DIMENSIONAL WEDGE PROBES (Used in Equation [7] to compute effect of errors in measured pressures when $r(P_L)/P_L = r(P_S)/P_S$.)

$$G = \frac{\sqrt{2}}{f} \frac{f_M}{f} \frac{e_M}{e_a} \quad [8]$$

In the second case, where $r(P_L) = r(P_S) = r(P)$, the probable error in computed Mach number is given by

$$r(M) = g \frac{r(P)}{P} \quad [9]$$

and is proportional to the ratio of the probable error in the measured pressures to the free-stream static pressure. The error coefficient g is defined by

$$g = \frac{\sqrt{\left(\frac{P}{P_L}\right)^2 + \left(\frac{P}{P_S}\right)^2}}{\frac{f_M}{f} \frac{e_M}{e_a}} \quad [10]$$

Qualitatively, one can see that the error in Mach number will be low if the pressure errors are small relative to the measured pressures and if the relative rate of change of the pressure ratio with Mach number is large.⁶ Quantitatively, the values of G and g may be evaluated analytically for a number of pressure-ratio combinations where wedge, static, or pitot probes are used. As an example, consider the combination where pitot pressures are measured in front of and behind the oblique shock from a wedge probe ($P_L = P_{n1}$ and $P_S = P_{n2}$). The pressure ratio f is equal to d/bc . Substituting into Equation [8]

$$G = \frac{\sqrt{2}}{d} \frac{b_M}{b} \frac{c_M}{c} \frac{e_M}{e_a} \left(\frac{d_a}{d} - \frac{c_a}{c} \right)$$

⁶ So that G and g will be small.

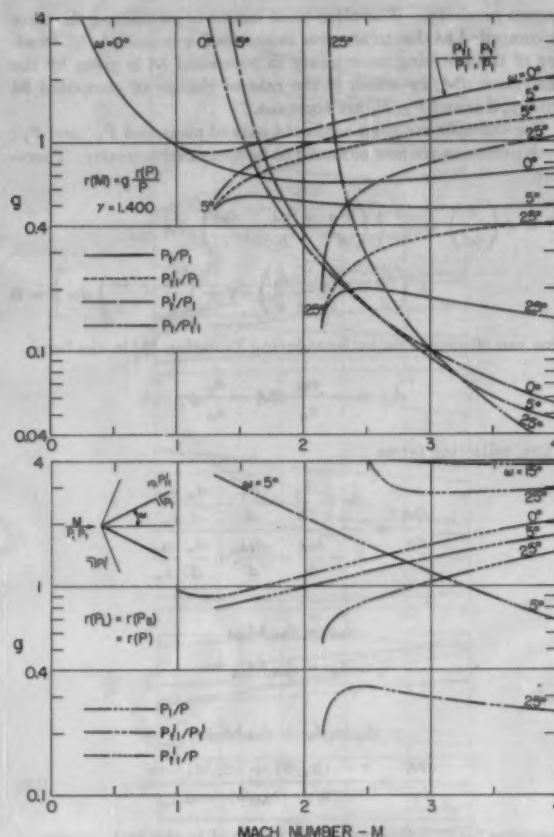


FIG. 7 FUNCTION g FOR TWO-DIMENSIONAL WEDGE PROBES (Used in Equation [9] to compute effect of errors in measured pressures when $r(P_L) = r(P_S) = r(P)$.)

or, since $d_M = d_M M_{1M}$ and $d_a = d_M M_{1a}$

$$G = \frac{-\sqrt{2}}{h + (b_M/b) - n} \quad [11]$$

Likewise, from Equation [10]

$$g = -\frac{\sqrt{(c/d)^2 + (1/b)^2}}{h + (b_M/b) - n} \quad [12]$$

A list of formulas for the coefficients G and g is presented in the third and fourth columns of Table 1. Figs. 6 and 7 show the value of these coefficients plotted against Mach number for a few values of wedge angle. It is easily seen that a very large change in the probable error in computed Mach number can accompany a change in the pressure-ratio combination used or in the probe angle ω . The best combination depends upon the Mach number and upon the relative values of the probable errors in the two measured pressures.

Error in Ratio of Specific Heats γ . All the formulas for Mach number are functions of γ as well as pressure ratio. Therefore any error in the assumed value of γ will be reflected in an error in computed Mach number. The uncertainty in the value of γ for air at low pressures and moderate temperatures is quite small (5), but considerable uncertainty exists at higher temperatures or pressures, if the air is wet, or if the gas composition is not

known precisely. Therefore some means of estimating the error in computed M due to an error in assumed γ is needed. A measure of the resulting uncertainty in computed M is given by the derivative $dM/d\gamma$ which is the rate of change of computed M with γ , if ω and P_L/P_S are constant.

For example, consider again the case of measured P_{a1}' and P_{t1}' ; both pressures are now assumed to be measured correctly. Therefore

$$df = d \left(\frac{d}{bc} \right) = \frac{d}{bc} \left[\left(\frac{dM}{d} - \frac{bM}{b} - \frac{cM}{c} \right) dM + \left(\frac{d\gamma}{d} - \frac{b\gamma}{b} - \frac{c\gamma}{c} \right) d\gamma + \left(\frac{d\alpha}{d} - \frac{c\alpha}{c} \right) d\alpha \right] = 0$$

One can eliminate $d\alpha$ by introducing Equation [3] in the form

$$d\alpha = -\frac{e_M}{e_a} dM - \frac{e_\gamma}{e_a} d\gamma$$

Thus, collecting terms

$$\frac{dM}{d\gamma} = \frac{r - \frac{b\gamma}{b} + \frac{d\gamma}{d} - \frac{d\alpha}{d} \frac{e_\gamma}{e_a}}{h + \frac{bM}{b} - \frac{dM}{d} + \frac{d\alpha}{d} \frac{e_M}{e_a}}$$

Since

$$dM = dM_1 M_{1M}$$

$$d\alpha = dM_1 M_{1\alpha}$$

and⁷

$$d\gamma = d\gamma + dM_1 M_{1\gamma}$$

$$\frac{dM}{d\gamma} = \frac{r - (b\gamma/b) + (d\gamma/d) - s}{h + (bM/b) - n} \dots \dots \dots [13]$$

Formulas for this derivative are collected in the fifth column of Table 1 for 10 cases. Fig. 8 shows the value of the derivative for a few values of ω . It is obvious that some combinations of pressure ratio and probe angle are inherently more sensitive to errors in γ than are others.

The derivative corresponding to the pressure ratio P_1/P becomes infinite and changes sign at a Mach number which depends on the included angle of the probe. The existence of this undesirable behavior may be demonstrated in another way by using a power series⁸ in ω for computing P_1/P . Since

$$\frac{dM}{d\gamma} = -\frac{\frac{\partial(P_1/P)}{\partial\gamma}}{\frac{\partial(P_1/P)}{\partial M}} \dots \dots \dots [14]$$

a formula for $dM/d\gamma$ involving powers of ω may be obtained by differentiating the coefficients in the power series. Curves plotted from Equation [14] show the same characteristics as those plotted from Equation [13]. The derivative becomes infinite at the Mach number at which P_1/P is a minimum for a given ω , see Fig. 2; that is, when the denominator in Equation [14] becomes zero. The reason for the behavior of the P_1/P curves in Fig. 8 is therefore apparent; with the wrong value of γ it may be impossible to find a value of M which corresponds to a low enough pressure ratio P_1/P .

⁷ The $d\gamma$ to the left of the equal sign is the partial derivative of the pressure ratio d with respect to γ with M and α constant, and the $d\gamma$ to the right is the partial derivative with M_1 constant.

⁸ E.g., equation (149) of NACA TN 1428.

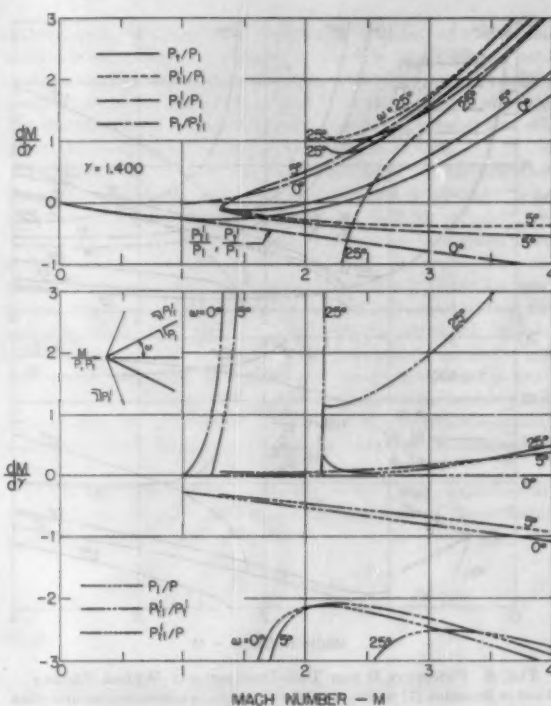


FIG. 8 DERIVATIVE $dM/d\gamma$ FOR TWO-DIMENSIONAL WEDGE PROBES (Used to compute effect of error in assumed ratio of specific heats.)

Error in Deflection Angle ω . When measurements are made with a wedge probe, an error in the assumed flow-deflection angle ω may be present as a result of errors in assumed free-stream flow direction, probe alignment, or in probe construction. The value of $dM/d\omega$ will be used as a measure of the sensitivity of the computed Mach number to errors in wedge deflection angle ω .

Considering that P_{a1}' and P_{t1}' are measured correctly and $d\gamma = 0$

$$df = d \left(\frac{d}{bc} \right) = \frac{d}{bc} \left[\left(\frac{dM}{d} - \frac{bM}{b} - \frac{cM}{c} \right) dM + \left(\frac{d\alpha}{d} - \frac{c\alpha}{c} \right) d\alpha \right] = 0$$

Also

$$d\omega = \cos^2 \omega d\epsilon = \cos^2 \omega (e_M dM + e_a d\alpha)$$

Combining to eliminate $d\alpha$

$$\frac{dM}{d\omega} = t \frac{dM_1 (M_{1\alpha}/d) - (c\alpha/c)}{h + (bM/b) - n} \dots \dots \dots [15]$$

where the parameter t contains a constant to convert the angle ω from radians to degrees. The right-hand column of Table 1 lists formulas for the other cases. From the curves plotted in Fig. 9 it can be seen that the magnitude of $dM/d\omega$ for the P_1/P case becomes excessive at certain Mach numbers. The reason is the same one that caused $dM/d\gamma$ to approach infinity. It might be noted that the denominators of the equations for G , q , $dM/d\gamma$, and $dM/d\omega$ for a particular pressure ratio are identical.

DISCUSSION

One important application of the foregoing error study is

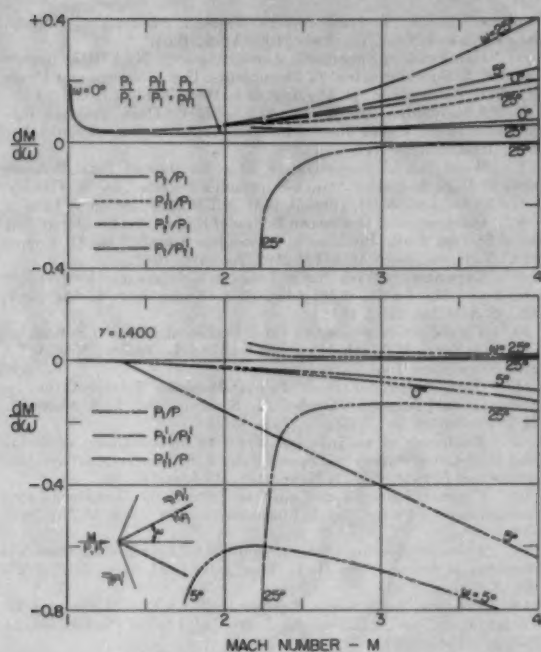


FIG. 9 DERIVATIVE $dM/d\omega$ FOR TWO-DIMENSIONAL WEDGE PROBES (Used to compute effect of error in assumed flow deflection angle ω measured in degrees.)

evaluating the relative merits of various probes which are used to calibrate supersonic wind tunnels. For this purpose, a cross plot against ω from Figs. 6, 7, 8, and 9 for the particular tunnel Mach number is useful. Fig. 10 is a sample plot for $M = 3.00$. In general, the smallest error can be expected if P_1 is measured (curves 2 and 5) and the largest if the static pressure ratio P_1/P (curve 1) is used. A final choice between the various pressure ratios will depend on the expected relative probable errors in the pressures, in γ and ω . If both γ and ω have relatively large errors, for example, P_{11}' and P should be measured with $\omega = 22$ deg, since both derivatives are zero for this combination. However, the effect of pressure errors will be much larger than with some other combinations. If, instead, both the pressures and ω are subject to errors but γ is known accurately, P_1/P_{11}' should be measured using a 22-deg wedge probe.

The analysis up to this point has been purely theoretical. A brief discussion of some possible sources of error is included here so as to present a more complete picture (6). The effects of angle of attack on P_1 and on P_{11}' have been discussed already by considering the effect of an error in ω . An angle of attack above about 15 deg also will decrease the reading of P_1' with a pitot tube (7). A static probe is even more sensitive to angle of attack (8, 9) and, therefore, should be aligned carefully with the flow.

Another source of error is the boundary layer which forms on the surface of the probe and which, in effect, alters the included angle of the probe, especially near the tip (10). Fig. 9 is of use in estimating the results of this change in effective ω .

If the probe is very small or the density very low, the measured P_1' will differ from the ideal value given by inviscid-flow theory (6). Sherman (11) shows that this effect is apparent when the Reynolds number based on the probe diameter is less than 300. This small value of Reynolds number is normally exceeded.

It has been shown that the smallest errors usually are associated with the pressure ratio P_1/P_{11}' . Application of this

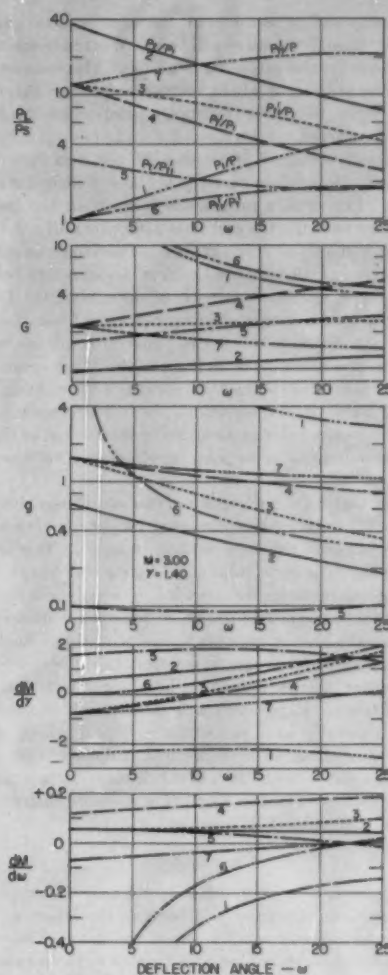


FIG. 10 CROSS PLOT AGAINST ω AT A FREE-STREAM MACH NUMBER OF 3.00 FOR TWO-DIMENSIONAL WEDGE PROBES

(Numbers beside curves signify measured pressure ratio according to following code: 1: P_1/P , 2: P_1/P_1 , 3: P_{11}'/P_1 , 4: P_1/P_1' , 5: P_1/P_{11}' , 6: P_{11}'/P_1' and 7: P_{11}'/P . Deflection angle ω is measured in degrees.)

theoretical conclusion must be tempered in practice because of the evidence presented in reference (12). In that paper it is shown that there is a loss in P_1 as the flow passes through a supersonic wind-tunnel nozzle, and that an inherent error exists in measuring P_1' with a blunt-nosed pitot tube. The presence of such systematic errors in the measured pressures would seriously affect the comparisons presented in Figs. 6, 7, and 10 which are theoretically correct only for random errors.

Errors also arise from an improper use of a probe. Nonuniformities in the free-stream flow affecting the flow between the tip of a probe and the pressure taps will affect the measured pressures (6). These pressures cannot be interpreted into terms of Mach number because the available coefficients are valid only when the free-stream flow is uniform. Fortunately, it is usually possible to make the probe small enough to enable one to apply the uniform flow coefficients with little error. Another example is provided by the static-pressure probe. A compression wave crossing the probe a short distance behind the pressure taps will

cause the measured pressure to be too high because part of the pressure rise through the wave will be transmitted upstream in the boundary layer on the probe surface (13). Measurements made in a transverse velocity gradient such as a boundary layer are also subject to error (6). For example, pitot-probe readings are affected by interference from a nearby wall (14).

An improperly designed probe also will result in incorrect pressure readings. A familiar example is the cylindrical static-pressure probe. The surface pressure is lower than the free-stream static pressure near the tip and rises asymptotically to the static pressure a few diameters downstream. Therefore the static-pressure holes are usually placed at least 8 diameters behind the beginning of the cylindrical portion of the probe (9). In the case of a wedge probe, a source of error can arise from disturbances originating at the ends of the probe. This error will not be present if the surface pressure taps lie in front of the Mach cones from the tips of the probe. Static-pressure readings will be changed by the presence of burrs or countersinking, by using large holes, or by drilling the pressure holes at an angle to the normal to the surface (6). These sources of error may be eliminated by careful shop work.

In an intermittent tunnel, or when test conditions change fairly rapidly, the pressure in the connecting tubing may not have time to stabilize before a pressure reading is made. This is another source of systematic error minimized by careful design (15).

The foregoing remarks are intended to be only a brief reminder of some of the various factors which must be considered by an aerodynamicist selecting pressure instrumentation. Each of these factors is important enough to warrant being the subject of a separate paper; the brief mention here is not intended to slight their importance. Experience will show which factors must be considered carefully in a particular case and which are unimportant. By combining the theoretical analysis of this paper and practical experience with the effects of these factors an aerodynamicist has a logical basis for selecting pressure instrumentation intended to determine Mach number.

CONCLUSIONS

Various pressure ratios which may be used to compute Mach number have been analyzed to determine the effect on the computed Mach number of small errors in the data. The results for two particular cases show that small errors in the measured pressures can result in a large error in the computed Mach number. The error arising from this source can be minimized by choosing the most favorable pair of measured pressures. Which pair should be chosen depends upon the Mach number and upon the relative magnitudes of the probable error in each measured pressure.

The effect of errors in the assumed ratio of specific heats and in the probe deflection angle also is analyzed. The resulting error in the Mach number can be reduced by selection of the measured pressures used to compute the Mach number.

It is shown that considerable care and foresight is required if the probable error in a Mach number computed from measured pressures is to be kept within acceptable limits.

BIBLIOGRAPHY

- 1 "On the Measurement of Surface Pressure With a Static Probe," by W. W. Willmarth, *Journal of the Aeronautical Sciences*, vol. 20, 1953, pp. 438-439.
- 2 "Tables of Supersonic Flow Around Cones," edited by Z. Kopal, Center of Analysis, Massachusetts Institute of Technology, Cambridge, Mass., Technical Report No. 1, 1947.
- 3 "Accuracy of Aerodynamic Flow Parameters Computed From Pressure Measurements Having Small Errors," by O. W. Nicks and F. W. Barry, North American Aviation, Inc., Report No. AL-1393, May 15, 1951.
- 4 "On the Errors Involved in Measuring Supersonic Mach

Numbers," by W. T. Lord and D. Beastall, Ministry of Supply, RAE Technical Note No. Aero 2100, April, 1951.

5 "Handbook of Supersonic Aerodynamics," NAVORD Report 1488, vol. 5, Superintendent of Documents, U. S. Government Printing Office, Washington, D. C., August 1, 1953, Table 1510.08.

6 "Aerodynamic Measurements," by R. C. Dean, Jr., Gas Turbine Laboratory, Massachusetts Institute of Technology, Cambridge, Mass., 1953, chapter III.

7 "Wind-Tunnel Investigation of a Number of Total-Pressure Tubes at High Angles of Attack-Supersonic Speeds," by W. Gracey, D. E. Coletti, and W. R. Russell, NACA TN 2261, January, 1951.

8 "Orientation of Orifices on Bodies of Revolution for Determination of Stream Static Pressure at Supersonic Speeds," by M. Cooper and C. V. Hamilton, NACA TN 2592, January, 1952.

9 "Experiments With Static Tubes in a Supersonic Airstream—Parts I and II," by D. W. Holder, R. J. North, and A. Chinneck, ARC, R & M No. 2782, 1953.

10 "Viscosity Corrections to Cone Probes in Rarefied Supersonic Flow at a Nominal Mach Number of 4," by L. Talbot, NACA TN 3219, November, 1954.

11 "New Experiments on Impact-Pressure Interpretation in Supersonic and Subsonic Rarefied Air Streams," by F. S. Sherman, TN 2995, September, 1953.

12 "Evidences of an Inherent Error in Measurement of Total-Head Pressure at Supersonic Speeds," by J. S. Murphy, *Aeronautical Engineering Review*, vol. 12, November, 1953, pp. 47-51.

13 "Conical Flow as a Result of Shock and Boundary-Layer Interaction on a Probe," by J. Lukaszewicz, ARC, R & M No. 2669, 1952.

14 "Factors Affecting Laminar Boundary Layer Measurements in a Supersonic Stream," by R. E. Blue and G. M. Low, NACA TN 2891, February, 1953.

15 "Pressure Response in Supersonic Wind-Tunnel Pressure Instrumentation," by A. L. Ducoffe, *Journal of Applied Physics*, vol. 24, 1953, pp. 1343-1354.

Appendix

$$a = \left(1 + \frac{\gamma - 1}{2} M^2\right)^{\frac{\gamma}{\gamma - 1}}$$

$$\frac{aM}{a} = \frac{\gamma M}{1 + \frac{\gamma - 1}{2} M^2}$$

$$\frac{a_\gamma}{a} = - \left[\frac{\ln \left(1 + \frac{\gamma - 1}{2} M^2\right)}{(\gamma - 1)^2} - \frac{\gamma M^2}{(\gamma - 1) \{2 + (\gamma - 1) M^2\}} \right]$$

$$b = \left(\frac{\gamma + 1}{2} M^2\right)^{\frac{\gamma}{\gamma - 1}} \left(\frac{2\gamma M^2 - \gamma + 1}{\gamma + 1}\right)^{\frac{1}{1 - \gamma}}$$

$$\frac{bM}{b} = \frac{2\gamma(2M^2 - 1)}{M(2\gamma M^2 - \gamma + 1)}$$

$$\frac{b_\gamma}{b} = \frac{1}{\gamma - 1} \left[1 - \frac{2M^2 - 1}{2\gamma M^2 - \gamma + 1} \right] - \frac{1}{(\gamma - 1)^2}$$

$$\ln \left[\frac{(\gamma + 1)^2 M^2}{2(2\gamma M^2 - \gamma + 1)} \right]$$

$$c = (\gamma + 1)/j$$

$$\frac{c_\alpha}{c} = - \frac{2\gamma M^2 \sin 2\alpha}{j}$$

$$\frac{c_\gamma}{c} = \frac{1}{\gamma + 1} - \frac{2m^2 - 1}{j}$$

d, d_γ, dM_1 — use formulas for b if $M_1 \geq 1$ and for a if $M_1 \leq 1$ replacing M by M_1 .

$$e = \frac{M^2 \sin 2\alpha - 2 \cot \alpha}{2 + M^2(\gamma + \cos 2\alpha)}$$

$$e_\alpha = \frac{2[M^2(\cos 2\alpha + e \sin 2\alpha) + \csc^2 \alpha]}{2 + M^2(\gamma + \cos 2\alpha)}$$

$$\frac{e_M}{e_\alpha} = \frac{2(\cot \alpha + e)}{M[M^2(\cos 2\alpha + e \sin 2\alpha) + \csc^2 \alpha]}$$

$$\frac{e_\gamma}{e_\alpha} = \frac{-M^2 e}{2[M^2(\cos 2\alpha + e \sin 2\alpha) + \csc^2 \alpha]}$$

$$h = \frac{c_\alpha}{c} \left[\frac{\tan \alpha}{M} - \frac{e_M}{e_\alpha} \right]$$

$$M_{1j} = \frac{(\gamma + 1)^2 M^2 m^3 - 4(m^2 - 1)(\gamma m^2 + 1)}{jk}$$

$$M_{1M} = \frac{m \sin \alpha [2(\gamma + 1)^2 M^2 - 8\gamma m^2 + 4(\gamma - 1) - M_1^2 \{(\gamma - 1)j + 2\gamma k\}]}{M_{1jk}}$$

$$M_{1\alpha} = \frac{M^2 \sin 2\alpha [(\gamma + 1)^2 M^2 - 8\gamma m^2 + 4(\gamma - 1) - M_1^2 \{(\gamma - 1)j + 2\gamma k\}]}{2M_{1jk}}$$

$$M_{1\gamma} = \frac{m^2}{2M_{1jk}} [2(\gamma + 1)^2 M^2 - 4(m^2 - 1) - jM_1^2] - \frac{M_1}{j} [m^2 - 0.5]$$

The equations collected in Table 1 involving P_1 or P_{11}' may be simplified for the limiting case that $\omega = 0$. The error coefficients G and g are identical to the coefficients for the corresponding pressure ratio obtained by removing the subscript 1 from the designation of the pressure ratio shown in the first column. Likewise the coefficient $dM/d\gamma$ may be obtained except for two cases for which the formulas reduce to

$$\frac{dM}{d\gamma} = -\frac{M(M^2 - 1)}{\gamma(M^2 - 2)} \text{ for } P_1/P$$

$$\frac{dM}{d\gamma} = 0 \text{ for } P_{11}'/P_1'$$

The equations for $dM/d\omega$ reduce to

$$\frac{dM}{d\omega} = \infty, \text{ for } P_1/P \text{ and } P_{11}'/P_1'$$

$$\frac{dM}{d\omega} = \frac{0.017453 M \left(1 + \frac{\gamma - 1}{2} M^2 \right)}{\sqrt{M^2 - 1}}, \text{ for } P_t/P_t, P_{11}'/P_{11}, \text{ and } P_t/P_{11}'$$

$$\frac{dM}{d\omega} = \frac{0.017453 M^2 (2\gamma M^2 - \gamma + 1)}{2(M^2 - 1) \sqrt{M^2 - 1}} \text{ for } P_t'/P_t$$

$$\frac{dM}{d\omega} = -\frac{0.017453 M(M^2 - 1)^2}{(2M^2 - 1) \sqrt{M^2 - 1}} \text{ for } P_{11}'/P$$

Discussion

W. G. CORNELL.⁹ Congratulations are due to the author for a rational approach to the problem of choosing instrumentation

⁹ Aerodynamics Engineer, Aircraft Gas Turbine Division, General Electric Company, Cincinnati, Ohio. Mem. ASME.

designed to yield stream Mach number from pressure measurements.

In his discussion of sources of error, the author states that it is usually possible to make a probe small enough to enable one to assume uniform stream conditions with little error. This depends somewhat upon the case considered. In the cases of large wind tunnels and aircraft models, the point is well taken. In the cases of small models and of turbomachinery, however, it is ordinarily not possible to make the probe small relative to flow-field dimensions. In such cases, one must consider the effect of the probe in distorting the flow field, as well as the effects of stream velocity gradient on probe response.

R. B. PEARCE.¹⁰ This paper supplies a convenient and useful tool for experimental aerodynamicists. Instrumentation can now be designed, and error analyses made, on a much more rational basis than in the past. His paper is a definite addition

to the field of supersonic aerodynamic testing

B. F. SHATTUCK.¹¹ The author centers his attention on the important problem of making "indirect measurements." In particular he calculates Mach number from directly measured pressures in several different well-known ways. The errors caused by the calculations are evaluated concisely and arranged in convenient form for the user. However, these error calculations are useful only if (1) the errors in making direct pressure measurements can be determined accurately, and (2) the errors involved in obtaining the idealized equations for Mach number can be evaluated. Both of these points become especially important at very high Mach number where viscosity may affect appreciably both the measurements of pressure and the form of the equations for calculating Mach number.

AUTHOR'S CLOSURE

The problem of probe size is always present. Among the solutions which have been used are calibrating to determine a correction factor, using a simple total-pressure probe which can be made only a few thousandths of an inch in diameter, or using optical measurements such as interferograms.

The error analysis presented in the paper may be used if the errors in the pressures γ and ω are random. However, if systematic errors, such as those discussed in the paper or mentioned by Mr. Cornell and Mr. Shattuck, are known to exist one must choose instrumentation which is least affected by the systematic errors¹² or estimate the amount of the error and correct for it. Whichever method is employed, an instrumentation engineer must rely on his background of experience with compressible flows.

¹⁰ Group Leader, Thermodynamics, Aerophysics Department, North American Aviation, Inc., Downey, Calif.

¹¹ Supervisor, Fluid Mechanics, General Electric Company, Cincinnati, Ohio.

¹² E.g., the effect of an incorrect value of γ may be minimized by making use of Fig. 8 in choosing instrumentation.

Some Aerodynamic Investigations in Centrifugal Impellers

By J. T. HAMRICK,¹ CLEVELAND, OHIO

Results of both theoretical and experimental investigations of flow in rotating impeller passages are presented. It is the purpose of this presentation to acquaint the designer with the manner in which losses arise, their effect upon the flow within the passage, and their over-all effect upon impeller performance. In addition, analysis and design methods based on isentropic-flow calculations are discussed and their application to the design of mixed-flow impellers is demonstrated.

NOMENCLATURE

The following nomenclature is used in the paper:

- c_a = speed of sound for stagnation conditions in inlet annulus
- c_p = specific heat of air at constant pressure
- D = per cent of distance from hub to shroud
- f_s = slip factor, ratio of absolute tangential velocity of air at exit to impeller speed at exit
- ΔH_{act} = actual enthalpy rise relative to impeller, based on impeller speed
- $[\Delta H_{ad}]$ = isentropic enthalpy rise relative to impeller required to produce a given relative total pressure
- J = mechanical equivalent of heat
- L = ratio of distance along a streamline from inlet to total distance from inlet to outlet
- P_0 = stagnation pressure in inlet annulus
- P_2 = stagnation pressure at $R = 1.5$ (at $R = 2.0$ for impeller in Fig. 22) in vaneless diffuser
- P_r = total pressure relative to rotating passage
- ΔP_r = difference between theoretical relative total pressure for the isentropic case and measured relative total pressure
- p = static pressure
- Q = ratio of flow velocity relative to impeller to velocity of sound at inlet stagnation conditions
- Q_t = flow rate, cfm
- R = ratio of impeller radius or radius in the diffuser to impeller tip radius
- r = radius, in. or ft
- T_0 = temperature at stagnation conditions in inlet annulus
- U = impeller-tip speed
- u = axial velocity, fps
- u_a = axial velocity far upstream of blade leading edge in inlet annulus
- W = weight flow, lb/sec
- β = relative flow direction on cylindrical flow surface (inset Fig. 20)

- β_a = relative flow direction far upstream of impeller inlet (inset Fig. 20)
- γ = ratio of specific heats
- δ = ratio of stagnation pressure in inlet annulus to standard sea-level pressure
- ϵ_i = inlet deviation angle (inset Fig. 20)
- η_{ad} = over-all adiabatic efficiency, ratio of isentropic work to actual work required to produce a given pressure ratio
- $\eta_{ad, rel}$ = relative adiabatic efficiency, ratio of ΔH_{ad} to ΔH_{act}
- θ = ratio of stagnation temperature in inlet annulus to standard sea-level temperature
- ω = angular velocity, radians/sec

INTRODUCTION

In an effort to create a better general understanding of the flow conditions in centrifugal compressors and to provide guidance in impeller design, NACA research in this field has been directed toward analysis of the flow in the rotating impeller passage. A number of theoretical solutions have been made for isentropic flow through both radial and mixed flow impellers (1, 2, 3, 4, for example).² These solutions provide insight into flow behavior with regard to blade loading, compressibility effects, eddy formations, and slip factor in the absence of viscosity. Studies of viscous effects have been made by experimental investigations of flow conditions in the rotating passages of two 48-in. impellers (5, 6, 7, 8, 9).

All of these investigations were preliminary in nature and no attempt was made to arrive at design coefficients or a family of shapes. Primary emphasis was placed upon the qualitative determination of the manner and extent of the departure of the viscous flow from the isentropic. This approach was made because of the complicated nature of the flow through the impeller and the many factors which affect the flow. Among these factors are boundary-layer build-up, relative inlet angle, clearance space between blades and shroud, and secondary flows. The effect of each of these alone upon the flow is difficult to evaluate because of interaction. For example, secondary flows which result from total pressure gradients in the hub-to-shroud plane may disperse the low-energy air in the boundary layer enough to prevent separation on the blades but, on the other hand, the shift of this low-energy air in the boundary layer may result in mixing losses comparable to those which result from separation. It is felt that if the designer can see the effects of this interaction even in the simplified case of the radial-inlet impeller he can utilize isentropic-flow solutions more effectively both for the design of more efficient impellers and the analysis of experimental data.

An attempt is made in this paper to show the effects of velocity distribution, off-design angles of entry, secondary flows, and flow through the blade-to-shroud clearance upon the efficiency and range of operation of the impeller. The effect of the loss distribution at the impeller exit upon the diffuser problem and over-all efficiency are discussed. Analysis and design methods based on isentropic-flow calculations are discussed and their application

¹ National Advisory Committee for Aeronautics, Lewis Flight Propulsion Laboratory.

Contributed by the Gas Turbine Power Division and presented at the Diamond Jubilee Semi-Annual Meeting, Boston, Mass., June 19-23, 1955, of THE AMERICAN SOCIETY OF MECHANICAL ENGINEERS.

NOTE: Statements and opinions advanced in papers are to be understood as individual expressions of their authors and not those of the Society. Manuscript received at ASME Headquarters, April 12, 1955. Paper No. 55-SA-53.

² Numbers in parentheses refer to the Bibliography at the end of the paper.

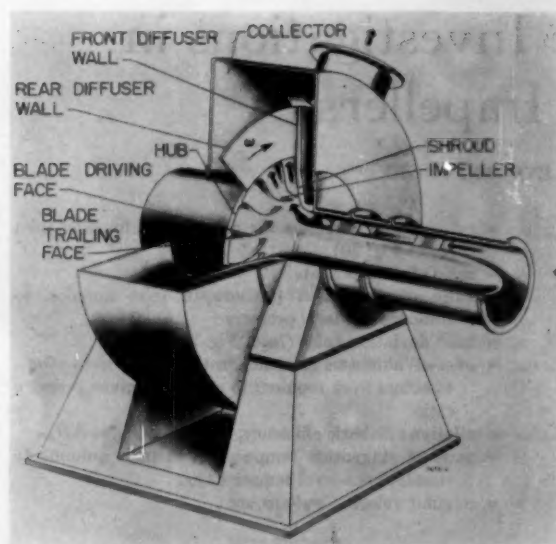


FIG. 1 48-IN. IMPELLER TEST RIG

to the design of mixed-flow impellers is demonstrated. The results presented in this paper were obtained from investigations conducted at the Lewis Flight Propulsion Laboratory of the National Advisory Committee for Aeronautics.

EXPERIMENTAL INVESTIGATIONS—RADIAL-FLOW IMPELLERS

Experimental Setup. A view of the 48-in. impeller test rig used in this investigation is shown in Fig. 1. Pressure-transfer cells for transmitting the pressures from the rotating impeller to stationary manometer tubes are contained in the bullet-nosed section upstream from the impeller inlet. Total and static pressure measurements were made at the encircled locations shown in Fig. 2(a). The total-pressure probes were distributed throughout the 18 passages so as to give the coverage shown with minimum blockage effects. Static pressures were measured only at the hub inasmuch as the investigations of reference (5) showed little or no static-pressure variation from hub to shroud at a given radial position. Total-pressure measurements were made at the encircled positions at the levels shown on the typical passage cross section in Fig. 2(b). This was accomplished by telescoping the probe shown in Fig. 2(c) successively from level 0 to level 5. One of 20 pressure-transfer cells is shown in Fig. 2(d). Because of the limited number of cells, it was necessary to switch probe or tap-to-cell connections and make five duplicate runs at each weight flow point to get complete coverage. All runs with pressure measurements in the impeller were made at an equivalent tip speed of 700 fps, an inlet pressure of 16 in. of mercury absolute, and ambient-air temperatures. Further instrumentation details are given in references (5, 9).

Study of Flow Distribution for Two Blade Shapes. Experimental results for two impellers, A and B, identical in shape except for blade camber and inlet nose section, are given in Figs. 3, 4, and 5. Both blades have the cross-sectional shape shown in Fig. 2(b). The difference in camber is shown roughly by the blade shapes in Fig. 5. Over-all adiabatic efficiency η_{ad} and over-all pressure ratio P_2/P_0 is shown for a range of corrected weight flows $W\sqrt{\theta/\delta}$ in Fig. 3. Despite their differences in camber and therefore their blade-loading distributions, the maximum adiabatic efficiencies of the two impellers are approximately the same. The efficiencies

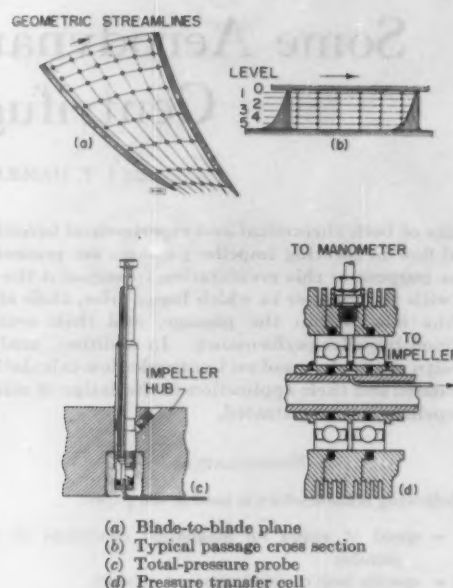


FIG. 2 INSTRUMENTATION DETAILS, 48-IN. RIG

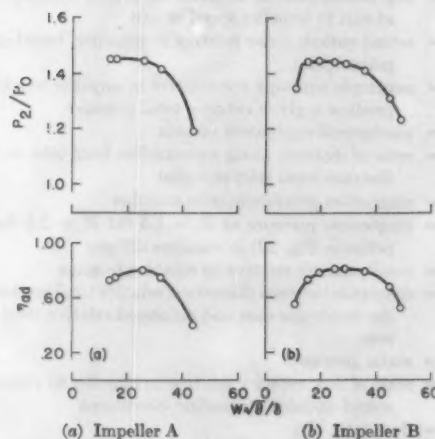


FIG. 3 OVER-ALL PERFORMANCE AT EQUIVALENT TIP SPEED OF 700 FPS

are relatively low; however, high efficiency was not an important factor in choosing a test vehicle inasmuch as the objective was to study viscous effects. The blade loading at maximum efficiency is given by Fig. 4, in which p/P_0 , the ratio of static pressure to total pressure at inlet, and Q , the ratio of velocity relative to the blades to speed of sound for inlet stagnation conditions, are plotted against radial distance. The values of Q are those for mid-passage height. For convenience of presentation the measurements taken nearest the blade driving and trailing faces are referred to respectively as driving and trailing-face values.

For impeller A the blade shows a tendency to unload gradually at the outlet radius. Unloading is referred to here as the attaining of equal static pressures on the driving and trailing faces at a given radius. Theoretical values obtained by the method of reference (2), as shown by the broken lines in Fig. 4(a), also indicate that impeller A unloads gradually at the outlet. This tendency is

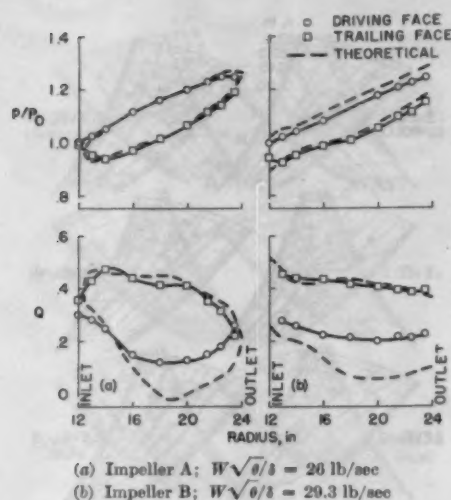


FIG. 4 VELOCITY AND STATIC PRESSURE DISTRIBUTIONS NEAR BLADE FACES FOR IMPELLER A AND B AT MAXIMUM EFFICIENCY

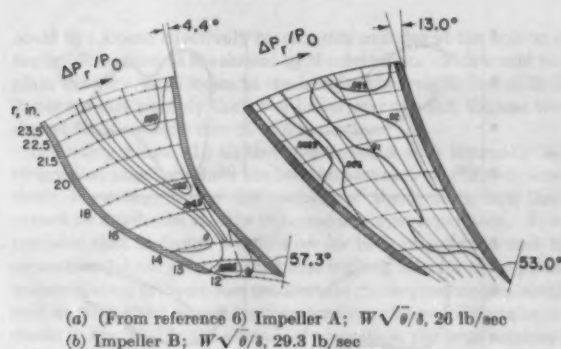


FIG. 5 TOTAL-PRESSURE-LOSS RATIO AT MEAN HEIGHT FOR TWO IMPELLERS AT POINTS OF MAXIMUM EFFICIENCY

not exhibited by the experimental data of impeller B and again the theoretical values agree with the trend, Fig. 4(b). It is indicated by these comparisons of experimental and theoretical static pressures that the blade static-pressure distribution and unloading characteristics can be predicted theoretically to a great extent.

The experimental relative velocity is somewhat higher on the driving face than is shown by the theoretical solution for both impellers and can be explained by considering the relationship of total and static pressures. On the driving face, losses are small as shown by the loss distribution in Fig. 5 and, therefore, the experimental relative total pressures are approximately equal to the theoretical. Total pressure loss $\Delta P_r/P_0$ in Fig. 5 is defined as the ratio of the difference between the theoretical and measured relative total pressure to inlet total pressure where the theoretical total pressure is

$$P_r = P_0 \left[1 + \left(\frac{\gamma - 1}{2} \right) \left(\frac{\omega r}{C_0} \right)^2 \right]^{\frac{\gamma}{\gamma - 1}}$$

For values of Q in the neighborhood of zero, if there are no losses, only approximately 1 per cent drop in static pressure is required to raise the value of Q to 0.10. Therefore very small

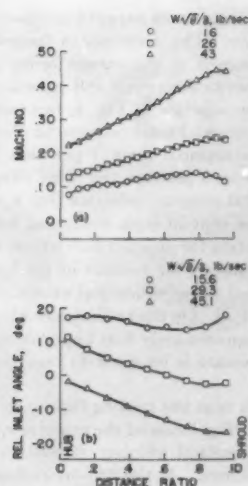
changes in static pressure were required to effect large changes in Q on the driving face. The difference in theoretical and experimental static pressure is of the correct order of magnitude to produce the difference in theoretical and experimental velocity on the driving face for impeller B, Fig. 4, but not for impeller A. However, the experimental total pressure on the driving face for impeller A (6) was approximately 1 per cent higher than the theoretical which would produce the same effect. This higher than theoretical total pressure indicates that a constant error of approximately 1 per cent in both static and total pressure was introduced in correcting for impeller-hub temperature and centrifugal force on the rotating air column in the hub of impeller A (reference 5) and that the experimental values of static pressures are too high in Fig. 4(a). On the trailing face where the velocity is higher (Q equals approximately 0.4) approximately a 5 per cent change in static pressure is required to raise the value of Q by 0.10.

Losses in the area near the trailing face as shown by the pressure-loss contours in Fig. 5 caused the experimental velocity to be lower than the theoretical velocity downstream of the 16-in. radius for both impellers. At the 23.5-in. radius in Fig. 4(a) the trailing-face velocity is noticeably lower than the driving-face velocity; therefore, even with unloading of the blade at the 24-in. radius, the velocities will not be the same on both sides of the blade at outlet because of the losses on the trailing face. The pressure-loss contours, Fig. 5, show higher losses for impeller A than for impeller B, possibly the result of the greater deceleration rate along the trailing face for impeller A.

Off-Design Conditions for Impeller B. In the initial investigations, which were made with impeller A, total pressures were measured at mean blade height only. The extent of the losses in the neighborhood of the trailing face could not be explained by the limited amount of data obtained from these measurements; therefore impeller B was instrumented to measure total pressures at the five levels as previously described. Surveys which showed large variations in velocity upstream of the inlet of impeller A also indicated that instrumentation at several levels was necessary in order to examine the effects of relative inlet-angle variations and losses at off-design conditions. Off-design conditions are defined as those for which significant losses result from too large an angle relative to the blade at inlet. Relative inlet angle is defined here as the angle between the flow direction at inlet and the driving face of the blade with flow directed at the driving face being positive.

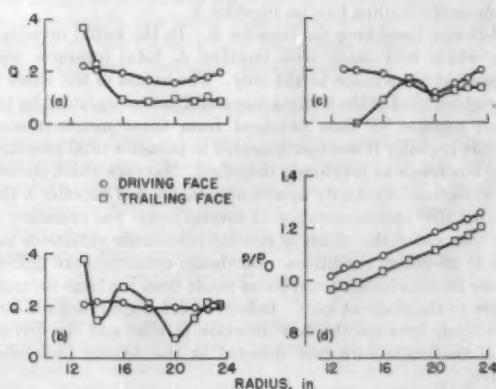
Inasmuch as the wall and hub shapes upstream of impellers A and B were identical and the amounts of blockage by the blades at inlet were approximately the same, it was not considered necessary to make new surveys for impeller B. The surveys were made 0.750 in. upstream of impeller A. Mach number for three weight flows for impeller A is plotted against distance ratio across the passage in Fig. 6(a). By interpolation, the Mach number distribution at inlet for impeller B was determined for three weight-flow rates and the approximate relative inlet-angle distribution was computed. Relative inlet angle is plotted against distance ratio across the passage in Fig. 6(b).

For the weight-flow rate of 15.6 lb there is a variation of 4 deg across the passage for an average relative inlet angle of approximately 16 deg. The effects of this large angle upon trailing-face velocity are shown in Figs. 7 and 8. The total pressure loss on the trailing face, Fig. 8, is smaller at the hub than at the shroud. The deceleration on the trailing face at the hub progresses to the 18-in. radius at which point maximum loss occurs. At level 3 and at the shroud the deceleration is more abrupt and the maximum loss occurs just inside the inlet on the trailing face. The varying velocity pattern, Figs. 7(b) and (c), from inlet to outlet along the trailing face, may be the result of secondary flows and flow through



(a) Mach number variation 0.75 in. upstream from impeller A inlet
(b) Relative angle of inlet, impeller B (based on inlet Mach number for impeller A)

FIG. 6 RELATIVE ANGLE OF INLET FOR IMPELLER B BASED ON MACH NUMBER DISTRIBUTION UPSTREAM OF IMPELLER A



(a) Hub (level 5) velocity ratio; (b) mean (level 3) velocity ratio; (c) shroud (level 0) velocity ratio; (d) all levels, static pressure ratio

FIG. 7 VELOCITY AND STATIC PRESSURE DISTRIBUTION ALONG BLADE SURFACES FOR EQUIVALENT WEIGHT FLOW OF 15.6 LB PER SEC

the blade-to-shroud clearance space. The velocity patterns for the weight-flow rate of 15.6 lb per sec, Fig. 7, differ from those at other weight flows in that the velocity on the trailing face is generally lower than that on the driving face. The losses which caused this condition did not greatly affect the static-pressure distribution, Fig. 7(d), which is similar in configuration to the theoretical distribution for the weight flow of 29.3 lb per sec, Fig. 4(b).

For the weight-flow rate of 45.1 lb per sec the relative inlet angle decreases from -2.0 near the hub to -17.0 near the shroud. The effects of this variation can be observed readily in Figs. 9 and 10. At the hub where the relative inlet angle is small the losses on the driving face are relatively small, Fig. 10, level 5. As the angle becomes more negative from hub to shroud the velocity gradient on the driving face near inlet becomes steeper, Figs. 9(b) and (c), and the losses correspondingly greater, reaching a $\Delta P_r/P_0$ of 0.16 at the shroud, Fig. 10, level 0. The drop in

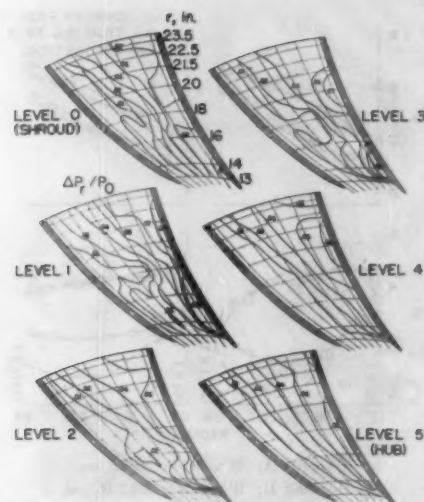
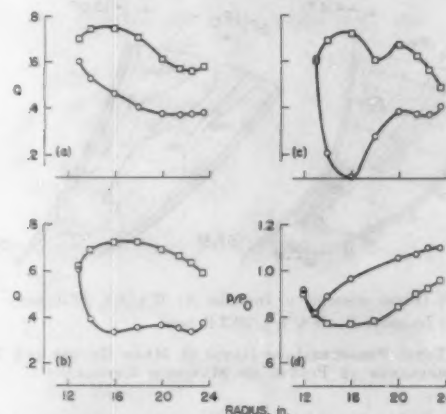


FIG. 8 TOTAL-PRESSURE-LOSS DISTRIBUTION IN ROTATING PASSAGE FOR SIX LEVELS BETWEEN HUB AND SHROUD AT CORRECTED WEIGHT FLOW OF 15.6 LB PER SEC



(a) Hub (level 5) velocity ratio; (b) mean (level 3) velocity ratio; (c) shroud (level 0) velocity ratio; (d) all levels, static pressure ratio

FIG. 9 VELOCITY AND STATIC PRESSURE DISTRIBUTION ALONG BLADE SURFACES FOR EQUIVALENT WEIGHT FLOW OF 45.1 LB PER SEC

static pressure between the 12 and 13-in. radii, Fig. 9(d), is probably the result of separation on the driving face.

The losses due to relative inlet-angle variation from hub to shroud for the weight-flow rate of 29.3 lb per sec (design weight flow) appear to be small as shown by the pressure-loss distribution in Fig. 11, even though the relative inlet angle is higher than 11 deg at the hub. This occurrence may be the result of angle deviation owing to thickness and taper as discussed in (10). As the fluid approaches the blade there is an increase in the axial component of velocity just upstream of the blade because of blade blockage which results in an effective change in the direction of the fluid relative to the rotating impeller. The change in relative inlet angle thus effected is called the inlet-deviation angle. It is difficult to allow for deviation in impeller B because of the manner in which the blades were finished off at inlet and the proximity of the survey probe to the blades. However, the relative inlet angle

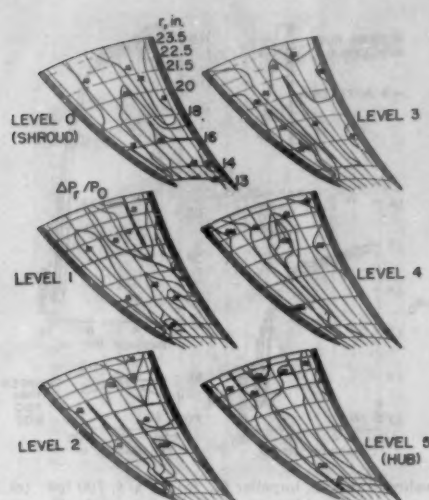


FIG. 10 TOTAL-PRESSURE-LOSS DISTRIBUTION IN ROTATING PASSAGE FOR SIX LEVELS BETWEEN HUB AND SHROUD AT CORRECTED WEIGHT FLOW OF 45.1 LB PER SEC

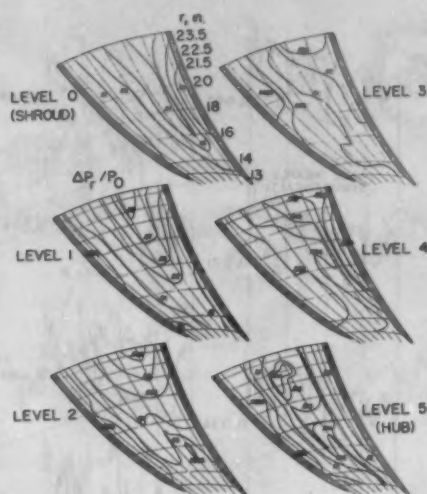


FIG. 11 TOTAL-PRESSURE-LOSS DISTRIBUTION IN ROTATING PASSAGE FOR SIX LEVELS BETWEEN HUB AND SHROUD AT CORRECTED WEIGHT FLOW OF 29.3 LB PER SEC

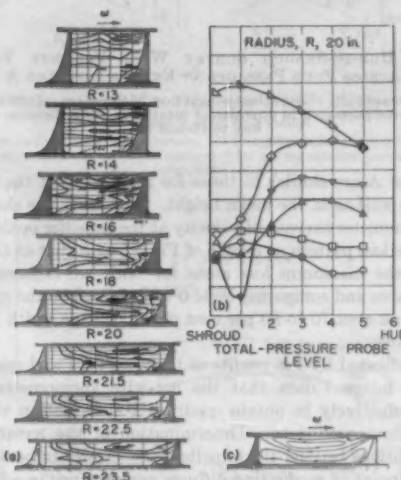
could be reduced effectively by as much as 5 deg at the hub to a negligible amount at the shroud by the deviation. This would explain the very small losses at the hub for the weight flow of 29.3 lb per sec and possibly the lower losses near the hub than at the shroud for the weight flow of 15.6 lb per sec.

Secondary Flows. In all the investigations with internally instrumented impellers there has been an accumulation of comparatively low-energy air in the vicinity of the trailing face that cannot be attributed readily to boundary-layer separation. It is probable that at design weight flow for both impellers A and B separation did not occur on the blade trailing face, for at no point is there a steep pressure-loss gradient (or static-pressure gradient) such as that which occurs for the negative relative inlet angles as shown in Fig. 10. In the absence of separation, the large accumulation of low-energy air must be attributed to secondary flows. Secondary flows are, in general, cross currents which are normal to the potential flow streamlines and are caused by hub-to-shroud gradients in total pressure which are also normal to the potential flow streamlines.

A classic example of secondary flow without attendant viscous losses in a rotating radial channel is given by Kramer and Stanitz (11). Visualization studies of secondary flow in cascades in which smoke was used are given in (12). For impellers that are not fully shrouded the flow through the blade-to-shroud clearance space from the driving face to the trailing face side also provides cross currents which complicate the flow picture and prevent an evaluation of secondary-flow effects alone.

A cross-sectional view of the pressure-loss ratio at various radii from inlet to outlet for design weight flow is given in Fig. 12(a). The velocity variations from hub to shroud across the geometric stream surfaces at the 20-in. radius are given in Fig. 12(b). As was previously mentioned, the variation in static pressure from hub to shroud across a geometric stream surface at a given radius for this impeller is negligible; therefore any variation in velocity from hub to shroud represents, in effect, a variation in total pressure.

Calculations based on the velocity variation in Fig. 12(b) were made to determine the approximate direction of secondary flows at the 20-in. radius. The possible secondary flow directions are given in Fig. 12(c). Along the hub and shroud the low-energy



(a) Cross-sectional view of total-pressure loss; (b) shroud-to-hub velocity profiles; (c) possible directions of secondary flow

FIG. 12 SECONDARY FLOW AND CLEARANCE EFFECTS FOR EQUIVALENT WEIGHT FLOW RATE OF 24.3 LB PER SEC

air in the boundary layer is moved toward the trailing face except in areas where the movement is offset by leakage through the blade-to-shroud clearance space. It appears that air of relatively high energy pours through the clearance space, expands into the area of the trailing face, and moves the low-energy air along the shroud to meet that coming from the driving face. The amount of energy involved in these secondary flows is a matter of debate. Probably the greatest losses come from the mixing downstream of the impeller outlet. With the flow of air from two directions at the shroud in the impeller passage there is a possibility that the low-energy air mass near the shroud at approximately 80 per cent of the passage width from the driving face is in the form of a vortex which upon dissipation would cause large losses.

Hot-wire anemometer surveys (13) show that the loss patterns

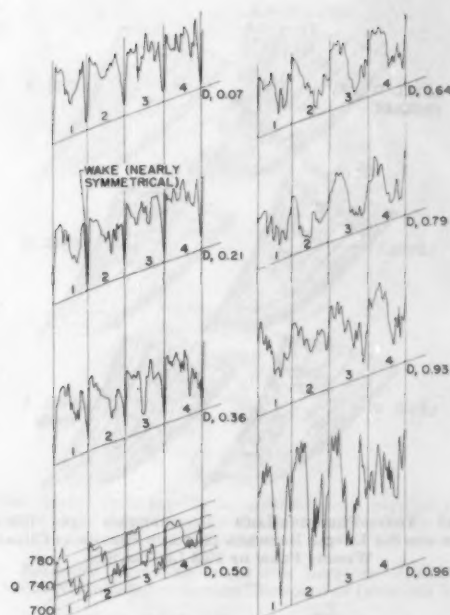


FIG. 13 HUB-TO-SHROUD SURVEY WITH VELOCITY VARIATION ACROSS FOUR PASSAGES AT EXIT OF IMPELLER A

(From reference (13). Equivalent weight flow 26 lb per sec. Driving-to-trailing face across passage is in direction of rotation ω . D is distance ratio from hub to shroud.)

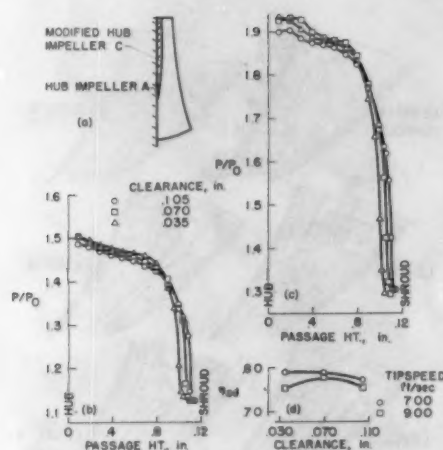
in impeller A are similar to those for impeller B at the hub and shroud as well as at the mean height. In Fig. 13 are shown hot-wire anemometer surveys of velocity at the impeller outlet. Comparing the loss pattern at level 5 of Fig. 11 with that at $D = 0.07$, Fig. 13, the maximum loss areas for both are adjacent to the trailing faces and comparing level 0 with $D = 0.96$ the maximum loss is in an area 70 to 80 per cent of the passage width from the driving face.

It is indicated by the results of these surveys and comparison with the internal data that the hot-wire anemometer can be utilized effectively to obtain qualitative information about the internal flow conditions. Determination of the nature of the flow conditions leaving the impeller is especially important from the standpoint of evaluating diffuser performance in addition to the aid it gives in analyzing flow conditions in the impeller.

Clearance Effects. The length of time required for internal flow measurements prevented the extension of these investigations to obtain relative total pressure-loss distributions for varying amounts of clearance between the blades and shroud. However, tests were made to determine the effect of varying clearance upon over-all efficiency and outlet total-pressure distribution for the impeller of reference (8). This is designated as impeller C in Fig. 14(a).

In choosing impeller C for these tests it was assumed that, with the lower blade height for a portion of the passage, the clearance effects would be more pronounced than for the unaltered height. Total pressure surveys from hub to shroud were made 0.5 in. downstream from the impeller outlet. The results are shown in the form of total-pressure ratio which is plotted against passage height in inches in Figs. 14(b) and (c), and comparison is made for three values of clearance at two tip speeds.

Over-all efficiency is shown in Fig. 14(d). The clearance for which maximum efficiency is obtained appears to be a function of



(a) Hub-shroud profile, impeller C; (b) $U/\sqrt{\theta}$, 700 fps; (c) $U/\sqrt{\theta}$, 900 fps; (d) over-all efficiency, impeller C

FIG. 14 EFFECT OF CLEARANCE VARIATION UPON PERFORMANCE AND TOTAL-PRESSURE DISTRIBUTION 0.5 IN. DOWNSTREAM FROM IMPELLER C

impeller speed. Although the level of total pressure is higher over most of the passage height for 0.035 clearance at 700 fps, Fig. 14 (c), the over-all efficiency is no better than for the 0.070 clearance.

A similar situation exists for the 0.035 and 0.105 clearances at 900 fps with maximum efficiency occurring at the 0.070 clearance. The efficiency in these cases may depend upon whether or not the boundary layer is scraped up next to the shroud or allowed to flow through the clearance space between the blade and shroud. In the smoke studies of Hansen, Herzig, and Costello (12), it was observed generally that for a cascade of blades bounded by a moving wall with clearance the boundary layer was scraped up by the blades with little or no flow through the clearance space. For the more heavily loaded blades of impeller B this was not the case. Apparently the scraping effect was nullified by the large pressure differential so that any build-up of boundary layer on the driving face was bled through the clearance. At the minimum clearance for impeller C (0.035 in.) it is possible that the scraping effect predominated and caused the efficiency to be lower than for the 0.070 clearance at the tip speed of 900 fps.

The foregoing surmise is based on an examination of hot-wire anemometer surveys for the three values of clearance at a tip speed of 700 fps, Fig. 15. The generally lower velocity immediately adjacent to the driving face at $D = 0.36$ and 0.50 for the 0.035 clearance indicates that complete bleeding of the boundary layer from the driving face has not occurred, perhaps because of the scraping effect. These velocity patterns at the exit of impeller C are, in general, similar to those for impeller A.

Mixing Losses. In the vaneless diffuser tests with a 12-in.-diam impeller in reference (14) the friction coefficients based on total pressure, Fig. 16, decreased from approximately 0.008 at the 7-in. radius to approximately 0.004 at the 9-in. radius. This change is attributed to a decrease in the mixing losses as the flow smooths out in moving to the 9-in. radius. A pictorial example of the smoothing-out process in the diffuser of impeller A is given by the hot-wire anemometer-survey results shown in Fig. 17. The survey was made at points along a radial line approximately midway between the vaneless diffuser walls.

Some indication of the magnitude of the mixing losses for impeller B may be obtained by comparing over-all impeller efficiency based on total-pressure measurements in the diffuser with

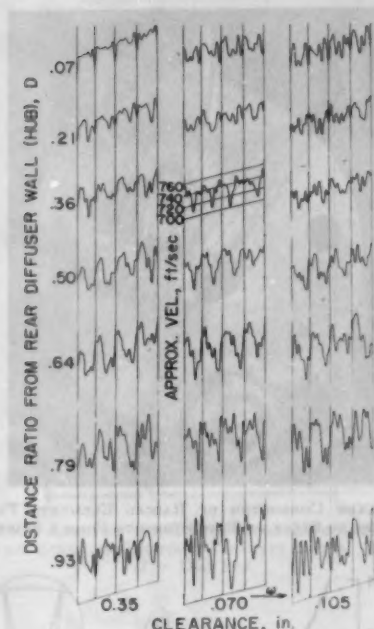


FIG. 15 HUB-TO-SHOULD SURVEYS WITH VELOCITY VARIATION ACROSS FOUR PASSAGES AT EXIT OF IMPELLER C FOR CHANGING BLADE-TO-SHOULD CLEARANCE
(Equivalent weight flow 26 lb per sec. Driving-to-trailing face across passage is in direction of ω ; $U/\sqrt{\theta} = 700$ fps.)

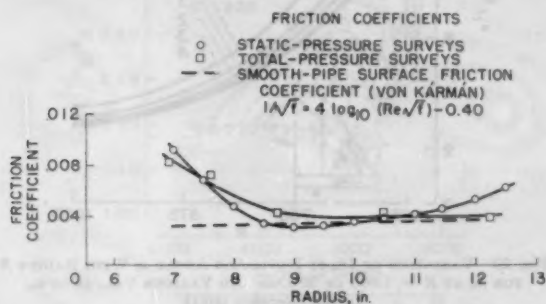


FIG. 16 VARIATION OF FRICTION COEFFICIENTS WITH RADIUS IN CONSTANT-AREA VANELESS DIFFUSER (14)

that based on impeller relative efficiency neglecting mixing losses. The comparison is made for four weight flows in Fig. 18. The efficiency based on total-pressure measurements in the diffuser where mixing losses are included is approximately six points lower than that based on relative efficiency neglecting mixing losses for all four weight flows. The methods and equations used in arriving at the values shown in Fig. 18 are given in the following paragraphs.

The over-all impeller efficiency was based on total pressure and temperature measured at the 36-in. radius in the diffuser with the total pressure corrected for losses to the 24-in. radius. The correction was made by means of reference (13) using a total-pressure friction coefficient of 0.0042. The value of 0.0042 corresponds approximately to the friction coefficient in smooth pipes, Fig. 16; therefore the correction is for surface friction losses only. As a result the losses due to mixing are charged to the efficiency thus computed.

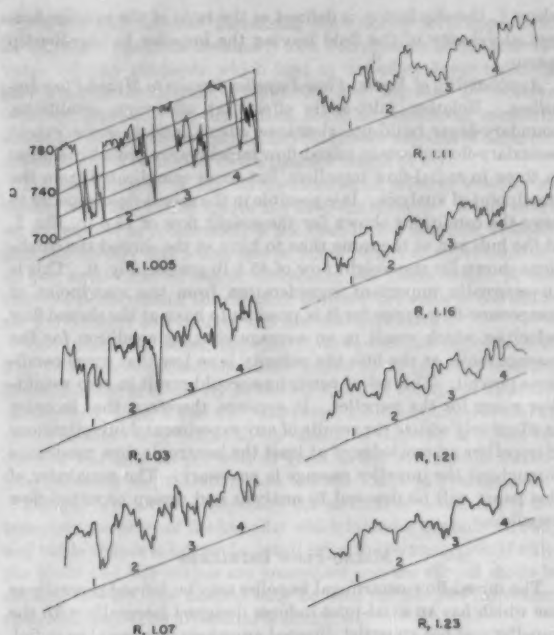


FIG. 17 RADIAL SURVEY IN DIFFUSER WITH VELOCITY VARIATION ACROSS FOUR PASSAGES
(Equivalent weight flow, 26 lb per sec. Driving-to-trailing face across passage is in direction of rotation ω . Numbers refer to successive passages. From reference (13).)

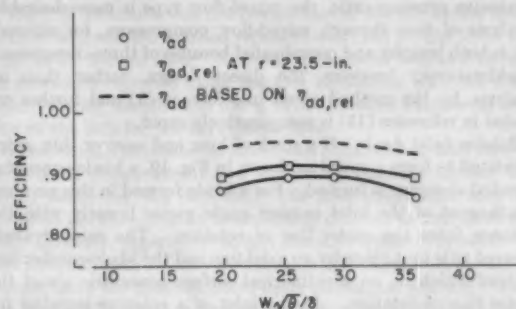


FIG. 18 EFFICIENCY, IMPELLER B

Relative adiabatic efficiency $\eta_{ad,rel}$ at a given radial position is defined (5) as the ratio ΔH_{ad} , the isentropic enthalpy rise relative to the impeller which will give the measured relative total pressure to ΔH_{act} , the actual increase in relative enthalpy based on impeller speed

$$\eta_{ad,rel} = \frac{\Delta H_{ad}}{\Delta H_{act}} = \frac{2gJc_pT_0 \left[\left(\frac{P_r}{P_0} \right)^{\frac{\gamma-1}{\gamma}} - 1 \right]}{\omega^2 r^2}$$

$\eta_{ad,rel}$ may be related to over-all impeller efficiency as follows, if there are no mixing losses (9)

$$\eta_{ad} = 1 - \frac{1 - \eta_{ad,rel}}{2f_s}$$

where f_s , the slip factor, is defined as the ratio of the average tangential velocity of the fluid leaving the impeller to impeller-tip speed.

Applicability of Radial-Flow-Impeller Results to Mixed-Flow Impellers. Relative inlet-angle effects at off-design conditions, boundary-layer build-up, clearance effects, and to some extent secondary-flow effects in mixed-flow impellers are probably similar to those in radial-flow impellers, but more complicated from the standpoint of analysis. It is possible in the mixed-flow impeller to have the conditions shown for the weight flow of 15.6 lb, Fig. 7, at the hub and at the same time to have at the shroud the conditions shown for the weight flow of 45.1 lb per sec, Fig. 9. This is an especially important consideration from the standpoint of compressor-flow range for it is possible to have at the shroud flow velocities which result in an average choking condition for the passage while at the hub the velocity is so low that surge conditions prevail. This set of conditions would result in zero weight-flow range for the impeller. It appears, therefore, that in order to effectively utilize the results of any experimental investigations of impellers a knowledge of at least the isentropic-flow conditions throughout the impeller passage is necessary. The remainder of this paper will be devoted to analysis and design of mixed-flow impellers.

MIXED-FLOW IMPELLERS

The mixed-flow centrifugal impeller may be defined generally as one which has an axial-inlet inducer designed integrally with the impeller and has an outlet directed anywhere from axial to radial. Blades with radial or near radial elements which are utilized in this type impeller are structurally rugged and as a result allow higher inlet-blade heights and higher maximum tip speeds than can be obtained with radial-inlet impellers which generally have cantilevered blades such as those of impellers A and B; therefore, from the standpoint of weight flow per unit frontal area and maximum pressure ratio, the mixed-flow type is more desirable. Analysis of flow through mixed-flow compressors, for example (3), is both lengthy and complicated because of three-dimensional considerations; however, the direct design, rather than an analysis, by the method given in reference (3) and further extended in reference (15) is comparatively rapid.

Relative Inlet Angle. If a stack of long and narrow thin strips is twisted to form a spiral as shown in Fig. 19, a blade consisting of radial elements is formed. For a blade formed in this manner, the tangent of the inlet camber angle varies linearly with the distance from the center line of rotation. The camber angle referred to is that made by an axial line and the blade-camber line both of which lie on a cylindrical surface concentric about the center line of rotation. At the inlet of a rotating impeller for which the inlet-air velocity is constant from hub to shroud the tangent of the angle of approach relative to the rotating impeller also varies linearly with r ; therefore, for very thin blades, the design for zero relative inlet angle from hub to shroud reduces to the problem of attaining constant axial velocity from hub to shroud in the inlet annulus.

For thick blades at inlet and for blades which vary in thickness from hub to shroud the effect of flow blockage must be taken into account. Stanitz (10) has made theoretical calculations to determine the effect of blade thickness and taper on the inlet-flow conditions for an axial inlet. Fig. 20 which was taken from reference (10) shows the effect of both thickness and blade taper on the inlet-flow direction. ϵ_i , the deviation angle (equal to $\beta_a - \beta$), is plotted against radius r . Terms u_a and β_a (inset, Fig. 20) are, respectively, the axial velocity and relative flow direction far upstream in the inlet annulus. β is the relative flow direction after deviation due to blade thickness and taper. The passage blockage in Fig. 20 varies from 40 per cent at the hub to 5 per cent at the

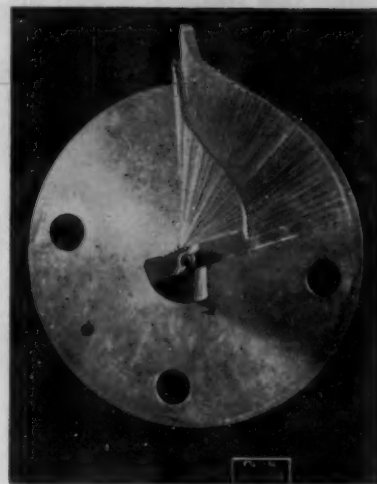


FIG. 19 BLADE CONSISTING OF RADIAL ELEMENTS FORMED BY TWISTING STACK OF THIN STRIPS TO FORM A SPIRAL

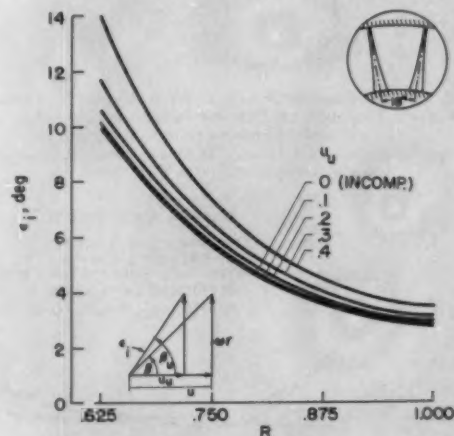


FIG. 20 VARIATION OF INLET DEVIATION ANGLE ϵ_i WITH RADIUS R FOR β_a AT $R = 1.000$ OF 60 DEG AND VARIOUS VALUES OF u_a [From reference (10).]

shroud ($R = 1.0$). Because of deviation angle, viscous effects, and sometimes distortion of the flow due to turning ahead of the inlet annulus, the determination of the blade angle at inlet for maximum over-all efficiency is often very difficult and must be determined experimentally; however, an awareness of the approximate size of the deviation angle is of great value in the initial design.

Analysis. Analysis of flow through mixed-flow impellers even by the relatively simple stream-filament method requires a large amount of time (240 to 480 hr computing time). The velocity distribution from the flow analysis of reference (3) is given in Fig. 21 and the performance results for this impeller from reference (16) are shown in Fig. 22. The velocity-contour lines in Fig. 21 show a steep velocity gradient with low velocity along the hub from a point midway through the impeller to the outlet. An analysis of the flow in the blade-to-blade plane of this impeller showed a large eddy on the driving face of the blade at the hub. If experimentally the reversal of flow which accompanies the for-

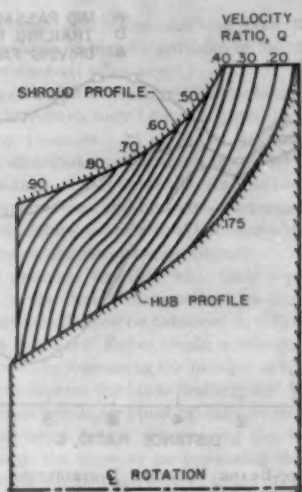


FIG. 21 FLOW ANALYSIS FOR CENTRIFUGAL IMPELLER IN MERIDIONAL PLANE, LINES OF CONSTANT-VELOCITY RATIO. $W = 8.743$; $U = 1331$ FPS

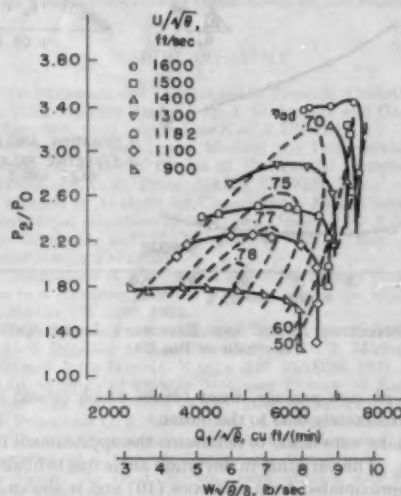


FIG. 22 PERFORMANCE CHARACTERISTICS OF MIXED-FLOW IMPELLER [From reference (16).]

mation of the eddy causes instability, a separation and rotating stall such as that discussed in reference (17) may occur. If the rotating stall does not result in surge or results in surge mild enough to allow operation at a lower weight flow, a second stall or surge point caused by too large a relative inlet angle will be reached. There are two surge points for some of the speeds of operation shown in Fig. 4 of reference (17) which may be the result of such an occurrence.

For the impeller of Fig. 22, the unstable eddy apparently caused violent surge at speeds of 1400 and 1500 fps (16), whereas at the other speeds it merely caused a reduction in efficiency with decreasing weight flow. The eddy may be eliminated by increasing the number of blades; however, this increases the surface friction and raises the manufacturing costs. The eddy also may be eliminated by increasing the velocity level in the region

where the eddy occurs. Increasing the velocity level appears to be the more desirable because it also decreases or eliminates adverse velocity gradients which lead to boundary-layer build-up and possible separation. However, any increase in relative velocity, especially at the outlet, must be considered carefully inasmuch as there is an ensuing increase in the amount of diffusion required and a reduction in the passage height at exit.

For the impeller of Fig. 21 an increase in relative velocity at outlet, from 300 to 600 fps for the 1300-fps tip speed, would cause an increase of approximately 8 per cent in the absolute velocity into the diffuser and a decrease in blade height of approximately 45 per cent. The effects of decreasing the blade height in the impeller or decreasing the distance between the walls of the diffuser are difficult to evaluate and are not well known.

The addition of balsa, impeller C, to radial-flow impeller A of Fig. 14 which decreased the blade height by 28 per cent resulted in a reduction in efficiency at the tip speed of 700 fps of approximately 0.01, Figs. 3 and 14. However, the blade aspect ratio at outlet (outlet blade height to tip radius) of impeller A before reduction was only 50 per cent as great as the average for mixed-flow impellers and therefore does not represent an average case.

Design. For a flow analysis by the method of reference (3) the complete geometry of the impeller which includes the hub, shroud, and blade shapes is known in detail prior to the analysis. If only the blade and hub shapes are prescribed and the shroud shape is allowed to vary, the method may be used for design (15) rather than analysis. The procedure is as follows:

Several stations are established from inlet to outlet along the hub and the first streamline is drawn in by estimate forming a streamtube adjacent to the hub. A velocity distribution is assigned along the hub and the equations of reference (3) are used to determine the velocity along the first streamline at normal lines drawn from the hub at each station. The average weight flow for the streamtube at each normal is then computed to check for continuity. If continuity has not been achieved the streamline spacing is revised and the solution repeated until the weight flows are equal at all normal lines. A second streamline is drawn in and the procedure repeated using the first streamline with the computed velocity distribution along it in the same manner as was done at the hub for the first streamtube.

When enough streamtubes have been computed to take care of the over-all design weight flow the final streamline defines the shroud shape for the impeller. The first streamtube may be started at the shroud or an intermediate position as well as at the hub. However, experience, so far, has shown that it is better to start with a smooth velocity distribution in the area where velocity changes have the greatest effect upon streamline spacing. This area is generally found to be near the hub where blade blockage is at a maximum.

Application of Design Method. The procedure described in the foregoing was used to redesign the shroud of the impeller of Fig. 21. A velocity distribution with very little deceleration along the hub was prescribed and the outlet velocity was increased. Approximately 75 hr of computing time were required. The resulting streamlines, velocity distribution, and shroud are shown in Fig. 23. The blade-shroud clearance space was included in the analysis but not in the design, therefore the design weight flow, Fig. 23, is slightly lower than that for the analysis, Fig. 21. The prescribed velocity along the hub and the resulting velocity distribution on the shroud are shown in Fig. 24 and compared with the velocity distribution obtained in the analysis.

With the new configuration the deceleration rate is generally reduced along the hub but remains approximately the same on the shroud. However, the path length for the decelerating flow on the shroud has been reduced. It is probable that with the higher over-all velocity level along the hub and elimination of the eddy

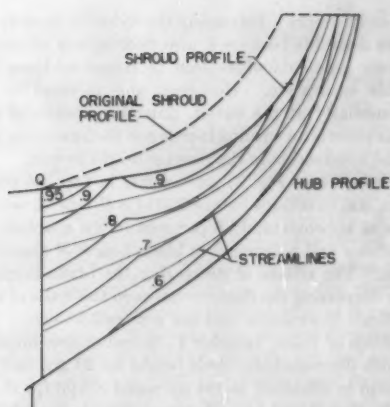


FIG. 23 STREAMLINES AND VELOCITY DISTRIBUTION FOR REDESIGNED SHROUD. $W = 8.384$; $U = 1331$ Fps

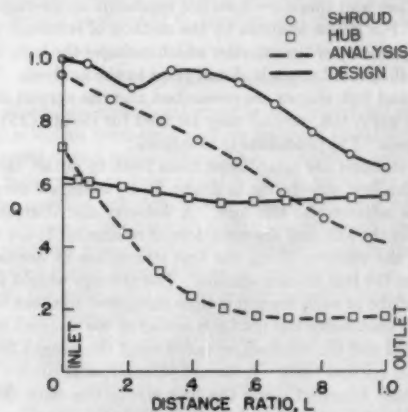


FIG. 24 COMPARISON OF ANALYSIS AND DESIGN VELOCITY DISTRIBUTIONS ON HUB AND SHROUD

the weight-flow range at the speeds above 1300 fps will be greatly increased. The sharp rise in velocity on the shroud which resulted from the prescribed velocity distribution along the hub is an example of the unpredictable results of prescribing the velocity along any given path especially where the path has a large amount of curvature as in this case.

The velocity distribution from blade to blade was computed by the method outlined in reference (3) and a correction for slip factor was made by the method of reference (2). This correction for slip factor which was not included in the results presented in Fig. 23 did not alter the streamline spacing but did result in a slightly higher relative velocity at exit because of the larger relative tangential component. The velocity distribution for the streamtube nearest the shroud is shown in Fig. 25.

The deceleration rate along the trailing face is approximately the same as that at mid-passage. The very large deceleration rate on the driving face is not expected to cause trouble inasmuch as all the experimental data from the internal instrumentation indicate that the boundary layer does not build up on the driving face. The small velocity difference from blade to blade from inlet to L equals 0.35 and the large difference thereafter is undesirable from the standpoint of blade-loading distribution. A redistribution of camber may be needed. This condition could be corrected to some extent without changing the camber by adding, in

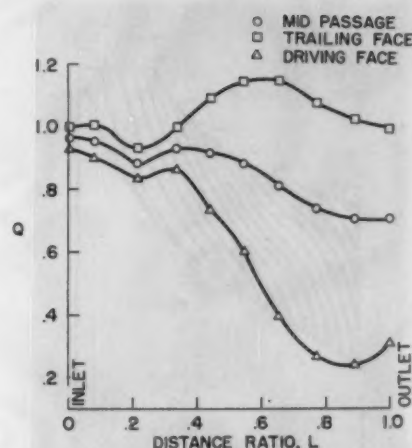


FIG. 25 BLADE-TO-BLADE VELOCITY DISTRIBUTION FOR STREAMTUBE NEAREST SHROUD IN FIG. 23

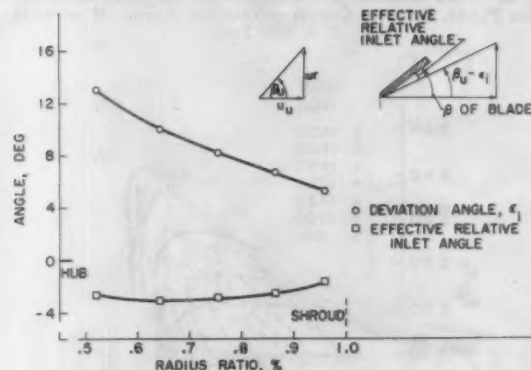


FIG. 26 DEVIATION ANGLE AND EFFECTIVE INLET ANGLE FOR IMPELLER OF FIG. 23

the middle of each passage, short blades which extend from L equals approximately 0.35 to the outlet.

Calculations were made to determine the approximate relative inlet angles. The variation in deviation angle due to blade blockage was approximated from reference (10) and is shown in Fig. 26. The upstream flow angle β_u minus the deviation angle ϵ_1 gives the effective flow angle at inlet. The difference in the effective inlet-flow angle and the blade-inlet angle β gives the effective relative inlet angle. The effective relative inlet angle, also shown in Fig. 26, is negative; therefore the maximum efficiency probably will occur at a lower weight flow than the design weight flow of 8.384 lb per sec.

CONCLUSION

In the design of an impeller it is desirable to obtain wide weight-flow range as well as high efficiency. Design flow conditions that are conducive to wide flow range such as low relative inlet angles, more nearly uniform flow conditions from hub to shroud, and blade loadings without eddy formations on the driving face of the blade may be approximated by methods reported herein. However, achievement of these conditions does not necessarily insure high efficiency. Boundary-layer build-ups along the hub and shroud surfaces bring about secondary flows and accumula-

tions of low-energy air. The resulting poor flow distribution causes mixing losses of high magnitudes in the diffuser, and consequently, low over-all efficiency.

The regions of high loss which result from boundary-layer build-up and secondary flows may be investigated by instrumentation of the rotating passages. In addition, qualitative information about the loss distribution at the passage outlet may be obtained from hot-wire-anemometer surveys. Results obtained from both internal instrumentation and hot-wire-anemometer surveys have been presented to show the effects of boundary-layer build-up and secondary flows on the internal-flow picture.

Theoretical analyses together with these experimental results indicate that in the design of impellers for high pressure ratio, optimum conditions cannot be achieved in all respects and compromises must be made. For example, a reduction in blade loading brought about by increasing the number of blades may reduce the deceleration rate on the blade trailing face, but the resulting reduction in boundary-layer build-up may be more than offset by increased skin-friction losses. Decreasing the over-all deceleration rate through the impeller by increasing the outlet velocity may again reduce the boundary-layer build-up only to have any gains offset by increased losses caused by the resulting decrease in outlet blade height. These results indicate a need for further investigation to determine the effects of such parameters as blade loading, deceleration rates, and blade aspect ratio upon impeller losses and the distribution of these losses at the impeller exit.

BIBLIOGRAPHY

- 1 "Two-Dimensional Compressible Flow in Centrifugal Compressors With Straight Blades," by J. D. Stanitz and Gaylord Ellis, NACA Rep. 954, 1950 (supersedes NACA TN 1932).
- 2 "A Rapid Approximate Method for Determining Velocity Distribution on Impeller Blades of Centrifugal Compressors," by J. D. Stanitz and V. D. Prian, NACA TN 2421, 1951.
- 3 "Method of Analysis for Compressible Flow Through Mixed-Flow Centrifugal Impellers of Arbitrary Design," by J. T. Hamrick, Ambrose Ginsburg, and W. M. Osborn, NACA Rep. 1082, 1952 (supersedes NACA TN 2165).
- 4 "Comparison of Two- and Three-Dimensional Potential-Flow Solutions in a Rotating Impeller Passage," by G. O. Ellis and J. D. Stanitz, NACA TN 2086, 1952.
- 5 "Experimental Investigation of Flow in the Rotating Passages of a 48-Inch Impeller at Low Speeds," by D. J. Michel, Ambrose Ginsburg, and John Mizisin, NACA RM E51D20, 1951.
- 6 "An Analysis of Flow in Rotating Passage of Large Radial-Inlet Centrifugal Compressor at Tip Speed of 700 Feet Per Second," by V. D. Prian and D. J. Michel, NACA TN 2584, 1951.
- 7 "Effect of Changing Passage Configuration on Internal-Flow Characteristics of a 48-Inch Centrifugal Compressor. I—Change in Blade Shape," by D. J. Michel, John Mizisin, and V. D. Prian, NACA TN 2706, 1952.
- 8 "Effect of Changing Passage Configuration on Internal-Flow Characteristics of a 48-Inch Centrifugal Impeller. II—Change in Hub Shape," by John Mizisin and D. J. Michel, NACA TN 2835, 1952.
- 9 "Study of Three-Dimensional Internal Flow Distribution Based on Measurements in a 48-Inch Radial-Inlet Centrifugal Impeller," by J. T. Hamrick, John Mizisin, and D. J. Michel, NACA TN 3101, 1954.
- 10 "Effect of Blade-Thickness Taper on Axial-Velocity Distribution at the Leading Edge of an Entrance Rotor-Blade Row With Axial Inlet and the Influence of This Distribution on Alignment of the Rotor Blade for Zero Angle of Attack," by J. D. Stanitz, NACA TN 2986, August, 1953.
- 11 "A Note on Secondary Flow in Rotating Radial Channels," by J. J. Kramer and J. D. Stanitz, NACA TN 3013, 1953.
- 12 "A Visualization Study of Secondary Flows in Cascades," by A. G. Hansen, H. Z. Herzog, and G. R. Costello, NACA TN 2947, 1953.
- 13 "Investigation of Flow Fluctuations at the Exit of a Radial-Flow Centrifugal Impeller," by J. T. Hamrick and John Mizisin, NACA RM E52H11, 1952.
- 14 "Friction Coefficients in a Vaneless Diffuser," by W. B. Brown, NACA TN 1311, 1947.
- 15 "A Rapid Approximate Method for the Design of Hub-Shroud Profiles of Centrifugal Impellers of Given Blade Shape," by K. J. Smith and J. T. Hamrick, NACA TN 3399, March, 1955.
- 16 "An Investigation of the Effect of Blade Curvature on Centrifugal-Impeller Performance," by R. J. Anderson, W. K. Ritter, and D. M. Dildine, NACA TN 1313, 1947.
- 17 "Compressor Surge and Stall Propagation," by H. W. Emmons, C. E. Pearson, and H. P. Grant, Trans. ASME, vol. 77, 1955, pp. 455-469.

Discussion

G. O. ELLIS.² The author and the NACA are to be congratulated for having conducted a carefully detailed investigation of the internal-flow conditions in centrifugal impellers and related the detailed picture to phenomena commonly measured by more conventional experimental efforts. This work not only provides a pattern upon which future investigations can be based but the discussion of the results should stimulate additional interpretations and constructive argument. The writer would appreciate having the author offer additional comment concerning the following points:

The first concerns the critical, or noncritical, nature of the flow on the driving face near the impeller inlet. The author does not expect large decelerations in this region to cause trouble inasmuch as all experimental data from internal instrumentation indicate that the boundary layer does not build up on the driving face of the blade. This opinion is shared by many thoughtful investigators. Ritter, Johnsen, Ginsburg, et al., however, demonstrated in NACA ARR E5J03, ARR E5I28, and TN 1313 that, at least for the configurations investigated, the efficiency is adversely affected by high loading (and therefore high deceleration rates on the driving face of the blade) near the impeller inlet. Also, as the author has demonstrated, the boundary layer is bled from the driving face and deposited somewhere near the trailing face by secondary flows. Thus, although the boundary layer is not likely to separate from the driving face, large decelerations which encourage boundary-layer growth in this region may increase the supply of low-energy fluid to the critical trailing-face region. It is suggested therefore that, pending further evidence, the velocities on the driving face should receive the same careful attention as those on the trailing face.

The second request for additional comment concerns the author's acceptance of Stanitz's conclusions regarding the effect of leading-edge thickness and taper. Referring to Dr. Stanitz's work (reference 10 to the paper), it is noted that in the solutions presented, a discontinuity in velocity exists along the leading edge of the blade. The velocities just upstream were calculated neglecting the blockage influence of the blade thickness while thick blades were assumed just downstream from the inlet. Deviation angles are calculated based on the downstream values of axial velocity while no change is assumed to occur in the relative tangential component of velocity. It can be reasonably argued that either the upstream calculated values of the tangential component or an average should give values of the deviation angle more in agreement with actual flow. Unfortunately, the deviation angle is greatly affected by this choice and, in fact, may be completely changed in direction near the hub.

Finally, considering Figs. 7, 8, 9, and 10 and the corresponding discussion in the paper, it seems that the concept of separation becomes confusing when applied to mixed-flow-type turbomachines. Even for potential flow the velocity along a line normal to a surface varies radically in direction as well as magnitude and the difference between a flow badly disrupted by secondary flows and separated flows is quite indistinct.

² Research Department, Carrier Corporation, Syracuse, N. Y.

M. G. RYAN.⁴ This paper is a very welcome addition to existing literature in the centrifugal-compressor field. Particularly interesting are the discussions of secondary-flow phenomena. It is hoped that research on secondary flows will continue.

In discussing clearance effects, the author explains the lower efficiency of the small-clearance impeller (0.035 in. clearance) by referring to the smoke tests of Hansen, Herzig, and Costello, reference (12) of the paper. He suggests that for this small clearance, the boundary layer on the shroud is no longer bled through the clearance space, but is scraped up onto the blade, thus causing larger losses.

The authors of reference (12), on the other hand, reached the conclusion that, in a compressor, the scraping-up of the boundary layer had a beneficial effect on flow conditions along the shroud, because the scraped-up fluid forms a vortex which replaced the tip vortex and at the same time the low-energy fluid from the blade suction surface was pulled off onto the shroud. It is true that reference (12) includes no loss figures. On the other hand, it is well known that shrouding axial compressor rows has a somewhat detrimental effect on performance, which would indicate that the losses due to a scraped-up vortex are slightly smaller than the tip losses encountered with a wall which is stationary relative to the blade (i.e., an attached shroud). Also, stationary cascade tests indicate that with a blade-tip clearance and stationary wall, losses are considerably higher than with zero clearance. These considerations throw considerable doubt on the author's tentative conclusions regarding the reason for increased loss at small tip clearance. Would he care to comment?

AUTHOR'S CLOSURE

The author thanks Messrs. Ellis and Ryan for their comments. In the references cited by Mr. Ellis the experimental results did not permit clear-cut conclusions regarding loading effects. There were variations other than blade shape such as change in cross-sectional passage area from inlet to outlet and in the case of the impellers of NACA TN 1313 unstable eddies on the blade driving face severely reduced range and efficiency. Further, high loading does not necessarily imply large decelerations. This would depend upon the amount of diffusion desired in the impeller passage. If a large amount of diffusion is desired, then there must be large

local decelerations on either the driving face near the inlet or the trailing face near the outlet. It has been demonstrated in numerous cases that separation does not occur on the driving face (except for severe negative relative inlet angles) and it has also been demonstrated in the elbow tests of NACA TN 3015 that there were low-energy air accumulations on the suction surface even though there was accelerating flow along all surfaces. Therefore it is the opinion of the author that if it is necessary to accept local decelerations in the passage it is better to take them on the driving face where separation is not likely to occur. The idea here is to avoid separation. Of course decelerations should be eliminated where possible.

The meaning of the comments regarding the work of Dr. Stanitz (10) is not clear enough to the author to allow comment other than that certainly there is a great need for more knowledge of the flow around the leading edges of blades both at design and off-design conditions. However, the work is considered by the author as an excellent guide in approximating the relative flow angle at inlet.

The concept of separation is confusing in rotating machines if velocity alone is used in determination of separation point. However, a static pressure drop along with a sudden loss in total pressure gives a more positive indication. It is possible that some of the losses on the trailing face, Figs. 7, 8, 9, and 10, are brought about by separation on that face but the smoothness of the static-pressure profiles is a strong indication that this is not the case.

With regard to Mr. Ryan's discussion of clearance effects, the conditions under which experiments of reference (12) were run were quite different from those of the subject paper as regards Reynolds number, Mach number, attainable circulation, and geometric shape. Therefore the dominating factors were not the same in both cases. As a result each individual case must be viewed on its own merits. In the subject paper the comparison is for varying amounts of clearance and not for shrouded versus unshrouded impellers. The complexity of the problem is such that conclusion regarding the merits of shrouding or not shrouding could not be drawn from these results. This is demonstrated by the fact that shrouding of a single impeller appears to be detrimental at high speeds and beneficial at low speeds as shown in NACA ARR E5H23.

⁴ Carrier Corporation, Syracuse, N. Y.

A Three-Dimensional Spherical Pitot Probe

By J. C. LEE¹ AND J. E. ASH,² CHICAGO, ILL.

The conventional method of applying the five-hole spherical pitot probe to three-dimensional flow measurements consists of either adjusting the probe until its axis points in the flow direction, or yawing the probe until the meridian plane passing through the center orifice contains the flow angle, and then making use of two-dimensional calibration curves for the flow determination in this plane. Both methods require adjustment of the probe, which, in general, is quite difficult to accomplish if the probe is mounted upon a rotating impeller. To avoid this difficulty a five-hole, three-dimensional spherical pitot probe has been developed and calibrated to measure static pressure and the magnitude and direction of the velocity vector for any arbitrary flow angle without adjustment of the probe.

NOMENCLATURE

The following nomenclature is used in the paper:

- w = free-stream velocity relative to probe
- p_s = free-stream static pressure
- ρ = specific mass
- ϕ = conical angle formed by velocity and probe axis
- δ = dihedral angle between flow plane and meridian plane
- α = conical angle formed by four symmetrical pressure holes and probe axis
- γ_n = angle between velocity vector and any n th pressure hole
- k = pressure-recovery factor

The subscripts 0, 1, 2, 3, 4 refer to the five pressure holes; the center hole has the subscript 0, and the holes bearing the subscripts 2, 0, 4 lie in the equatorial plane as shown in Fig. 2.

INTRODUCTION

Reliable experimental data for the flow field in rotating-blade cascades are scant mainly because of the lack of suitable flow-measuring instruments. For studying the flow phenomena in three-dimensional or mixed-flow rotating cascades, it is not only necessary to measure the static pressure and the flow velocity, but also the flow direction. In addition, the sensing probe must be sufficiently small to be capable of point measurement without appreciably affecting the flow in the passages because of its presence. Among the several types of pitot probes commonly used for measurement of flow direction, as well as flow velocity and static pressure, are the claw-type probe and the spherical probe.^{3,4} The common method of obtaining flow direction by means of these probes is the null system. The probe is adjusted along two perpendicular directions or planes, yaw and pitch, until the probe

axis points in the flow direction which is measured by protractor scales on the two planes. An alternative method consists of yawing the probe until the meridian plane contains the flow angle, or pitch angle, and using two-dimensional calibration curves for the flow measurements.^{5,6}

Both methods require adjustment of the probe, which, in general, is quite difficult to accomplish if the probe is mounted on a rotating impeller. To avoid this difficulty, a five-hole spherical pitot probe with a head diameter of 0.190 in. was made and calibrated three-dimensionally to measure static pressure, velocity, and flow direction in the rotating cascades.

The probe consists essentially of a tapered shaft with a 0.190-in.-diam spherical sensing head at the end, as shown in Fig. 1. The other end of the shaft is welded at a right angle to a crosspiece which is to be mounted between the two shrouds of the blade cascade during tests. On the spherical surface are five pressure holes of 0.016 in. diam, one along the shaft axis and four located symmetrically on the meridional and equatorial planes. The meridian plane passes through the axes of the shaft and of the crosspiece. Each of the four symmetrically spaced holes lies on a sphere radius which makes an angle of 40 deg with the probe axis. The crosspiece being at a sufficient distance downstream from the probe head causes no appreciable flow disturbance at the pickup. In addition, the symmetry of the probe design results in calibration curves which are symmetric for opposite pressure holes.

THEORETICAL CALIBRATION CURVES

The energy equation between a point in the free stream and the n th hole on the sphere is given by

$$p_n + \frac{w^2}{2} = p_n + \rho \frac{w_n^2}{2}; \quad n = 0, 1, 2, 3, 4, \dots \quad [1]$$

Solving this equation for the pressure at the n th hole yields

$$p_n = p_s + \rho \frac{w^2}{2} \left[1 - \left(\frac{w_n}{w} \right)^2 \right] \\ = p_s + k_n \rho \frac{w^2}{2} \dots \dots \dots [2]$$

$$\text{The pressure-recovery factor} \quad k_n = \left[1 - \left(\frac{w_n}{w} \right)^2 \right]$$

is a function of the Reynolds number and the orientation of the hole with respect to the stream γ_n . However, this factor becomes independent of the Reynolds number for sufficiently high velocities, and is only a function of γ_n which can be expressed in terms of the two angles ϕ and δ . By combining the equations for the pressure at each of the five holes, the following ratios may be obtained

$$\frac{k_1 - k_2}{k_3 - k_4} = \frac{p_1 - p_2}{p_3 - p_4} = X_{12}(\phi, \delta) \dots \dots \dots [3]$$

$$\frac{k_2 - k_4}{k_3 - k_1} = \frac{p_2 - p_4}{p_3 - p_1} = Y_{24}(\phi, \delta) \dots \dots \dots [3a]$$

¹ Armour Research Foundation, Illinois Institute of Technology.

² Associate Research Engineer, Heat Power Division, Armour Research Foundation, Technology Center. Assoc. Mem. ASME.

³ "Instrumentation for Axial-Flow Compressor Research," by C. A. Meyer and R. P. Benedict, Trans. ASME, vol. 74, 1952, pp. 1327-1336.

⁴ "Several Combination Probes for Surveying Static and Total Pressure and Flow Direction," by W. M. Schulte, G. C. Ashby, Jr., and J. R. Erwin, NACA TN 2830, November, 1952.

Contributed by the Gas Turbine Power Division and presented at the Diamond Jubilee Semi-Annual Meeting, Boston, Mass., June 19-23, 1955, of THE AMERICAN SOCIETY OF MECHANICAL ENGINEERS.

NOTE: Statements and opinions advanced in papers are to be understood as individual expressions of their authors and not those of the Society. Manuscript received at ASME Headquarters, April 15, 1955. Paper No. 55-SA-56.

⁵ "Three-Dimensional Flow Measuring Probe," by R. L. Hundstedt, Scientific Paper 1644, Westinghouse Research Laboratories, East Pittsburgh, Pa., February, 1952.

⁶ "Experiences With Flow Direction Instruments," by B. Eckert, NACA TM No. 969, March, 1941.

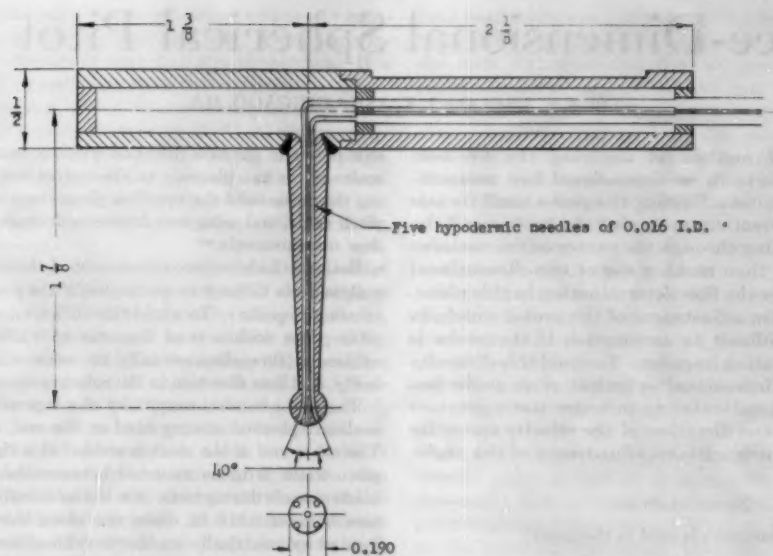


FIG. 1 CONSTRUCTIONAL DETAILS OF SPHERICAL PITOT

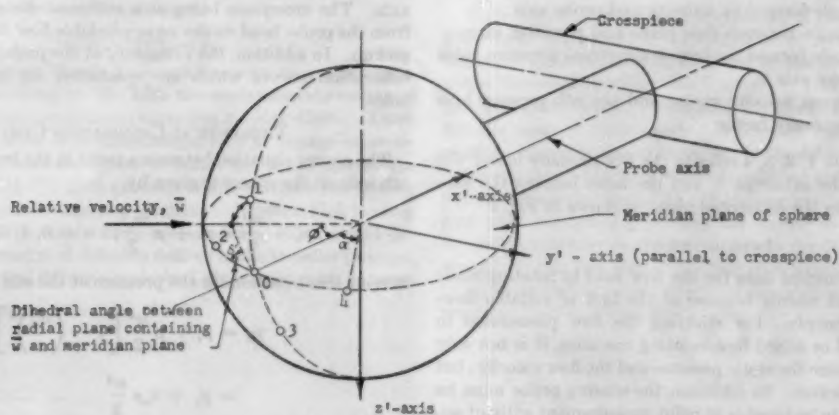


FIG. 2 NOTATION FOR SPHERICAL PROBE HEAD

Each of these ratios may be determined experimentally by measuring the pressure differences between the corresponding holes on the pitot sphere for a known orientation of the probe with respect to the free-stream velocity vector. The two functions of Equations [3] and [3a] implicitly give ϕ and δ , which determine the direction of the velocity, in terms of the ratio of

$$\frac{k_2 - k_1}{k_0 - k_1} \quad \text{and} \quad \frac{k_1 - k_3}{k_0 - k_3}$$

These ratios have finite values if δ is in the range $0 < \delta < 180^\circ$, Fig. 2. But in the range $-180^\circ < \delta < 0$, the ratios become infinite when the vector makes equal angles with holes 0 and 3. For this reason and also for the sake of symmetry, the graph of the two ratios defining flow direction and velocity is divided into two halves, $0 < \delta < 180^\circ$, and $-180^\circ < \delta < 0$. For the first half, the ratios given by Equations [3] and [3a] are used. For the second half, the ratios used are

$$\frac{k_1 - k_3}{k_0 - k_1} = \frac{p_1 - p_3}{p_0 - p_1} = X_{13}(\phi, \delta) \dots \dots \dots [4]$$

$$\frac{k_2 - k_4}{k_0 - k_1} = \frac{p_2 - p_4}{p_0 - p_1} = Y_{24}(\phi, \delta) \dots \dots \dots [4a]$$

The theoretical determination of the foregoing ratios of the pressure-recovery factors may be based upon potential flow around a sphere. For this case, the velocity at any point on the sphere surface corresponding to a radial line forming an angle γ_n with the w -direction is given by the equation⁷

$$w_n = \left(\frac{3}{2} \sin \gamma_n \right) w \dots \dots \dots [5]$$

This means that the pressure-recovery factor at the n th hole for potential flow is given by

⁷ "Theoretical Hydrodynamics," by L. M. Milne-Thomson, The MacMillan Company, New York, N. Y., second edition, 1950.

$$k_a = 1 - \frac{9}{4} \sin^2 \gamma_a \dots \dots \dots [6]$$

and the ratio of the pressure-recovery factors is

$$\begin{aligned} \frac{k_1 - k_3}{k_0 - k_3} &= \frac{\sin^2 \gamma_2 - \sin^2 \gamma_1}{\sin^2 \gamma_3 - \sin^2 \gamma_0} \\ &= \frac{\cos^2 \gamma_1 - \cos^2 \gamma_2}{\cos^2 \gamma_0 - \cos^2 \gamma_3} \dots \dots \dots [7] \end{aligned}$$

The ratios of the other pressure-recovery factors are given by similar expressions.

The angle γ_a is related to ϕ and δ by the equations of spherical trigonometry

$$\left. \begin{aligned} \cos \gamma_0 &= \cos \phi \\ \cos \gamma_1 &= \cos \phi \cos \alpha + \sin \alpha \sin \delta \sin \phi \\ \cos \gamma_2 &= \cos \phi \cos \alpha + \sin \alpha \cos \delta \sin \phi \\ \cos \gamma_3 &= \cos \phi \cos \alpha - \sin \alpha \sin \delta \sin \phi \\ \cos \gamma_4 &= \cos \phi \cos \alpha - \sin \alpha \cos \delta \sin \phi \end{aligned} \right\} \dots \dots [8]$$

Making use of these relations, we have the functions representing the theoretical ratios of the pressure-recovery factors

$$\begin{aligned} (X_{132}) &= \frac{2 \sin 2\alpha \sin \delta \sin 2\phi}{2 \sin^2 \alpha (\cos^2 \phi - \sin^2 \delta \sin^2 \phi) + \sin 2\alpha \sin \delta \sin 2\phi} \dots \dots [9] \end{aligned}$$

$$(Y_{241}) = \frac{2 \sin 2\alpha \cos \delta \sin 2\phi}{2 \sin^2 \alpha (\cos^2 \phi - \sin^2 \delta \sin^2 \phi) + \sin 2\alpha \sin \delta \sin 2\phi} \dots \dots [9a]$$

These ratios are plotted in Fig. 3. Because of perfect symmetry, only the first quadrant in which δ ranges from zero to 90 deg is shown.

The foregoing functions are used to determine the direction of the velocity. The magnitude of the velocity may be determined by applying the general pressure equation to the center hole and one of the other four holes, say, hole (3), which will give the equation

$$p_0 - p_3 = \rho \frac{w^2}{2} (k_0 - k_3)$$

From this the velocity is

$$w = \sqrt{\frac{2}{\rho} \frac{p_0 - p_3}{k_0 - k_3}} \dots \dots \dots [10]$$

Equations [6] and [8] may be used to determine the theoretical relation of $(k_0 - k_3)$ to ϕ and δ

$$\begin{aligned} k_0 - k_3 &= \frac{9}{4} (\cos^2 \gamma_0 - \cos^2 \gamma_3) \\ &= \frac{9}{4} [\sin^2 \alpha (\cos^2 \phi - \sin^2 \delta \sin^2 \phi) \\ &\quad + \frac{1}{2} (\sin 2\alpha \sin 2\phi \sin \delta)] \dots \dots [11] \end{aligned}$$

The curves for determining the flow direction and velocity obtained by experimental calibration are shown in Fig. 4. The dotted curves are the constant $k_0 - k_3$ or $k_0 - k_1$ curves. The experimental curves in Fig. 4 are not very symmetrical because of the slight misalignment of the holes, especially the center hole (0) which was found to be off the axis about 2 deg toward hole (4). In general, Fig. 4 checks fairly well with the theoretical curves in

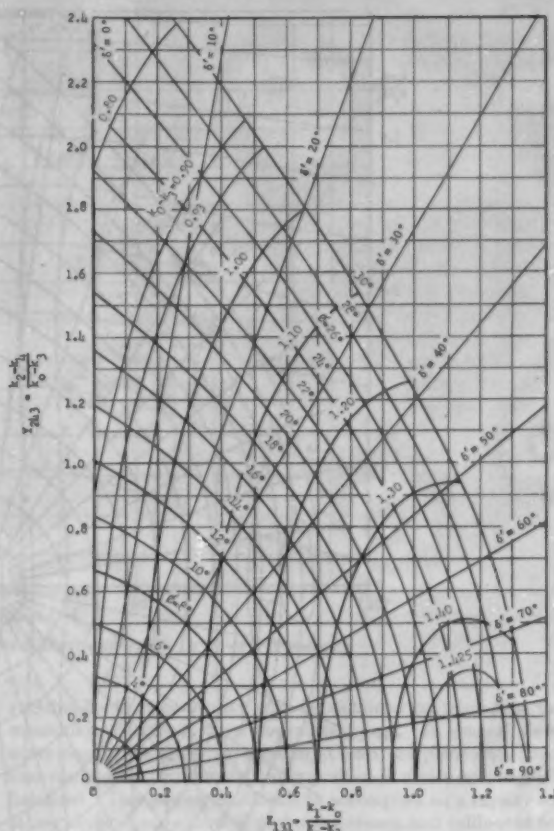


FIG. 3 THEORETICAL CALIBRATION CURVES FOR THE 5-HOLE SPHERICAL PITOT PROBE

Fig. 3. The latter were computed on the assumptions of potential flow and zero post effect.

After the magnitude and direction of the velocity have been determined, the static pressure of the free stream is given directly by Equation [2] for the center hole

$$p_s = p_0 - k_0 \rho \frac{w^2}{2} \dots \dots \dots [12]$$

The theoretical value of k_0 is given by Equation [6], where γ_0 is identical to the cone angle ϕ

$$k_0 = 1 - \frac{9}{4} \sin^2 \phi \dots \dots \dots [13]$$

The theoretical curves for k_0 and the corresponding experimental calibration curves are shown in Fig. 5. The deviation of the experimental curves from the theoretical one is mainly due to the misalignment of the center hole (0).

CALIBRATION

The spherical probe was calibrated in the test stand which is shown schematically in Fig. 6. The calibration fixture consists of two concentric rings in a gimbal mounting. The bottom ring is pivoted along its diameter in the table mounting, with the pivot axis perpendicular to the nozzle axis. The tilting angle is measured with a protractor on the pivot axis and is equal to the cone angle ϕ between the velocity vector of the flow and the shaft axis

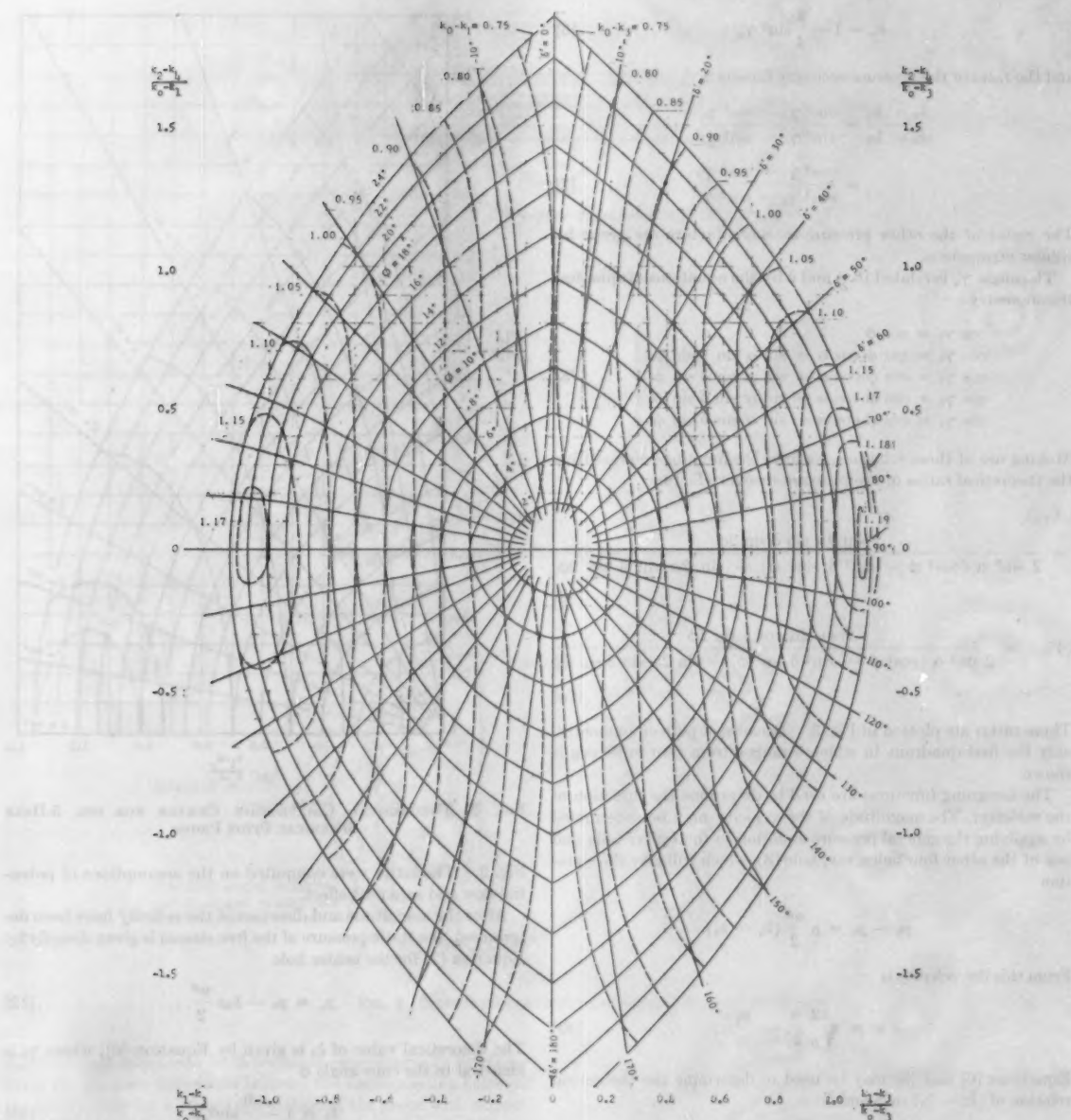


FIG. 4 CALIBRATION OF SPHERICAL PITOT FOR DETERMINATION OF MAGNITUDE AND DIRECTION OF FLOW

of the probe. The top ring rotates over the bottom ring which has protracted angular divisions to measure the dihedral angle δ . The probe is mounted on the top ring with its shaft axis coinciding with the ring axis and with the center of the spherical probe on the pivot axis of the bottom ring. By this arrangement the center of the sphere remains on the nozzle axis and fixed in position with any change of cone angle and dihedral angle. Thus the error caused by nonuniformity of nozzle air velocity with change of these angles is minimized.

APPLICATION

This spherical pitot probe was designed mainly for measuring the relative flow through rotating three-dimensional blade cascades. The relative flow through such cascades is steady provided the guide cascades in the upstream or downstream are remotely located. In such cases, the response speed of the pressure readings can be sacrificed in favor of small orifice holes and connecting tubings. Thus the size of the probe head can be reduced, and the errors due to differences in centrifugal heads of the holes at dif-

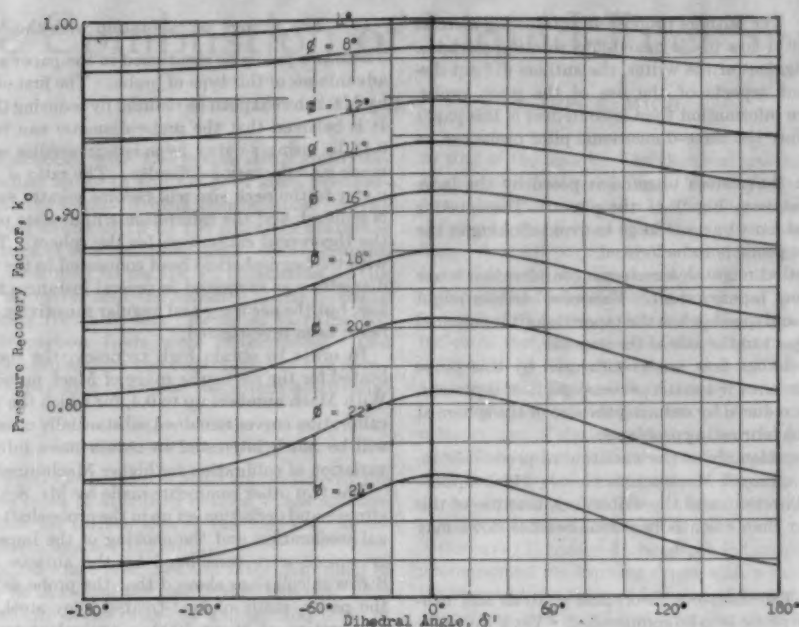


FIG. 5 CALIBRATION OF SPHERICAL PITOT FOR DETERMINATION OF STATIC PRESSURE

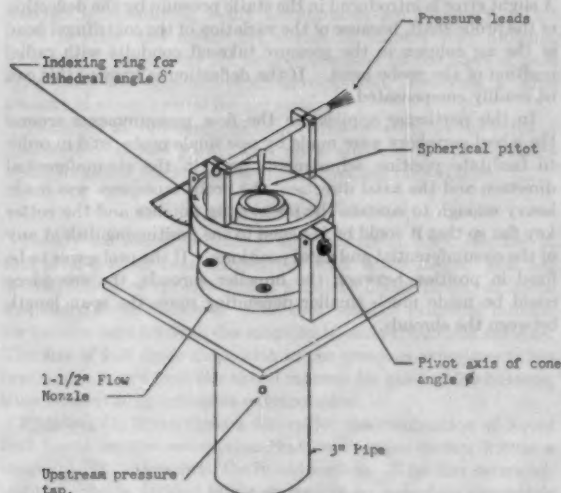


FIG. 6 SPHERICAL PITOT-PROBE CALIBRATION FIXTURE

ferent radii from the axis of the rotating cascade are minimized.

The probe can be mounted on the impeller without any provision for yawing. The pressure readings are taken off from the impeller shaft through rotation seals. Viscous drag mercury seals were developed for this purpose and found to perform satisfactorily.

SUMMARY AND CONCLUSIONS

The accurate three-dimensional measurement of internal flow is necessary for further development in the field of mixed-flow subsonic turbomachinery. Steady-state measurements within a

rotating-blade cascade may only be obtained by mounting the measuring instrument upon the rotating part. In general, flow-surveying probes must be yawed in at least one plane until pressure readings on two symmetrically positioned orifice openings are balanced. This yawing is difficult to accomplish on a rapidly rotating element. A spherical probe was chosen and calibrated for three-dimensional measurements without yawing. Satisfactory measurements were obtained in actual blade cascades by this method. The probe is quite sensitive to direction; in general, an accuracy of better than 1 deg for ϕ and 2 deg for δ can be expected. The accuracy for the velocity and static pressure is estimated to be about 3 per cent. The inherent disadvantages of this type of probe are the limited operating range of Reynolds number (4×10^5 to 1.5×10^6) and the change of calibration when the probe is held close to the wall.

ACKNOWLEDGMENT

This work was done at the Armour Research Foundation as part of the research program on "Investigation of Three-Dimensional Cascades" sponsored by the Aeronautical Research Laboratory of Wright Air Development Center under Contract No. AF33(616)-2369.

Discussion

W. G. CORNELL.^{*} Congratulations are due to the authors on an interesting and valuable paper. A probe which does not require operational realignment is indeed useful for experimental investigations of turbomachinery.

The authors minimize two important effects, which merit further attention: (a) The probe calibration will be affected by the large stream velocity gradients which exist in high-performance impellers; (b) the calibration will be a function of the level of stream Mach number.

^{*} Aerodynamics Engineer, Aircraft Gas Turbine Division, General Electric Company, Cincinnati, Ohio. Mem. ASME.

F. C. SCHWENK.⁹ The authors propose an interesting method for the measurement of flow inside mixed-flow rotating cascades. However, in the judgment of the writer, the authors did not discuss some important aspects of the use of the pitot probe. Actually, much more information than is contained in this paper will be required before the three-dimensional pitot probe can be utilized.

The first problem that comes to mind is posed by the large diameter of the crosspiece, Fig. 1 of the paper. The rotating cascade to be studied must be quite large to avoid choking in the passage in which the probe is to be located.

Another question that might deserve some consideration is one of stresses in the long tapered shaft. Excessive stresses might occur for high rotational speeds when the tapered shaft is mounted nonradially with respect to the axis of the impeller.

It is also expected that flow angles measured by this probe in a cascade will be in error if a static pressure gradient is present. Such an error can be reduced by reducing the size of the sphere at the expense of causing fabricating problems.

There is also a question about the variation of probe calibration with changes in approach Mach-number level. Mach number should affect the calibration, and the writer feels that use of this pitot probe for other than essentially incompressible flows may be difficult.

F. S. WEINIG.¹⁰ The complete theoretical analysis and calibration of this 5-hole probe is to be commended. Yet if the probe is not to be used in a quite large test vehicle, the problem remains of extending the calibration to a field where velocity gradients exist. The real difficulty then, because of the velocity gradient, would be that the corrections, in general, had to be different as to the causes of this gradient whether potential, as by curvature of the streamlines, or nonuniformity of energy, as in the shear flow of the boundary layer or of secondary flow.

AUTHORS' CLOSURE

The two major questions raised by all three discussers, Messrs. Cornell, Schwenk, and Weinig are:

- (a) The change of calibration with large velocity gradients.

⁹ Lewis Laboratory, National Advisory Committee for Aeronautics, Washington, D. C.

¹⁰ Manager, Aerodynamics, Aircraft Gas Turbine Division, General Electric Company, Cincinnati, Ohio. Mem. ASME.

- (b) The change of calibration with the Mach number level.

These two points as mentioned in the paper are the inherent disadvantages of this type of probe. The first effect, as pointed out by Mr. Schwenk, can be reduced by reducing the size of the sphere. It is believed that the probe diameter can be reduced to about 0.13 in. using smaller hypodermic needles without introducing much manufacturing difficulty. The ratio of the probe head diameter to the neck size will become greater as the head diameter is reduced, and the calibration will deviate more and more from the theoretical calibration for the sphere. The use of a probe with the hemispherical head connected to the neck with the same diameter was suggested in several instances to reduce the probe size, but the accuracy and angular sensitivity of such a probe has never been investigated.

In order to obtain high accuracy, the probe should be calibrated for the particular range of Mach number to be measured. With Mach numbers up to 0.4, for which the probe was used, the calibration curves remained substantially constant. The authors will be much interested to obtain more information about the variation of calibration for higher Mach-number levels.

The two other comments made by Mr. Schwenk regarding the stresses and deflection set up in the probe shaft under high centrifugal acceleration and the choking of the impeller passage by the crosspiece were considered by the authors during the design. Stress calculations showed that the probe as shown in Fig. 1 of the paper, made of heat-treated alloy steel, was safe up to an acceleration of about 5000 *g*, equivalent to operating a 24-in. diameter wheel at about 4000 rpm with the probe mounted on the periphery and shaft axis perpendicular to the impeller radius. A slight error is introduced in the static pressure by the deflection of the probe shaft, because of the variation of the centrifugal head of the air column in the pressure take-off conduits with radial position of the probe head. If the deflection is known, this can be readily compensated.

In this particular application the flow measurements around the wheel periphery were made by one single probe, and in order to facilitate position adjustment, both in the circumferential direction and the axial direction, the probe crosspiece was made heavy enough to contain the positioning notches and the cotter key flat so that it could be fastened to the positioning disk at any of the circumferential and axial positions. If the probe was to be fixed in position between the impeller shrouds, the crosspiece could be made much smaller depending upon the span length between the shrouds.

The Combustion of Liquid-Fuel Spray¹

By J. A. BOLT² AND T. A. BOYLE,³ ANN ARBOR, MICH.

This paper is concerned with the evaporation and combustion of liquid-fuel spray in the range of sizes predominantly used in aircraft gas-turbine combustors. Spray of uniform-size fuel drops of 70 to 130 microns diameter was produced by means of a spinning disk. Photographic techniques were developed to obtain an indication of the rate of change of diameter and the velocity of the burning drops, while moving freely in air. Rates of burning for several pure hydrocarbon fuels were determined. The experimental work emphasizes the complexity of the combustion of a fuel spray and the need for much additional work.

INTRODUCTION

BURNING of liquid fuel is aided in many applications by the use of various types of atomizing nozzles, whose function it is to increase the surface area of the fuel and, consequently, the rates of evaporation and burning.

Our knowledge of the exact processes and rates of burning of liquid-fuel drops in furnaces and turbines is very meager. This is due to the complexity of the processes and the difficulties of measurement under the actual burner conditions.

This lack of knowledge hampers application of rational methods to the design of combustors for gas turbines. When a rational analysis is attempted, many assumptions are necessary. This leads to error and makes the design of burners very difficult. As a result, these units are largely designed on the basis of past experience and trial-and-error development, involving a large amount of experimental burner testing.

Therefore all fundamental information relating to the rates of combustion of fuel spray, and an evaluation of the variables which influence the process are of the greatest importance.

SURVEY OF PAST WORK

Nearly all the experimental and analytical work relating to this problem has been carried out with single drops; this has involved flooded spheres which simulate liquid drops, or drops suspended from filaments. The drop sizes of principal interest for turbine burners lie in the range up to several hundred microns. The size of fuel drops dealt with in the previous experiments has been much larger than the size of interest for gas-turbine burners, thus necessitating extensive extrapolation.

Spalding (1, 2)⁴ outlines a theory for the combustion of liquid fuel based on the assumption that combustion occurs within a stagnant film adjacent to the liquid surface. The film surrounding the drop is divided into two regions by a surface concentric

to that of the liquid. The chemical reaction is assumed to take place at the dividing surface. The fuel vapor passes by diffusion from the liquid surface to the burning surface, while the oxygen diffuses to this surface from the outer boundary of the stagnant film. A small portion of the heat of combustion is conducted inward to heat the liquid and provide the latent heat of vaporization of the fuel. The main portion of the heat of combustion is conducted outward toward the gas stream. This analysis indicates that the rate of combustion of a liquid fuel is greatly influenced by the phenomena of heat transfer, diffusion, and evaporation. Evaluation of these phenomena has been hindered by difficulties involved in the analysis of the gases and the measurement of the temperatures near the flame zone. Spalding was able to complete his analysis by making simplifying assumptions for many of these factors. Experimental work was conducted employing flooded spheres of approximately 1 1/2 in. diam to support some of his theory.

Godsave (3) ignited drops suspended on a vertical filament and photographed the burning drops with a motion-picture camera. He observed the rates of burning of various fuels and pure hydrocarbons, and found that over the range of drop sizes investigated (1000 to 2000 microns), the burning drops decreased in size at a mass rate proportional to the first power of their diameter. The burning rate may be expressed by an evaporation constant, as defined by the following equation

$$D^3 = D_0^3 - \lambda t$$

where

D = drop diameter at any time, t

D_0 = drop diameter at $t = 0$

λ = evaporation constant having the dimensions of length³/time

t = elapsed burning time

He also obtained experimental evidence that the rate of combustion is chiefly dependent on the enthalpy of the liquid and on the latent heat of vaporization, rather than on properties such as the volatility of the fuel. Spalding (1, 2) also stated that the fuel properties having the predominant effect on the combustion rate are the heat of combustion, the latent heat of vaporization, and the specific heat of the vapor. Since these properties do not vary greatly for the usual hydrocarbon fuels, it is reasonable to expect that the combustion rates will be quite similar. Thus the difference in burning rates for gasoline and diesel fuel is due mainly to the difference in time required to reach equilibrium temperature. Spalding points out the importance of these conclusions, since they indicate the futility of trying to accelerate combustion by means of additives.

EXPERIMENTAL METHOD SELECTED

This work was undertaken in an effort to avoid the following sources of experimental error:

- 1 Complications arising from filament or wire suspension.
- 2 An undesirable degree of extrapolation to obtain data for the drop size of principal interest.
- 3 Indefiniteness resulting from dealing with a wide range of drop sizes.
- 4 Use of an isolated drop instead of a drop under the influence of its neighbors.

¹ Results of an investigation conducted at the Engineering Research Institute of the University of Michigan, under contract with Wright Air Development Center, Wright-Patterson Air Force Base.

² Professor of Mechanical Engineering, University of Michigan. Mem. ASME.

³ Assistant Professor of Mechanical Engineering, University of Michigan. Assoc. Mem. ASME.

⁴ Numbers in parentheses refer to the Bibliography at the end of the paper.

Contributed by the Gas Turbine Power Division and presented at the Diamond Jubilee Semi-Annual Meeting, Boston, Mass., June 19-23, 1955, of THE AMERICAN SOCIETY OF MECHANICAL ENGINEERS.

NOTE: Statements and opinions advanced in papers are to be understood as individual expressions of their authors and not those of the Society. Manuscript received at ASME Headquarters, May 10, 1955. Paper No. 55-SA-67.

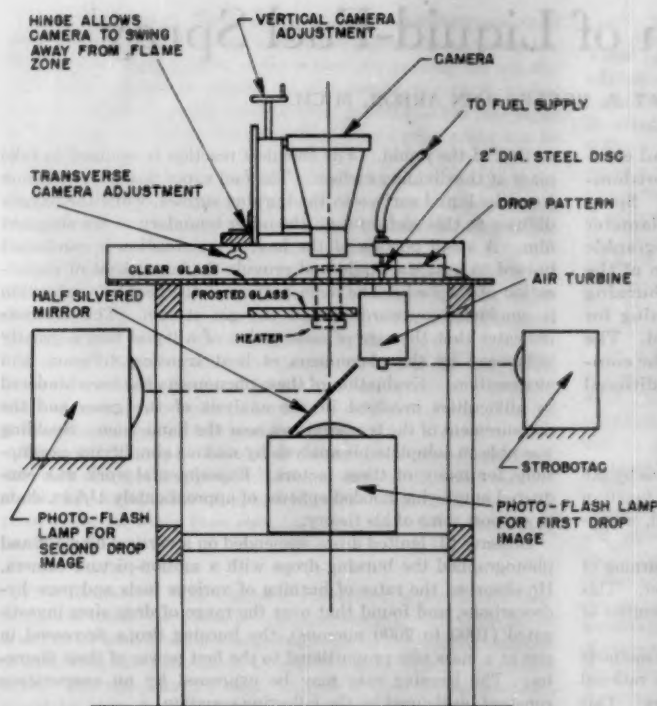


FIG. 1 EQUIPMENT FOR MAKING, BURNING, AND PHOTOGRAPHING UNIFORM-SIZE FUEL DROPS

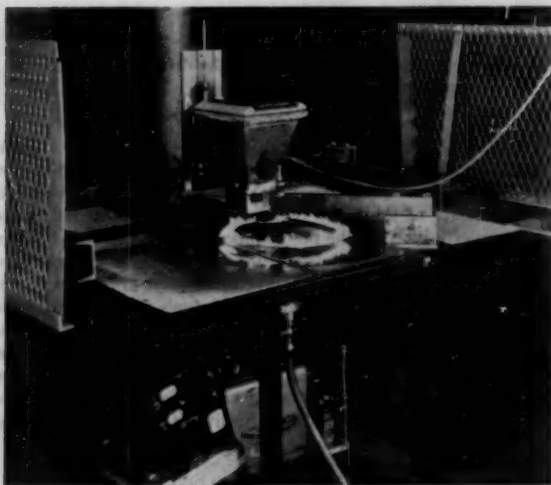


FIG. 2 TEST STAND WITH BURNING FUEL SPRAY

The experimental procedure utilized an application of photographic analysis to a uniform-drop-size spray as it was burned. This paper describes the development of a method for the problem, and reviews the results which have been obtained to date. Some aspects of it constitute only a progress report, since the investigation is continuing.

The equipment used for most of these tests is illustrated in Figs. 1 and 2.

SPINNING-DISK SPRAYER

The need for a uniform-drop-size fuel spray adequate to sustain a combustion process was best met by spray from a spinning-disk sprayer. During the early stages of this work other means were tried, but the spinning disk was considered the most suitable. The work of May (4) and Walton and Prewett (5) had established the uniformity of spray from a spinning disk; however, the work of Friedman (6) indicated that when these sprayers were loaded heavily, the uniformity of the spray diminished. For the work reported here the spray was considered uniform when it exhibited a standard mean deviation of 5 microns or less. However, as the spray burns, the range of sizes increases.

Within the limits thus established, a spinning-disk sprayer supplied spray that was adequate in quantity and acceptably uniform in size. The satellite drops formed traveled 3 or 4 in. radially and were carried upward. These satellite drops were not present in the region of the flame as long as the rate of fuel supply to the disk was kept relatively low. Conditions representative of much of the work reported are as follows: Fuel supply, 12 cc/min; disk diameter, 2 in.; disk speed, 8000 rpm; drop size entering flame, 90 microns.

The disk was turned by an air turbine, mounted with its axis vertical. The disk was held in the collet chuck on the turbine shaft and supplied spray in the form of a horizontal sheet. Turbine control was effected through a pressure regulator and the speed was measured with a strobotac.

Drops formed at the edge of the disk traveled in a straight, virtually horizontal path for 6 or 8 in.; then, as their outward velocity was reduced, they dropped to the surface of the stand on which the turbine was mounted. A bunsen flame, moved through the region in which the drop velocity was sufficiently reduced, initiated a sustained flame in the form of a ring around the disk. A portion of the flame was then photographed, and the size and velocity of drops appearing on the photographs were determined.

PHOTOGRAPHIC SPRAY ANALYSIS

The basic arrangement of equipment used to photograph the burning spray was patterned after that of York and Stubbs (7). A General Electric photolight was directed through the region of spray to be photographed. The transmitted light yielded a silhouette photograph of the drops within the camera field at the instant the light was flashed. The intensity of the flash was controlled by the location of the light and of the ground-glass diffusing screen.

For determining velocities, two photolights were used, see Fig. 1. They supplied light to a half-silvered mirror and then through the spray to the camera. The second photolight was fired at a known interval after the first so that knowledge of the distance between the two images of a drop would permit determining its velocity. An alternative method utilized a single photolight powered in sequence from six capacitors, which produced six flashes in rapid sequence. With this arrangement, an ordinary six-cylinder automobile-engine ignition-unit assembly was used, being turned at approximately 1700 rpm. The primary circuit-breaker points of the ignition unit were used to time the trigger circuit of the photolight, and the secondary distributor system was used to connect each of the six 2-microfarad condensers in sequence to the photolight electrodes.

Photographs were taken with the camera axis either vertical or horizontal. The orientation of camera and lights to the spinning disk for each scheme is shown in Figs. 3 and 4.

Photographs taken with the apparatus arrangement shown in Fig. 3 (orientation A) will be referred to as A photographs. With this arrangement the plane of focus of the camera can be approximately coincident with the plane of spray supplied to the flame. The A photographs taken without flame present revealed many drops, and it was through a considerable number of these photographs that the capability of the disk sprayer was confirmed. More than 300 drop images have appeared on some of the 4 × 5-in. negatives. Inasmuch as the camera magnification

was 3, and the Jones and Lamson comparator used for examining the negatives provided an additional magnification of 10, the drop images that were measured were 30 times actual size. Careful examination of negatives showing about 300 drop images indicated that over 90 per cent of the drop diameters were within a 5-micron range. To obtain this degree of uniformity of drops, the balance of the disk and air turbine and the quality of the turbine bearings must be excellent.

COMBUSTION OF UNIFORM SPRAY

After establishing the limits of uniformity of the spray, a series of A photographs was taken through a flame supplied by the uniform spray. The plane of focus was located in the lower part of the flame. In general, these photographs, Figs. 5 and 6, showed spray of the original size toward the entering side of the field. The spray then showed a quite regular reduction of size as the fuel drops proceeded to traverse the 1 or 1½ in. through the flame. The drops could thus be observed in successive regions where the mean diameter was reduced from 90 to 100 microns down to 40 to 60 microns. Heated air supplied from below for combustion permitted burning a somewhat larger drop size and produced a more stable flame. The conditions represented in Fig. 5 are original size, 130 microns; original velocity, approximately 2 fps; minimum-size drop visible, 40 microns; minimum velocity, about 0.5 fps. When examining Figs. 5 and 6, it must be remembered that the original negative provided much clearer images of the drops than the printed photograph shown.

Concurrent work was carried out which resulted in a number of B photographs, as shown in Fig. 7. In these the number of drops was considerably reduced; however, the location of the drops in the vertical plane within the flame could be determined.

METHOD OF EVALUATION

Because of the larger number of drop images obtainable on one negative, the A photographs served as the principal source of data. The negatives were placed within a transparent plastic shield and viewed with a comparator. The shield carried a grid of lines which appeared, together with the photographic image, on the comparator screen. The spaces between lines were numbered, and these served as designation for the several zones into which the photograph was divided. This is illustrated for a typical negative in Fig. 8. Within the actual flame the distance represented by one of these zones was 0.083 in. measured along the line of travel of the drops. On the comparator screen the zone appeared to be 2½ in. in width. Drops within these zones were counted and measured, and the distance between the two images of each drop was determined. This information, together with the knowledge of the time duration between flashes, yielded the velocity of each drop.

A mean diameter and mean velocity were determined for the drops appearing in each zone. These mean characteristics were ascribed to the spray appearing in the successive zones. The time needed for the drops to proceed to a particular zone, and thus experience a reduction in mean drop size, was then obtained by summing up the times necessary to traverse the intervening zones at the observed mean velocities. Data from several negatives were combined by considering only those zones in which the size was observed to change, designating as zero the last zones in which original-size drops appeared.

RESULTS

The experimental work described made possible the determination of the average time required to burn representative drops of various liquid fuels in an actual spray. These times

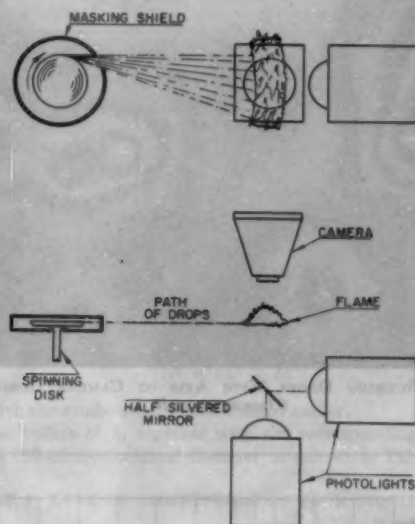


FIG. 3 ORIENTATION A OF SPINNING DISK AND PHOTOLIGHTS WITH CAMERA AXIS VERTICAL

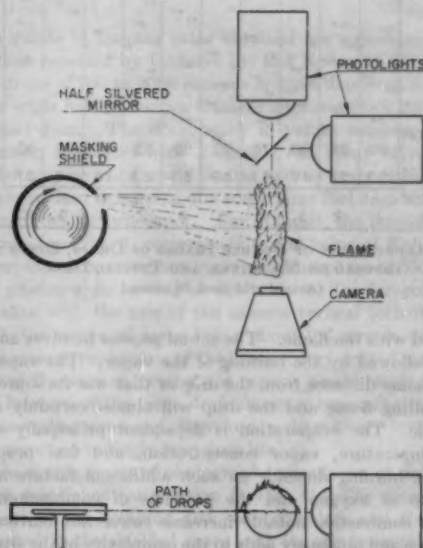


FIG. 4 ORIENTATION B OF SPINNING DISK AND PHOTOLIGHTS WITH CAMERA AXIS HORIZONTAL



FIG. 5 TYPICAL VIEW OF BURNING KEROSENE DROPS, 130 MICRONS ORIGINAL SIZE, ORIENTATION A



FIG. 6 TYPICAL VIEW OF BURNING KEROSENE DROPS, 100 MICRONS ORIGINAL SIZE

were based on observations made as the drops were reduced from 100 or 130 microns original diameter to about 50 microns.

It was noted that there is no single burning rate for all the drops in a given spray, but rather that their burning rates vary over a wide range. This, of course, is the result of the different conditions of burning for each drop. The term "burning rate" may be misleading, since it implies that the droplet is intimately

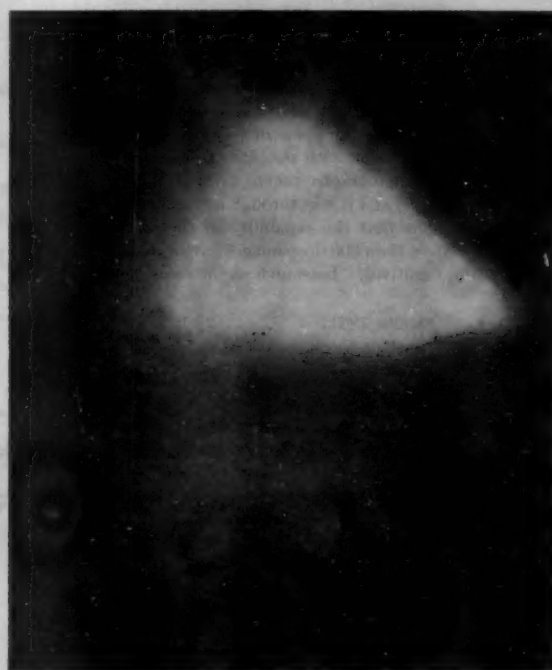


FIG. 7 BURNING DROPS WITH AXIS OF CAMERA HORIZONTAL (ORIENTATION B)

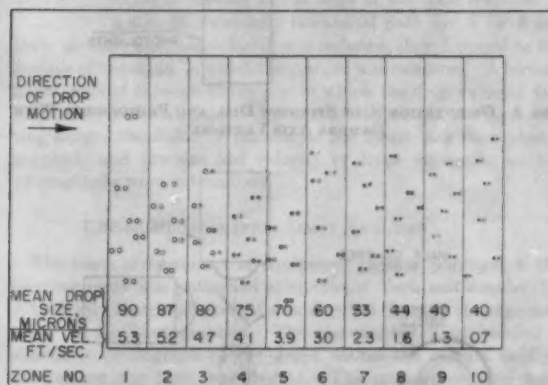


FIG. 8 ILLUSTRATION OF DOUBLE IMAGES OF DROPS, ZONES SUPERIMPOSED ON NEGATIVES, AND TYPICAL DATA (Actual grid used 20 zones.)

associated with the flame. The actual process involves an evaporation followed by the burning of the vapor. The vapor may burn at some distance from the droplet that was its source, and this resulting flame and the drop will almost certainly not be concentric. The evaporation is dependent principally on the local temperature, vapor concentration, and fuel properties, while the burning depends on such additional factors as concentration of oxygen and the products of combustion. The action of combustion notably increases convection currents and turbulence and obviously adds to the complexity of the situation.

Plots of the averaged data are shown in Fig. 9. These values for the four fuels shown represent data from many photographs

and are average rates for the entire process. The plotted curves substantiate the theory that drop diameter squared varies linearly with time.

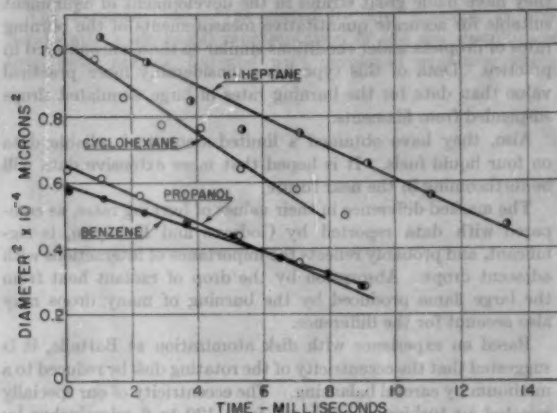


FIG. 9 BURNING RATES OF FUEL SPRAY

The slope of these lines is the constant λ for the particular fuel, as previously defined. Given a value of λ for a particular fuel, the time for evaporation and burning of a given-size drop readily can be obtained from the equation

$$D^2 = D_0^2 - \lambda t$$

for which the symbols have been defined earlier.

These values of λ , together with the corresponding life of a drop of 100 microns original diameter, are shown in Table 1.

TABLE 1 RATE OF COMBUSTION OF FOUR LIQUID FUELS

Fuel	λ (mm ² /sec)	Time to evaporate 100 μ drops, sec
Benzene	0.0033	0.03
Cyclohexane	0.0066	0.015
n-Propyl alcohol	0.0046	0.022
n-Heptane	0.0047	0.021

The values of burning rates obtained are approximately one half those reported by Godsave (3) and Kobayasi (8) for much larger drops of 700 to 2000 microns original diameter, burning in still air while held on a silica filament approximately 200 microns (0.2 mm) diam. The discrepancy in values suggests that the phenomena associated with a burning fuel spray of very small drop size may be more nearly similar to drop evaporation in a hot atmosphere than to burning of a single large fuel drop surrounded by flame from its own vapor. For example, the burning rate of n-heptane (see Fig. 9) corresponds to the value of Kobayasi (9) for n-heptane drops evaporating in an atmosphere of 530 C.

The photographs serving as the basis for the foregoing work were taken with the axis of the camera vertical (orientation A, Fig. 3), the region of focus being about 0.6 mm in depth and located close to the bottom of the flame. Any drift of small drops up out of the zone of focus of the camera would result in an apparent increase of the mean drop diameter remaining in focus in each succeeding zone and, therefore, a deceptively low value of λ with a correspondingly long drop life.

To check this, series of photographs were taken at right angles to those mentioned (orientation B, Fig. 4). The drops coming from part of the spinning disk were shielded, and the camera was located in the shielded space with its axis tangential to the group of drops that was burning. When viewed in this manner, the flame presented a roughly triangular outline and revealed

the drop images concentrated along the lower boundary of the flame, Fig. 7.

Series of these photographs were analyzed for the purpose of checking the values presented in the foregoing. These showed a much smaller number of drops per photograph, but gave approximately the same result.

Motion pictures taken at a rate up to 3000 frames per second also revealed quite clearly the motion and decrease in size of the drops throughout most of their combustion cycle. This technique is being developed further, and it is expected that it will yield significant information.

It is interesting to note that as the spray proceeded through the flame the size uniformity diminished rapidly. Fig. 10 represents the range and distribution of drop size appearing in suc-

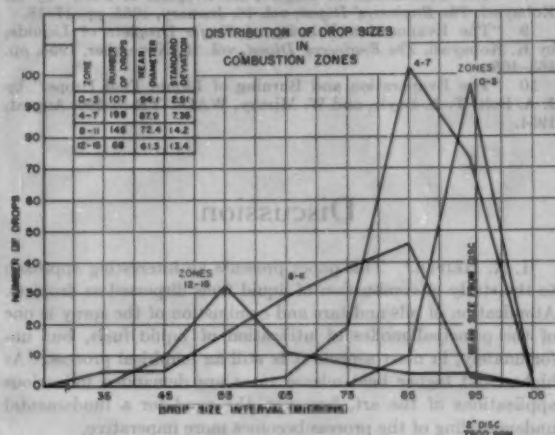


FIG. 10 DISTRIBUTION OF DROP SIZES IN COMBUSTION ZONES FOR KEROSENE DROPS

cessive zones throughout the flame. As the spray proceeds through a distance of a little over 1 in. (13 zones), the mean diameter of the drops is reduced from 94 to 61 microns. At the same time, the range of sizes in representative zones increased considerably, and the standard mean deviation showed a corresponding increase from 2.9 to 13.4 microns.

CONCLUSIONS

- 1 A successful photographic technique has been developed for observing the burning rates of small fuel drops in free flight.
- 2 The data support the idea that there is a linear relationship between the drop diameter squared and time for burning.
- 3 The action of combustion creates a high degree of turbulence.
- 4 There is a very large variety of circumstances of the burning process, causing drops to vaporize at different rates; an important factor in the tests reported was the drop position relative to the principal flame zone.
- 5 The uniformity of the drop diameter of a spray diminishes rapidly as burning proceeds.
- 6 The combustion of a fuel spray is a very complex process, requiring much more theoretical and experimental work.

ACKNOWLEDGMENT

The financial assistance of the Powerplant Laboratory, Wright Air Development Center, and permission to publish this material taken largely from a USAF report (10) are gratefully acknowledged.

BIBLIOGRAPHY

- 1 "Combustion of Liquid Fuel in a Gas Stream," by D. B. Spalding, *Fuel*, vol. 29, 1950, pp. 2-7, 25-32.
- 2 "Combustion of Fuel Particles," by D. B. Spalding, *Fuel*, vol. 30, 1951, pp. 121-130.
- 3 "The Burning of Single Drops of Fuel," by G. A. E. Godsave, National Gas Turbine Establishment, England, Report R87, 1951.
- 4 "An Improved Spinning Top Homogeneous Spray Apparatus," by R. R. May, *Journal of Applied Physics*, vol. 20, 1951, p. 932.
- 5 "Production of Sprays and Mists of Uniform Drop Size," by W. H. Walton and W. C. Prewett, *Proceedings of the Physical Society*, vol. 62, part 6, section B, 1949, pp. 341-350.
- 6 "Centrifugal Disk Atomization," by S. J. Friedman, F. A. Gluckert, and W. R. Marshall, Jr., *Chemical Engineering Progress*, vol. 48, April, 1952, pp. 181-191.
- 7 "Photographic Analysis of Sprays," by J. L. York and H. E. Stubbs, *Trans. ASME*, vol. 74, 1952, pp. 1157-1162.
- 8 "The Combustion of Single Fuel Droplets of Fuel," by K. Kobayasi, *The Engineers' Digest*, vol. 16, January, 1955, pp. 17-18.
- 9 "The Evaporation Velocity of Single Droplets of Liquids," by K. Kobayasi, *The Engineers' Digest*, vol. 15, November, 1954, pp. 463-465.
- 10 "The Evaporation and Burning of Liquid Fuel Drops," by J. A. Bolt, T. A. Boyle, and W. Mirsky, WADC TR 54-390, August, 1954.

Discussion

H. R. HEIPLE.³ This paper presents an interesting approach to the study of combustion of liquid fuels dispersed as droplets. Atomization of oils and tars and combustion of the spray is one of the principal modes of utilization of liquid fuels, but unfortunately, in most aspects it is still an empirical process. As higher and higher heat-release rates are demanded in various applications of the art, however, the need for a fundamental understanding of the process becomes more imperative.

The techniques outlined by the authors appear to be one means for obtaining this fundamental information. Use of high-speed motion pictures seems to be a particularly valuable method for studying the mechanisms involved. Use of other methods for photographing the droplets in the flame, specifically the "schlieren" arrangement, is suggested as a technique for obtaining additional data.

Confirmation of the equation proposed by Godsave relating burning rate to an evaporation constant is interesting, particularly in view of the difference in order of magnitude of the sizes of droplets studied. The authors suggest that the differences between the values of burning rates obtained in this investigation and in other studies may indicate different evaporation or combustion mechanisms. It is also possible that the evaporation constant λ is a function of vapor pressure as well as of other physical properties of the system and, as a consequence, varies with droplet size. The range of droplet sizes studied is small (less than an order of magnitude) and an extension of the study to establish the constancy of λ seems to be in order.

Although investigations with sprays of uniformly sized droplets is desirable to establish mechanisms, the sprays obtained in practice are far from uniform with respect to droplet size. A study of nonuniform sprays should be made at some time to determine whether interaction occurs in the simultaneous burning of droplets with diameters differing by an order of magnitude. Information obtained in such a study might explain certain phenomena that are encountered in the field (such as the metastable blue-flame combustion occasionally observed with pressure atomizing burners) and disclose means for utilizing desirable processes and suppressing the undesirable ones.

³ Shell Oil Company, Searsville, N. J.

J. M. PILCHER.⁶ It appears that the authors of this paper have made two major contributions to the study of the complex processes involved in the combustion of a fuel spray. First, they have made great strides in the development of equipment suitable for accurate quantitative measurements of the burning rates of droplets under conditions similar to those encountered in practice. Data of this type have considerably more practical value than data for the burning rates of large simulated drops suspended from filaments.

Also, they have obtained a limited amount of reliable data on four liquid fuels. It is hoped that more extensive data will be forthcoming in the near future.

The marked difference in their values of burning rates, as compared with data reported by Godsave and Kobayasi, is significant, and probably reflects the importance of interactions with adjacent drops. Absorption by the drop of radiant heat from the large flame produced by the burning of many drops may also account for the difference.

Based on experience with disk atomization at Battelle, it is suggested that the eccentricity of the rotating disk be reduced to a minimum by careful balancing. The eccentricity of our specially selected air turbine was reduced from 120 to 6 microns by careful balancing of the combined shaft and disk.

A. A. PUTNAM.⁷ The authors are to be congratulated on a fine piece of work. The technique they have developed will be of great value to other workers in this field. Their finding of a difference of a factor of 2 between single-droplet and multiple-droplet combustion rates indicates that far more work of this type is needed before we fully understand the combustion of liquid fuels.

The writer would like to bring to the authors' attention a recent article by Tanasawa.⁸ This report analyzes a similar set of data, but gives more attention to the statistical representation of the data. The authors' comments on the relation of this paper to their work would be of value.

AUTHORS' CLOSURE

Mr. Heiple's comments and suggestions are appreciated. We agree that an extension of the study to establish the constancy of λ over a greater range of drop sizes is desirable, and this was one of our original objectives. However, difficulties relating to formation of uniform drops as well as their combustion over a wider range of sizes with the equipment used imposed limitations. We also undertook application of schlieren techniques but experienced difficulties in obtaining satisfactory focus because of the shape and irregular movement of the flame.

We also agree with Mr. Heiple that further development of the high-speed photographic technique is desirable, and as stated in the paper, we expect to do this. When this paper was presented a 16-mm film of five minutes' duration was shown of burning fuel spray taken at 3000 frames per second, with several arrangements of back and side lighting. This film aroused considerable interest. Additional work is needed to be more certain of the exact optical relationship between the actual drop size and the size of the images seen on the film. More than 3000 frames per second and the use of 35 mm in place of 16-mm film would also be desirable.

We concur with Mr. Pilcher concerning the need for careful

⁶ Assistant Chief, Combustion and Applied Physics Division, Battelle Memorial Institute, Columbus, Ohio. Mem. ASME.

⁷ Assistant Division Chief, Battelle Memorial Institute, Columbus, Ohio. Mem. ASME.

⁸ "On the Combustion Rate of a Group of Fuel Particles Injected Through a Swirl Nozzle," by Yasuji Tanasawa in "The Technology Reports of the Tohoku University," Japan, vol. 18, 1954.

The Aerothermopressor—A Device for Improving the Performance of a Gas-Turbine Power Plant

By A. H. SHAPIRO,¹ K. R. WADLEIGH,² B. D. GAVRIL,³ AND A. A. FOWLE,⁴ CAMBRIDGE, MASS.

Theoretical and experimental investigations of a novel gas-dynamics device having no moving parts yet performing the function of a compressor, are described. This device, called the "Aerothermopressor," exploits the possibility of raising the total pressure of a high-speed gas stream through cooling of the gas. When placed at the exhaust of a gas turbine, the Aerothermopressor will reduce the exhaust pressure, thereby improving both fuel economy and power capacity per unit of air flow. Basic elements of the apparatus comprise a nozzle which accelerates hot gas into an evaporation section; a water-injection system which delivers finely atomized water into the high-speed stream; an evaporation section in which the gas is cooled and most of the water evaporated; and, finally, a diffuser in which the gas stream is decelerated and the static pressure increased.

Although the Aerothermopressor is simple in structural arrangement, the physical processes occurring within it are exceedingly complex in their details. The simultaneous effects on the gas stream of droplet drag, evaporative cooling, area variation, and wall friction lead to many regimes of operation, including the hitherto unknown passage from subsonic to supersonic speeds in a constant-area duct. Theoretical calculations of a one-dimensional nature, involving for the gas stream the equations of continuity, momentum, and energy, and for the liquid-droplet cloud the equations of motion, heat transfer, and mass transfer, have been carried out on a high-speed, electronic digital computer. The theory reproduces all the behavior patterns of experimental units and is in generally good quantitative agreement with the experimental data.

The results of experiments on a small-scale, constant-area unit of 2.13 in. diam are presented and compared with theoretical calculations. The experiments and theory both show that a net stagnation rise is possible only with gas flows greater than about 2 lb/sec; below this value the

detrimental effects of wall friction completely absorb the gains due to cooling. In the range of 25 lb/sec a net stagnation pressure rise of about 10 per cent seems assured, while 20 per cent seems possible.

Early tests on a recently completed medium-scale unit of 25 lb/sec capacity have already demonstrated a net overall rise in stagnation pressure.

NOMENCLATURE

The following nomenclature is used in the paper:

- A = cross-sectional area of duct
- c = speed of sound in gas phase
- c_p = specific heat at constant pressure of gas phase
- c_{p1} = specific heat of water in droplet
- c_{p12} = mean value of c_p between 1 and 2
- C_D = drag coefficient of droplet
- d = volume-surface mean-droplet diameter
- d_0 = value of d immediately after atomization
- d_{0f} = value of d_0 given by Nukiyama and Tanasawa formula (4)⁵
- D = duct diameter
- \mathcal{D} = diffusivity of water vapor into air
- $E = dp_0/p_0 M^2$
- f = skin-friction coefficient of pipe
- G = see Equation [8b]
- h_a = specific enthalpy of air
- h_l = specific enthalpy of liquid water in droplet
- h_v = specific enthalpy of water vapor
- h_D = film coefficient of mass transfer (Equation [42])
- h_T = film coefficient of heat transfer (Equation [45a])
- h_0 = stagnation enthalpy of gas phase
- h_{0a} = stagnation enthalpy of air
- h_{0v} = stagnation enthalpy of water vapor
- k = ratio of specific heats for gas phase
- L = length of evaporation section
- \mathcal{L} = latent heat of water vapor at temperature T_1
- M = Mach number of gas phase, V/c
- Nu_D = Nusselt number for mass transfer, $h_D D/\mathcal{D}$
- Nu_T = Nusselt number for heat transfer, $h_T D/k$
- p = static pressure of gas phase
- p_0 = stagnation pressure of gas phase
- P_0 = stagnation of pressure of mixture (Equation [28])
- Pr = Prandtl number, $c_p \mu/k$
- Q = heat added per unit mass of gas
- R = gas constant of gas phase
- R_a = gas constant of air
- R_v = gas constant of water vapor
- \bar{R} = universal gas constant
- Rey = relative Reynolds number of droplet, $(\rho d|V - V_1|)/\mu$
- Sc = Schmidt number, $\mu/\rho \mathcal{D}$
- t = time

⁵ Numbers in parentheses refer to the Bibliography at the end of the paper.

¹ Professor of Mechanical Engineering, Massachusetts Institute of Technology. Mem. ASME.

² Associate Professor of Mechanical Engineering, Massachusetts Institute of Technology. Mem. ASME.

³ Division of Industrial Co-Operation Staff Member, Department of Mechanical Engineering, Massachusetts Institute of Technology. Assoc. Mem. ASME.

⁴ Assistant Professor of Mechanical Engineering, Massachusetts Institute of Technology.

Some of the work reported here was supported financially by the Office of Naval Research and by the Bureau of Ships, Department of the Navy. Reproduction of this article in whole or in part is permitted for any purpose by the United States Government.

Contributed by the Gas Turbine Power Division and presented at the ASME Diamond Jubilee Semi-Annual Meeting, Boston, Mass., June 10-23, 1955, of THE AMERICAN SOCIETY OF MECHANICAL ENGINEERS.

NOTE: Statements and opinions advanced in papers are to be understood as individual expressions of their authors and not those of the Society. Manuscript received at ASME Headquarters, May 10, 1955. Paper No. 55-SA-65.

- T = absolute temperature of gas phase
 T_l = temperature of droplet
 T_0 = stagnation temperature of gas phase
 V = gas velocity
 V_l = droplet velocity
 w = mass rate of gas flow
 w_a = mass rate of air flow
 w_l = mass rate of water flow
 w_{l0} = mass rate of water injected
 W = molecular weight of gas phase
 W_a = molecular weight of air
 W_v = molecular weight of water vapor
 x = fraction evaporated, w/Ω_0
 y = V_l/V
 Y = see Equation [13]
 z = longitudinal distance from inlet plane
 Z = see Equation [58]
 α = θ_0/T (see Equation [26])
 β = see Table 3
 ϵ = diffuser loss coefficient (see Eq. [55])
 η_c = compressor efficiency
 η_t = turbine efficiency
 θ_0 = mixture stagnation temperature (see Equation [26])
 κ = thermal conductivity of gas phase
 μ = viscosity of gas phase
 ρ = mass density of gas phase
 ρ_l = mass density of water in droplet
 ρ_{sl} = spatial mass density of saturated water vapor at droplet surface
 ρ_{∞} = spatial mass density of water vapor far from droplet surface
 τ_w = shear stress at pipe wall
 ω = specific humidity of gas phase, lb of water per lb of air
 Ω_0 = initial water-air ratio, w_{l0}/w_a

Subscripts

- 1 = at inlet of evaporation section
 2 = at exit of evaporation section
 3 = at exit of diffuser
 a = air
 l = water
 v = water vapor

1 INTRODUCTION

1.1 Object

The purpose of this paper is to present both an introduction and a progress report on a novel aerothermodynamic device which performs the function of a compressor but which requires only an extremely simple mechanical structure having no moving parts. Basically, the Aerothermopressor is a duct within which atomized water evaporates into a high-speed stream of high-temperature gas, thereby inducing a rise in isentropic stagnation pressure of the gas stream. One of the most attractive applications of the Aerothermopressor is as an auxiliary for improving the performance of a gas-turbine plant.

The plan of the paper is (a) to develop the basic ideas and the theory of the Aerothermopressor, (b) to illustrate its application to the gas-turbine plant, (c) to discuss the factors entering into the design of an Aerothermopressor and the considerations for handling them, (d) to present the theoretical and experimental results thus far obtained, and (e) to evaluate the future prospects of the Aerothermopressor and name the crucial problems which it faces.

1.2 Basic Concept and Preliminary Theory of Aerothermopressor

A glance at the history of typical inventions shows that almost

without exception the theory of a device follows the conception of its mechanical arrangement. The Aerothermopressor seems to be one of those rare instances wherein a theoretical analysis revealed the practical possibilities; in fact, the mode of operation of the Aerothermopressor is so far removed from that intuitive sense which usually underlies invention, that one can hardly imagine its having been rationally conceived prior to the theoretical advances in gas dynamics of the past decade.

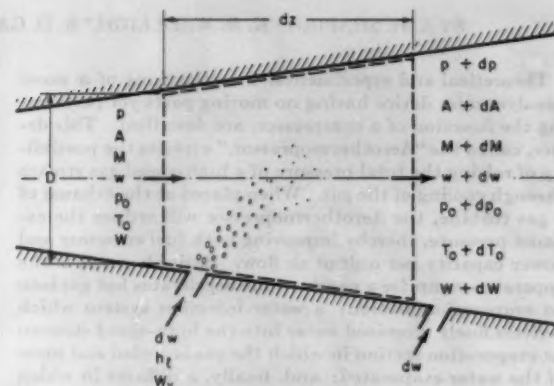


FIG. 1 ILLUSTRATES ONE-DIMENSIONAL PROCESS ON WHICH EQUATION [1] IS BASED

Preliminary Analysis. The formula which motivated the developments reported here, presented by Shapiro and Hawthorne (1) in 1947, indicates how the isentropic stagnation pressure of a gas stream, Fig. 1, is affected by the various external influences which may alter the state of the stream

$$\frac{dp_0}{p_0} = -\frac{kM^2}{2} \left[\frac{dT_0}{T_0} + 4f \frac{dz}{D} + 2(1-y) \frac{dw}{w} - \frac{1}{1 + \frac{k-1}{2} M^2} \frac{dW}{W} \right] \dots [1]$$

This equation, which is derived from the continuity, momentum, and energy equations for a perfect gas, is the result of a one-dimensional analysis of a simple model in which the external influences considered include changes in the stagnation temperature, pipe-wall friction, and the stepwise injection and evaporation of liquid with a concomitant change in molecular weight of the gas phase. The quantities appearing in this one-dimensional analysis may be thought of as representing certain average properties of the actual duct flow. The local stagnation pressure p_0 is the pressure which the stream would reach if it were isentropically decelerated to rest in steady flow; similarly, the local stagnation temperature T_0 is the absolute temperature which the stream would reach if it were adiabatically decelerated to rest in steady flow. The symbol k denotes the ratio of specific heats; M , the local Mach number; f , the pipe-wall skin-friction coefficient; D , the local hydraulic diameter of the duct; z , longitudinal distance along the duct; w , the local mass rate of flow of the gas phase; W , the local molecular weight of the gas phase; and y , the ratio of forward component of liquid-injection velocity to gas velocity. In each infinitesimal interval dz , the mass dw of liquid is assumed to be injected into the gas per unit time, and to be completely evaporated and mixed at the end of the interval.

What Equation [1] shows clearly is that the stagnation pressure

tends to be reduced by wall friction, by the aerodynamic drag associated with the injection of liquid (assuming $y = V_1/V < 1$), and by a reduction in molecular weight. Changes in cross-sectional area do not in themselves alter the local rate of change of stagnation pressure. Most significant for our purpose, however, is the observation that a reduction in stagnation temperature (i.e., cooling of the gas flow) tends to increase the stagnation pressure. Moreover, Equation [1] indicates that the effects noted are the result of a dynamic process, as evidenced by the proportionality of the stagnation-pressure change to the square of the Mach number, and that they may not be produced by thermodynamic changes in a static system. To obtain significant changes in p_0 , therefore, it is evident, even from this preliminary analysis, that operation at high subsonic speeds or supersonic speeds may be necessary.

The only possibility for increasing the stagnation pressure is through a process in which the decrease in stagnation temperature can be accomplished in such a way that the adverse effects seen in Equation [1] are outweighed. Two practical possibilities come to mind; i.e., the first involves the use of ordinary heat exchangers, and the second involves the evaporation of a volatile liquid into the air stream.

Futility of Heat Exchangers. For an ordinary heat exchanger in which the air flows through a tube having cooled walls, Equation [1] is simplified to the form

$$\frac{dp_0}{p_0} = -\frac{kM^2}{2} \left[\frac{dT_0}{T_0} + 4f \frac{dx}{D} \right] \dots \dots \dots [2]$$

Detailed analysis of this Equation [1], employing Reynolds analogy between friction and heat transfer, shows that the stagnation pressure loss produced by wall friction always exceeds the stagnation pressure rise attainable by cooling. Consequently heat exchangers cannot accomplish the desired result.

Evaporative Cooling. In order to determine whether evaporative cooling offers any prospects whatsoever, the analysis will for this purpose be simplified in a favorable way by assuming that the frictional term of Equation [1] is negligible compared with the other terms, and, conservatively, that the liquid is injected with negligible forward velocity. Then Equation [1] may be written

$$\frac{dp_0}{p_0} = -\frac{kM^2}{2} \left[\frac{dT_0}{T_0} + 2 \frac{dw}{w} - \frac{dW}{W} \right] \dots \dots \dots [3]$$

The energy equation may be written approximately, ignoring the kinetic-energy increase of the injected fluid, by equating the decrease of stagnation enthalpy of the gas stream to the enthalpy rise of the evaporated liquid

$$-w c_p dT_0 \cong (h_2 - h_1) dw \dots \dots \dots [4]$$

where c_p is the specific heat at constant pressure of the gas phase, h_2 is the enthalpy of the injected liquid after it has been evaporated and brought to thermal equilibrium with the gas, and h_1 is the enthalpy of the injected liquid.

For the change in molecular weight, we find, from the definition of molecular weight for a gas mixture, the formula

$$\frac{dW}{W} = \left(1 - \frac{W}{W_*} \right) \frac{dw}{w} \dots \dots \dots [5]$$

where W_* is the molecular weight of the evaporated liquid.

Substituting Equations [4] and [5] into Equation [3], we obtain

$$\frac{dp_0}{p_0} = -\frac{kM^2}{2} \left[2 - \frac{h_2 - h_1}{c_p T_0} - 1 + \frac{W}{W_*} \right] \frac{dw}{w} \dots \dots \dots [6]$$

From this relation it may be seen that the criterion for a rise in stagnation pressure is that

$$\frac{h_2 - h_1}{c_p T_0 \left(1 + \frac{k-1}{2} M^2 \right)} - \frac{W}{W_*} - 1 > 2 \dots \dots \dots [7]$$

Now, other things being the same, liquids with large latent heats are most likely to meet the criterion of Equation [7], inasmuch as $(h_2 - h_1)$ is of the order of magnitude of the latent heat. Hence water seems to be the desirable choice for the Aerothermopressor because, apart from obvious economic reasons, it has a larger latent heat than almost any other fluid. To gain some concept of orders of magnitude, Table 1 sets out approximate values of the left-hand side of Equation [7] for evaporation of liquid water into air.

TABLE 1 VALUES IN EQUATION [7]

T_0 (deg R)	$M = 0$	$M = 1$	$M = 2$	$M = 3$	$M = 4$
500.....	7.4	7.4	7.1	6.8	6.3
1000.....	4.4	4.3	4.0	3.7	3.6
2000.....	2.9	2.7	2.4	2.1	2.1

Comparing the figures in Table 1 with the criterion of Expression [7], it may be concluded that there is indeed a possibility for increasing the stagnation pressure by evaporating water into a high-speed stream of air, and that this possibility exists over a wide range of stagnation temperature and Mach number.

In interpreting Table 1 it is well to recall (a) that water can be evaporated into the air only so long as the latter is not saturated with water vapor, and (b) that the amount of evaporation which can be effected per unit length of duct depends on the driving temperature difference essential for heat transfer between the gas and the liquid. These considerations, when combined with the values of Table 1 and the form of Equation [1] (including the wall-friction term), demonstrate that the maximum rise in stagnation pressure will be obtained when the stagnation temperature is neither excessively high nor excessively low, and with Mach numbers which are neither excessively large nor excessively small.

1.3 Application of Aerothermopressor to Gas-Turbine Plant

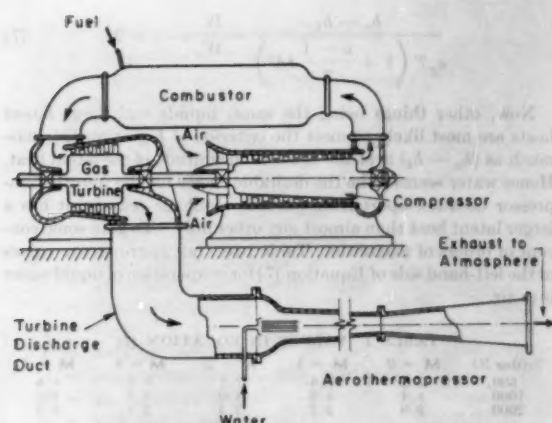
Of the various applications of the Aerothermopressor which have been considered, its use in improving both the performance and the characteristics of a gas-turbine plant seems to be one of the most promising as well as one of reasonably immediate application.

Cycle Arrangements. The most obvious place for the Aerothermopressor is at the exhaust of the power turbine in the simple gas-turbine cycle, Fig. 2(a), where the Aerothermopressor is supplied (at no expense, as it were) with a stream of hot air at sufficiently high temperature to make significant increases in stagnation pressure possible. If the Aerothermopressor produces a rise in stagnation pressure and also discharges to the atmosphere, it follows that the stagnation pressure at the turbine exit will be reduced below atmospheric, thus making the Aerothermopressor analogous to the condenser in a steam power plant.

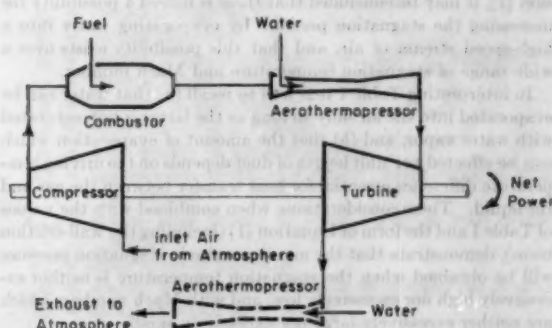
A second cycle arrangement is shown in Fig. 2(b). Here more fuel is burned per unit of air flow than in the cycle of Fig. 2(a), the compensating advantages being that the pressure at the turbine inlet is increased while at the same time the mass rate of flow through the turbine is augmented. Nothing stands in the way of installing a second Aerothermopressor at the turbine exhaust, as suggested by the dashed lines of Fig. 2(b), thus compounding the improvements in performance.

Effects on Performance. In Figs. 3(b) and 3(c) are shown the results of cycle calculations for the simple cycle of Figs. 2(a) and 3(a), illustrating the advantages mentioned previously.

It may be seen that the reduction of back pressure betters the performance and the characteristics of the gas-turbine plant in a number of ways: (a) The specific fuel consumption is reduced;



(a) At exit of turbine



(b) Between burner and turbine

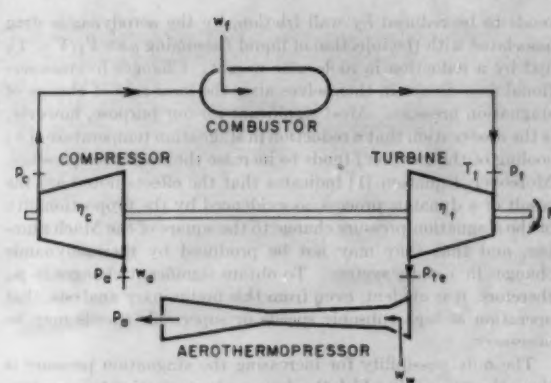
FIG. 2 APPLICATION OF AEROTHERMOPRESSOR TO SIMPLE GAS TURBINE

(b) the specific air consumption is decreased, i.e., the power capacity of a given size of machine is increased; (c) the optimum compressor ratio is reduced in inverse proportion to the square root of the pressure ratio across the Aerothermopressor; and (d) the net work ratio is increased, thus making the plant performance less sensitive to such design variables as turbine-inlet temperature and compressor and turbine efficiencies and, consequently, permitting acceptable performance with less stringent specifications on these variables than would otherwise be possible.

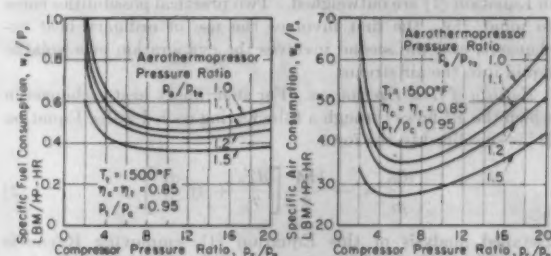
With a high turbine-inlet temperature and with high values of turbine and compressor efficiencies, Fig. 3(b), the percentage improvements in fuel economy and in power capacity are approximately equal to the percentage rise in stagnation pressure across the Aerothermopressor. For example, with a compressor pressure ratio of 4, a stagnation pressure ratio across the Aerothermopressor of 1.2 produces a reduction in specific fuel consumption and specific air consumption of 20 per cent.

With a low turbine-inlet temperature and low component efficiencies, Fig. 3(c), the improvements in performance are even more marked, and may well change the situation from one of marginal net power output to one of reasonably acceptable performance.

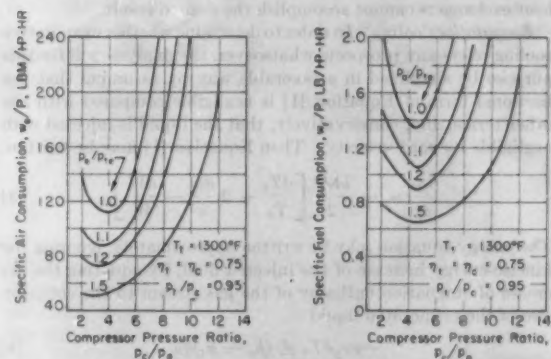
Comparison of Aerothermopressor With Regenerator. In the embodiment of Figs. 2(a) and 3(a), the Aerothermopressor must compete with the regenerator, the latter being the conventional scheme for utilizing the energy in the high-temperature exhaust



(a) Cycle arrangement



(b) Fuel economy and power capacity for favorable cycle parameters



(c) Fuel economy and power capacity for unfavorable cycle parameters

FIG. 3 EFFECT OF AEROTHERMOPRESSOR ON PERFORMANCE OF GAS-TURBINE PLANT

gas. At this writing it does not seem that the Aerothermopressor can match the improvement in fuel economy accessible to the regenerator. On the other hand, the Aerothermopressor brings about a reduction in specific air consumption (i.e., a rise in power capacity) of magnitude equal to the reduction in specific fuel consumption, whereas the regenerator, by virtue of its frictional pressure drop, produces a slight loss in power capacity. What may be even more important in many practical applications is that an effective regenerator robs the gas-turbine plant of the compactness and lightness which often is the outstanding claim of the gas turbine over rival prime movers. As will be seen, the Aerothermopressor is sufficiently small and light as not to be at a

TABLE 2 THERMODYNAMIC LIMITS OF PERFORMANCE

Inlet conditions				Outlet conditions (air saturated)			
Air		Water		Water/air ratio		p/p_0	
T_0 , deg F	p_0 , psia	T_0 , deg F	p_0 , psia		T_0 , deg F	p/p_0	p/p_0
740	10.0	60	14.7	0.128	166	32.0	3.2
740	14.7	60	14.7	0.125	180	45.0	3.1
1040	10.0	60	14.7	0.185	214	67.0	6.7
1040	12.0	60	14.7	0.183	222	78.6	6.6
1040	14.7	60	14.7	0.181	230	92.3	6.5
1340	10.0	60	14.7	0.241	267	142.5	14.3
1340	14.7	60	14.7	0.234	284	190.1	12.9
1040	14.7	60	14.7	0.181	230	92.3	6.5
1040	14.7	100	14.7	0.187	230	89.8	6.1
1040	14.7	60	14.7	0.181	230	92.3	6.5
1040	14.7	60	3000	0.182	231	93.0	6.4

disadvantage in this respect, except perhaps for automotive applications. A final compensating advantage of the Aerothermopressor is that it is structurally simple and not subject to the serious problems of fouling and corrosion which blight the status of the regenerator.

1.4 Effect of Size on Aerothermopressor Performance

So important is the scale effect in the Aerothermopressor that it seems desirable to conclude this introduction with an explanation of this phenomenon before proceeding to more detailed considerations.

For given gas properties at the beginning of the evaporation section and a given initial droplet cloud, the necessary length of the evaporation section is roughly established by the residence time required for the droplets substantially to be evaporated. If the gas and water flows are quadrupled, for example, the cross-sectional area of the duct will also be quadrupled, but such gas properties as velocity, pressure, temperature, etc., will at corresponding sections be nearly the same as before. Accordingly, the required residence time and the required length will also be unchanged, but the length-diameter ratio of the duct will be only half as large as in the first instance. Since the stagnation pressure loss associated with pipe friction is roughly proportional to the length-diameter ratio, Equation [1], the net rise in stagnation pressure will be greater for the case with the larger air flow. This influence of air flow on the relative prominence of frictional effects is furthermore magnified because the net rise in stagnation pressure of Equation [1] turns out to be a comparatively small difference between comparatively large quantities.

What all this amounts to is that below a certain scale of air flow the Aerothermopressor is doomed to failure; there is a critical size for which the Aerothermopressor will be on the verge of producing a rise in stagnation pressure; and above this critical size (which, according to our present knowledge, is in the diameter range of 2 to 3 in.) the attainable stagnation-pressure rise mounts rapidly as the scale of air flow is increased.

2 THEORY OF AEROTHERMOPRESSOR

2.1 Thermodynamic Limit of Performance

One of the first questions that comes to mind in evaluating a new device like the Aerothermopressor is, what is the maximum performance of which it is theoretically capable? This may be answered on purely thermodynamic grounds by considering a steady-flow process in which the streams of inlet air and inlet water are brought together in a hypothetical apparatus having no thermodynamic irreversibilities, and producing an exit stream of air saturated with water vapor. As in the actual Aerothermopressor, it is assumed that the reversible apparatus does not exchange heat or work with the surroundings.

The analysis, for given initial properties of air and water requires that (a) the stagnation enthalpy increase for the water equal the corresponding decrease for the air, (b) the entropy rise of

the water equal the corresponding decrease for the air, and (c) the exit stream be saturated. Pertinent results of the calculations⁶ are shown in Table 2 for a variety of inlet conditions.

The over-all stagnation-pressure ratio of the gas stream (shown in the last column) is seen to depend primarily on the inlet stagnation temperature of the air. Variations in the inlet air pressure, inlet water pressure, and inlet water temperature exert relatively small influence on the over-all stagnation-pressure ratio.

So attractive are the figures in the last column of Table 2 that a word of caution is necessary lest they be given too much weight. More detailed investigation discloses that it does not seem possible in a real Aerothermopressor even to approach the reversible mixing of air and water upon which Table 2 is predicated. The main sources of irreversibility in the Aerothermopressor are (a) wall friction, (b) aerodynamic drag on the accelerating droplets, (c) heat transfer from the air to the droplets across a finite temperature difference, and (d) mass transfer of water vapor from the droplets to the air stream across a finite difference in partial pressure. As later discussions of the detailed mechanisms of the Aerothermopressor will show, there seems to be no means by which a device having the general character of the Aerothermopressor can simultaneously reduce all these irreversibilities to small proportions.

A corollary of these remarks is that the last column of Table 2, while giving absolute thermodynamic limits, does not give a realistic view of what the actual ceiling to Aerothermopressor performance might be. Thus we are presently in the irritating status of not really knowing what is the best performance which might be reasonably expected of the Aerothermopressor, and it appears that detailed calculations like those of Section 2.7 may be necessary for its prediction.

Still a further corollary is that the effects of inlet air and water temperature and of inlet pressure shown in Table 2 are probably not representative of their effects in an actual Aerothermopressor. Inasmuch as irreversibilities play such a strong role in the Aerothermopressor, the influence of the afore-mentioned properties might be realized most forcefully through their effects on the irreversibilities, and this of course is an aspect totally absent from the analysis underlying Table 2.

2.2 One-Dimensional Analysis of Aerothermopressor

Because wall friction dictates a small length-diameter ratio for the Aerothermopressor, the continuously distributed injection and evaporation suggested by Fig. 1 does not represent a good design. In order to approximate maximum droplet residence times, it seems desirable for most of the water to be injected near the beginning of the evaporation section, as suggested in Fig. 2(a). For a real Aerothermopressor, therefore, Equations [6] and [7] do not adequately represent what occurs, even though they are surely

⁶ The analysis and calculations were made by Mr. Alve Erickson, Instructor in Mechanical Engineering, Massachusetts Institute of Technology.

indicative of the true state of affairs inasmuch as the analysis on which they are based does, in fact, take account (albeit according to a somewhat distorted model) of the principal physical phenomena.

Definition of One-Dimensional Model. In order to obtain a better insight into the details of the Aerothermopressor process, however, and also to provide a more precise theory for numerical calculations, it is necessary to develop an analysis which is in better accord with the true events. In the model we now adopt, the flow is treated as one-dimensional (i.e., no radial variations in any properties of either the gas stream or the droplet cloud,) and the droplets are assumed to be of uniform size. Since atomization occurs very quickly, it is further assumed that at the inlet plane of the evaporation section, spherical droplets of equal size are uniformly distributed over the cross section and have the velocity and temperature with which they left the injection nozzles.

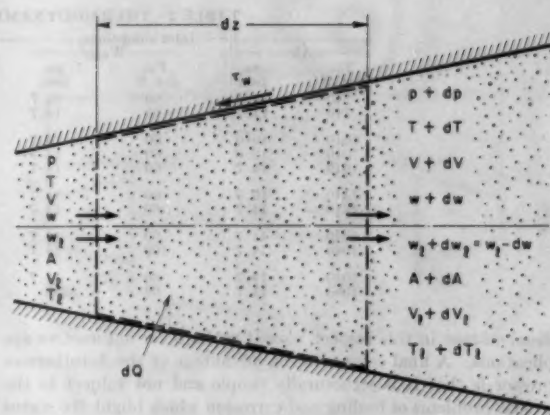
At any section of cross-sectional area A , the gas flows at the mass rate w and has a certain velocity V , pressure p , temperature T , and composition ω . Simultaneously, the droplet cloud has a certain droplet diameter d and its own mass rate of flow w_i , velocity V_i , and temperature T_i . A distance dz further downstream, the afore-mentioned properties of both the gas stream and droplet cloud have been altered in consequence of the combined effects of wall friction, change in cross-sectional area, droplet drag, heat transfer, and evaporation; the latter three phenomena result respectively from the differences between the two phases in velocity, temperature, and partial pressure of the water vapor.

Influence Coefficients. For the infinitesimal interval dz , Fig. 4(a), the analysis is based upon a simultaneous solution of the following equations written in differential form: (a) The governing equations representing conservation of mass, the momentum theorem, and the first law of thermodynamics, (b) the equation of state of a perfect-gas mixture having variable specific heat and obeying the Gibbs-Dalton law of partial pressures and enthalpies, and (c) the definitions of Mach number, gas-phase stagnation temperature and pressure, and mixture stagnation temperature and pressure. Details of the analysis are given in Appendix A, and the results are summarized by the system of influence coefficients presented in Table 3. The influence coefficients are simply the coefficients in the algebraic relations connecting the variables of the left-hand column with the variables of the top row. For example

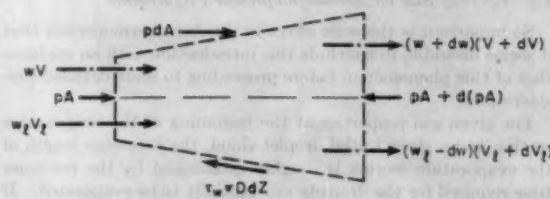
$$\frac{dM^2}{M^2} = - \frac{2 \left(1 + \frac{k-1}{2} M^2 \right) \frac{dA}{A}}{1 - M^2} + \frac{(1 + kM^2) \left(1 + \frac{k-1}{2} M^2 \right) \frac{dQ}{c_p T_0} - \frac{w_i}{w} \frac{dh_i}{c_p T_0} + \dots, \text{etc.}}{1 - M^2}$$

Behavior of Stream Properties Under Influence of Area Change—Heat Transfer, Evaporation, Wall Friction, and Droplet Acceleration. Apart from their utility for numerical calculations, the influence coefficients of Table 3 reveal clearly how the stream behaves under the action of area change, friction, and so on. A discussion of these influence coefficients at this point will help later to explain the complex and varied behavior patterns exhibited by the Aerothermopressor as well as point the way to rules for design.

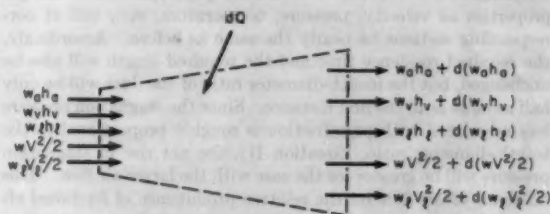
Detailed investigation of orders of magnitude shows that of the variables at the top of Table 3, those which predominate in the actual Aerothermopressor process are the terms involving area change (dA/A), evaporation (dw/w), wall friction ($4f/dz/D$), and droplet acceleration ($w_i dV_i/wV$). How these effects tend to change the stream properties is summarized in Table 4. Although the table is self-explanatory, some additional remarks will emphasize the most important results.



(a) Nomenclature and control volume



(b) Forces and momentum fluxes for control volume



(c) Fluxes of enthalpy and kinetic energy for control volume

FIG. 4 ILLUSTRATES ONE-DIMENSIONAL ANALYSIS OF APPENDIX A

Area Change. This has no direct effect on any of the local rates of change of the stagnation properties. Its greatest importance is that it gives the designer some control over the Mach number and the temperature of the stream.

Heat Transfer and Changes in Liquid Temperature. The term in dQ represents external heat exchange between the two-phase stream and the duct wall; while the term in dh_i represents the excess of all the heat received by the droplet cloud over the enthalpy rise of the evaporated liquid. Net energy extraction from the gas stream either through a negative value of dQ or through a positive value of dh_i tends to produce a gain in stagnation pressure, a reduction in stagnation temperature, and a change in Mach number away from unity (M decreases at subsonic speeds, but increases at supersonic speeds).

Evaporation. The terms involving dw/w represent several phenomena: (a) The energy exchange associated with the enthalpy increase of the evaporated liquid, (b) the energy exchange associated with changes in kinetic energy of the evaporated liquid as its velocity changes from that of the liquid to that of the gas, and (c) the momentum exchange associated with the acceleration of the evaporated liquid. For most intervals of the Aerothermo-

TABLE 3 INFLUENCE COEFFICIENTS

	$\frac{dA}{A}$	$\frac{dQ - \frac{w}{c_p} dh_2}{c_p T_0}$	$\frac{dw}{w}$	$4f \frac{dz}{D}$	$\frac{w_2}{w} \frac{dV_1}{V}$	$\frac{dW}{W}$	$\frac{dk}{k}$
$\frac{dM^2}{M^2}$	$\frac{2(1 + \frac{k-1}{2} M^2)}{1-M^2}$	$\frac{(1 + kM^2)(1 + \frac{k-1}{2} M^2)}{1-M^2}$	$-\frac{(1 + kM^2)(1 + \frac{k-1}{2} M^2)}{1-M^2} \left[\frac{h_2 - h_1 + \frac{V^2}{2}(1-y^2)}{c_p T_0} \right] + \frac{2(1 + \frac{k-1}{2} M^2)}{1-M^2} [1 + (1-y)kM^2]$	$\frac{kM^2(1 + \frac{k-1}{2} M^2)}{1-M^2}$	$\frac{(kM^2)}{1-M^2} \times \left[2(1 + \frac{k-1}{2} M^2) - \frac{k-1}{k} (1 + kM^2)y \right]$	$-\frac{1 + kM^2}{1-M^2}$	-1
$\frac{dV}{V}$	$-\frac{1}{1-M^2}$	$\frac{1 + \frac{k-1}{2} M^2}{1-M^2}$	$-\frac{1 + \frac{k-1}{2} M^2}{1-M^2} \left[\frac{h_2 - h_1 + \frac{V^2}{2}(1-y^2)}{c_p T_0} \right] + \frac{1 + (1-y)kM^2}{1-M^2}$	$\frac{kM^2}{2(1-M^2)}$	$\frac{kM^2 - (k-1)M^2 y}{1-M^2}$	$-\frac{1}{1-M^2}$	0
$\frac{dp}{p}$	$\frac{kM^2}{1-M^2}$	$\frac{kM^2(1 + \frac{k-1}{2} M^2)}{1-M^2}$	$\frac{kM^2(1 + \frac{k-1}{2} M^2)}{1-M^2} \left[\frac{h_2 - h_1 + \frac{V^2}{2}(1-y^2)}{c_p T_0} \right] - 2 + \frac{1 + (k-1)M^2 y}{1 + \frac{k-1}{2} M^2}$	$\frac{kM^2(1 + (k-1)M^2)}{2(1-M^2)}$	$-\frac{kM^2}{1-M^2} [1 + (k-1)M^2(1-y)]$	$\frac{kM^2}{1-M^2}$	0
$\frac{dT}{T}$	$\frac{(k-1)M^2}{1-M^2}$	$\frac{(1 - kM^2)(1 + \frac{k-1}{2} M^2)}{1-M^2}$	$-\frac{kM^2(1 + \frac{k-1}{2} M^2)}{1-M^2} \left[\frac{h_2 - h_1 + \frac{V^2}{2}(1-y^2)}{c_p T_0} \right] + (k-1)M^2 [1 + kM^2(1-y)]$	$-\frac{k(k-1)M^4}{2(1-M^2)}$	$-\frac{(k-1)M^2}{1-M^2} [y + kM^2(1-y)]$	$\frac{(k-1)M^2}{1-M^2}$	0
$\frac{dT_0}{T_0}$	0	1	$-\frac{h_2 - h_1 + \frac{V^2}{2}(1-y^2)}{c_p T_0}$	0	$-\frac{(k-1)M^2 y}{1 + \frac{k-1}{2} M^2}$	$\frac{\frac{k-1}{2} M^2}{1 + \frac{k-1}{2} M^2}$	$\frac{M^2/2}{1 + \frac{k-1}{2} M^2}$
$\frac{d\theta_0}{\theta_0}$	0	$\frac{1 + \frac{k-1}{2} M^2}{a}$	$-\frac{1 + \frac{k-1}{2} M^2}{a} \left[\frac{h_2 - h_1 + \frac{V^2}{2}(1-y^2)}{c_p T_0} \right] - \frac{\frac{k-1}{2} M^2 (1 + \frac{w}{w_2} y^2)}{a}$	0	0	$\frac{\frac{k-1}{2} M^2 (1 + \frac{w}{w_2} y^2)}{a}$	$\frac{M^2/2 (1 + \frac{w}{w_2} y^2)}{a}$
$\frac{dp_0}{p_0}$	0	$-\frac{k}{2} M^2$	$\frac{k}{2} M^2 \left[\frac{h_2 - h_1 + \frac{V^2}{2}(1-y^2)}{c_p T_0} - 2(1-y) \right]$	$-\frac{k}{2} M^2$	$-\frac{kM^2}{2} \left[2 - \frac{(k-1)M^2 y}{1 + \frac{k-1}{2} M^2} \right]$	$\frac{\frac{k}{2} M^2}{1 + \frac{k-1}{2} M^2}$	$\frac{(\frac{k}{2} M^2)}{(k-1)^2} \left[\frac{1 + \frac{k-1}{2} M^2}{1 + \frac{k-1}{2} M^2} \right]$
$\frac{dp_2}{p_0}$	0	$-\frac{k}{2} M^2$	$\frac{1}{2} M^2 \left(1 + \frac{k-1}{2} M^2 \right) \left(1 + \frac{w}{w_2} y^2 \right) \left[\frac{h_2 - h_1 + \frac{V^2}{2}(1-y^2)}{c_p T_0} \right] - \frac{kM^2}{2a} \left(1 + \frac{w}{w_2} y^2 \right) y^2 - kM^2(1-y)$	$-\frac{k}{2} M^2$	$-kM^2(1-y)$	$\frac{kM^2}{2a} \left(1 + \frac{w}{w_2} y^2 \right)$	$\frac{k}{(k-1)^2} \left[\frac{a-1}{a} - \ln a \right]$

Definitions:

$$y = V_1/V$$

$$a = \theta_0/T = 1 + (1 + \frac{w}{w_2} y^2) \frac{k-1}{2} M^2$$

$$T_0/T = 1 + \frac{k-1}{2} M^2$$

$$\beta = \frac{h_2 - h_1}{c_p T_0} + \frac{\frac{k-1}{2} M^2}{1 + \frac{k-1}{2} M^2} (1-y^2)$$

$$p_0/p = (T_0/T)^{\frac{k}{k-1}}$$

$$p_0/p = (\theta_0/T)^{\frac{k}{k-1}}$$

Note: The table summarizes the algebraic relations between the variables of the left-hand column and the variables of the top row, and is to be interpreted in the manner,

$$\frac{dM^2}{M^2} = \frac{2(1 + \frac{k-1}{2} M^2)}{1-M^2} \frac{dA}{A} + \frac{(1 + kM^2)(1 + \frac{k-1}{2} M^2)}{1-M^2} \frac{dQ - \frac{w}{c_p} dh_2}{c_p T_0} + \dots \text{etc.}$$

pressor process the first two effects (embodied in the term β) are by far the most important, and therefore Table 4 shows the effects due to the β -term alone. With this assumption, the criterion for a rise in p_0 is that $\beta > 2(1-y)$, which indicates that the stream is more apt to rise in stagnation pressure after the droplet cloud has been accelerated than in the period immediately following injection.

Wall Friction. Of all the independent variables in Table 3, the wall friction term $4f dz/D$ is the only one which cannot assume negative values—that is, the term dz is by definition always positive, and the friction coefficient, according to the second law of thermodynamics, may never be negative. Consequently, both stagnation pressures are reduced with any increase in length, thus pointing to the prime requirement of accomplishing the evaporation in the minimum possible distance.

Changes in Liquid Velocity. The term in dV_1 must be interpreted with the necessary condition that the liquid is accelerated only while it is traveling more slowly than the gas ($y < 1$), and is

decelerated only while traveling more rapidly ($y > 1$). It represents two physical phenomena: (a) The drag (or thrust, as the case may be) of the liquid droplets on the gas stream, and (b) the work done by the gas on the liquid when the latter is accelerated. By virtue of its manner of definition, the mixture stagnation temperature θ_0 is unaffected directly by changes in liquid velocity, whereas the gas stagnation temperature T_0 reflects the work effect, liquid acceleration reducing T_0 and deceleration increasing T_0 . Liquid drag always decreases the gas stagnation pressure p_0 ; liquid thrust (negative dV_1) usually, but not always, increases p_0 (the exception being when y is quite large compared with unity). Of particular interest is the fact that the mixture stagnation pressure P_0 is altered by changes in liquid velocity only when y is different from unity. Strangely enough, both liquid drag and liquid thrust decrease P_0 . This is so because changes in P_0 are the result of the irreversibilities in the acceleration or deceleration process, and the irreversibility reduces P_0 whether the aerodynamic force is occasioned by the droplets moving faster than the gas or vice

TABLE 4 BEHAVIOR OF STREAM PROPERTIES UNDER INFLUENCE OF AREA CHANGE, EVAPORATION, WALL FRICTION, AND DROPLET DRAG

		Area increase produces (a)	Evaporation produces (b)	Wall friction produces (c)	Liquid acceleration produces (d)
Mach Number, M	subsonic	decrease	decrease (h)	increase	increase (e)
	supersonic	increase	increase (h)	decrease	decrease (e)
Gas Velocity, V	subsonic	decrease	decrease (h)	increase	increase (e)
	supersonic	increase	increase (h)	decrease	decrease (e)
Pressure, p	subsonic	increase	increase (h)	decrease	decrease (e)
	supersonic	decrease	decrease (h)	increase	increase (e)
Temperature, T	subsonic	increase	decrease (h)	decrease	decrease (e)
	supersonic	decrease	increase (h)	increase	increase (e)
Gas Stagnation Temperature, T_0	subsonic	nil	decrease	nil	decrease (f)
	supersonic	nil	decrease	nil	decrease (f)
Mixture Stagna- tion Temperature θ_0	subsonic	nil	decrease	nil	nil (g)
	supersonic	nil	decrease	nil	nil (g)
Gas Stagnation Pressure, p_0	subsonic	nil	increase (h)	decrease	decrease (e)
Mixture Stagna- tion Pressure, P_0	subsonic	nil	increase (h)	decrease	decrease (e)
	supersonic	nil	increase (h)	decrease	decrease (e)

Notes: (a) Opposite effects for area decrease.
 (b) Opposite effects for condensation.
 (c) Opposite effects are impossible.
 (d) When $y < 1$, $dV > 0$; when $y > 1$, $dV < 0$.
 (e) Dependent upon magnitude of y for liquid deceleration.
 (f) Opposite effect for liquid deceleration.
 (g) Same effect for liquid deceleration.
 (h) Based on β only, and generally correct for β in excess of two; otherwise effects are indeterminate.

versa. When the acceleration or deceleration is brought about so slowly that the droplets follow closely the speed of the gas stream (y tending toward unity), the acceleration or deceleration tends to occur reversibly, and the loss in P_0 approaches zero.

Molecular Weight. As indicated by Equation [5], the term dW/W is controlled by the evaporation term dw/w and by the composition of the gas phase together with the molecular weights of air and water vapor. The evaporation of water (molecular weight 18) into air (molecular weight 29) reduces the molecular weight of the gas phase. With dW/W negative, Table 3 shows that the change in molecular weight induced by evaporation tends to decrease the stagnation temperatures and pressures and to drive the Mach number toward unity.

Specific Heat. Since k for water vapor is about 1.3 as compared with about 1.4 for air, evaporation yields negative values of dk/k . This in turn tends to increase the Mach number, decrease the stagnation temperatures, and increase the stagnation pressures.

Subsonic Versus Supersonic Speeds. Examination of Tables 3 and 4 shows that, almost without exception, the effects of heat transfer, wall friction, etc., on the Mach number, gas velocity, pressure, and temperature are of opposite signs at subsonic and supersonic speeds. This is a well-known phenomenon of gas dynamics, but it is of particular interest and importance here be-

cause the multiplicity of phenomena occurring simultaneously in the Aerothermopressor may, by any of several combinations, bring about either choking or continuous transition through the speed of sound (3). More will be said about this later.

Regarding the four stagnation properties, on the other hand, the effects observed at supersonic speeds are the same as those at subsonic speeds.

2.3 Description of Aerothermopressor Behavior

With the help of the concepts developed in the preceding section, it is now possible to explain the many types of flow patterns exhibited by the Aerothermopressor.

For simplicity, we begin with an Aerothermopressor having a long constant-area evaporation section and with a subsonic Mach number at the plane of water injection, Fig. 5. In the entry plane the gas flows at high velocity and temperature, and the liquid is injected at low velocity and temperature. The most important phenomena are those of droplet drag, evaporation, and wall friction. Although these three effects of course occur simultaneously, each is predominant over some portion of the process. An appreciation of this fact is essential for a qualitative understanding of the Aerothermopressor operation.

Regime I—Droplet Drag Predominant. During the droplet acceleration period which accompanies and follows atomization, wall

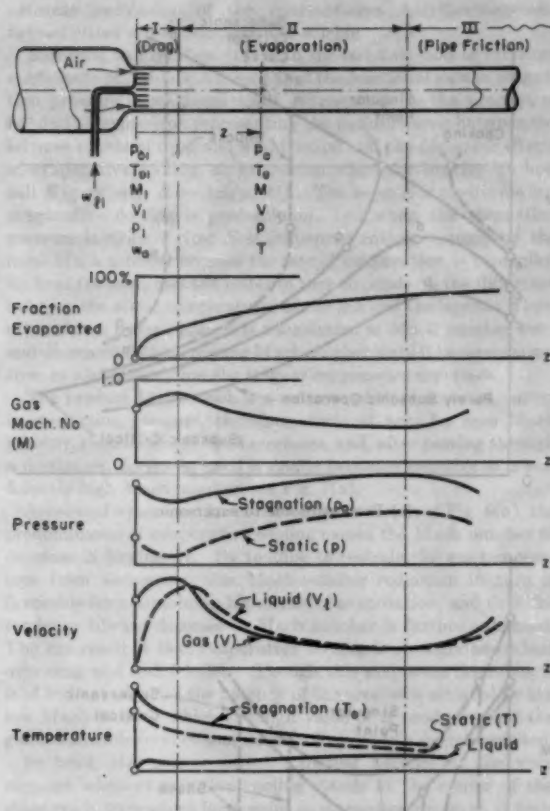


FIG. 5 SCHEMATIC REPRESENTATION OF BEHAVIOR OF SUBSONIC, CONSTANT-AREA AEROTHERMOPRESSOR

friction is comparatively negligible because the large velocity difference produces huge accelerations and excellent conditions for heat transfer to the droplet cloud. Although the effects of heat transfer and evaporation are enormous, they are, nevertheless, outweighed by the effects of droplet drag. We may therefore speak of Regime I as the zone in which drag is so predominant that it controls the qualitative behavior of the stream. According to Table 4, therefore, the Mach number increases, the static pressure decreases, the stagnation pressures decrease, the gas velocity increases, and the static and stagnation temperatures decrease.

At first the velocity and temperature differences between the gas and liquid are so great that they produce enormous rates of evaporation, droplet-velocity increase, gas-temperature decrease, and liquid-temperature increase. These high rates, however, diminish the driving velocity and temperature differentials, with the consequence that the afore-mentioned rates decrease as the process proceeds.

In the case of liquid temperature, an increase is reflected in a greatly magnified evaporation rate, which in turn tends to cool the droplet (the vapor pressure varies approximately as the fifteenth power of the absolute temperature in the applicable range). Therefore the droplets rapidly tend to approach the wet-bulb temperature of the gas stream, in which state the heat received from the gas is equal to the enthalpy rise of the evaporated material. The local wet-bulb temperature does not vary much, and so the droplets remain at nearly constant temperature (in the neighborhood of 150 F) for virtually the entire process.

Regime II—Droplet Evaporation Predominant. As the velocity difference between gas and liquid decreases (y tending toward unity), the effects of droplet drag decay much more rapidly than the effects of evaporation, the latter being substantial even for zero velocity difference. A point is reached, therefore, where the evaporative phenomena counterbalance the drag phenomena, and there ensues a zone in which evaporation predominates and controls the behavior of the stream.

Table 4 shows that in Regime II the Mach number decreases, the static and stagnation pressures increase, the gas velocity decreases, and the stagnation and static temperatures decrease.

An unexpected result is induced by the gas deceleration in Regime II. At some point in the vicinity of the transition from Regime I to Regime II, the gas velocity is diminished to the previously increased droplet velocity. While the gas further decelerates because of evaporation, the liquid tends to retain its momentum, and thus the liquid soon finds itself traveling more rapidly than the gas and consequently being decelerated. For most of Regime II the liquid velocity is slightly greater than the gas velocity, with the velocity spread being constantly narrowed. Correspondingly, the momentum and energy returned to the gas stream induces changes in gas-stream properties opposite to those experienced in Regime I. For example, the negative drag in Regime II assists in the recovery of the stagnation pressure lost in Regime I. It should be noted that these effects are proportional to the mass of liquid involved, which steadily decreases as evaporation proceeds. Hence less is returned to the stream in Regime II than taken from it in Regime I.

Regime III—Wall Friction Predominant. In the course of Regime II, the evaporation rate becomes ever smaller as the surface area of the droplets decreases and as the velocity and temperature differences promoting heat transfer are eaten away. Ultimately a stage is reached where pipe friction, which hitherto has lurked in the background as a weak contender, takes over by default.

In Regime III, where wall friction is controlling, Table 4 indicates that the Mach number and gas velocity once again rise, and the static and stagnation pressures fall.

Little need be said about Regime III except that it has no place in a well-designed Aerothermopressor. Nothing is to be gained, and much can be lost, by allowing the evaporation section to be so long that evaporative cooling is outweighed by pipe friction. The stream should be allowed to enter a decelerating diffuser some distance before the transition from Regime II to Regime III.

Transition Through Speed of Sound. As observed in Fig. 5 and Table 4, the predominance of drag in Regime I drives the Mach number toward unity, while the predominance of evaporative cooling in Regime II drives the Mach number away from unity. This permits a continuous transition through Mach number unity at the crossover point where droplet drag and evaporative cooling nullify each other (3); what happens is analogous to the passage through the speed of sound in an isentropic Laval nozzle, wherein the tendencies of the contracting section to force the Mach number toward unity and of the diverging section to force it away from unity are exactly nullified at the geometric throat.

The longitudinal Mach-number distributions are shown in Fig. 6(a) for a subsonic entry. For a low initial Mach number, M rises from a to b (drag controlling), then decreases (evaporation controlling). An increase of initial Mach number from a to c increases from b to d the Mach number at which evaporation begins to control over drag. There is a unique initial Mach number (depending of course on such parameters as initial stagnation temperature, water-air ratio, etc.), called the "critical Mach number," for which the crossover point occurs exactly at Mach number unity. This condition yields curve $e-f$, downstream of which the Mach number may either ascend into the supersonic region or descend into the subsonic region, for either event satisfies the

requirement of Table 4 that, in the region where evaporation controls, the Mach number proceed away from unity. Whether the flow follows the subsonic curve $f-g$ or the supersonic curve $f-h$ depends on the back pressure of the system, just as in the case of the Laval nozzle. Thus, contrary to widely held belief, it is possible for a flow to pass from subsonic velocity to supersonic velocity in a duct of constant area.

Mathematically, the transition through point f may be interpreted in terms of the algebraic relation for dM^2/M^2 represented by the first line of influence coefficients of Table 3. For our present purpose we may write this as

$$\frac{dM^2}{dz} = \frac{G(z)}{1 - M^2} \dots \dots \dots [8a]$$

where

$$G \equiv M^2 \left(1 + \frac{k-1}{2} M^2 \right) \left[-2 \frac{d(\log A)}{dz} + \frac{(1 + kM^2)}{c_p T_0} \left(\frac{dQ}{dz} - \frac{w_1}{w} \frac{dh_1}{dz} \right) + \dots \right] \dots \dots [8b]$$

in which, for a given case, G is a function of z alone inasmuch as all the stream properties, M , T , p , etc., and their derivatives, dM/dz , dT/dz , etc. . . . are functions of z alone.

From what has been said before, the sign of G depends on whether drag or evaporation is controlling. The sign of dM^2/M^2 , however, depends not only on the sign of G , but also upon whether the flow is subsonic or supersonic, as summarized in Table 5.

TABLE 5 SIGN OF dM^2/dz

	$M < 1$	$M = 1$	$M > 1$
$G > 0$ (drag controls).....	+	=	-
$G = 0$	0	indeterminate	0
$G < 0$ (evaporation controls)	-	=	+

For subsonic flow, Table 5 clearly shows a maximum in the curves $M(z)$ at the point where $G = 0$ (i.e., evaporation and drag evenly balanced), a rising Mach number in Regime I, and a falling Mach number in Regime II. What is of additional interest is that dM^2/dz is of the indeterminate form $0/0$ when G passes through zero as M becomes unity; it is this mathematical singularity which permits passage through Mach number unity. The slope of the Mach number curve at point f may be found by applying L'Hospital's rule to Equation [8a], from which it is found (3) that

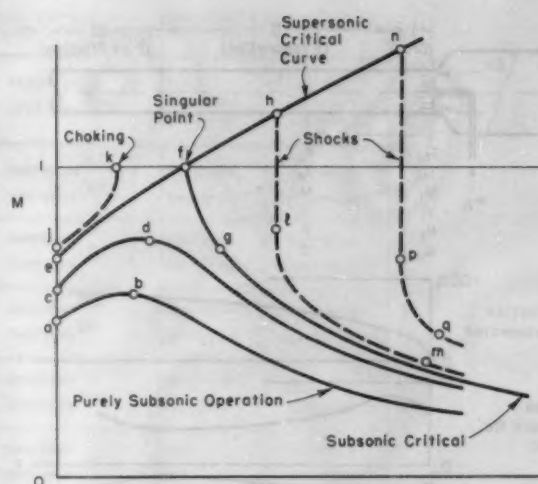
$$\left(\frac{dM}{dz} \right)_f = \pm \sqrt{- \left(\frac{dG}{dz} \right)_f} \dots \dots \dots [8c]$$

Thus, when $M = 1$ and $G = 0$, the flow may be continued only if G is decreasing, and in that case there are two solutions having slopes of equal magnitude but opposite sign, one proceeding to supersonic speed and the other to subsonic.

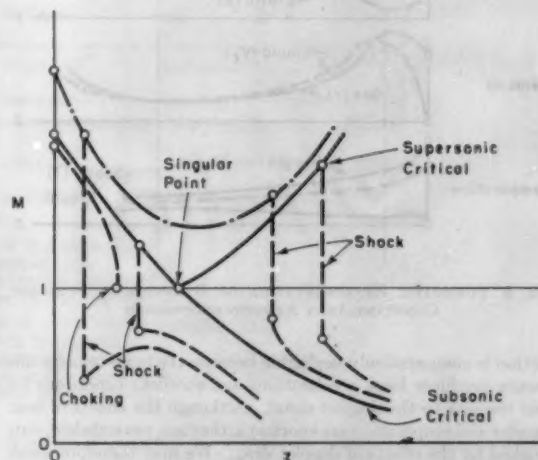
The critical curve $e-f-g$ and $e-f-h$ is a singular curve in the family of solutions of Equation [8a], and the point f is known as a saddle point singularity.

Choking. Referring again to Fig. 6(a), an increase of initial Mach number from e to j causes the Mach number to reach unity while drag is still controlling (i.e., with G still positive). Under these conditions it is impossible for the solution to be continued (3), and we say that the flow is choked. In practice, the flow represented by the curve $j-k$ is possible only if the duct area is increased at k or earlier. If the duct continues at constant area, a steady flow with initial Mach number j may not be realized, and the highest initial Mach number which is possible is that at e , hence the term critical Mach number.

Shock Waves. When the flow becomes supersonic on the branch



(a) From subsonic to supersonic



(b) From supersonic to subsonic

FIG. 6 CONTINUOUS PASSAGE THROUGH SPEED OF SOUND

$f-h$ of Fig. 6(a), still another feature in the form of normal shocks may add to the variety of possible flow patterns. These take the flow from supersonic speed to subsonic speed, after which the Mach number decreases according to Table 5. Thus, depending on the back pressure, such Mach-number distributions as $e-f-h-l-m$ or $e-f-n-p-q$ may be observed.

Supersonic Entry. All the discussion relating to Figs. 5 and 6(a) refer to a subsonic initial Mach number. For a supersonic Mach number at the plane of injection the situation is analogous; there will be the same three predominating regimes already described, but the directions of change will in many instances be different. A descriptive picture of the flow may, however, be constructed from Tables 4 and 5, and Fig. 6(b) shows some of the Mach-number distributions which may arise.

2.4 Self-Frustrating Tendency of Constant-Area Aerothermopressor

Perceptive readers may have already noticed in Fig. 6(a) a

neurotic inclination of the constant-area Aerothermopressor toward either self-emasculation or suicide.

Referring to Equation [1], or to the last two lines of influence coefficients of Table 3, it is seen that the fractional gain in stagnation pressure is mathematically represented by the product of M^2 and an expression representing the net difference between the adverse effects of drag and wall friction and the favorable effects of evaporative cooling, an expression which for brevity we now call E (precisely, $E = dp_0/p_0 M^2$). The term E is positive when evaporative cooling is predominant, i.e., when the stagnation pressure is rising. Now E is influenced rather strongly by the local Mach number because the rate of evaporation is controlled by heat transfer, and the latter in turn depends on the difference between the static temperatures of the gas and the liquid. Thus, other things being equal, E is a maximum at Mach number zero, and decreases with increasing Mach number until it becomes negative, at which condition the stagnation pressure decreases.

The product $M^2 E$, which is a measure of the fractional change in stagnation pressure, therefore starts at zero for zero Mach number, then increases as M increases, and, after passing through a maximum, decreases until it finally becomes negative at a sufficiently high Mach number, see Fig. 7(a).

Subsonic Impotence. In all the subsonic curves of Fig. 6(a), the predominance of evaporative cooling causes the Mach number to decrease in Regime II. By tending to restrain the gas temperature from decreasing, this Mach-number reduction in turn is favorable for maintaining high rates of evaporation, and thus the tendency toward decrease in Mach number is further enhanced. The net result is that evaporative cooling is strongly ascendant over drag and wall friction. Though this may seem desirable, it is of little avail, since the potency of the process is vitiated by the low Mach number which the high value of E produces, and the gains realizable from evaporative cooling are to a degree forfeited.

In brief, the process is self-defeating because at the very moment when evaporative cooling stands at the center of the stage ready to produce large gains in stagnation pressure, it finds itself with equal fervor reducing the Mach number to the point where what should be a shout is only a whisper!

Supersonic Suicide. Suppose now that the flow has achieved the supersonic curve $e-f-h-n$ of Fig. 6(a). Having arrived in Regime II, evaporative cooling pushes the flow to higher and higher Mach numbers, both effects inducing a rapid drop in the gas temperature. As a consequence, the evaporation rate is seriously reduced. Ultimately, the rate of evaporation is reduced to such a negligible amount that the stream would scarcely change state any further except for the effects of wall friction which are now predominant. To be sure, the decelerating influence of wall friction permits a slight revival in the rate of evaporation, but this only produces a battle of attrition in which evaporation occurs only in so far as the changes brought about by wall friction permit it to, and no net gain is possible.

The suicidal tendency is now revealed: At supersonic speeds, the predominance of evaporative cooling increases the Mach number, paving the way for wall friction to become predominant and thus negating the benefits of further evaporation.

Importance of Mach-Number Control. What may the designer, acting in the role of psychiatrist, do to assure a more healthy behavior of the Aerothermopressor, with the aim of extracting the maximum possible rise in stagnation pressure? He may, in fact, do a great deal, by controlling the Mach-number distribution either through the medium of changes in cross-sectional area of the evaporation section or through the introduction of additional water at downstream stations. The former possibility is discussed below.

In subsonic flow, a decrease in area is at first required to prevent the Mach number from falling too rapidly. At supersonic

speeds the area must also be diminished in order to prevent the Mach number from becoming too high. In either case, however, as the process proceeds, a point is reached at which it is desirable to have a falling Mach number in order to maintain the evaporation rate, and this ultimately dictates an increase in area at some subsonic speed. Thus the evaporation section merges continuously with the diffuser, and there is no real line of demarcation between the two.

From this discussion emerges the significance of area control as a means for achieving maximum performance. More is said on this important subject in Sections 2.5 and 2.6.

Mach-number control by additional water injection depends on the fact that immediately after injection the drag of the additional water tends to predominate, and this provides a means whereby the Mach number may be pushed toward unity.

2.5 Selecting Best Area Variation in Evaporation Section

The discussion in the preceding section may be given an approximate analytical form which provides a design method for selecting a variation in cross-sectional area which is at least in the neighborhood of that for optimum performance.

Detailed calculations of the type shown in Section 2.7 indicate that the total distance occupied by Regime I is only a few inches, and that only a small fraction of the evaporation occurs during this period. In Regime II, where most of the evaporation occurs, the droplets have a speed very near that of the gas stream (i.e., $y \approx 1$), and the liquid temperature is nearly constant at a value differing little from the local wet-bulb temperature. By assuming that $y = 1$, and that the liquid temperature is constant and equal to an average value of the wet-bulb temperature, Equation [38] expressing the fractional rise in stagnation pressure per unit of humidity increase, $(1/P_0)(dP_0/d\omega)$ may be derived, as shown in Appendix B.

Design Procedure for Regime II. As explained in Appendix B, the choice of the parameters T_{01} , Ω_0 , d_0 , Nu , and f/D permits the construction of the curves such as shown in Fig. 7(a). For each value of ω , the curves show clearly the insignificant gains achievable at low Mach numbers, and the rapidly deteriorating performance at excessively high Mach numbers.

To appreciate Fig. 7(a), we first ask, what is the criterion for best performance? The answer is simply that the net stagnation pressure rise of the entire process be a maximum. Now this does not necessarily require that the most stagnation pressure rise be realized for each increment evaporated, for a sacrifice at an early stage may augment the potentialities at a later stage. Consequently, the maximization of the over-all stagnation-pressure rise is no simple matter, transcending by far in difficulty the conventional variational problem of the calculus. Dealing with this in its full complexity necessarily hinges on the numerical integrations discussed in Section 2.7. With the present simplified design procedure, there is no better choice than to make the plausible assumption that a design which maximizes the stagnation pressure rise for each interval of evaporation will, in fact, also approximate the design which gives maximum over-all rise in stagnation pressure.

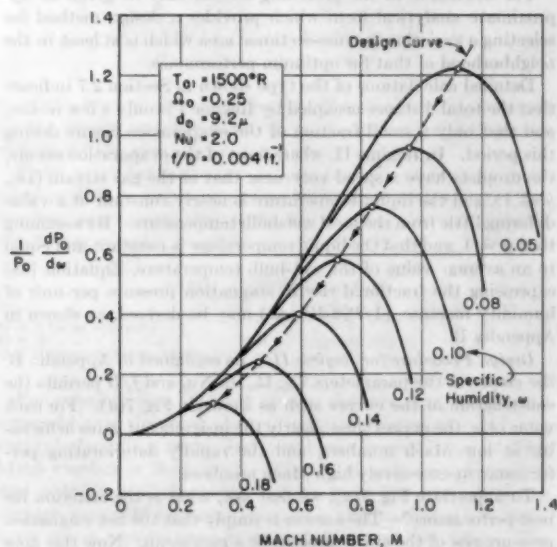
The foregoing statement is equivalent to saying that the dashed line, labelled "design curve" in Fig. 7(a), passing through the maximum points of the curves of constant ω , yields at least a first approximation to the best Aerothermopressor design in Regime II. Transferring each point of the design curve to Fig. 7(b), we obtain the solid line representing the optimum variation of M with ω . The solid curve of Fig. 7(c) is determined by plotting the value of $dP_0/P_0 d\omega$ at each point of the design curve against the corresponding value of ω ; this curve represents the maximum fractional rise in stagnation pressure per unit of evaporation. By integrating the area under the curve of Fig. 7(c), the change in

stagnation pressure associated with a given amount of evaporation may then be computed. From the equation of continuity it is then possible to calculate the cross-sectional area for each value of ω . Then, using Equation [37], the longitudinal co-ordinate of each point may be determined by numerical integration, thus establishing the shape of this portion of the Aerothermopressor.

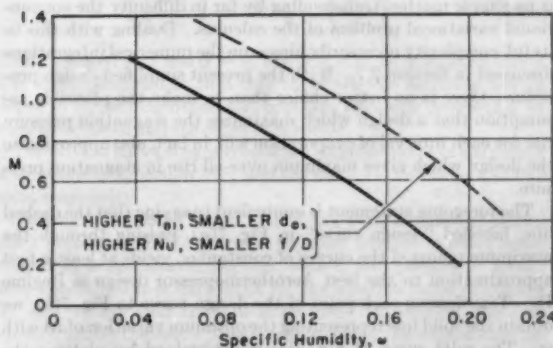
The method described is found to lead to the result that the Mach number must be decreased as the evaporation proceeds. This generally dictates a reduction in cross-sectional area in the early part of Regime II, followed by an increase in the later part.

Effects of Initial Parameters on Best Design. Figs. 7(b) and 7(c) illustrate with dashed lines the comparative positions of the design curves which result from Fig. 7(a) for different values of the initial parameters more favorable to effective operation. Such more effective operation comes from higher values of T_{01} and Nu , and from lower values of d_0 and f/D .

Under these circumstances the curves of constant ω in Fig. 7(a)



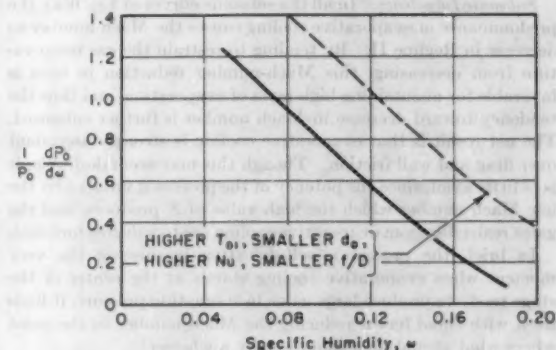
(a) Typical curves of fractional rate of change of mixture stagnation pressure with specific humidity as a function of Mach number, with local specific humidity as a parameter, and for constant values of T_{01} , Ω_0 , d_0 , Nu , f/D



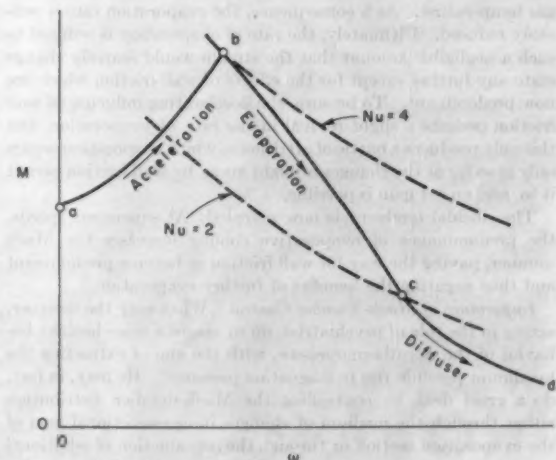
(b) Optimum curve of Mach number versus humidity, corresponding to design curve of Fig. 7(a). Dashed curve, shows comparative position of optimum curve for more favorable values of parameters

are displaced upward and to the right. This in turn moves the corresponding design curves of Figs. 7(b) and 7(c) upward. Thus, with more favorable initial parameters, the level of operating Mach numbers is higher, and greater increases in stagnation pressure per unit of evaporation may be achieved.

Evaluation of Simplified Design Procedure. The principal defect of the method outlined in the foregoing is that it is incapable of revealing the correct Nusselt number to be used at each stage. To determine Nu requires an evaluation of the velocity difference between the phases, and this can be found only from a consideration of the entire past history of the process. The $dP_0/P_0 d\omega$ analysis gives recognition only to the present state of affairs, and does not look to the past or to the future. During the course of the process, the value of Nu changes continuously, and a series of charts like that of Fig. 7(a), each with a different value of Nu , would be really necessary for establishing the best design (assuming that Nu were known at each point). This limitation is more important than it might at first seem to be, because the comparatively small difference between the total beneficial effects of evaporative cooling and the total detrimental actions of drag makes a change in Nu from, say, 2 to 4, most significant in reorientating the optimum variation of M with ω .



(c) Optimum curve of $dP_0/P_0 d\omega$ versus humidity, corresponding to design curve of Fig. 7(a). Dashed curve shows comparative position of optimum curve for more favorable values of parameters



(d) Illustrates optimal Mach-number variation of entire Aerothermopressor

FIG. 7 APPROXIMATE OPTIMIZATION METHOD, BASED ON ANALYSIS OF APPENDIX B

What all this means is that the $dP_0/P_0 d\omega$ method cannot give the Aerothermopressor the advantages which might accrue from control of the Nusselt number. For example, by choosing what might appear to be a comparatively unfavorable Mach-number distribution at one stage, the ensuing acceleration or deceleration of the stream might be used to establish large velocity differences and correspondingly large Nusselt numbers, with the consequence that increased gains in stagnation pressure realized at a later stage might more than compensate for the mediocre performance accepted at the earlier stage.

Thus the $dP_0/P_0 d\omega$ analysis advises the Aerothermopressor to "live for the present only, with no thought for the future," and consequently cannot by itself give the final answer to the question of how the Aerothermopressor should be designed. On the other hand, it certainly represents a starting point for a more adequate approach such as that outlined in Section 2.7, and it is hoped that ultimately a study of specific results generated by the rather involved procedure of Section 2.7 will in turn suggest some simple rules of thumb with which the results of the comparatively simple $dP_0/P_0 d\omega$ method may be modified to be more closely in accord with the best design.

2.6 Some Design Considerations

Disarmingly simple as it is in structural arrangement, the Aerothermopressor is host to a bewildering variety of physical events. These phenomena, constituting fundamentally mass conservation, momentum effects, and energy effects for both the droplet cloud and the gas stream, are strongly interrelated. Consequently the designer, in attempting to give due weight to each factor influencing performance, is faced in the Aerothermopressor with a large number of conflicting tendencies. The best design is, as usual, a compromise among these. What is baffling is that at present there seems to be no simple way for evaluating the relative importance of each effect and thus of arriving at clear-cut design rules. No doubt a combination of sufficient experimental data with worked-out numerical cases such as those of Section 2.7 will some day help in this regard.

Having made these rather discouraging remarks, we may immediately add that much is indeed known in a qualitative way about the influences of the most important design variables. This knowledge is important not only because it reveals pitfalls, but also because it usually suggests how experimental information can be used in improving a given design. Therefore we shall discuss the major elements of the Aerothermopressor, state the decisions facing the designer in each, and present the major considerations by which the design choices may be made.

Design Specifications. In a specific situation, we are confronted by design values of air flow (w_a), initial stagnation temperature (T_{a0}), and initial stagnation pressure (p_{a0}), although the magnitudes of the two latter quantities are in some degree dependent on the performance of the Aerothermopressor itself. In addition, there may be a range of these three parameters specified in the area of off-design operation.

Control of Aerothermopressor. Once a particular unit has been built, at least three procedures are possible for adjusting to off-design conditions or for compensating for imperfections in design:

(a) By far the easiest scheme is to control the rate of water injection at the inlet, thereby governing the water-air ratio. Presumably it would be routine procedure for the operator to adjust the water flow to the point of maximum stagnation-pressure rise. At best, however, this method can take care of off-design conditions or lapses in design only approximately.

(b) "Trimming" of the lengthwise Mach-number variation may be accomplished by means of variable-area devices such as a central plug or a series of concentric sleeves located along the axis of the Aerothermopressor. This would detract considerably from the

mechanical simplicity which the Aerothermopressor otherwise possesses.

(c) Trimming of the lengthwise Mach-number variation may be achieved also by the injection of auxiliary water at several stations along the evaporation section. Even though the effectiveness of the auxiliary water may be slightly impaired through a loss in residence time, the effectiveness of the main injected water might be augmented sufficiently to effect a net gain.

Aerothermopressor Components. For purposes of isolating and dealing separately with the principal phenomena, it is convenient to think of the Aerothermopressor as comprising the following elements: (a) The air nozzle which accelerates the hot air from the low-speed upstream section into the high-speed section; (b) the water-injection system; (c) the "acceleration" section, in which occur atomization and the major portion of the droplet acceleration; (d) the evaporation section, in which evaporation is generally controlling and where most of the evaporation occurs; and (e) the diffuser, which ultimately decelerates the stream to low speeds and terminates the process.

Each of these components will now be considered separately.

Air Nozzle. Two questions arise here: (a) How high should be the Mach number M_1 at the nozzle exit (which is also the plane of water injection), and (b) what shape should the nozzle have?

For the specified values of w , p_{a0} , and T_{a0} , the diameter at the nozzle exit determines the Mach number M_1 . If M_1 is excessively large, the stagnation-pressure loss associated with the droplet acceleration may be prohibitive; however, if it is too small, the droplet diameter will be comparatively large, and the required length of the evaporation section will be excessive, leading to intolerable frictional losses. The best value of M_1 in each case must, therefore, be determined either by experiment or by calculations of the type illustrated in Section 2.7.

The influence of the Mach-number level on the length required for evaporation may be seen from the following approximate considerations: For air atomization, the droplet diameter d_d varies inversely with the air velocity V (reference 4). Since the distance traveled by each droplet during its acceleration period is a very small fraction of the total distance L required for evaporation, L may be approximated by supposing that the droplet moves with the same velocity as the air. From considerations of heat transfer

$$-\frac{\rho_l(h_g - h_l)\pi d^2}{2} \frac{dd}{dt} = h_T \pi d^2 (T - T_l)$$

For very low Reynolds numbers, $h_T d/k = 2$. Substituting this value of h_T , and integrating the equation, we find that the time for complete evaporation follows the law $t \sim d^2$. In addition, the length L is proportional to the product of V and t . Therefore

$$L \sim Vt \sim (1/d)(d^2) \sim d \sim 1/V$$

and the required length is seen to be inversely proportional to the velocity. For a given length, a greater fraction of total evaporation occurs at high air speeds than at low, even though high air speed means a comparatively small residence time.

Regarding the shape of the air nozzle, the main considerations here are that (a) it should be longitudinally as short as possible so that any massive part of the water-injection system may easily be placed in a low-velocity region, and (b) it should avoid adverse pressure gradients on the walls large enough to induce boundary layer separation.

Water-Injection System. The requirements of the water-injection system are that (a) the droplet cloud produced should have the smallest possible volume-surface mean drop size, (b) the drop-size spectrum be such that the mass fraction of the drops lying above the volume-surface mean size is not too large, (c) the droplet cloud should be uniformly distributed over the cross section,

and (d) the parasitic stagnation-pressure loss associated with the aerodynamic drag of the injection system should be a minimum.

Without precluding the possibility of other arrangements which may prove more favorable, most of the effort thus far has been given to a "porcupine" type of injector, comprising small tubes in parallel, with the water injected at low speed into the high-speed air approximately at the exit of the air nozzle. Little more can be said now about the injection system except that the lack of precise information concerning the drop size produced is perhaps the weakest link connecting theory and experiment.

The best water-air ratio results from a compromise between two opposing effects; that is, as the water flow is increased, the acceleration drag is increased (unfavorable), but the amount of evaporation occurring in a given distance is also increased (favorable). Fortunately, this is a matter which in each case can be very easily settled on an operating Aerothermopressor.

Acceleration Section. Within the very few inches of length constituting the acceleration section, the droplet cloud is formed and accelerated approximately to the gas speed, and of the order of $1/4$ the total evaporation occurs. Because of the exceedingly short length (5) and the extra complexity of the processes in this region, it may prove unfeasible to attempt any Mach-number control by means of area variations in this zone.

A considerable loss of stagnation pressure occurs in the acceleration section. The loss of stagnation pressure associated only with the acceleration of the droplet masses (disregarding heat transfer and evaporation) is illustrated by the following values (5) for a water-air ratio of 0.2 (the loss is approximately linear with water-air ratio):

M_1	p_{01}/p_{01}	P_{01}/P_{01}
0.3	0.978	0.988
0.4	0.957	0.977
0.5	0.927	0.961
0.615 (choked)	0.846	0.933

These losses are of the same order as the net gain in the Aerothermopressor, thus emphasizing strongly the necessity of careful design at every point in order to achieve acceptable performance.

For the limiting case of very low Mach number, a formula for the irrecoverable loss of stagnation pressure due to droplet acceleration may be derived. From momentum considerations, the pressure change ($p_B - p_A$) due to the acceleration of the drops from zero speed to the gas speed V without area change is given by

$$p_A - p_B = \frac{w_i V}{A} = \frac{w_i}{w_a} \rho_a V^2 \dots \dots \dots [9]$$

and is equal to the loss in gas stagnation pressure during the acceleration. If the mixture is then reversibly decelerated to zero speed, the pressure p_C attained is calculated by considering the two-phase mixture to be homogeneous with the appropriate density

$$p_C = p_B + \left(1 + \frac{w_i}{w_a}\right) \frac{\rho_a V^2}{2} \dots \dots \dots [10]$$

Accordingly, the net loss in stagnation pressure is given by

$$\left(p_A + \frac{1}{2} \rho_a V^2\right) - p_C = \frac{w_i}{w_a} \frac{\rho_a V^2}{2} = \frac{w_i}{w_a} \frac{k p M^2}{2} \dots [11]$$

That is, the minimum conceivable net loss in stagnation pressure is one dynamic head multiplied by the water-air ratio, and is exactly one half the loss in gas stagnation pressure during the acceleration.

The best water-injection velocity is governed by the opposing considerations that (a) a low water injection velocity results in small drops but large acceleration loss, whereas (b) a high water injection velocity gives large drops but small acceleration loss.

The required number of injection points depends on the angle of spread of the droplet spray. From the data obtained thus far, it appears that the best number probably lies within the range of $1/2$ to 2 injection points per square inch of cross section.

Evaporation Section. The primary considerations for the design of the evaporation section have been discussed in Sections 2.4 and 2.5.

Diffuser. No precise line of demarcation in terms of the Aerothermopressor process can be made between evaporation section and diffuser, inasmuch as significant evaporation and droplet deceleration effects occur within the diffuser. A substantial portion of the evaporation may occur in that portion of the evaporation section which has a geometrically diverging cross section. Moreover, the gas decelerates and the pressure rises in virtually the entire length of the evaporation section.

Granting these facts, a stage is ultimately reached in the Aerothermopressor process where the main objective is to decelerate the stream and recover pressure efficiently. This part of the apparatus is arbitrarily called the diffuser. The best conventional diffuser is a cone of approximately 6 deg included angle. A consideration of the concurrent phenomena of evaporation and droplet deceleration occurring in the Aerothermopressor diffuser, however, can be interpreted to suggest a somewhat longer diffuser in order better to exploit these additional phenomena. The diffuser of smaller angle makes the revived evaporation in the diffuser more effective because it causes the evaporation to occur at relatively higher Mach numbers; and it adds to the efficiency of droplet deceleration by causing the droplets to remain more nearly at the gas speed (6).

Optimum Mach-Number Distribution for Entire Aerothermopressor. Guided by a combination of the qualitative considerations presented in this Section, together with approximate design method for Regime II given in Section 2.5 and the results obtained by the more complete theoretical method discussed later in the next Section, the nature of the optimum Mach-number distribution for the entire Aerothermopressor may be rationally anticipated. The discussion is illustrated schematically in Fig. 7(d).

From a consideration of the importance of maintaining a large temperature difference for heat transfer, we may confidently expect that the position of maximum Mach number (point b) should occur near the beginning of the process where the humidity is low and the stagnation temperature high.

Now, referring to the approximate method for Regime II, large values of the relative Reynolds number can be established only in the part of the process where the Mach number is high and where large accelerations and decelerations are possible. Thus in the neighborhood immediately downstream of point b, the curve of M versus ω will be that of Fig. 7(b) for a Nusselt number of about 4. Near the end of the evaporation region the Mach number is necessarily smaller, the speed of sound is lower, and large accelerations or decelerations are no longer possible. Together with the fact that the droplet diameter is also smaller, all this implies that the relative Reynolds number is quite small. Therefore, near the end of the evaporation section (point c), the curve of M versus ω should be like that of Fig. 7(b) for a Nusselt number of about 2.

Assuming that point c represents the location where the rate of stagnation pressure rise has virtually vanished, the curve c-d will represent the diffuser. The latter, as explained previously, will most probably be a cone of half-angle somewhat less than 3 deg.

The best inlet Mach number (point a) cannot be foreseen easily, as it depends on the best compromise between small droplet size and small acceleration drag. In some cases the inlet Mach number might be the highest of the entire process, and then M would decrease continuously.

The value of ω at point b is determined by the advantage of making the Mach number rise from a to b occur as quickly as possible, with the restraint, however, that too rapid an acceleration will maintain such large differences in velocity that large losses in P_0 will be produced. It seems extremely important to choose the location and Mach number of point b wisely, for the nature of the entire process calls for the maximum exploitation of the benefits of cooling in the very region where evaporation is most predominant, where the temperature differential is still large, and where there exists the possibility of operating locally at large Mach numbers. Immediately downstream of point b is where the maximum gains are to be won, and if they are not won there, they are forever forfeited.

In summary then, the best Mach-number distribution for subsonic entry appears to call for a soaring rise of Mach number in the acceleration zone, followed by a gradual decrease in Mach number in Regime II (involving a gradual transition from the curve $Nu \cong 4$ to that for $Nu \cong 2$), and concluded by a fairly rapid decrease of Mach number in the diffuser.

2.7 Numerical Calculations of Aerothermopressor Process

Because of its complexity, its many diverse design considerations, and the fact that only by great care can a poor design be avoided, a successful future for the Aerothermopressor may depend as much on the development of a rational theory as on experimental development. The latter goes slowly, and may be of greatest significance in helping to form a theoretical design method which adequately represents Aerothermopressor performance. Then we may look to the theory for such matters as determining the optimum cross-sectional area variation, extrapolating performance to unknown ranges of supply pressures and temperatures, and predicting off-design performance.

Theoretical Model for Analysis. The analysis considered is purely one-dimensional: in any cross-sectional plane (a) the gas velocity, temperature, and pressure are uniform, and (b) the droplet velocity, temperature, size, and spatial density are uniform. In addition, it is assumed that the droplets are atomized immediately upon injection, and that no subsequent atomization or agglomeration occurs.

Variables of the Analysis. At the entry plane of the Aerothermopressor (section 1), the initial conditions may be characterized by seven quantities, of which the first six are intensive and the last extensive:

- (i) p_{01} , inlet-gas stagnation pressure
- (ii) T_{01} , inlet-gas stagnation temperature
- (iii) M_1 , inlet Mach number
- (iv) Ω_0 , inlet water-air ratio
- (v) T_{l1} , inlet-liquid temperature
- (vi) V_{l1} , inlet-liquid velocity
- (vii) A_1 , inlet cross-sectional area

Note that p_{01} , T_{01} , M_1 , and A_1 together determine the air-flow rate w_a , so that w_a could be used in place of A_1 . Furthermore, for a given style of water injector, we may anticipate that the listed variables will determine the initial droplet diameter d_0 .

The duct itself may have a shape which might be characterized by relating the area ratio to the distance z from the inlet plane. For example, we might write

$$\frac{A}{A_1} = 1 + \alpha_1 \frac{z}{\sqrt{A_1}} + \alpha_2 \frac{z^2}{A_1} + \dots \quad [12]$$

where α_1 , α_2 , etc., are dimensionless numbers defining the duct shape.

At any section z downstream of the inlet plane, having a local cross-sectional area A , the state of the stream may be characterized by six intensive quantities:

- (i) p , gas pressure
- (ii) T , gas temperature
- (iii) M , Mach number
- (iv) ω , specific humidity
- (v) T_l , liquid temperature
- (vi) V_l , liquid velocity

Governing Equations. Thus for specified values of the seven initial variables and a specified duct shape, six physically independent equations are necessary for establishing the six required properties at each station z . These six equations are fundamentally (a) the equations of continuity, momentum, and energy for the gas stream, and (b) the equations of mass transfer, heat transfer, and drag for the droplet cloud.

The three governing equations for the gas stream are derived in Appendix A, and their simultaneous solution has already been summarized by means of the influence coefficient equations of Table 3. In these equations the terms dw/w and dW/W are dependent on mass transfer (evaporation) from the droplets; the term dk/k is dependent upon changes in temperature and humidity of the gas stream; the term in $d\dot{h}$ is dependent on the mass transfer and heat transfer for the droplets; and the term in dV_l is dependent on the drag forces between the droplet and gas. Therefore a complete analytical formulation of the problem requires that the equations of Table 3 be augmented by the three equations of mass transfer, heat transfer, and drag for the droplets. The derivation of the latter equations is presented in Appendix C.

Numerical Solution of Equations. The system of ordinary, simultaneous, nonlinear, differential equations just referred to seems to be well beyond the possibility of analytical integration, and numerical solution is therefore necessary. After a brief experience with working out solutions by hand computation, it became evident that real progress could be made only by a much more rapid calculation procedure. The problem was accordingly programmed for the Whirlwind I computer, a high-speed, electronic, digital machine at the Massachusetts Institute of Technology.

Although extended discussion of the means of solution is inappropriate here, it may be mentioned in passing that some of the difficulties encountered during the development of this numerical treatment involved (a) adequately large high-speed memory, (b) tolerably small truncation error without excessively large computational time, (c) tendency of the numerical solution toward serious instability, and (d) establishment of the singular solution passing continuously through Mach number unity. More details are given by Gavril (8).

At the present time the fourth-order Runge-Kutta method of numerical integration is used, but the general scheme of calculation may be more easily illustrated by considering the first-order (Euler) method of numerical integration. In the latter the basic idea is to calculate the increment at a point using only the first term of the Taylor series expansion about the point, for example

$$\Delta M^2 \cong (dM/dx)\Delta x$$

Suppose that the initial values of the problem are given, and that the fraction evaporated, $x \equiv \omega/\Omega_0$, which is taken as running variable, is divided into many small intervals Δx . The finite-difference equations are then solved for each interval, and the properties computed for the end of the interval are then available for use in the next interval.

To illustrate, imagine that the calculations have been carried to a certain value of z , where the values of ω , d , V_l , T_l , p , T , V , M , z , and A are all known. Then, for an increment in humidity Δx ; the values of Δd and $\Delta \omega$ are calculated from Equation [41]; ΔT_l is computed from Equation [45b] with Equations [43],

[43a], [44], [46], and [47]; Δt is found from Equation [45a] with Equations [46] and [47]; ΔV_i is obtained from Equation [48] with Equations [49]; and, finally, the distance Δz , in which the foregoing changes in droplet properties occur, is determined by Equation [50]. Assuming that the duct shape is known ΔA may be found for the corresponding Δz . All the increments in the top row of Table 3 are now known for the step under consideration, and the corresponding changes in gas properties, ΔM^2 , Δp , ΔV , etc., may be reckoned from the equations of Table 3. Having carried out these calculations, the droplet and gas properties are completely determined at the end of the humidity interval, and all is in readiness for repeating the procedure within the next humidity interval.

It should be noted here that the solution is propagated by the fact that at any section z , where all the stream properties are known, it is possible to calculate the first derivative of each property by means of the equations of Appendix C and Table 3. The increment in each property can therefore be determined by any of the conventional numerical procedures. One of the crucial aspects of such a calculation is that each successive value depends on previous values.

Present Status of Numerical Calculations. At the present writing a considerable number of integrations have been carried out for the constant-area Aerothermopressor and a smaller number for the variable-area case. Currently, work is proceeding on a promising scheme for systematically optimizing the parameters and the area variation controlling performance, but this has not yet progressed to the point where results may be reported. Many of the results thus far obtained have been presented by Gavril (8). A few are presented here for illustration, and in Section 2 we shall present additional computed results for comparison with the experimental results.

Constant-Area, Subsonic Aerothermopressor Process. Fig. 8 shows the results of numerical calculations for the case of a constant-area unit with an initial Mach number of 0.7, a water-air ratio of 0.20, initial stagnation conditions of 1500 deg R and 14.7 psia, a friction parameter f/D of 0.004 ft⁻¹ (corresponding to $f = 0.004$ with a duct of 12 in. diam), and an initial droplet diameter of 13.8 microns [as computed from the Nukiyama and Tanasawa formula (4)]. All the varied phenomena previously described as occurring in Regimes I, II, and III are seen here quantitatively. Noteworthy points include: (a) Regime I is of the order of only 0.1 ft in length, although the actual delay in atomization will increase this somewhat; (b) the liquid overtakes the gas in about 0.4 ft; (c) about 10 per cent of the water is evaporated in Regime I and about 30 per cent at the end of the droplet acceleration period; (d) the 7 per cent loss in stagnation pressure incurred in Regime I is not recovered until about 50 per cent of the water injected is evaporated, thus placing the burden of winning a net gain on the remaining part of the process; (e) the net rise in stagnation pressure is about 6 per cent; (f) the required length of evaporation section is of the order of 4 ft, and the droplet residence time is of the order of 0.01 sec.

Constant-Area, Supersonic Aerothermopressor Process. Fig. 9 is for the same case as Fig. 8 except that the initial Mach number is 1.5 and the corresponding initial droplet diameter is 7.34 microns (based on the risky extrapolation of the Nukiyama and Tanasawa drop-size formula to supersonic speeds). Here again the distinct phenomena of Regime I, II, and III are clearly evident, although they are generally of opposite character to the subsonic case. The lengths of Regime I and of the evaporation zone are roughly the same as those in Fig. 8. The liquid temperature, however, is about 70 F as compared with about 140 F for the subsonic case, due primarily to the lower pressure level. From a consideration of the Mach number and temperature variations, it appears that the net stagnation pressure rise of some 6 per cent could be con-

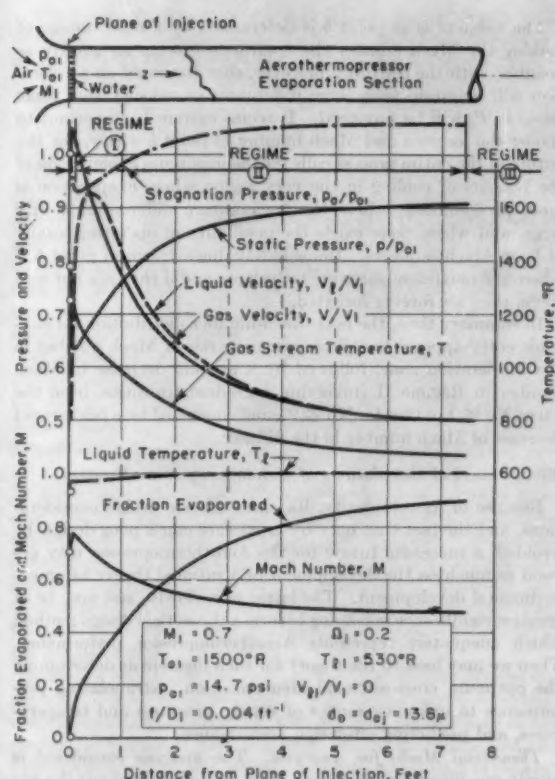


FIG. 8 TYPICAL THEORETICAL CALCULATIONS FOR SUBSONIC, CONSTANT-AREA OPERATION

siderably augmented by decreasing the cross-sectional area of the duct at about 1 ft from the inlet in such a way that the Mach number would be reduced.

Effect of Varying Initial Parameters for Subsonic, Constant-Area Operation. With regard to certain initial parameters, namely, f/D_1 , d_0 and T_{01} , it can be said with assurance that a given change will be either undesirable or desirable. Specifically, the performance will improve as f/D_1 and d_0 decrease and as T_{01} increases (except at very high values of the latter). This will generally be true irrespective of the values of such other parameters as Ω_0 , M_1 , p_{01} , V_{l1}/V_1 , and area variation, although the effect on performance associated with alterations in any of the variables f/D_1 , d_0 , and T_{01} will, of course, depend greatly on the values of all the parameters.

Considering, on the other hand, the parameters Ω_0 , M_1 , p_{01} , and V_{l1}/V_1 , we can only state vaguely that whether or not increases in these will improve or detract from the net stagnation-pressure rise depends on the specific values of these variables as well as those of f/D_1 , d_0 , T_{01} , and of the area variation. The reason for this indeterminacy, as explained before, is that an increase (or decrease) of any of the variables Ω_0 , M_1 , p_{01} , and V_{l1}/V_1 has both favorable and unfavorable aspects; in some circumstances the favorable aspects will hold the upper hand; in others the unfavorable aspects will predominate.

These remarks show that the effects of Ω_0 , M_1 , p_0 , and V_{l1}/V_1 can hardly be deduced from a few comparisons, and that hasty conclusions drawn from a few cases might be dangerous. What is more, a really meaningful study of the effects of Ω_0 , M_1 , p_0 , and

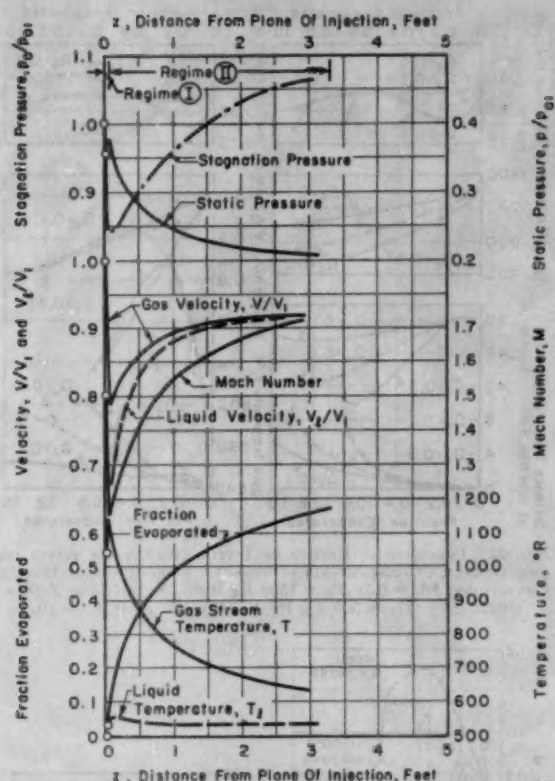


FIG. 9 TYPICAL THEORETICAL CALCULATIONS FOR SUPERSONIC CONSTANT-AREA OPERATION INITIAL CONDITIONS: $M_i = 1.5$; $T_{i0} = 1500$ deg R; $p_{e0} = 14.7$ psia; $f/D_i = 0.004$ ft⁻¹; $\Omega_0 = 0.15$; $T_{i0} = 530$ deg R; $V_{i0}/V_i = 0$; $d_0 = d_{0f} = 7.34\mu$

V_{i0}/V_i requires a selection of the optimum area variation for each set of initial variables for otherwise a favorable case might unfairly be compared with an unfavorable one. This really implies that determination of the optimum area variation and optimum values of the initial parameters must be made simultaneously. The studies already made may be far from those desiderata, so no attempt will be made here to evaluate systematically the influence of Ω_0 , M_i , p_{e0} , and V_{i0}/V_i .

Regarding f/D_i , d_0 , and T_{i0} , it is well to repeat that the magnitudes of the effects on performance are, in fact, strongly dependent on all the other initial variables and on the area variation, although the direction of the effects is not in doubt. Recognizing in advance that the results of one comparison may not be meaningful in other circumstances, we nevertheless shall present certain specific results for the sake of illustrating the influence of the variables f/D_i , Ω_0 , and d_0 .

Effect of Size. With values of the other variables remaining the same, Fig. 10 shows the effect of variations in rate of air flow on subsonic, constant-area operation. The parameter f/D_i shown in Fig. 10 varies approximately inversely with the square root of the air flow. For a value of f in the neighborhood of 0.004, the three values of f/D_i correspond to duct diameters of approximately ∞ , 12 in., and 2 in.

The curves of temperature, velocity, and distance versus fraction evaporated are nearly independent of f/D_i . The curves of p , p_0 , and M , however, show a strong dependency. As f/D_i in-

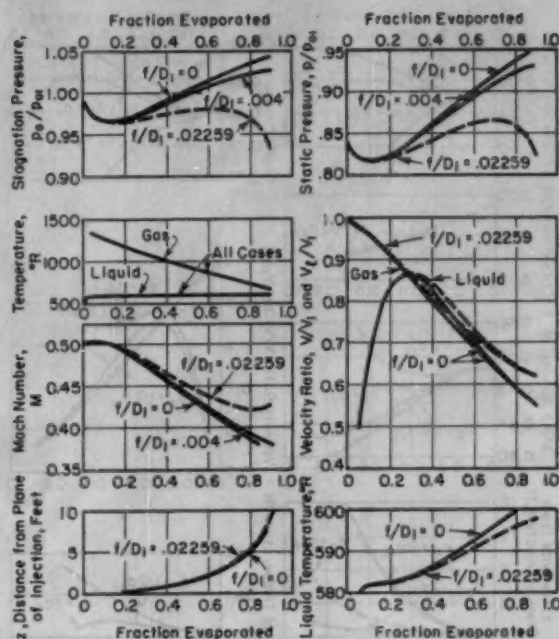


FIG. 10 THEORETICAL EFFECT OF SIZE ON SMALL-SCALE, CONSTANT-AREA, SUBSONIC OPERATION. INITIAL CONDITIONS: $M_i = 0.5$; $T_{i0} = 1500$ deg R; $p_{e0} = 14.7$ psia; $\Omega_0 = 0.2$; $T_{i0} = 530$ deg R; $V_{i0}/V_i = 0$; $d_0 = d_{0f} = 19\mu$

creases, Regime III sets in earlier (Regime III is absent when $f/D_i = 0$), and the maximum stagnation pressure is decreased. A net rise in p_0 seems impossible if f/D_i exceeds a certain value. There seems to be little difference between the cases $f/D_i = 0$ and $f/D_i = 0.004$, yet the former would be very superior if the optimum area variation were employed for each case.

Effect of Droplet Size. Assuming that the initial droplet size may be varied independently of M_i through the injector design, or that the droplet size produced differs from that of the Nukiyama and Tanasawa formula (4), Fig. 11 shows how a case of small-scale, subsonic, constant-area operation would be altered if the droplet size were either one half or twice as large as the Nukiyama and Tanasawa value (d_{0f}).

The influence of d_0 is seen to be enormous, and would be even greater if each case had the optimum area variation. For 80 per cent fraction evaporated, the distances required are 1 ft, 5 ft, and 20 ft (approximately a square law, see Section 2.6) for the three droplet sizes. With $d_0 = 2d_{0f}$ evaporation never becomes predominant over wall friction, while with $d_0 = d_{0f}/2$, a net stagnation pressure rise appears possible even with a 2-in.-diam duct.

These results illustrate two conclusions of paramount significance: (a) Nothing is more crucial to effective performance than an atomization system producing very small drops, and (b) the weakest link between theory and experiment is a lack of knowledge of the actual drop-size spectrum produced in the Aerothermopressor.

Effect of Water-Air Ratio. Again with a reminder concerning the inadvisability of drawing general conclusions, we show in Fig. 12 the effect of water-air ratio on a specific case of subsonic, constant-area performance.

Noting that here the amount of water required to saturate the air stream is in the neighborhood of $\Omega_0 \approx 0.2$ it is seen that the values of 0.1 and 0.3 correspond, respectively, to a considerable

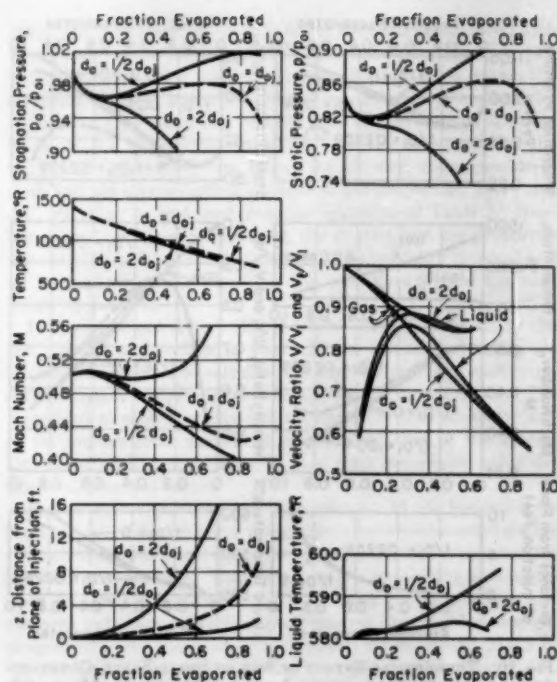


FIG. 11 THEORETICAL EFFECT OF INITIAL DROP SIZE ON SMALL-SCALE, CONSTANT-AREA, SUBSONIC OPERATION. INITIAL CONDITIONS: $M_1 = 0.5$; $T_{01} = 1500$ deg R; $p_{01} = 14.7$ psia; $f/D_1 = 0.0226$ ft $^{-1}$; $\Omega_0 = 0.2$; $T_{01} = 530$ deg R; $V_{01}/V_1 = 0$; $d_0 = d_{0i} = 10\mu$

water deficiency and a considerable water excess. As Ω_0 increases, both the drag and evaporation phenomena are strengthened; Regimes II and III each set in at earlier values of x , but at about the same distance z . Evaporation barely achieves some predominance for $\Omega_0 = 0.1$ and is most forceful for $\Omega_0 = 0.3$. A deficiency of water seems to be more detrimental than an excess, a result confirmed by experiment. The best performance seems to be obtained for a value of Ω_0 greater than that required for saturation, although it is of considerable practical consequence that the net stagnation pressure rise as well as the position of maximum p_0 are relatively insensitive to Ω_0 .

Passage Through Speed of Sound. Fig. 13(a) illustrates constant-area operation at various subsonic initial Mach numbers, and shows the extreme sensitivity of the flow to the initial Mach number when it is in the neighborhood of the critical. To pass through the speed of sound, the calculations give $M_1 = 0.74289$, whereas $M_1 = 0.74$ gives purely subsonic operation with a peak Mach number of 0.93 while $M_1 = 0.75$ leads to choking at $x \approx 0.1$. On the supersonic branch of the critical curve the rapid rise of Mach number soon brings on Regime III, and frictional choking ensues in the vicinity of $x = 0.57$.

Fig. 13(b) illustrates the corresponding curves of gas-stagnation pressure. The corresponding static pressure variations are shown in Fig. 27, where they are compared with experimental data.

Shocks. Once supersonic speeds have been reached, there exists the possibility of normal discontinuities (shocks) in the gas phase. These may occur at various positions, depending on the back-pressure level. In the calculations it was assumed that the gas stream passed through an adiabatic, normal shock as though the droplet cloud were not present, and the properties of the droplet cloud on the downstream side of the shock were assumed the same as those on the upstream side.

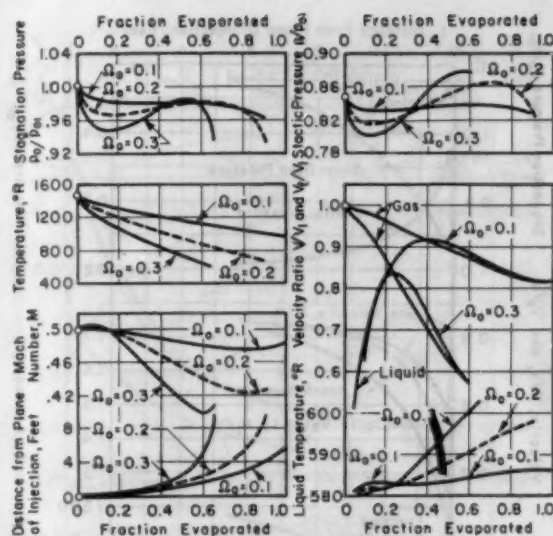


FIG. 12 THEORETICAL EFFECT OF INITIAL WATER-AIR RATIO ON SMALL-SCALE, CONSTANT-AREA, SUBSONIC OPERATION. INITIAL CONDITIONS: $M_1 = 0.5$; $T_{01} = 1500$ deg R; $p_{01} = 14.7$ psia; $f/D_1 = 0.0226$ ft $^{-1}$; $T_{01} = 530$ deg R; $V_{01}/V_1 = 0$; $d_0 = d_{0i} = 10\mu$

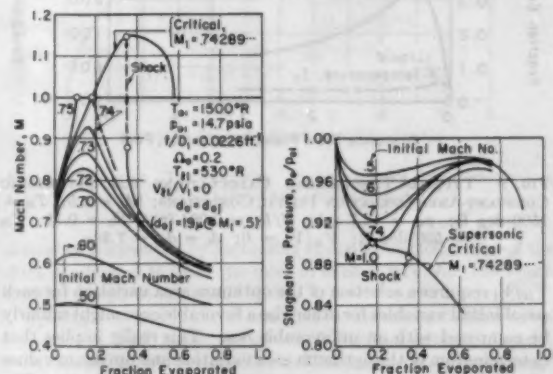


FIG. 13 THEORETICAL CURVE OF CONSTANT-AREA OPERATION AT VARIOUS SUBSONIC INITIAL MACH NUMBERS, ILLUSTRATING CONTINUOUS PASSAGE AT CRITICAL INITIAL MACH NUMBER THROUGH SPEED OF SOUND, AND NORMAL SHOCKS ON SUPERSONIC CRITICAL BRANCH. CORRESPONDING CURVES OF STATIC PRESSURE ARE SHOWN IN FIG. 27

Figs. 13(a) and 13(b) show operation on the supersonic critical with a shock at $x = 0.35$, the performance downstream of the shock being typically subsonic. Following a slight drop in stagnation pressure across the shock itself, there is a rapid rate of rise brought on by the deceleration of the droplets and a high evaporation rate resulting from comparatively large differences in velocity and temperature.

Control of Cross-Sectional Area. How considerable are the gains to be won by proper control of the cross-sectional area is illustrated in Fig. 14. On this chart the base run for purposes of comparison is the constant-area supersonic critical curve with $T_{01} = 1500$ deg R, $p_{01} = 14.7$ psia, $f/D_1 = 0.004$ ft $^{-1}$, $\Omega_0 = 0.25$, and $d_0 = d_{0i} = 13.4\mu$, for which the critical Mach number is $M_1 = 0.727$ The striking feature of this constant-area case is its earlier mentioned suicidal character; after passing through

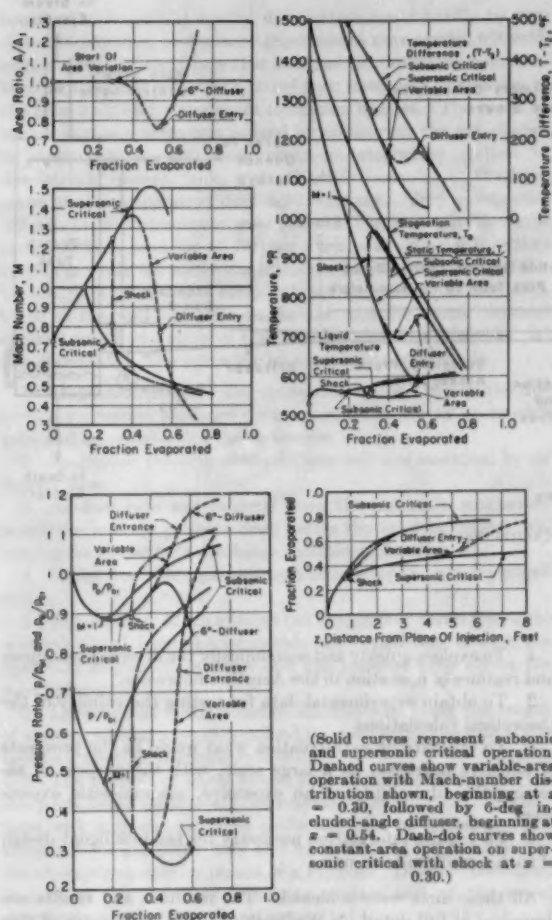


FIG. 14 ILLUSTRATES THEORETICAL IMPROVEMENT BY CONTROL OF CROSS-SECTIONAL AREA. INITIAL CONDITIONS: $M_1 = 0.727$; $T_{01} = 1500$ deg R; $p_{01} = 14.7$ psia; $f/D_1 = 0.004$ ft $^{-1}$; $T_{11} = 530$ deg R; $V_{11}/V_1 = 0$; $d_0 = d_{01} = 13.4$ μ ; $\Omega_0 = 0.25$

Mach number unity, the Mach number is pushed to such high values by evaporative cooling that the temperature potential for heat transfer is severely depressed and, after about 48 per cent fraction evaporated, wall friction gains control, and the stagnation pressure declines rapidly before it is ever able to ascend even to its initial value.

By inserting a normal shock at $x = 0.30$ ($M = 1.26$), the gas temperature is not allowed to fall too rapidly, and there is a notable gain in performance, the net stagnation pressure rise being more than 10 per cent.

With operation at constant area on the subsonic critical curve, the maximum rise in stagnation pressure is seen to be in the neighborhood of 7 or 8 per cent.

In the light of the discussions of Sections 2.4 and 2.5 and of other considerations too lengthy for discussion here, the Mach-number distribution shown in Fig. 14 was described. In this figure the solid lines represent operation on the subsonic and supersonic critical curves for a unit of about 12 in. diam. The variable-area case (dashed line) is compounded of (a) constant-area operation on the supersonic critical up to $c = 0.30$, (b)

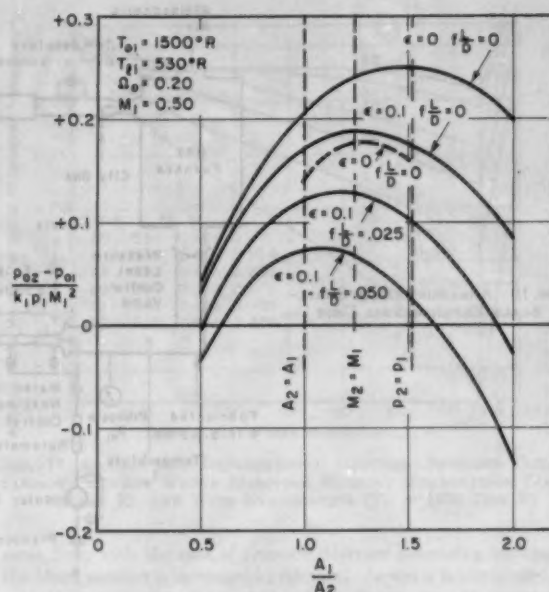


FIG. 15 TYPICAL RESULTS OF CALCULATIONS BASED ON "LOW-VELOCITY" DISCONTINUITY ANALYSIS. DASHED CURVE SHOWS RESULTS OF "EXACT" DISCONTINUITY ANALYSIS

variable-area operation from $x = 0.30$ to $x = 0.54$ with the Mach-number distribution illustrated, and (c) operation in a conical diffuser of 6-deg included angle for $x > 0.54$. It may be seen that the maximum area reduction is 25 per cent of the initial area, and that the diffuser begins shortly after the position of minimum area. What is of greatest practical importance is that, in the variable-area case shown, a stagnation pressure rise of more than 18 per cent is indicated.

The foregoing example is only an isolated instance presented merely to show the importance of Mach-number control, and is illustrative of the improvements to be gained whether this control is brought about by area control or by lengthwise water injection. In this example the Mach-number variation was chosen arbitrarily and would be the optimum only through coincidence. As mentioned earlier, more systematic ways of determining the optimum are under development. Only fragmentary results of this more systematic study are available, the most important practical conclusion thus far being that with $T_{01} = 1500$ deg R and an air flow of about 20 lb/sec, a stagnation pressure rise of more than 20 per cent seems to be attainable provided that the drop size is that of the Nukiyama-Tanasawa formula (4).

2.8 Approximate Discontinuity Analysis

For real insight into the details of the Aerothermopressor process, or for knowledgeable optimization of the area variation, we have no better procedure at the moment than the extended numerical integrations described in Section 2.7. But for the approximate computation of the order of magnitude of attainable performance, a comparatively simple algebraic method may be constructed.

Rather than dealing accurately with the history of the process, the approximate analysis proceeds on the assumption that in the evaporation section the curve of pressure versus area may be represented as a straight line. The core of the analysis is then the integral equations of continuity, momentum, and energy connecting the inlet and exit states of the evaporation section.

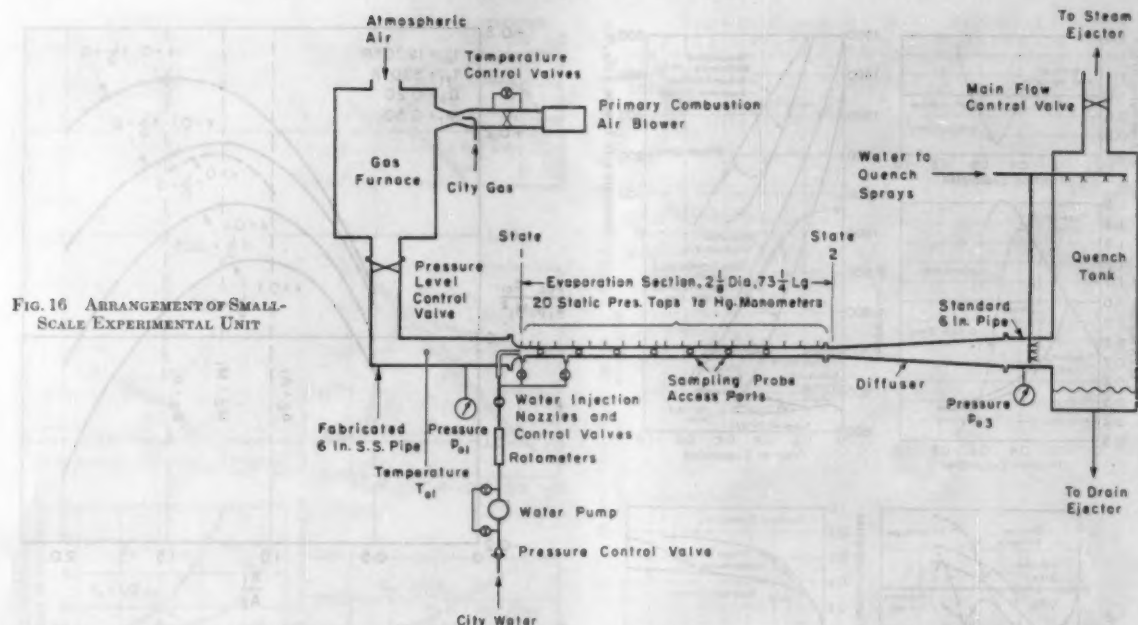


FIG. 16 ARRANGEMENT OF SMALL-SCALE EXPERIMENTAL UNIT

At low Mach numbers an especially simple form of the analysis becomes usable.

Details of the analysis are recorded in Appendix D, and a typical set of computed results is shown in Fig. 15. More extended analyses of the discontinuity type together with a wealth of numerical results are presented in reference (8).

In Fig. 15 the solid curves represent the low Mach-number analysis. For comparison, the dashed curve shows how, for the case of no friction in the evaporation section and diffuser, the results are modified when the more accurate iterative calculation procedure of Appendix D is used. With the inlet parameters shown, an abscissa of 1.0, of course, corresponds to constant area; 1.24 corresponds to equal Mach number at inlet and exit; and 1.51 corresponds to equal pressures at inlet and exit.

A glance at the results of Section 2.7 shows that the linear pressure-area relationship is a crude approximation. Nevertheless, it is believed that as far as gross orders of magnitude are concerned, the curves of Fig. 15 are significant in respect to the attainable stagnation-pressure rise and in displaying the effects of area change, wall friction, and diffuser loss. Among the conclusions that may be drawn are the following:

- 1 With a diffuser loss coefficient of 0.1, a diameter of 1 ft, a length of 6 ft, and $f = 0.004$, a stagnation-pressure rise approaching 20 per cent is possible.
- 2 A net rise in stagnation pressure is not possible if fL/D exceeds approximately 0.075 (for $f \leq 0.005$, this limits L/D to 15).
- 3 Area decrease is definitely beneficial, and the optimum amount of area contraction increases as the frictional effects are minimized.

3 EXPERIMENTS WITH A SMALL-SCALE CONSTANT-AREA AERO-THERMOPRESSOR

3.1 Objective of Small-Scale Experiment

The experiments to be described were carried out on a scale of air flow so small that there was no expectation of a net rise in stagnation pressure. Instead the goals were as follows:

- 1 To explore quickly and economically the diverse phenomena and regimes of operation in the Aerothermopressor.
- 2 To obtain experimental data for testing the validity of the theoretical calculations.
- 3 To estimate by extrapolation what would be the prospects of effective operation on a large scale, with the purpose of assessing the advisability of an expensive, medium-scale experiment.
- 4 To acquire information necessary for the intelligent design of such a medium-scale unit.

All these aims were achieved. The methods and results are described in full detail by Wadleigh (9), and a summary of this work is presented here.

3.2 Details of Apparatus

Flow System. Powered by a steam-jet ejector at the downstream end, the entire system, Fig. 16, operated at subatmospheric pressure. Air from the atmosphere was drawn into a gas-fired combustion chamber; from the latter the heated air passed through two mixing elbows and a straightening length to the upstream stagnation section; thence through a converging, accelerating nozzle into the evaporation duct; and, after being cooled by water evaporation, into a conical diffuser of 6-deg included angle; finally, the air flowed through a large quench tank to the jet pump via a control valve by means of which the back pressure on the Aerothermopressor was adjusted.

Test Duct. As the objective was to obtain basic data rather than maximum performance, the evaporation duct was of constant area, 2.13 in. diam and 73 in. long. The test section was fitted with twenty static pressure taps on the wall, and with eight access ports for introduction of measuring probes.

Water-Injection System. Atomization of the so-called "gas-atomization" type was achieved by introducing water at low speed into the high-velocity air stream at the beginning of the 2.13-in. evaporation duct. Since the type of water-injection system which would best yield the desirable features of small droplets

together with uniform spatial distribution could hardly be predicted in advance, preliminary experiments were carried out with some twenty different injection schemes (9), involving combinations of axial-flow water jets, radial-flow water jets originating in the pipe wall, and water-sheet formation nozzles. The merit of each injection system was judged by comparing the net change in stagnation pressure from upstream stagnation section to downstream quench tank, with all other variables at the inlet plane of the evaporation duct held constant. Very substantial differences in performance were found. The best injection system, and that used for all further work, was an axial injection system in which the water was introduced at the inlet plane of the 2.13-in. duct by means of seven tubes of dimensions 0.125 in. OD, 0.110 in. ID, with one tube on the axis and the others disposed symmetrically on a circle of 1.25 in. diam.

Measurements. The following measurements were made:

- 1 Stagnation pressure and stagnation temperature in the upstream stagnation section were measured directly by an impact tube and a multishielded thermocouple.
- 2 Stagnation pressure at the diffuser exit was measured by an impact tube.
- 3 Air-flow rate was inferred from the upstream stagnation properties and the pressure drop across the inlet bellmouth, assuming for the latter a discharge coefficient of unity.
- 4 Water flow was measured by a rotameter and a sharp-edged orifice.
- 5 Entrance-air Mach number (at the plane of water injection) was calculated from the isentropic law connecting it with the upstream stagnation pressure and the pressure drop across the inlet bellmouth.
- 6 Longitudinal static-pressure distributions along the length of the test section were determined by connecting the wall static taps to a multiple manometer board.
- 7 The amount of water evaporated at the sections where access ports were available was determined by transversing these sections with a special sampling probe designed for withdrawing a sample of the gas phase only and by measuring the humidity of the air-vapor sample by means of a Foxboro "Dewcel" indicator. Details of the humidity-measuring system and of the novel sampling probe are given in reference (9).

Control of Variables. In the apparatus described, the significant parameters which could be controlled were (a) the upstream stagnation pressure p_{01} , (b) the upstream stagnation temperature T_{01} ; (c) the water-air ratio Ω_0 , and (d) either the initial Mach number M_1 , or, in the case of choked flow where M_1 was uniquely determined by p_{01} , T_{01} , and Ω_0 , the position of a normal shock in the test section.

These were varied in a systematic manner during the course of the tests.

3.3 Experimental Results

We present here selected results which illustrate the theoretical considerations of Section 2 and which also show the influences of the controllable parameters. Here again the reader is cautioned that the effects of these parameters in a small-scale, constant-area apparatus are generally not the same as in a large-scale unit having an optimum area variation.

Comparison of Flows With and Without Evaporation. Fig. 17 illustrates in an unmistakable way the powerful influence of that evaporative cooling which is the heart of the Aerothermopressor process.

The three runs with $T_{01} = 1500$ deg R constitute essentially adiabatic flows. With no water injection ($\Omega_0 = 0$) the process is the one-dimensional Fanno-line process (reference 2, chapter 6) and exhibits a constantly falling static pressure typical of sub-

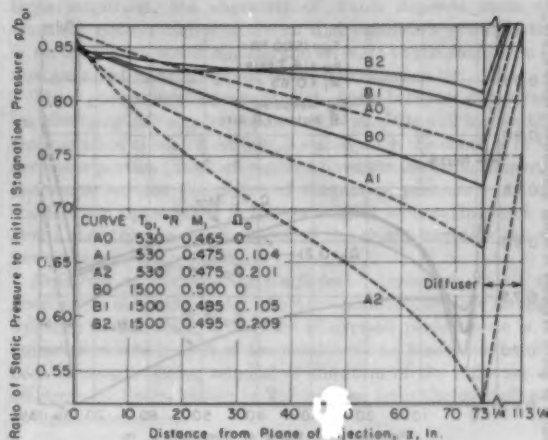


FIG. 17 SMALL-SCALE EXPERIMENTAL RESULTS, SHOWING COMPARISON BETWEEN WATER INJECTION WITHOUT EVAPORATION ($T_{01} = 530$ deg R), AND WITH EVAPORATION ($T_{01} = 1500$ deg R)

sonic flow, with the rate of pressure decrease increasing because the Mach number is increased by friction. As water is introduced, with Ω_0 first equal to 0.1 and then 0.2, a larger drop in pressure than before occurs near the inlet because of droplet drag; after the first few inches, the droplet drag is small, and the pressure drop is primarily that of pipe friction. However, the rate of frictional pressure drop is greater at the larger values of Ω_0 because the droplet drag increases the Mach numbers at which friction occurs throughout the duct. For the case $T_{01} = 530$ deg R and $\Omega_0 = 0.2$, in fact, the flow at the duct exit is nearly choked; i.e., the Mach number is nearly unity.

The case of $\Omega_0 = 0$ at $T_{01} = 1500$ deg R is again essentially adiabatic and is directly comparable with the case of $\Omega_0 = 0$ at $T_{01} = 530$ deg R. The small difference in the rates of pressure drop for these two Fanno-line runs is present because of a difference in initial Mach number and also because the pipe-friction factor f is altered by the difference in length Reynolds number between the two cases.

Turning to the curves for $T_{01} = 1500$ deg R with water injection, we see pronounced differences owing to the evaporative cooling which is now present. Whereas for $T_{01} = 530$ deg R (i.e., no evaporation) water injection increases the pressure drop, with $T_{01} = 1500$ deg R (i.e., strong evaporation) water injection decreases the pressure drop. It seems safe to say also that the Mach-number rise here when evaporation occurs is less than when evaporation does not occur.

Effect of Water-Air Ratio. Certain aspects of the phenomena just discussed are brought out more clearly in Fig. 18, for which the initial Mach number of 0.65 is higher than that for the runs shown in Fig. 16, thus magnifying the pressure gradients. The fact that cooling at subsonic speeds does indeed tend to decrease the Mach number was clearly evidenced by this series of runs, inasmuch as it was not even possible to operate at $M_1 = 0.65$ with no water injection, the initial Mach number for choking when operating dry being less than 0.65.

For each value of Ω_0 , the three characteristic regimes discussed in Section 2.3 are observed:

1 **Regime I.** For a distance of about 2 in. the pressure falls rapidly because of droplet drag. The magnitude of this initial pressure drop is roughly proportional to the rate of water flow, i.e., to Ω_0 .

2 **Regime II.** A rapidly rising pressure occurs in the next 20

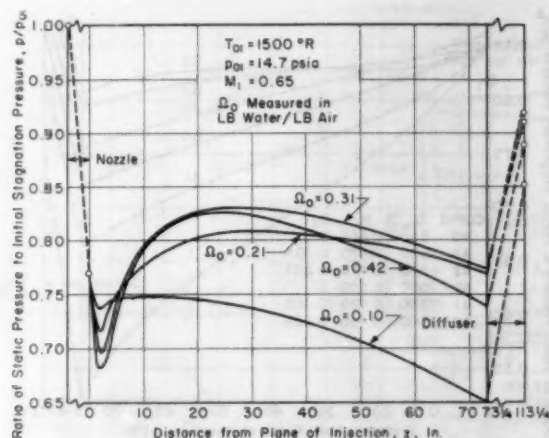


FIG. 18 SMALL-SCALE EXPERIMENTAL RESULTS, SHOWING EFFECT OF WATER-AIR RATIO

in. or so, where evaporative cooling is predominant. The maximum rate of pressure rise increases as Ω_0 increases, chiefly because an increased Ω_0 means a greater amount of heat-transfer surface in the droplet cloud. For such a small Ω_0 as 0.10, the net rise is rather small and reaches its peak at $z \approx 10$ in.; in this case there is scarcely enough surface to accomplish much cooling, and the droplet cloud vanishes comparatively rapidly because the driving temperature differential is not decreased very much by cooling of the gas. With values of Ω_0 between 0.2 and 0.4 the pressure rise exceeds the loss in Regime I, such that at $z \approx 25$ in. the pressure is higher than in the inlet plane. The maximum pressure in the duct and also at the diffuser exit is obtained with $\Omega_0 \approx 0.3$, this being the water-air ratio for which the balance between pressure rise due to cooling and pressure drop due to droplet acceleration and wall friction is an optimum. For low values of Ω_0 , the distance z to the point of maximum pressure increases as Ω_0 increases because the droplet cloud persists for greater distances. For high values of Ω_0 , on the other hand, the distance decreases as Ω_0 increases because the gas stream tends toward saturation more quickly.

3 Regime III. After the rate of evaporation has been reduced sufficiently by the falling gas temperature and diminishing droplet diameter, wall friction gains control. The pressure begins to drop, and the rate of pressure fall grows as evaporation becomes weaker and weaker.

Passage Through Mach Number Unity. Fig. 19 shows the pressure distributions obtained with constant values of T_{01} , p_{01} , and Ω_0 , but with varying initial Mach numbers M_1 .

The curves for $M_1 = 0.48$ and $M_1 = 0.65$ are for values of back pressure so high that the entire flow is subsonic. Qualitatively similar to those of Fig. 18, they demonstrate as well the dynamic character of the events in the sense that the pressure gradients grow as the Mach number ascends.

All the remaining curves of Fig. 19 are for the critical initial Mach number, $M_1 \approx 0.78$, for which evaporation becomes predominant over drag just at the point where the local Mach number is unity. The lowermost curve in Fig. 19 is for the greatest possible length of supersonic flow in the test section and, except for a shock near the exit, corresponds to the supersonic critical curve shown in Fig. 13. The branch curves rising precipitously from this lowermost curve represent normal shocks followed by subsonic flow.

Shock Configurations. Considering in more detail the lower-

most curve in Fig. 19, it is seen that the pressure falls and the Mach number rises to unity in Regime I, up to $z \approx 2$ in.; the pressure continues to fall and the Mach number rises to substantial supersonic values in Regime II, up to $z \approx 28$ in.; then, because of wall friction, the pressure begins to rise and the Mach number to fall in Regime III, up to $z \approx 55$ in. However, the duct length is too great for supersonic flow to continue to the exit, for in the absence of shocks, the Mach number would reach the choking value of unity before the exit. Therefore a shock must stand somewhere in the duct. For very low back pressures (e.g., condition 2 in Fig. 19), the shock is at its furthestmost possible position downstream, that is, at the position for which the subsonic flow following the shock becomes choked at the duct exit. In this case the shock lies in the range of z between 55 and 62 in., and $M = 1$ at the duct exit; the flow in the diverging diffuser (now operating as a nozzle) then accelerates to supersonic speeds, and is again decelerated to subsonic speeds by means of a shock in the "diffuser," the shock having a loss in stagnation pressure suf-

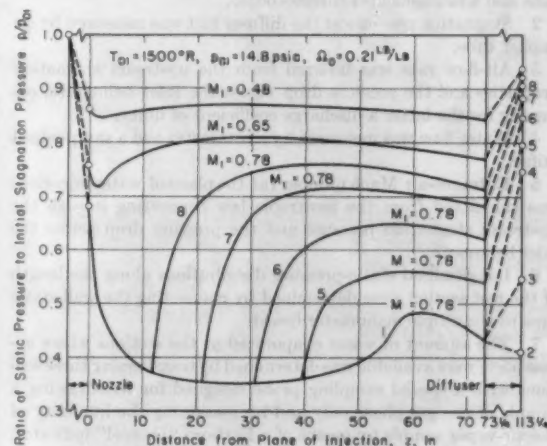


FIG. 19 SMALL-SCALE EXPERIMENTAL RESULTS, SHOWING EFFECT OF INITIAL MACH NUMBER, CONTINUOUS PASSAGE THROUGH SPEED OF SOUND, AND SHOCKS IN SUPERSONIC REGIME

ficiently high to match the prescribed low back pressure. The lowermost curve therefore exhibits an amazing range of gas dynamics phenomena, comprising two continuous accelerations through the speed of sound (albeit by different mechanisms), two normal compression shocks, three distinct regions of subsonic flow, and two distinct regions of supersonic flow.

As the back pressure is increased, say, from condition 2 to condition 3, the shock in the diffuser moves upstream to lower supersonic Mach numbers, but the flow in the duct is completely unaltered. When the back pressure reaches condition 4, however, the diffuser shock disappears in the duct exit where $M = 1$, and this then represents the limit of operation with choked flow at the duct exit, and with the furthestmost downstream position of the shock in the duct.

A further rise in back pressure over that for condition 4 therefore causes the shock in the duct to move upstream. As the back pressure is increased the shock continuously and successively moves from position 1 to positions 5, 6, 7, and 8. For all the latter modes of operation the flow following the shock and at the duct exit is subsonic. Following the shock, the pressure at first rises because of subsonic cooling and deceleration of the liquid droplets, and subsequently falls because of subsonic friction.

Because of the now-familiar shock-boundary-layer interaction,

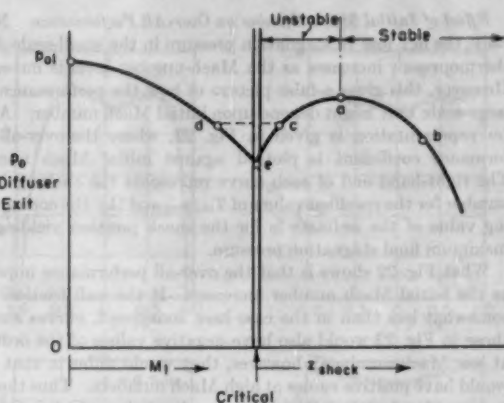


FIG. 20 ILLUSTRATES SCHEMATICALLY SHOCK POSITIONS FOR STABLE AND UNSTABLE OPERATION

the shocks, rather than being discontinuities, occupy a distance of about 8 in., corresponding to about four duct diameters.

Stable Versus Unstable Operation at the Critical Mach Number. Attempts to operate on the subsonic branch of the critical curve or with shocks further upstream than the position corresponding to curve 8 were unsuccessful. When the back pressure was raised slightly above that of condition 8 (corresponding to curve 8), the entire flow became highly unsteady, with large surges in pressure, flow rate, and shock position.

This strange behavior may be explained by reference to the schematic diagram of Fig. 20, which refers to a small-scale Aerothermopressor in which there is at all times a net loss in stagnation pressure from inlet to diffuser exit. Consider an experimental arrangement in which p_{01} , T_{01} , and Ω_0 are fixed and in which, at least for the present, steady flow is assumed possible. Then, as M_1 increases from zero, the value of p_0 at the diffuser exit will at first decrease because the net loss in p_0 is roughly proportional to M_1^2 . This loss continues until M_1 reaches its critical value, after which M_1 may increase no further, and we may use the position of the shock as the controllable variable governing performance. From the theoretical consideration of Section 2, there will be a particular position of the shock (point a) in Fig. 20 for best performance. In Fig. 19, therefore, the curve of p_0 versus shock position will first rise to point a, and will subsequently fall as the shock moves further downstream.

Now, operation at a point to the right of a, such as at b, is stable in the sense that a slight variation in the imposed back pressure will induce a change in Aerothermopressor operation of such nature as to make the delivered exit pressure adjust to the imposed back pressure. For example, suppose that steady operation prevails at b, and that the imposed back pressure is suddenly increased slightly. This will generate a small compression wave which will propagate upstream until it reaches the shock, and its interaction with the shock will force the latter slightly upstream. But the latter event increases the delivered back pressure and thus the Aerothermopressor adjusts stably to the imposed disturbance.

Operation at a point such as c on the portion of the curve between a and c, on the other hand, is unstable. If, after an assumed steady operation at c, the imposed back pressure is suddenly raised slightly, the generated compression wave will on reaching the shock again move the latter upstream. But this reduces the delivered exit pressure, with the result that conditions are further from equilibrium than before, and the point of operation is driven toward e. There ensues an oscillatory mode of

large amplitude, the character of which depends upon the transient characteristics of the air and water-flow systems, that is, on the way in which p_{01} , T_{01} , and Ω_0 react to the changes in air flow pursuant to M_1 dropping below its critical value.

These phenomena are reminiscent of the behavior of converging-diverging diffusers for supersonic flow. It is well known that the operation of such a diffuser is stable when the shock is in the divergent portion (in which region a downstream displacement of the shock reduces the delivered stagnation pressure), but unstable when the shock is in the convergent section (in which region a downstream displacement of the shock increases the delivered stagnation pressure).

Definition of Performance Coefficient. Inasmuch as all the phenomena occurring within the Aerothermopressor are strongly dynamic in character, a measure of over-all performance is required from which most of the sensitivity to Mach number has been removed. Being mindful of the form of the influence coefficients for dp_0/p_0 shown in Table 3, we form the over-all performance coefficient

$$\frac{p_{03} - p_{01}}{p_{01} M_1^2}$$

where p_{03} is the stagnation pressure at the diffuser exit.

Although the use of this dimensionless figure of performance does in fact illuminate the results, it seems in place once again to state that the value of this performance coefficient depends not only on p_{01} , T_{01} , Ω_0 , M_1 , and length of evaporation section, but also on the actual duct diameter and on the area variation, because both friction and area change act to alter the local Mach number.

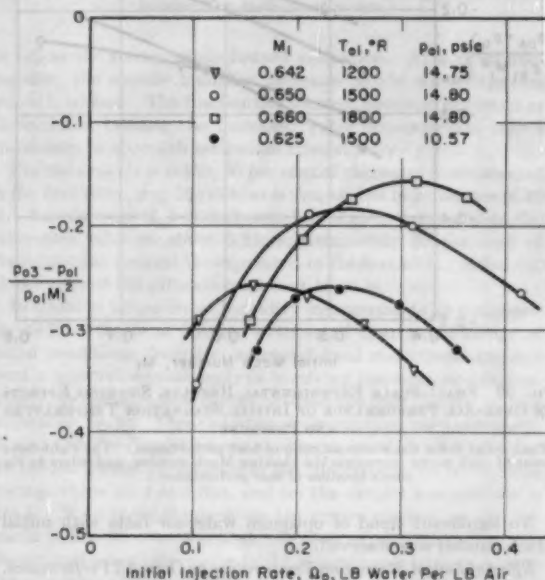


FIG. 21 SMALL-SCALE EXPERIMENTAL RESULTS, SHOWING EFFECTS ON OVER-ALL PERFORMANCE OF WATER-AIR RATIO, INITIAL STAGNATION TEMPERATURE, AND INITIAL STAGNATION PRESSURE (Each point is for initial Mach number or shock position of best performance.)

Effect of Water-Air Ratio on Over-All Performance. The curves of Fig. 21 are typical of the variation in over-all performance when the water-injection rate is varied and the initial stagnation conditions and Mach number all held constant. For each set of initial parameters (M_1 , T_{01} , p_{01}), there is an optimum value of Ω_0 .

Below this optimum Ω_0 , the total amount of cooling is weak compared with wall friction; above this value, the added droplet drag cannot be offset by evaporative cooling because of the tendency of the stream to reach saturation too quickly. The performance is less sensitive to variations in Ω_0 above the optimum value, however, than to variations below the optimum; i.e., excessive water is not as detrimental to performance as a deficiency. The curves are fortunately quite flat near their peaks, and so the precise adjustment of the water flow is not critical.

As might be expected from the theoretical considerations, an increase in T_{01} requires an increase in Ω_0 . For example, with $p_{01} = 14.8$ psia, the following table shows the optimum values of Ω_0 at several temperatures:

T_{01} , deg R	1200	1500	1800
Ω_0	0.16	0.24	0.31

Fig. 21 shows also that the optimum water-air ratio is substantially independent of p_{01} .

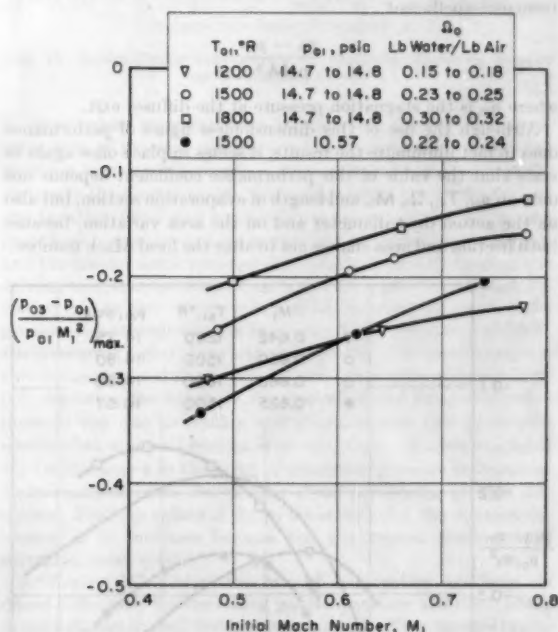


FIG. 22 SMALL-SCALE EXPERIMENTAL RESULTS, SHOWING EFFECTS ON OVER-ALL PERFORMANCE OF INITIAL STAGNATION TEMPERATURE AND PRESSURE

(Each point is for the water-air ratio of best performance. The right-hand point of each curve represents the choking Mach number, and refers to the shock location of best performance.)

No significant trend of optimum water-air ratio with initial Mach number was observed.

Effect of Initial Stagnation Temperature on Over-All Performance. From Fig. 21 it may be seen that, with a given initial Mach number, the best performance attainable with the appropriate value of Ω_0 is improved as the initial stagnation temperature is raised. The same result is obvious also from Fig. 22, which shows only the best performance at each Mach number and temperature. An increase in the temperature difference available for cooling, as well as an increase in the saturation humidity, account in a simple manner for the better performance at high temperatures. On the same grounds it is easy to understand also why the optimum water-air ratio rises as the initial stagnation temperature increases, at least in the range of the latter under consideration.

Effect of Initial Mach Number on Over-All Performance. Naturally, the net loss in stagnation pressure in the small-scale Aerothermopressor increases as the Mach-number level is increased. However, this gives a false picture of how the performance of a large-scale unit might depend upon initial Mach number. A better representation is given in Fig. 22, where the over-all performance coefficient is plotted against initial Mach number. The right-hand end of each curve represents the choking Mach number for the specified values of T_{01} , p_{01} , and Ω_0 ; the corresponding value of the ordinate is for the shock position yielding the maximum final stagnation pressure.

What Fig. 22 shows is that the over-all performance improves as the initial Mach number increases. If the wall friction were somewhat less than in the case here considered, curves such as those in Fig. 22 would also have negative values of the ordinate at low Mach numbers; however, they would differ in that they would have positive values at high Mach numbers. Thus there is, in general, a certain initial Mach number below which a rise in p_0 cannot be achieved, and above which the net rise in stagnation pressure mounts rapidly as the initial Mach number is increased. The explanation of this behavior is related to the effect of M_1 on droplet diameter; as M_1 increases, the droplet diameter decreases, and a greater fraction of the water is evaporated in the given length of duct, as described previously in Section 2.6 and as shown later in Fig. 26.

Effect of Initial Stagnation Pressure on Over-All Performance. Figs. 21 and 22 also show a considerable worsening in performance as the inlet stagnation pressure is reduced. For fixed values of M_1 , T_{01} , and Ω_0 , the influence of decreasing p_{01} may be felt in several ways, namely, (a) through an increase in initial droplet diameter produced by decreased atomization forces; (b) through a reduction in heat-transfer coefficient and in drag effects produced by lessened relative Reynolds numbers; (c) through an increase in pipe-friction factor produced by the decrease in pipe Reynolds number; (d) through the lowered wet-bulb temperature and the

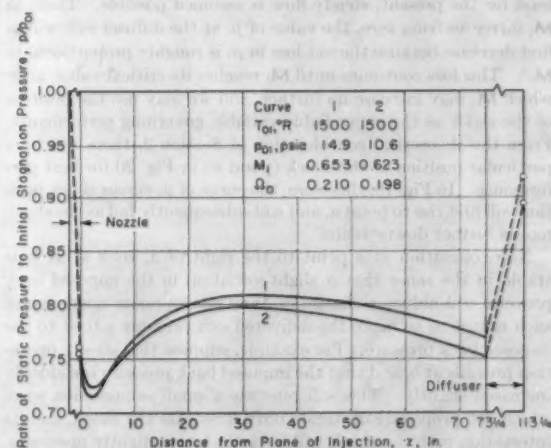


FIG. 23 SMALL-SCALE EXPERIMENTAL RESULTS, SHOWING EFFECT OF STAGNATION-PRESSURE LEVEL ON STATIC PRESSURE DISTRIBUTION

increased vapor-carrying capacity of the stream before saturation is reached; and (e) through an increase in the mass-transfer coefficient associated with an increase in the mass diffusivity.

As heat transfer rather than mass transfer is controlling in the evaporation process effects (d) and (e) are probably of small consequence. Furthermore, it is hard to imagine effect (c) as accounting for the results seen in Figs. 21 and 22.

Some additional relevant facts appear in Fig. 23, which show

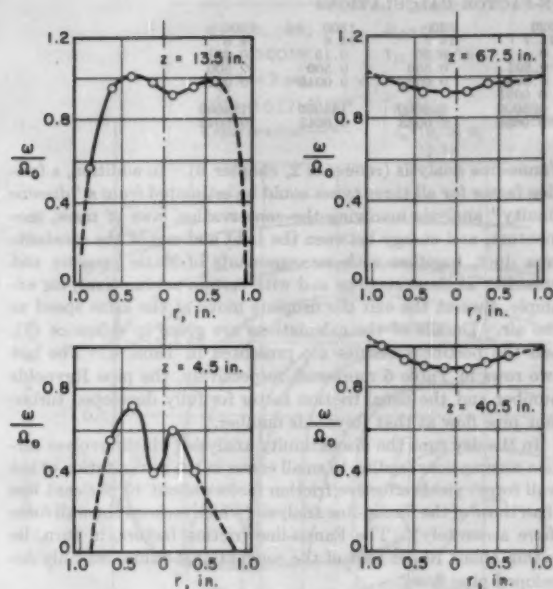


FIG. 24 SMALL-SCALE EXPERIMENTAL RESULTS, SHOWING HUMIDITY PROFILES AT SEVERAL LONGITUDINAL CROSS SECTIONS: $M_1 = 0.502$; $\Omega_0 = 0.150$; $T_{01} = 1500$ deg R; $p_{01} = 14.6$ psia

the longitudinal pressure distributions at two pressure levels with comparable (but slightly different) values of M_1 and Ω_0 . Taking note of the comparative values of M_1 and Ω_0 , what is most striking is the enormous difference in the rates of pressure rise at the beginning of Regime II. In the theoretical calculations of reference (8), the effect of p_{01} under conditions of unchanged d_0 was found to be extremely small; i.e., the net influence of item (b) in the foregoing list was found to be unimportant. Accordingly, the evidence points to items (a) as being controlling, i.e., that the effect of initial stagnation pressure is strongest through its influence on drop size.

Evaporation Profiles. For fixed initial conditions, Fig. 24 shows typical profiles of specific humidity at four different transverse cross sections of the flow.

Near the inlet, at $z = 4.5$, the humidity profile reflects the deficiencies of the water-injection system in achieving uniform distribution. However, even in the short distance of 4.5 in., an astonishing amount of evaporation has occurred, thus testifying to the tremendous heat-transfer surface of a droplet cloud.

Further downstream, a rapid straightening of the humidity profile is observed, until at $z = 67.5$ in. the profile is nearly flat. By virtue of the large droplet inertia, it does not seem likely that the turbulence of the stream does much to redistribute the droplets in a more uniform way. What the data suggest, rather, is that the turbulent migrations of the gas itself rapidly mix those portions of the gas in contact with many droplets with those portions in contact with few. Or from a different point of view, each piece of gas courses turbulently through the different parts of the droplet cloud, and thus experiences the average water distribution. If this picture is true, uniformity of the spray distribution on a fine-grained scale may not be critically important, so long as uniformity on a large-grained scale is achieved. Weight is added to this picture of highly turbulent gas motion by the observation in Fig. 24 that the gas humidity at $r \approx 0.5$ in. decreases as the gas goes from $z = 13.5$ in. to $z = 40.5$ in.; this can only be ac-

counted for by the mixing of the very humid gas at $r \approx 0.5$ in. with the much less humid gas near the walls.

Ultimately, the humidity is higher near the walls than at the center. This seems to be the result of the velocity profile in the duct, which grants to droplets near the walls a longer residence time than to those at the center.

Longitudinal Rate of Evaporation. By integrating humidity profiles such as those of Fig. 24, we obtain the open-point curves of Fig. 25, showing now average humidity increases with longitudinal distance. There is evident here the very rapid initial rate of evaporation followed by a decreasing rate which continues

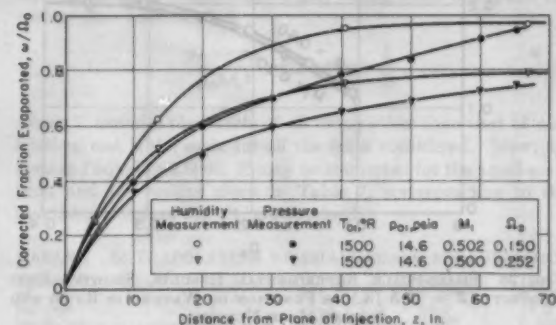


FIG. 25 SMALL-SCALE EXPERIMENTAL RESULTS, SHOWING FRACTION EVAPORATED VERSUS LONGITUDINAL DISTANCE (Open points refer to direct humidity measurements. Closed points are inferred from static pressure data.)

to fall as the stream tends toward saturation. At a given duct position, the specific humidity increases as the water-injection rate is increased. The fraction evaporated, however, decreases as Ω_0 increases because the increased water concentration causes the stream to approach saturation more rapidly.

For the case $\Omega_0 = 0.150$, 50 per cent of the water is evaporated in the first 10 in., and 95 per cent is evaporated in a distance of 40 in. For the case $\Omega_0 = 0.252$, which is slightly greater than the saturation value of about 0.21, approximately 50 per cent of the saturation amount is evaporated in the first 10 in., and about 85 per cent of the saturation amount in 40 in.

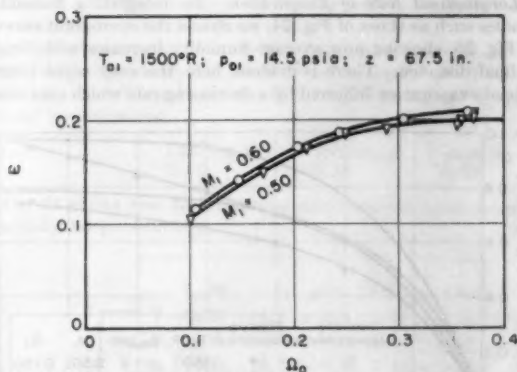
In addition to the direct humidity measurements, it was possible to infer the local fraction evaporated from a knowledge of initial conditions, from the measured local static pressure, and from a one-dimensional analysis involving the equations of continuity, momentum, and energy between the inlet and the section in question (9, 8). Three additional assumptions were necessary, to wit: (a) The droplet moves at the gas speed, (b) the value for the pseudo friction factor used in the analysis may be taken at an average value for f of 0.004, and (c) the droplet temperature is 130 F. With these assumptions the curves marked by the full points in Fig. 25 were obtained. Because of assumption (a), the discontinuity analysis can be fairly accurate only at considerable distance from the inlet. Where the assumption $V_d/V = 1$ is a fairly good one, the validity of the calculated humidity will depend on the choice of the value used for f . With conventional values of the friction factor, this discontinuity analysis leads to values of humidity which are too high. A comparison of the direct humidity data with those inferred from the pressure measurements indicates similar trends and orders of magnitude, with the quantitative agreement improving as z increases.

Total Water Evaporated. Fig. 26 shows how the specific humidity near the end of the duct ($z = 67.5$ in.) varies with water-air ratio (Ω_0) and initial Mach number (M_1).

For a fixed value of M_1 , the exit specific humidity increases

TABLE 6 RESULTS OF FRICTION-FACTOR CALCULATIONS

T_{01} , deg R.....	1500	1500	530	530	1500	1500
p_{01} , psia.....	14.5	10.9	14.7	14.7	14.6	14.6
z_0	0	0	0	0.30	0.15	0.25
M_1	0.597	0.597	0.595	0.500	0.500	0.500
f (discontinuity) analysis.....	0.0034	0.0034	0.0032	0.0035	0.0040	0.0046
f (Fanno-line).....	0.0038	0.0038	0.0035	0.0035	0.0040	0.0046
$\rho_1 V_1 D_1 / \mu_1$	175000	128000	805000	502000	154000	154000
$0.046 (\rho_1 V_1 D_1 / \mu_1)^{-1/4}$	0.0041	0.0044	0.0032	0.0033	0.0043	0.0043

FIG. 26 SMALL-SCALE EXPERIMENTAL RESULTS, SHOWING EXIT HUMIDITY ($Z = 67.5$ IN.) AS FUNCTION OF WATER-AIR RATIO AND INITIAL MACH NUMBER

with Ω_0 because the total amount of heat-transfer surface in the droplet cloud is proportional to Ω_0 . As Ω_0 proceeds above 0.3, however, the exit specific humidity tends to level off owing to the stream having become nearly saturated at a specific humidity of about 0.21, such that the exit humidity can scarcely increase no matter how much water is fed in.

How important a role is played by drop size is shown strikingly in Fig. 26, where it may be seen that for fixed values of T_{01} , p_{01} , and Ω_0 , the exit humidity increases as M_1 increases. This despite the fact that the residence time of the droplets is less at the higher Mach numbers. As shown in Section 1.6, the length required for complete evaporation varies approximately in inverse proportion to the initial Mach number; in a given length the total amount evaporated increases as M_1 increases.

Wall-Friction Factor. In order to interpret the small-scale experimental data and to predict the performance of large-scale units, knowledge of the effective friction factor f is desirable. The value of f may well be different from that for ordinary fully developed pipe flows for several reasons: (a) The water cloud probably tends to make the velocity profile more uniform; (b) evaporation alters the density and viscosity profiles; (c) near the pipe inlet the boundary layer surely does not fill the pipe; (d) in much of the evaporation section the static pressure is rising, which is opposite to the falling pressure characteristic of simple pipe flow; (e) impingement of water on the walls, crashing of droplets into the boundary layer, and tearing of water off the walls, all must have some influence on the skin-friction coefficient. These effects are separate and complex and for the present it is necessary to simply lump them all into an "effective" friction factor.

Values of the effective friction factor under various circumstances were evaluated from three types of experiments:

- 1 Dry runs at low and high temperatures.
- 2 Wet runs at low temperature and therefore with no evaporation.
- 3 Wet runs at high temperature, with considerable evaporation.

For type 1, the friction factor could be determined from the

Fanno-line analysis (reference 2, chapter 6). In addition, a friction factor for all three types could be estimated from a "discontinuity" analysis involving the conservation laws of mass, momentum, and energy between the inlet and exit of the constant-area duct, together with measurements of static pressure and humidity at these stations and with certain assumptions, for example, that at the exit the droplets move at the same speed as the air. Details of the calculations are given in reference (9), and the pertinent results are presented in Table 6. The last two rows in Table 6 represent, respectively, the pipe Reynolds number and the usual friction factor for fully developed turbulent pipe flow at that Reynolds number.

In the dry runs the discontinuity analysis (which involves certain assumptions leading to small errors in the computation of the wall force) yields effective friction factors about 10 per cent less than those of the Fanno-line analysis (which reckons the wall force more accurately). The Fanno-line friction factors, in turn, lie within about 10 per cent of the conventional values for fully developed pipe flows.

The injection of water seems to raise the effective friction factor by some 10 to 20 per cent. Whether by coincidence or otherwise, the effective friction factor for the wet runs is in close agreement with the conventional friction factor for fully developed pipe flow.

3.4 Comparison of Theory and Experiment

We turn now to a comparison of the experimental results of

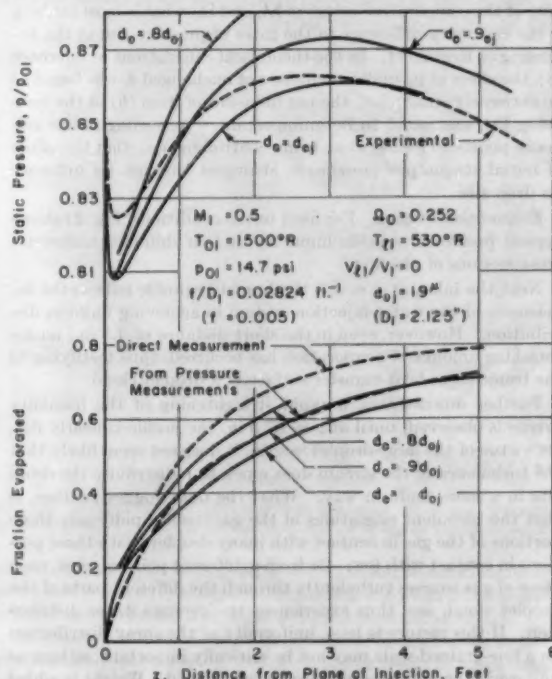


FIG. 27 COMPARISON OF SMALL-SCALE EXPERIMENTAL RESULTS (DASHED CURVES) WITH THEORETICAL CALCULATIONS (SOLID CURVES) FOR COMPLETELY SUBSONIC OPERATION

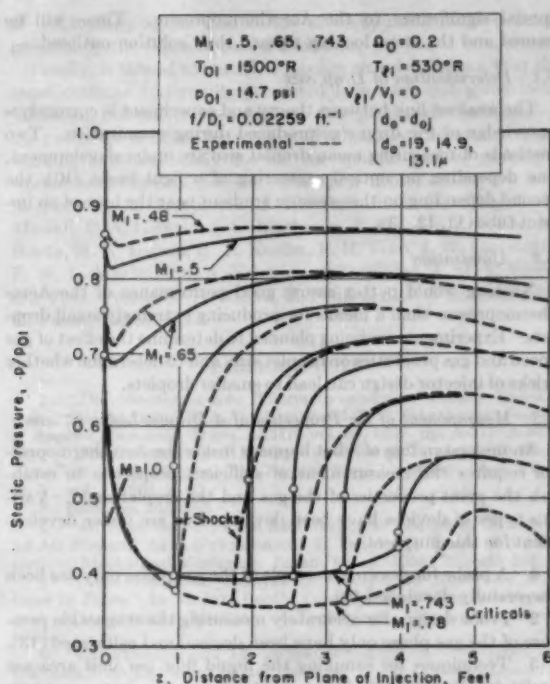


FIG. 28. COMPARISON OF SMALL-SCALE EXPERIMENTAL RESULTS (DASHED CURVES) WITH THEORETICAL CALCULATIONS (SOLID CURVES) FOR SUBSONIC-SUPERSONIC OPERATION

Section 3.3 with those computed using the theoretical method of Section 2.7.

Fig. 27 shows, in addition to the observed curves of Fig. 25 for $\Omega_0 = 0.252$, the corresponding theoretical curves computed with $f = 0.005$ and the Nukiyama and Tanasawa drop size of 10 microns as well as with slightly smaller drop sizes. The measured and theoretical curves are of the same general character, and the agreement is not disappointing when one considers the broad sweep of physical phenomena which the theory attempts to model.

In Fig. 28 are shown the theoretical curves corresponding to the observed critical curves of Fig. 19. The theoretical critical Mach number of 0.74 compares favorably with the measured value of 0.78, and the theory gives a gratifying accurate picture of the different regimes of operation, including the interposition of shocks with subsequent subsonic operation.

These results speak well for the theory as a means of estimating performance of a large-scale unit, and as a basis for determining the optimum area variation.

3.5 Extrapolation of Small-Scale Experimental Data to Larger Sizes

Other things remaining the same, the main effect of increasing the air-flow capacity of the unit is in reducing the importance of the term $4fL/D$ and therefore diminishing the stagnation pressure loss caused by pipe friction. However, it is no easy matter to estimate this size effect, as a change in pipe friction alters the Mach-number distribution in the test duct, and this in turn modifies the stagnation-pressure changes associated with cooling, drag, etc. The extrapolation can be made only if the Mach-number distributions are the same in the two cases (it is found that humidity distribution is quite insensitive to changes in $4fL/D$).

As the comparatively large wall friction in the small-scale constant-area unit tends to force the Mach number toward unity (Table 4), an equivalent Mach-number distribution in a large-scale unit requires area changes to accomplish the same result. This means that the comparison to be made in the following is between the small-scale constant-area unit and a large-scale unit in which the area is constantly reduced in such a way as to give the same Mach number at each value of s as in the small-scale unit.

Based on the foregoing reasoning, we may proceed as follows. Inasmuch as all the phenomena, except that of wall friction, are alike in the cases considered, we may (using Table 3) express the performance coefficient as

$$\frac{p_{01} - p_{01}}{p_{01} M_1^2} = Y - 2fk \frac{L}{D} \dots \dots \dots [13]$$

where Y includes the effects of all terms other than that of wall friction, and is the same for all the cases considered. Now, assuming f equal to 0.0040, Y may be computed for the small-scale unit, and the results given in Table 7, corresponding to the maximum points of Fig. 21, are obtained.

TABLE 7. EXTRAPOLATION OF SMALL-SCALE PERFORMANCE

T_{01} , deg R.	1200	1500	1800
M_1	0.777	0.780	0.783
p_{01} , psia.	14.7	14.7	14.7
w , lb/sec.	0.755	0.677	0.612
f	0.0040	0.0040	0.0040
D , in.	1.35	1.35	1.35
L/D	2.13	2.13	2.13
Ω_0	34.5	34.5	34.5
Ω_1	0.17	0.24	0.31
$(p_{01} - p_{01})/p_{01} M_1^2$ max.	-0.23	-0.16	-0.13
Y	0.15	0.22	0.25
$L/D = 20$	0.95	1.00	1.02
$L/D = 15$	0.99	1.03	1.05
$L/D = 10$	1.02	1.07	1.08
$L/D = 5$	1.05	1.10	1.12
$L/D = 0$	1.06	1.13	1.15

The results under the dashed line in Table 7 represent extrapolated performance for the large-scale unit.

To gain some estimate of size, we observe from the pressure and humidity data that a length of about 5-ft is required. A diameter of 1 ft would correspond to an air flow of about 25 lb/sec, or that of a gas turbine of about 1500 net horsepower. With $L/D = 5$, a stagnation-pressure reduction at the turbine exit of about 10 per cent is seen from Table 7 to be possible when $T_{01} = 1500$ deg R.

There seems little doubt that the large-scale performance just estimated may be achieved as a minimum. It seems equally likely that considerably better performance is attainable, the reasons being as follows:

1 Only a strange coincidence could assure that the Mach-number distributions involved in the foregoing calculations are the optimum for each combination of p_{01} , T_{01} , Ω_0 , M_1 , and f/D_1 . What is more, in large-scale units the optimum values of Ω_0 , M_1 , and length will surely differ from those in smaller units.

2 The friction factor should be less for large units than for small because of a small favorable pipe Reynolds number.

3 Little attention was given to diffuser design in the small-scale unit, and gains may very likely be won by careful attention to this element of the apparatus.

4 Undesirable effects associated with water near the walls can be minimized in larger units.

Therefore the extrapolations should be considered conservative, and the extrapolated performance of large-scale units shown in the foregoing table as assured levels, with a considerable margin of improvement possible.

As explained before, the extrapolated performance refers to a

large-scale unit having an area variation that will produce the same Mach-number distribution as in the small-scale unit. Considerable practical importance is therefore attached to the question of how much area variation is required to assure the attainment of extrapolated performance. This may be estimated from the influence coefficients in the first line of Table 3. To obtain the same Mach-number variation in a variable-area unit without friction as in a constant-area unit with friction, it is only necessary to set equal to the terms in dA/A and in $4f dz/D$ appearing in the equation for dM^2/M^2 , remembering that the terms involving dw/w will be the same in both instances. Thus we obtain

$$\frac{dA}{A} = -\frac{kM^2}{2} 4f \frac{dz}{D}$$

as the sought-for criterion. Lacking precise information as to the Mach-number distribution in the small-scale unit, we may only compute the over-all change in area in terms of some average value of M^2 . Thus we may write

$$\frac{\Delta A}{A} \cong -\frac{k}{2} \overline{M^2} 4f \frac{L}{D}$$

Taking $k \cong 1.35$, $f = 0.004$, $L/D = 34.5$, and using a value of $\overline{M^2} \cong 0.7$, we obtain $\Delta A/A \cong -0.26$. This means that the exit area must be approximately three fourths of the inlet area in a unit so large that friction is negligible. Whether this is the best area reduction for a large-scale unit remains problematical. The actual manner of area variation required to obtain the Mach-number distribution of the small-scale unit cannot of course be found from this simplified calculation.

4 MEDIUM-SCALE AEROTHERMOPRESSOR EXPERIMENT

At the time of this writing, there is under preliminary test a medium-scale Aerothermopressor, 11 in. diam, with a maximum available air flow of 25 lb/sec. For these preliminary tests the evaporation section is of constant outside diameter and is thoroughly instrumented. Area variations will subsequently be provided by means of internal tapered plugs; this general approach is thought best suited to determining optimum area variation most quickly and economically.

In Section 2 it was shown that the greater portion of the evaporation section should be of diminishing area in order to establish a desirable Mach-number variation. In the small-scale constant-area unit, the comparatively large frictional effects accomplished the same Mach-number variation as that which would result from an area reduction of about one fourth in the absence of friction. Therefore the Mach-number distribution of the medium-scale constant-area unit is less favorable than that of the small-scale constant-area unit. Accordingly, it may be expected that the medium-scale constant-area unit will not have as good performance as the extrapolated performance shown in Table 7.

Despite the handicaps accompanying this medium-scale constant-area unit until mentioned, the preliminary tests have already yielded the gratifying result of a net rise in stagnation pressure of about 3 per cent from the upstream stagnation section to the diffuser exit. What is important here is the positive proof of the Aerothermopressor principle, rather than the smallness of the net rise achieved under unfavorable circumstances. There is every reason to believe that substantial improvements lie ahead, ready to be gained by intelligent control of the cross-sectional area.

5 ASSOCIATED PROBLEMS

The research and development discussed in this report have brought to the fore a number of technical problems which are of

special significance to the Aerothermopressor. These will be named and the steps looking toward their solution outlined.

5.1 Determination of Drop Size

The weakest link between theory and experiment is currently a knowledge of the drop size produced during atomization. Two methods of measuring mean droplet size are under development, one depending on optical scattering of a light beam (10), the second depending on the pressure gradient near the hose of an impact tube (11, 12, 13).

5.2 Atomization

Nothing would better assure good performance of the Aerothermopressor than a means for producing extremely small droplets. Experiments are being planned to determine the effect of gas speed and gas properties on droplet size, and to determine whether tricks of injector design can lead to smaller droplets.

5.3 Measurement of the Properties of a Droplet-Laden Stream

An understanding of what happens inside the Aerothermopressor requires the measurement of sufficient properties to establish the point properties of the gas and the droplet cloud. Various types of devices have been developed or are under development for this purpose:

- 1 A probe for drawing a sample of the gas phase only has been successfully developed (9).
- 2 Probe designs for accurately measuring the stagnation pressure of the gas phase only have been devised and calibrated (13).
- 3 Techniques for sampling the liquid flow per unit area are under development (13, 14).
- 4 A scheme for determining the droplet velocity has received some experimental attention and appears promising (13).

CONCLUSIONS

1 The wide variety of gas-dynamics phenomena observable within the Aerothermopressor are explainable in terms of heat transfer, evaporation, droplet drag, wall friction, and cross-sectional area variation.

2 Experiment and theory both show that the Aerothermopressor can produce a net rise in stagnation pressure with mass flows of about 2 lb/sec or greater.

3 A net rise in stagnation pressure has already been won in a 25-lb/sec unit, and in this size the theory suggests that rises of perhaps 20 per cent are achievable. The latter figure would lead to improvements in both fuel economy and power capacity of a simple gas-turbine plant of about 20 per cent.

4 The theoretical analysis of the Aerothermopressor gives a generally correct picture of its performance.

5 With high subsonic Mach numbers at the inlet, the required length of evaporation section is about 5 ft, and for an initial stagnation temperature of 1500 deg R, the optimum water-air ratio is in the neighborhood of 0.25.

ACKNOWLEDGMENTS

Most of the experimental work described here was carried out under the sponsorship of the Office of Naval Research and Bureau of Ships, and their financial assistance is gratefully acknowledged.

The experimental work has been done in the Gas Turbine Laboratory of M. I. T., with the assistance and co-operation of the laboratory staff.

For the use of the 25-lb/sec air supply, thanks are given to the Fuels Research Laboratory of M. I. T.

All the numerical computations were carried out on Whirlwind I, an electronic, digital computer at the Massachusetts Institute

of Technology. The availability of computer time was made possible by the Office of Naval Research.

Finally, it should be stated, if it is not already obvious, that the considerations and results presented here were not given birth fullblown, but rather were evolved slowly through the stimulating exchange of ideas between staff members and students, all working enthusiastically toward the specific goal of making a workable Aerothermopressor. For their contributions we wish to thank C. A. Templeton, J. R. Wish, R. A. Hawkins, L. V. Mowell, P. A. Gisvold, J. C. Matheson, P. Plender, E. Feher, M. Booth, H. K. Larson, R. E. Kosiba, F. H. Vose, J. W. Carpenter, F. W. L. Martin, 3rd, A. Erickson, J. Dussourd, J. M. McGrew, Jr., V. G. Pesek, G. E. Keeler, J. Fenske, J. B. Cheatham, Jr., H. Foust, and M. Tefft.

BIBLIOGRAPHY

- 1 "The Mechanics and Thermodynamics of Steady One-Dimensional Gas Flow," by A. H. Shapiro and W. R. Hawthorne, *Journal of Applied Mechanics*, Trans. ASME, vol. 69, 1947, pp. A-317-A-336.
- 2 "The Dynamics and Thermodynamics of Compressible Fluid Flow," by A. H. Shapiro, The Ronald Press Company, New York, N. Y., vol. 1, 1954, p. 83.
- 3 *Ibid.*, pp. 255-260.
- 4 "An Experiment on the Atomization of Liquid by Means of an Air Stream," by S. Nukiyama and Y. Tanasawa, *Trans. of the Society of Mechanical Engineers, Japan*, vol. 4, 1938, Reports 1-6.
- 5 "One-Dimensional Analysis of Steady-Flow Air-Water Mixtures in Pipes," by Merson Booth, thesis for Naval Engineering degree, Massachusetts Institute of Technology, Cambridge, Mass., 1953.
- 6 "Experimental and Theoretical Investigation of Subsonic Air Diffusers With Entrained Liquid Droplets," by E. G. Feher, thesis for SM degree, Massachusetts Institute of Technology, Cambridge, Mass., 1953.
- 7 "Evaporation From Drops," by W. E. Rans and W. R. Marshall, Jr., *Chemical Engineering Progress*, vol. 48, 1952, pp. 141-146, 173-180.
- 8 "A Theoretical Investigation of the Thermodynamic and Dynamic Effects of Water Injection Into High-Velocity, High-Temperature Gas Streams," by B. D. Gavril, thesis for ScD degree in Mechanical Engineering, Massachusetts Institute of Technology, Cambridge, Mass., 1954.
- 9 "An Experimental Investigation of a Small Scale Aerothermopressor—A Device for Increasing the Stagnation Pressure of a High-Temperature, High-Velocity Gas Stream by Evaporative Cooling," by K. R. Wadleigh, thesis for ScD degree in Mechanical Engineering, Massachusetts Institute of Technology, Cambridge, Mass., 1953.
- 10 "The Photometric Measurement of Particle Size," by J. B. Cheatham, Jr., thesis for SB degree in Mechanical Engineering, Massachusetts Institute of Technology, Cambridge, Mass., 1954.
- 11 "Measurement of Droplet Size in an Aerosol by a Modified Impact Probe," by G. E. Keeler, thesis for MS degree in Mechanical Engineering, Massachusetts Institute of Technology, Cambridge, Mass., 1954.
- 12 "Investigation of Aerodynamic Droplet Measuring Probe," by V. G. Pesek, thesis for SB degree in Mechanical Engineering, Massachusetts Institute of Technology, Cambridge, Mass., 1954.
- 13 "Theoretical and Experimental Investigation of a Deceleration Probe," by Jules Dussourd, thesis for ScD degree in Mechanical Engineering, Massachusetts Institute of Technology, Cambridge, Mass., 1954.
- 14 "A Sampling Technique for a Measurement of Water-Air Ratio of a High-Speed Spray-Laden Air Stream," by R. E. Kosiba and F. H. E. Vose, thesis for Naval Engineering degree, Massachusetts Institute of Technology, Cambridge, Mass., 1953.

Appendix A

DERIVATION OF INFLUENCE COEFFICIENTS

The analysis is most conveniently carried out by casting the definitions and physical laws applicable to the infinitesimal control volume of Fig. 4 into the form of logarithmic differentials. The gas mixture is assumed to obey the perfect-gas law and the Gibbs-Dalton law, but with variable specific heats.

Definition of Mach Number. For a perfect gas

$$M^2 \equiv \frac{V^2}{C^2} = \frac{V^2 W}{k R T} \quad [14]$$

$$\frac{dM^2}{M^2} = 2 \frac{dV}{V} + \frac{dW}{W} - \frac{dk}{k} - \frac{dT}{T} \quad [15]$$

Perfect-Gas Law

$$p = \rho R T / W \quad [16]$$

$$\frac{dp}{p} = \frac{d\rho}{\rho} + \frac{dT}{T} - \frac{dW}{W} \quad [17]$$

Conservation of Mass. With w the mass rate of flow of the gas phase, and A the net cross-sectional area for gas flow

$$w = \rho A V \quad [18]$$

$$-\frac{dw}{w} = \frac{dw}{w} = \frac{d\rho}{\rho} + \frac{dA}{A} + \frac{dV}{V} \quad [19]$$

Momentum Theorem. Taking account of the pressure and shear forces acting on the control volume, and of the momentum fluxes entering and leaving, we have (Fig. 4b)

$$\begin{aligned} p dA - d(pA) - \tau_w \pi D dz \\ = (w + dw)(V + dV) + (w_1 - dw)(V_1 + dV_1) \\ - wV - w_1 V_1 \end{aligned}$$

Introducing the definition of local skin-friction coefficient

$$\tau_w \equiv f \frac{1}{2} \rho V^2$$

simplifying, and rearranging in dimensionless form with the help of the relation $\rho V^2 = k p M^2$, the momentum equation becomes

$$\begin{aligned} \frac{dp}{p} + k M^2 \frac{dV}{V} + \frac{k M^2}{2} \left(4f \frac{dz}{D} + 2 \frac{w_1}{w} \frac{dV_1}{V} \right) \\ + k M^2 (1 - y) \frac{dw}{w} = 0 \quad [20] \end{aligned}$$

Energy Equation. Considering the heat transfer dQ from the walls and the fluxes of enthalpy and kinetic energy, Fig. 4(c), the first law of thermodynamics is written as

$$w dQ = d(w_2 h_2) + d(w_1 h_1) + d(w_1 V_1^2 / 2) + d(w_2 V_2^2 / 2)$$

For a mixture of perfect gases following the Gibbs-Dalton law

$$\frac{w_2}{w} dh_2 + \frac{w_1}{w} dh_1 = c_p dT$$

Moreover, from continuity

$$w = w_2 + w_1$$

$$dw = dw_2 = -dw_1$$

Combining these, simplifying, and rearranging, the energy equation becomes

$$\begin{aligned} \frac{dT}{T} + (k-1) M^2 \frac{dV}{V} + \left[\frac{h_2 - h_1 + \frac{V^2}{2} (1-y^2)}{c_p T} \right] \frac{dw}{w} \\ - \frac{dQ - \frac{w_1}{w} dh_1}{c_p T} + \frac{w_1}{w} (k-1) M^2 y \frac{dV_1}{V} = 0 \quad [21] \end{aligned}$$

Formation of Influence Coefficients. Equations [15], [17], [19], [20], and [21] constitute five simultaneous linear algebraic equations among twelve differential variables: dM^2/M^2 , dp/p , $d\rho/\rho$, dT/T , dV/V , dW/W , dw/w , dk/k , dA/A , dV_i/V_i , dV_i/V_i , and $[dQ - (w_i/w)dh_i]/c_p T$. Therefore seven of these may be chosen as independent, and the remaining five may be computed from the values of these seven independent variables. For the latter, the last seven are selected, inasmuch as these represent most directly the influence of the duct geometry and of the droplet acceleration and evaporation on the gas properties. Solving the equations simultaneously in the manner outlined, the influence coefficients appearing in the first four lines of Table 3 are obtained.

Gas-Stagnation Temperature. The stagnation temperature of the gas phase alone is defined as the temperature which would be reached if the gas phase were steadily and adiabatically decelerated to zero speed without interacting with the liquid. Placing its exact variation within the scheme of the influence coefficients is complex because k varies during the deceleration. Since the effect of this variation in k is very small, and for the sake of obtaining results simple and instructive in form, a pseudostagnation temperature is defined as in the foregoing, except that the gas is assumed to have constant k during the deceleration. Then (2)

$$T_0/T = 1 + \frac{k-1}{2} M^2 \dots [22]$$

$$\frac{dT_0}{T_0} = \frac{dT}{T} + \frac{\frac{k-1}{2} M^2}{1 + \frac{k-1}{2} M^2} \frac{dM^2}{M^2} + \frac{\frac{kM^2}{2}}{1 + \frac{k-1}{2} M^2} \frac{dk}{k} \dots [23]$$

from which the fifth line of Table 3 is found.

Gas Stagnation Pressure. The stagnation pressure of the gas phase alone is defined as the pressure which would be reached if the gas phase were steadily, reversibly, and adiabatically decelerated to zero speed without interacting with the liquid. As above, we define a pseudostagnation pressure based on the assumption of unchanged k during the deceleration. Then (2)

$$p_0/p = \left(1 + \frac{k-1}{2} M^2\right)^{\frac{k}{k-1}} \dots [24]$$

$$\begin{aligned} \frac{dp_0}{p_0} = \frac{dp}{p} + \frac{\frac{kM^2/2}{1 + \frac{k-1}{2} M^2} \frac{dM^2}{M^2}}{\frac{kM^2/2}{1 + \frac{k-1}{2} M^2} \frac{dM^2}{M^2}} + \left[\frac{\frac{kM^2/2}{(k-1) \left(1 + \frac{k-1}{2} M^2\right)} - \frac{k}{(k-1)^2} \right. \\ \left. \log \left(1 + \frac{k-1}{2} M^2\right) \right] \frac{dk}{k} \dots [25] \end{aligned}$$

from which the seventh line of Table 3 is found.

Mixture Stagnation Temperature. For certain purposes a consideration of the stagnation properties of the mixture of gas and droplets is more revealing than that of the gas phase alone. Here the question arises of how to define the mixture stagnation properties; that is, what are the interactions between the droplets and gas during the fictitious decelerations? After reflection on the various possibilities, what seem most useful are definitions which differ from the previous definitions only in that they take account of the kinetic energy of the droplets. Therefore the mixture stag-

nation temperature is defined as the gas temperature which would be reached if the mixture were steadily and adiabatically decelerated to zero speed with only mechanical (i.e., no heat transfer or evaporation) interactions between the gas and droplets. Then, again using the notion of a pseudostagnation temperature for constant k during the deceleration

$$c_p \theta_0 \equiv c_p T + \frac{V^2}{2} + \frac{w_i}{w} \frac{V_i^2}{2} = c_p T_0 + \frac{w_i}{w} \frac{V_i^2}{2}$$

which, after some manipulation becomes

$$\begin{aligned} \theta_0 &\equiv T \left[1 + \left(1 + \frac{w_i}{w} \frac{V_i^2}{V^2}\right) \frac{k-1}{2} M^2 \right] \\ &= T_0 \left[\frac{1 + \left(1 + \frac{w_i}{w} \frac{V_i^2}{V^2}\right) \frac{k-1}{2} M^2}{1 + \frac{k-1}{2} M^2} \right] \equiv \alpha T \dots [26] \end{aligned}$$

or, in differential form

$$\begin{aligned} \frac{d\theta_0}{\theta_0} = \frac{1}{\alpha} \left(1 + \frac{k-1}{2} M^2\right) \frac{dT_0}{T_0} + (k-1) \frac{M^2 y}{\alpha} \left(\frac{w_i}{w} \frac{dV_i}{V}\right) \\ - \frac{k-1}{2} \frac{M^2 y^2}{\alpha} \left(1 + \frac{w_i}{w}\right) \frac{dw}{w} + \frac{k-1}{2} \frac{M^2 y^2}{\alpha} \frac{w_i}{w} \frac{dW}{W} \\ + \frac{M^2 y^2}{2\alpha} \frac{w_i}{w} \frac{dk}{k} \dots [27] \end{aligned}$$

from which the sixth line of Table 3 is found.

Mixture Stagnation Pressure. Analogously with the mixture stagnation temperature, we define the mixture stagnation pressure as the gas pressure which would be reached if the mixture were steadily, reversibly, and adiabatically decelerated to zero speed with only mechanical interactions between the gas and droplets. For the deceleration to be reversible, the gas alone must first change speed until it is at the same speed as the droplets; then the two phases must decelerate together so slowly that the difference in velocity between the phases is at each point vanishingly small. Since the gas undergoes isentropic changes during the defined process, the pseudostagnation pressure P_0 obtained by ignoring variations in k during the deceleration is found with the help of Equation [26] to be

$$\begin{aligned} \frac{P_0}{p} &= \left(\frac{\theta_0}{T}\right)^{\frac{k}{k-1}} \\ &= \left[1 + \left(1 + \frac{w_i}{w} \frac{V_i^2}{V^2}\right) \frac{k-1}{2} M^2\right]^{\frac{k}{k-1}} \dots [28] \end{aligned}$$

$$\begin{aligned} \frac{dP_0}{P_0} = \frac{dp}{p} + \frac{k}{k-1} \left(\frac{d\theta_0}{\theta_0} - \frac{dT}{T}\right) \\ - \frac{k}{(k-1)^2} \left(\log \frac{\theta_0}{T}\right) \frac{dk}{k} \dots [29] \end{aligned}$$

from which the last line of Table 3 is found.

Appendix B

ANALYSIS FOR APPROXIMATE OPTIMIZATION PROCEDURE IN REGIME II

With the aim of obtaining an explicit and simple design procedure, the following assumptions are made which are approximately valid in Regime II: (a) $y = 1$; (b) T_i is constant; and (c) the influence of the dk/k term on stagnation pressure is negligible. For the purpose to which the present analysis is later

put, a consideration of the gas stagnation pressure p_0 leads down a blind alley (because the analysis would indicate speciously that p_0 could locally be made to rise most rapidly by extreme decelerations which would profit p_0 through the momentum of the droplets), and so we shall deal with the mixture stagnation pressure P_0 .

Approximate Equation for dP_0/P_0

Using the assumptions listed in the foregoing, Table 3 yields for dP_0/P_0 the expression

$$\frac{dP_0}{P_0} = \frac{kM^2}{2} \left[\frac{\left(1 + \frac{k-1}{2} M^2\right) \left(1 + \frac{w_i}{w}\right) \frac{h_0 - h_i}{c_p T_0}}{1 + \left(1 + \frac{w_i}{w}\right) \frac{k-1}{2} M^2} \right. \\ \left. - \frac{1 + \frac{w_i}{w}}{1 + \left(1 + \frac{w_i}{w}\right) \frac{k-1}{2} M^2} \right] \frac{dw}{w} + \frac{kM^2}{2} \left[-4f \frac{dz}{D} \right. \\ \left. + \frac{1 + \frac{w_i}{w}}{1 + \left(1 + \frac{w_i}{w}\right) \frac{k-1}{2} M^2} \frac{dW}{W} \right] \dots [30]$$

In what follows, we shall express dW and dz in terms of dw , and thus we shall obtain an expression showing the amount of stagnation-pressure rise per unit of evaporation.

Introduction of Specific Humidity

Using the definitions of local specific humidity ($\omega \equiv w_0/w_a$) and of initial water-air ratio ($\Omega_0 \equiv w_{00}/w_a$), we may form the following equations relating the mass-flow terms of Equation [30] to the specific humidity

$$1 + \frac{w_i}{w} = 1 + \frac{w_{i0} - w_0}{w_a + w_0} = \frac{w_a + w_{i0}}{w_a + w_0} = \frac{1 + \Omega_0}{1 + \omega} \dots [31]$$

$$\frac{dw}{w} = \frac{dw_0}{w_a + w_0} = \frac{d(w_0/w_a)}{1 + (w_0/w_a)} = \frac{d\omega}{1 + \omega} \dots [32]$$

Change of Droplet Diameter

Assuming the existence of a droplet cloud of uniform size, and that neither further atomization nor agglomeration occurs in Regime II, the number of droplets per unit time passing any section will be unchanged. The mass rate of water flow will therefore be proportional to the cube of the droplet diameter

$$\left(\frac{d}{d_0}\right)^3 = \frac{w_{i0} - w_0}{w_{i0}} = \frac{\Omega_0 - \omega}{\Omega_0} \dots [33]$$

Differentiating, we get

$$dd = -\frac{d_0^3}{3d^2} \frac{dw_0}{w_{i0}} = -\frac{d_0}{3} \left(\frac{\Omega_0 - \omega}{\Omega_0}\right)^{-2/3} \frac{d\omega}{\Omega_0} \dots [34]$$

Evaluation of dW/W

The molecular weight of the mixture of gases is related to the molecular weights of the component species by

$$W = \frac{w_0 + w_a}{w_0/w_a + w_a/w_a} = W_a \frac{1 + \omega}{1 + \omega(W_a/W_0)} \dots [35]$$

Hence Equation [5] becomes, after rearrangement

$$\frac{dW}{W} = \frac{(W_0/W_a) - 1}{(W_0/W_a) + \omega} \frac{d\omega}{1 + \omega} \dots [36]$$

Heat Transfer to Droplet

Since, by assumption, the droplet temperature is unaltered, and the droplet and gas have the same speed, the amount of heat transferred between gas and droplet during the time interval dt may be equated to the enthalpy change of that portion of the droplet which evaporates. Thus

$$h_i \pi d^2 (T - T_i) dt = -\pi d^2 \rho_l \frac{dd}{2} (h_0 - h_i)$$

The distance traveled by the droplet during the time dt is

$$dz = V dt = \frac{M}{\sqrt{1 + \frac{k-1}{2} M^2}} \sqrt{kRT_0}$$

Combining these relations, employing Equations [33] and [34], and expressing the heat-transfer coefficient by the Nusselt number through the definition

$$Nu_T \equiv h_i d / \kappa; \quad h_i = (Nu_T \kappa) / d$$

we get

$$dz = \frac{1}{6(Nu_T)} \frac{h_0 - h_i}{T - T_i} \frac{\rho_l d_0^2}{\kappa} \frac{M}{\sqrt{1 + \frac{k-1}{2} M^2}} \\ \sqrt{kRT_0} \left(\frac{\Omega_0 - \omega}{\Omega_0}\right)^{-1/3} \frac{d\omega}{\Omega_0} \dots [37]$$

Working Formula for $dP_0/P_0 d\omega$

Setting Equations [31], [32], [36], and [37] into Equation [30], simplifying and rearranging, we finally obtain

$$\frac{1}{P_0} \frac{dP_0}{d\omega} = \frac{kM^2}{2} \left\{ \frac{1 + \Omega_0}{1(1 + \omega)^2 \left(1 + \frac{1 + \Omega_0}{1 + \omega} \frac{k-1}{2} M^2\right)} \right. \\ \left[\left(1 + \frac{k-1}{2} M^2\right) \frac{h_0 - h_i}{c_p T_0} - \frac{1 + \omega}{(W_0/W_a) + \omega} \right] \\ - \frac{2}{3} \frac{f/D}{(Nu_T)} \frac{(h_0 - h_i)}{T_0 - T_i} \frac{\sqrt{1 + \frac{k-1}{2} M^2}}{\left(1 + \frac{k-1}{2} M^2\right)} \frac{\rho_l d_0^2}{\kappa} \frac{M \sqrt{kRT_0}}{\Omega_0 \left(1 - \frac{\omega}{\Omega_0}\right)^{1/3}} \right\} \dots [38]$$

Calculation of T_0

Considering the energy equation relating the properties at the Aerothermopressor inlet to those at any section where $y = 1$, we may write

$$w_0 h_{010} + w_{10} h_{10} = w_0 h_{01} + w_{10} h_{11} + w_1 \frac{V^2}{2} + w_2 h_{20} \dots [39]$$

The enthalpy changes may be closely approximated by

$$h_{010} - h_{00} \cong c_{p0}(T_{01} - T_0) \\ h_{10} - h_1 \cong \mathcal{L} + c_{p1}(T_0 - T_{01}) + c_{p2}(T_{01} - T_1) \\ h_{11} - h_{10} \cong c_{p1}(T_1 - T_{01})$$

and the term $V^2/2$ may be expressed as

$$\frac{V^2}{2} = \frac{M^2 kRT_0}{2 \left(1 + \frac{k-1}{2} M^2\right)}$$

Introducing these into the energy equation, the local stagnation temperature may be solved for as

$$T_0 \cong \frac{1 + \frac{k-1}{2} M^2}{(1 + \omega) + (1 + \Omega_0) \frac{k-1}{2} M^2} \times \left[(1 + \omega) T_{01} - \frac{\omega \mathcal{L}}{c_p} - \Omega_0 \frac{c_{pi}}{c_p} (T_i - T_{i0}) - \omega \frac{c_{pe}}{c_p} (T_{01} - T_i) \right] \quad [40]$$

Estimate of Nusselt Number

The value of Nu_T depends upon the relative Reynolds number between droplet and gas stream (7). If γ were exactly unity, this Reynolds number would be zero, and Nu_T would be 2.00. Although γ may be so close to unity that it may be so assumed for the purpose of Equation [30], its deviation from unity may generate a sufficiently high Reynolds number to give Nusselt numbers substantially greater than 2.00. To find the local value of Nu_T , therefore, would require integrating the entire set of governing equations of the Aerothermopressor after the manner of Section 2.7. But this is exactly what we wish to avoid in the present simplified design method. Fortunately, the numerical integrations of the type of Section 2.7 show that in Regime II, the value of Nu_T lies between 2 and 4, thus setting upper and lower limits on Nu_T which are not excessively apart.

Method of Constructing Curves of $dP_0/P_0 d\omega$

Suppose that in a given case the conditions at the Aerothermopressor inlet, i.e., T_{01} , Ω_0 , and d_0 , are known. In Regime II the value of T_i may be set equal to the average wet-bulb temperature, which, for the range of pressures and temperatures encountered, is generally not far from 140 F. A particular value of Nu between 2 and 4 is also selected. In addition, we choose an appropriate average value of f/D , neglecting the variations of diameter, inasmuch as these amount only to some 10 or 20 per cent in the range of interest.

Then, for each combination of M and ω , Equations [38] and [39] allow the value of $dP_0/P_0 d\omega$ to be calculated. Thus it is possible to construct curves of $dP_0/P_0 d\omega$ versus M , with ω as a parameter, as exemplified by the chart of Fig. 7(a).

Appendix C

GOVERNING PHYSICAL EQUATIONS FOR DROPLETS

Consider a single droplet of diameter d , velocity V_i , and temperature T_i , journeying in a gas stream of velocity V , temperature T , pressure p , and specific humidity ω . As the mean distance between droplets is of the order of 10 droplet diameters or more, mutual interactions between the droplets are ignored, and the gaseous medium surrounding each droplet is imagined as infinite in extent.

Droplet Diameter Versus Stream Humidity

Since the droplets are uniform and incompressible, and of unchanged number per unit time, the mass rate of liquid flow at any section is proportional to the cube of the droplet diameter. Thus the local humidity, which is a measure of the loss in liquid mass flow, is given by

$$x \equiv \frac{\omega}{\Omega_0} = 1 - \left(\frac{d}{d_0} \right)^3$$

or, after differentiation, the change in droplet diameter is related to the change in humidity by

$$\frac{dd}{d_0} = -\frac{1}{3} \frac{dx}{(d/d_0)^3} = -\frac{1}{3} \frac{d\omega/\Omega_0}{(d/d_0)^3} \quad [41]$$

Mass Transfer

The reduction in droplet diameter is the result of transfer of mass from the saturated water vapor at the surface of the droplet to the external gaseous medium. The resulting rate of change of mass is expressed in terms of the mass-transfer coefficient, the surface area, and the "driving force" which constitutes the difference in spatial mass concentration

$$-\frac{d}{dt} \left(\frac{\pi}{6} d^3 \rho_l \right) = h_D (\pi d^2) (\rho_{s1} - \rho_{s\infty})$$

which simplifies to

$$\frac{dd}{dt} = -\frac{2h_D}{\rho_l} (\rho_{s1} - \rho_{s\infty}) \quad [42]$$

For the coefficient h_D , we have used the seemingly satisfactory (at least for solid spheres with small temperature differences and mass-transfer rates) correlation of Ranz and Marshall (7)

$$Nu_D = 2 + 0.6(Sc)^{1/4} (Re)^{1/2} \quad [43]$$

where

$$Nu_D \equiv h_D d / \mathcal{D}; \quad Sc \equiv \mu / \rho \mathcal{D}; \quad Re \equiv (\rho d |V - V_i|) / \mu \quad [43a]$$

In evaluating the driving potential, ρ_{s1} is taken as the reciprocal of the specific volume of saturated water vapor at the temperature T_i ; $\rho_{s\infty}$ is computed from the perfect-gas law of mixtures as

$$\rho_{s\infty} = \frac{p}{R_s T} \frac{\omega}{1 + \omega W_a / W_g} \quad [44]$$

Heat Transfer

From a consideration of the first law of thermodynamics, the rate of heat transfer to the droplet is equal to the sum of the rate of enthalpy change of both the evaporated and unevaporated water. Thus

$$h_T (\pi d^2) (T - T_i) = \left(\frac{\pi d^3}{6} \rho_l \right) \frac{d}{dt} (c_{pi} T_i) - \mathcal{L} \frac{d}{dt} \left(\frac{\pi d^3}{6} \rho_l \right)$$

which simplifies to

$$\frac{dT_i}{dt} = \frac{6h_T}{\rho_l c_{pi}} (T - T_i) + \frac{3\mathcal{L}}{c_{pi}} \frac{dd}{dt} \quad [45a]$$

where \mathcal{L} is the latent heat at the temperature T_i . Using Equations [41] and [42], this may be written in the alternate form

$$\frac{dT_i}{dx} = -\frac{1}{c_{pi}(1-x)} \left[\mathcal{L} - \frac{h_T}{h_D} \frac{(T - T_i)}{\rho_{s1} - \rho_{s\infty}} \right] \quad [45b]$$

The heat-transfer coefficient h_T has also been taken from the correlation of Ranz and Marshall (7)

$$Nu_T = 2 + 0.6(Pr)^{1/4} (Re)^{1/2} \quad [46]$$

where

$$Nu_T \equiv h_T d / \kappa; \quad Pr \equiv c_{pi} \mu / \kappa \quad [47]$$

Droplet Acceleration

Employing the conventional definition of drag coefficient for blunt bodies like spheres, we may equate the net force on the particle to the product of mass and acceleration. Thus

$$C_D \left(\frac{\pi}{4} d^2 \right) \frac{\rho}{2} (V - V_i) |V - V_i| = \rho_l \frac{\pi d^3}{6} \frac{dV_i}{dt}$$

from which

$$\frac{dV_1}{dt} = \frac{3}{4} (C_D \text{Rey}) \frac{\mu}{\rho_1 d^2} (V - V_1) \dots [48]$$

In the numerical calculations the well-established correlation between C_D and Rey for solid spheres has been approximated by

$$\left. \begin{aligned} C_D &= 24/\text{Rey} & \text{for } 0 < \text{Rey} \leq 1 \\ C_D &= 24/\text{Rey}^{1/2} & \text{for } 1 \leq \text{Rey} \leq 390 \\ C_D &= 0.45 & \text{for } 390 \leq \text{Rey} < \infty \end{aligned} \right\} \dots [49]$$

Displacement of Droplet

The distance dz along the duct traveled by the droplet cloud in the time dt is given by

$$dz/dt = V_1 \dots [50]$$

Appendix D

APPROXIMATE DISCONTINUITY ANALYSIS

Governing Integral Equations

Let section 1 be the inlet plane and section 2 the exit plane of the Aerothermopressor, and let the entire water input be evaporated completely at section 2 (it is known from other considerations that excess water has little effect on performance). Then we may write the following conservation equations between sections 1 and 2:

Energy

$$(h_{0e2} - h_{0e1}) + \Omega_0(h_{0e2} - h_{0e1}) + \Omega_0(h_{0e1} - h_{11}) = 0$$

or

$$(1 + \Omega_0)c_{p12}(T_{0e} - T_{01}) = -\Omega_0(h_{0e1} - h_{11})$$

$$\frac{T_{0e}}{T_{01}} = \frac{T_2}{T_1} \frac{1 + \frac{k_2 - 1}{2} M_2^2}{1 + \frac{k_1 - 1}{2} M_1^2} = 1 - \frac{\Omega_0}{1 + \Omega_0} \frac{h_{0e1} - h_{11}}{c_{p12}T_{01}} \dots [51]$$

Continuity

$$\frac{V_2}{V_1} = (1 + \Omega_0) \frac{\rho_1}{\rho_2} \frac{A_1}{A_2} \dots [52]$$

Definition of Mach Number

$$M_1^2 = \frac{V_1^2 W_1}{k_1 R T_1}; \quad M_2^2 = \frac{V_2^2 W_2}{k_2 R T_2} \dots [53]$$

Equation of State

$$\frac{\rho_2}{\rho_1} = \frac{W_2}{W_1} \frac{T_1}{T_2} \frac{p_2}{p_1} \dots [54]$$

Momentum Equation. Omitting wall friction for the present

$$p_1 A_1 - p_2 A_2 + \int_1^2 p dA = - \int_1^2 A dp = \rho_1 A_1 V_1 [(1 + \Omega_0)V_2 - V_1]$$

To compute the definite integral requires a detailed knowledge of the drop history, which we are here avoiding. As shown by Wadleigh (9), the results are insensitive to the way in which A varies with p , and so we have arbitrarily chosen a linear variation

$$\frac{dp}{dA} = \text{const} = \frac{p_2 - p_1}{A_2 - A_1}$$

Evaluating the integral in the momentum equation, and simplifying, we get

$$\frac{p_2 - p_1}{k_1 p_1 M_1^2} = \frac{2}{1 + \frac{A_2}{A_1}} \left[1 - (1 + \Omega_0) \frac{V_2}{V_1} \right] \dots [55]$$

Stagnation Pressure. The well-known isentropic relation gives

$$\frac{p_0}{p} = \left(1 + \frac{k-1}{2} M^2 \right)^{\frac{k}{k-1}} \dots [56a]$$

As shown in reference (2), page 95, the isentropic stagnation pressure may also be expressed approximately, at least in terms up to order M^4 , as

$$\frac{p_0 - p}{p} = \frac{k M^2}{2} \left(1 + \frac{M^2}{4} + \dots \right)$$

Retaining only the terms of order M^2 , we may form

$$\frac{(p_{02} - p_{01})_\infty}{k_1 p_1 M_1^2} \cong \frac{p_2 - p_1}{k_1 p_1 M_1^2} + \frac{1}{2} \frac{p_2}{p_1} \frac{k_2 M_2^2}{k_1 M_1^2} - \frac{1}{2} \dots [56b]$$

where the subscript infinity here refers to infinite duct size, for which the wall friction is indeed zero.

First-Order Solution. Explicit algebraic solution of the foregoing set of equations for

$$(p_{02} - p_{01})/k_1 p_1 M_1^2$$

seems impossible. For low Mach numbers, however, such a solution may be approximated. Having in mind the assumption of low Mach numbers, we may, according to Equation [55], set $p_2/p_1 \cong 1$ in Equations [54] and [56]; and we may further set $T_{0e}/T_{01} \cong T_2/T_1$ in Equation [51]. Algebraic combination of Equations [52], [53], and [54] then yields

$$\frac{k_2 M_2^2}{k_1 M_1^2} \cong (1 + \Omega_0) \left(\frac{A_1}{A_2} \right) Z \dots [57]$$

where

$$Z \equiv (1 + \Omega_0) \frac{A_1}{A_2} \frac{W_1}{W_2} \frac{T_2}{T_1} \dots [58]$$

In addition, algebraic combination of Equations [52], [54], and [55] produces

$$\frac{p_2 - p_1}{k_1 p_1 M_1^2} \cong \frac{2}{1 + \frac{A_2}{A_1}} [1 - (1 + \Omega_0)Z] \dots [59]$$

The calculation procedure is now as follows, for given values of

$$M_1, T_1, \Omega_0, \text{ and } A_2/A_1$$

(a) T_2 is calculated from the low Mach-number approximation for Equation [51].

(b) $k_2 M_2^2/k_1 M_1^2$ is calculated from Equation [57].

(c) $(p_2 - p_1)/k_1 p_1 M_1^2$ is calculated from Equation [59].

(d) $(p_{02} - p_{01})_\infty/k_1 p_1 M_1^2$ is calculated from Equation [56b].

Exact Discontinuity Solution. If more accurate results than those obtainable from the low Mach-number analysis are desired, trial-and-error solution of Equations [51], [52], [53], [54], [55], and [56a] is necessary, the approximate solution serving as a useful starting point. First we derive several required formulas.

Eliminating V_1/V_2 from Equation [55] with the help of Equations [52] and [54], we obtain

$$\frac{p_2 - p_1}{k_1 p_1 M_1^2} = \frac{2}{1 + \frac{A_2}{A_1}} \left\{ 1 - \frac{(1 + \Omega_0)Z}{1 + \frac{2k_1 M_1^2}{1 + \frac{A_2}{A_1}} [1 - (1 + \Omega_0)Z]} \right\} \quad [60]$$

Solution of this for p_2/p_1 yields

$$\frac{p_2}{p_1} = 1 + \frac{2k_1 M_1^2}{1 + \frac{A_2}{A_1}} \left\{ 1 - \frac{(1 + \Omega_0)Z}{1 + \frac{2k_1 M_1^2}{1 + \frac{A_2}{A_1}} [1 - (1 + \Omega_0)Z]} \right\} \quad [61]$$

Then, employing Equations [60], [52], and [54], the value of $k_2 M_2^2/k_1 M_1^2$ may be found from Equation [53] as

$$\frac{k_2 M_2^2}{k_1 M_1^2} = \frac{(1 + \Omega_0) \frac{A_1}{A_2} Z}{\left\{ 1 + \frac{2k_1 M_1^2}{1 + \frac{A_2}{A_1}} [1 - (1 + \Omega_0)Z] \right\}^2} \quad [62]$$

The exact expression for the stagnation pressure ratio may be found from Equation [56a] as

$$\left(\frac{p_{02}}{p_{01}} \right) = \frac{p_2}{p_1} \left(\frac{1 + \frac{k_2 - 1}{2} M_2^2}{1 + \frac{k_1 - 1}{2} M_1^2} \right)^{k_2/(k_2 - 1)} \quad [63]$$

in which the value of p_2/p_1 is that given by Equation [51].

Assuming that values of M_1 , T_1 , Ω_0 , and A_2/A_1 have been selected, the numerical calculations may be carried out in the following order:

- Guess M_2 , using the low Mach-number analysis as a guide.
- Compute the corresponding T_2 from Equation [51].
- Evaluate Z from Equation [58].
- Check whether the guessed value of M_2 is correct by computing M_2 from Equation [62].
- Using the value of M_2 from Equation [62], repeat steps (a) to (d) until satisfactory convergence is obtained. Only two trials are usually necessary.
- Calculate $(p_2 - p_1)/p_1$ from Equation [60].
- Solve Equation [63] for (p_{02}/p_{01}) .

Effects of Wall Friction and Diffuser Loss. We may now take account of wall friction in a manner which is in the same vein as the approximations already made. Taking note of the influence coefficients of Table 2, the change in p_0 associated with wall friction may be expressed as

$$\frac{(p_{02} - p_{01})_f}{p_{01}} \cong - \frac{k \bar{M}^2}{2} 4f \frac{L}{D} \quad [64]$$

where $k \bar{M}^2$ is the arithmetic mean of $k_1 M_1^2$ and $k_2 M_2^2$.

Besides wall friction, there is a loss in the diffuser which may be expressed as a per cent loss of stagnation pressure in terms of a loss coefficient ϵ

$$\epsilon = - \frac{(\Delta p_0)_{diff}}{\frac{1}{2} k_2 p_2 M_2^2} \quad [65]$$

Linearly superposing the losses due to wall friction and the diffuser on the previous results, we obtain

$$\frac{p_{02} - p_{01}}{k_1 p_1 M_1^2} \cong \frac{(p_{02} - p_{01})_e}{k_1 p_1 M_1^2} - \frac{1}{2} \frac{k \bar{M}^2}{k_1 M_1^2} \frac{p_{01}}{p_1} 4f \frac{L}{D} - \frac{\epsilon}{2} \frac{k_2 M_2^2}{k_1 M_1^2} \frac{p_2}{p_1} \quad [66]$$

Discussion

D. H. DICKSTEIN.⁷ In this paper a very complex phenomenon has been given a very thorough treatment. The phenomenon has been taken apart, examined, and the numerous aspects of its inner workings clearly distinguished from one another in an excellent fashion as one could wish at this time. The paper is an excellent application of analysis and its tool, high-speed computing, to a problem which otherwise would have been quite mysterious and which would have required experimental work of mammoth scope.

Faced with the same basic problem, within the past year the writer has solved the same equations as those solved in this paper. However, the wealth of interpretation of the solutions and the precise experimental work validating the theory of the paper came as a welcome surprise. The writer took the equations describing gas flow with evaporation, friction, etc., from the paper of Shapiro and Hawthorne and developed three equations describing evaporation of the liquid spray. These three equations are identical to those of the paper.

Solutions to the three drop equations—heat transfer, mass transfer, and Newton's law—plus seven of Shapiro and Hawthorne's equations were obtained using the automatic computing facilities at Evendale, Ohio. Thus the history of the evaporating spray traveling along a duct was obtained.

As emphasized in the paper, decreasing the initial drop size is of prime importance in shortening the time required for vaporization, and consequently maximizing performance. Therefore work is in order toward devices to inject minimum size drops.

R. E. ENGLISH.⁸ This investigation of the Aerothermopressor is an impressive one. The salient characteristics of the Aerothermopressor in improving the gas-turbine cycle appear to be as follows:

- 1 With a comparatively small addition to engine volume and weight, this mechanically simple device will increase both the power per unit size and thermal efficiency of a simple gas-turbine engine.
- 2 The gains in thermal efficiency are not as large as obtainable by means of other devices, such as a regenerator.
- 3 For good performance, the rate of water flow is about ten times the rate of fuel flow.

Use of an Aerothermopressor is thus most advantageous in those applications for which a large water supply is readily available and for which bulk and weight supersede the desire for highest thermal efficiency. Ships and locomotives appear to be the most likely beneficiaries. The high liquid consumption rules out aircraft and automobiles, and for central power stations the requirement of highest thermal efficiency will predominate.

The authors state the principle that theoretical understanding occasionally leads to evolution of a different mechanical arrangement that results in improved performance. This principle can be applied to increase thermal efficiency over that obtained with the Aerothermopressor. As Table 2 implies, large gains in thermal efficiency are potentially obtainable by reversible evaporation of

⁷ Fluid Mechanics Unit, Aircraft Gas Turbine Division, Aerodynamics, General Electric Company, Cincinnati, Ohio.

⁸ Aeronautical Research Scientist, National Advisory Committee for Aeronautics, Cleveland, Ohio.

water to cool the exhaust gases. But, as the authors phrase it, "It does not seem possible in a real Aerothermopressor even to approach the reversible mixing of air and water upon which Table 2 is predicated." A different mechanical arrangement might permit a closer approximation of reversible evaporation. One such possibility is to extend the expansion in the turbine to a pressure considerably below atmospheric pressure. A portion of the water could be injected into this low-pressure gas stream and the resulting cooled mixture compressed a small amount by an engine-driven compressor. Additional injections of water could be followed by additional compressions until atmospheric pressure is reached. If the energy of the initial expansion were delivered to a turbine rather than being stored in kinetic energy, the losses resulting from droplet drag and wall friction could be greatly reduced. Less rapid evaporation of the water would then be acceptable, and the reversible process would be more closely approximated.

R. V. KLEINSCHMIDT.¹ On reading this paper the writer was reminded of the old definition of a physical chemist as "a person who made very inaccurate measurements on very impure substances." The authors appear to have made a rather futile mathematical analysis of a device whose practical utility the writer seriously questions. The writer does not mean to blame the authors for this, as the subject is one of those intriguing invitations to "beat the game" which are great fun to play with, but which leave us empty-handed and frustrated.

The writer first studied their work over a year ago, and the main advance since that time seems to be a laboratory demonstration of the fact that a slight rise in stagnation pressure is possible. To the writer this seems quite obviously possible. Whether a practical application can be achieved the writer regards as highly questionable, especially in view of the high temperatures and large amounts of water involved.

The paper is full of strange inconsistencies in thought. For example: Heat exchangers are ruled out because of the influence of friction factor, but in the next paragraph the "analysis will . . . be simplified . . . by assuming that the frictional term of Equation [1] is negligible." Immediately afterward the authors assume that "the liquid is injected with negligible forward velocity," and in the next sentence but one they "ignore" the kinetic energy increase of the injected fluid, these being admittedly the two major forms of loss in the system.

Later in the "Introduction," the amazing statement is made that "Nothing stands in the way of installing a second Aerothermopressor in the turbine exhaust," though the gas at this point is obviously partially saturated by the adiabatic expansion in the turbine of the previously heavily loaded gases from the first Aerothermopressor. Incidentally, anyone familiar with gas-turbine cycles knows that the injection of water in the position of the first Aerothermopressor results in an almost prohibitive loss in efficiency.

In Section 2.1 the authors propose "a hypothetical apparatus having no thermodynamic irreversibilities." The writer would very much like to know how they propose, even hypothetically, to inject water into a hot-gas stream "reversibly." The writer's brand of thermodynamics requires that some regard be paid to the facts of life. At the end of the section the authors do, in effect, apologize for this approach, but why put it in at all? The writer is also amused by the naïve little sentence at the end of the first paragraph of Section 2.2, and in the next paragraph, "the droplets are assumed to be of uniform size," is a condition, the attainment of which would be worth many times the possible

value of any Aerothermopressor. The writer need not weary the reader with further examples.

The real trouble with this paper is a very serious and basic one in our whole approach to engineering in educational institutions. We are so enamored of the solving of mathematical equations, that we teach our students that any distortion of the facts is worth while just so long as we can thereby integrate the differential equation. We must use mathematics to show that we know how to use it whether it is useful or not.

Seriously, the writer feels that our young engineers should be taught to analyze problems in physical terms and in economic terms before they spend months in detailed analysis. In Section 2.6 the authors have given a good engineering analysis of the real problems of design and performance. These and the experimental results presented are, to the writer altogether discouraging, in comparison with other ways of improving gas-turbine efficiency. The writer gravely doubts if the results, here presented, are worth the very substantial expenditure of public funds that was required to obtain them.

AUTHORS' CLOSURE

The authors thank Mr. Dickstein for his complimentary remarks and agree that research aimed at atomization with minimum-drop size is well worth while.

Mr. English's summary of the salient characteristics of the Aerothermopressor as applied to a gas-turbine cycle is endorsed by the authors. Besides ships and locomotives, however, there are certain types of stationary installations, those having a low-load factor, where the low cost and increased-power capacity of the Aerothermopressor may make it economically more suitable than a regenerator.

It is quite true, as Mr. English mentions, that the energy in the exhaust gas may also be utilized by installation of an auxiliary turbine, cooler, and auxiliary compressor. The work of the auxiliary turbine exceeds that of the auxiliary compressor, and thus the net fuel economy is improved. The cooling may be done in a conventional surface heat exchanger, or by evaporation of water at low speeds and virtually static conditions, or by evaporation of water at high gas speeds with a concurrent rise in total pressure. A cycle scheme of this type was patented some thirty years ago. It goes without saying that such an arrangement adds very greatly to the complexity of the plant and increases rather than decreases the capital cost per unit of net horsepower installed. On the other hand, it will undoubtedly yield a considerable improvement in fuel economy. Now that gas-turbine-power sets have found some small place in the industrial spectrum of prime movers, it would seem well worth while to study this cycle arrangement from the points of view of capital cost, fuel economy, and flexibility in operation.

The authors approach their reply to Dr. Kleinschmidt's discussion with incredulity, embarrassment, and diffidence: Incredulity, because it hardly seems possible that a mature engineer of some standing would allow so irresponsible and venomous a statement to be printed over his name. Embarrassment, because the discussion is more revealing of the spirit in which it was written than of anything connected with the paper. And diffidence, because additional valuable journal space must be used to reply to a discussion apparently composed of errors and bias in equal parts.

It seems best to begin with the third, fourth, and fifth paragraphs of Dr. Kleinschmidt's discussion, for these contain definite technical statements with which one can at least come to grips frontally. These paragraphs bear a common stamp: Every statement in them is either wrong or misleading.

Dr. Kleinschmidt finds it "a strange inconsistency in thought" that heat exchangers are ruled out as a means of obtaining a rise

¹ Consulting Engineer, Stoneham, Mass. Life Mem. ASME.

in total pressure because of friction, while in the next paragraph the "analysis will . . . be simplified . . . by assuming that the frictional term of Equation [1] is negligible." This feeling on Dr. Kleinschmidt's part can only mean that he does not realize that an Aerothermopressor and a heat exchanger are altogether different in construction and principle of operation. In a surface heat exchanger, the heat transfer and the wall friction go hand in hand at every element of tube surface. With a certain amount of cooling goes an inevitable amount of wall friction, and the latter always produces a loss in total pressure greater than the gain produced by the cooling. In the Aerothermopressor, on the other hand, the cooling of the gas stream does not occur at the wall of the duct, and there is no inescapable connection between the amount of cooling and the amount of wall friction. For successively larger units, in fact, the total pressure loss due to wall friction becomes progressively smaller. The analysis in question is one where the object was to determine whether the gain in total pressure due to cooling could ever exceed the inescapable loss in total pressure due to the acceleration of the liquid droplets. For this purpose, wall friction, which is indeed very small in large units, was omitted from the analysis. The results of the analysis, which are embodied in Table 1, show that with the evaporation of water into air, there is, in fact, a comfortable margin of net pressure rise, and demonstrate that a sufficiently large Aerothermopressor will work. In sum, what Dr. Kleinschmidt finds strangely inconsistent is a statement of the type that oranges are different from apples, or that heat exchangers are different from Aerothermopressors. Incidentally, it is only to obtain the simple criterion of workability of Equation [7] that wall friction is ignored; in the more complete analysis leading to Table 3, and in the numerical calculations, it is taken account of fully.

Dr. Kleinschmidt also finds a strange inconsistency in thought in the assumption that "the liquid is injected with negligible forward velocity," although shortly afterward the authors "(ignore) the kinetic energy increase of the injected fluid," in spite of (quoting Dr. Kleinschmidt) "these being admittedly the two major forms of loss in the system." The complaint here, the authors infer, is not with the conservative assumption of injection with negligible velocity, which leads to an unfavorably large loss of total pressure due to the momentum increase of the water. Rather it is the subsequent neglect, in the energy equation, Equation [4], of the kinetic-energy increase of the water. In Equation [4], the magnitude of the kinetic-energy change of the water is very small compared with the change of enthalpy in the transition from water to steam and the subsequent superheating. For example, the enthalpy change is of the order of 1200 Btu per lb of injected water, while even at a speed of, say, 1300 ft per sec, the kinetic energy increase is only 34 Btu per lb of injected water. The authors feel that an approximation involving less than 3 per cent error is warranted, especially when the object is to arrive at a simple criterion, without lengthy computation, of whether a scheme will or will not work. The analysis in question is again the preliminary one leading to Equation [7] and Table 1; in the more complete analysis leading to Table 3 which later supersedes it, and in the numerical calculations, the kinetic-energy change of the liquid water is, in fact, fully accounted for, but this naturally makes the analysis more complicated. It is well to point out that the velocity change of the injected liquid can not be ignored in the momentum equation, where it is sizeable compared with the other terms in the same equation. For example, a speed of 1300 ft per sec in air at 1000 F corresponds to a momentum flux per unit area almost exactly equal to the static pressure in value. Therefore changes in speed of that magnitude cannot be ignored in terms of its effect on the static pressure. It is the *momentum* increase of the injected water which leads to

the loss of total pressure which is associated with acceleration.

It should not be surprising that what can be ignored for one purpose cannot be ignored for another one. For instance, when water flows steadily through a long pipe we treat it as incompressible; but when a valve is closed at the end, initiating water hammer, the compressibility of the water is central to the treatment of the pressure wave. When we calculate the power output from a steam turbine, we may ignore the change in gravitational potential energy from inlet to exit because it is so small compared with the enthalpy changes; but in a hydraulic turbine the change in elevation is all-important. In the Aerothermopressor, the kinetic-energy change of the injected liquid makes only a tiny contribution to the energy equation, but its momentum change makes a major contribution in the momentum equation.

Dr. Kleinschmidt next finds "amazing" the authors' statement that "Nothing stands in the way of installing a second Aerothermopressor in the turbine exhaust," although, quoting Dr. Kleinschmidt, "the gas at this point is obviously partially saturated by the adiabatic expansion in the turbine of the previously heavily loaded gases from the first Aerothermopressor." If Dr. Kleinschmidt had taken the trouble to perform a simple thermodynamic calculation he would have found that, for a given temperature at turbine exhaust, the presence of water vapor in the turbine exhaust allows *more* rather than less liquid water to be subsequently injected and evaporated before saturation is reached. This may seem paradoxical at first, but the explanation is simple. The presence of water vapor increases the specific heat of the exhaust mixture. This reduces the temperature fall produced by a given amount of evaporation, and since vapor pressure varies rapidly with temperature, more water may thus be evaporated before saturation is reached.

In the same paragraph, Dr. Kleinschmidt says that "anyone familiar with gas-turbine cycles knows that the injection of water in the position of the first Aerothermopressor results in an almost prohibitive loss in efficiency." Here again a few simple calculations might have averted ill-founded conclusions. If, with a fixed-turbine-inlet temperature, the temperature at the combustor exit is increased by burning more fuel, and the gas is then cooled by evaporation of water, the fuel consumption is increased and the power is also increased because of the increased mass flow through the turbine. In the conventional cycle, with no Aerothermopressor effect, the net specific-fuel consumption is increased, and Dr. Kleinschmidt's statement is true. But if the evaporation also increases the total pressure, this augments the turbine power still further. Whether the specific fuel consumption is, on the whole, better or worse than in the simple cycle, then depends on how much rise in total pressure may be realized. Some calculations made by the authors show that there is some possibility of improving the fuel economy with an Aerothermopressor between the combustor and turbine.

Next, Dr. Kleinschmidt attacks thermodynamics itself. He challenges a kind of thermodynamical reasoning which has served engineers long and well when he scornfully refers to the authors' examination of "a hypothetical apparatus having no thermodynamic irreversibilities," and asks that some regard be paid to the facts of life. The authors submit that nothing could be more realistic than to establish what is the maximum performance that one can possibly extract thermodynamically, for then one knows it is futile to hope for more. If the analysis had shown a total pressure rise of no more than ten or twenty per cent with no irreversibilities present, this would immediately have choked off any further effort on the scheme. But since the analysis showed that the limits on performance were far beyond this, it was possible to proceed with the knowledge that one was at least not bucking the thermodynamic facts of life. The authors cannot help but wonder how many times Dr. Kleinschmidt, in the ordi-

nary course of his work, has calculated the power one might get from a steam turbine if there were no friction. What is more, the authors feel that, had they not carried out such an analysis, they would have been criticized (and rightly so) for violating the principle that practical engineers should always determine what is the maximum theoretical performance of which the apparatus they are studying is capable.

In response to Dr. Kleinschmidt's query as to the hypothetical process by which water may be mixed reversibly with a hot-gas stream, the authors will point out that the customary hypothetical frictionless nozzles and diffusers, as well as semipermeable membranes, are involved. The combination of these into a hypothetically reversible device is left to the mechanical ingenuity of Dr. Kleinschmidt.

Many readers will know of the delightful books by Stephen Potter on "Lifemanship" and "Gamesmanship." More recently he has published an article on the principles of "Reviewmanship," and it is to be hoped that this will soon be followed by one on "Discussmanship." Mr. Potter will find four brilliant examples of the last-named art in the brief space of the fifth paragraph of Dr. Kleinschmidt's discussion.

(1) There is a world of difference between the authors' "considering a hypothetical apparatus having no thermodynamic irreversibilities" and Dr. Kleinschmidt's statement that the authors "propose" such an apparatus. By implying that the authors put forward the reversible device as a practical embodiment, Dr. Kleinschmidt was able to slay the dragon which he had himself created. And, contrary to Dr. Kleinschmidt's statement, the authors did not in the least "apologize" for such an analysis. As pointed out earlier, such an analysis is essential to fixing on the absolute limits of performance, and the authors would have been seriously at fault if they had not carried it out. The principle of Discussmanship illustrated here falls in the general category of: "call the dog a bad name, and then hang him for being bad."

(2) No explanation is given by Dr. Kleinschmidt of precisely what is amusing and what is naive when he states that "The writer is also amused by the naive little sentence at the end of the first paragraph of Section 2.2." This principle of Discussmanship might be described in the general terms: "adopting an air of faint superiority, make politely contemptuous but vague remarks of a veiled nature, with the added implication that only a dolt would fail to understand them."

(3) Dr. Kleinschmidt, in discussing the assumption of uniform drop size, pontificates that "the attainment of (this) would be worth many times the possible value of any Aerothermopressor." The authors note that Dr. Kleinschmidt has not questioned the simplifying assumption of uniform droplet size for purposes of analysis; a further analysis which takes account of the drop-size spectrum shows, in fact, that the assumption of uniform size leads to only minor inaccuracies in the analysis. What Dr. Kleinschmidt does do is a supreme example of another general principle of Discussmanship: "inferentially suggest in innocent language that the authors should have spent their efforts in a different field of research altogether."

(4) Every expert at Discussmanship has one final ace up his sleeve. Dr. Kleinschmidt is not found wanting. When every trick has been played, and the bag is quite empty, the practiced Discussman ends casually with some artfully considerate phrase such as Dr. Kleinschmidt's: "The writer need not weary the reader with further examples."

One can only admire Dr. Kleinschmidt's omniscient statement that "To the writer a slight rise in stagnation pressure

seems quite obviously possible." It was never obviously possible to the authors, nor to any one of their acquaintance, that energy extraction could produce a rise in total pressure; under static conditions, in fact, cooling tends to produce reductions in pressure. Nor were they ever convinced that a rise was possible until after a great amount of both theoretical and experimental work had been done. Many besides the authors would like Dr. Kleinschmidt to explain why it is "obvious" that some rise in total pressure is possible and why it is also "obvious" that this rise is slight but not great.

Dr. Kleinschmidt considers that "the high temperatures and large amounts of water involved make practical application questionable." There are other grounds on which the practical application of the Aerothermopressor will yet turn, but not these. The temperatures discussed in the paper are those normally to be expected at the exhaust of a gas turbine. The water requirements are not negligible, but they amount to only about one per cent of the condenser-cooling-water consumption in a condensing steam plant of equal-power capacity.

Not content with finding fault with the Aerothermopressor research, Dr. Kleinschmidt must needs overflow with a haymaker swing at "our whole approach to engineering in educational institutions." To the authors this brings to mind the story of the elephant and the blind men, each of whom described the elephant in terms of the one portion of the anatomy which he could feel. There may be some schools guilty of Dr. Kleinschmidt's charges, but in the main such a statement only reflects a lack of knowledge of the facts.

The authors are in no position to discuss Dr. Kleinschmidt's feelings on the question of whether or not the expenditure of public funds on the Aerothermopressor research is justified. But granted that government sponsorship of research is a fact of these times, the authors are fully prepared to argue that a portion of this research is well spent on projects whose success is not assured from the first. Most researches whose end products can be foreseen have a pedantic quality. They are necessary, and they must not be scorned, but it would be fatal not to support at the same time directions of research which, though risky, are bold and unconventional.

It is frightening to realize that, in 1939, there was so little imagination and courage in government support of aircraft-engine research that the amount of work being done on jet engines was minuscule, if not zero. By 1946 all development of piston engines had ceased and all funds went to turbine-engine research, but this happened only because the boldness and vigor of German and British development had made any other course absurd. Fortunately for our safety, a very different attitude imbued the atom-bomb development. By citing these cases the authors do not wish to imply in any way that the Aerothermopressor represents a significant advance. However, the authors do hold that it is to the best interests of the country that unconventional technical ideas founded on sound principles be investigated on a scale of effort in keeping with the potential rewards and the likelihood of success. It is all too easy and, for some, too satisfying, to find reasons why any new idea is foolish and bound to fail. Such an attitude is worse than passivity, for it is hostile to the reasoned enthusiasm which makes engineering developments come to life.

Regarding the Aerothermopressor itself, more work remains to be done before it is known whether it is effective enough to deserve practical application. The authors have enjoyed carrying forward their research on the Aerothermopressor in such a spirit of inquiry and hope that it will be possible to continue the work until the question is reasonably settled.

A New Electrical Analog Method for the Solution of Transient Heat-Conduction Problems

By G. LIEBMANN,¹ ALDERMASTON, BERKSHIRE, ENGLAND

A new resistance-network analog method for the solution of heat-flow problems under transient conditions is described. In this method, electrical networks represent the difference equations which approximate the differential equations governing the problem to be solved. Temperature is represented by voltage, the spatial features of the problem by a network of parallel resistances, and the thermal constants by series resistances. A solution in steps δt of time is obtained by successive readjustments of potentiometers supplying the voltages to the network. The new method is very flexible, the time interval δt and the thermal constants being adjustable during the progress of the work. It can be applied to problems of considerable complexity. One of its outstanding features is its "stability." Accuracies of better than 1 per cent can be obtained.

INTRODUCTION

THE analytical solution of heat-flow problems under transient conditions often proves forbiddingly complicated and sometimes even impossible. In recent years, more and more attention has, therefore, been given to graphical,² numerical,³ and analog⁴ methods. While these methods do not usually lead to solutions of high accuracy, they may give the solutions in a relatively short time and often can deal with problems of greater complexity than is practicable with the analytical methods.

The most general mathematical description of heat conduction in a composite body is the equation

$$\text{div} (K \text{ grad } U) = c\rho \frac{\partial U}{\partial t} \dots \dots \dots [1]$$

subject to given initial and boundary conditions. In Equation [1] U is the temperature, K the thermal conductivity, c the specific heat, ρ the density, and t the time.

The heat capacity ($c\rho$) and thermal conductivity K appearing in Equation [1] may be functions of the co-ordinates (x, y, z) or (r, θ) as well as of the temperature U .

The new electrical analog method described in this paper can deal with any of these conditions, simple or complex. Its main characteristic arises from the fact that it uses finite intervals of

space and time. This distinguishes it from the earlier capacitance-resistance analog method (Beuken, 1937; Paschakis and Baker, 1942), in which finite intervals of space are used, but real time, continuously variable, is used as the independent variable. While the new method does not therefore possess the attribute of an automatically proceeding solution, it allows just for this reason the choice of an arbitrary time scale, which can be changed at will, and it permits the arbitrary interruption of the process of solution to make adjustments to the parameters of the problem. This gives great flexibility to the new method and makes it suitable for attacking problems of considerable complexity. While the new method can deal effectively and speedily with simple cases, it has also been applied successfully to large-scale problems. A brief preliminary account of the method was given at the "General Discussion on Heat Transfer" in London, England, in September, 1951 (Liebmann, 1951). The extension of the method to problems of heat transfer across a surface or of internal heat generation under nonstationary conditions will be discussed in a later paper.

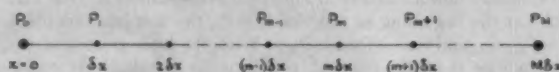


FIG. 1 POINTS AT FINITE INTERVALS δx USED IN DIFFERENCE APPROXIMATION TO PARTIAL DIFFERENTIAL EQUATION

If the body is uniform and isotropic, Equation [1] has the simpler form

$$\nabla^2 U = \frac{1}{D} \frac{\partial U}{\partial t} \dots \dots \dots [2]$$

∇^2 being the Laplacian operator, and in the case of one-dimensional problems, e.g., a slab of width and height large compared with its thickness, this simplifies further to

$$\frac{\partial^2 U}{\partial x^2} = \frac{1}{D} \frac{\partial U}{\partial t} \dots \dots \dots [3]$$

where

$$D = K/c\rho \dots \dots \dots [4]$$

is the diffusivity.

PRINCIPLE OF NEW ANALOG METHOD

The new analog method, basically, is an electrical resistance-network method for solving step-by-step finite-difference equations which are approximations to the partial differential Equations [1] to [3]. The difference equations underlying the analog method are those also used by the author to solve heat-conduction problems numerically by the relaxation technique (Liebmann, 1955); e.g., the finite-difference approximation to Equation [3] is

$$(U_{m-1,n} - 2U_{m,n} + U_{m+1,n})/(\delta x)^2 = (U_{m,n} - U_{m,n-1})/D\delta t \dots [5]$$

where $U_{m,n}$ is the temperature at the point P_m , at the distance $x = m\delta x$ from the boundary $x = 0$, see Fig. 1, at the time $t = n\delta t$

¹ Senior Research Physicist, Associated Electrical Industries, Ltd., Research Laboratory.

² Schmidt, 1924; Jaeger, 1950 (see references at the end of the paper).

³ Schmidt, 1942; Emmons, 1943; Dusenberre, 1945; Eyres, Hartree, Ingham, Jackson, Sarjant, and Wagstaff, 1946; Crank and Nicolson, 1947; Dusenberre, 1949; Allen and Severn, 1951.

⁴ Moore, 1936; Beuken, 1937; Paschakis and Beuken, 1938; Paschakis and Baker, 1942; McCann and Wils, 1949; Coyle, 1951.

Contributed by the Heat Transfer Division and presented at the Diamond Jubilee Semi-Annual Meeting, Boston, Mass., June 19-23, 1955, of THE AMERICAN SOCIETY OF MECHANICAL ENGINEERS.

NOTE: Statements and opinions advanced in papers are to be understood as individual expressions of their authors and not those of the Society. Manuscript received at ASME Headquarters, May 21, 1954. Paper No. 55-SA-15.

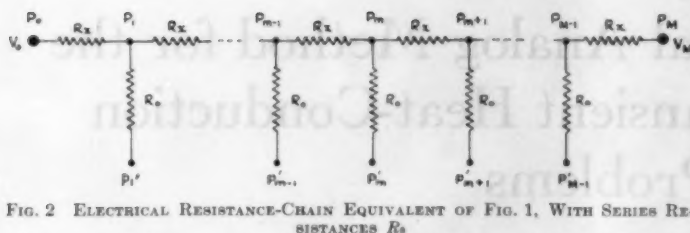


Fig. 2 ELECTRICAL RESISTANCE-CHAIN EQUIVALENT OF FIG. 1, WITH SERIES RESISTANCES R_s

since the beginning ($t = 0$); δx and δt are the finite space and time intervals in which the solution is worked. As discussed in the other paper, the solutions of heat-conduction problems based on Equation [5] are stable for all values of the parameter

$$\alpha = (\delta x)^2 / D \delta t \dots \dots \dots [6]$$

It is shown there that an error ϵ made at the time $(n-1)\delta t$ at the point P_m is, in a first approximation, reduced to an error $\alpha\epsilon/(2+\alpha)$ at the time $n\delta t$ at P_m , but spreads at the same time to the points neighboring on P_m in geometrically decreased manner by the factor $1/(2+\alpha)$; hence single errors become damped out as the solution proceeds, and randomly distributed errors will cancel rapidly.

The high degree of stability of Equation [5] is very advantageous in the new analog method, because the error cancellation just mentioned applies to the experimental errors in the analog measurement of the temperature function. Moreover, as δt may be chosen without any restriction by a stability condition, it may be chosen in such a way that the solution can be completed in relatively few steps.

Consider now a chain of M equal value resistances R_s , see Fig. 2. Let the beginning of this chain be P_0 , the first junction point be P_1 , etc., and the end point P_M . With the later generalization to two or three-dimensional problems in mind, these resistances R_s will be called the "network resistances." To each junction point P_1, \dots, P_m, \dots a resistance of value R_0, \dots is connected, the free terminals of these resistances, called "series resistances," being the points P'_1, \dots, P'_m, \dots . Let the value of R_0 be related to that of R_s by the formula

$$R_0 = \frac{D \delta t}{(\delta x)^2} R_s \dots \dots \dots [7]$$

The chain of resistances R_s may then be considered a one-dimensional "model" of a body in which the heat-conduction phenomena can be fully described by one spatial co-ordinate x and are therefore determined by Equation [3]. The junction points P_1, \dots, P_m, \dots correspond to points $x = \delta x, \dots, x = m\delta x, \dots$ in the real body, the end points P_0 and P_M corresponding to its boundaries. Temperatures are then represented by the voltages in the model, i.e.

$$U_{m,n} = a V_{m,n} \dots \dots \dots [8]$$

where a is a conversion constant, its numerical value depending on the temperature and voltage scales used.

Let the end points P_0 and P_M of the chain of network resistances R_s be connected to potential sources of values V_0 and V_M , corresponding to the prescribed boundary temperatures U_0 and U_M , and voltages $V_{1,0}, \dots, V_{m,0}, \dots$ corresponding to the prescribed initial temperatures $U_{1,0}, \dots, U_{m,0}, \dots$ be applied to the terminals ("feeding points") P'_1, \dots, P'_m, \dots , of the series resistances R_0 . Then the voltages $V_{1,1}, \dots, V_{m,1}, \dots$ will appear at the "network" junctions P_1, \dots, P_m, \dots , and these voltages $V_{m,1}$ will correspond to the temperatures $U_{m,1}$ in the body, represented by the model, at the time $t = \delta t$. If the network voltages

$V_{m,1}$ are measured and the voltages at the terminals P'_m are then made equal to $V_{m,1}$, the voltage $V_{m,2}$ will appear at the network junctions, corresponding to the temperatures $U_{m,2}$ at the time $t = 2\delta t$, and so on. Generally, if the voltages $V_{m,n-1}$, representing the temperatures $U_{m,n-1}$ at the points $x = m\delta x$ at the time $t = (n-1)\delta t$ are applied to the terminals P'_m , the voltages $V_{m,n}$ corresponding to $U_{m,n}$, the temperatures at the time $t = n\delta t$, appear in the network.

To prove this statement, consider the section of the network between points P_{m-1} and P_{m+1} , as shown in Fig. 3. According to Kirchhoff's law

$$\sum_{i=1}^3 i_i = 0$$

where i_1, i_2, i_3 are the currents flowing into the junction point P_m . As

$$i_1 = (V_{m-1,n} - V_{m,n})/R_s, \quad i_2 = (V_{m+1,n} - V_{m,n})/R_s$$

and

$$i_3 = (V_{m,n-1} - V_{m,n})/R_0$$

one has

$$V_{m-1,n} - 2V_{m,n} + V_{m+1,n} = (V_{m,n} - V_{m,n-1})R_s/R_0 \dots [9]$$

This equation is formally identical with the difference Equation [5] if the relative values of R_s and R_0 satisfy the Relation [7].

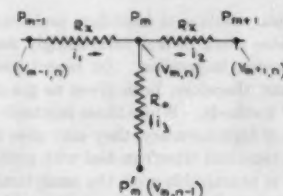


Fig. 3 RESISTANCE-NETWORK STAR AT POINT P_m (FIGS. 1 AND 2) SHOWING BRANCH CURRENTS i_1, i_2 , AND i_3

Hence the voltage relations in the described network model represent the difference Equation [5] which approximates the partial differential Equation [3], within close limits, set by the accuracy of voltage measurements and the tolerances of the resistance values (see section Experimental Tests).

The solution of a heat-conduction problem by the described analog model has therefore essentially the characteristics imposed by the finite-difference approximation, Equation [5]; i.e., the solution is subject to the truncation errors $O(\delta x)^2$ and $O(\delta t)$ of this approximation, but it is stable for any value of δx or δt chosen to work out the solution of the problem. In particular, it is possible to reset at will the value of δt , by readjusting the values of the resistances R_0 during the progress of the work.

PRACTICAL REALIZATION OF ANALOG METHOD

A practical realization of the discussed resistance-network analog method is achieved by adding the required voltage sources and a measuring circuit to the network shown in Fig. 3. This results in the electrical-circuit arrangement of Fig. 4. The voltages $V_{m,n-1}$ are provided by a number of low-resistance potentiometers (slide wires) $\dots D_m \dots$, the tapping points of the potentiometers being connected to the terminals P'_m of the $R_{0,m}$ resistances. These potentiometers are connected across a voltage source E . The network or potentiometer voltages are measured

by connecting a probe Pr to the network stud or potentiometer tapping where the measurement is desired and adjusting the tapping point of the potentiometer bridge B , or of the potentiometer D_m so that the meter M shows no current flowing through the probe circuit. The network voltages are therefore expressed in relative units, the relative terminal voltage of the source E having the value $V = 1$.

If the boundary temperature at P_0 is a function of the time, the potentiometer D_0 is appropriately readjusted after the required number of time intervals δt .⁵

A modification of the network arrangement, Fig. 4, which gives greater working speed, is shown in Fig. 5. The potentiometers D_m are duplicated (denoted by D_m' and D_m'') and a change-over switch S_m is provided. Instead of measuring all network voltages $V_{m,n}$ with the help of the bridge B , recording the results and then resetting all potentiometers D_m from their previous settings $V_{m,n-1}$ to the values $V_{m,n}$, the second potentiometer D_m'' which is not in circuit, of each pair D_m' and D_m'' , is balanced directly against the network voltage $V_{m,n}$. When this has been done for all potentiometers D_m'' , all switches S_m are simultaneously switched over so that now the potentiometers D_m'' , set to the voltages $V_{m,n}$, are in circuit. At the network nodes P_m the voltages $V_{m,n+1}$ have appeared through this, and the potentiometers D_m' , which are not in circuit now, are balanced to these new values $V_{m,n+1}$. Then the switches are changed over again and so on. Network voltages are only recorded where and when required.⁶

EXPERIMENTAL APPARATUS FOR APPLICATION OF METHOD

An experimental apparatus was constructed to study the practical application of the method as described in the foregoing sections. The apparatus comprises the complete equipment, including measuring circuits, etc., with the exception of the resistance network proper. This was done to secure greater flexibility, because it is then possible to use the new apparatus in conjunction with any type of resistance network analog. For instance, the apparatus was used in co-operation with existing linear networks and (x, y) and (r, z) -networks. As the main purpose of constructing the apparatus was to study the method, an apparatus providing for only 41 network points was built.⁷ The experimental model has a height of 38 in. and a width of 30 in. Eighty-two potentiometers D_m' and D_m'' are represented by straight resistance wires (21 SWG Eureka wire) of 25 in. length, strung out above vertical $1/8$ -in.-wide grooves in a vertical bakelite panel. The end contacts are made by pulling the resistance wires over the sharp edges of two heavy horizontal copper bars, let into the bakelite panel, and clamping the ends of the resistance wires down on the copper bars. Good electrical contact is essential as the resistance of the potentiometers must be low compared with the network resistances to avoid interaction of the voltages at the potentiometer sliders which are interconnected through the resistance network. The potentiometer sliders are phosphor-bronze leaf springs carried on $3/8$ -in.-long, $1/8$ -in.-wide brass blocks sliding in the grooves of the bakelite panel and making, in turn, contact with thin copper strips lying at the

⁵ The extension of the resistance-network arrangement of Fig. 4 to the solution of problems involving heat transfer at prescribed rates at boundary points, or heat generated at interior points, requires additional series resistances $R_{0,m}'$, as will be discussed in a later paper.

⁶ The described technique can be turned into an automatic method by providing a servomotor system which carries out automatically the required potentiometer-balancing operations (see British Patent Specification 684, 989).

⁷ An automatic analog apparatus with 200 network points is now under construction.

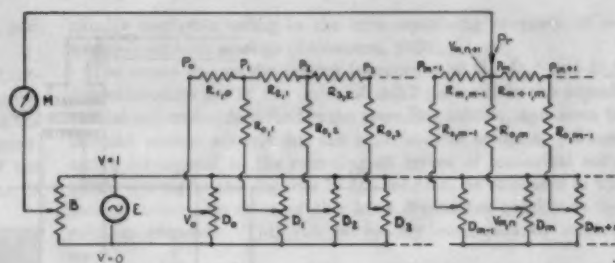


FIG. 4 LINEAR RESISTANCE NETWORK, REPRESENTING SEMI-INFINITE, HEAT-INSULATED BAR, OR SEMI-INFINITE SOLID, WITH PRESCRIBED BOUNDARY TEMPERATURE U_0 REPRESENTED BY VOLTAGE V_0 AT $x = 0$

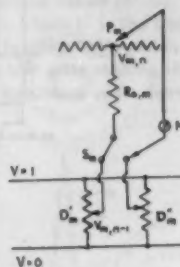


FIG. 5 RESISTANCE-NETWORK USING TWO ALTERNATIVE SETS OF FEEDING POTENTIOMETERS FOR TEMPORARY STORAGE OF TEMPERATURE VALUES

bottoms of the grooves; the contact to these copper strips is made from the back of the bakelite panel.

Horizontal lines are ruled across the front of the bakelite panel, so that the position of the sliders gives a direct reading of the network voltages $V_{m,n}$. Hence, during the operation of the apparatus, the solution of the problem appears in the form of two "graphs," the positions of one set of sliders giving the temperature distribution at the time $n\delta t$ and the positions of the other set of sliders giving the temperature distribution at $(n+1)\delta t$. The two sets of sliders are distinguished by a color code.

The $R_{0,m}$ and $R_{0,m}'$ resistances⁸ are miniature wire-wound adjustable rheostats, arranged in a sloping panel in front of the vertical bakelite panel. Each of these resistances comprises in series a rheostat of 5000 ohms for coarse adjustment, and a rheostat of 120 ohms for fine adjustment, or to represent short-time intervals δt , and so on.

The circuit arrangement of the apparatus is shown in Fig. 6. The $R_{0,m}$ and $R_{0,m}'$ resistances are connected through telephone-jack sockets J_m' and J_m'' . A telephone jack plug J can then be used to insert any of these resistances into the fourth arm of a built-in Wheatstone bridge, the straight wire potentiometer B (of same construction as the D_m' and D_m'' potentiometers) and the multiplier W forming the other arms. In this way, it is easy to reset quickly any of the $R_{0,m}$ or $R_{0,m}'$ resistances during the solution of a problem.

All change over switches S_m (as discussed with reference to Fig. 5) are ganged together, so that the solution can be advanced by δt , after all D -potentiometers have been reset, by operating a single switch lever. This lever operates at the same time an electrical counter which counts the number of switching operations, i.e., the number n of time intervals δt since the beginning. By pressing any of the individual spring-loaded double-pole S_m' switches, one can connect the balance indicator M (an amplifier with miniature cathode-ray-tube indicator) into any of the

$\epsilon = \epsilon_1 + \epsilon_2$ in the type of problem solved by Equation [1], particularly at the beginning of the solution (n small).

The experimental errors ϵ_2 can be subdivided into the adjustment errors of the D_m' and D_m'' potentiometers during the progress of the solution, and the errors arising in the setting up of the model, i.e., the errors in the values of the R_s and R_0 resistances. The influence of the errors occurring in the setting up of the model, which lie in practice in the range 0.2 to 1 per cent, is

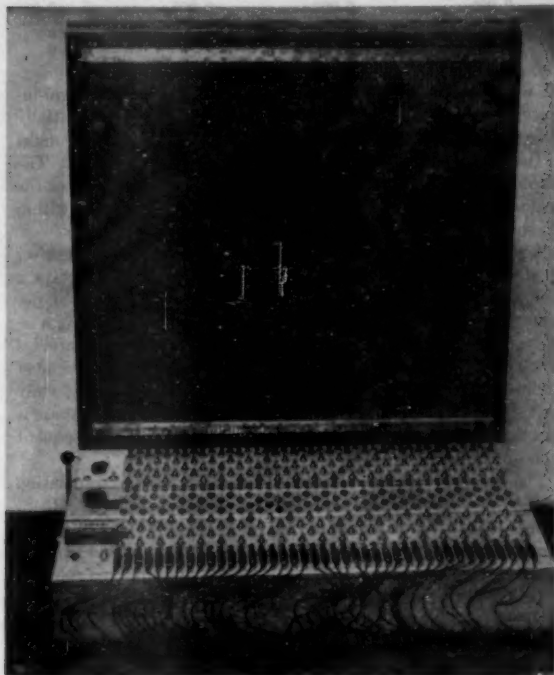


FIG. 7 PHOTOGRAPH OF ANALOG APPARATUS ACCORDING TO FIG. 6. [Sloping panel contains, counting from back to front, switches S_m' , rheostats $R_{s,m}$ (coarse and fine), telephone-jack sockets, J_m' and J_m'' , rheostats $R_{s,m}'$ (coarse and fine), connectors C , and outlet terminals O . The miniature c.r.o. balance indicator M , bridge multiplier W , switch S_m , and an electrical counter for time intervals n are seen near the left end of the sloping panel. Straight wire potentiometers D_m' and D_m'' are visible on vertical panel.]

usually negligible owing to the error-equalizing property of resistance-network analogs (Liebmann, 1950).

The errors due to the setting inaccuracy of the D_m' and D_m'' potentiometers are of the order of ± 0.2 per cent in the experimental apparatus described in the preceding section, and seem to account almost entirely for the experimental errors ϵ_2 . These errors correspond to the rounding-off errors of numerical solutions. Owing to the stability of the solution, as discussed in the second section, an error of this kind diminishes quickly as the solution proceeds. This can be readily confirmed by experiment.

In solving the linear bar problem on the analog apparatus, with $\delta x = 1$ cm, $D = 0.125$ cm²/sec, and $\delta t = 4$ sec, a setting error of 10 per cent, from $U/U_0 = 0.311$ to $U/U_0 = 0.411$, was introduced after $t = 16\delta t$, at $x = 4$, and the solution was thereafter continued in the ordinary way, giving values U'/U_0 . In Fig. 8 the error $\epsilon' = (U'/U_0) - (U/U_0)$, where U is the undisturbed analog solution, is plotted as a function of position x along the bar for several time intervals $n'\delta t$ after making the error.

It is seen that the maximum error decreases, roughly in geo-

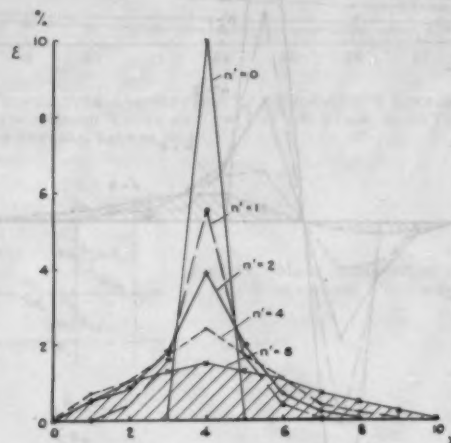


FIG. 8 ERROR ϵ' IN PER CENT OF U_0 AFTER SEVERAL TIME INTERVALS n' DUE TO SINGLE VOLTAGE-SETTING ERROR OF 10 PER CENT AT TIME INTERVAL $n' = 0$ ($D = 0.125$ cm²/sec, $\delta t = 4$ sec.)

TABLE 1 TEMPERATURE DISTRIBUTION IN SEMI-INFINITE SOLID INITIALLY AT ZERO TEMPERATURE

$D = 0.125$ cm²/sec, $\delta x = 1$ cm, $\delta t = 8$ sec, $\alpha = \frac{(\delta x)^2}{D\delta t} = 1$

$\epsilon = (U/U_0)_{\text{max}} - (U/U_0)_{\text{calc}}$ $\epsilon_1 = (U/U_0)_{\text{max}} - (U/U_0)_{\text{calc}}$ $\epsilon_2 = (U/U_0)_{\text{max}} - (U/U_0)_{\text{calc}}$ $\epsilon = \epsilon_1 + \epsilon_2$

$n\delta t$ (sec)	ϵ			ϵ_1			ϵ_2			ϵ		
	$(U/U_0)_{\text{calc}}$	$(U/U_0)_{\text{max}}$	$(U/U_0)_{\text{min}}$	$(U/U_0)_{\text{calc}}$	$(U/U_0)_{\text{max}}$	$(U/U_0)_{\text{min}}$	$(U/U_0)_{\text{calc}}$	$(U/U_0)_{\text{max}}$	$(U/U_0)_{\text{min}}$	$(U/U_0)_{\text{calc}}$	$(U/U_0)_{\text{max}}$	$(U/U_0)_{\text{min}}$
0	1	1	1	0	0	0	1	1	1	0	0	0
1	0.803	0.793	0.792	-0.010	-0.011	0.001	0.901	0.902	0.899	0.001	-0.002	0.003
2	0.617	0.601	0.601	-0.016	-0.016	0	0.803	0.803	0.800	0.000	-0.003	0.003
3	0.453	0.435	0.435	-0.018	-0.017	-0.001	0.708	0.704	0.704	-0.004	-0.004	0.000
4	0.317	0.300	0.303	-0.017	-0.014	-0.003	0.617	0.611	0.613	-0.006	-0.004	-0.002
5	0.211	0.201	0.203	-0.010	-0.008	-0.002	0.532	0.524	0.527	-0.008	-0.005	-0.003
6	0.133	0.128	0.131	-0.005	-0.002	-0.003	0.453	0.446	0.448	-0.007	-0.005	-0.002
7	0.080	0.082	0.082	0.002	0.002	0	0.381	0.378	0.376	-0.003	-0.005	0.002
8	0.046	0.050	0.049	0.004	0.003	0.001	0.317	0.317	0.312	0.000	-0.005	0.005
9	0.024	0.024	0.029	0.000	0.005	-0.005	0.260	0.255	0.256	-0.005	-0.004	-0.001
10	0.012	0.015	0.016	0.003	0.004	-0.001	0.211	0.208	0.208	-0.003	-0.003	0.000
11	0.006	0.009	0.008	0.003	0.002	0.001	0.168	0.168	0.166	0.000	-0.002	0.002
12	0.003	0.005	0.004	0.002	0.001	0.001	0.133	0.133	0.131	0.000	-0.002	0.002
13	0.001	0.003	0.001	0.002	0.001	0.001	0.104	0.103	0.102	-0.001	-0.002	0.001
14	0	0	0	0	0	0	0.080	0.077	0.079	-0.003	-0.001	-0.002
15							0.061	0.057	0.060	-0.004	-0.001	-0.003
16							0.045	0.044	0.045	-0.001	0.000	-0.001
17							0.034	0.035	0.033	0.001	0.001	0.002
18							0.024	0.026	0.024	0.002	0.002	0.002
19							0.018	0.020	0.017	0.002	-0.001	0.003
20							0.012	0.016	0.012	0.004	0.000	0.004
25							0.002	0.005	0.001	0.003	-0.001	0.004
30							0	0	0	0	0	0

TABLE 2 REDUCTION OF SYSTEMATIC ERRORS IN MEASURED TEMPERATURE DISTRIBUTION THROUGH EXTRAPOLATION
(Temperature distribution in semi-infinite solid initially at zero temperature)

$x(\text{cm})$	$D = 0.125 \text{ cm}^2/\text{sec}, \quad \delta x = 1 \text{ cm}, \quad t = 16 \text{ sec}$					
	$(U/U_0)_{\text{calc}}$	$(U/U_0)_{\text{meas}}$	ϵ	$(U/U_0)_{\text{calc}}$	$(U/U_0)_{\text{meas}}$	ϵ
0	1	1	0	1	1	0
1	0.617	0.585	-0.032	0.599	-0.018	-0.004
2	0.317	0.293	-0.024	0.303	-0.014	-0.004
3	0.133	0.135	0.002	0.135	0.002	0.002
4	0.046	0.057	0.011	0.051	0.005	-0.001
5	0.012	0.028	0.016	0.018	0.006	0.004
6	0.003	0.005	0.002	0.005	0.002	0.002
7	0.001	0	-0.001	0.002	0.001	0.003
8	0	0	0	0	0	0
9	0	0	0	0	0	0

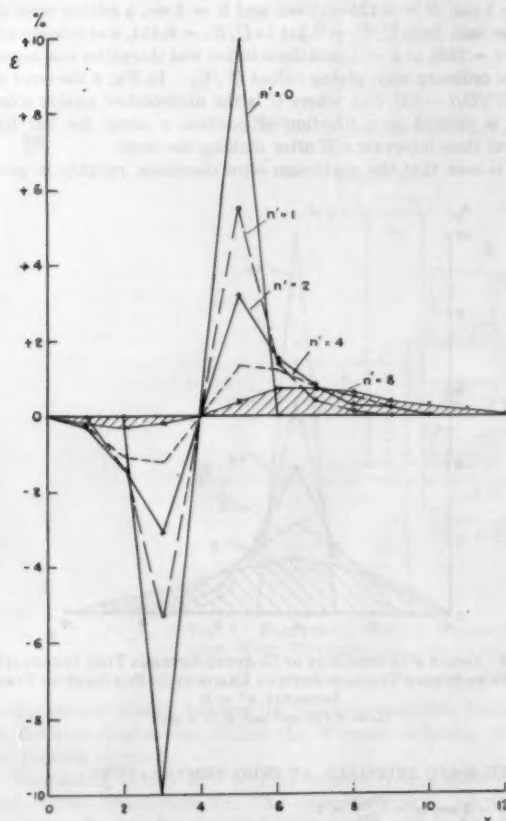


FIG. 9 ERROR ϵ IN PER CENT OF U_0 AFTER SEVERAL TIME INTERVALS n' DUE TO TWO VOLTAGE-SETTING ERRORS OF EQUAL AMOUNT (10 PER CENT) BUT OPPOSITE SIGN AT TIME INTERVAL $n' = 0$
($D = 0.125 \text{ cm}^2/\text{sec}, \delta t = 4 \text{ sec.}$)

metric progression, with the number n' of time intervals since the introduction of the error, while spreading out over more and more adjacent points. The total area under the error curve remains constant, except for some loss of error ("liquidation") at the boundary $x = 0$ ($U = U_0$) for larger values of n' . Hence a local setting error eventually will be spread over all network points, and if there are equal amounts of positive and negative errors, as is probable in most solutions, these will soon cancel. This is illustrated by Fig. 9, in which after $t = 16\delta t$ a negative error of 10 per cent was introduced at $x = 3$, and a positive error of 10 per cent at $x = 5$.

The convergence of the analog solution is illustrated in Fig.

10, which refers to the temperature distribution in a semi-infinite solid, or linear insulated bar ($D = 0.125 \text{ cm}^2/\text{sec}$) initially at temperature $U = 0$, the end of which is suddenly brought to the temperature $U_0 = 1$, at the time $t = 0$ ($n = 0$). The graphs show $|\epsilon|_{\text{max}}$, the maximum error irrespective of sign, of the analog solution which occurs at the time $n\delta t$ anywhere within the solid.

A great range of time intervals was used. It is seen that, after an initial maximum error of a few per cent, there is always a monotonic decrease of the maximum error to well below 1 per cent after a reasonably large number of time intervals, say, $n = 20$, very nearly independently of the length of the time interval δt . This confirms the earlier statement that one can choose, over a wide range, arbitrary values of δt , or of the mesh-size δx . Only for very small values of δt , or more specifically for $\alpha \gg 1$, there is an initial rise in $|\epsilon|_{\text{max}}$ with increasing n before its subsequent monotonic decrease.

The initial error can be reduced greatly by the extrapolation method discussed in the paper on the relaxation solution (Liebmann, 1955). In this method, a problem is first worked with a time interval δt_1 , giving the solution U_1 , and then with a time interval $\delta t_2 = \delta t_1/2$, giving the solution U_2 . An improved solution U_3 is then obtained by adding the difference ($U_2 - U_1$) to U_1 . The degree of improvement is shown by the results of Table 2.

GENERALIZATION OF THE ANALOG METHOD

Practical problems in heat conduction are mostly of a two or three-dimensional nature, and often involve several materials of different thermal properties. Then the more general heat-conduction Equation [1] has to be solved. The analog method discussed in the foregoing is applicable to these more complex problems without appreciable change. The only difference is that now the resistance-network model is of a correspondingly more complicated nature, being, e.g., a two-co-ordinate network model, and that different values of the thermal conductivity K may have to be used in different parts of the model. Also, from a practical point of view, it is often useful to employ unequal co-ordinate intervals; e.g., one uses a coarse mesh where temperatures are expected to change slowly only, and a finer mesh where a rapid temperature change is anticipated, or a complicated shape has to be represented.

The resistance-network representation of the finite-difference approximations to equations of the type of Equation [1], in Cartesian or cylindrical co-ordinates, with locally different values of thermal conductivity K , and unequal mesh sizes or subdivided meshes, has been discussed elsewhere (Liebmann, 1954). The equation considered there is $\text{div } K \text{ grad } U = g$, and the results given can be directly transferred through replacing $g = g_0$ at the point P_0 at the time $n\delta t$ by

$$[cp(\partial U/\partial t)]_{P_0} = (cp)_0(U_{0,n} - U_{0,n-1})/\delta t$$

where $(cp)_0$ is the averaged value of cp within the volume element surrounding P_0 .

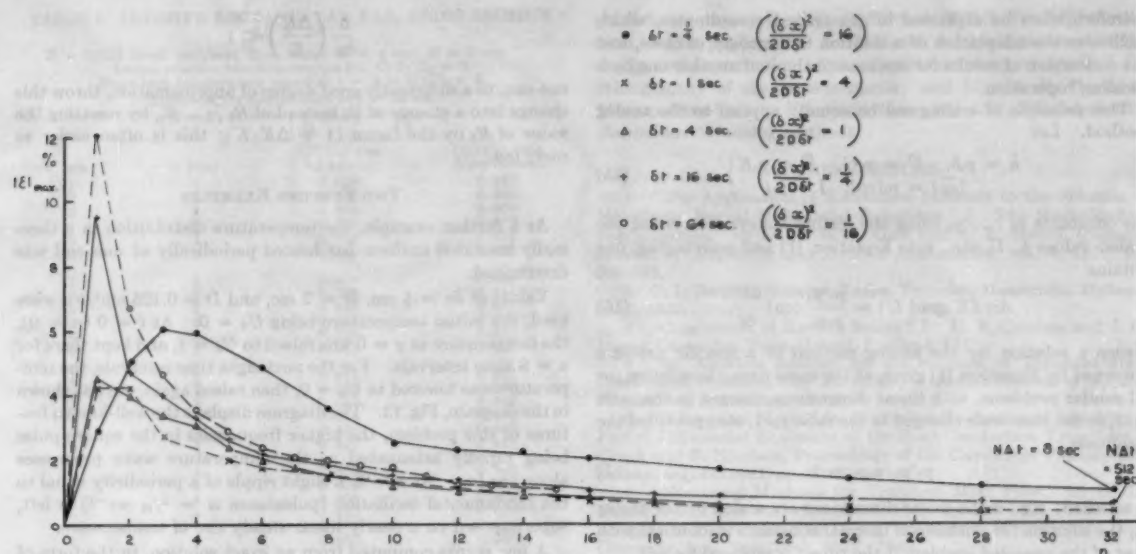


FIG. 10 MAXIMUM ABSOLUTE ERROR $|\epsilon|_{\max}$ IN PER CENT OF U_0 IN TEMPERATURE DISTRIBUTION OF SEMI-INFINITE LINEAR HEAT-INSULATED BAR, INITIALLY AT TEMPERATURE $U = 0$, THE TEMPERATURE AT $x = 0$ BEING RAISED TO $U_0 = 1$ AT $t = 0$ ($n = 0$), AS FUNCTION OF NUMBER n OF TIME INTERVALS, FOR SEVERAL VALUES OF Δt ($D = 0.125 \text{ cm}^2/\text{sec.}$)

In a two-dimensional model, for instance, mesh intervals δx_1 , δx_2 , and δy_1 , δy_2 , as shown in Fig. 11, may be used, the mean thermal conductivities between P_0 and P_1 being K_1 , etc. It is convenient to express the thermal conductivities K_m as multiples k_m of a standard value K_0

$$K_m = k_m K_0 \dots \dots \dots [10]$$

The "resistance-network star," Fig. 12, with the voltages $V_{m,n}$ at its terminals P_m , and the voltage $V_{m,n-1} = aU_{m,n-1}$ at the feeding point P_0 , then represents the finite-difference equation replacing Equation [1] if the resistance R_1 has this value

$$R_1 = \frac{2\delta x_1}{(\delta y_1 + \delta y_2)k_1} R_N \dots \dots \dots [11]$$

and similarly for R_2 , R_3 , R_4 (see Liebmann, 1954), whereas

$$R_0 = \frac{4K_0\delta t}{(\delta x_1 + \delta x_2)(\delta y_1 + \delta y_2)(c\rho)_0} R_N \dots \dots \dots [12]$$

R_N being a suitable standard value of resistance.

For $k_1 = \dots = k_4 = 1$, and $\delta x_1 = \delta x_2 = \dots = \delta x$, the expression for R_0 reduces to $R_0 = (D\delta t R_N)/(\delta x)^2$, which is identical with Equation [7], whereas $R_1 = \dots = R_4 = R_N$.

The design data for a resistance network for solving three-dimensional heat-conduction problems of rotational symmetry follow in a similar way from the formulas given in the paper by Liebmann (1954). Curved boundaries can be represented in a resistance-network analog model; rules for the required modifications have been discussed in an earlier paper (Liebmann, 1952).

Anisotropic values of K as expressed by $k_1 = k_2 = \beta k_3 = \beta k_4$, or a sudden change of medium, as determined by $k_1 \neq k_3$, can be easily represented by a corresponding choice of the values of $R_1 \dots R_4$. If a sudden change of medium affects also the values of $(c\rho)$, the required value of R_0 is determined by evaluating its reciprocal G_0

$$G_0 = \sum_1^4 G_p \dots \dots \dots [13]$$

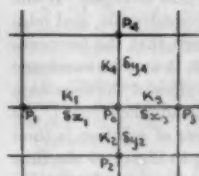


FIG. 11 MESH SUBDIVISION IN TWO DIMENSIONAL PROBLEMS

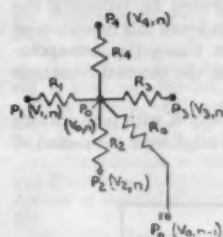


FIG. 12 RESISTANCE-NETWORK STAR AT POINT P_0 OF FIG. 11

where each conductance G_p is given by

$$G_p = \frac{A_p c_p \rho_p}{K_0 \delta t} G_N \dots \dots \dots [14]$$

Here, A_p is the part of the area $(\delta x_1 + \delta x_2)(\delta y_1 + \delta y_2)/4$ around point P_0 to which the values c_p and ρ_p are assigned, suitably averaged over the area A_p and $G_N = 1/R_N$.

UNITS AND SCALING

In this paper, CGS units are used throughout, but in applying the analog method, and any apparatus carrying this into effect, one can use any system of units, as long as all dimensions, thermal constants, and other data are consistently expressed in the same system of units.

It is found in many formal solutions of problems which permit rigorous analysis that the solution depends on the parameter $u = x^2/Dt$, and not separately on x or t . Formal solutions can

therefore often be expressed in generalized co-ordinates, which facilitates the adaptation of a solution to a variety of cases, and the conversion of results for one case to those of another one by a "scaling" operation.

This principle of scaling can be equally applied to the analog method. Let

$$\bar{h} = p_1 h, \quad \bar{U} = p_2 U, \quad \bar{K} = p_3 K \quad \left\{ \begin{array}{l} (\bar{c}\bar{p}) = p_4 (cp), \quad \bar{t} = p_5 t \end{array} \right\} \dots \dots \dots [15]$$

the constants $p_1 \dots p_5$ being the scaling factors. Inserting the scaled values \bar{h} , \bar{U} , etc., into Equation [1] and rearranging, one obtains

$$\text{div} (K \text{ grad } U) = \frac{p_1^2 p_4}{p_2 p_5} (cp) \frac{\partial U}{\partial t} \dots \dots \dots [16]$$

Hence a solution by the analog method of a specific problem governed by Equation [1] gives, at the same time, the solution for all similar problems, with linear dimensions changed in the ratio $p_1:1$, or the time scale changed in the ratio $p_5:1$, etc., provided the condition

$$p_1^2 p_4 / p_2 p_5 = 1 \dots \dots \dots [17]$$

is satisfied; e.g., if the linear dimensions are scaled by the factor p_1 , the solution for unchanged thermal constants is identical with that of the unscaled problem if the time t is replaced by $p_1^2 t$.

REPRESENTATION OF VARIABLE THERMAL CONSTANTS

If the thermal constants, e.g., K or (cp) , are functions of the temperature, it is necessary to reset some of the resistances during the progress of the solution to represent these changes. If the changes of the data with temperature are considerable, and relatively coarse δx and δt intervals are used such that the temperature rises are great between successive steps, it may be necessary to use an iterative method. In this, the values of the constants are set, in the first obtained solution, for the advance from U_n to U_{n+1} according to the value U_n . The process of solution is then repeated, using the constants corresponding to $U_{n+1/2}$ of the first solution when proceeding from U_n to U_{n+1} in the second solution. If need be, the solution is further improved by repeating the second solution, etc. Very often one can avoid this repetition of solutions by estimating the temperature $U_{n+1/2}$ (by extrapolation), and set the resistances to represent the thermal constants at this estimated value of $U_{n+1/2}$.

If changes ΔK of the thermal conductivity K with temperature cannot be disregarded, but are relatively small over the period of a time interval δt , such that

$$\frac{\partial}{\partial x} \left(\frac{\Delta K}{K} \right) \ll 1$$

one can, to a sufficiently good degree of approximation, throw this change into a change of R_0 instead of $R_1 \dots R_4$, by resetting the value of R_0 by the factor $(1 + \Delta K/K)$; this is often easier to carry out.

TWO FURTHER EXAMPLES

As a further example, the temperature distribution in a thermally insulated uniform bar heated periodically at one end was determined.

Values of $\delta x = 1$ cm, $\delta t = 2$ sec, and $D = 0.125$ cm²/sec were used, the initial temperature being $U_0 = 0$. At $t = 0$ ($n = 0$), the temperature at $x = 0$ was raised to $U_0 = 1$, and kept there for $n = 8$ time intervals. For the next eight time intervals, the temperature was lowered to $U_0 = 0$, then raised again, etc., as shown in the diagram, Fig. 13. The diagram displays the well-known features of this problem, the higher frequencies in the square pulse being rapidly attenuated as the temperature wave progresses along the bar. At $x = 5$, a slight ripple of a periodicity equal to the fundamental oscillation (pulsatance $\omega = 1/2$ sec⁻¹) is left, superimposed on a nearly linear steady rise of temperature.

A few points computed from an exact solution, in the form of an infinite Fourier series,⁹ are shown as dots in Fig. 13. The vertical bars indicate the calculated phase delay δ for the fundamental oscillation $\delta = x(\omega/2D)^{1/2}$. The calculated values agree very well with the analog solution. However, it is much quicker to obtain the analog solution than to work out the formal solution for a sufficiently great number of points. The advantage of the analog method would be further increased if additional complications were introduced into the problem, e.g., if the on-off ratio of the heat pulse, or its height were changed.

An application to a two-dimensional problem is illustrated by the results given in Table 3. This table gives the analog solution for the temperature distribution at $t = 32$ sec ($n = 16$) over the rectangular cross section of a mild-steel bar of 12 cm \times 8 cm, the initial temperature being $U = 0$, and the surface temperature being raised at the time $t = 0$ from $U = 0$ to $U = U_0$. The fourth column of Table 3 shows for comparison the corresponding calculated values found by interpolating Russell's (1936) graphs. Agreement between the analog values and the calculated values is seen to be very satisfactory.

⁹ Carslaw and Jaeger, 1947, p. 50.

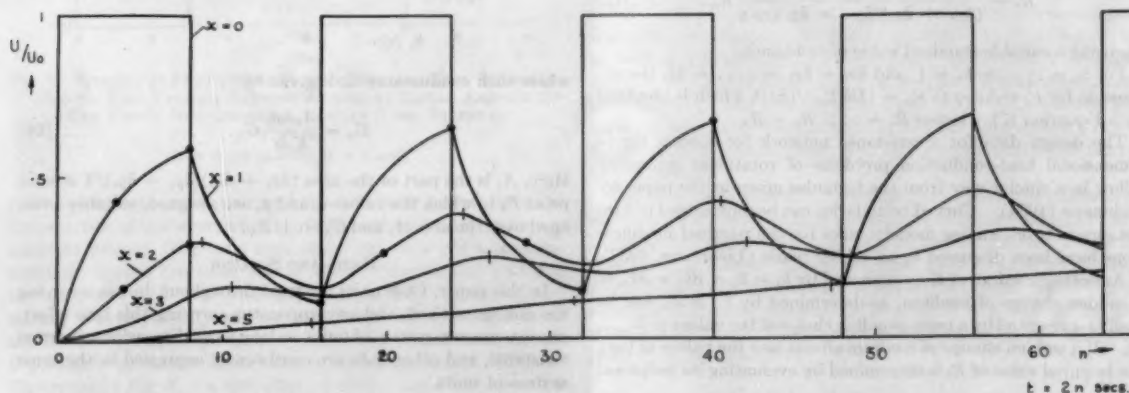


FIG. 13 TEMPERATURE DISTRIBUTION AS FUNCTION OF TIME AT SEVERAL POSITIONS x IN SEMI-INFINITE LINEAR HEAT-INSULATED STEEL BAR HEATED PERIODICALLY AT $x = 0$
($D = 0.125$ cm²/sec, $\delta t = 2$ sec.)

TABLE 3 INFINITE RECTANGULAR BAR, CROSS SECTION $2L \times 2B$

$D = 0.125$ (iron) cm²/sec; $L = 6$ cm; $B = 4$ cm; $M = 3$ sec
 Initial relative temperature (at $t < 0$) $U/U_0 = 0$
 Boundary temperature raised at $t = 0$ to $U/U_0 = 1$
 Temperature distribution at $t = 32$ sec
 $U = U_0$ at $x = \begin{cases} 0 & \text{and } y = 0 \\ 12 & \end{cases}$

x (cm)	y (cm)	(U/U_0) exp by analog	(U/U_0) calc from Russell
1	1	0.923	0.925
2	1	0.835	0.860
3	1	0.806	0.809
4	1	0.774	0.777
5	1	0.756	0.759
6	1	0.749	0.752
1	2	0.859	0.861
2	2	0.736	0.741
3	2	0.646	0.647
4	2	0.587	0.588
5	2	0.553	0.555
6	2	0.543	0.542
1	3	0.816	0.821
2	3	0.659	0.667
3	3	0.542	0.546
4	3	0.464	0.470
5	3	0.420	0.423
6	3	0.407	0.411
1	4	0.803	0.806
2	4	0.634	0.638
3	4	0.506	0.517
4	4	0.422	0.425
5	4	0.375	0.379
6	4	0.363	0.360

NOTE: Accuracy of measurement: ± 0.2 per cent.

Expected systematic error of measurement: less than 0.9 per cent.
 Accuracy of interpolation from Russell's calculated values: 0.5 per cent.

CONCLUSION

Experience so far gained with the new analog method has shown it to be a very versatile method which can be successfully handled by persons who have only very moderate mathematical skill. While it is not as fast as the older capacitance-resistance analog method, it is free from some of its sources of error (see Paschke and Heisler, 1944), and it appears more flexible. The new method is very much faster than the previously used numerical methods. Even in cases where a formal solution is known, it is often quicker to obtain the analog solution than to evaluate the formal solution numerically for a great number of points. Using the described extrapolation method, one can with reasonable care obtain solutions which are accurate to ± 0.5 per cent; this is usually a higher accuracy than that with which the thermal constants of the investigated problem are known.

The main application of the new method may be in problems which require a great number of mesh points for their representation, e.g., the temperature distribution in systems of complicated geometry, or of very complex composition, and in problems of intrinsic difficulty, e.g., those where the thermal properties are functions of time or temperature.¹²

However, quite simple small-scale apparatus may be improvised with the means available in most laboratories, as only a number of resistances (rheostats) and simple measuring equipment is required. It should then be possible to solve many relatively complex problems with sufficient speed and accuracy.

The method is, of course, not limited to heat-conduction problems, but can deal with any problem described by an equation of the type of Equation [1] or [2], e.g., diffusion and mass-flow problems.

ACKNOWLEDGMENTS

The author wishes to thank Dr. T. E. Allibone, F.R.S., the Director of the A.E.I. Research Laboratory, for permission to

¹² For instance, it has been used to investigate the temperature distribution in steam and gas turbines and in rocket motors under various operating conditions.

publish this paper; Prof. D. R. Hartree, F.R.S., for helpful criticism of this paper; Mr. A. C. Heath for his assistance in the design and construction of the experimental apparatus and for taking many of the measurements; and Mr. M. B. Coyle, of Metropolitan-Vickers Electrical Company Ltd., for interesting discussions on analog methods.

REFERENCES

- 1 "The Application of Relaxation Methods to the Solution of Nonelliptic Partial Differential Equations. I. The Heat-Conduction Equation," by D. N. de G. Allen and R. T. Savorn, *Quarterly Journal of Mechanics and Applied Mathematics*, vol. 4, 1951, pp. 209-223.
- 2 C. L. Beuken, *Econom. Techn. Tydschr.*, Maastricht, Holland, no. 1, 1937.
- 3 "Conduction of Heat in Solids," by H. S. Carslaw and J. C. Jaeger, Clarendon Press, Oxford, England, 1947.
- 4 "An Air-Flow Analogy for the Solution of Transient Heat Conduction Problems," by M. B. Coyle, *British Journal of Applied Physics*, vol. 2, 1951, pp. 12-17.
- 5 "A Practical Method for Numerical Evaluation of Solutions of Partial Differential Equations of the Heat-Conduction Type," by J. Crank and P. Nicolson, *Proceedings of the Cambridge Philosophical Society*, vol. 43, 1947, pp. 50-67.
- 6 "Numerical Methods for Transient Heat Flow," by G. M. Dushinberre, *Trans. ASME*, vol. 67, 1945, pp. 703-712; "Numerical Analysis of Heat Flow," by G. M. Dushinberre, McGraw-Hill Book Company, Inc., New York, N. Y., 1949.
- 7 "The Numerical Solution of Heat-Conduction Problems," by H. W. Emmons, *Trans. ASME*, vol. 65, 1943, pp. 607-615.
- 8 "The Calculation of Variable Heat Flow in Solids," by N. R. Eyres, D. R. Hartree, J. Ingham, R. Jackson, R. J. Sarjant, and J. B. Wagstaff, *Philosophical Transactions of the Royal Society of London, England, series A*, vol. 240, 1946-1948, pp. 1-57.
- 9 "A Schmidt Mechanism for Approximate Solution of the Equation of Linear Flow of Heat in a Medium Whose Thermal Properties Depend on the Temperature," by J. C. Jaeger, *Journal of Scientific Instruments*, vol. 27, 1950, pp. 226-227.
- 10 "Solution of Partial Differential Equations With a Resistance Network Analogue," by G. Liebmann, *British Journal of Applied Physics*, vol. 1, 1950, pp. 92-103.
- 11 "Proceedings of the General Discussion on Heat Transfer, The Institution of Mechanical Engineers, London, England, 1951, pp. 300-301; discussion by G. Liebmann.
- 12 "The Solution of Waveguide and Cavity-Resonator Problems With the Resistance-Network Analogue," by G. Liebmann, *Proceedings IEE*, vol. 90, part 4, 1952, Monograph No. 38, pp. 260-272.
- 13 "Resistance-Network Analogues With Unequal Meshes or Subdivided Meshes," by G. Liebmann, *British Journal of Applied Physics*, vol. 5, 1954, pp. 362-366.
- 14 "The Solution of Transient Heat Flow and Heat Transfer Problems by Relaxation," by G. Liebmann, *British Journal of Applied Physics*, vol. 6, 1955, pp. 129-135.
- 15 "Application of Electric-Analog Computers to Heat-Transfer and Fluid-Flow Problems," by G. D. McCann, Jr., and C. H. Wiltz, *Journal of Applied Mechanics*, *Trans. ASME*, vol. 71, 1949, pp. 247-258.
- 16 "The Hydrocal; a Hydrodynamic Calculating Machine for Solving Unsteady-State Problems in Heat Transfer and Other Types of Diffusion," by A. D. Moore, *Industrial and Engineering Chemistry*, vol. 28, 1936, pp. 704-708.
- 17 "A Method for Determining Unsteady-State Heat Transfer by Means of an Electrical Analogy," by V. Paschke and H. D. Baker, *Trans. ASME*, vol. 64, 1942, pp. 105-112.
- 18 "Die Berechnung der Durchwärmungszeiten von Gutstücken auf Grund der relativen Mindertemperatur," by V. Paschke and C. L. Beuken, *Elektrotechnik und Maschinenbau*, vol. 56, 1938, pp. 98-100.
- 19 "The Accuracy of Measurements in Lumped R-C Cable Circuits as Used in the Study of Transient Heat Flow," by V. Paschke and M. P. Heisler, *Trans. AIEE*, vol. 63, 1944, pp. 165-171.
- 20 "Some Mathematical Considerations on the Heating and Cooling of Steel," by T. F. Russell, *Iron and Steel Institute, Special Report No. 14*, 1936, pp. 149-187.
- 21 "Beiträge zur technischen Mechanik und technischen Physik," by E. Schmidt, *August Föppl-Festschrift*, Berlin, Germany, 1924, pp. 179-189; "Das Differenzenverfahren zur Lösung von Differentialgleichungen der nichtstationären Wärmeleitung, Diffusion und Impulsausbreitung," by E. Schmidt, *Forschung*, vol. 13, 1942, pp. 177-185.

Discussion

G. M. DUSINBERRE.¹¹ Every organization now using resistance-capacitance analogs, or contemplating their use, can profitably study the considerations of flexibility, simplicity, accuracy, and low cost, which are features of the author's method.

According to the usual finite-difference representation, we consider each "future" temperature an explicit function of the "present" temperature of the region in question and of the other regions in thermal contact. This remains the preferred method for manual calculation and probably also for digital-computer work. The author, in essence, writes the future temperatures as functions simultaneously of each other and the present temperatures taken singly. This would seem to add confusion to a simple picture. It would greatly complicate a manual solution. But the simultaneity is taken care of by a resistance network only slightly more complicated than that required for a steady-state problem, and there is often a gain in the elimination of convergence criteria. As compared with the resistance-capacitance network there is an advantage in being able to represent any variation of the physical properties, with convenience and accuracy.

It must be noted that while the method permits a large time interval without losing mathematical stability, still, judgment must be used in taking advantage of this feature. Often a transient-temperature calculation is made for the purpose of estimating stress due to temperature gradients. Then if one uses too large a time interval, one obscures the very point of interest.

The writer has been interested in the prediction of transients in heat exchangers. Here an important term is dt/dx , which is used to evaluate the heat transported by flow of the fluid. It is often, in fact usually, the case that the term d^2t/dx^2 is negligible. In this case he has not been able to apply the author's method.

But if the term involving d^2t/dx^2 is larger than the term involving dt/dx , as may be the case with liquid metals at low rates of flow, then he finds it possible to use the author's method. It requires resistances increasing in a geometrical proportion, so that if the two terms were nearly equal it would not be very practical.

It is to be hoped that the author or some other interested person can extend the application of this analog in a more general way to problems involving fluid flow.

VICTOR PASCHKIS.¹² The author, well known for his many contributions to techniques of solving heat-conduction problems, is to be congratulated not only for an ingenious new method but also for an outstanding clear and complete presentation.

In fact, his considerations are so exhaustive and his analysis of errors is so outstanding that but little remains to be asked.

The writer, working mainly with the resistance-capacitance-type analog mentioned by the author, is of course particularly interested in a comparison of the new method with the older one.

The author points out that his method is slower than the older method. Does this remark refer only to the electrical computing time or also to the coding time? Particularly for complicated problems with temperature-dependent parameters and problems involving several materials, it would appear that the preparation of the computing circuit would require considerably more effort than the R-C network.

The new method trades the error due to leakage in capacitances, inherent in the R-C network, for errors due to finite time steps

and due to inaccuracies in voltages $V_{m,n-1}$ which may be caused by the potentiometers, unless extreme precautions are taken.

With reference to Fig. 12 of the paper, a discussion of the additional error in unequal lumping would be very interesting.

AUTHOR'S CLOSURE

In his encouraging remarks, Professor Dusinberre has compared the new analog method with the more familiar numerical techniques of solving transient heat-conduction problems by a process of explicit forward integration. While the new analog is based on an implicit method in which the transient problem is, in fact, replaced by a series of boundary-value problems of the Poisson type, it is this type of problem which is most conveniently and speedily solved by the resistance-network analog. As Professor Dusinberre has pointed out, one has to use one's judgment concerning the length of time interval most appropriate to the problem under investigation, as the optimum-time interval is no longer determined by the "stability" criterion of the numerical forward integration method. In the analog method one will often use a short time interval during the period when a critical change of temperature occurs, and a long time interval during other periods, as the change of time interval is so easily effected.

The problem of the transient condition in the heat exchanger is a difficult one, and one cannot see how this can be solved in its general form by the present analog method. However, if the heat transport through mass flow is either rather smaller or considerably greater than the heat transport through conduction in the liquids, solution by the analog technique appears possible. The type of resistance-network analog to be used for solving the first one of these two cases has been stated by Professor Dusinberre. The second case might be solved by representing the heat transfer between the heat-exchanger pipe and the liquids by a resistance-network model, as will be discussed in the following paper on solving heat-transfer problems. The difficulty in the case of the heat exchanger is that the local temperatures in the liquids, and hence the heat-transfer rates, are depending on the general temperature distribution in the exchanger. However, it appears feasible to overcome this difficulty by carrying out an iterative process for each time interval δt .

In reply to Dr. Paschkis, it is the actual computing time which is longer in the new analog method because for each time interval a series of potentiometer adjustments has to be made, whereas the solution proceeds automatically, and usually at a much faster rate, in the resistance-capacitance analog. The coding time, i.e., the time necessary to determine the values of the component parts of the analog model and to set these values in the analog apparatus, should be the same in the new method as in the resistance-capacitance analog. This applies, in principle, also to the resetting of component values, during the progress of the solution to allow for the variation of some parameters. But whereas one is bound by the automatic rate of progress of the solution in the resistance-capacitance method, which requires for this reason techniques which are either restricted in accuracy or which involve a greater amount of instrumentation, one may find it often an advantage that one can interrupt the progress of the solution at will in the new analog method and make all required readjustments of parameters at leisure before continuing.

Concerning the question of errors, as was discussed in Section 2, Experimental Tests of Analog Method, the inaccuracies in the voltages, $V_{m,n-1}$, were found to be of the order of ± 0.2 per cent for the apparatus described in the paper; all measurements were taken with ordinary care and without extensive precautions. This leaves the errors due to the finite steps of space and time. These errors can be estimated from the finite difference approximations which have been used by considering the influence of

¹¹ Professor of Mechanical Engineering, The Pennsylvania State University, State College, Pa. Fellow ASME.

¹² Technical Director, Heat and Mass Flow Analyser Laboratory, Engineering, Columbia University, New York, N. Y. Mem. ASME.

the neglected higher-order terms of the approximations. It is indeed one of the advantages of the new analog method that it permits a more precise assessment of these errors.

The additional errors due to unequal lumping can be appreciated most easily by reference to the finite-difference approximation [5]. For different interval lengths adjacent to the point P_m , say, δx_{m+1} between P_{m+1} and P_m , and δx_m between P_m and P_{m-1} , this equation changes to

$$\begin{aligned} 2(U_{m+1,n} - U_{m,n})/\delta x_{m+1}(\delta x_m + \delta x_{m+1}) &+ 2(U_{m,n} - U_{m-1,n})/\delta x_m(\delta x_m + \delta x_{m+1}) \\ &- [(\delta x_{m+1} - \delta x_m)/3](\partial^3 U/\partial x^3)_{m,n} \\ &= (U_{m,n} - U_{m,n-1})/D\delta t \dots \dots \dots [5a] \end{aligned}$$

For $\delta x_{m+1} = \delta x_m$, Equation [5a] is identical with [5] but for unequal interval lengths a third-order correction term proportional to the difference between the two mesh intervals appears in the finite difference approximation. This would be equivalent to an error ΔU in the progressing analog solution of

$$\Delta U = -[D\delta t(\delta x_{m+1} - \delta x_m)/3](\partial^3 U/\partial x^3)_{m,n}$$

This error ΔU can be estimated in retrospect by evaluation of $(\partial^3 U/\partial x^3)$. For the two-dimensional case of Figs. 11 and 12, a more complicated but similarly constructed correction term applies.

DURING the past few years, the electrical analog method has been applied to a wide variety of heat conduction problems. This method has been found to be particularly useful in the solution of problems involving transient heat conduction. The method is based on the principle of conservation of energy, and it is possible to obtain a solution for the temperature distribution at any time during the transient process. The method is particularly useful in the solution of problems involving heat conduction in solids of irregular shape, and it is possible to obtain a solution for the temperature distribution at any time during the transient process.

The first step in the solution of a heat conduction problem by the electrical analog method is to construct an electrical circuit which is equivalent to the heat conduction problem. This is done by replacing the heat conduction problem by an equivalent electrical circuit. The heat conduction problem is then solved by solving the electrical circuit. The solution of the electrical circuit is then used to determine the temperature distribution in the heat conduction problem. The method is particularly useful in the solution of problems involving transient heat conduction. The method is based on the principle of conservation of energy, and it is possible to obtain a solution for the temperature distribution at any time during the transient process. The method is particularly useful in the solution of problems involving heat conduction in solids of irregular shape, and it is possible to obtain a solution for the temperature distribution at any time during the transient process.

The second step in the solution of a heat conduction problem by the electrical analog method is to construct an electrical circuit which is equivalent to the heat conduction problem. This is done by replacing the heat conduction problem by an equivalent electrical circuit. The heat conduction problem is then solved by solving the electrical circuit. The solution of the electrical circuit is then used to determine the temperature distribution in the heat conduction problem. The method is particularly useful in the solution of problems involving transient heat conduction. The method is based on the principle of conservation of energy, and it is possible to obtain a solution for the temperature distribution at any time during the transient process. The method is particularly useful in the solution of problems involving heat conduction in solids of irregular shape, and it is possible to obtain a solution for the temperature distribution at any time during the transient process.



Fig. 1. Schematic diagram of electrical circuit used for solving heat conduction problems

The third step in the solution of a heat conduction problem by the electrical analog method is to construct an electrical circuit which is equivalent to the heat conduction problem. This is done by replacing the heat conduction problem by an equivalent electrical circuit. The heat conduction problem is then solved by solving the electrical circuit. The solution of the electrical circuit is then used to determine the temperature distribution in the heat conduction problem. The method is particularly useful in the solution of problems involving transient heat conduction. The method is based on the principle of conservation of energy, and it is possible to obtain a solution for the temperature distribution at any time during the transient process. The method is particularly useful in the solution of problems involving heat conduction in solids of irregular shape, and it is possible to obtain a solution for the temperature distribution at any time during the transient process.

The fourth step in the solution of a heat conduction problem by the electrical analog method is to construct an electrical circuit which is equivalent to the heat conduction problem. This is done by replacing the heat conduction problem by an equivalent electrical circuit. The heat conduction problem is then solved by solving the electrical circuit. The solution of the electrical circuit is then used to determine the temperature distribution in the heat conduction problem. The method is particularly useful in the solution of problems involving transient heat conduction. The method is based on the principle of conservation of energy, and it is possible to obtain a solution for the temperature distribution at any time during the transient process. The method is particularly useful in the solution of problems involving heat conduction in solids of irregular shape, and it is possible to obtain a solution for the temperature distribution at any time during the transient process.

The fifth step in the solution of a heat conduction problem by the electrical analog method is to construct an electrical circuit which is equivalent to the heat conduction problem. This is done by replacing the heat conduction problem by an equivalent electrical circuit. The heat conduction problem is then solved by solving the electrical circuit. The solution of the electrical circuit is then used to determine the temperature distribution in the heat conduction problem. The method is particularly useful in the solution of problems involving transient heat conduction. The method is based on the principle of conservation of energy, and it is possible to obtain a solution for the temperature distribution at any time during the transient process. The method is particularly useful in the solution of problems involving heat conduction in solids of irregular shape, and it is possible to obtain a solution for the temperature distribution at any time during the transient process.

Thermal Properties of Titanium Alloys and Selected Tool Materials

By E. G. LOEWEN,¹ CAMBRIDGE, MASS.

Thermal conductivity has been determined of five titanium alloys, four high-speed-steel alloys, and four types of tungsten-carbide tool materials, over a temperature range of 200 to 1000 F. In addition, the specific heat of two titanium alloys has been found between 70 and 1400 F.

INTRODUCTION

DURING recent theoretical investigations (1, 2)² of cutting-tool temperatures it became evident that there were not sufficient data available on the thermal conductivity and specific heat at elevated temperatures of many important materials, especially titanium alloys. Using fairly conventional methods the thermal conductivities of five titanium alloys, four high-speed steels, and four types of carbide tool materials were measured up to 1000 F. In addition the specific heat of two titanium alloys was determined over a range of 70 to 1400 F.

APPARATUS

Thermal conductivity was found from the measurement of the temperature gradient in a $\frac{1}{4}$ -in.-diam rod, one end of which was heated and the other end cooled by a constant-flow calorimeter. A guard tube was used to approach one-dimensional heat flow as closely as possible. The apparatus is quite similar to that described by Donaldson (3) and is shown in Fig. 1. It differs from that of Van Dusen and Shelton (4) in that the calorimeter allows absolute measurement of the heat flow through the specimen without reference to other materials. A more elegant method has been proposed by Hogan and Sawyer (5) but it requires more elaborate instrumentation than we had available. The heater consisted of a stainless-steel block containing four Globar heaters fed from a variable transformer. The 2-in.-diam calorimeter was made of brass and contained hermetically sealed counterflow passages for the water flow. The water was supplied from a constant-head (15-ft) tank, fed by tap water passing through an electric tubular heater, a simple arrangement that kept temperature variations to less than 0.5 deg F per hr. The small temperature rise in the water passing through the calorimeter was measured by means of a calibrated 5-junction differential chromel-alumel thermocouple and precision potentiometer to the nearest 0.01 deg F. The water flow rate was determined from the time taken to fill a 500-ml flask. The temperature gradient in the specimen was found from four No. 22-gage chromel-alumel couples butt-welded and inserted in 0.05-in.-diam holes drilled through the center of the bar, points 3 in. above and below, and one 2 in. below the center. The guard tube was 3 in. diam and had a separate auxiliary heater wound around its base which could be adjusted for optimum guard-to-specimen temperature match. A

cooling coil wound around the top of the guard was fed from the same water supply as the calorimeter. Thermocouples inserted in the guard at the same levels as those in the specimen allowed corrections to be made for heat transfer between guard and specimen. The space inside the guard tube was filled with Fuller's earth, the outside was insulated with firebrick, and the top of the apparatus was insulated with rockwool. The maximum attainable temperature was determined by the damage to be tolerated; no readings were made above 1250 F.

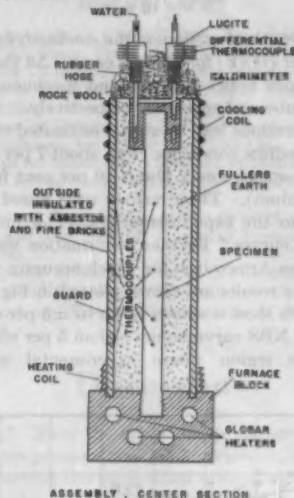


FIG. 1 SKETCH OF THERMAL-CONDUCTIVITY APPARATUS

Specific heat was measured by heating to a known temperature a $\frac{1}{4} \times 2$ -in. cylindrical specimen in a vertical copper-tube furnace, a simplified version of apparatus described by Ginnings, Douglas, and Ball (6). The heat content of the specimen was determined by allowing it to drop into a solid copper calorimeter. This calorimeter consisted of a 5-lb cylinder with a hollow center and automatically closing lid; it was located in a thermos flask and a 5-junction chromel-alumel couple was used to follow changes in its temperature. Continuous recording made it a simple matter to apply cooling corrections.

EXPERIMENTAL ACCURACY

The coefficient of thermal conductivity k was calculated from the one-dimensional Fourier heat-flow equation

$$Q = kA \frac{d\theta}{dx} \dots \dots \dots [1]$$

where Q is the heat flowing through section A having a temperature gradient $d\theta/dx$. Errors can be discussed in terms of these quantities. For the equation to apply we must have truly steady-state conditions. By means of a simple bucking circuit a sensitive recording millivoltmeter kept constant track of the temperature of the hot end of the specimen. Most readings were made

¹ Assistant Professor, Mechanical Engineering Department, Massachusetts Institute of Technology. At present, The Taft-Peirce Manufacturing Company, Woonsocket, R. I. Mem. ASME.

² Numbers in parentheses refer to Bibliography at end of paper. Contributed by the Heat Transfer Division and presented at a joint session of the Heat Transfer Division and the Research Committee on Metal Processing at the Diamond Jubilee Semi-Annual Meeting, Boston, Mass., June 19-23, 1955, of THE AMERICAN SOCIETY OF MECHANICAL ENGINEERS.

NOTE: Statements and opinions advanced in papers are to be understood as individual expressions of their authors and not those of the Society. Manuscript received at ASME Headquarters, April 12, 1955. Paper No. 55-SA-45.

when this temperature varied less than 2 deg F per hr. Errors in measuring A can be considered negligible. Errors due to substituting $\Delta\theta/\Delta x$ for $d\theta/dx$ are also negligible. Changes in A due to thermal expansion at high temperatures are compensated for in part by an increase in specimen length. This effect has been neglected because the maximum error so introduced is only ~ 1 per cent. Uncertainty in the distance between couples, the readings from the calibrated thermocouples, contact potentials, unsteady state, etc., combine to give an estimated 1 to 2 per cent error in $\Delta\theta/\Delta x$. It is the measurement of Q that has the greatest amount of uncertainty associated with it. Calorimeter calibration, slight fluctuations in water temperature and rate of flow, parasitic heat flow through insulating material result in probable errors of 2 to 5 per cent in Q . The errors decrease as the specimen conductivity or the temperature increases. With very low-conductivity materials (titanium) it is necessary to correct Q for heat transfer Q_1 between guard and specimen

$$Q_1 = \frac{L(2\pi)k_1\Delta\theta}{\ln r_2/r_1} \quad [2]$$

where L is the length of section, k_1 the conductivity of the insulator [0.05 Btu/(hr)(ft)(F) for Fuller's earth], $\Delta\theta$ the average temperature difference between guard and specimen, r_2 and r_1 the radii of guard tube and specimen, respectively.

These considerations lead to a total estimated error of about 5 per cent for a medium conductor (Fe), about 7 per cent for a poor conductor (high-speed steel), about 10 per cent for a very poor conductor (titanium). These values were found to correspond approximately to the experimental scatter of individual points from the mean curves. Further confirmation was obtained by running a test on Armco iron for which accurate values of k are known (7). The results are shown plotted in Fig. 2. While experimental points show a scatter of up to ± 5 per cent, the mean differs from the NBS curve no more than 5 per cent, even in the low-temperature region where experimental errors are the greatest.

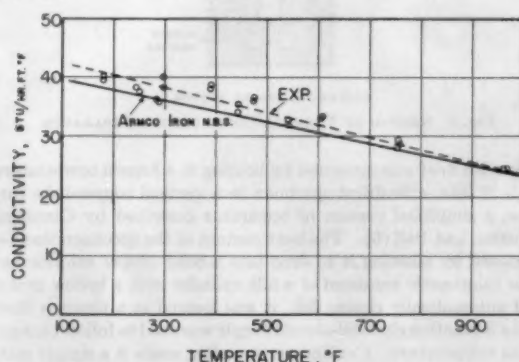


FIG. 2 THERMAL CONDUCTIVITY OF ARMCO IRON
(Circles represent experimental points. NBS curve is shown solid.)

In the specific-heat measurements the enthalpy H , as a function of the temperature θ , is the primary quantity measured. Errors in H are due to uncertainty in the initial and final temperatures of the specimen (1 per cent), calorimetric measurement (2 per cent), calorimeter calibration (2 per cent). Polynomial equations were found that best fitted the experimental data points of H , so that C_p could be found by simple differentiation: $C_p = dH/d\theta$. The uncertainty u in the value of C_p so determined will be a function of the temperature and can be represented approximately by $u = \pm(3 + 0.005\theta)$ per cent, where θ is the temperature in deg F.

EXPERIMENTAL RESULTS

Thermal conductivity of four different carbide-tool materials are shown in Fig. 3. CA-4 and K-6 are cast-iron grades containing only tungsten carbide and a small amount of cobalt binder. CA-2 and K2S are steel-cutting grades containing titanium and tantalum carbide in addition to tungsten carbide as well as an increased amount of cobalt.

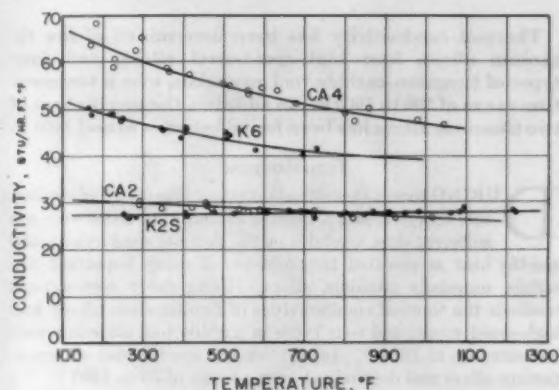


FIG. 3 THERMAL CONDUCTIVITY OF FOUR CARBIDE-TOOL MATERIALS

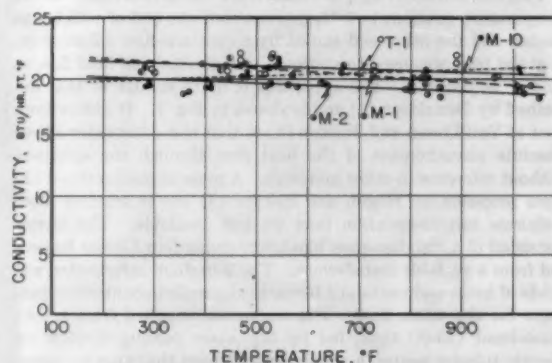


FIG. 4 THERMAL CONDUCTIVITIES OF T1, M1, M2, M10 ANNEALED HIGH-SPEED STEEL

TABLE 1 NOMINAL COMPOSITION OF HIGH-SPEED-STEEL ALLOYS

Alloy	W	Cr	Per cent V	Mo	Fe
T1.....	18	4	1	..	77
M1.....	1.5	4	1	8.5	85
M2.....	6	4	2	5	83
M10.....	..	4	2	8	86

The conductivities of four grades of high-speed steel are shown in Fig. 4. Their nominal composition is shown in Table 1. The specimens were in the annealed condition. Differences between them and with temperature are hardly noticeable and it is evident that for many practical purposes a single value of 21 Btu/(hr)(ft)(F) will be a satisfactory figure to use.

Differences in conductivity between titanium alloys, as shown in Figs. 5 and 6, are also not very great, except that commercially pure titanium (75A) has a higher conductivity than the alloys, just as one would expect. The composition of five of the alloys used is given in Table 2, that for Ti 75A (1) and Ti 150A (1) is not known but evidently not quite the same as Ti 75A (2) and Ti 150A (2). Variation of conductivity with temperature is seen to be small.

TABLE 2 COMPOSITION OF TITANIUM ALLOYS

Alloy	H	C	N	O	Fe	Cr	Mn	Mo	Ti
Ti 75A (2)	0.0068	0.06	0.048	0.131	0.07	99.75
Ti 130A	0.0069	0.05	0.034	0.177	0.20	..	6.50	..	93.21
Ti 150A (2)	0.0092	0.05	0.076	0.105	1.40	2.71	95.65
Re-55	0.0073	0.08	0.028	0.123	0.12	99.64
Cr-Mo	0.0077	0.02	0.032	0.131	0.13	3.38	..	2.10	96.30

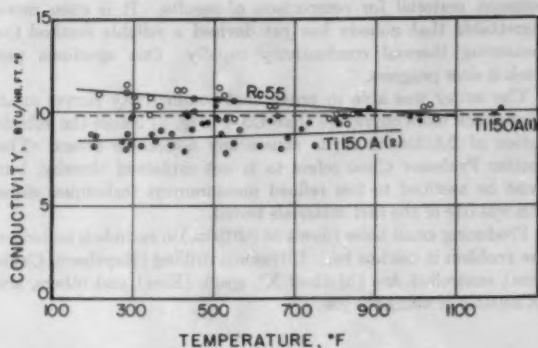


FIG. 5 THERMAL CONDUCTIVITY OF Ti 75A, Ti 130A, AND Cr-Mo TITANIUM ALLOYS

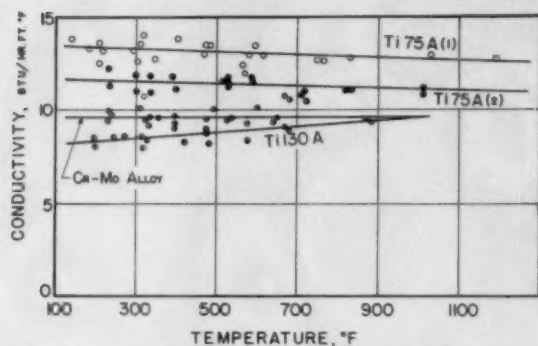


FIG. 6 THERMAL CONDUCTIVITY OF Ti 150A AND RC 55 TITANIUM ALLOYS

The specific heat (C_p) of Ti 75A and Ti 150A of nominal composition were found to be

$$\text{Ti 75A: } C_p = 0.125 + 4.8 \times 10^{-4}(\theta - 70)^2 \text{ Btu/lb F}$$

$$\text{Ti 150A: } C_p = 0.130 + 4.8 \times 10^{-4}(\theta - 70)^2 \text{ Btu/lb F}$$

where θ is the temperature in deg F.

Caution is in order if these equations are to be extrapolated above the maximum temperature of the experiments (1400 F). The values between room temperature and 212 F were checked independently by heating the specimens in steam and dropping them into a water calorimeter. The results so obtained were

$$\text{Ti 75A: } C_p = 0.129 \pm 2 \text{ per cent (at 140 F) Btu/lb F}$$

$$\text{Ti 150A: } C_p = 0.131 \pm 3 \text{ per cent}$$

and agree with the equations just given.

It is obvious that the specific heat of titanium increases rapidly with temperature. This fact was confirmed when the new values were used in conjunction with the analysis given in (1) to calculate the temperatures at the tip of a lathe tool machining titanium. Instead of giving absurdly high values, as the previously published values of C_p had done, the calculated temperatures agree quite well with direct experimental measurement of the cutting temperatures (2).

ACKNOWLEDGMENT

Part of the work reported was sponsored by the Allegheny-Ludlum Steel Company. The same company also furnished machined specimens of CA2 and CA4 carbides and specimens of Ti 75 (1) and Ti 150A (1). Watertown Arsenal furnished the remaining titanium specimens and was responsible for the chemical analysis reported in Table 2. The Kennametal Company furnished the specimens of K6 and K2S. The advice of Prof. L. R. Vianey, formerly of M.I.T., and the assistance of Messrs. R. Gleason, A. Maculaitis, and A. S. Tweedie in carrying out many of the experiments is gratefully acknowledged.

BIBLIOGRAPHY

- 1 "On the Analysis of Cutting-Tool Temperatures," by E. G. Loewen and M. C. Shaw, Trans. ASME, vol. 76, 1954, pp. 217-232.
- 2 "Machining Titanium," by M. C. Shaw and collaborators, published by Machine Tool Division, Mechanical Engineering Department, M.I.T., 1954.
- 3 "Apparatus for Determining Thermal Conductivity," by J. W. Donaldson, *Metallurgia*, vol. 2, 1930, pp. 150-154.
- 4 "Apparatus for Measuring Thermal Conductivity of Metals Up to 600 C.," by M. S. Van Dusen and S. M. Shelton, *Journal of Research*, NBS, vol. 12, 1934, p. 429.
- 5 "The Thermal Conductivity of Metals at High Temperature," by C. L. Hogan and R. E. Sawyer, *Journal of Applied Physics*, vol. 23, 1952, pp. 177-180.
- 6 "Heat Capacity of Sodium," by D. C. Ginnings, T. B. Douglas, and A. F. Ball, NBS Res. Paper RP 2110, vol. 45, 1950, pp. 23-33.
- 7 NBS Report on "Thermal Conductivity of Armco Iron," pre-publication 1953.

Discussion

B. T. CHAO.³ Since the analytical procedure for estimating metal-cutting temperature was made available, much useful information concerning the mechanism of tool failure has been obtained. One major handicap in applying the analysis is the lack of adequate data of the thermal properties of the tool and work materials. The author is to be congratulated on the fine piece of work reported here. There is at present great need for additional similar work.

In calculating the thermal conductivity of the test specimen from Equation [1] of the paper, the author replaced $d\theta/dx$ by $\Delta\theta/\Delta x$, and stated that the error in doing so was negligible. The Δx used were either 2 or 3 in. No $\Delta\theta$ values were reported. Actually, the error resulting from such a substitution may be small or large depending on (a) the rate of change of the thermal conductivity of the specimen material with temperature and (b) the range of temperature concerned. For a material whose conductivity does not vary as temperature changes, the temperature-distance relation for the apparatus described will be linear, and, consequently, $d\theta/dx$ and $\Delta\theta/\Delta x$ are identical. However, if the conductivity exhibits a strong temperature dependency, and the temperature difference across the hot and cold end of the specimen is large, such a substitution may introduce appreciable error inasmuch as the Δx selected by the author are relatively coarse. Examination of Fig. 3 shows that the data scatter for CA4 carbide is considerably larger than that of other carbides listed, particularly in the lower-temperature range where the temperature

³ Associate Professor of Mechanical Engineering, University of Illinois, Urbana, Ill.

dependency of its conductivity is stronger. Such observation seems to support the foregoing discussion.

Fig. 4 of the paper gives conductivity values of four different kinds of high-speed steel in the annealed state. It is well known that changes in microstructure of steels oftentimes produce a significant change in their electrical and thermal properties.⁴ A quenched medium or high C steel tempered to a high hardness has a lower conductivity than the same steel in the annealed state. It seems, therefore, that the data will be more useful if the conductivity values of high-speed steels were determined from quenched and tempered specimens (corresponding to the condition in service) rather than from the annealed specimens.

Finally, the writer would like to know the technique which the author used to produce 0.05-in.-diam holes in cemented-carbide materials.

⁴ "Heat Transfer," by Max Jakob, John Wiley & Sons, Inc., New York, N. Y., vol. 1, 1950, chapter 6.

AUTHOR'S CLOSURE

Professor Chao was too modest in his discussion to point out that he, too, has been measuring thermal properties of important engineering materials. Since he used a different method it is regrettable that we did not happen to choose at least one common material for comparison of results. It is even more regrettable that nobody has yet devised a reliable method for measuring thermal conductivity rapidly. One specimen per week is slow progress.

The writer was able to prove that conductivity curves must have much more curvature than CA-4 (Fig. 3) before the substitution of $\Delta\theta/\Delta x$ for $d\theta/dx$ causes any noticeable errors. The scatter Professor Chao refers to is not explained thereby, but must be ascribed to less refined measurement techniques since this was one of the first materials tested.

Producing small holes (down to 0.010 in.) in carbide is no longer the problem it used to be. Ultrasonic drilling (Raytheon, Cavitron), controlled Arc (Method X), spark (Elox), and others, are all capable of doing the job.

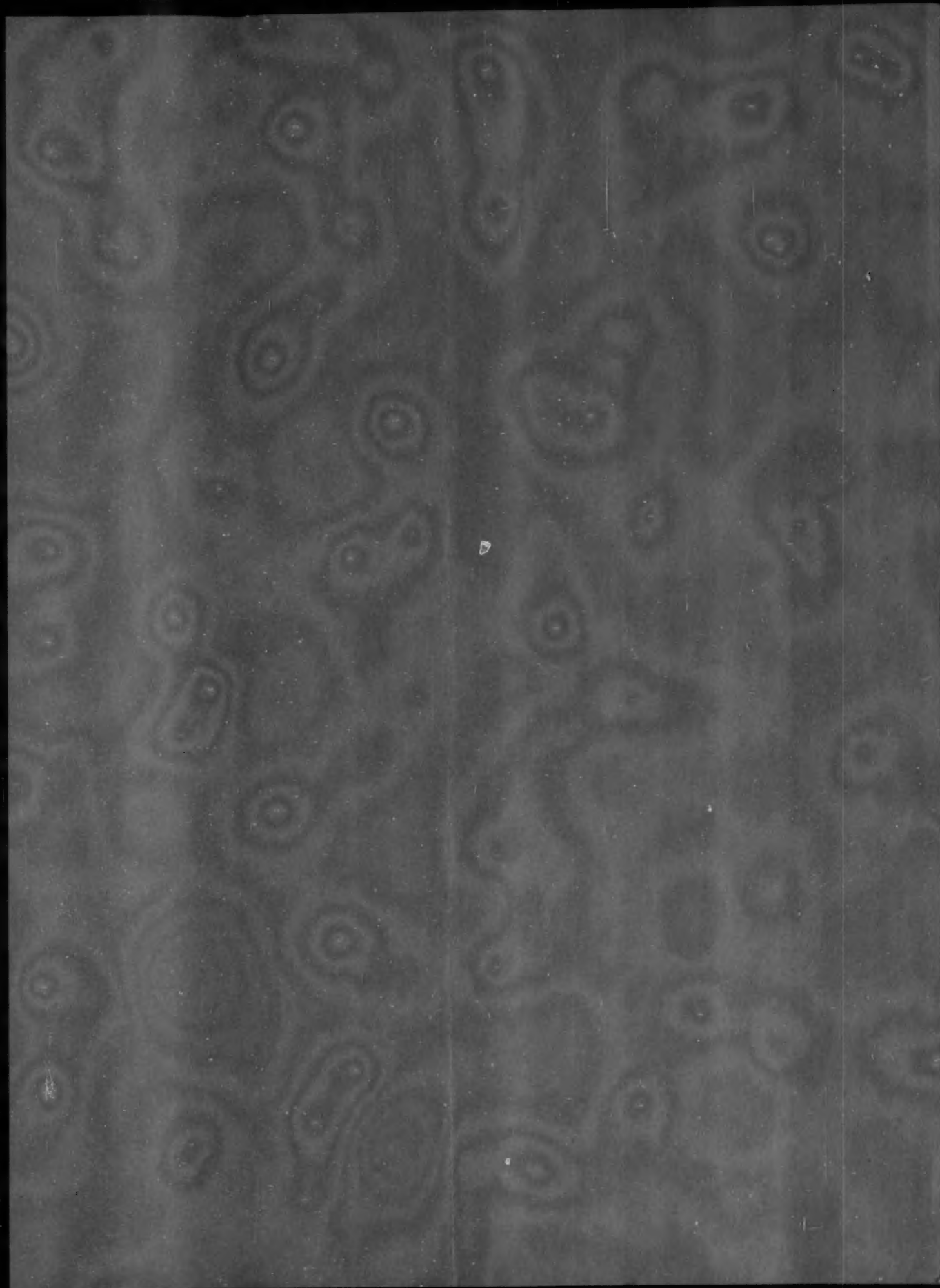




the following are the main points of the paper:

The first point is that the evidence for the existence of a 'true' race is very weak. The second point is that the evidence for the existence of a 'true' race is very weak. The third point is that the evidence for the existence of a 'true' race is very weak. The fourth point is that the evidence for the existence of a 'true' race is very weak. The fifth point is that the evidence for the existence of a 'true' race is very weak. The sixth point is that the evidence for the existence of a 'true' race is very weak. The seventh point is that the evidence for the existence of a 'true' race is very weak. The eighth point is that the evidence for the existence of a 'true' race is very weak. The ninth point is that the evidence for the existence of a 'true' race is very weak. The tenth point is that the evidence for the existence of a 'true' race is very weak.

The conclusion is that the evidence for the existence of a 'true' race is very weak.



A New ASME Publication

FREQUENCY RESPONSE

Coverage: The entire field from basic theory to experimental techniques.

Authorship: Top experts on frequency response in U. S. and abroad.

The book includes papers presented at the 1953 ASME Frequency Response Symposium plus eight additional articles. In nine sections and 372 pages it:

orients the reader in regard to historical developments, fundamental theory, and significant advances;

treats linear, nonlinear, sampling, and statistical approaches;

illustrates application of experimental methods of frequency response to process controls, servomechanism design, and power systems;

presents discussions of many of the papers;

includes a bibliography of important works on frequency response.

Size: 8½" × 11"

Illustrations: 428

Binding: cloth

Price: \$7.50

(20% discount to
ASME members)

TABLE OF CONTENTS

Fundamentals

The Regeneration Theory—H. Nyquist

Early History of the Frequency-Response Field—A. C. Hall

*The Frequency-Response Method: A Brief Survey—R. H. Macmillan (England)

Frequency-Response Data Presentation, Standards and Design Criteria—R. Oldenburger

A Bibliography of the Frequency-Response Method as Applied to Automatic-Feedback-Control Systems—A. M. Fuchs

Analysis of Regulating Systems With Particular Reference to Speed Control—R. H. Macmillan (England)

Frequency-Response Aids

*Frequency-Response Computational Aids—K. Izawa (Japan)

Sine-Wave Generators—D. W. St. Clair, L. W. Erath, and S. L. Gillespie

Servo, Airplane, and Power System Applications

The Frequency-Response Approach to the Design of a Mechanical Servo—H. A. Helm

Application of Frequency-Analysis Techniques to Hydraulic Control Systems—A. C. Hall

Frequency-Response Method Applied to the Study of Turbine Regulation in the Swedish Power System—V. Oja

Experimental Flight Methods for Evaluating Frequency-Response Characteristics of Aircraft—G. A. Smith and W. C. Triplett

Process Control

Control-System Behavior Expressed as a Deviation Ratio—J. M. L. Janssen (Holland)

Frequency-Response Analysis and Controllability of a Chemical Plant—A. R. Altman (England)

*Frequency-Response Analysis of Continuous Flow Systems—H. Kramers and G. Alberda (Holland)

*Response and Phase-lag of Thermometers—E. G. J. Eykman and C. J. D. M. Verhagen (Holland)

Transient Response

Determination of Transient Response From Frequency Response—A. Leonhard (Germany)

The Use of Zeros and Poles for Frequency Response or Transient Response—W. R. Evans

*A Method of Estimating Dynamic Characteristics of Physical Systems—S. Lees

Optimum Controls

A Uniform Approach to the Optimum Adjustment of Control Loops—R. C. Oldenbourg

Synthesis of Optimum Feedback Systems Satisfying a Power Limitation—J. H. Westcott (England)

Nonlinear Techniques

*On Some Nonlinear Phenomena in Regulatory Systems—L. C. Goldfarb (Russia)

Recent Advances in Nonlinear Servo Theory—J. M. Loeb (France)

Approximate Frequency-Response Methods for Representing Saturation and Dead Band—H. Chestnut

Stability Characteristics of Closed-Loop Systems With Dead Band—C. H. Thomas

Sampling Controls

*Frequency Method of Analyzing Intermittent Regulating Systems—Y. Z. Tsytkin (Russia)

*The Pulse Transfer Function and Its Application to Sampling Servo Systems—R. H. Barker (England)

Statistical Methods

A Statistical Approach to Servomechanisms and Regulators—M. J. Pelegrin (France)

* New articles not previously published.

THE AMERICAN SOCIETY OF MECHANICAL ENGINEERS
29 W. 39th St.
New York 18, N. Y.

